

NASA Contractor Report 189070

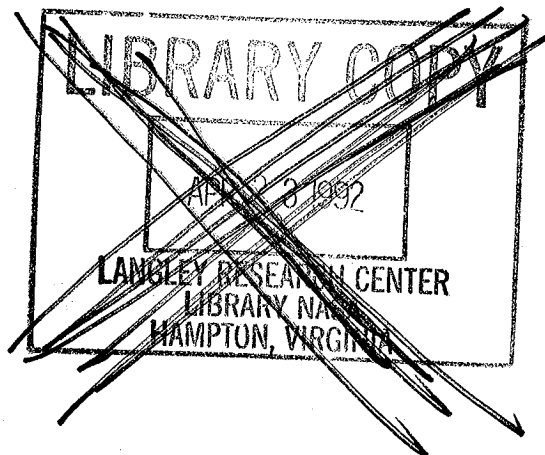
NASA-CR-189070
19920011279

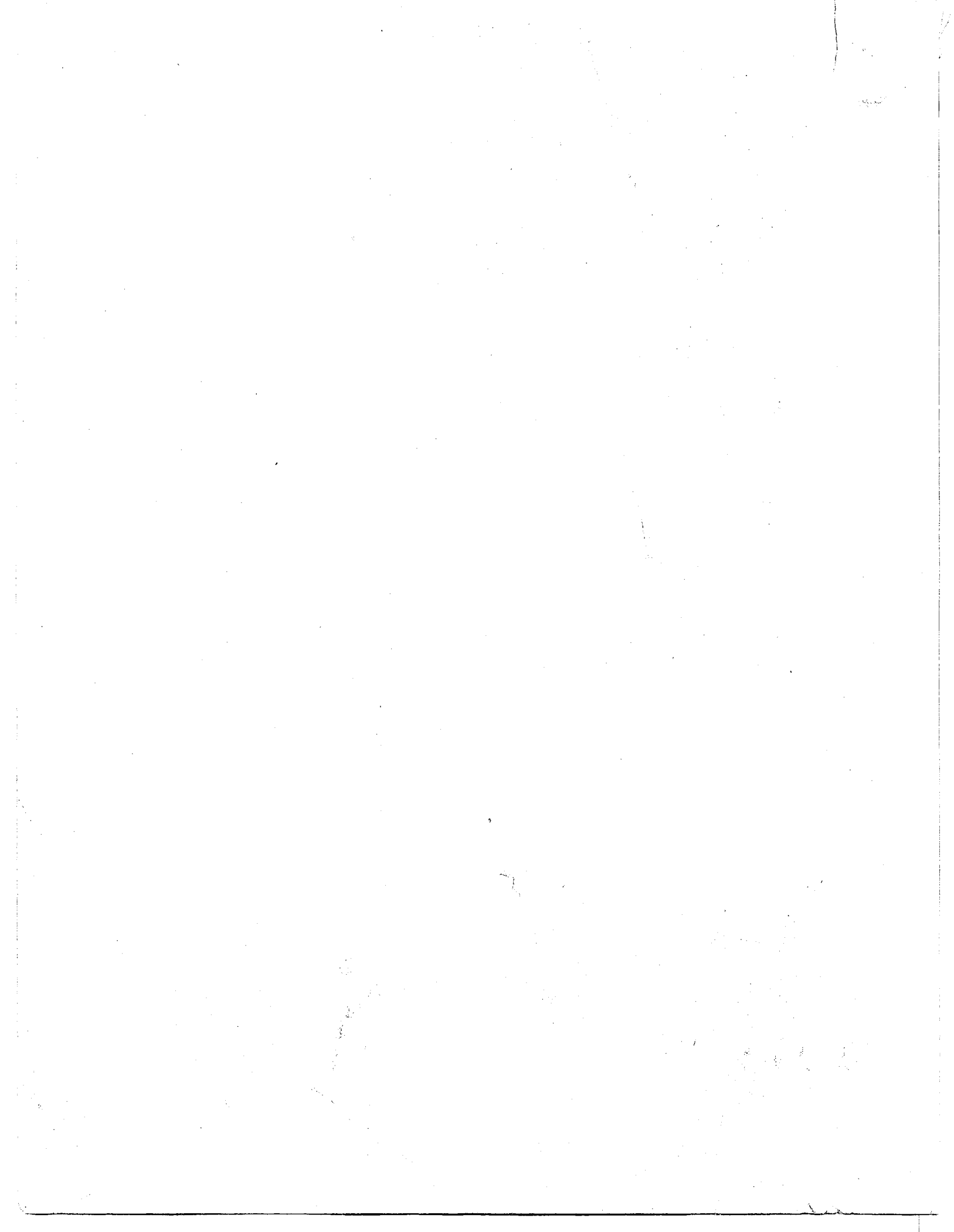
Superelement Methods in High Temperature Metal Matrix Composites

Daniel Trowbridge
University of Akron
Akron, Ohio

November 1991

Prepared for
Lewis Research Center
Under Grant NAG3-50





ABSTRACT

An investigation into fiber fracture and debonding in metal matrix composites is conducted using the finite element method. The superelement finite element technique was used to model a metal matrix composite under various loading condition and with varying degrees of fiber debonding. The use of superelements saved many man hours by allowing for alteration of only the primary superelement to manipulate partial bonding for the entire model. The composite's material properties were calculated and the effects of fiber debonding on these properties were noted. The internal stress state of the composite while under various loads was also investigated. Special interest was devoted to the change in stress state as a result of increasing fiber debonding.

ACKNOWLEDGEMENTS

I wish to express my thanks to my wife for her support and patience during my studies. I wish to express sincere gratitude to John Caruso and Dr. C. C. Chamis for their technical and moral support in producing this document. The author would also like to express his appreciation for the direction and assistance provided by Dr. D. G. Fertis and Dr. P. Chang and the support provided through the NASA Lewis Research Center under the NAG 3-50 grant.

TABLE OF CONTENTS

	Page
LIST OF TABLES	vi
LIST OF FIGURES	vii
LIST OF SYMBOLS	xxxiv
CHAPTER	
1. INTRODUCTION	1
2. OBJECTIVE	5
3. BACKGROUND	6
4. THEORETICAL	24
5. PROCEDURE	28
6. RESULTS	52
6.1 Room Temperature Moduli with Center Fiber Debonding	53
6.2 Room Temperature Poisson's Ratio with Center Fiber Debonding	54
6.3 Room Temperature Shear Moduli with Center Fiber Debonding	55
6.4 Room Temperature Thermal Expansion Coefficients with Center Fiber Debonding	56
6.5 High Temperature Moduli with Center Fiber Debonding	58
6.6 High Temperature Poisson's Ratio with Center Fiber Debonding	59
6.7 High Temperature Shear Moduli with Center Fiber Debonding	60

6.8	High Temperature Thermal Expansion Coefficients with Center Fiber Debonding	61
6.9	Room Temperature Moduli with All Fibers Debonding	62
6.10	Room Temperature Poisson's Ratio with All Fibers Debonding	63
6.11	Room Temperature Shear Moduli with All Fibers Debonding	65
6.12	Room Temperature Thermal Expansion Coefficients with All Fibers Debonding	65
6.13	High Temperature Moduli with All Fibers Debonding	67
6.14	High Temperature Poisson's Ratio with All Fibers Debonding	68
6.15	High Temperature Shear Moduli with All Fibers Debonding	69
6.16	High Temperature Thermal Expansion Coefficients with All Fibers Debonding	70
7.	MICROSTRESSES	71
7.1	Loading: σ_{xx}^e	71
7.1	Loading: σ_{yy}^e	85
7.1	Loading: σ_{yx}^e	135
7.1	Loading: σ_{yz}^e	142
7.1	Loading: Temperature Load	149

8. CONCLUSIONS	179
9. SUMMARY	181
REFERENCES	183
APPENDIX	185

LIST OF TABLES

TABLE		PAGE
5.1	Calculated Material Properties for all P100-Graphite Model	29
5.2	Composite Material Properties – No Debonding	30
5.3	Room Temperature Constitutive Material Properties	31
5.4	High Temperature Constitutive Material Properties	37

LIST OF FIGURES

FIGURE		PAGE
1.1	Finite Element Mesh of Composite Unit Cell	3
3.1	Composite Model	8
3.2	Modeling of Fiber Disbond	10
3.3	Composite Model, Faces and Layers	13
3.4	Model Dimensions	14
3.5	Locations of Stress Plots	23
5.1	Effect of Center Fiber Debonding on Modulus at Room Temperature	33
5.2	Effect of Center Fiber Debonding on Poisson's Ratio at Room Temperature	34
5.3	Effect of Center Fiber Debonding on Shear Modulus at Room Temperature	35
5.4	Effect of Center Fiber Debonding on Thermal Expansion Coefficient at Room Temperature	36
5.5	Effect of Center Fiber Debonding on Modulus at High Temperature	38
5.6	Effect of Center Fiber Debonding on Poisson's Ratio at High Temperature	39
5.7	Effect of Center Fiber Debonding on Shear Modulus at High Temperature	40
5.8	Effect of Center Fiber Debonding on Thermal Expansion Coefficient at High Temperature	41
5.9	Effect of Total Fiber Debonding on Modulus at Room Temperature	43

5.10	Effect of Total Fiber Debonding on Poisson's Ratio at Room Temperature	44
5.11	Effect of Total Fiber Debonding on Shear Modulus at Room Temperature	45
5.12	Effect of Total Fiber Debonding on Thermal Expansion Coefficient at Room Temperature	46
5.13	Effect of Total Fiber Debonding on Modulus at High Temperature	48
5.14	Effect of Total Fiber Debonding on Poisson's Ratio at High Temperature	49
5.15	Effect of Total Fiber Debonding on Shear Modulus at High Temperature	50
5.16	Effect of Total Fiber Debonding on Thermal Expansion Coefficient at High Temperature	51
7.1	σ_{11} Normalized Microstresses, O-A Direction, 0.0% Debonding, σ_{xx}^e Loading	72
7.2	σ_{11} Normalized Microstresses, O-A Direction, 1.39% Debonding, σ_{xx}^e Loading	74
7.3	σ_{11} Normalized Microstresses, O-A Direction, 2.78% Debonding, σ_{xx}^e Loading	75
7.4	σ_{11} Normalized Microstresses, O-A Direction, 4.17% Debonding, σ_{xx}^e Loading	76
7.5	σ_{11} Normalized Microstresses, O-A Direction, 5.56% Debonding, σ_{xx}^e Loading	77

7.6	σ_{11} Normalized Microstresses, O-A Direction, 6.94% Debonding, σ_{xx}^e Loading	78
7.7	σ_{11} Normalized Microstresses, O-A Direction, 8.33% Debonding, σ_{xx}^e Loading	79
7.8	σ_{11} Normalized Microstresses, O-A Direction, 9.72% Debonding, σ_{xx}^e Loading	80
7.9	σ_{11} Normalized Microstresses, O-A Direction, 11.11% Debonding, σ_{xx}^e Loading	81
7.10	σ_{11} Normalized Microstresses, O-C Direction, 0.0% Debonding, σ_{xx}^e Loading	82
7.11	σ_{11} Normalized Microstresses, O-C Direction, 5.56% Debonding, σ_{xx}^e Loading	83
7.12	σ_{11} Normalized Microstresses, O-C Direction, 11.11% Debonding, σ_{xx}^e Loading	84
7.13	σ_{31} Normalized Microstresses, O-A Direction, 0.0% Debonding, σ_{xx}^e Loading	86
7.14	σ_{31} Normalized Microstresses, O-A Direction, 5.56% Debonding, σ_{xx}^e Loading	87
7.15	σ_{31} Normalized Microstresses, O-A Direction, 11.11% Debonding, σ_{xx}^e Loading	88

7.16	σ_{31} Normalized Microstresses, O—C Direction, 0.0% Debonding, σ_{xx}^e Loading	89
7.17	σ_{31} Normalized Microstresses, O—C Direction, 5.56% Debonding, σ_{xx}^e Loading	90
7.18	σ_{31} Normalized Microstresses, O—C Direction, 11.11% Debonding, σ_{xx}^e Loading	91
7.19	σ_{12} Normalized Microstresses, O—C Direction, 0.0% Debonding, σ_{xx}^e Loading	92
7.20	σ_{12} Normalized Microstresses, O—C Direction, 5.56% Debonding, σ_{xx}^e Loading	93
7.21	σ_{12} Normalized Microstresses, O—C Direction, 11.11% Debonding, σ_{xx}^e Loading	94
7.22	σ_{22} Normalized Microstresses, O—A Direction, 0.0% Debonding, σ_{yy}^e Loading	95
7.23	σ_{22} Normalized Microstresses, O—A Direction, 1.39% Debonding, σ_{yy}^e Loading	96
7.24	σ_{22} Normalized Microstresses, O—A Direction, 2.78% Debonding, σ_{yy}^e Loading	97
7.25	σ_{22} Normalized Microstresses, O—A Direction, 4.17% Debonding, σ_{yy}^e Loading	98

7.26	σ_{22} Normalized Microstresses, O—A Direction, 5.56% Debonding, σ_{yy}^e Loading	99
7.27	σ_{22} Normalized Microstresses, O—A Direction, 6.94% Debonding, σ_{yy}^e Loading	100
7.28	σ_{22} Normalized Microstresses, O—A Direction, 8.33% Debonding, σ_{yy}^e Loading	101
7.29	σ_{22} Normalized Microstresses, O—A Direction, 9.72% Debonding, σ_{yy}^e Loading	102
7.30	σ_{22} Normalized Microstresses, O—A Direction, 11.11% Debonding, σ_{yy}^e Loading	103
7.31	σ_{22} Normalized Microstresses, O—B Direction, 0.0% Debonding, σ_{yy}^e Loading	105
7.32	σ_{22} Normalized Microstresses, O—B Direction, 5.56% Debonding, σ_{yy}^e Loading	106
7.33	σ_{22} Normalized Microstresses, O—B Direction, 11.11% Debonding, σ_{yy}^e Loading	107
7.34	σ_{22} Normalized Microstresses, O—C Direction, 0.0% Debonding, σ_{yy}^e Loading	108
7.35	σ_{22} Normalized Microstresses, O—C Direction, 5.56% Debonding, σ_{yy}^e Loading	109

7.36	σ_{22}	Normalized Microstresses, O–C Direction, 11.11% Debonding, σ_{yy}^e Loading	110
7.37	σ_{11}	Normalized Microstresses, O–A Direction, 0.0% Debonding, σ_{yy}^e Loading	112
7.38	σ_{11}	Normalized Microstresses, O–A Direction, 5.56% Debonding, σ_{yy}^e Loading	113
7.39	σ_{11}	Normalized Microstresses, O–A Direction, 11.11% Debonding, σ_{yy}^e Loading	114
7.40	σ_{11}	Normalized Microstresses, O–B Direction, 0.0% Debonding, σ_{yy}^e Loading	116
7.41	σ_{11}	Normalized Microstresses, O–B Direction, 1.39% Debonding, σ_{yy}^e Loading	117
7.42	σ_{11}	Normalized Microstresses, O–B Direction, 2.78% Debonding, σ_{yy}^e Loading	118
7.43	σ_{11}	Normalized Microstresses, O–B Direction, 4.17% Debonding, σ_{yy}^e Loading	119
7.44	σ_{11}	Normalized Microstresses, O–B Direction, 5.56% Debonding, σ_{yy}^e Loading	120
7.45	σ_{11}	Normalized Microstresses, O–B Direction, 6.94% Debonding, σ_{yy}^e Loading	121

7.46	σ_{11} Normalized Microstresses, O-B Direction, 8.33% Debonding, σ_{yy}^e Loading	122
7.47	σ_{11} Normalized Microstresses, O-B Direction, 9.72% Debonding, σ_{yy}^e Loading	123
7.48	σ_{11} Normalized Microstresses, O-B Direction, 11.11% Debonding, σ_{yy}^e Loading	124
7.49	σ_{11} Normalized Microstresses, O-C Direction, 0.0% Debonding, σ_{yy}^e Loading	125
7.50	σ_{11} Normalized Microstresses, O-C Direction, 5.56% Debonding, σ_{yy}^e Loading	126
7.51	σ_{11} Normalized Microstresses, O-C Direction, 11.11% Debonding, σ_{yy}^e Loading	127
7.52	σ_{33} Normalized Microstresses, O-B Direction, 0.0% Debonding, σ_{yy}^e Loading	129
7.53	σ_{33} Normalized Microstresses, O-B Direction, 5.56% Debonding, σ_{yy}^e Loading	130
7.54	σ_{33} Normalized Microstresses, O-B Direction, 11.11% Debonding, σ_{yy}^e Loading	131
7.55	σ_{23} Normalized Microstresses, O-A Direction, 0.0% Debonding, σ_{yy}^e Loading	132

7.56	σ_{23} Normalized Microstresses, O–B Direction, 0.0% Debonding, σ_{yy}^e Loading	133
7.57	σ_{23} Normalized Microstresses, O–C Direction, 0.0% Debonding, σ_{yy}^e Loading	134
7.58	σ_{12} Normalized Microstresses, O–A Direction, 0.0% Debonding, σ_{yx}^e Loading	136
7.59	σ_{12} Normalized Microstresses, O–A Direction, 5.56% Debonding, σ_{yx}^e Loading	137
7.60	σ_{12} Normalized Microstresses, O–A Direction, 11.11% Debonding, σ_{yx}^e Loading	138
7.61	σ_{12} Normalized Microstresses, O–B Direction, 0.0% Debonding, σ_{yx}^e Loading	139
7.62	σ_{12} Normalized Microstresses, O–B Direction, 5.56% Debonding, σ_{yx}^e Loading	140
7.63	σ_{12} Normalized Microstresses, O–B Direction, 11.11% Debonding, σ_{yx}^e Loading	141
7.64	σ_{12} Normalized Microstresses, O–C Direction, 0.0% Debonding, σ_{yx}^e Loading	143
7.65	σ_{12} Normalized Microstresses, O–C Direction, 5.56% Debonding, σ_{yx}^e Loading	144

7.66	σ_{12} Normalized Microstresses, O-C Direction, 11.11% Debonding, σ_{yx}^e Loading	145
7.67	σ_{23} Normalized Microstresses, O-A Direction, 0.0% Debonding, σ_{yz}^e Loading	146
7.68	σ_{23} Normalized Microstresses, O-A Direction, 5.56% Debonding, σ_{yz}^e Loading	147
7.69	σ_{23} Normalized Microstresses, O-A Direction, 11.11% Debonding, σ_{yz}^e Loading	148
7.70	σ_{23} Normalized Microstresses, O-B Direction, 0.0% Debonding, σ_{yz}^e Loading	150
7.71	σ_{23} Normalized Microstresses, O-B Direction, 5.56% Debonding, σ_{yz}^e Loading	151
7.72	σ_{23} Normalized Microstresses, O-B Direction, 11.11% Debonding, σ_{yz}^e Loading	152
7.73	σ_{23} Normalized Microstresses, O-C Direction, 0.0% Debonding, σ_{yz}^e Loading	153
7.74	σ_{23} Normalized Microstresses, O-C Direction, 5.56% Debonding, σ_{yz}^e Loading	154
7.75	σ_{23} Normalized Microstresses, O-C Direction, 11.11% Debonding, σ_{yz}^e Loading	155

7.76	σ_{11} Normalized Microstresses, O–A Direction, 0.0% Debonding, Thermal Loading	156
7.77	σ_{11} Normalized Microstresses, O–A Direction, 1.39% Debonding, Thermal Loading	157
7.78	σ_{11} Normalized Microstresses, O–A Direction, 2.78% Debonding, Thermal Loading	158
7.79	σ_{11} Normalized Microstresses, O–A Direction, 4.17% Debonding, Thermal Loading	159
7.80	σ_{11} Normalized Microstresses, O–A Direction, 5.56% Debonding, Thermal Loading	160
7.81	σ_{11} Normalized Microstresses, O–A Direction, 6.94% Debonding, Thermal Loading	161
7.82	σ_{11} Normalized Microstresses, O–A Direction, 8.33% Debonding, Thermal Loading	162
7.83	σ_{11} Normalized Microstresses, O–A Direction, 9.72% Debonding, Thermal Loading	163
7.84	σ_{11} Normalized Microstresses, O–A Direction, 11.11% Debonding, Thermal Loading	164
7.85	σ_{11} Normalized Microstresses, O–C Direction, 0.0% Debonding, Thermal Loading	166
7.86	σ_{11} Normalized Microstresses, O–C Direction, 5.56% Debonding, Thermal Loading	167
7.87	σ_{11} Normalized Microstresses, O–C Direction, 11.11% Debonding, Thermal Loading	168
7.88	σ_{31} Normalized Microstresses, O–A Direction, 0.0% Debonding, Thermal Loading	170

7.89	σ_{31} Normalized Microstresses, O—A Direction, 5.56% Debonding, Thermal Loading	171
7.90	σ_{31} Normalized Microstresses, O—A Direction, 11.11% Debonding, Thermal Loading	172
7.91	σ_{31} Normalized Microstresses, O—C Direction, 0.0% Debonding, Thermal Loading	173
7.92	σ_{31} Normalized Microstresses, O—C Direction, 5.56% Debonding, Thermal Loading	174
7.93	σ_{31} Normalized Microstresses, O—C Direction, 11.11% Debonding, Thermal Loading	175
7.94	σ_{12} Normalized Microstresses, O—A Direction, 0.0% Debonding, Thermal Loading	176
7.95	σ_{12} Normalized Microstresses, O—A Direction, 5.56% Debonding, Thermal Loading	177
7.96	σ_{12} Normalized Microstresses, O—A Direction, 11.11% Debonding, Thermal Loading	178
A.1	σ_{11} Normalized Microstresses, O—C Direction, 0.0% Debonding, σ_{xx}^e Loading	187
A.2	σ_{11} Normalized Microstresses, O—C Direction, 1.39% Debonding, σ_{xx}^e Loading	188
A.3	σ_{11} Normalized Microstresses, O—C Direction, 2.78% Debonding, σ_{xx}^e Loading	189
A.4	σ_{11} Normalized Microstresses, O—C Direction, 4.17% Debonding, σ_{xx}^e Loading	190

A.5	σ_{11} Normalized Microstresses, O—C Direction, 5.56% Debonding, σ_{xx}^e Loading	191
A.6	σ_{11} Normalized Microstresses, O—C Direction, 6.94% Debonding, σ_{xx}^e Loading	192
A.7	σ_{11} Normalized Microstresses, O—C Direction, 8.33% Debonding, σ_{xx}^e Loading	193
A.8	σ_{11} Normalized Microstresses, O—C Direction, 9.72% Debonding, σ_{xx}^e Loading	194
A.9	σ_{11} Normalized Microstresses, O—C Direction, 11.11% Debonding, σ_{xx}^e Loading	195
A.10	σ_{31} Normalized Microstresses, O—A Direction, 0.0% Debonding, σ_{xx}^e Loading	196
A.11	σ_{31} Normalized Microstresses, O—A Direction, 1.39% Debonding, σ_{xx}^e Loading	197
A.12	σ_{31} Normalized Microstresses, O—A Direction, 2.78% Debonding, σ_{xx}^e Loading	198
A.13	σ_{31} Normalized Microstresses, O—A Direction, 4.17% Debonding, σ_{xx}^e Loading	199
A.14	σ_{31} Normalized Microstresses, O—A Direction, 5.56% Debonding, σ_{xx}^e Loading	200

A.15	σ_{31} Normalized Microstresses, O—A Direction, 6.94% Debonding, σ_{xx}^e Loading	201
A.16	σ_{31} Normalized Microstresses, O—A Direction, 8.33% Debonding, σ_{xx}^e Loading	202
A.17	σ_{31} Normalized Microstresses, O—A Direction, 9.72% Debonding, σ_{xx}^e Loading	203
A.18	σ_{31} Normalized Microstresses, O—A Direction, 11.11% Debonding, σ_{xx}^e Loading	204
A.19	σ_{31} Normalized Microstresses, O—C Direction, 0.0% Debonding, σ_{xx}^e Loading	205
A.20	σ_{31} Normalized Microstresses, O—C Direction, 1.39% Debonding, σ_{xx}^e Loading	206
A.21	σ_{31} Normalized Microstresses, O—C Direction, 2.78% Debonding, σ_{xx}^e Loading	207
A.22	σ_{31} Normalized Microstresses, O—C Direction, 4.17% Debonding, σ_{xx}^e Loading	208
A.23	σ_{31} Normalized Microstresses, O—C Direction, 5.56% Debonding, σ_{xx}^e Loading	209
A.24	σ_{31} Normalized Microstresses, O—C Direction, 6.94% Debonding, σ_{xx}^e Loading	210

A.25	σ_{31} Normalized Microstresses, O—C Direction, 8.33% Debonding, σ_{xx}^e Loading	211
A.26	σ_{31} Normalized Microstresses, O—C Direction, 9.72% Debonding, σ_{xx}^e Loading	212
A.27	σ_{31} Normalized Microstresses, O—C Direction, 11.11% Debonding, σ_{xx}^e Loading	213
A.28	σ_{12} Normalized Microstresses, O—C Direction, 0.0% Debonding, σ_{xx}^e Loading	214
A.29	σ_{12} Normalized Microstresses, O—C Direction, 1.39% Debonding, σ_{xx}^e Loading	215
A.30	σ_{12} Normalized Microstresses, O—C Direction, 2.78% Debonding, σ_{xx}^e Loading	216
A.31	σ_{12} Normalized Microstresses, O—C Direction, 4.17% Debonding, σ_{xx}^e Loading	217
A.32	σ_{12} Normalized Microstresses, O—C Direction, 5.56% Debonding, σ_{xx}^e Loading	218
A.33	σ_{12} Normalized Microstresses, O—C Direction, 6.94% Debonding, σ_{xx}^e Loading	219
A.34	σ_{12} Normalized Microstresses, O—C Direction, 8.33% Debonding, σ_{xx}^e Loading	220

A.35	σ_{12} Normalized Microstresses, O-C Direction, 9.72% Debonding, σ_{xx}^e Loading	221
A.36	σ_{12} Normalized Microstresses, O-C Direction, 11.11% Debonding, σ_{xx}^e Loading	222
A.37	σ_{22} Normalized Microstresses, O-B Direction, 0.0% Debonding, σ_{yy}^e Loading	223
A.38	σ_{22} Normalized Microstresses, O-B Direction, 1.39% Debonding, σ_{yy}^e Loading	224
A.39	σ_{22} Normalized Microstresses, O-B Direction, 2.78% Debonding, σ_{yy}^e Loading	225
A.40	σ_{22} Normalized Microstresses, O-B Direction, 4.17% Debonding, σ_{yy}^e Loading	226
A.41	σ_{22} Normalized Microstresses, O-B Direction, 5.56% Debonding, σ_{yy}^e Loading	227
A.42	σ_{22} Normalized Microstresses, O-B Direction, 6.94% Debonding, σ_{yy}^e Loading	228
A.43	σ_{22} Normalized Microstresses, O-B Direction, 8.33% Debonding, σ_{yy}^e Loading	229
A.44	σ_{22} Normalized Microstresses, O-B Direction, 9.72% Debonding, σ_{yy}^e Loading	230

A.45	σ_{22} Normalized Microstresses, O–B Direction, 11.11% Debonding, σ_{yy}^e Loading	231
A.46	σ_{22} Normalized Microstresses, O–C Direction, 0.0% Debonding, σ_{yy}^e Loading	232
A.47	σ_{22} Normalized Microstresses, O–C Direction, 1.39% Debonding, σ_{yy}^e Loading	233
A.48	σ_{22} Normalized Microstresses, O–C Direction, 2.78% Debonding, σ_{yy}^e Loading	234
A.49	σ_{22} Normalized Microstresses, O–C Direction, 4.17% Debonding, σ_{yy}^e Loading	235
A.50	σ_{22} Normalized Microstresses, O–C Direction, 5.56% Debonding, σ_{yy}^e Loading	236
A.51	σ_{22} Normalized Microstresses, O–C Direction, 6.94% Debonding, σ_{yy}^e Loading	237
A.52	σ_{22} Normalized Microstresses, O–C Direction, 8.33% Debonding, σ_{yy}^e Loading	238
A.53	σ_{22} Normalized Microstresses, O–C Direction, 9.72% Debonding, σ_{yy}^e Loading	239
A.54	σ_{22} Normalized Microstresses, O–C Direction, 11.11% Debonding, σ_{yy}^e Loading	240

A.55	σ_{11} Normalized Microstresses, O–A Direction, 0.0% Debonding, σ_{yy}^e Loading	241
A.56	σ_{11} Normalized Microstresses, O–A Direction, 1.39% Debonding, σ_{yy}^e Loading	242
A.57	σ_{11} Normalized Microstresses, O–A Direction, 2.78% Debonding, σ_{yy}^e Loading	243
A.58	σ_{11} Normalized Microstresses, O–A Direction, 4.17% Debonding, σ_{yy}^e Loading	244
A.59	σ_{11} Normalized Microstresses, O–A Direction, 5.56% Debonding, σ_{yy}^e Loading	245
A.60	σ_{11} Normalized Microstresses, O–A Direction, 6.94% Debonding, σ_{yy}^e Loading	246
A.61	σ_{11} Normalized Microstresses, O–A Direction, 8.33% Debonding, σ_{yy}^e Loading	247
A.62	σ_{11} Normalized Microstresses, O–A Direction, 9.72% Debonding, σ_{yy}^e Loading	248
A.63	σ_{11} Normalized Microstresses, O–A Direction, 11.11% Debonding, σ_{yy}^e Loading	249
A.64	σ_{11} Normalized Microstresses, O–C Direction, 0.0% Debonding, σ_{yy}^e Loading	250

A.65	σ_{11} Normalized Microstresses, O—C Direction, 1.39% Debonding, σ_{yy}^e Loading	251
A.66	σ_{11} Normalized Microstresses, O—C Direction, 2.78% Debonding, σ_{yy}^e Loading	252
A.67	σ_{11} Normalized Microstresses, O—C Direction, 4.17% Debonding, σ_{yy}^e Loading	253
A.68	σ_{11} Normalized Microstresses, O—C Direction, 5.56% Debonding, σ_{yy}^e Loading	254
A.69	σ_{11} Normalized Microstresses, O—C Direction, 6.94% Debonding, σ_{yy}^e Loading	255
A.70	σ_{11} Normalized Microstresses, O—C Direction, 8.33% Debonding, σ_{yy}^e Loading	256
A.71	σ_{11} Normalized Microstresses, O—C Direction, 9.72% Debonding, σ_{yy}^e Loading	257
A.72	σ_{11} Normalized Microstresses, O—C Direction, 11.11% Debonding, σ_{yy}^e Loading	258
A.73	σ_{33} Normalized Microstresses, O—B Direction, 0.0% Debonding, σ_{yy}^e Loading	259
A.74	σ_{33} Normalized Microstresses, O—B Direction, 1.39% Debonding, σ_{yy}^e Loading	260

A.75	σ_{33} Normalized Microstresses, O-B Direction, 2.78% Debonding, σ_{yy}^e Loading	261
A.76	σ_{33} Normalized Microstresses, O-B Direction, 4.17% Debonding, σ_{yy}^e Loading	262
A.77	σ_{33} Normalized Microstresses, O-B Direction, 5.56% Debonding, σ_{yy}^e Loading	263
A.78	σ_{33} Normalized Microstresses, O-B Direction, 6.94% Debonding, σ_{yy}^e Loading	264
A.79	σ_{33} Normalized Microstresses, O-B Direction, 8.33% Debonding, σ_{yy}^e Loading	265
A.80	σ_{33} Normalized Microstresses, O-B Direction, 9.72% Debonding, σ_{yy}^e Loading	266
A.81	σ_{33} Normalized Microstresses, O-B Direction, 11.11% Debonding, σ_{yy}^e Loading	267
A.82	σ_{12} Normalized Microstresses, O-A Direction, 0.0% Debonding, σ_{yx}^e Loading	268
A.83	σ_{12} Normalized Microstresses, O-A Direction, 1.39% Debonding, σ_{yx}^e Loading	269
A.84	σ_{12} Normalized Microstresses, O-A Direction, 2.78% Debonding, σ_{yx}^e Loading	270

A.85	σ_{12} Normalized Microstresses, O—A Direction, 4.17% Debonding, σ_{yx}^e Loading	271
A.86	σ_{12} Normalized Microstresses, O—A Direction, 5.56% Debonding, σ_{yx}^e Loading	272
A.87	σ_{12} Normalized Microstresses, O—A Direction, 6.94% Debonding, σ_{yx}^e Loading	273
A.88	σ_{12} Normalized Microstresses, O—A Direction, 8.33% Debonding, σ_{yx}^e Loading	274
A.89	σ_{12} Normalized Microstresses, O—A Direction, 9.72% Debonding, σ_{yx}^e Loading	275
A.90	σ_{12} Normalized Microstresses, O—A Direction, 11.11% Debonding, σ_{yx}^e Loading	276
A.91	σ_{12} Normalized Microstresses, O—B Direction, 0.0% Debonding, σ_{yx}^e Loading	277
A.92	σ_{12} Normalized Microstresses, O—B Direction, 1.39% Debonding, σ_{yx}^e Loading	278
A.93	σ_{12} Normalized Microstresses, O—B Direction, 2.78% Debonding, σ_{yx}^e Loading	279
A.94	σ_{12} Normalized Microstresses, O—B Direction, 4.17% Debonding, σ_{yx}^e Loading	280

A.95	σ_{12} Normalized Microstresses, O-B Direction, 5.56% Debonding, σ_{yx}^e Loading	281
A.96	σ_{12} Normalized Microstresses, O-B Direction, 6.94% Debonding, σ_{yx}^e Loading	282
A.97	σ_{12} Normalized Microstresses, O-B Direction, 8.33% Debonding, σ_{yx}^e Loading	283
A.98	σ_{12} Normalized Microstresses, O-B Direction, 9.72% Debonding, σ_{yx}^e Loading	284
A.99	σ_{12} Normalized Microstresses, O-B Direction, 11.11% Debonding, σ_{yx}^e Loading	285
A.100	σ_{12} Normalized Microstresses, O-C Direction, 0.0% Debonding, σ_{yx}^e Loading	286
A.101	σ_{12} Normalized Microstresses, O-C Direction, 1.39% Debonding, σ_{yx}^e Loading	287
A.102	σ_{12} Normalized Microstresses, O-C Direction, 2.78% Debonding, σ_{yx}^e Loading	288
A.103	σ_{12} Normalized Microstresses, O-C Direction, 4.17% Debonding, σ_{yx}^e Loading	289
A.104	σ_{12} Normalized Microstresses, O-C Direction, 5.56% Debonding, σ_{yx}^e Loading	290

A.105	σ_{12} Normalized Microstresses, O–C Direction, 6.94% Debonding, σ_{yx}^e Loading	291
A.106	σ_{12} Normalized Microstresses, O–C Direction, 8.33% Debonding, σ_{yx}^e Loading	292
A.107	σ_{12} Normalized Microstresses, O–C Direction, 9.72% Debonding, σ_{yx}^e Loading	293
A.108	σ_{12} Normalized Microstresses, O–C Direction, 11.11% Debonding, σ_{yx}^e Loading	294
A.109	σ_{23} Normalized Microstresses, O–A Direction, 0.0% Debonding, σ_{yz}^e Loading	295
A.110	σ_{23} Normalized Microstresses, O–A Direction, 1.39% Debonding, σ_{yz}^e Loading	296
A.111	σ_{23} Normalized Microstresses, O–A Direction, 2.78% Debonding, σ_{yz}^e Loading	297
A.112	σ_{23} Normalized Microstresses, O–A Direction, 4.17% Debonding, σ_{yz}^e Loading	298
A.113	σ_{23} Normalized Microstresses, O–A Direction, 5.56% Debonding, σ_{yz}^e Loading	299
A.114	σ_{23} Normalized Microstresses, O–A Direction, 6.94% Debonding, σ_{yz}^e Loading	300

A.115	σ_{23} Normalized Microstresses, O—A Direction, 8.33% Debonding, σ_{yz}^e Loading	301
A.116	σ_{23} Normalized Microstresses, O—A Direction, 9.72% Debonding, σ_{yz}^e Loading	302
A.117	σ_{23} Normalized Microstresses, O—A Direction, 11.11% Debonding, σ_{yz}^e Loading	303
A.118	σ_{23} Normalized Microstresses, O—B Direction, 0.0% Debonding, σ_{yz}^e Loading	304
A.119	σ_{23} Normalized Microstresses, O—B Direction, 1.39% Debonding, σ_{yz}^e Loading	305
A.120	σ_{23} Normalized Microstresses, O—B Direction, 2.78% Debonding, σ_{yz}^e Loading	306
A.121	σ_{23} Normalized Microstresses, O—B Direction, 4.17% Debonding, σ_{yz}^e Loading	307
A.122	σ_{23} Normalized Microstresses, O—B Direction, 5.56% Debonding, σ_{yz}^e Loading	308
A.123	σ_{23} Normalized Microstresses, O—B Direction, 6.94% Debonding, σ_{yz}^e Loading	309
A.124	σ_{23} Normalized Microstresses, O—B Direction, 8.33% Debonding, σ_{yz}^e Loading	310

A.125	σ_{23} Normalized Microstresses, O–B Direction, 9.72% Debonding, σ_{yz}^e Loading	311
A.126	σ_{23} Normalized Microstresses, O–B Direction, 11.11% Debonding, σ_{yz}^e Loading	312
A.127	σ_{23} Normalized Microstresses, O–C Direction, 0.0% Debonding, σ_{yz}^e Loading	313
A.128	σ_{23} Normalized Microstresses, O–C Direction, 1.39% Debonding, σ_{yz}^e Loading	314
A.129	σ_{23} Normalized Microstresses, O–C Direction, 2.78% Debonding, σ_{yz}^e Loading	315
A.130	σ_{23} Normalized Microstresses, O–C Direction, 4.17% Debonding, σ_{yz}^e Loading	316
A.131	σ_{23} Normalized Microstresses, O–C Direction, 5.56% Debonding, σ_{yz}^e Loading	317
A.132	σ_{23} Normalized Microstresses, O–C Direction, 6.94% Debonding, σ_{yz}^e Loading	318
A.133	σ_{23} Normalized Microstresses, O–C Direction, 8.33% Debonding, σ_{yz}^e Loading	319
A.134	σ_{23} Normalized Microstresses, O–C Direction, 9.72% Debonding, σ_{yz}^e Loading	320

A.135	σ_{23} Normalized Microstresses, O—C Direction, 11.11% Debonding, σ_{yz}^e Loading	321
A.136	σ_{11} Normalized Microstresses, O—C Direction, 0.0% Debonding, Thermal Loading	322
A.137	σ_{11} Normalized Microstresses, O—C Direction, 1.39% Debonding, Thermal Loading	323
A.138	σ_{11} Normalized Microstresses, O—C Direction, 2.78% Debonding, Thermal Loading	324
A.139	σ_{11} Normalized Microstresses, O—C Direction, 4.17% Debonding, Thermal Loading	325
A.140	σ_{11} Normalized Microstresses, O—C Direction, 5.56% Debonding, Thermal Loading	326
A.141	σ_{11} Normalized Microstresses, O—C Direction, 6.94% Debonding, Thermal Loading	327
A.142	σ_{11} Normalized Microstresses, O—C Direction, 8.33% Debonding, Thermal Loading	328
A.143	σ_{11} Normalized Microstresses, O—C Direction, 9.72% Debonding, Thermal Loading	329
A.144	σ_{11} Normalized Microstresses, O—C Direction, 11.11% Debonding, Thermal Loading	330
A.145	σ_{31} Normalized Microstresses, O—A Direction, 0.0% Debonding, Thermal Loading	331
A.146	σ_{31} Normalized Microstresses, O—A Direction, 1.39% Debonding, Thermal Loading	332

A.147	σ_{31} Normalized Microstresses, O–A Direction, 2.78% Debonding, Thermal Loading	333
A.148	σ_{31} Normalized Microstresses, O–A Direction, 4.17% Debonding, Thermal Loading	334
A.149	σ_{31} Normalized Microstresses, O–A Direction, 5.56% Debonding, Thermal Loading	335
A.150	σ_{31} Normalized Microstresses, O–A Direction, 6.94% Debonding, Thermal Loading	336
A.151	σ_{31} Normalized Microstresses, O–A Direction, 8.33% Debonding, Thermal Loading	337
A.152	σ_{31} Normalized Microstresses, O–A Direction, 9.72% Debonding, Thermal Loading	338
A.153	σ_{31} Normalized Microstresses, O–A Direction, 11.11% Debonding, Thermal Loading	339
A.154	σ_{31} Normalized Microstresses, O–C Direction, 0.0% Debonding, Thermal Loading	340
A.155	σ_{31} Normalized Microstresses, O–C Direction, 1.39% Debonding, Thermal Loading	341
A.156	σ_{31} Normalized Microstresses, O–C Direction, 2.78% Debonding, Thermal Loading	342
A.157	σ_{31} Normalized Microstresses, O–C Direction, 4.17% Debonding, Thermal Loading	343
A.158	σ_{31} Normalized Microstresses, O–C Direction, 5.56% Debonding, Thermal Loading	344
A.159	σ_{31} Normalized Microstresses, O–C Direction, 6.94% Debonding, Thermal Loading	345

A.160	σ_{31}	Normalized Microstresses, O—C Direction, 8.33% Debonding, Thermal Loading	346
A.161	σ_{31}	Normalized Microstresses, O—C Direction, 9.72% Debonding, Thermal Loading	347
A.162	σ_{31}	Normalized Microstresses, O—C Direction, 11.11% Debonding, Thermal Loading	348
A.163	σ_{12}	Normalized Microstresses, O—C Direction, 0.0% Debonding, Thermal Loading	349
A.164	σ_{12}	Normalized Microstresses, O—C Direction, 1.39% Debonding, Thermal Loading	350
A.165	σ_{12}	Normalized Microstresses, O—C Direction, 2.78% Debonding, Thermal Loading	351
A.166	σ_{12}	Normalized Microstresses, O—C Direction, 4.17% Debonding, Thermal Loading	352
A.167	σ_{12}	Normalized Microstresses, O—C Direction, 5.56% Debonding, Thermal Loading	353
A.168	σ_{12}	Normalized Microstresses, O—C Direction, 6.94% Debonding, Thermal Loading	354
A.169	σ_{12}	Normalized Microstresses, O—C Direction, 8.33% Debonding, Thermal Loading	355
A.170	σ_{12}	Normalized Microstresses, O—C Direction, 9.72% Debonding, Thermal Loading	356
A.171	σ_{12}	Normalized Microstresses, O—C Direction, 11.11% Debonding, Thermal Loading	357

LIST OF SYMBOLS

α = Thermal Expansion Coefficient.

ν = Poisson's ratio.

σ = Stress or microstress.

ϵ = Strain.

A = Area

s = Physical dimension of the model.

E = Young's Modulus.

F = Force

G = Shear Modulus.

1 = Laminate coordinate axis system.

2 = Laminate coordinate axis system.

3 = Laminate coordinate axis system.

X = Global coordinate axis system.

Y = Global coordinate axis system.

Z = Global coordinate axis system.

u = Displacement in X or 1 direction.

v = Displacement in Y or 2 direction.

w = Displacement in Z or 3 direction.

Subscripts:

lnm = Laminate level properties, where $n=1,2,3$ and $m=1,2,3$.

xx, yy, zz, yx, \dots = Global level properties.

a, b, c, \dots = Subscripts to describe grid faces across width
and height.

$1, 2, 3, \dots$ = Subscripts to describe grid faces along length.

Superscripts:

e = Effective value.

Arrays and Vectors:

$[K]$ = Stiffness matrix.

$\{ u \}$ = Displacement vector.

$\{ P \}$ = Load vector.

$[G]$ = Boundary transformation.

Array and Vector Subscripts:

f = Statically independent or "free" variable.

a = Contains exterior degrees of freedom.

o = Contains interior degrees of freedom.

Array and Vector Superscripts:

a = Partial solution as a result of interior loadings.

o = Partial solution as a result of exterior loadings.

CHAPTER 1

INTRODUCTION

Composite materials have increased in importance as an engineering material for aerospace applications due to their high strength-to-weight ratio. Composite materials are increasingly being used in high temperature applications. To meet the need for high temperature composite materials, metal matrix and ceramic matrix materials have been utilized. Analysis and evaluation of these materials and their properties are very important if reliable designs are to be produced.

In recent years the finite element procedure has been shown to be a viable method of structural analysis. A useful alternative in the evaluation of structures with repeated geometry is substructuring using the superelement method. Substructuring involves the partitioning of a finite element mesh into separate collections of elements called substructures. Each substructure is solved separately and then combined. Using superelements is virtually the same as substructuring, both in its mathematical implementation and in concept, with the primary exception being the user interface [1]. The superelement technique involves defining an image by copying, rotating, or mirroring a portion of a conventional finite element mesh ("conventional" shall imply a non-super-element approach). This image can be described as a structural building block and may be repeatedly included as part of the overall structure.

No modeling data is required for the description of the image other than a list of its boundary points and information on its orientation with respect to the initial representation [2].

Traditionally, fibrous composite materials have been modeled as structures with evenly spaced fibers surrounded by a matrix material, the fibers having consistent diameters and running parallel throughout the composite. Though, in reality, some deviations from this geometry may be present, past work has shown that the assumption of consistent spacing is a good one [3][4].

The repeated geometry of the idealized composite readily lends itself to representation by the superelement technique. By conventionally modeling a unit cell of composite material and then imaging that unit cell, a composite structure of desired dimensions may be described. Analysis by the superelement technique is quite efficient and more easily implemented than conventional finite element methods.

The composite superelement mesh is of modular nature, consisting of a unit cell (figure 1.1) and images of the unit cell; therefore, discontinuities can easily be added by substituting a conventional mesh, which models the discontinuity, in place of one of the images. This conventional mesh can also be imaged to simulate multiple discontinuities within the composite material. Some discontinuities of interest that can be modeled in this manner are partial bonding and fiber fracture, both common in metal matrix composite materials. The modular nature of the superelement model also allows for efficient representation of hybrid and aligned short fiber composite materials. The hybrid composite can be modeled by changing the fiber material properties of two separate primary superelements and using these primaries and their images to build the desired

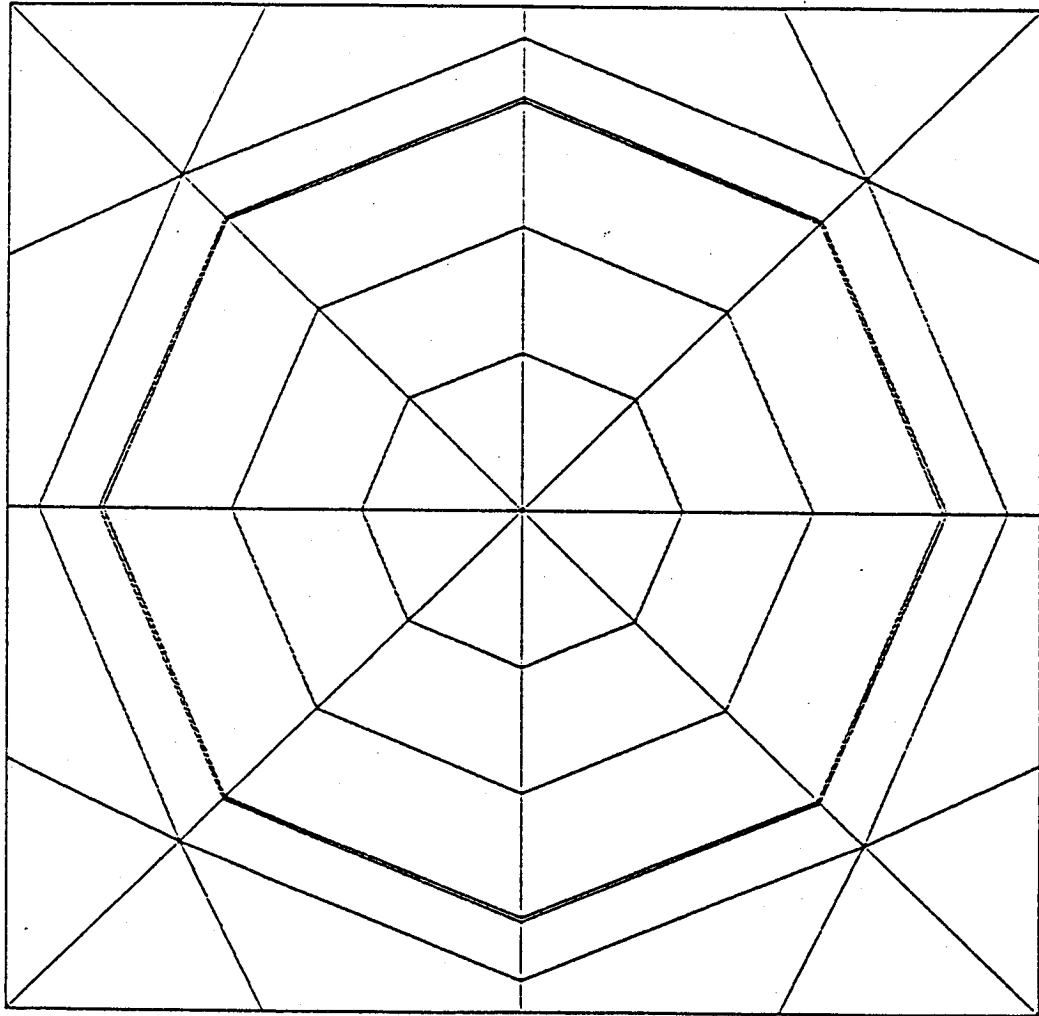


Figure 1.1 – Finite Element Mesh of Composite Unit Cell

structure. An aligned short fiber composite may be formed by including sections of pure matrix between lengths of fibers. The generation of a bead-filled composite may be accomplished using similar methods.

Once a superelement mesh is determined to be void of modeling inaccuracies, it can then be altered to investigate new areas of composite technology without the high cost of experimental analysis. Some of these areas may be the use of hollow reinforcing fibers or fibers with non-circular cross section. The effect of variations in fiber diameter along the fiber's length could also be investigated.

CHAPTER 2

OBJECTIVE

The objective of this paper is to show the degradation of various properties of metal matrix composite materials in relation to the amount of fiber disbond. The work also shows the mechanics of load transfer from the surrounding material to the debonded fiber. Since the debonding is only for a fraction of the length of the fiber, the fiber becomes structurally active in the bonded region and a gradient of load transfer from the matrix to the fiber can be witnessed. In the region where there is no connectivity between the fiber and the surrounding matrix, it is expected that the fiber will deform rigidly relative to the rest of the structure; therefore, theoretically, there will be no stresses in this region of the fiber.

CHAPTER 3

BACKGROUND

The composite system considered for this work is P100—Graphite/Copper. Analyses for high temperature and room temperature constituent material properties were considered. The utilization of copper for the metal matrix material is significant because of its relatively low thermal resistivity coefficient, which allows for a high rate of heat transfer. Thermal stresses in metal matrix composites can be very high due to the difference in the thermal expansion coefficients of the constituents. The high thermal conductivity of the copper matrix allows for the dissipation of heat energy, causing a decrease in thermal straining and a subsequent lowering of the stress state in the composite.

A problem arises when choosing properties to describe each of the constituent materials because the state of the material, and thus its properties, depends on the history of the material. An important factor in the material's behavior is its rate of cooling during the fabrication process. The rate of cooling determines the degree of crystallization. If copper is quickly cooled it will tend to be more amorphous, with many small crystals, and therefore more ductile. If it is cooled slowly it will have time for larger crystals to form and will be more brittle in nature [5]. It is difficult to test the *in situ* state of the copper after fabrication

of the composite; therefore, average material properties for the copper matrix must be assumed. This assumption may be a source of error when comparing finite element results to actual test data.

The superelement method is a form of substructuring used in the MacNeal Schwendler Corporation (MSC) version of NASTRAN where the computer takes on most of the bookkeeping burden as well as doing the entire analysis in one computer run. For this study Version 61 of MSC NASTRAN was used in the superelement analysis. All NASTRAN finite element work was done on a Cray-XMP supercomputer utilizing a solid state storage device. The database for each run was saved on the Cray and restarted using the next set of boundary conditions. This method allowed for faster computer turnaround during analysis.

The cases chosen are but a few of a multitude of possible partial bonding configurations. However, these cases are sufficient to demonstrate the load transfer and stress concentration effects of this phenomena and help to understand the effects of partial bonding on the composite's material properties. In the cases examined here, all fibers are running parallel to each other with their longitudinal axes in the X direction. Methods exist for transforming the material properties calculated from this fiber orientation to other material axis systems [6].

The mesh that was employed in this work consisted of a cluster of nine fibers in a three by three matrix (figure 3.1) and represents a fiber volume ratio of 0.466. The initial version of the mesh was fabricated with the center cell modeled as a primary superelement and all surrounding cells were images of that primary. This mesh was utilized when no fibers were debonded and when all nine

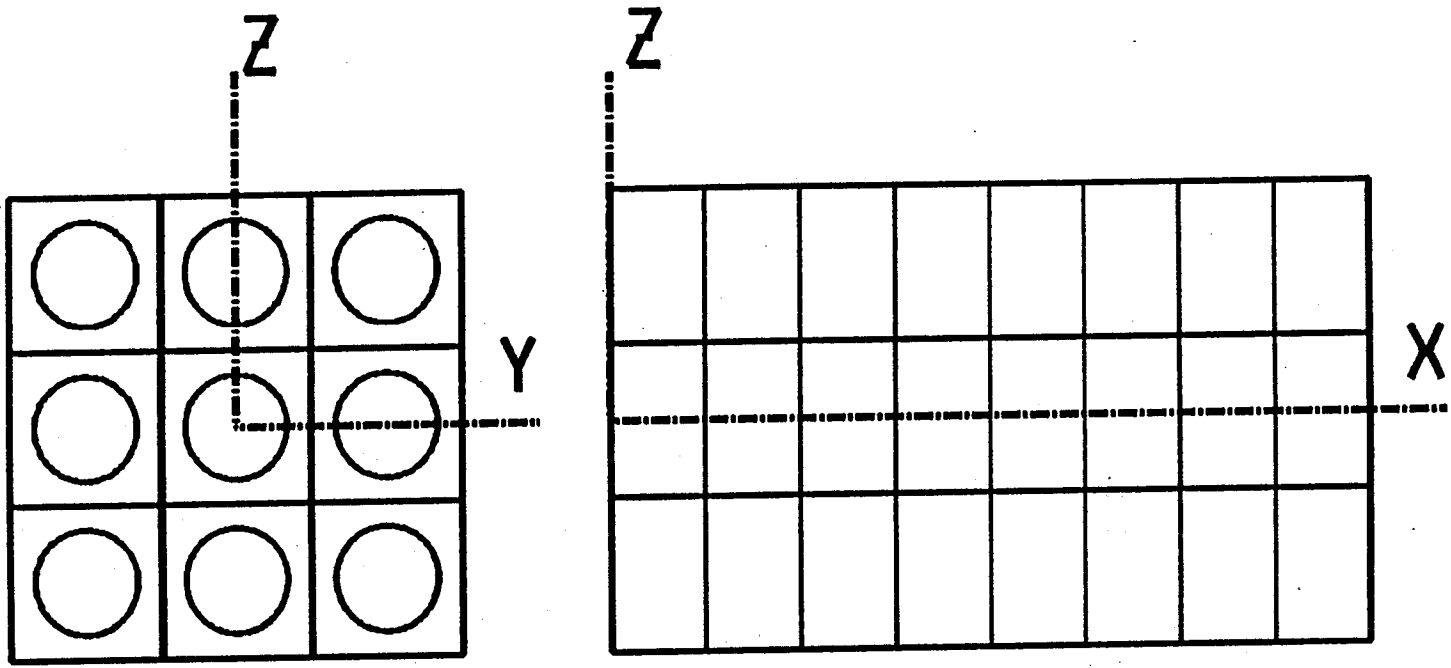


Figure 3.1 – Composite Model

fibers were debonded equally. Another mesh was formulated for when only the center fiber of the nine cell model was debonded. For this case the center cell was modeled using conventional finite element methods. The primary superelement was defined to be to one side of the center fiber and the remaining perimeter superelements were modeled as images of this one. Minor modifications were made to each of the meshes to allow for the modeling of varied amounts of disbond between fiber and matrix.

The methodology utilized to include the disbond is described briefly here. Duplicate grid points were defined for all grids around the circumference of the fiber, at the interface between fiber and matrix. This duplicate grid point was included in the analysis only when the portion of fiber where it resided was to be debonded from the matrix. The debonding took place when the connectivity cards that define the perimeter of the fiber were altered so that one of the duplicate grids was associated with the fiber, and one with the matrix. No connectivity then exists across the interface, producing a crack of zero width, with fiber on one side and matrix on the other (figure 3.2). In the work described here, the total circumference of a fiber was released together. Future work may include analyses where the fiber is not totally circumferentially disbonded, but this was not approached here. The amount of disbond was varied by debonding different lengths of fiber as described above. No attempt was made to find the loading at which the debonding will take place. Instead, interest was placed on the effect of debonding on the composite's material properties.

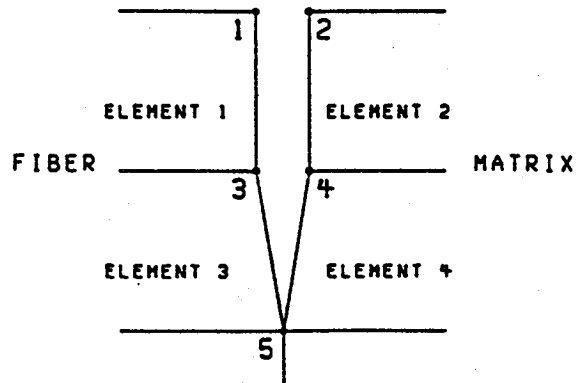
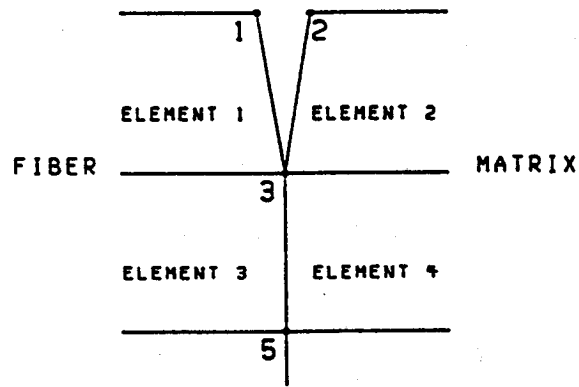
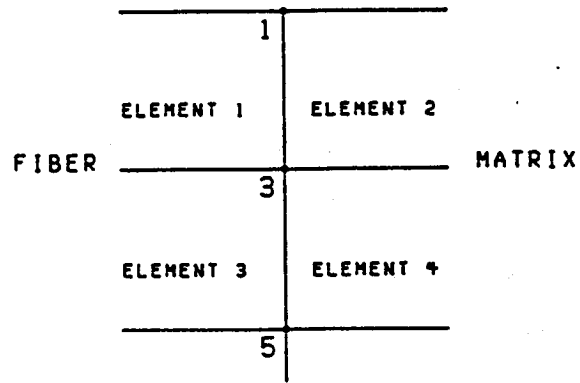


Figure 3.2 – Modeling of Fiber Disbond

In the model adopted for this work, thin elements were placed around the circumference of the fibers (figure 1.1). For the work discussed here, this thin layer was defined to be matrix material but was included for future work intended for this mesh. These elements have large aspect ratios but have been shown not to significantly effect the material property calculations under the loading conditions used. This layer allows for the ability to include an interphase region which is common in metal matrix composites. This interphase region is formed *in situ* from a chemical reaction between the fiber material and matrix material during the fabrication process [7]. It can also be used to model a coating on the fiber which can decrease areas of high stress. Reference [8] provides a discussion on this effect. This interface is commonly the most highly stressed area of a composite material. It is advantageous to lower the stress concentrations in these areas by placing a material of intermediate modulus or a ductile one between the fiber and the matrix. When a graded modulus interphase is employed, the interphase layer is defined to be one of intermediate modulus and the modulus ratio of any two neighboring components is lowered thus lowering stress concentrations due to modulus mismatch. If the interface region is defined to be a ductile material then local deformation capability is built into this area of stress risers resulting in at least partial dampening of the stress concentration effects due to modulus mismatch.

The following are the procedures used to calculate ply material properties from the finite element output. These methods are consistent with the mechanics of materials approach to solid structures [9].

ν_{113} , ν_{112} , and E_{111} are obtained from the same loading conditions. In this case the front face is fixed in the X ($u_1 = 0.0$) and the back face is displaced in the X ($u_9 = u$) (figure 3.3). Lines of geometric symmetry on the top and side faces are restricted from motion in such a way to insure symmetry once the model is loaded.

E_{111} is calculated by finding the total force over the displaced face and dividing this force by the area of this face yielding an equivalent applied stress (figure 3.4).

$$\sigma_{111}^e = \frac{\Sigma F}{A_1} \quad 3.1$$

The strain is then calculated by dividing the applied displacement by the length of the specimen.

$$\epsilon_{111} = \frac{u}{s_1} \quad 3.2$$

σ_{111}^e is divided by ϵ_{111} to equal Young's modulus in the 11 direction.

$$E_{111} = \frac{\sigma_{111}^e}{\epsilon_{111}} \quad 3.3$$

ν_{112} is found by finding the average deflection in the Y direction as a result of the enforced displacement in the X. Dividing this deflection by the width of the model yields a strain in the 22.

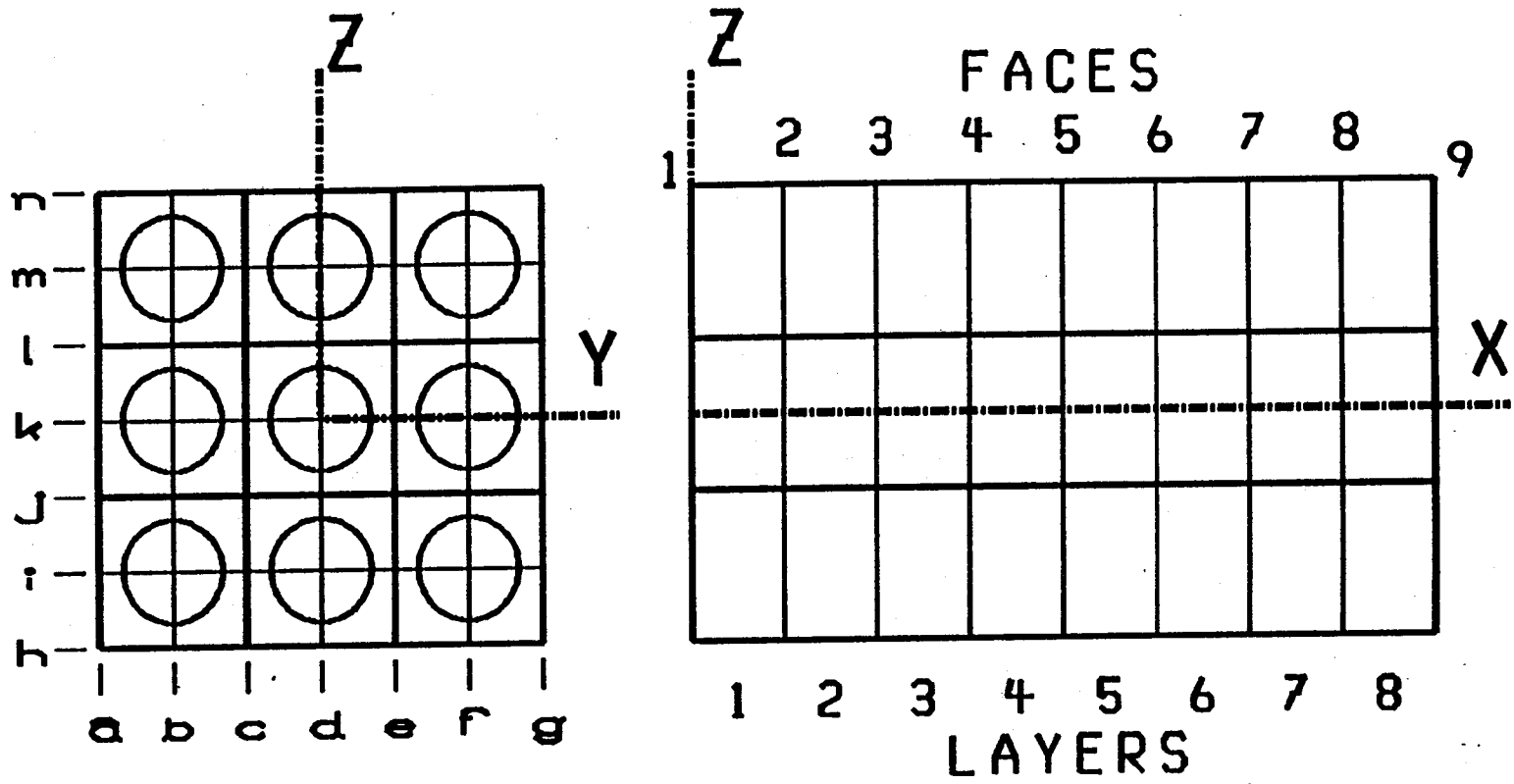
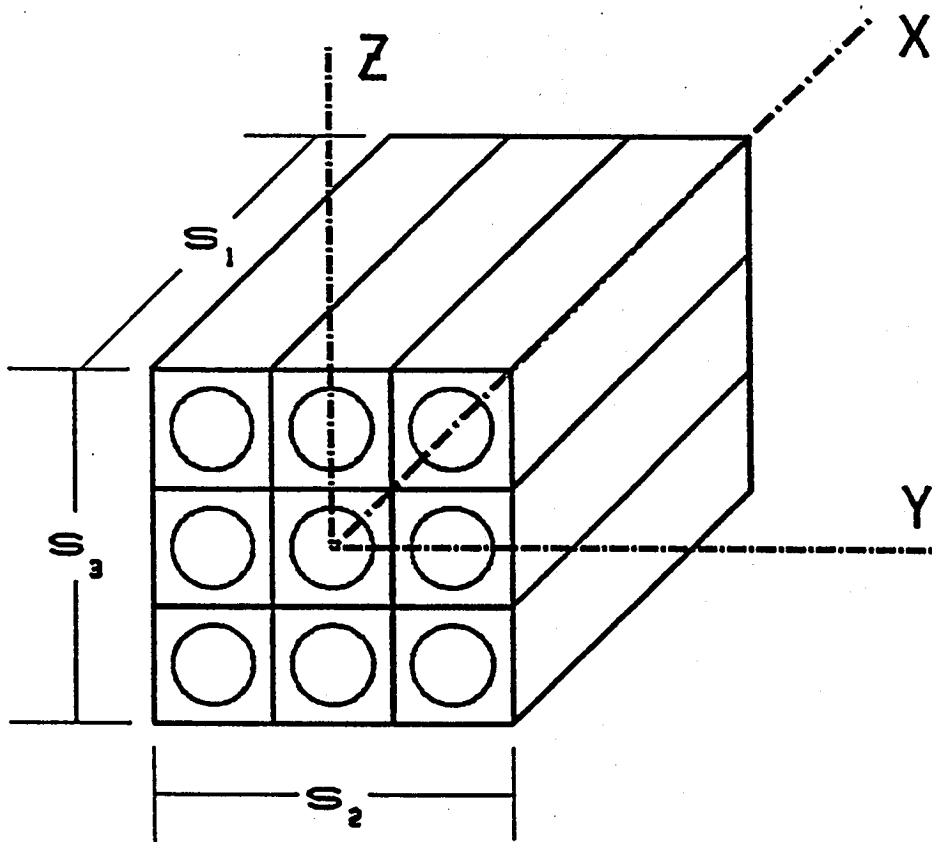


Figure 3.3 – Composite Model, Faces and Layers



$$A_1 = s_2 \times s_3$$

$$A_2 = A_3 = s_1 \times s_2$$

Figure 3.4 – Model Dimensions

$$\epsilon_{122} = \frac{v}{s_2} \quad 3.4$$

The Poisson's ratio, ν_{112} , is calculated from equation 3.5.

$$\nu_{112} = \frac{-\epsilon_{122}}{\epsilon_{111}} \quad 3.5$$

ν_{113} is found by similar methods.

$$\epsilon_{133} = \frac{w}{s_3} \quad 3.6$$

$$\nu_{113} = \frac{-\epsilon_{133}}{\epsilon_{111}} \quad 3.7$$

ν_{123} and E_{122} are both calculated from the same loading conditions. The face with the negative Y direction as its normal is fixed in the Y direction ($v_a = 0.0$) (figure 3.3) and the face with the positive Y direction as its normal has an enforced displacement in the positive Y direction ($v_g = v$) resulting in tension transverse to the fiber direction. The equivalent applied stress is then calculated by averaging the resultant forces over the face and dividing by the face's area.

$$\sigma_{122}^e = \frac{\Sigma F_{22}}{A_2} \quad 3.8$$

In calculating E_{122} the strain in the 22 is required. The strain is calculated by dividing the applied displacement by the width of the specimen.

$$\epsilon_{122} = \frac{v}{s_2} \quad 3.9$$

The equivalent stress divided by this strain is equal to Young's modulus in the 22 direction.

$$E_{122} = \frac{\sigma_{122}^e}{\epsilon_{122}} \quad 3.10$$

ν_{123} is found by finding the average deflection in the Z direction as a result of the enforced displacement in the Y. Dividing this deflection by the height of the model yields the strain in the transverse direction (33).

$$\epsilon_{133} = \frac{w}{s_3} \quad 3.11$$

The ratio of the strain in the 33 over the strain in the 22 yields the Poisson's ratio in the 23.

$$\nu_{123} = \frac{-\epsilon_{133}}{\epsilon_{122}} \quad 3.12$$

E_{133} and ν_{132} are calculated from another unique set of boundary conditions. In this case, the face whose normal is in the negative Z direction is fixed in the Z ($w_h = 0.0$) (figure 3.3), and the face whose normal is in the positive Z direction is displaced in the Z ($w_n = w$). The equivalent applied stress is computed by averaging the forces on the face where the deflection was applied and dividing by the area of that side.

$$\sigma_{133}^e = \frac{\Sigma F_{33}}{A_3} \quad 3.13$$

E_{133} is calculated by dividing this equivalent stress by the strain in the 33 direction. The strain in the 33 is ascertained by dividing the applied displacement in the Z by the height of the specimen.

$$\epsilon_{133} = \frac{w}{s_3} \quad 3.14$$

The equivalent stress is divided by this strain and is equal to Young's modulus in the 33 direction.

$$E_{133} = \frac{\sigma_{133}^e}{\epsilon_{133}} \quad 3.15$$

The first step in finding ν_{132} is obtaining the average deflection in the Y direction as a result of the enforced displacement in the Z. Dividing this deflection by the width of the model yields a strain in the 22.

$$\epsilon_{122} = \frac{v}{s_2} \quad 3.16$$

The ratio of this strain over the strain in the 33 yields the Poisson's ratio, ν_{132} .

$$\nu_{123} = \frac{-\epsilon_{122}}{\epsilon_{133}} \quad 3.17$$

For the determination of G_{121} , an enforced displacement in the X direction was placed on the face with the positive Y axis as its normal. The shear strain was then calculated by dividing this displacement by the width of the model.

$$\epsilon_{121} = \frac{u}{s_2} \quad 3.18$$

A FORTRAN program was used to glean and sum the resulting grid forces on this face from the NASTRAN output deck to achieve an equivalent applied force. The effective shear stress in the 21 direction is then calculated by dividing this force by the area over which it is applied.

$$\sigma_{121}^e = \frac{\Sigma F_{121}}{A_2} \quad 3.19$$

The shear strain for small displacements is given by the enforced deflection divided by the width of the specimen. G_{121} is obtained by dividing the shear stress in the 21 direction by the shear strain.

$$G_{121} = \frac{\sigma_{121}^e}{\epsilon_{121}} \quad 3.20$$

G_{131} is found by similar methods. For this calculation the face with the positive Z axis for its normal is used for the location of the enforced displacement.

$$\epsilon_{131} = \frac{u}{s_3} \quad 3.21$$

$$\sigma_{131}^e = \frac{\Sigma F_{131}}{A_3} \quad 3.22$$

$$G_{131} = \frac{\sigma_{131}^e}{\epsilon_{131}} \quad 3.23$$

G_{123} can be obtained by applying an enforced displacement in the positive Z direction to the side whose normal is the positive Y axis. The total resulting force on this face is calculated from the finite element output. This total shear force in the 23 direction is divided by the area of the side over which it was applied, resulting in the average shear stress in the 23 direction.

$$\sigma_{123}^e = \frac{\Sigma F_{123}}{A_2} \quad 3.24$$

The small displacement shear strain in the 23 is then calculated by dividing the applied displacement in the Z direction by the width of the model.

$$\epsilon_{123} = \frac{w}{s_2} \quad 3.25$$

G_{123} is calculated by dividing the effective shear stress, σ_{123}^e , by ϵ_{123} .

$$G_{123} = \frac{\sigma_{123}^e}{\epsilon_{123}} \quad 3.26$$

α_{111} , α_{122} , and α_{133} are all found by the same loading conditions. In this case a plane in the center of the model, with the positive X direction acting as its normal, is restricted from movement in the X direction ($u_x = 0.0$). This restriction assures symmetry about the center of the model. Again, lines of symmetry are enforced on the sides of the model. A thermal load is then applied to the model, $T = T_o$.

The first step in finding α_{111} is determining the average of the displacements on the end with the positive X axis as its normal and dividing by the length of the model, s_1 , resulting in the strain in the 11 due to the change in temperature.

$$\epsilon_{111} = \frac{u}{s_1} \quad 3.27$$

Now, by dividing the strain by the change in temperature, one can obtain the thermal expansion coefficient in the 11 direction.

$$\alpha_{111} = \frac{\epsilon_{111}}{\Delta T} \quad 3.28$$

α_{122} is found by taking the average displacement in the Y direction and dividing by the change in temperature and the width.

$$\alpha_{122} = \frac{v}{(\Delta T)(s_2)} \quad 3.29$$

The calculation of α_{133} is similar to that of α_{122} , with the exception being that the average displacement in the Z is divided by the change in temperature and by the height of the model [10].

$$\alpha_{133} = \frac{w}{(\Delta T)(s_3)} \quad 3.30$$

In all of the previous loading conditions boundary conditions were applied to enforce displacement symmetry. On each face of the above loading conditions and for each degree of debonding investigated, normalized constituent microstresses in three directions, each starting in the center of the model and moving toward the perimeter, were determined. These lines can be referenced easily by referring to the line segments defined in each of the three directions. The first line is from the middle of the center fiber to the edge of the mesh in the positive Z direction (line segment O-A). The second starts in the center of the

center fiber and diagonally bisects the angle between the positive Y and positive Z directions, forming a 45 degree angle with each and lying in the same plane (line segment O-C). The last line of stresses, again, starts at the middle point of the centermost fiber and ends at the edge of the mesh running in the positive Y direction (line segment O-B) (figure 3.5). A FORTRAN code was written to acquire constituent microstresses in the 11, 22, 33, 12, 23, and 31 directions along these lines and normalize them with respect to the equivalent applied stress. The normalized microstresses were gathered into tables and, if they were found to be significant relative to the ultimate stress of the constituent material in which they appeared, they were plotted. These plots allow for the investigation of areas of high stress due to debonding. These microstresses are not obtainable experimentally because they are internal to the structure.

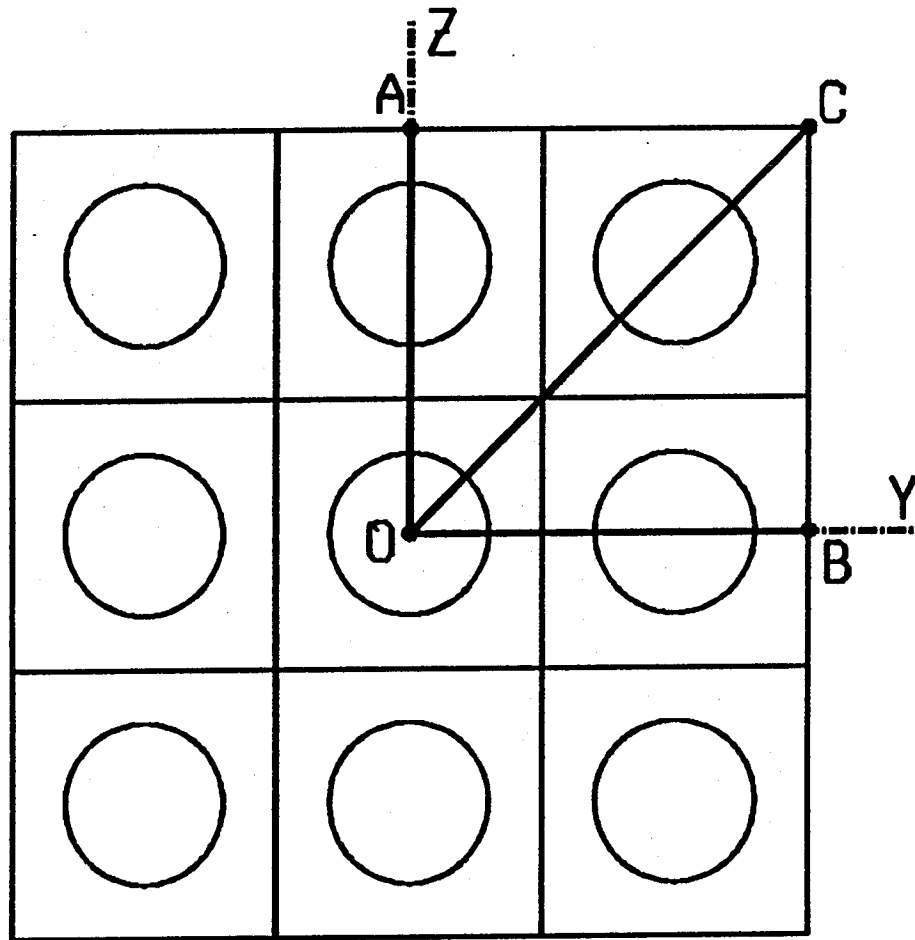


Figure 3.5 – Locations of Stress Plots

CHAPTER 4

THEORETICAL

The superelement method is a form of substructuring used in MSC NASTRAN. The important difference between substructuring and the use of superelements is that in the use of superelements most of the logistics of maintaining the substructure is done by the program and not the user. Mathematically, the use of superelements is equivalent to substructuring [11, 12, & 13]. A brief description of substructuring theory follows.

Consider the static analysis equation

$$\left[K_{ff} \right] \left\{ u_f \right\} = \left\{ P_f \right\} \quad 4.1$$

where $\left[K_{ff} \right]$ is the stiffness matrix, $\left\{ u_f \right\}$ is displacement vector and the vector $\left\{ P_f \right\}$ is the load vector. The "f" subscript indicates statically independent or "free" variables and reflects the elimination of degrees of freedom due to multipoint and single-point constraints. These matrices can be partitioned into the a-set and the o-set where the o-set includes all interior degrees of freedom of the superelement and the a-set includes all exterior degrees of freedom. This is given by the equation

$$\begin{bmatrix} [\bar{K}_{aa}] & [K_{ao}] \\ [K_{oa}] & [\bar{K}_{oo}] \end{bmatrix} \begin{Bmatrix} \{u_a\} \\ \{u_o\} \end{Bmatrix} = \begin{Bmatrix} \{\bar{P}_a\} \\ \{P_o\} \end{Bmatrix} \quad 4.2$$

Multiplying yields

$$[\bar{K}_{aa}] \{u_a\} + [K_{ao}] \{u_o\} = \{\bar{P}_a\} \quad 4.3$$

and

$$[K_{oa}] \{u_a\} + [\bar{K}_{oo}] \{u_o\} = \{P_o\} \quad 4.4$$

The bar over a variable indicates the quantity is a partition of its parent matrix.

Solving the second equation for the o-set variables yields

$$\{u_o\} = [K_{oo}]^{-1} \{P_o\} - [K_{oo}]^{-1} [K_{oa}] \{u_a\} \quad 4.5$$

Defining new terms we have

$$\{u_o\} = \{u_o^0\} + [G_{oa}] \{u_a\} \quad 4.6$$

where

$$\{u_o^o\} \equiv [K_{oo}]^{-1} \{P_o\} \quad 4.7$$

and

$$[G_{oa}] \equiv -[K_{oo}]^{-1} [K_{oa}] \quad 4.8$$

The quantity, $\{u_o^o\}$, is the partial solution obtained when loads are placed on interior points and external points are constrained. If no loads exist on points interior to the superelement then $\{u_o^o\}$ is null. Every superelement in the structure has a $\{u_o^o\}$ vector. The other part of the interior displacement solution is found by combining equations 4.8 and 4.4 yielding

$$\{u_o^a\} = [G_{oa}] \{u_a\} \quad 4.9$$

which is the displacement due to boundary point motion. Again, a $\{u_o^a\}$ vector is found for each superelement in the structure. The total solution is found by superposition of these two partial solutions. Combining the above equations yields equation 4.10.

$$[K_{aa}] \{u_a\} = \{P_a\} \quad 4.10$$

where

$$\left[K_{aa} \right] \equiv \left[\left[\bar{K}_{aa} \right] + \left[G_{oa} \right]^T \left[K_{oa} \right] \right] \quad 4.11$$

and

$$\left\{ P_a \right\} \equiv \left\{ \left\{ \bar{P}_a \right\} + \left[G_{oa} \right]^T \left\{ P_o \right\} \right\} \quad 4.12$$

The $\left[K_{aa} \right]$ matrix is the stiffness of the superelement with respect to its boundary points and exists for each superelement. The $\left\{ P_a \right\}$ vector is representative of the boundary loads that are transferred to the rest of the structure.

These partial solutions are stored and later added to the remainder of the structure. It is these matrices that, under conventional substructuring, would have to be manipulated by the user, whereas in the superelement technique the computer maintains this database.

The mechanics of material approach to calculating material properties from finite element output is based on the definitions of the properties themselves. Boundary conditions are applied so as to do away with any ill effects of the loading that might change the calculated property. Bending is one such ill effect. A description of the utilization of the mechanics of material approach for the calculation of composite material properties was addressed earlier.

CHAPTER 5

PROCEDURE

The initial investigation into partial bonding was preceded by some test cases to confirm the accuracy of the methods used to obtain the material properties from the finite element output. To do this, the mesh was executed using a monolithic material, P100-graphite (the fiber material). The loading cases discussed earlier were applied to the model and the monolithic material properties were back-calculated. These properties were compared to those of P100-graphite used as input to the finite element code. The calculated material properties obtained from the finite element output were very close to those used as input (table 5.1). This confirms the viability of this method of calculating composite material properties.

A set of reference finite element runs were then executed. These runs contained no debonding. Material properties were calculated from the output of these finite element runs (table 5.2). Caruso and Chamis [14] calculated composite material properties using similar methods and compared them to those predicted by Hopkins and Chamis [15] with very good correlation.

Debonding of a single fiber in the center of the nine cell model was now considered. Room temperature (70° F) constitutive material properties were used (table 5.3). In all loading conditions described here, fibers that were to be debonded did not have an applied displacement assigned to them. This allowed

**CALCULATED MATERIAL PROPERTIES
FOR ALL P100-GRAPHITE MODEL**

	UNITS	CONSTITUTIVE P100- GRAPHITE PROPERTIES	CALCULATED P100- GRAPHITE PROPERTIES
E_{111}	psi	105.0×10^6	105.0039201×10^6
E_{122}	psi	0.90×10^6	0.900165249×10^6
E_{133}	psi	0.90×10^6	0.900165249×10^6
G_{112}	psi	1.10×10^6	1.100001462×10^6
G_{123}	psi	0.70×10^6	0.6999990253×10^6
G_{113}	psi	1.10×10^6	1.100001462×10^6
ν_{112}	in/in	0.200	0.2000547581
ν_{123}	in/in	0.250	0.2496567996
ν_{113}	in/in	0.200	0.2000547581
α_{111}	in/in/°F	-0.90×10^{-6}	-0.90×10^{-6}
α_{122}	in/in/°F	5.60×10^{-6}	5.60×10^{-6}
α_{133}	in/in/°F	5.60×10^{-6}	5.60×10^{-6}

Table 5.1 – Calculated Material Properties for all P100–Graphite Model

COMPOSITE MATERIAL PROPERTIES
 NO DEBONDING - ALL FIBERS LOADED
 P100- GRAPHITE / COPPER

	UNITS	COMPOSITE PROPERTIES
E_{111}	psi	58.03×10^6
E_{122}	psi	7.19×10^6
E_{133}	psi	7.19×10^6
G_{112}	psi	3.36×10^6
G_{123}	psi	2.66×10^6
G_{113}	psi	3.36×10^6
ν_{112}	in/in	0.291
ν_{123}	in/in	0.246
ν_{113}	in/in	0.291
a_{111}	in/in/°F	1.11×10^{-6}
a_{122}	in/in/°F	11.41×10^{-6}
a_{133}	in/in/°F	11.41×10^{-6}

Table 5.2 – Composite Material Properties – No Debonding

ROOM TEMPERATURE CONSTITUTIVE MATERIAL PROPERTIES
P100- GRAPHITE / COPPER

	UNITS	FIBER	MATRIX
E_{11}	psi	105.0×10^6	17.0×10^6
E_{22}	psi	0.90×10^6	17.0×10^6
E_{33}	psi	0.90×10^6	17.0×10^6
G_{12}	psi	1.10×10^6	6.54×10^6
G_{23}	psi	0.70×10^6	6.54×10^6
G_{13}	psi	1.10×10^6	6.54×10^6
ν_{12}	in/in	0.200	0.300
ν_{23}	in/in	0.250	0.300
ν_{13}	in/in	0.200	0.300
α_{11}	in/in/°F	-0.90×10^{-6}	9.80×10^{-6}
α_{22}	in/in/°F	5.60×10^{-6}	9.80×10^{-6}
α_{33}	in/in/°F	5.60×10^{-6}	9.80×10^{-6}

Table 5.3 – Room Temperature Constitutive Material Properties

these fibers to behave as if they had been fractured. Debonding due to stress increases resulting from a broken fiber is a common occurrence in metal matrix composites. In this first series of runs, debonding was propagated from only one end of the model, producing an asymmetric disbond. Each element around the circumference of the fiber was allowed to debond using the methods described earlier. The debonding was done for each successive layer of elements along the length of the fiber. After the mesh was changed to reflect the next layer of debonding, the loading conditions were applied and material properties calculated. Results were plotted for each of the material properties versus percent disbond of the total mesh (figures 5.1 - 5.4). Least-squares linear regression was used to obtain equations for these lines. This allowed the results to be used as aid in the prediction of composite property degradation due to fiber debonding [16]. These plots show the properties affected most by debonding and to what degree they are affected. These results can also be used indicate partial bonding in cases where material properties deviated from predicted values. When suspecting the presence of partial bonding, closer attention should be paid to those properties found to be more sensitive to the presence of the fiber debonding.

The next series of runs had the same geometry as those mentioned above except that high temperature constituent material properties were used along with the symmetric debonding (table 5.4). The material properties found in table 5.4 were obtained from the METCAN (Metal Matrix Composite Analyzer) computer code [17]. The temperature selected was 1500° F. Here, all debonding was done symmetrically with respect to the center of the model. The results of the material property calculations are shown in figures 5.5 through 5.8.

EFFECT OF FIBER DEBONDING ON MODULUS - E111, E122, E133

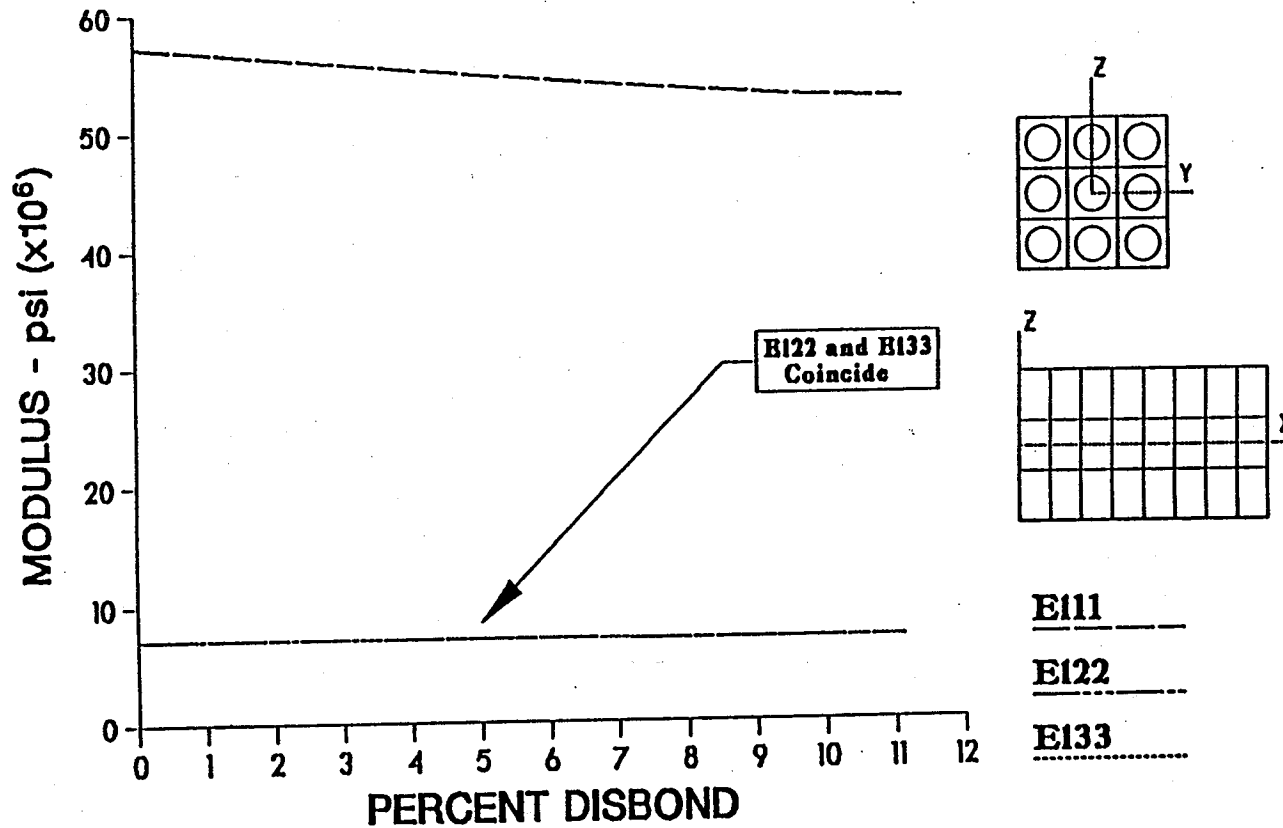


Figure 5.1 – Effect of Center Fiber Debonding on Modulus at Room Temperature

EFFECT OF FIBER DEBONDING ON POISSONS RATIO - ν_{112} , ν_{113} , ν_{123} , ν_{132}

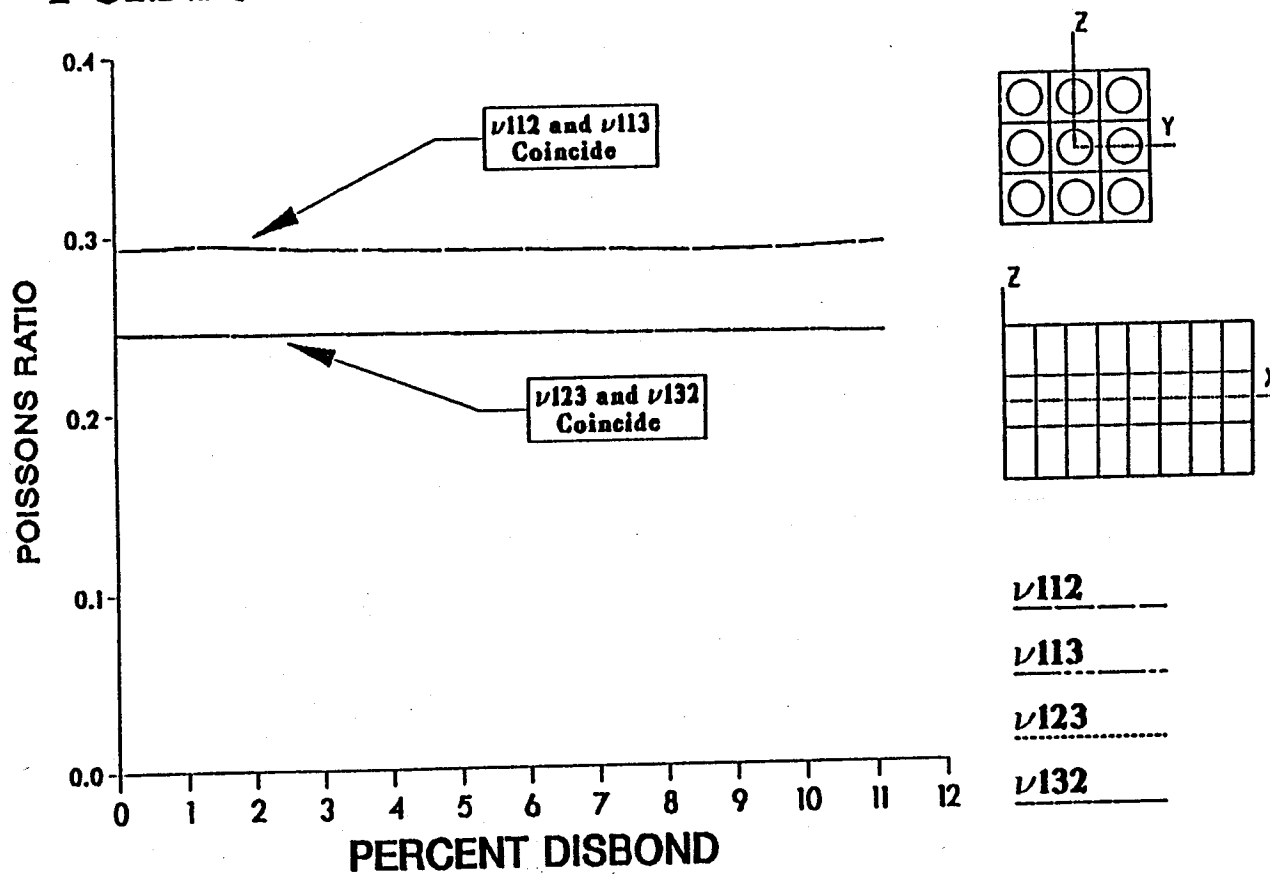


Figure 5.2 — Effect of Center Fiber Debonding on Poisson's Ratio at Room Temperature

EFFECT OF FIBER DEBONDING ON SHEAR MODULUS - G_{12} , G_{13} , G_{23}

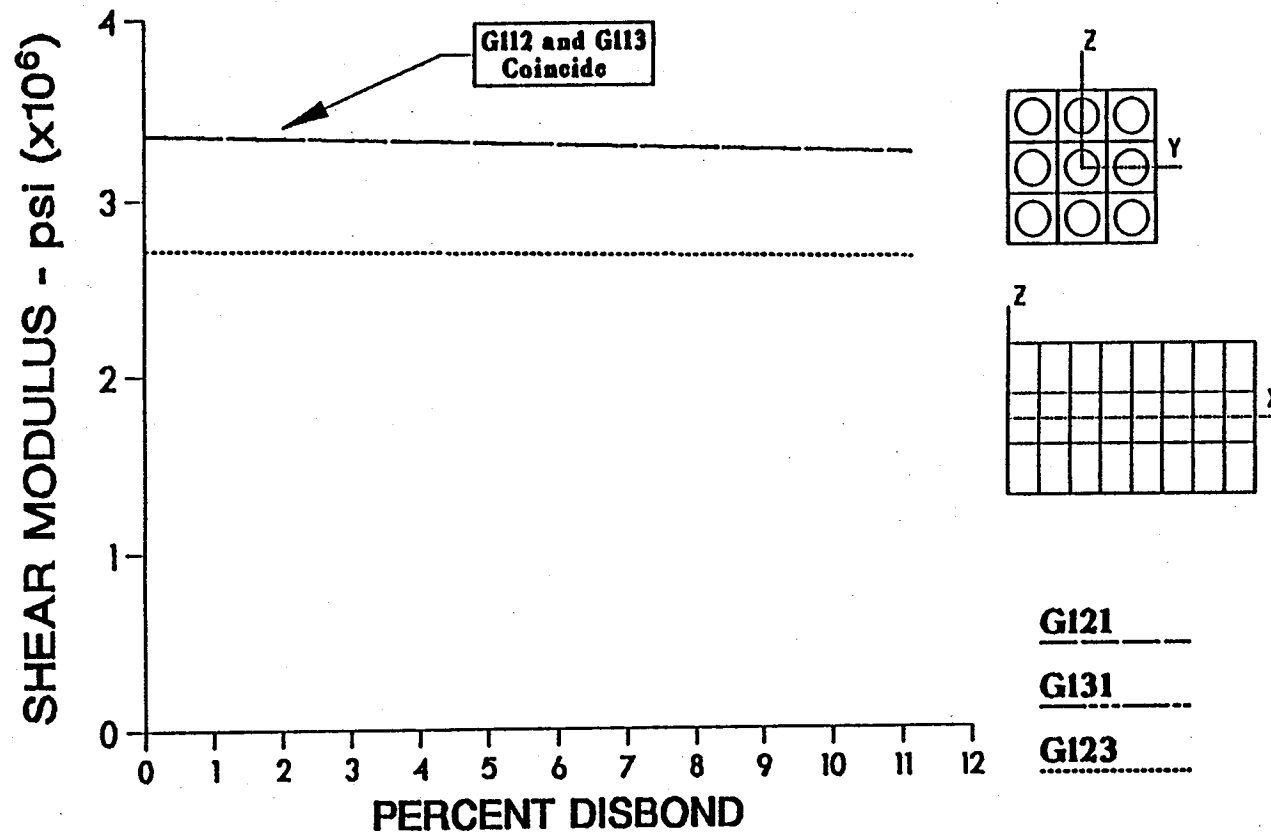


Figure 5.3 – Effect of Center Fiber Debonding on Shear Modulus at Room Temperature

**EFFECT OF FIBER DEBONDING ON
THERMAL EXPANSION COEFFICIENT (TEC) - α_{111} , α_{122} , α_{133}**

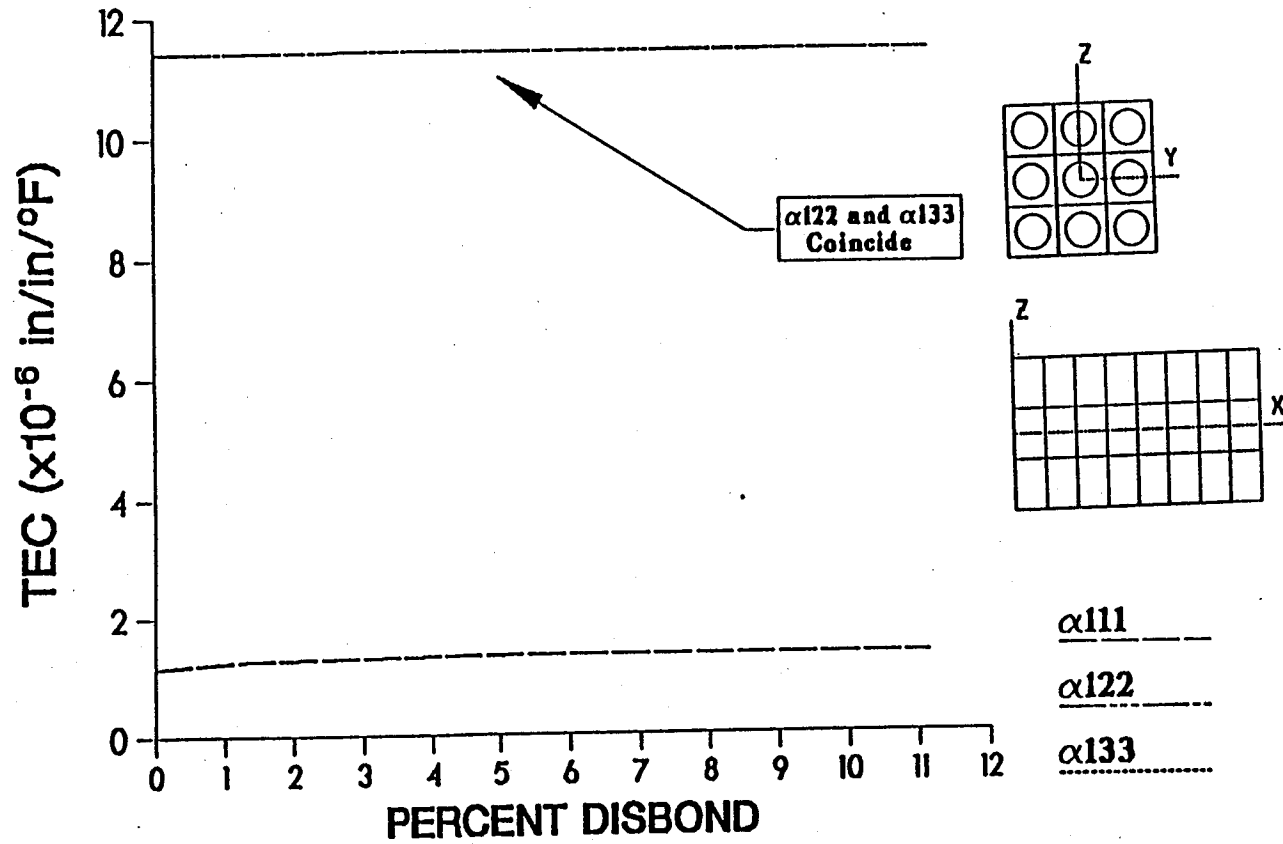


Figure 5.4 – Effect of Center Fiber Debonding on Thermal Expansion Coefficient at Room Temperature

HIGH TEMPERATURE (1500° F) CONSTITUITIVE MATERIAL PROPERTIES

P100-GRAPHITE / COPPER

	UNITS	FIBER	MATRIX
E_{11}	psi	93.8×10^6	8.87×10^6
E_{22}	psi	0.904×10^6	8.87×10^6
E_{33}	psi	0.904×10^6	8.87×10^6
G_{12}	psi	0.982×10^6	3.41×10^6
G_{23}	psi	0.625×10^6	3.41×10^6
G_{13}	psi	0.982×10^6	3.41×10^6
ν_{12}	in/in	0.179	0.300
ν_{23}	in/in	0.223	0.300
ν_{13}	in/in	0.179	0.300
α_{11}	in/in/°F	-1.008×10^{-6}	19.55×10^{-6}
α_{22}	in/in/°F	6.27×10^{-6}	19.55×10^{-6}
α_{33}	in/in/°F	6.27×10^{-6}	19.55×10^{-6}

Table 5.4 – High Temperature Constitutive Material Properties

EFFECT OF FIBER DEBONDING ON MODULUS - E111, E122, E133 HIGH TEMPERATURE (1500 °F)

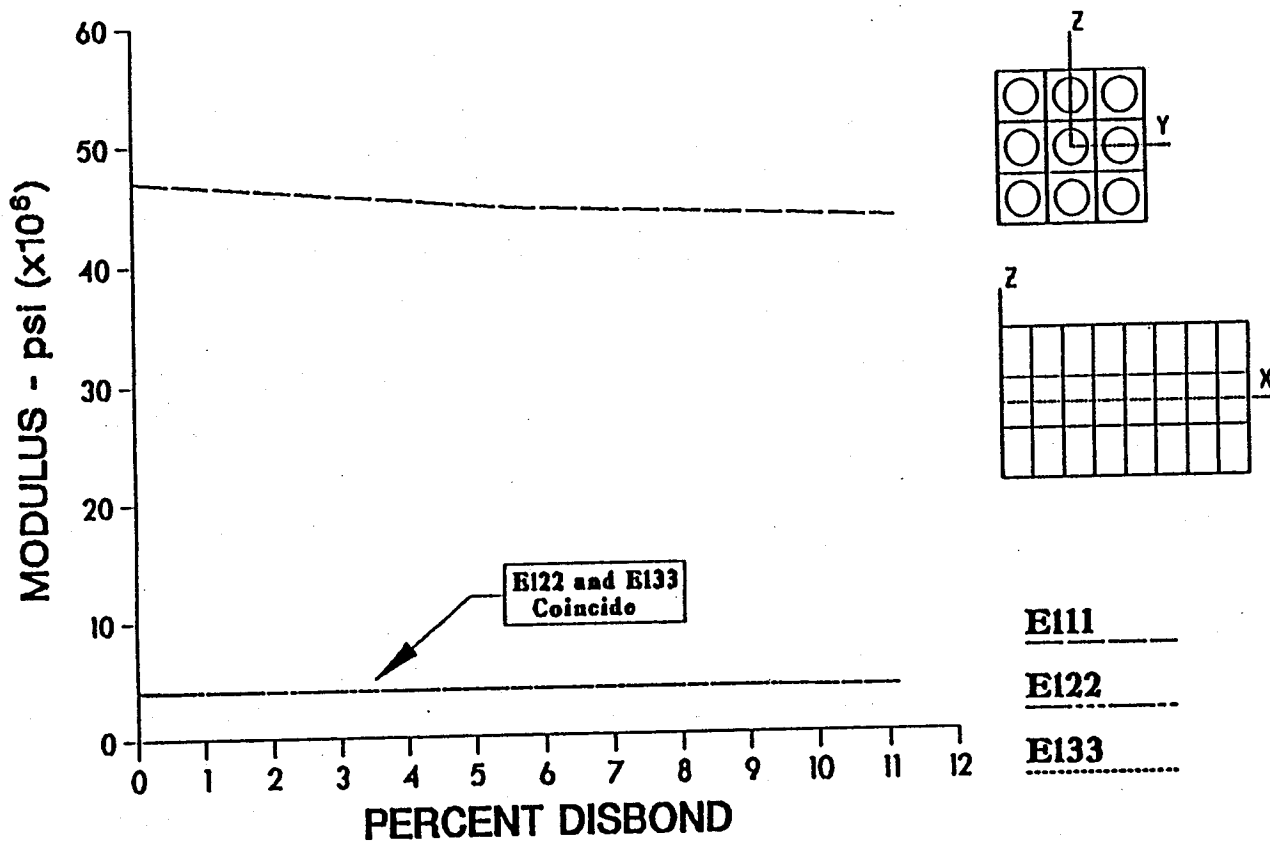


Figure 5.5 – Effect of Center Fiber Debonding on Modulus at High Temperature

EFFECT OF FIBER DEBONDING ON POISSONS RATIO - ν_{112} , ν_{113} , ν_{123} , ν_{132} HIGH TEMPERATURE (1500 °F)

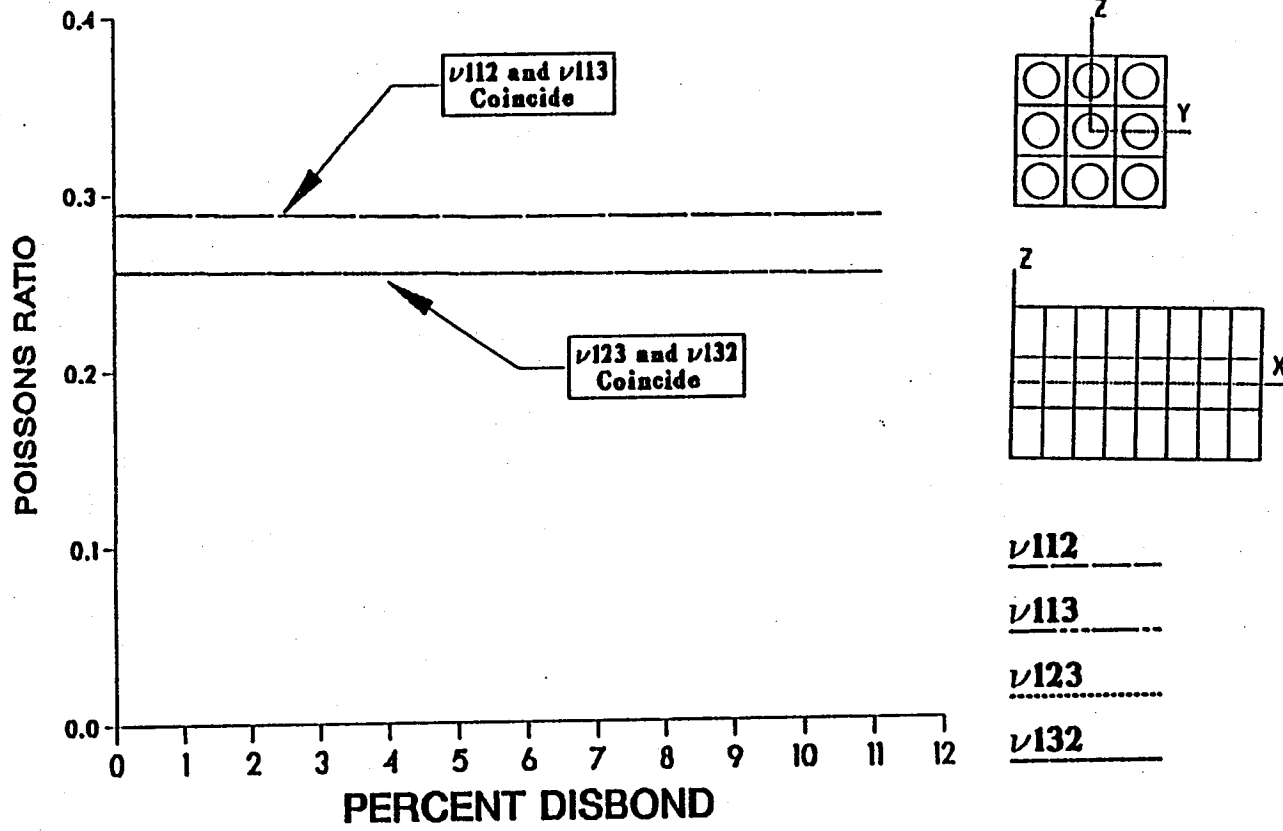


Figure 5.6 – Effect of Center Fiber Debonding on Poisson's Ratio at High Temperature

EFFECT OF FIBER DEBONDING ON SHEAR MODULUS - G_{12} , G_{13} , G_{23} HIGH TEMPERATURE (1500 °F)

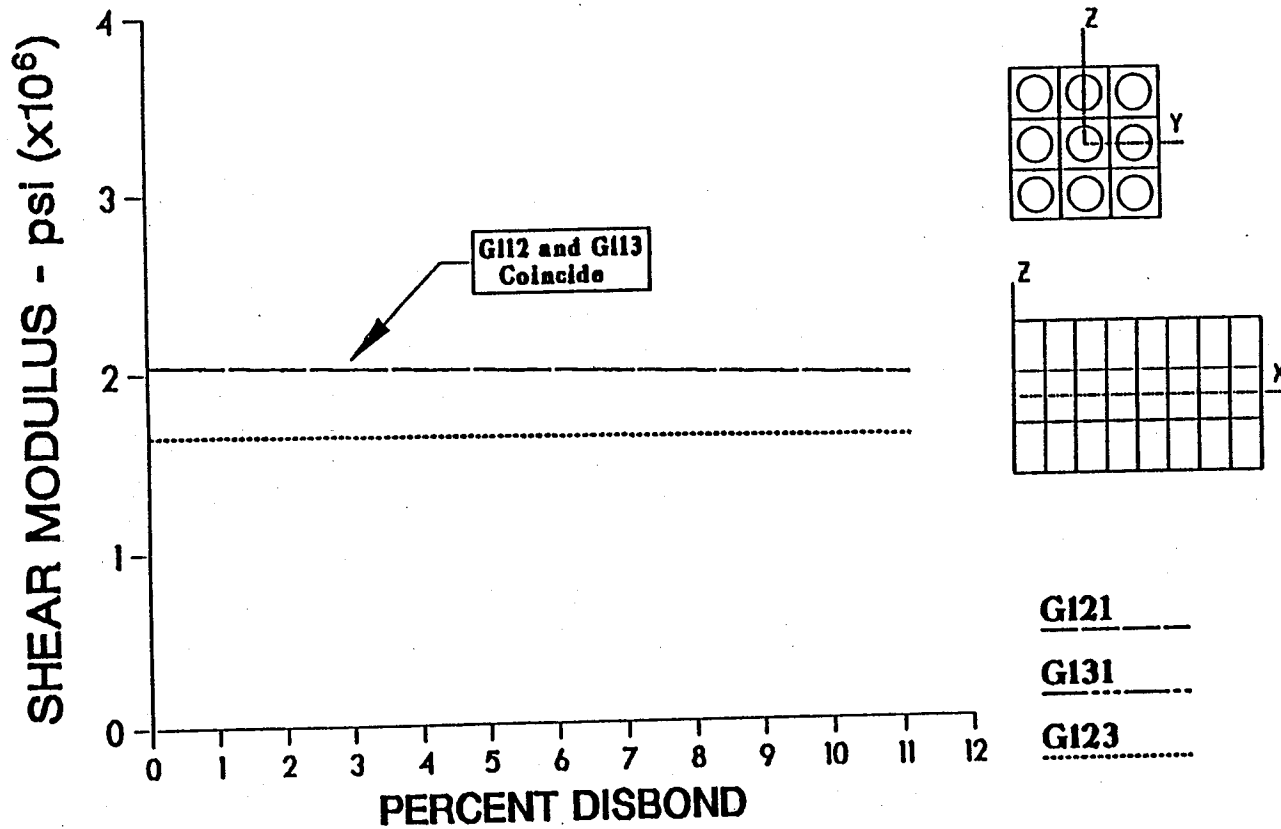


Figure 5.7 – Effect of Center Fiber Debonding on Shear Modulus at High Temperature

**EFFECT OF FIBER DEBONDING ON
THERMAL EXPANSION COEFFICIENT (TEC) - α_{111} , α_{122} , α_{133}
HIGH TEMPERATURE (1500 °F)**

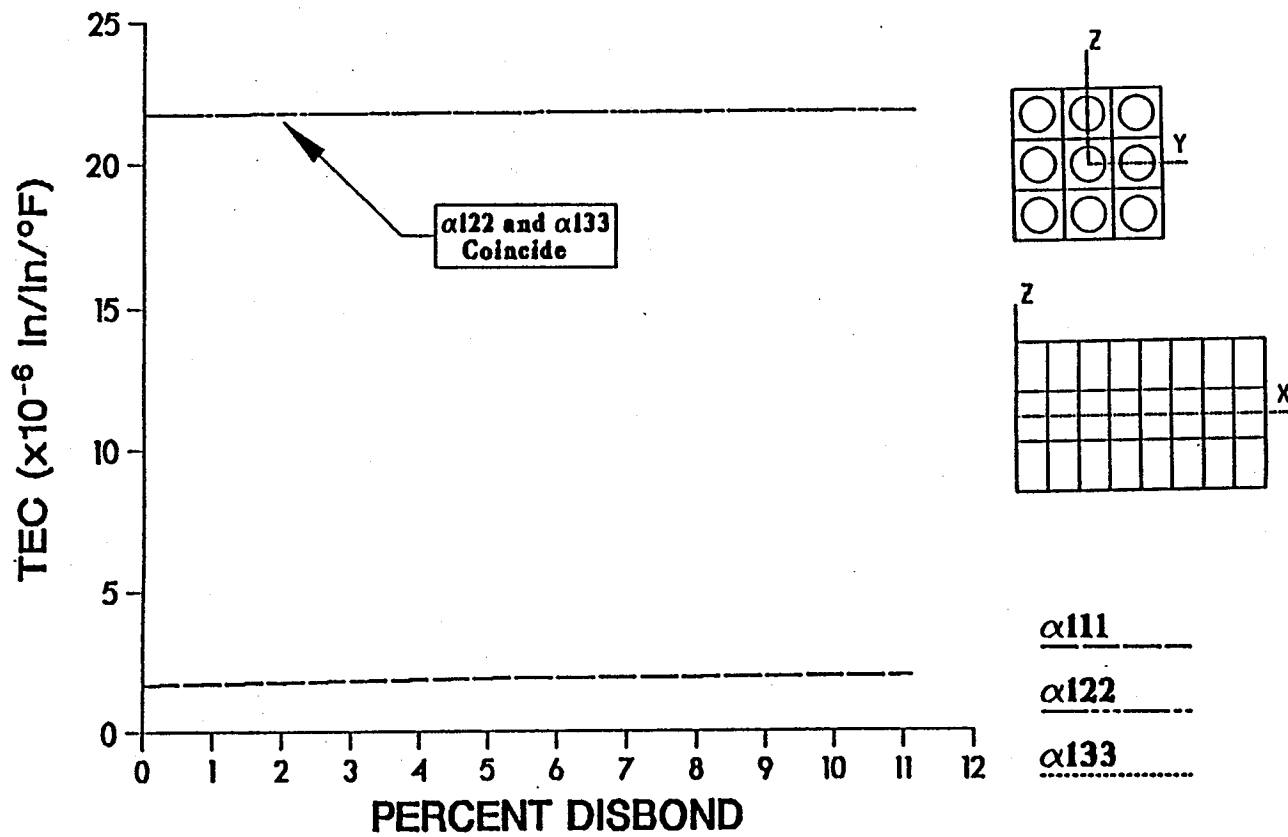


Figure 5.8 – Effect of Center Fiber Debonding on Thermal Expansion Coefficient at High Temperature

Note that these plots reflect a little over eleven percent debonding of the entire composite. This is a result of releasing only the center fiber for these cases considered here. The 11% debonding value shown on these plots represents the point at which the center fiber is totally debonded and the surrounding eight fibers are fully bonded to the matrix. This yields just over eleven percent (or one ninth) of the total circumferential area of all fibers not bonded to the matrix. When the center fiber is considered completely debonded it is still connected to the matrix material by a ring of nodes in the plane of symmetry. This residual attachment of the fiber's circumference to the matrix material can add some stiffness transversely and in shear.

The next series of conditions considered were when all nine fibers in the model were debonded symmetrically and room temperature conditions were imposed. Debonding was obtained by simultaneously removing the connectivity between fiber and matrix for two individual finite element lengths, one from each end of the model, to assure symmetry. In this case the percent debonding can go up to 100% of the total fiber length. Once again, the connectivity of a ring of nodes in the plane of symmetry around each fiber was maintained at 100% debonding. Material properties were calculated by applying each of the loading conditions described earlier. These results were plotted to show the effect of fiber debonding on each property when all fibers were equally debonded (figures 5.9 – 5.12). As before, the least-squares method was used to fit an equation to each of these lines.

Fiber debonding was then evaluated for high temperature conditions. All nine fibers were released as described above using material properties that reflected a use temperature of 1500° F. Material properties were calculated and

EFFECT OF FIBER DEBONDING ON MODULUS - E11, E122, E133

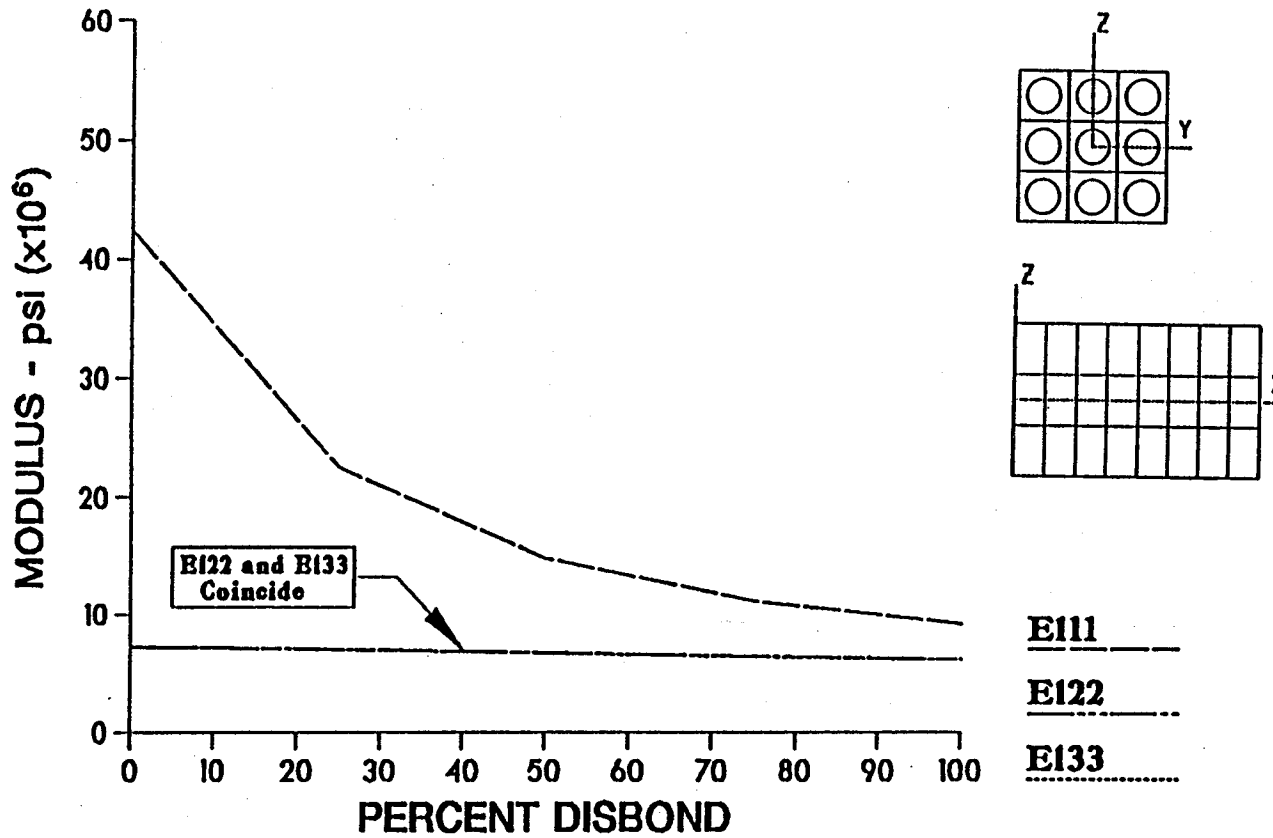


Figure 5.9 – Effect of Total Fiber Debonding on Modulus at Room Temperature

EFFECT OF FIBER DEBONDING ON POISSONS RATIO - ν_{112} , ν_{113} , ν_{123} , ν_{132}

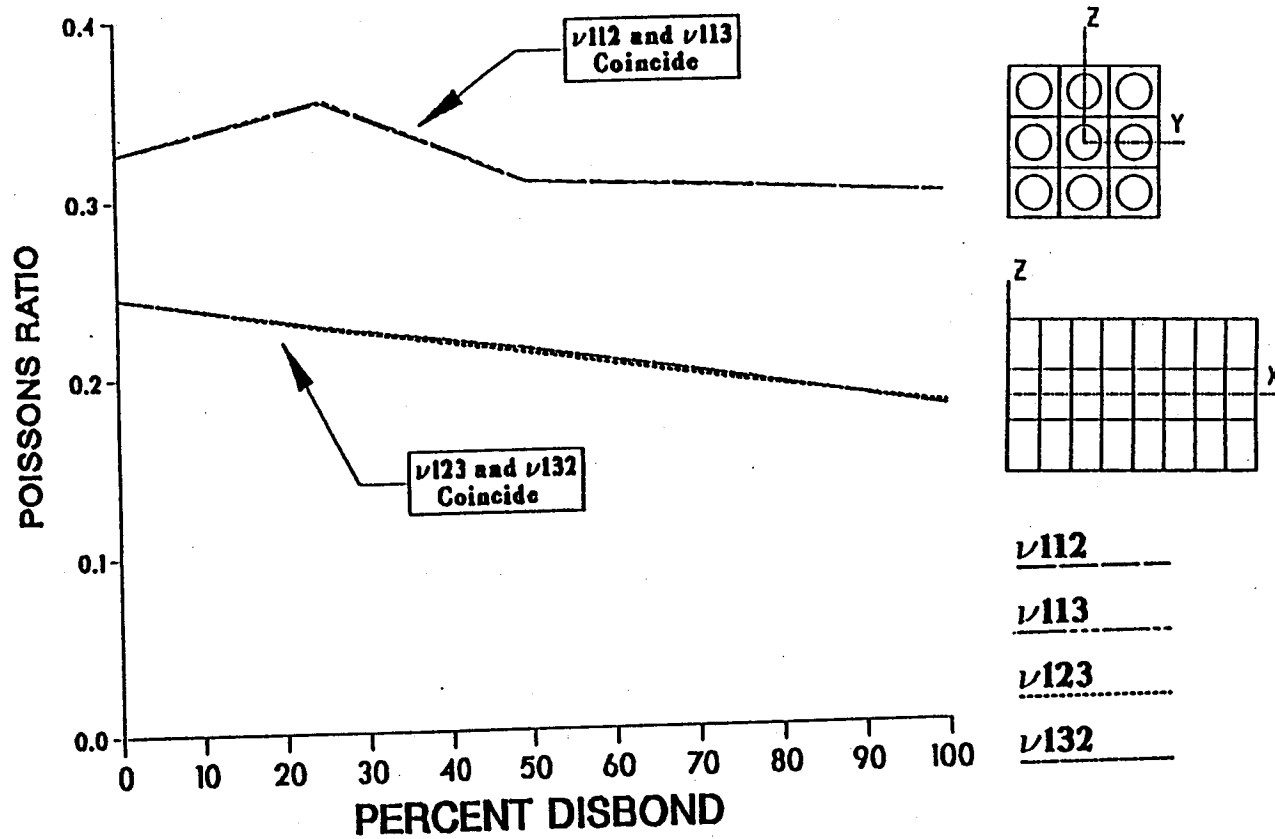


Figure 5.10 - Effect of Total Fiber Debonding on Poisson's Ratio at Room Temperature

EFFECT OF FIBER DEBONDING ON SHEAR MODULUS - G121, G131, G123

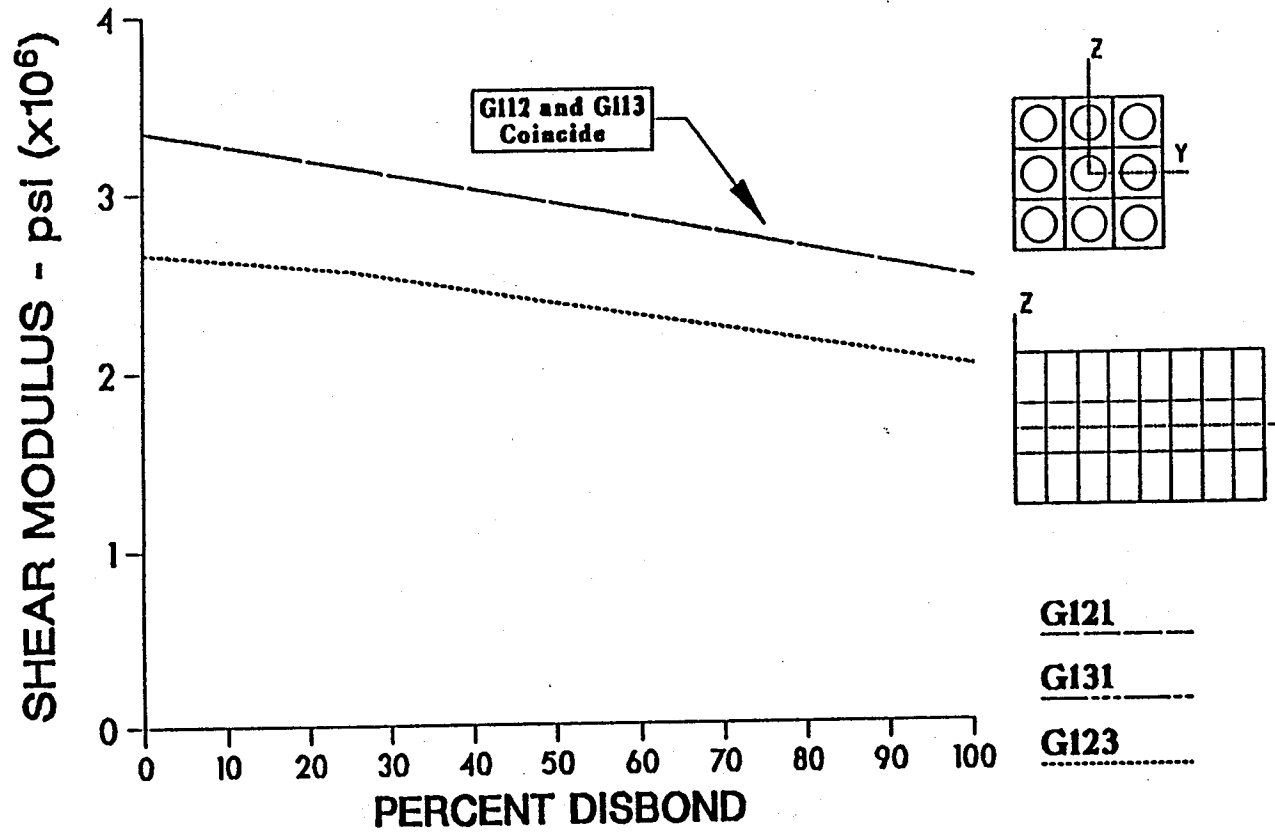


Figure 5.11 – Effect of Total Fiber Debonding on Shear Modulus at Room Temperature

**EFFECT OF FIBER DEBONDING ON
THERMAL EXPANSION COEFFICIENT (TEC) - α_{11} , α_{122} , α_{133}**

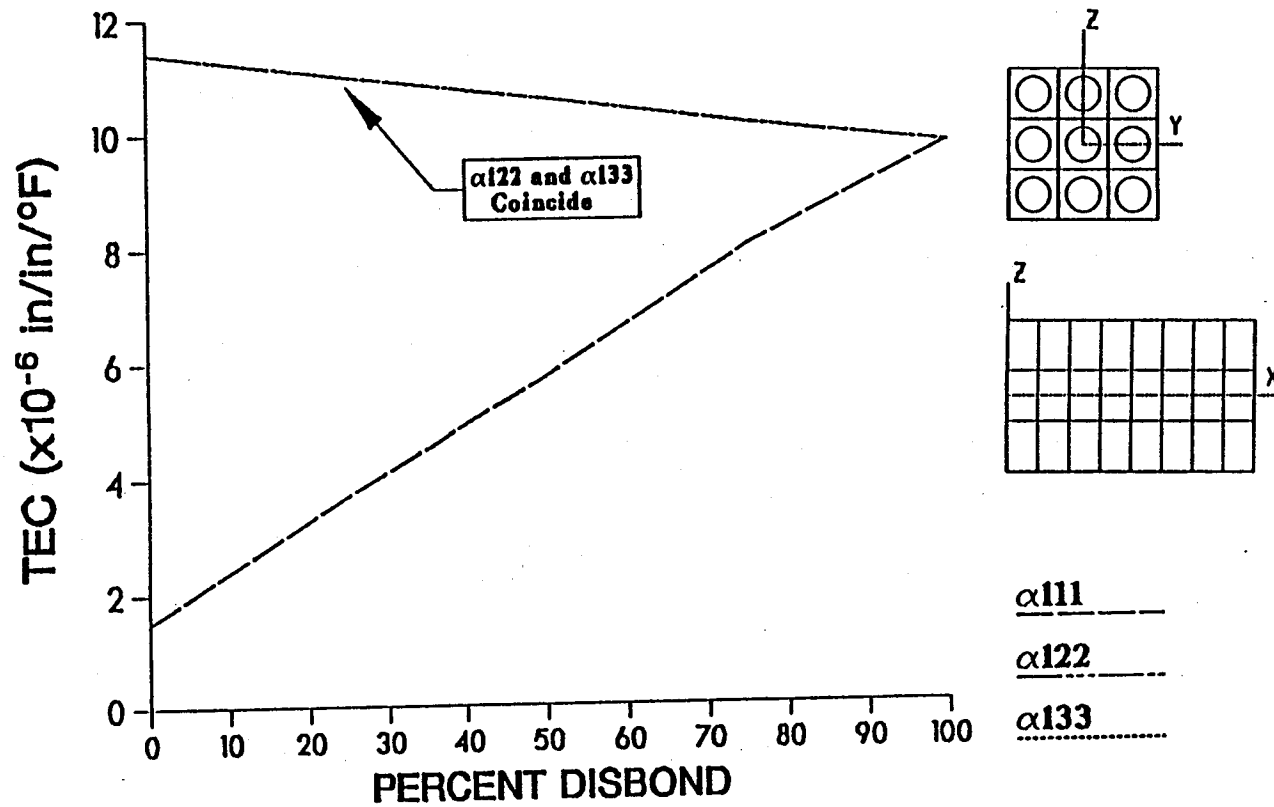


Figure 5.12 – Effect of Total Fiber Debonding on Thermal Expansion Coefficient at Room Temperature

plotted for varying degrees of fiber debonding ranging from 0% to 100% debonding (figures 5.13 - 5.16). These results show the effect of high temperature on composite material properties with fibers debonding in groups. Least-square equations describing the material property changes due to this effect were calculated and are discussed later.

EFFECT OF FIBER DEBONDING ON MODULUS - E111, E122, E133 HIGH TEMPERATURE (1500 °F)

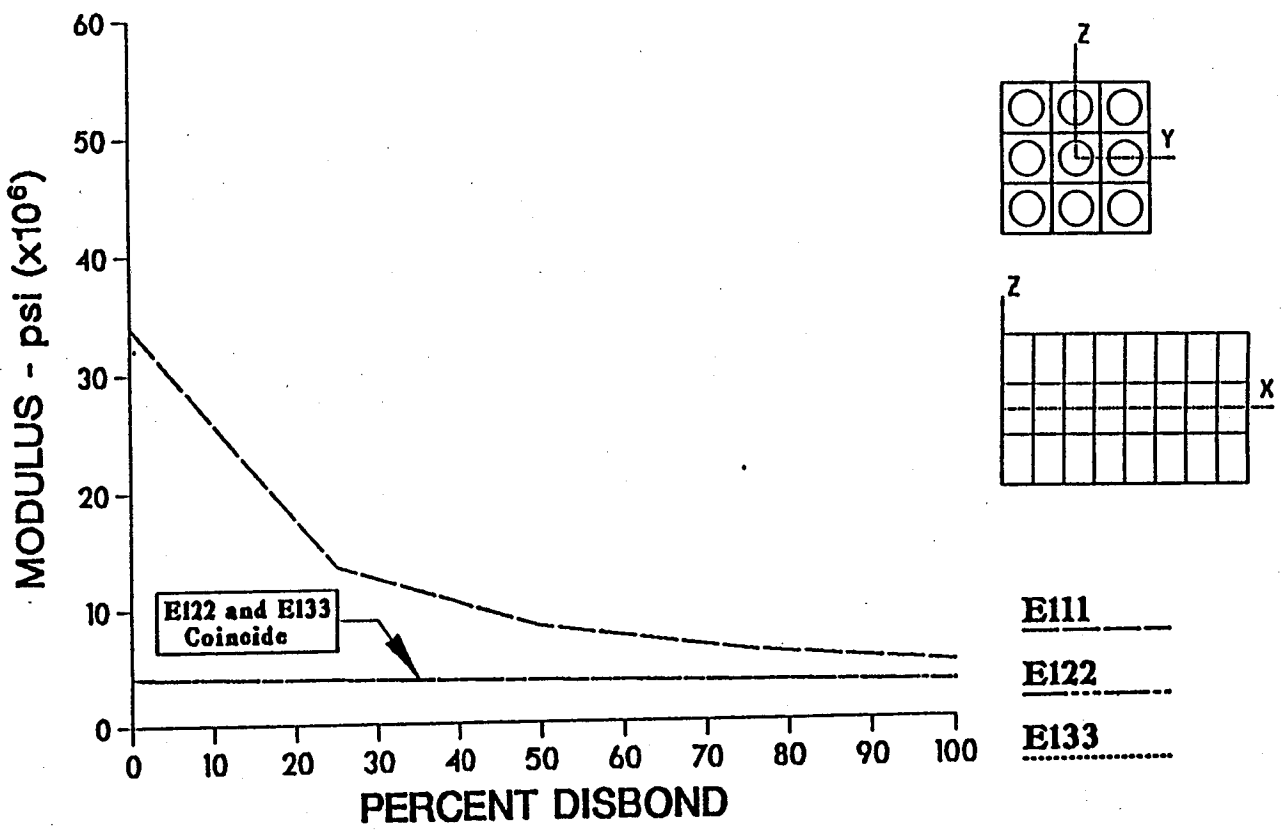


Figure 5.13 – Effect of Total Fiber Debonding on Modulus at High Temperature

**EFFECT OF FIBER DEBONDING ON
POISSONS RATIO - ν_{112} , ν_{113} , ν_{123} , ν_{132}
HIGH TEMPERATURE (1500 °F)**

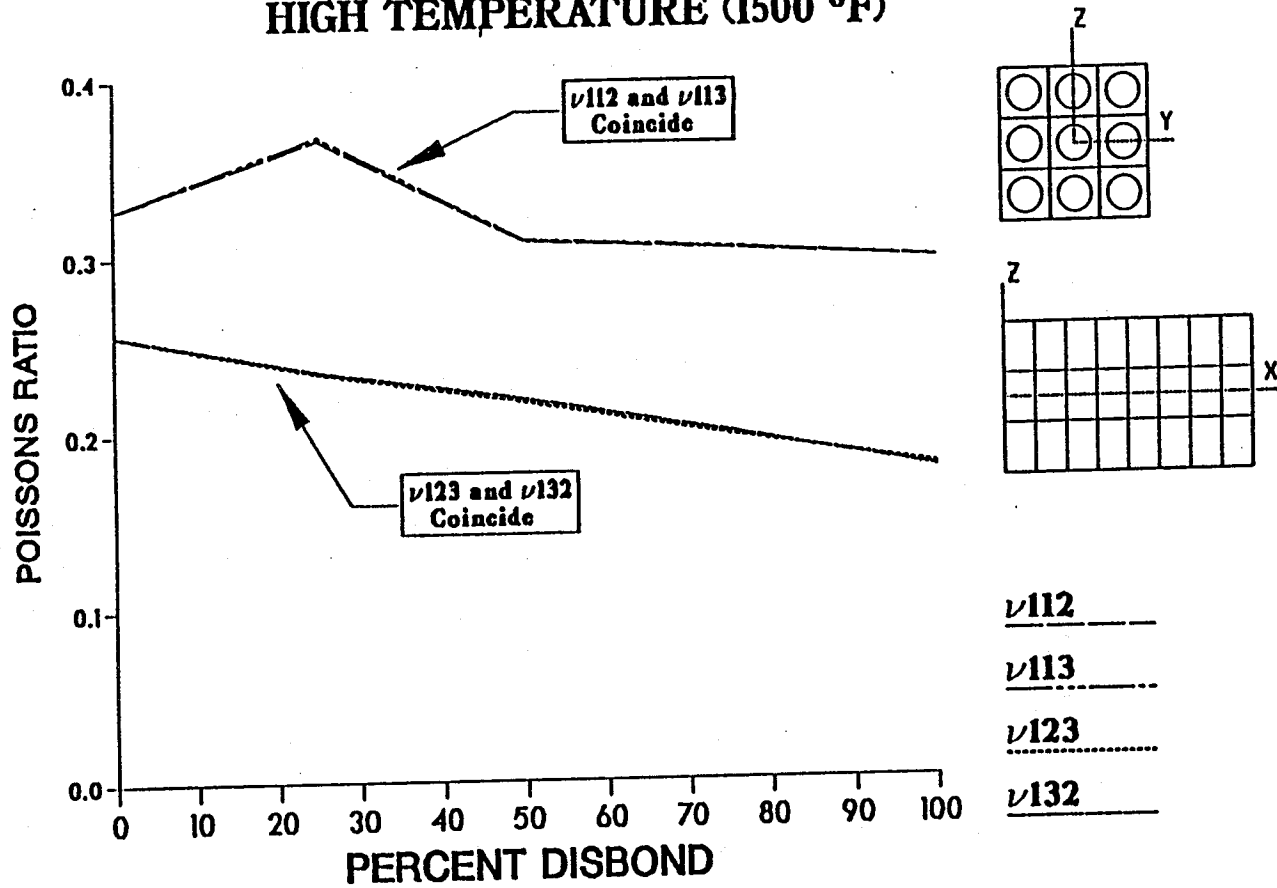


Figure 5.14 – Effect of Total Fiber Debonding on Poisson's Ratio at High Temperature

**EFFECT OF FIBER DEBONDING ON
SHEAR MODULUS - G_{12} , G_{13} , G_{23}
HIGH TEMPERATURE (1500 °F)**

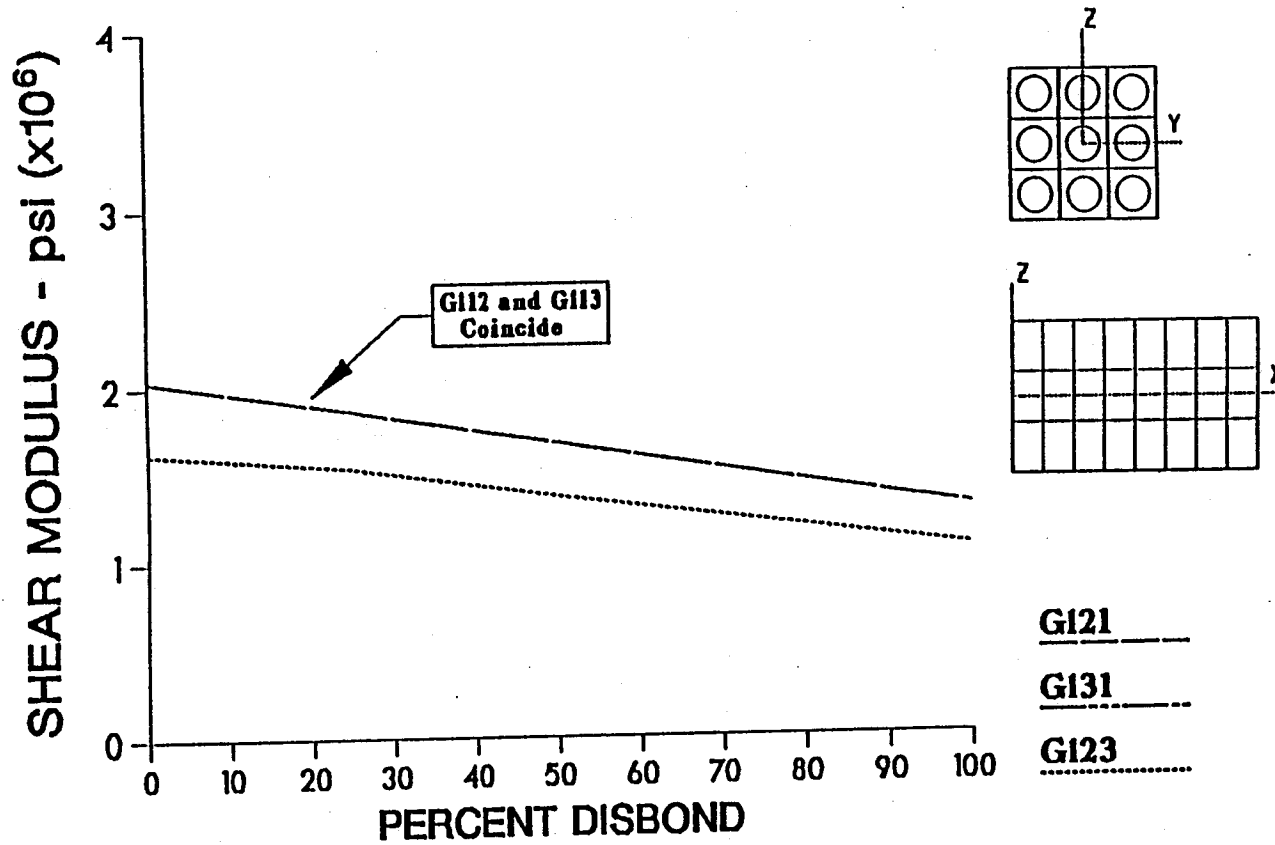


Figure 5.15 – Effect of Total Fiber Debonding on Shear Modulus at High Temperature

**EFFECT OF FIBER DEBONDING ON
THERMAL EXPANSION COEFFICIENT (TEC) - α_{111} , α_{122} , α_{133}
HIGH TEMPERATURE (1500 °F)**

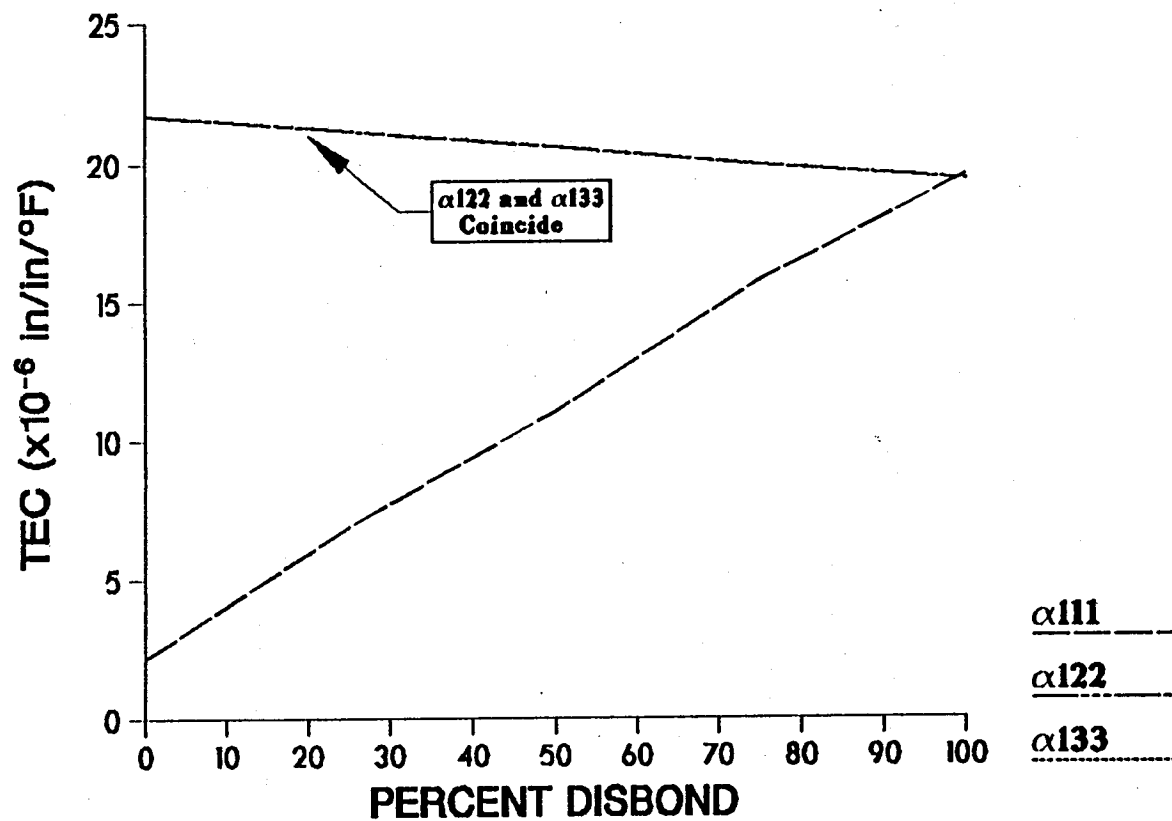


Figure 5.16 – Effect of Total Fiber Debonding on Thermal Expansion Coefficient at High Temperature

CHAPTER 6

RESULTS

The degradation in the following material properties is influenced by the difference in the corresponding fiber and matrix material properties. As the fibers become structurally inactive then the matrix material properties will have a more significant role in determining the composite's global properties. If the difference between fiber and matrix properties is not great then little change will be seen globally. Therefore there are two parts in assessing the sensitivity of a composite's material properties to fiber debonding: 1) the physical interaction between fiber and matrix as stresses are transferred between the two and 2) the relative difference between the constituent's material properties. Therefore, while viewing the following results, consideration must be given to the fact that although a property is declared to be insensitive to debonding using these materials (P100/Copper) the apparent insensitivity may be due to a small difference in constituent material properties. In some cases, it will be seen that a composite material property can be lower than that of the lowest constituent property.

6.1) Room Temperature Moduli with Center Fiber Debonding

Consider the results portrayed in figure 5.1. This figure shows the degradation of the modulus in the 11, 22 and 33 directions due to debonding of the center fiber only. These results reveal that the longitudinal modulus has decreased by about 8% while debonding was at 11.1% of the total circumferential fiber area in the model. When the least squares function approximation is used to quantify this line the resulting equation is found to be

$$E_{111} = 5.706 \times 10^7 - (4.368 \times 10^5)P \quad 6.1$$

where "P" is the percent of circumferential fiber area that is debonded.

E_{122} and E_{133} were solved for by utilizing the results from different loading conditions but were consistently calculated to be virtually equally to each other as shown by the coincident lines on figure 5.1. Because of the geometry of the idealized composite, properties in the 22 and 33 directions should be equivalent [17]. The coincidence of these lines suggest the validity of this approach. These lines can be approximated by the equation

$$E_{122} = E_{133} = 7.191 \times 10^6 - (9.499 \times 10^3)P \quad 6.2$$

The percent decrease in E_{122} and E_{133} for 11.1% total fiber area debonding is 1.5%. From these results it can be concluded that E_{111} is more sensitive to fiber

debonding than the transverse moduli. Even still, the decrease in the longitudinal modulus is reasonably small considering E_{f11} is 6 times greater than E_m . From further results it will become evident that E_{111} is the property that is the second most sensitive to fiber debonding.

6.2) Room Temperature Poisson's Ratio with Center Fiber Debonding

The effect of fiber debonding on Poisson's ratio for center fiber debonding is depicted in figure 5.2. Once again there is consistency with expected results since ν_{112} coincides with ν_{113} and ν_{123} coincides with ν_{132} and each were solved using the output from different loading conditions. The least squares approximation for ν_{112} and ν_{113} is given by

$$\nu_{112} = \nu_{113} = 0.293 - (3.590 \times 10^{-4})P \quad 6.3$$

When the center fiber is completely debonded (11.1% total fiber length debonding), ν_{112} and ν_{113} have degraded by 0.5%. This is a very small amount and may be considered insignificant implying that ν_{112} and ν_{113} are quite insensitive to fiber debonding. This insensitivity may be due to the small difference between ν_{f12} and ν_m (ν_m is 1.5 times larger than ν_{f12}).

ν_{123} and ν_{132} have a least squares approximation of

$$\nu_{123} = \nu_{132} = 0.246 - (3.327 \times 10^{-4})P \quad 6.4$$

Since ν_m is 1.2 times greater than ν_{f23} and a 1.6% decrease in ν_{123} is witnessed when total center fiber debonding is achieved; it can be concluded that geometric effects dominate over the effect of the relative increase in the role of the higher matrix Poisson's ratio. From these results we can truly say that ν_{123} is more sensitive to fiber debonding than ν_{112} . Given the same amount of debonding, there was relatively less degradation of ν_{112} than ν_{123} even though the difference between the constituent's respective Poisson's ratios was greater.

6.3) Room Temperature Shear Moduli with Center Fiber Debonding

The decrease in shear moduli due to center fiber debonding is shown in figure 5.3. As can be expected, G_{112} and G_{113} are coincident, even though they are calculated from the results of different loading conditions. G_{112} decreased by 3% as a result of complete debonding of the center fiber. Note that G_m is six times larger than G_{f12} and yet there is a decrease in G_{112} as increasing amounts of the center fiber become structurally inactive. The least squares linear approximation of the G_{112} and G_{113} is given by

$$G_{112} = G_{113} = 3.357 \times 10^6 - (9.495 \times 10^3)P \quad 6.5$$

Figure 5.3 also shows the effect of center fiber debonding on G_{123} . The value of G_{123} decreased by 2% when the center fiber was completely debonded, a decrease of structurally active fiber by 11.1%. Note again that though G_{f23} is nine times less than G_m , there is a decrease in G_{123} as more of the fiber is

debonded. Matrix properties would be expected to play a more significant role in the determination of the composite's global properties as increasing amounts of the fiber become structurally inactive. The approximate equation for the degradation of G_{123} is given by

$$G_{123} = 2.720 \times 10^6 - (4.780 \times 10^3)P \quad 6.6$$

G_{112} , G_{113} as well as G_{123} can be considered to be relatively insensitive to the debonding of the center fiber due to the small changes in these material properties.

6.4) Room Temperature Thermal Expansion Coefficients with Center Fiber Debonding

The thermal expansion coefficients are plotted in figure 5.4. The lines representing the transverse thermal expansion coefficients are coincident, as to be expected. The debonding conditions considered here produced a decrease in the transverse thermal expansion coefficients by 0.3%. This decrease is minimal and may be considered to be insignificant. Note also that α_m is only 1.75 times greater than α_{f22} . The least squares approximation of α_{122} and α_{133} is given by

$$\alpha_{122} = \alpha_{133} = 1.141 \times 10^{-5} + (3.003 \times 10^{-9})P \quad 6.7$$

The line describing the change in the longitudinal thermal expansion coefficient is also displayed in figure 5.4. α_{111} increased by 17.1% when the center fiber was totally debonded, which is equivalent to 11.1% debonding of the total fiber area. The longitudinal thermal expansion coefficient for the fiber material is negative but α_m is positive. This difference may be the cause of such a dramatic increase in α_{111} . Of all the material properties considered so far, α_{111} seems to be the most sensitive to center fiber debonding. This increase in α_{111} may be considered significant. The least squares linear approximation of the line depicting the increase in α_{111} on figure 5.4 is given by

$$\alpha_{111} = 1.226 \times 10^{-6} + (1.362 \times 10^{-8})P \quad 6.8$$

Analysis of the curve depicting the increase in α_{111} indicates that most of the increase occurs initially and then the line tends to decrease in slope. This implies a slightly nonlinear relationship between α_{111} and the amount of center fiber debonding. Using a second order least squares equation to approximate the equation of this line we find

$$\alpha_{111} = 1.171 \times 10^{-6} + (4.783 \times 10^{-8})P - (3.079 \times 10^{-9})P^2 \quad 6.9$$

6.5) High Temperature Moduli with Center Fiber Debonding

Center fiber debonding at high temperature is now to be considered. The model was changed slightly to allow for symmetric debonding and the constituent material properties were adjusted to reflect a use temperature of 1500°F. In figure 5.5 the degradation of longitudinal and transverse moduli is represented. E_{111} is seen to decrease by 7.3% when the center fiber is completely debonded. This is less of a decrease than observed for room temperature E_{111} , but this difference is not significant. The least squares linear approximating equation for the line depicting the decrease of E_{111} in figure 5.5 follows

$$E_{111} = 4.681 \times 10^7 - (3.096 \times 10^5)P \quad 6.10$$

The longitudinal modulus of the fiber alone is over 10 times greater than that of the matrix. Since 11.1% of the structural effect of the fiber mass has been removed due to the total debonding of the center fiber yet only a 7.3% decrease in E_{111} is witnessed and considering E_{f11} is ten times E_m then the conclusion is that the change in E_{111} brought about by center fiber debonding is significant, but not as significant as the change seen in α_{111} .

E_{122} and E_{133} are shown to be coincident in figure 5.5. Ignoring geometric effects and considering that E_m is 11 times greater than E_{f22} , it would be expected that as the center fiber becomes structurally inactive and the matrix material gains a larger relative percentage in the determination of the composite's properties, there would be an increase in the composite's transverse modulus. Due to geometric effects, the opposite occurs. E_{122} is shown to have

decreased by 2% when the center fiber is debonded. This decrease is not significant in magnitude and is mainly due to the reduced effective cross-sectional area, and the subsequent reduced transverse stiffness of the composite, as resulting from the debonding of the center fiber. The least squares equation describing the decrease is given by

$$E_{122} = E_{133} = 4.063 \times 10^6 - (7.879 \times 10^3)P \quad 6.11$$

This decrease may be due to the fact that when the fiber debonds there is, in effect, a cylindrical void where the fiber use to be. This hole removes some of the stiffness from the model resulting in a lower transverse modulus. Note that this decrease is almost of the same percentage as the room temperature decrease in E_{122} and E_{133} .

6.6) High Temperature Poisson's Ratio with Center Fiber Debonding

In figure 5.6 the Poisson's ratios of the composite are plotted. Note again, ν_{112} runs coincident with ν_{113} , and ν_{123} is coincident with ν_{132} . ν_{112} and ν_{123} both decrease by approximately 1.5% when the center fiber is debonded fully. The least squares linear equation for ν_{112} and ν_{113} is given by

$$\nu_{112} = \nu_{113} = 0.289 - (3.726 \times 10^{-4})P \quad 6.12$$

and for ν_{123} and ν_{132} it is

$$\nu_{123} = \nu_{132} = 0.256 - (3.718 \times 10^{-4})P \quad 6.13$$

When compared to the room temperature results, it is evident that there is a small increase in the change of ν_{112} and ν_{113} , and the change in ν_{123} and ν_{132} is about the same. From these results it may be concluded that temperature has little effect on the rate of degradation of these material properties even though the actual value of the properties may be different due to the use temperature.

ν_{112} , ν_{113} , ν_{123} and ν_{132} may all be considered to be relatively insensitive to center fiber debonding.

6.7) High Temperature Shear Moduli with Center Fiber Debonding

The effect of high temperature fiber debonding on shear moduli is shown in figure 5.7. G_{112} and G_{113} have degraded by almost 5% with the debonding of the center fiber. It is important to note that G_m is 3.5 times greater than G_{f12} and G_{f13} . In this case, G_m is 3.5 times greater than G_{f12} , yet G_{112} decreases as the matrix material's structural role increases. The least squares approximation of G_{112} and G_{113} is given by

$$G_{112} = G_{113} = 2.042 \times 10^6 - (8.532 \times 10^3)P \quad 6.14$$

The change in G_{112} and G_{113} at room temperature was 3% and at high temperature it was 5% when the center fiber was debonded. These changes represent the slope of the lines on their respective graphs. The difference in these slopes is not significant.

G_{123} is also represented by a line on figure 5.7. G_{123} , at high temperature, had degraded by almost 3% when the center fiber had totally debonded. G_m is 5.5 times greater than G_{f23} . Geometric effects dominate and the results indicate a decrease in G_{123} . Again, G_{123} at high temperature has been shown to degrade by approximately the same amount as at room temperature.

$$G_{123} = 1.651 \times 10^6 - (4.093 \times 10^3)P \quad 6.15$$

G_{112} , G_{113} and G_{123} can all be said to be relatively insensitive to center fiber debonding.

6.8) High Temperature Thermal Expansion Coefficients with Center Fiber Debonding

Figure 5.8 contains the plots that represent the changes in thermal expansion coefficients at high temperature as the center fiber is debonded. Note that the lines representing α_{122} and α_{133} are coincident. α_{122} and α_{133} increased by less than 1%, an insignificant amount. The least squares approximation for α_{122} and α_{133} is given by

$$\alpha_{122} = \alpha_{133} = 2.174 \times 10^{-5} + (1.761 \times 10^{-8})P \quad 6.16$$

In figure 5.8, α_{111} shows an increase by 17.3% when the center fiber is completely debonded which represents a decrease in effective fiber area of 11.1%. This substantial increase is due to the fact that α_{f11} is negative and α_m is positive. The least squares approximation of α_{111} is given by

$$\alpha_{111} = 1.709 \times 10^{-6} + (2.612 \times 10^{-8})P \quad 6.17$$

This change in α_{111} is significant and close to the percent change in α_{111} at room temperature.

6.9) Room Temperature Moduli with All Fibers Debonding

The case when all fibers are debonded at room temperature is now considered. The effect of all the fibers debonding on the moduli of the composite is plotted in figure 5.9. The degradation of E_{111} is now obviously non-linear. E_{111} , with 100% fiber debonding, has decreased by 78.2% and is lower than E_m . The cylindrical holes left by the debonded fibers decrease the stiffness of the composite, much like a sponge. The composite can actually have a lower modulus than that of the matrix alone. Though the fibers are still defined in the finite element model the connectivity has been removed, in effect producing a large cylindrical voids along the debonded length. Displacements may then cause the fiber and matrix materials to overlap. Of course this is not realistic and is a

result of the way the modeling was done. This affect may cause the calculation of material properties to be to conservative. The least squares quadratic approximation of the equation for E_{111} is given by

$$E_{111} = 4.132 \times 10^7 - (7.685 \times 10^5)P + (4.573 \times 10^3)P^2 \quad 6.18$$

E_{122} and E_{133} are coincident and appear to be linear as seen in figure 5.9. E_{122} and E_{133} decreased by only 15% with 100% fiber debonding. Note that E_m is 19 times greater than E_{f11} . Therefore the decrease in E_{122} and E_{133} is due to the cylindrical voids in the model. The linear approximation for E_{122} and E_{133} is given by

$$E_{122} = E_{133} = 7.216 \times 10^6 - (1.069 \times 10^4)P \quad 6.19$$

6.10) Room Temperature Poisson's Ratio With All Fibers Debonding

At low levels of fiber debonding, up until about 25% debonding, ν_{112} increases. Since u is an enforced displacement and does not change, then v must be increasing in this range.

$$\nu_{112} = \frac{-\epsilon_{122}}{\epsilon_{111}} = \frac{-\frac{v}{s_2}}{\frac{u}{s_1}} = \frac{-v \times s_1}{u \times s_2} \quad 6.20$$

After 25% debonding, ν decreases with increasing debonding. The initial rise may be due to the fact that the Poisson's ratio of the fiber is smaller than that of the matrix and E_{f22} is also less than E_m . Therefore, as the fibers are released there is reduced composite stiffness in the transverse direction. As more fiber is released, geometric effects begin to control. Deflections transverse to the fiber direction are seen more in the shrinking diameters of the hollow cylinders, created by the removal of the continuity between fiber and matrix, than in displacements on the external surface of the model where the average displacement was calculated. A cubic least squares approximation was used to describe this effect.

$$\nu_{112} = \nu_{113} = 0.328 + (1.901 \times 10^{-3})P - (6.007 \times 10^{-5})P^2 + (3.826 \times 10^{-7})P^3 \quad 6.21$$

ν_{123} and ν_{132} are again coincident as seen in figure 5.10. 100% debonding brought about a decrease in ν_{123} and ν_{132} of 26.7%. The value at 100% debonding is less than that of the matrix alone. This may be due to the spongy effect of the debonded composite, where a significant percentage of the transverse displacements take place in the cylinders left by the debonded fibers, resulting in less transverse strain. The least squares approximation for the curves of ν_{123} and ν_{132} at room temperature and 0% to 100% debonding is given by

$$\nu_{123} = \nu_{132} = 0.244 - (6.532 \times 10^{-4})P \quad 6.22$$

6.11) Room Temperature Shear Moduli With All Fibers Debonding

Figure 5.11 represents the results of debonding on the shear moduli at room temperature. G_{123} decreased by 24% when the fibers were completely debonded and, as with ν_{123} , its value is less than that of the pure matrix. The least squares approximation of the degradation of G_{123} is given by

$$G_{123} = 2.690 \times 10^6 - (6.606 \times 10^3)P \quad 6.23$$

G_{112} and G_{113} are again coincident as seen in figure 5.11. Both these properties decreased by 25% when 100% debonding had been achieved. As before, at 100% debonding, these properties are lower in value than that of the matrix material alone, presumably due to the sponge effect discussed earlier. The linear approximation of this degradation is given by the following equation

$$G_{112} = G_{113} = 3.350 \times 10^6 - (8.430 \times 10^3)P \quad 6.24$$

6.12) Room Temperature Thermal Expansion Coefficients With All Fibers Debonding

Figure 5.12 shows the change in the composite's thermal expansion coefficients when debonding is taken from 0% to 100% at room temperature. α_{111}

increases drastically as the debonding increases. At 100% debonding, α_{111} has increased by 557%. The value of α_{111} at 100% debonding is virtually identical to that of the matrix alone. The least squares equation for the increase in α_{111} is given by

$$\alpha_{111} = 1.570 \times 10^{-6} + (8.357 \times 10^{-8})P \quad 6.25$$

The degradation of α_{122} and α_{133} is also depicted in figure 5.12. Both α_{122} and α_{133} degraded by only 14% when all fibers were completely debonded. This is a very insignificant amount. The significance in these results is that the final value for α_{122} and α_{133} is virtually equal to α_m . This would tend to imply that the sponge effect discussed earlier has little effect on thermal expansion. The equation for this degradation is given by

$$\alpha_{122} = \alpha_{133} = 1.140 \times 10^{-5} - (1.658 \times 10^{-8})P \quad 6.26$$

It is significant to note that α_{111} , α_{122} , and α_{133} all approach α_m when the composite is approaching a quasi-monolithic state. Here, geometric effects seem to have little effect.

6.13) High Temperature Moduli With All Fibers Debonding

Consider now high temperature (1500°F) conditions while debonding takes place. In figure 5.13 the moduli of the nine cell model are plotted as the percent disbond is increased. Note that E_{111} is non-linear and degrades rapidly during initial debonding but tends to stabilize as debonding approaches 100%. This curve is similar in shape to that of room temperature E_{111} except it is shifted down the ordinate. The total decrease in E_{111} is 85.6% and its value at 100% debonding is lower than that of the matrix alone. Again, this is probably due to the sponge effect. The least squares quadratic approximation of E_{111} is given by

$$E_{111} = 3.237 \times 10^7 - (7.352 \times 10^5)P + (4.727 \times 10^3)P^2 \quad 6.27$$

The effect of high temperature does not seem to significantly change the rate of degradation of the longitudinal modulus due to debonding but it does change the actual value of the modulus at any given degree of debonding.

E_{122} and E_{133} are shown to coincide in figure 5.13. E_{122} and E_{133} both degrade by 20.6% at 100% fiber disbond. Note also that E_m is 11 times greater than E_{f22} and E_{f33} . The least squares approximation of the plot of E_{122} and E_{133} is given by the following equation

$$E_{122} = E_{133} = 4.084 \times 10^6 - (8.471 \times 10^3)P \quad 6.28$$

It is of interest to note that the difference between E_{111} and E_{122} at 100% disbond may be attributed to the geometry of the "holes" left by the debonding fibers. It would be expected that at 100% debonding the composite would display isotropic behavior except for the effect of the "holes" left by the debonded fibers. The presences of these cylindrical "holes" also allow the composite moduli to be lower than that of the matrix alone.

6.14) High Temperature Poisson's Ratio With All Fibers Debonding

Figure 5.14 shows the effect of fiber debonding on the Poisson's ratios at high temperature for all fibers debonding. In this figure ν_{112} and ν_{113} are coincident as well as ν_{123} and ν_{132} . As with the room temperature results, ν_{112} increases initially and then begins to decrease at about 25% debonding. The total decrease in ν_{112} and ν_{113} , from 0% debonding to 100% debonding, is 9.1%.

$$\nu_{112} = \nu_{113} = 0.330 + (2.633 \times 10^{-3})P - (7.972 \times 10^{-5})P^2 + (5.041 \times 10^{-7})P^3 \quad 6.29$$

ν_{123} and ν_{132} decrease linearly with fiber debonding as seen in figure 5.14. These material properties decreased by 29.6% when 100% debonding was reached. The equation approximating ν_{123} and ν_{132} is given by

$$\nu_{123} = \nu_{132} = 0.255 - (7.522 \times 10^{-4})P \quad 6.30$$

6.15) High Temperature Shear Moduli With All Fibers Debonding

As in figure 5.11, G_{112} and G_{113} are coincident in figure 5.15. This figure shows a linear decrease in G_{112} and G_{113} with fiber debonding. G_{112} and G_{113} decreased by 35.7% when the composite was at 100% debonding even though G_m is 3.5 times greater than G_{f12} . This is the same trend seen at room temperature. The least squares approximation of the line representing G_{112} and G_{113} is given by

$$G_{112} = G_{113} = 2.036 \times 10^6 - (7.264 \times 10^3)P \quad 6.31$$

The degradation of G_{123} , as seen in figure 5.15, is slightly non-linear both at high temperature and at room temperature (figure 5.11). G_{123} shows a slight increase in slope after about 25% debonding. This increase is so slight; that a linear approximation of the line was used, as in the room temperature case. The linear approximation of G_{123} obtained by the least squares method is given by

$$G_{123} = 1.652 \times 10^6 - (5.690 \times 10^3)P \quad 6.32$$

The total decrease in G_{123} is 34.2% at 100% disbond with G_m being 5.5 times greater than G_{f23} . Here again, as in many of the cases presented, there is a higher value of the matrix's property yet a decrease in the composite's property is witnessed with increasing levels of debonding. This trend must again be attributed to the effect of the cylindrical "holes" left by the debonding fiber.

6.16) High Temperature Thermal Expansion Coefficients With All Fibers Debonding

Figure 5.16 depicts the change in the composite's thermal expansion coefficients through the range of 0% to 100% debonding at 1500°F. As the percent disbond increased, a significant increase in α_{111} was evident. At 100% debonding, α_{111} had increased by 799% and was virtually the same as α_{122} and α_{133} at 100% debonding. This implies that the cylindrical "holes" do not affect the isotropic thermal expansion behavior of the completely debonded composite. The linear approximation for this increase in α_{111} is given by the equation

$$\alpha_{111} = 2.359 \times 10^{-6} + (1.748 \times 10^{-7})P \quad 6.33$$

α_{122} and α_{133} are also shown in figure 5.16. These values degrade with the increasing debonding of fibers. Though α_{122} and α_{133} decreased by 10.7% in the range from 0% to 100% fiber debonding, this is not a significant decrease in these values. The decrease is described by the equation

$$\alpha_{122} = \alpha_{133} = 2.174 \times 10^{-5} - (2.370 \times 10^{-8})P \quad 6.34$$

CHAPTER 7

MICROSTRESSES

Profiles of microstresses through the composite model were plotted to allow for the investigation of the stress states in the fiber and the matrix materials under different loadings. These microstresses were normalized with respect to the equivalent applied load. The loading conditions used are the same ones described earlier to find the composite's material properties. Some of these stress plots are described here and additional results are given in the appendix. Plots of microstresses were obtained only for loading conditions which produced microstresses that were significant with respect to the failure stress of the constituent in which they appeared.

7.1) Loading: σ_{xx}^e

Consider figure 7.1, each line represents the microstresses on each of the nine faces of grid points in the model (figure 3.3). This particular plot represents the normalized constituent microstresses in the 11 direction as a result of an enforced displacement in the XX direction when no debonding has been modeled. The stresses shown here are plotted along a line running from the center of the model, point "O", to point "A" on the edge of the model. Since the center fiber is not loaded, a low stress state can be seen in face 9, the unloaded

face. There is also an increase in the stress level on the inside edge of the surrounding fibers at face 9. This is the result of the additional load they must carry before it is transferred to the center fiber. The lines depicting the stress states in faces 8 and 9 are coincident in these figures. Since there are eight surrounding fibers that carry the additional load, the effect on each is not very great. Further inside the composite the stresses are transferred to the fiber through the matrix and an equal load sharing between all fibers is achieved. The figure shows that the center fiber has reached a nearly full stress state at about half the length of the model.

Figures 7.2 through 7.9 represent the constituent microstresses at varying levels of debonding of the center fiber. As debonding progresses, the load can not be transferred sufficiently through the depleted fiber-matrix interfacial area. The result is a center fiber that is less structurally active. Stress levels in the surrounding fibers increase as a result of the debonding, but since there is a community of fibers surrounding the debonding fiber, this increase is minimal.

A slight stress gradient is formed along the length of the surrounding fibers as debonding increases. This stress gradient begins to decrease as total center fiber debonding is approached. In figure 7.9, total center fiber debonding has been reached and the load that was once carried by the center fiber has been transferred to the community of surrounding fibers. At this stage the longitudinal load gradients have been eliminated and no significant increase in the stress levels of the surrounding fibers exists. Figures 7.10 through 7.12 show similar results by plotting the normalized constituent microstresses along the line segment O-C.

EFFECT OF 1.39% FIBER LENGTH DEBONDING ON CONSTITUENT MICROSTRESSES (σ_{11}) DUE TO A LOAD IN THE XX-DIRECTION

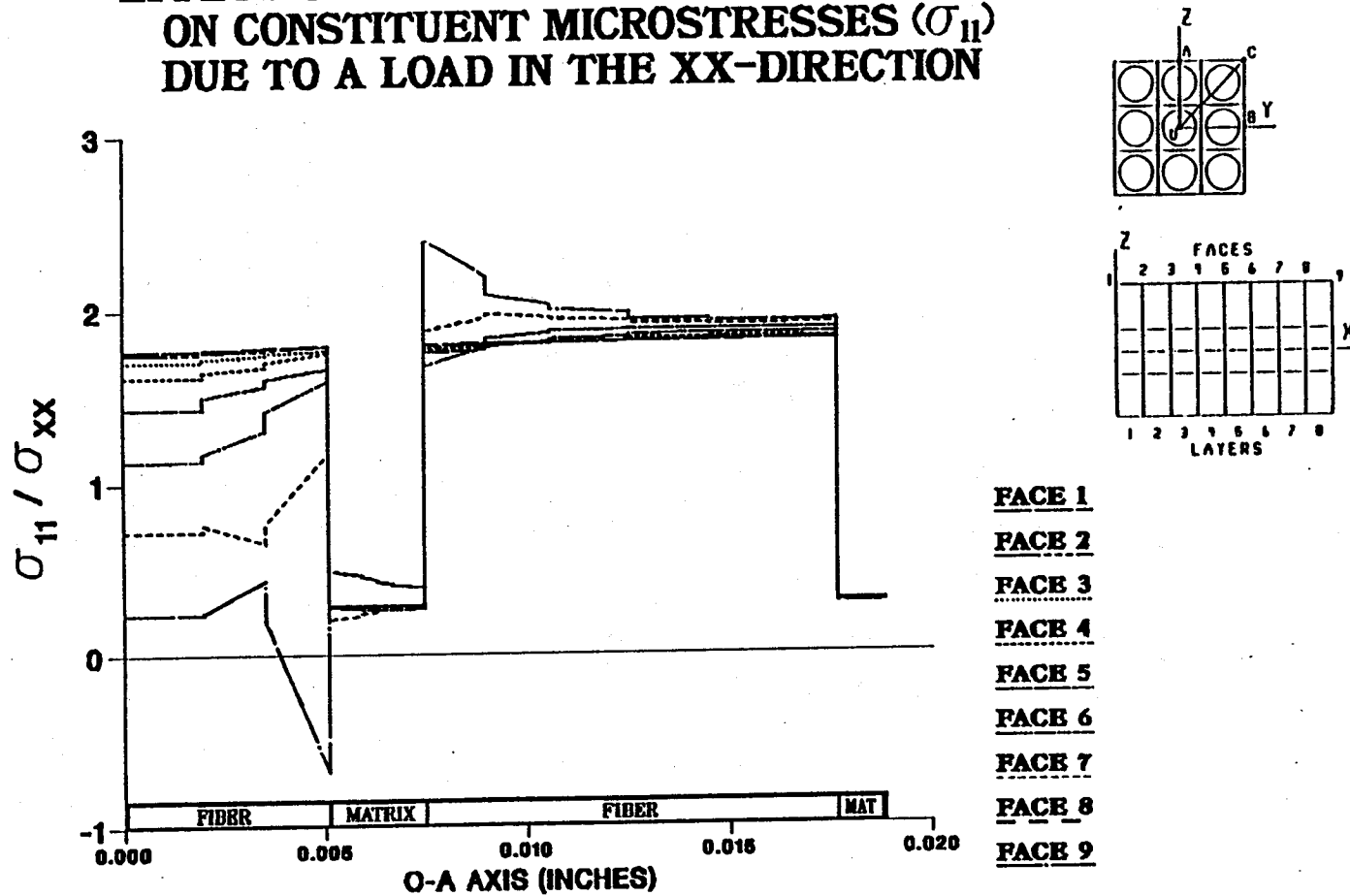


Figure 7.2 — σ_{11} Normalized Microstresses, O-A Direction, 1.39% Debonding, σ_{xx}^e Loading

EFFECT OF 2.78% FIBER LENGTH DEBONDING ON CONSTITUENT MICROSTRESSES (σ_{11}) DUE TO A LOAD IN THE XX-DIRECTION

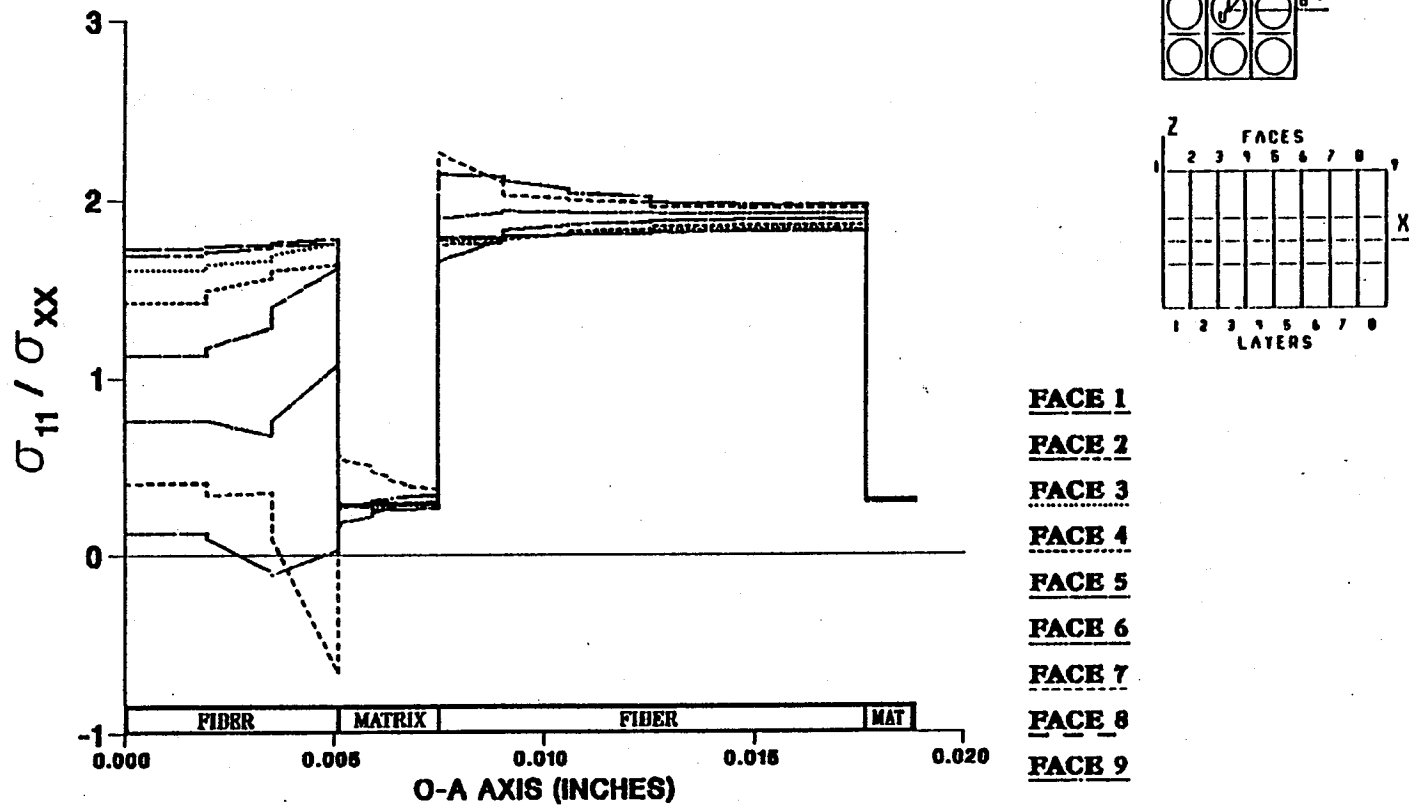


Figure 7.3 - σ_{11} Normalized Microstresses, O-A Direction, 2.78% Debonding, σ_{xx}^e Loading

EFFECT OF 4.17% FIBER LENGTH DEBONDING ON CONSTITUENT MICROSTRESSES (σ_{11}) DUE TO A LOAD IN THE XX-DIRECTION

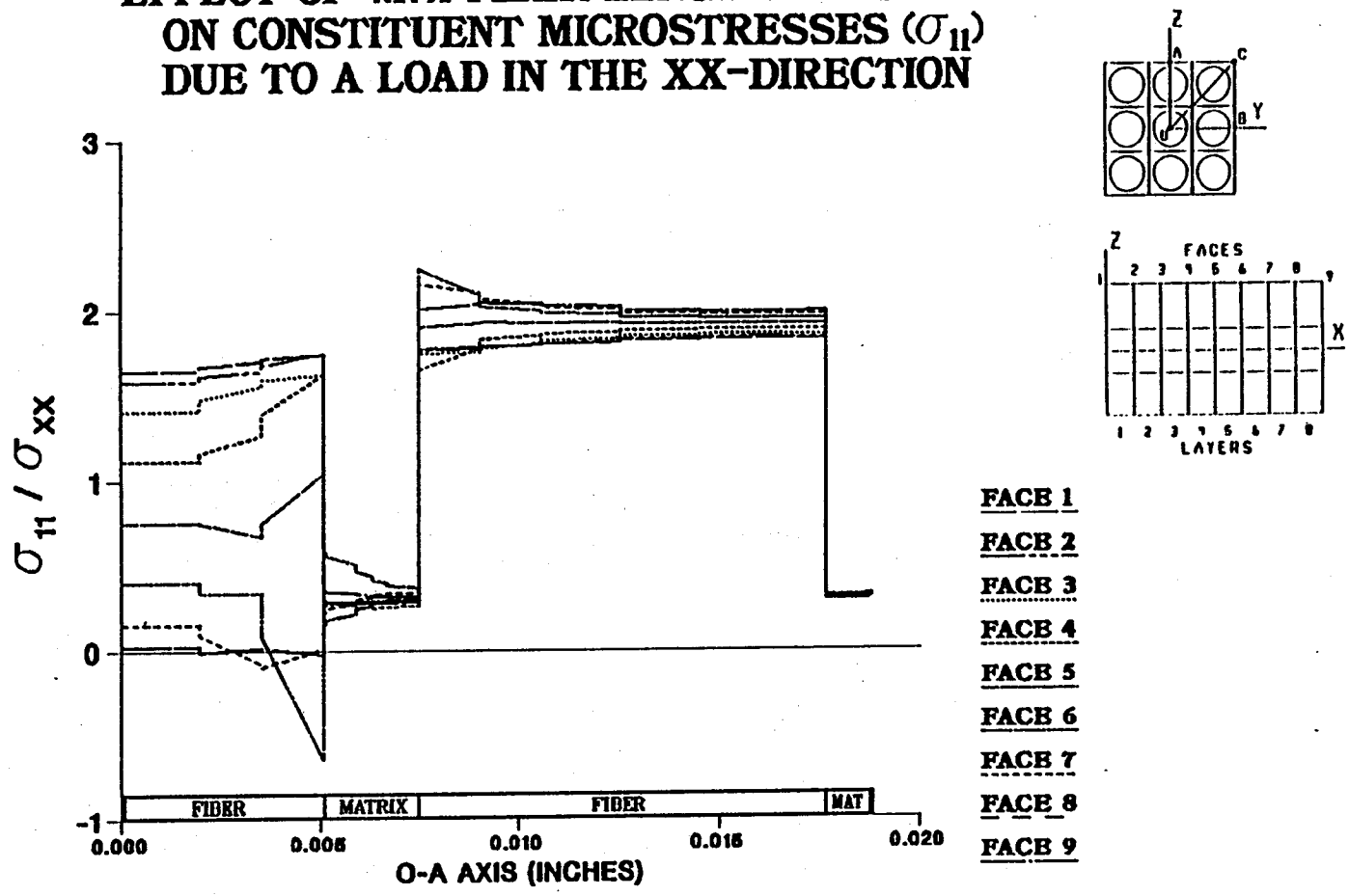
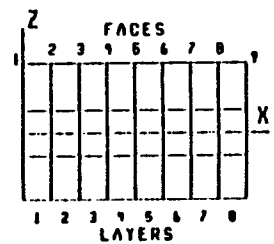
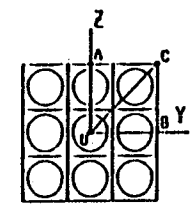
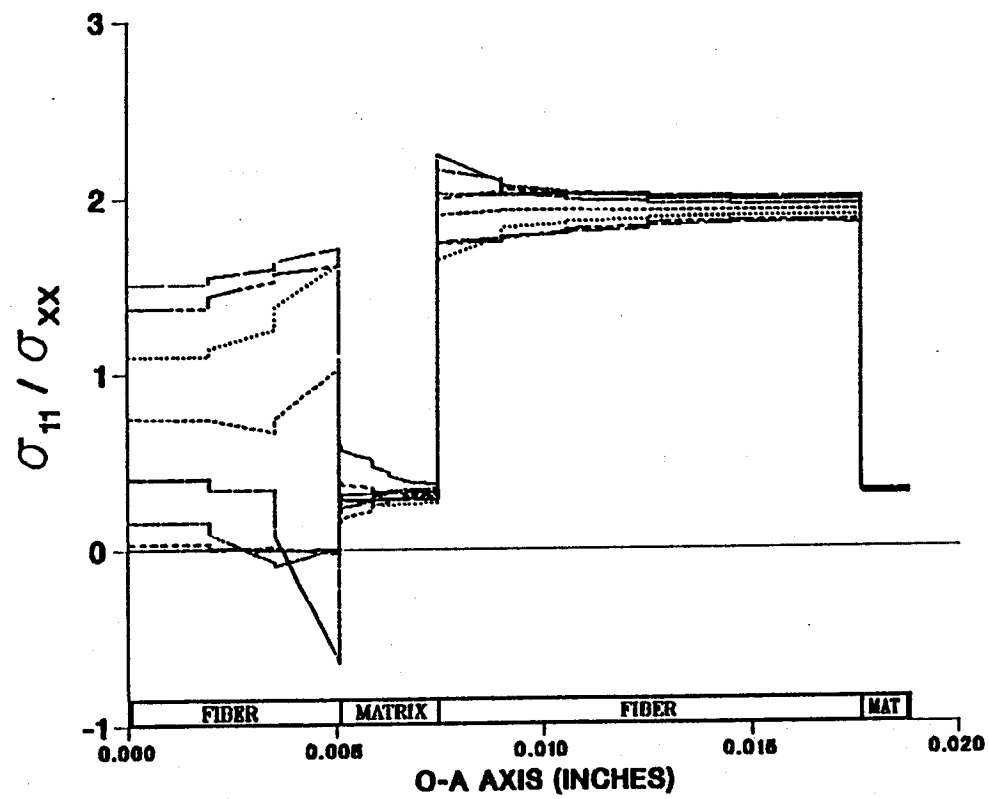


Figure 7.4 - σ_{11} Normalized Microstresses, O-A Direction, 4.17% Debonding, σ_{xx}^e Loading

EFFECT OF 5.56% FIBER LENGTH DEBONDING ON CONSTITUENT MICROSTRESSES (σ_{11}) DUE TO A LOAD IN THE XX-DIRECTION



- FACB 1
- FACB 2
- FACB 3
- FACB 4
- FACB 5
- FACB 6
- FACB 7
- FACB 8
- FACB 9

Figure 7.5 - σ_{11} Normalized Microstresses, O-A Direction, 5.56% Debonding, σ_{xx}^e Loading

EFFECT OF 6.94% FIBER LENGTH DEBONDING ON CONSTITUENT MICROSTRESSES (σ_{11}) DUE TO A LOAD IN THE XX-DIRECTION

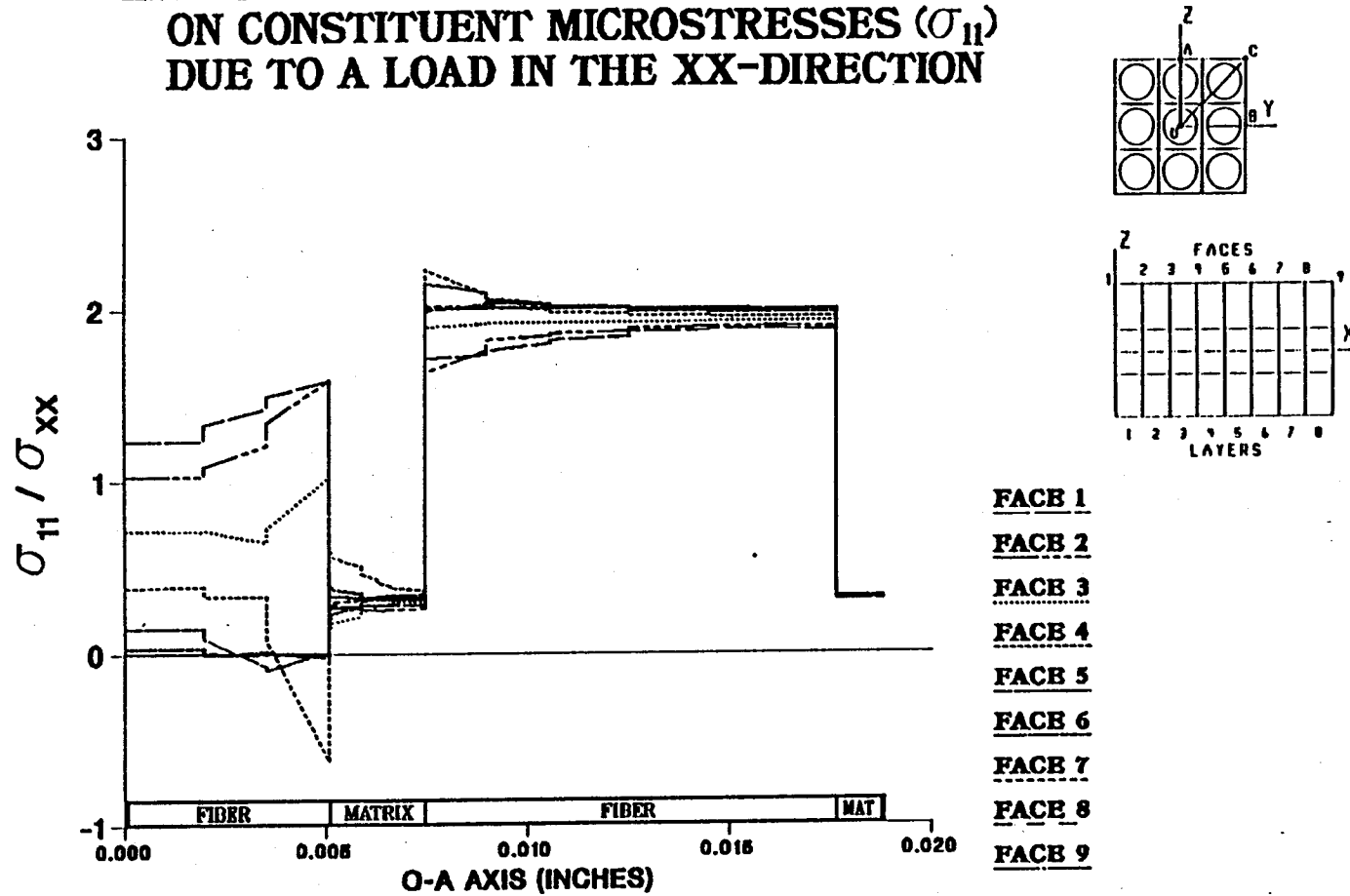


Figure 7.6 - σ_{11} Normalized Microstresses, O-A Direction, 6.94% Debonding, σ_{xx}^e Loading

EFFECT OF 8.33% FIBER LENGTH DEBONDING ON CONSTITUENT MICROSTRESSES (σ_{11}) DUE TO A LOAD IN THE XX-DIRECTION

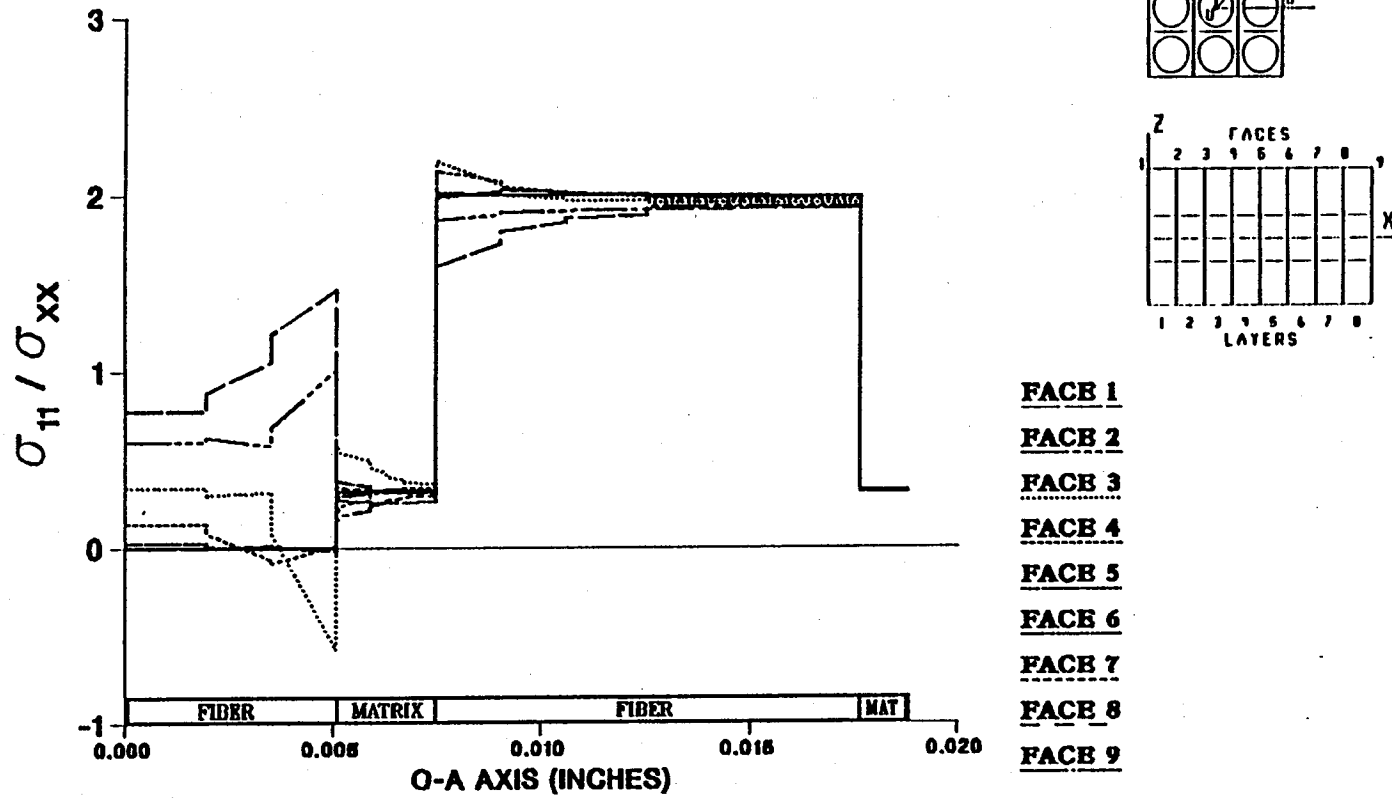
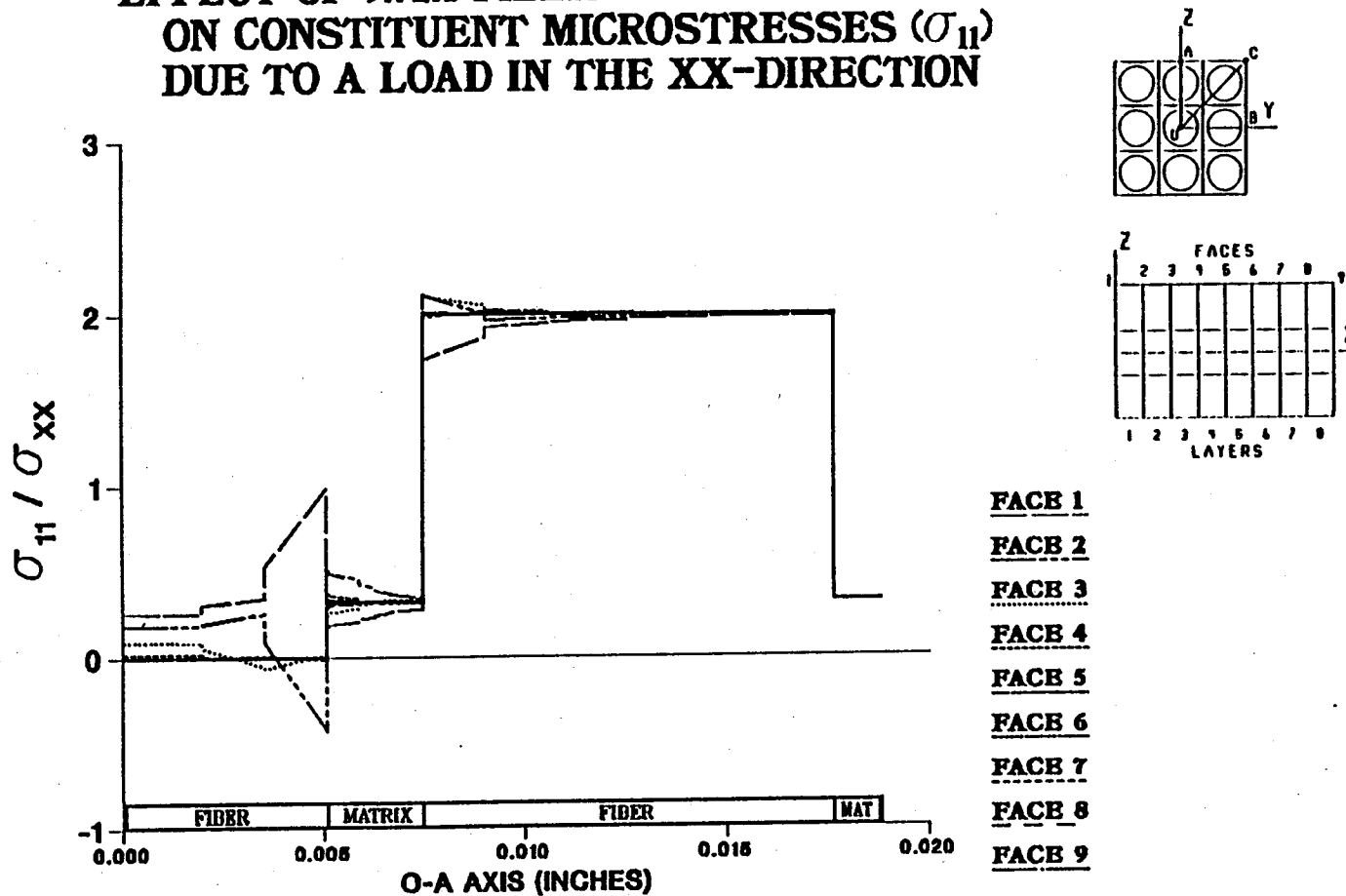


Figure 7.7 - σ_{11} Normalized Microstresses, O-A Direction, 8.33% Debonding, σ_{xx}^e Loading

EFFECT OF 9.72% FIBER LENGTH DEBONDING ON CONSTITUENT MICROSTRESSES (σ_{11}) DUE TO A LOAD IN THE XX-DIRECTION



- FACE 1
- FACE 2
- FACE 3
- FACE 4
- FACE 5
- FACE 6
- FACE 7
- FACE 8
- FACE 9

Figure 7.8 - σ_{11} Normalized Microstresses, O-A Direction, 9.72% Debonding, σ_{xx}^e Loading

EFFECT OF 11.11% FIBER LENGTH DEBONDING ON CONSTITUENT MICROSTRESSES (σ_{11}) DUE TO A LOAD IN THE XX-DIRECTION

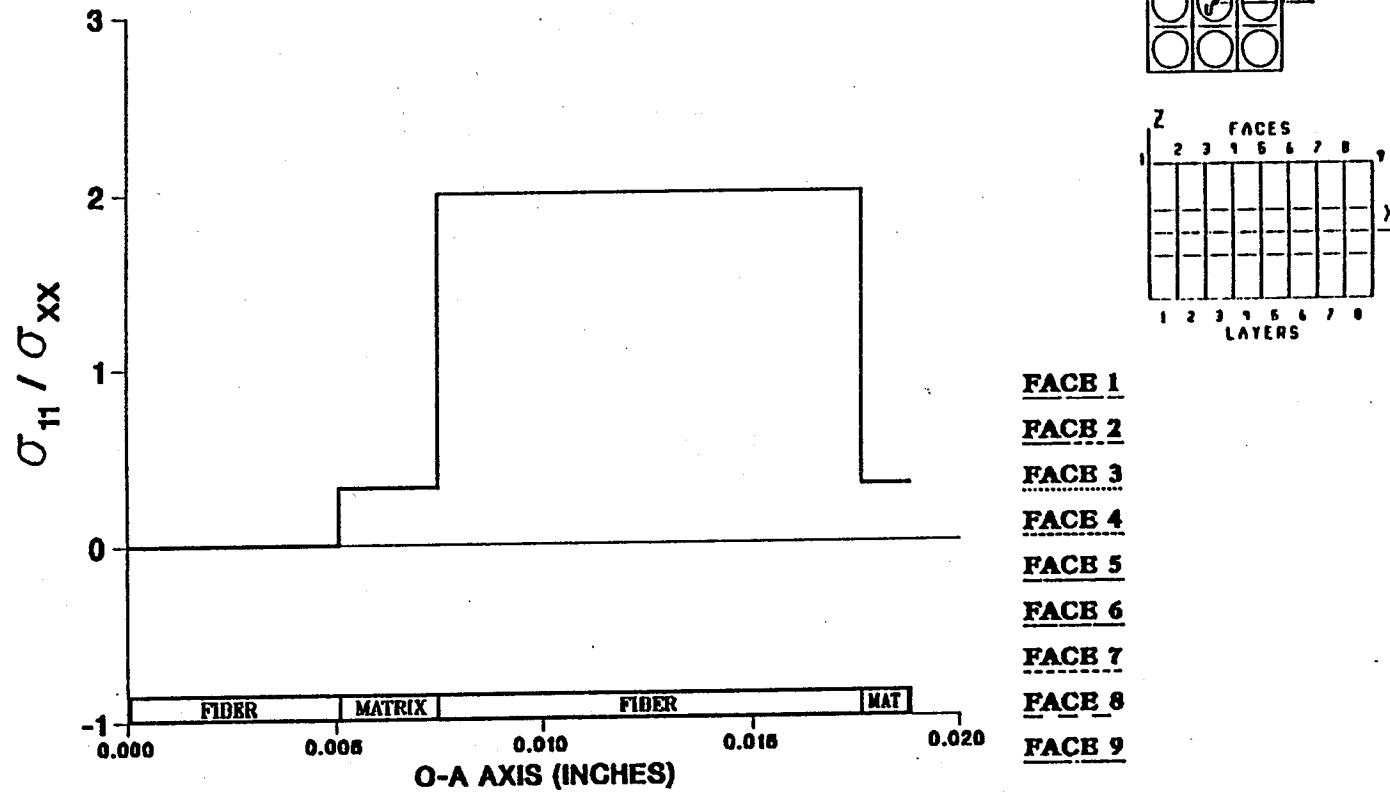
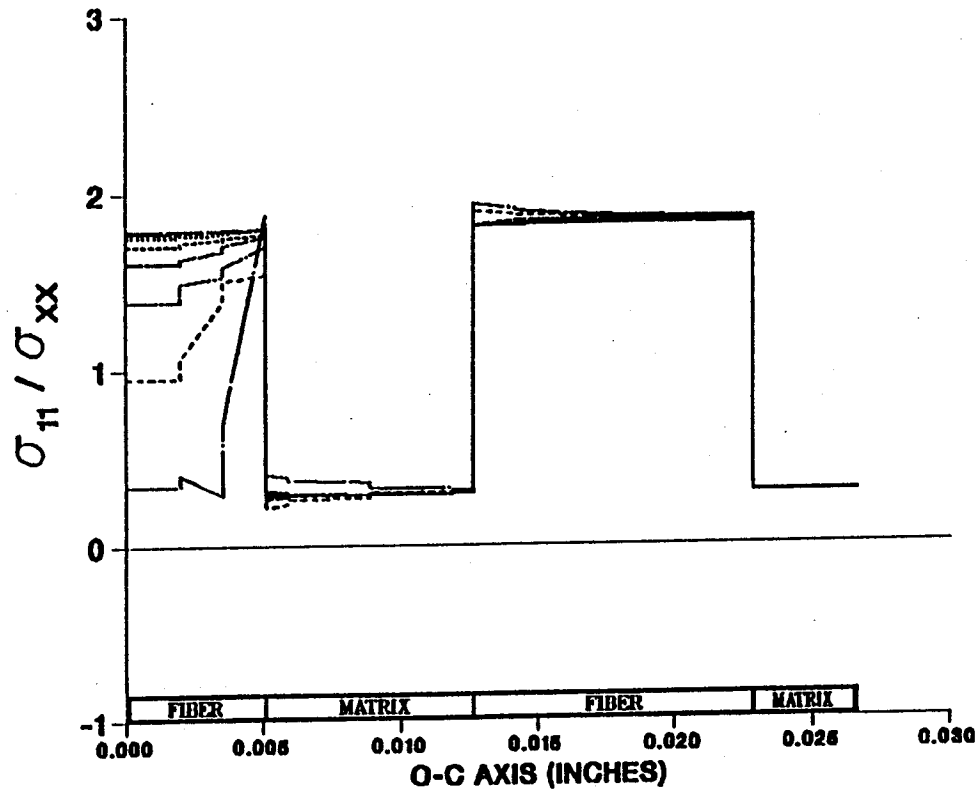
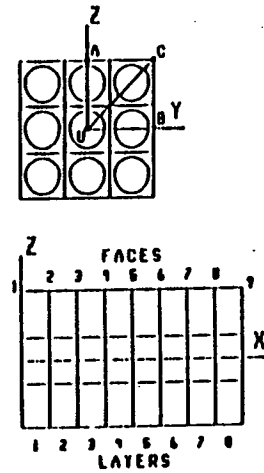


Figure 7.9 - σ_{11} Normalized Microstresses, O-A Direction, 11.11% Debonding, σ_{xx}^e Loading

EFFECT OF 0.0% FIBER LENGTH DEBONDING ON CONSTITUENT MICROSTRESSES (σ_{11}) DUE TO A LOAD IN THE XX-DIRECTION



- FACE 1
- FACE 2
- FACE 3
- FACE 4
- FACE 5
- FACE 6
- FACE 7
- FACE 8
- FACE 9

Figure 7.10 - σ_{11} Normalized Microstresses, O-C Direction, 0.0% Debonding, σ_{xx}^e Loading

EFFECT OF 5.56% FIBER LENGTH DEBONDING ON CONSTITUENT MICROSTRESSES (σ_{11}) DUE TO A LOAD IN THE XX-DIRECTION

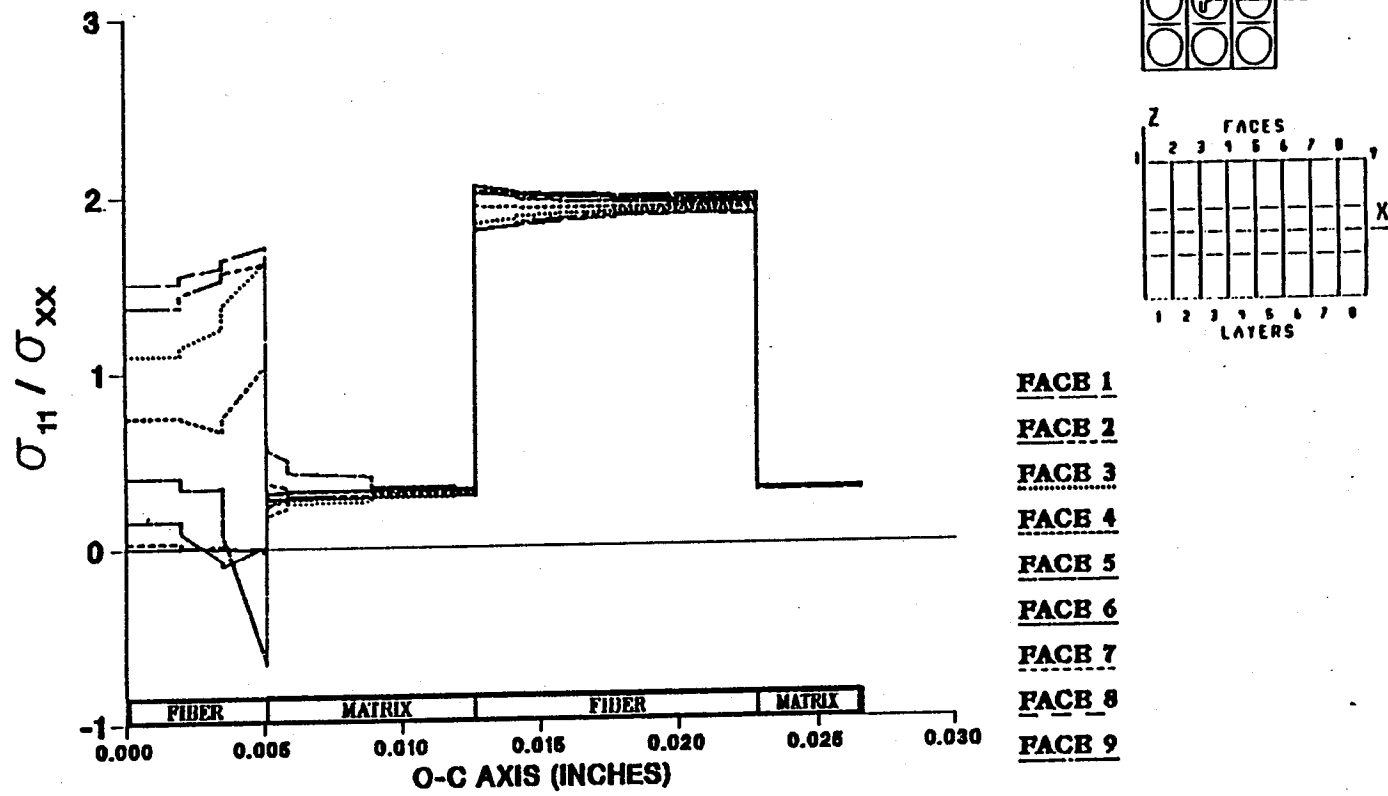
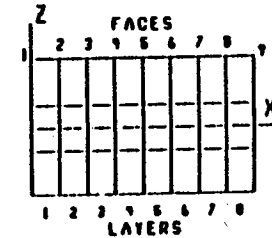
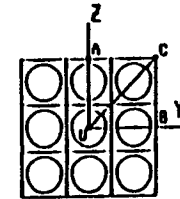
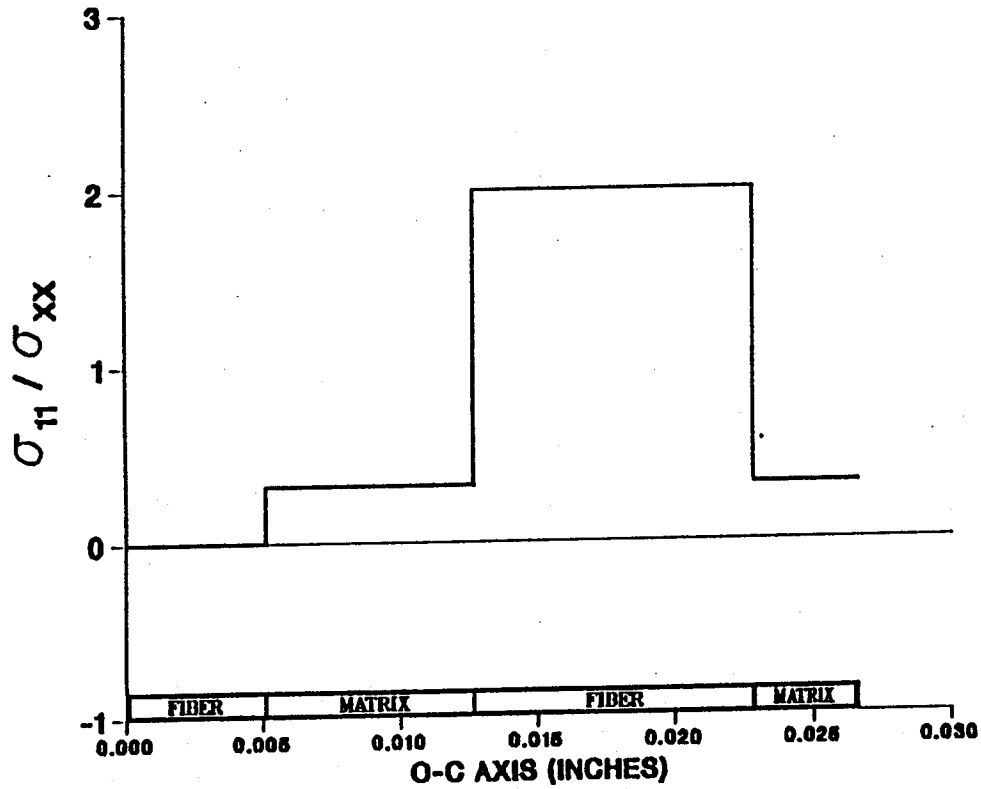


Figure 7.11 - σ_{11} Normalized Microstresses, O-C Direction, 5.56% Debonding, σ_{xx}^e Loading

EFFECT OF 11.11% FIBER LENGTH DEBONDING ON CONSTITUENT MICROSTRESSES (σ_{11}) DUE TO A LOAD IN THE XX-DIRECTION



- FACE 1
- FACE 2
- FACE 3
- FACE 4
- FACE 5
- FACE 6
- FACE 7
- FACE 8
- FACE 9

Figure 7.12 - σ_{11} Normalized Microstresses, O-C Direction, 11.11% Debonding, σ_{xx}^e Loading

Figures 7.13 through 7.15 and 7.16 through 7.18 show the shear stresses in the 13, σ_{13} , along directions defined by the line segments O—A and O—C, respectively. These shear stresses transfer the load to the debonding fiber and are most significant at the interface of the debonding fiber and the matrix. The longitudinal shear stresses tend to be highest at the face where the debonding is initiated and the fiber begins to be structurally active. Note that when completely debonded, the shear stresses drop to virtually zero because there is no load transfer to the center fiber.

Figures 7.19 to 7.21 also display the effect of center fiber debonding on longitudinal shear stresses (σ_{12}). These results are similar to those discussed above.

7.2) Loading: σ_{yy}^e

Figures 7.22 through 7.30 represent the resulting constituent microstresses due to an enforced displacement transverse to the fiber direction. These graphs show the microstresses along a line defined by the line segment O—A as the amount of center fiber debonding increases. In this transverse loading condition the matrix material carries most of the load and the fiber is strained the most. This is to be expected due to the relatively low transverse modulus of the fiber as compared to that of the matrix material. Since the fibers are not structurally dominate when loaded transversely, the effect of the debonding of the center fiber is not as significant as in the axially loaded case. As debonding progresses, stress risers are evident in the matrix material bordering on the debonding fiber. Also, no significant increase occurs in the load

EFFECT OF 0.0% FIBER LENGTH DEBONDING ON CONSTITUENT MICROSTRESSES (σ_{31}) DUE TO A LOAD IN THE XX-DIRECTION

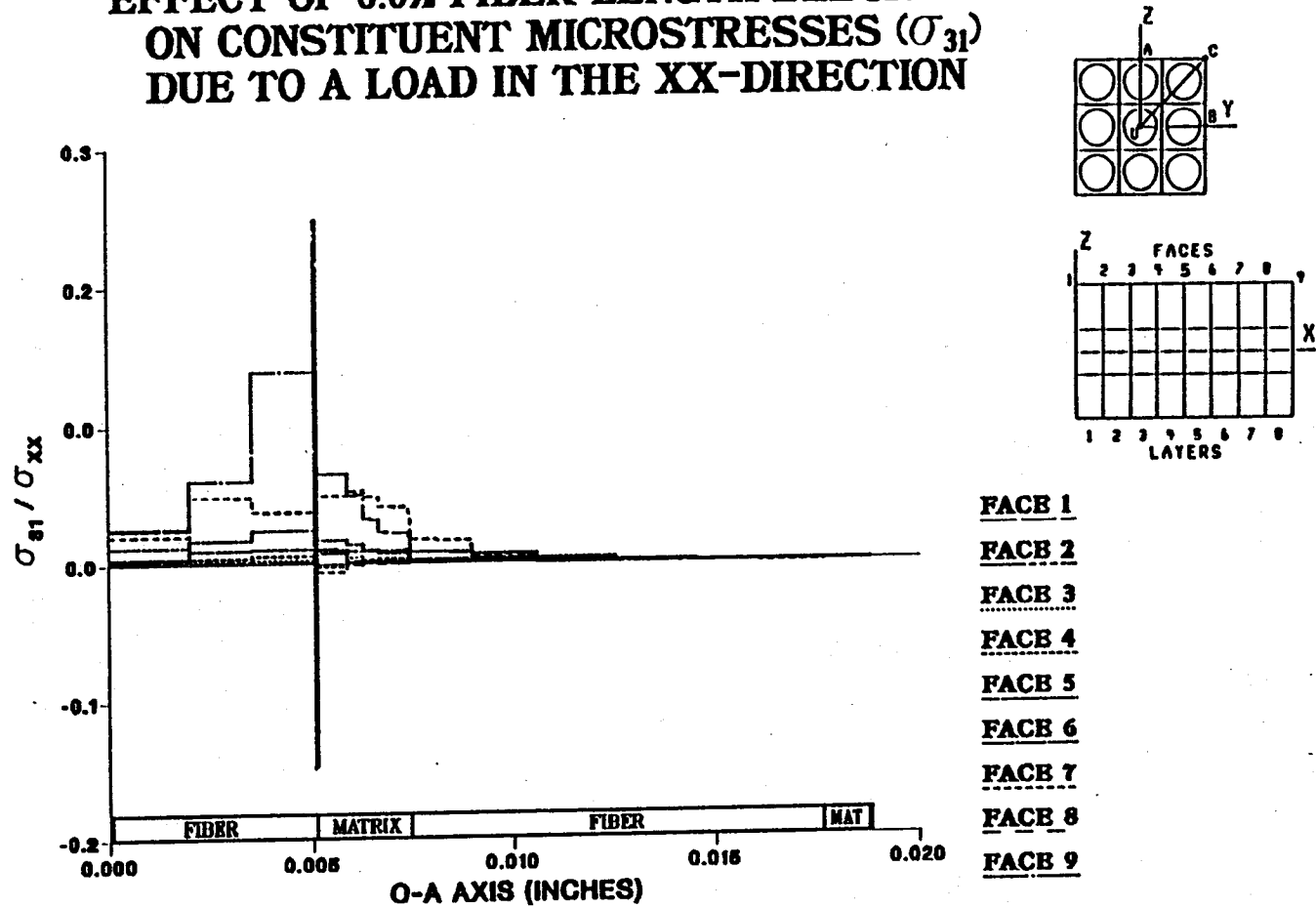


Figure 7.13 - σ_{31} Normalized Microstresses, O-A Direction, 0.0% Debonding, σ_{xx}^e Loading

EFFECT OF 5.56% FIBER LENGTH DEBONDING ON CONSTITUENT MICROSTRESSES (σ_{31}) DUE TO A LOAD IN THE XX-DIRECTION

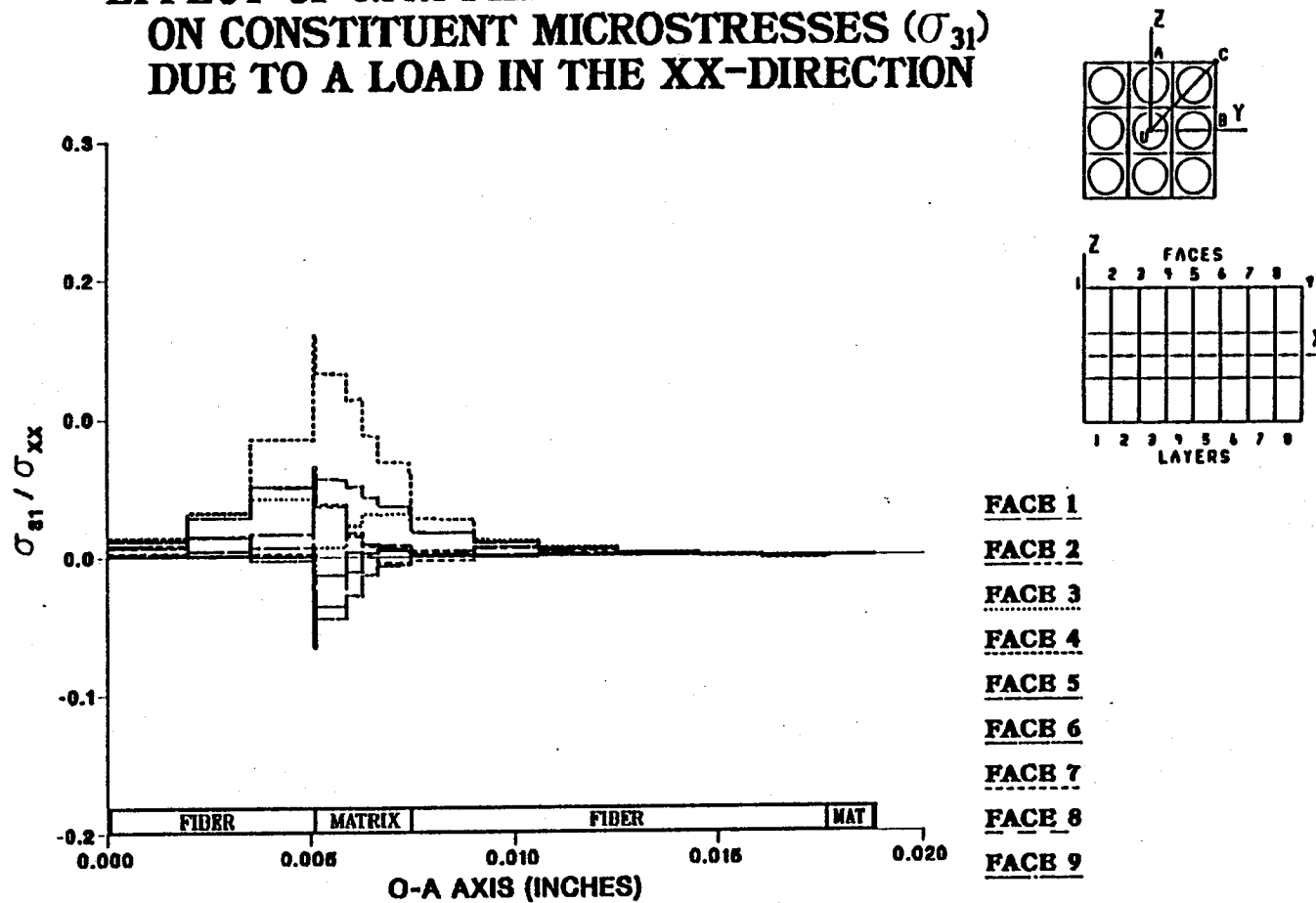


Figure 7.14 - σ_{31} Normalized Microstresses, O-A Direction, 5.56% Debonding, σ_{xx}^e Loading

EFFECT OF 11.11% FIBER LENGTH DEBONDING ON CONSTITUENT MICROSTRESSES (σ_{31}) DUE TO A LOAD IN THE XX-DIRECTION

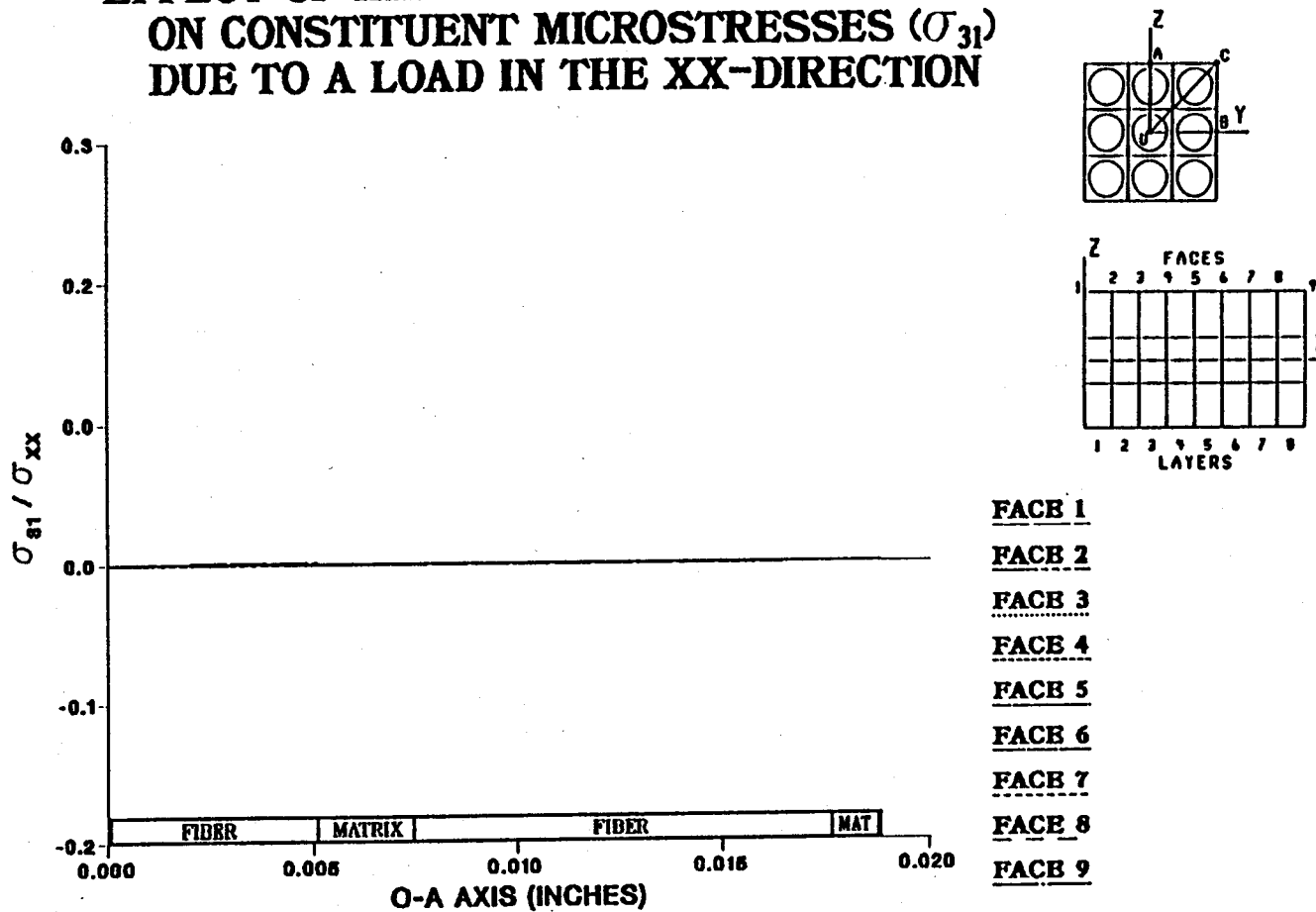


Figure 7.15 - σ_{31} Normalized Microstresses, O-A Direction, 11.11% Debonding, σ_{xx}^e Loading

EFFECT OF 0.0% FIBER LENGTH DEBONDING ON CONSTITUENT MICROSTRESSES (σ_{31}) DUE TO A LOAD IN THE XX-DIRECTION

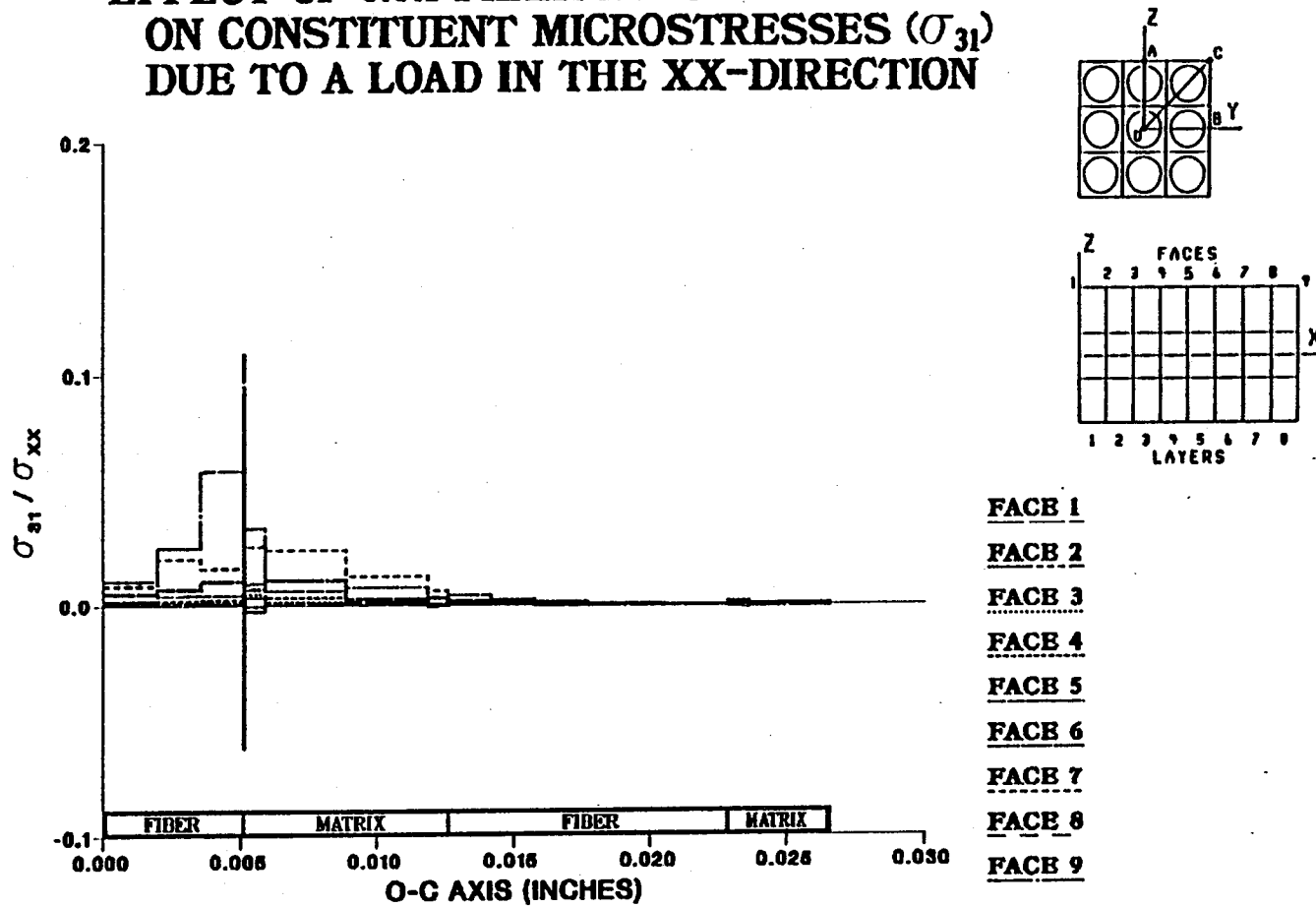


Figure 7.16 - σ_{31} Normalized Microstresses, O-C Direction, 0.0% Debonding, σ_{xx}^e Loading

EFFECT OF 5.56% FIBER LENGTH DEBONDING ON CONSTITUENT MICROSTRESSES (σ_{31}) DUE TO A LOAD IN THE XX-DIRECTION

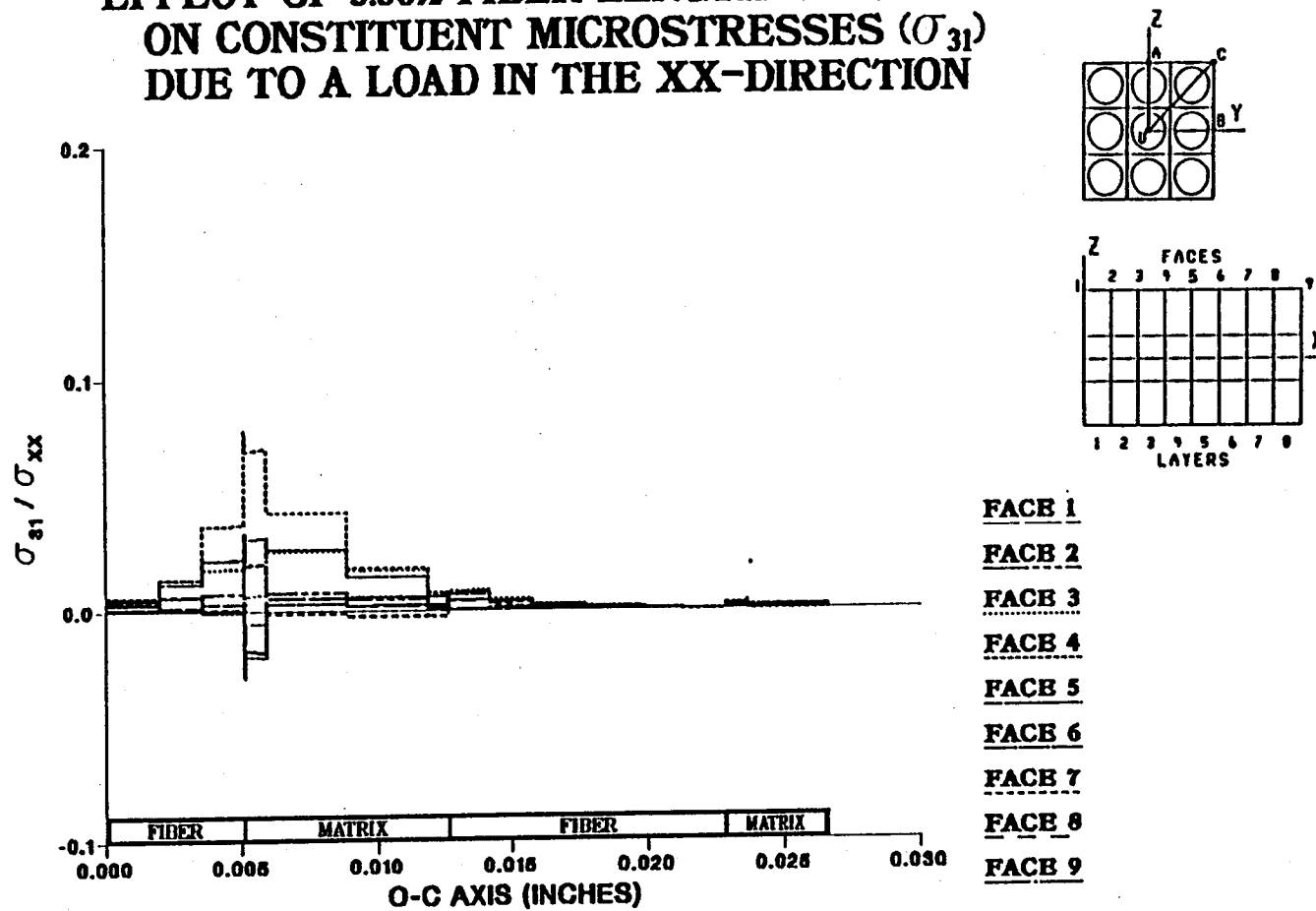
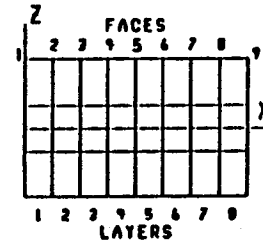
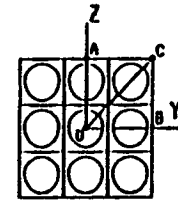
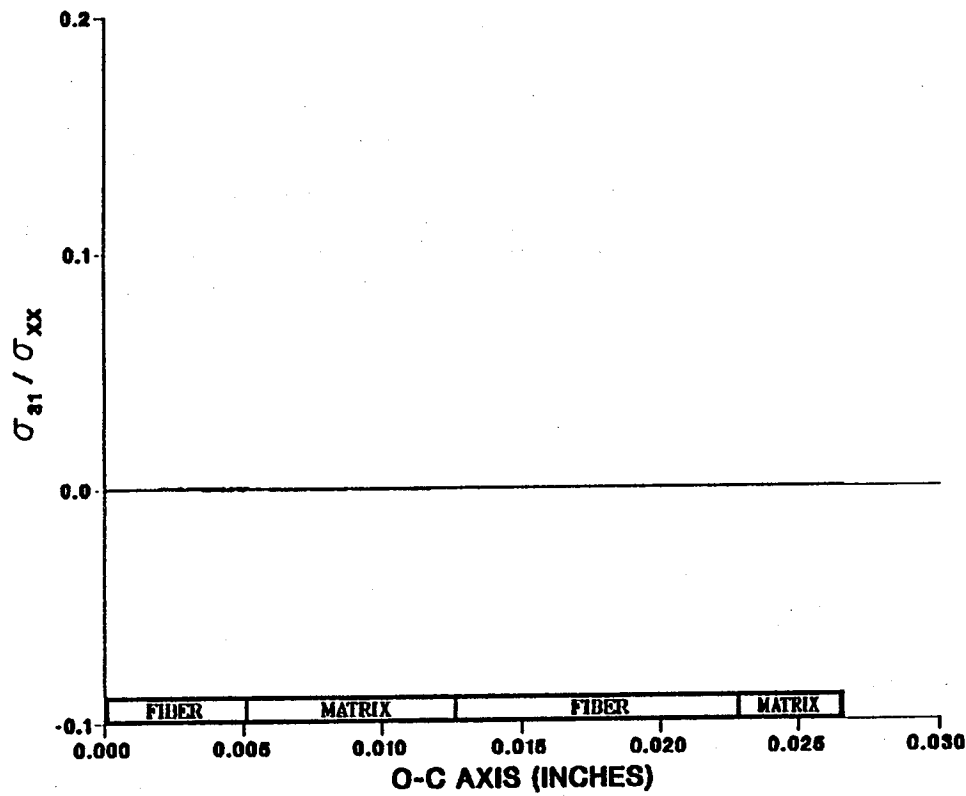


Figure 7.17 - σ_{31} Normalized Microstresses, O-C Direction, 5.56% Debonding, σ_{xx}^e Loading

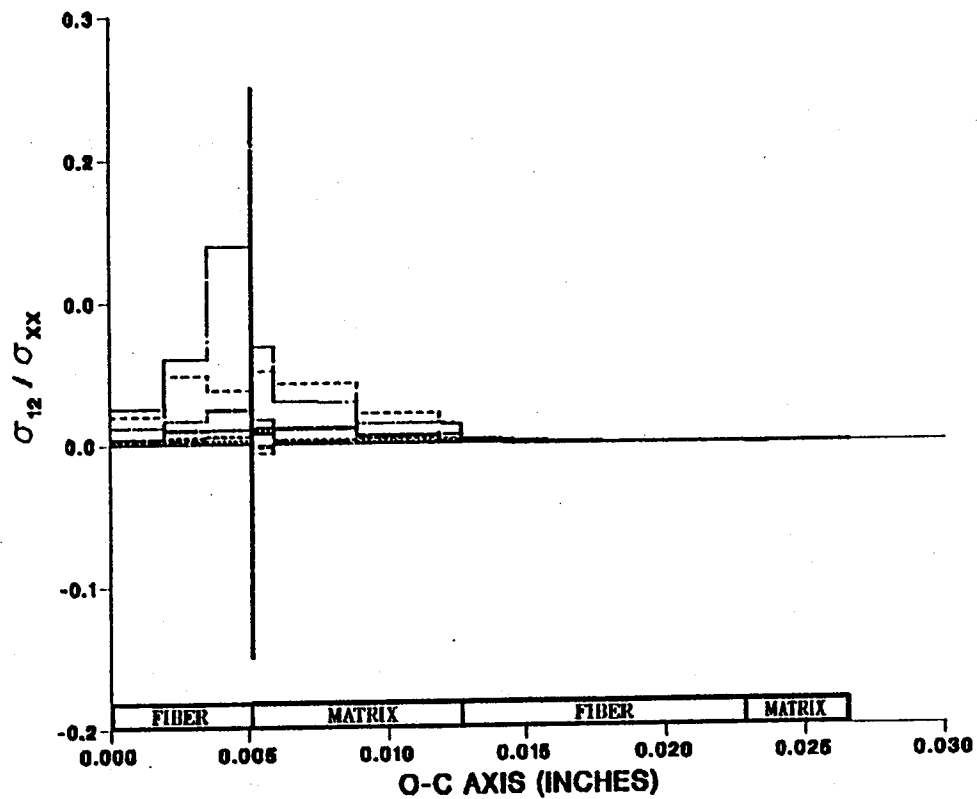
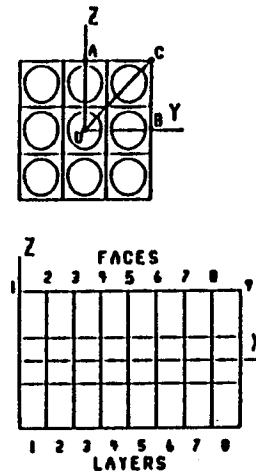
EFFECT OF 11.11% FIBER LENGTH DEBONDING ON CONSTITUENT MICROSTRESSES (σ_{31}) DUE TO A LOAD IN THE XX-DIRECTION



- FACE 1
- FACE 2
- FACE 3
- FACE 4
- FACE 5
- FACE 6
- FACE 7
- FACE 8
- FACE 9

Figure 7.18 - σ_{31} Normalized Microstresses, O-C Direction, 11.11% Debonding, σ_{xx}^e Loading

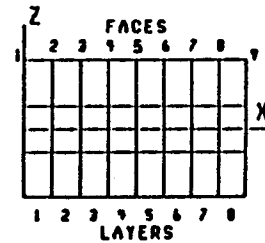
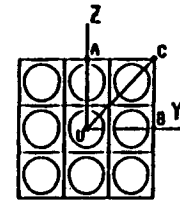
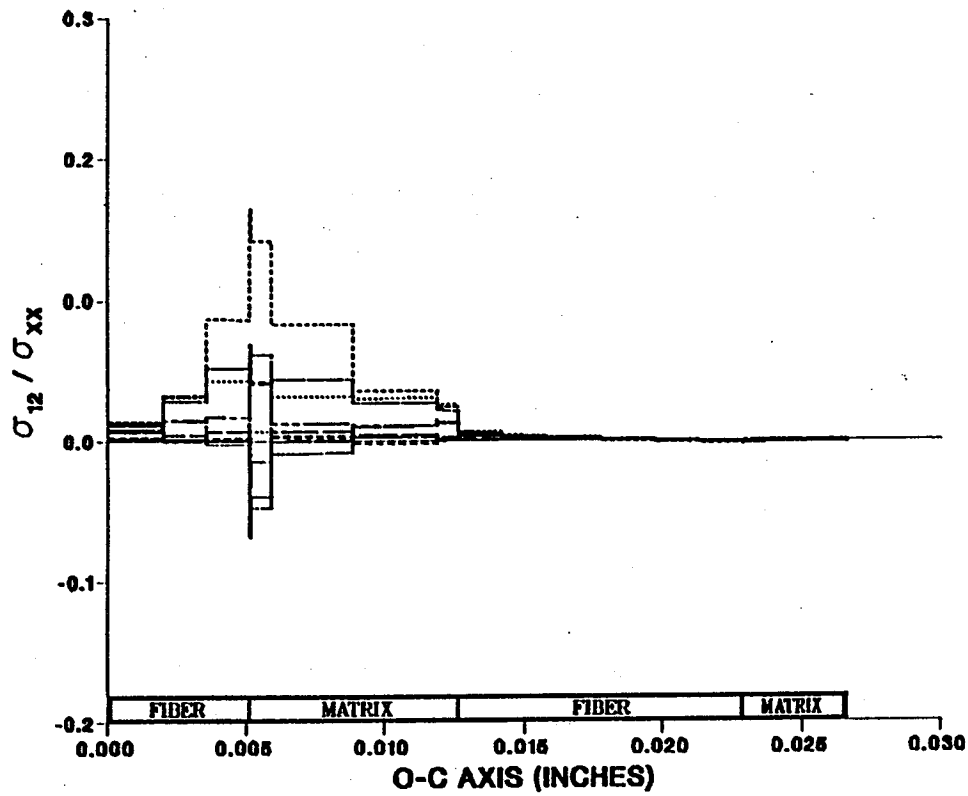
EFFECT OF 0.0% FIBER LENGTH DEBONDING ON CONSTITUENT MICROSTRESSES (σ_{12}) DUE TO A LOAD IN THE XX-DIRECTION



- FACE 1
- FACE 2
- FACE 3
- FACE 4
- FACE 5
- FACE 6
- FACE 7
- FACE 8
- FACE 9

Figure 7.19 — σ_{12} Normalized Microstresses, O-C Direction, 0.0% Debonding, σ_{xx}^e Loading

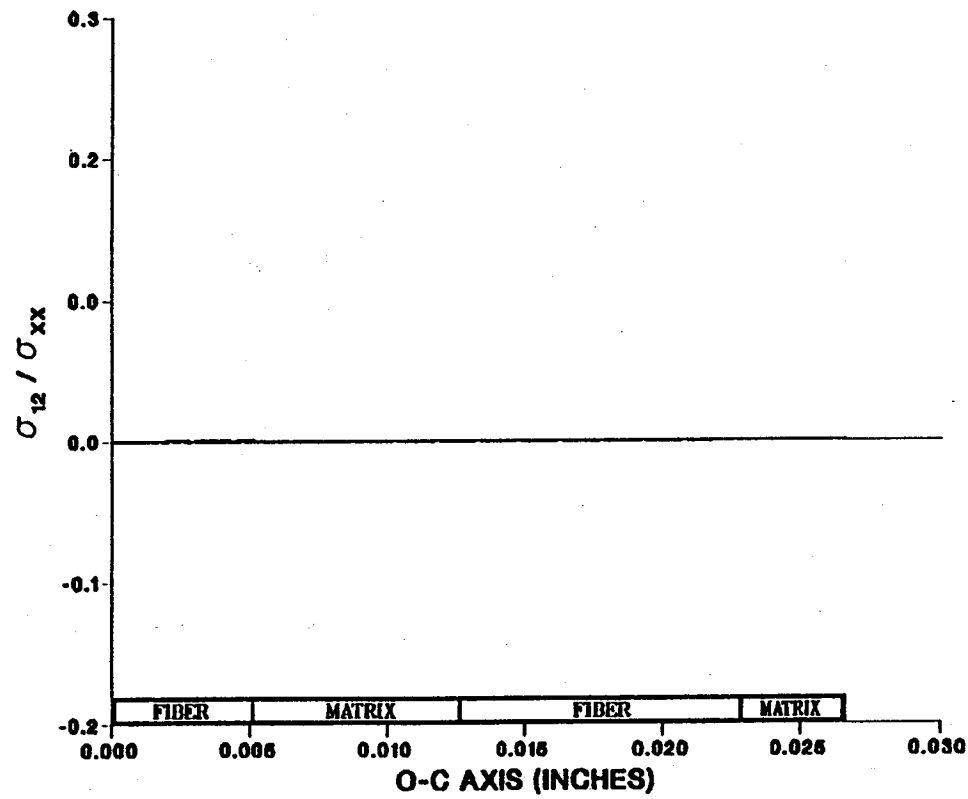
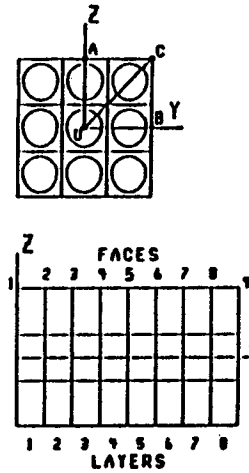
EFFECT OF 5.56% FIBER LENGTH DEBONDING ON CONSTITUENT MICROSTRESSES (σ_{12}) DUE TO A LOAD IN THE XX-DIRECTION



- FACE 1
- FACE 2
- FACE 3
- FACE 4
- FACE 5
- FACE 6
- FACE 7
- FACE 8
- FACE 9

Figure 7.20 — σ_{12} Normalized Microstresses, O-C Direction, 5.56% Debonding, σ_{xx}^e Loading

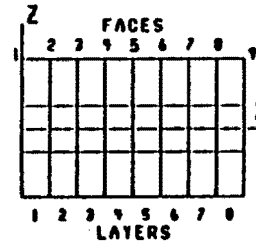
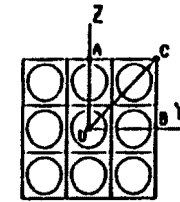
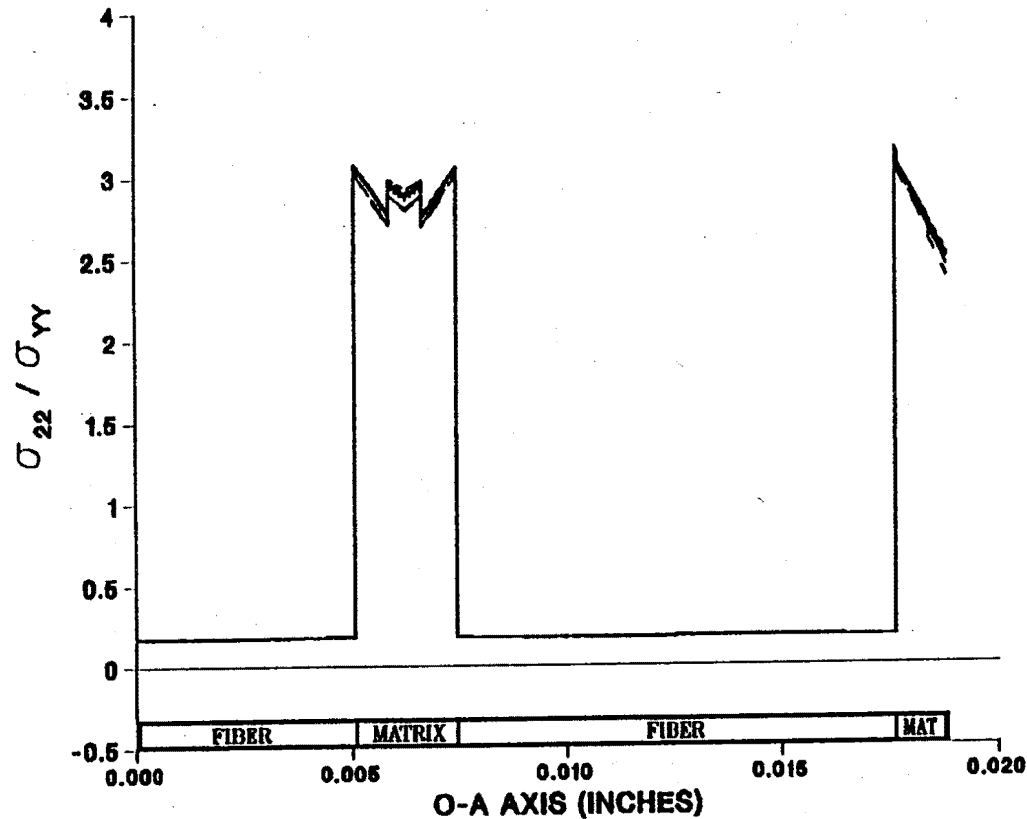
EFFECT OF 11.11% FIBER LENGTH DEBONDING ON CONSTITUENT MICROSTRESSES (σ_{12}) DUE TO A LOAD IN THE XX-DIRECTION



- FACE 1
- FACE 2
- FACE 3
- FACE 4
- FACE 5
- FACE 6
- FACE 7
- FACE 8
- FACE 9

Figure 7.21 - σ_{12} Normalized Microstresses, O-C Direction, 11.11% Debonding, σ_{xx}^e Loading

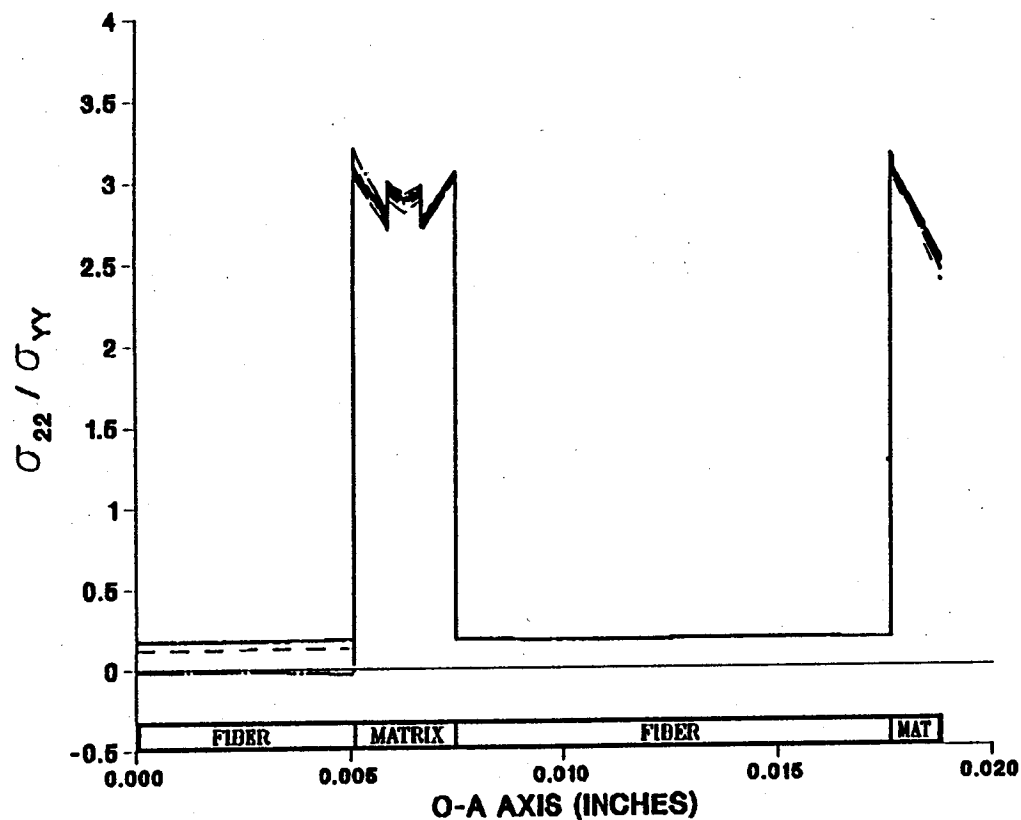
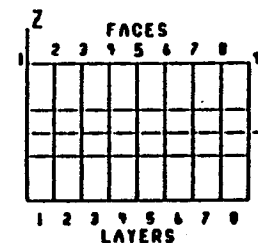
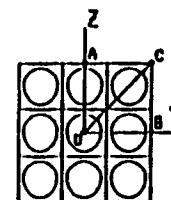
EFFECT OF 0.0% FIBER LENGTH DEBONDING ON CONSTITUENT MICROSTRESSES (σ_{22}) DUE TO A LOAD IN THE YY-DIRECTION



- FACE 1
- FACE 2
- FACE 3
- FACE 4
- FACE 5
- FACE 6
- FACE 7
- FACE 8
- FACE 9

Figure 7.22 - σ_{22} Normalized Microstresses, O-A Direction, 0.0% Debonding, σ_{yy}^e Loading

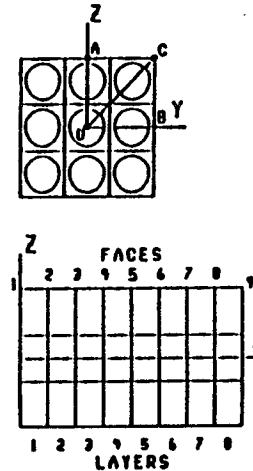
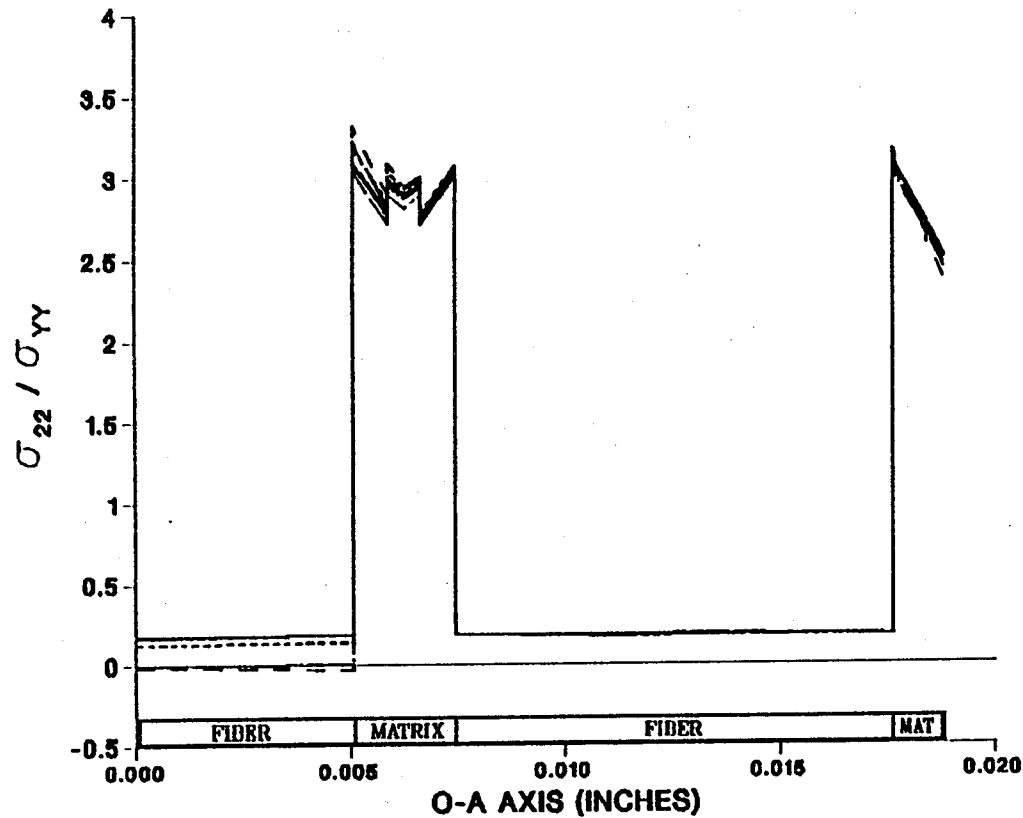
EFFECT OF 1.39% FIBER LENGTH DEBONDING ON CONSTITUENT MICROSTRESSES (σ_{22}) DUE TO A LOAD IN THE YY-DIRECTION



- FACE 1
- FACE 2
- FACE 3
- FACE 4
- FACE 5
- FACE 6
- FACE 7
- FACE 8
- FACE 9

Figure 7.23 - σ_{22} Normalized Microstresses, O-A Direction, 1.39% Debonding, σ_{yy}^e Loading

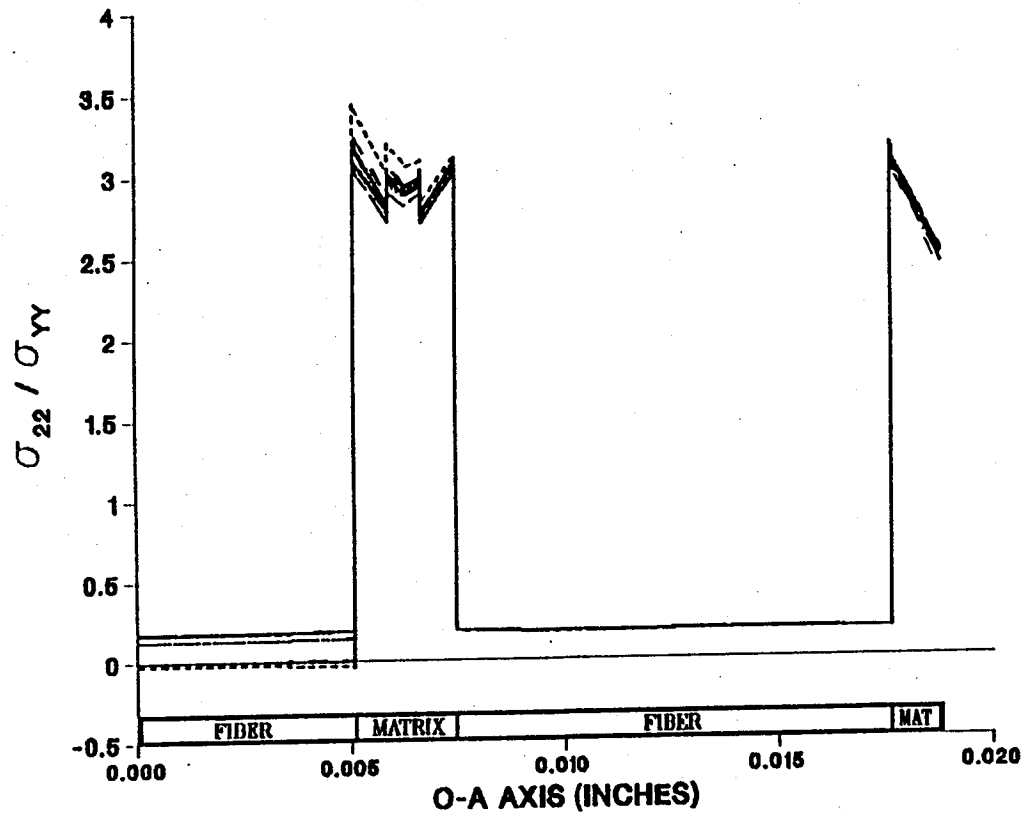
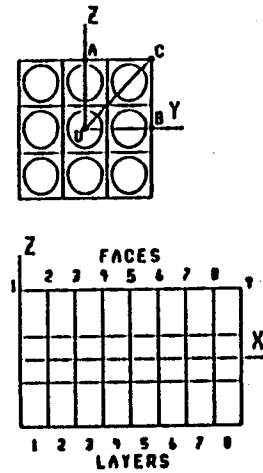
EFFECT OF 2.78% FIBER LENGTH DEBONDING ON CONSTITUENT MICROSTRESSES (σ_{22}) DUE TO A LOAD IN THE YY-DIRECTION



- FACE 1
- FACE 2
- FACE 3
- FACE 4
- FACE 5
- FACE 6
- FACE 7
- FACE 8
- FACE 9

Figure 7.24 - σ_{22} Normalized Microstresses, O-A Direction, 2.78% Debonding, σ_{yy}^e Loading

EFFECT OF 4.17% FIBER LENGTH DEBONDING ON CONSTITUENT MICROSTRESSES (σ_{22}) DUE TO A LOAD IN THE YY-DIRECTION



- FACE 1
- FACE 2
- FACE 3
- FACE 4
- FACE 5
- FACE 6
- FACE 7
- FACE 8
- FACE 9

Figure 7.25 - σ_{22} Normalized Microstresses, O-A Direction, 4.17% Debonding, σ_{yy}^e Loading

EFFECT OF 5.56% FIBER LENGTH DEBONDING ON CONSTITUENT MICROSTRESSES (σ_{22}) DUE TO A LOAD IN THE YY-DIRECTION

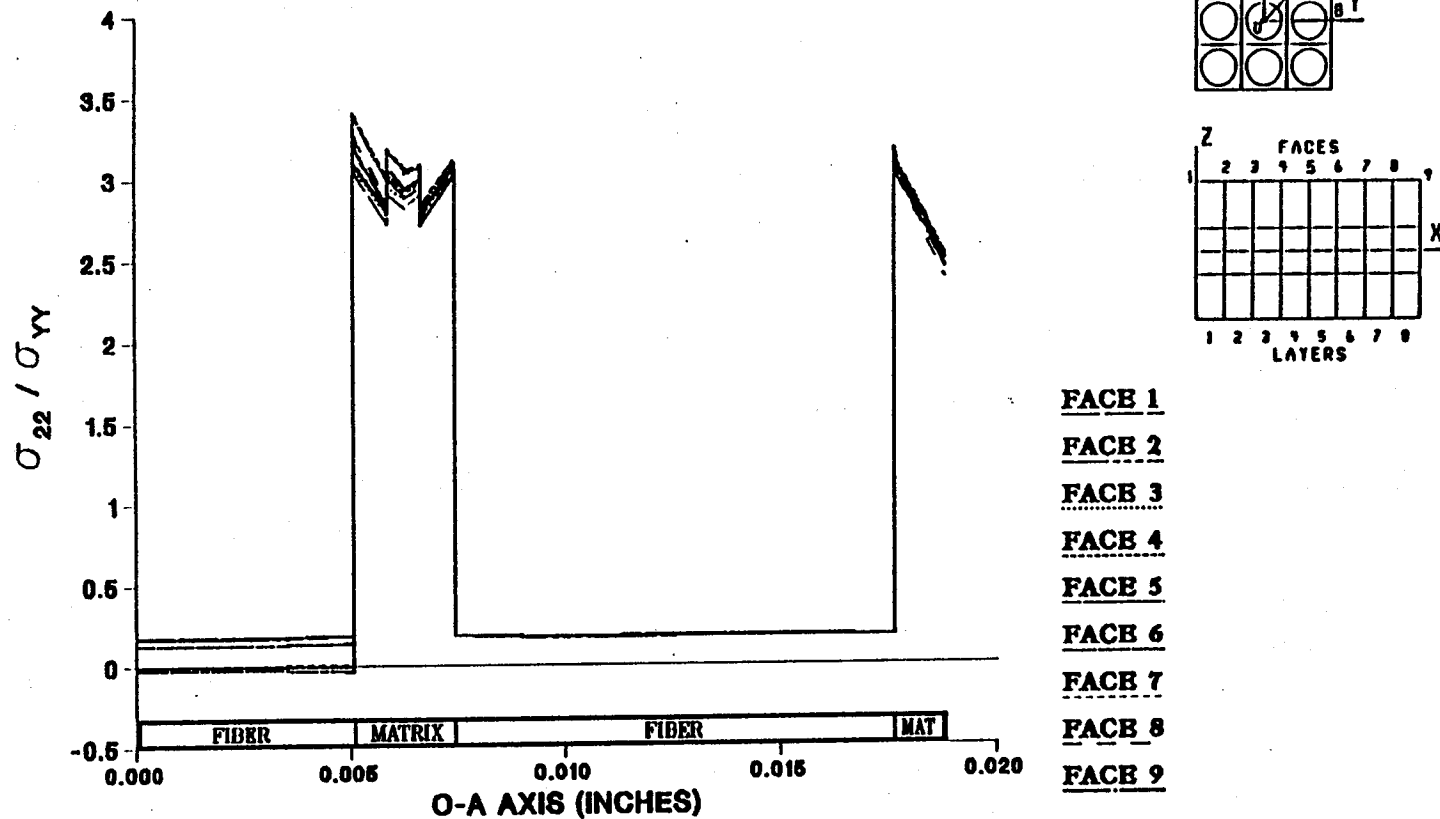
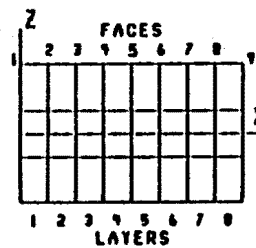
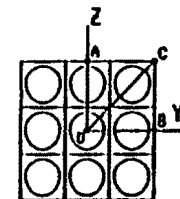
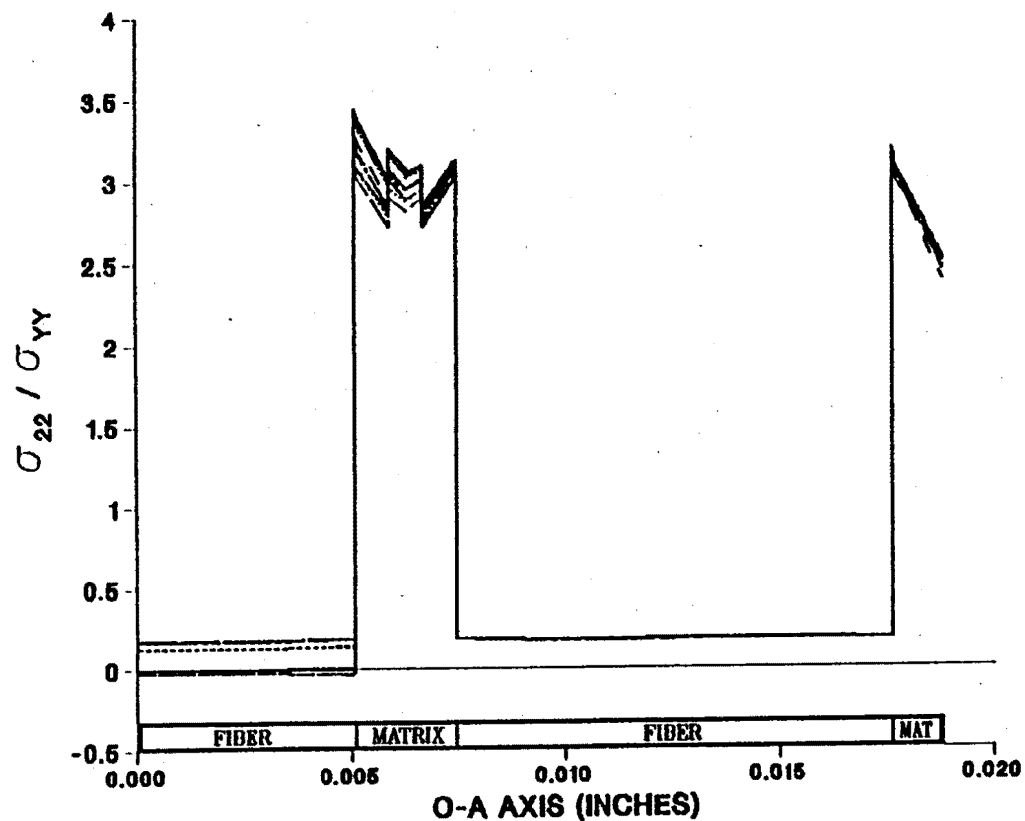


Figure 7.26 - σ_{22} Normalized Microstresses, O-A Direction, 5.56% Debonding, σ_{yy}^e Loading

EFFECT OF 6.94% FIBER LENGTH DEBONDING ON CONSTITUENT MICROSTRESSES (σ_{22}) DUE TO A LOAD IN THE YY-DIRECTION

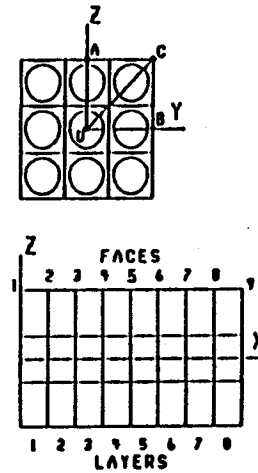
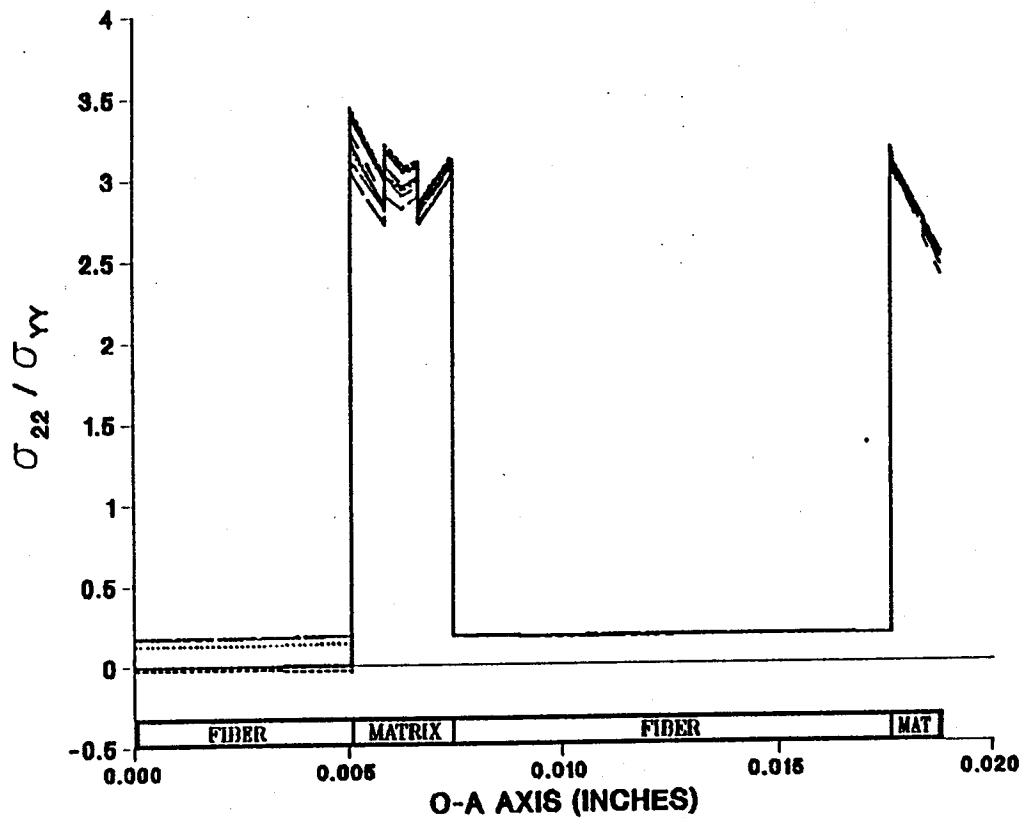
100



- FACE 1
- FACE 2
- FACE 3
- FACE 4
- FACE 5
- FACE 6
- FACE 7
- FACE 8
- FACE 9

Figure 7.27 — σ_{22} Normalized Microstresses, O-A Direction, 6.94% Debonding, σ_{yy}^e Loading

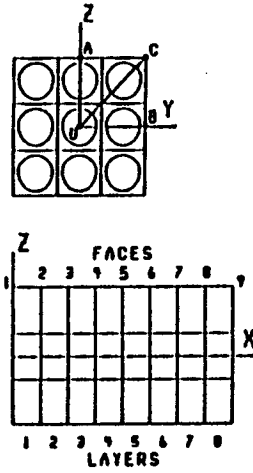
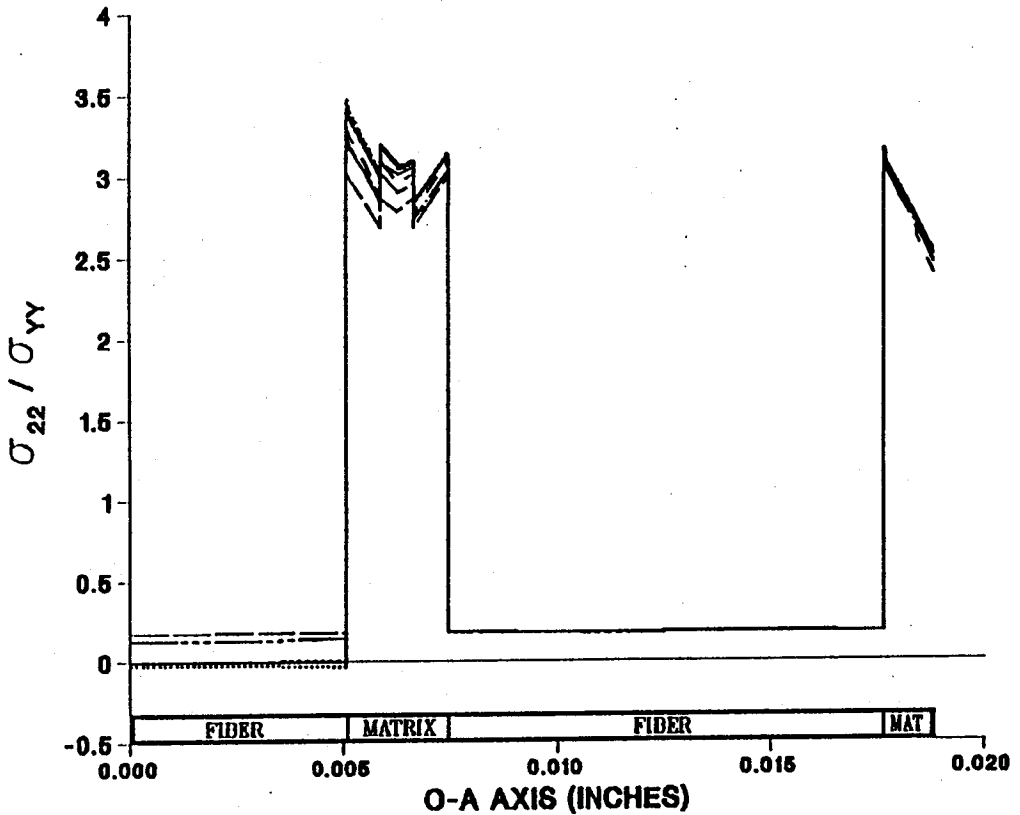
EFFECT OF 8.33% FIBER LENGTH DEBONDING ON CONSTITUENT MICROSTRESSES (σ_{22}) DUE TO A LOAD IN THE YY-DIRECTION



- FACE 1
- FACE 2
- FACE 3
- FACE 4
- FACE 5
- FACE 6
- FACE 7
- FACE 8
- FACE 9

Figure 7.28 - σ_{22} Normalized Microstresses, O-A Direction, 8.33% Debonding, σ_{yy}^e Loading

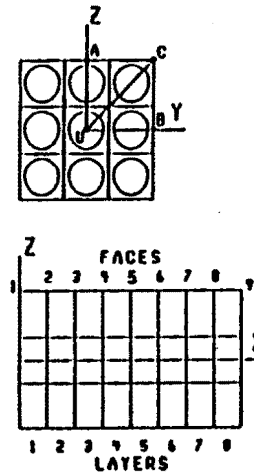
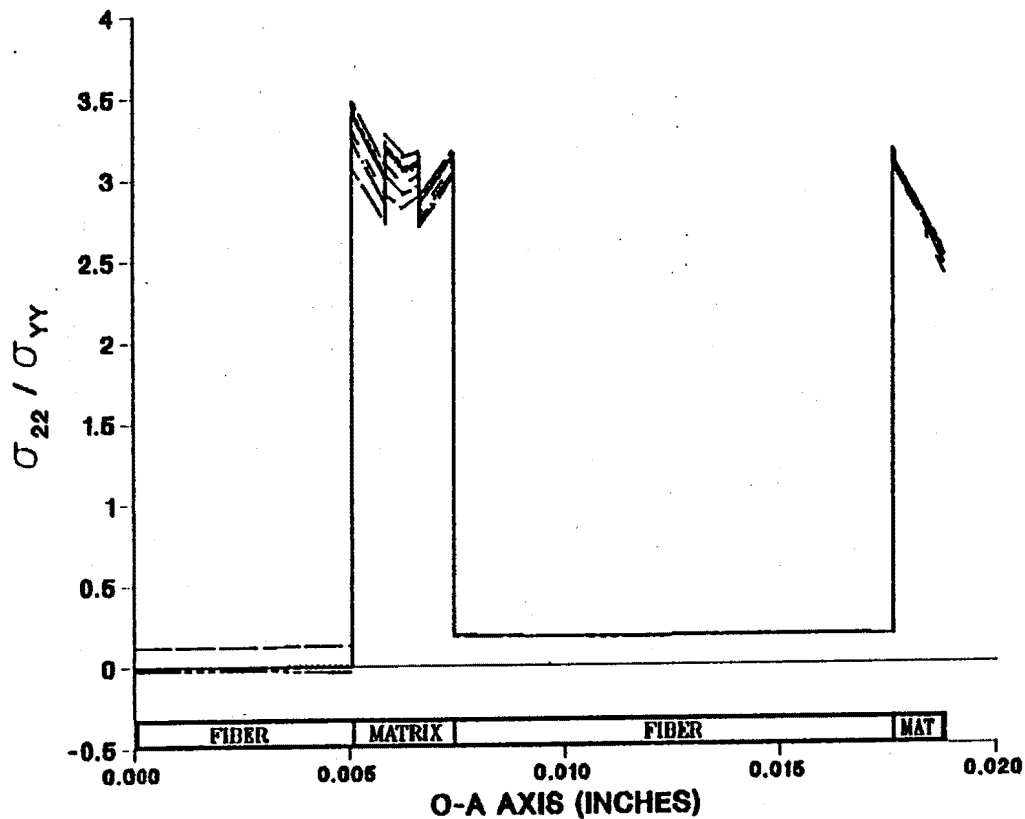
**EFFECT OF 9.72% FIBER LENGTH DEBONDING
ON CONSTITUENT MICROSTRESSES (σ_{22})
DUE TO A LOAD IN THE YY-DIRECTION**



- FACE 1
- FACE 2
- FACE 3
- FACE 4
- FACE 5
- FACE 6
- FACE 7
- FACE 8
- FACE 9

Figure 7.29 – σ_{22} Normalized Microstresses, O–A Direction, 9.72% Debonding, σ_{yy}^e Loading

EFFECT OF 11.11% FIBER LENGTH DEBONDING ON CONSTITUENT MICROSTRESSES (σ_{22}) DUE TO A LOAD IN THE YY-DIRECTION



- FACE 1
- FACE 2
- FACE 3
- FACE 4
- FACE 5
- FACE 6
- FACE 7
- FACE 8
- FACE 9

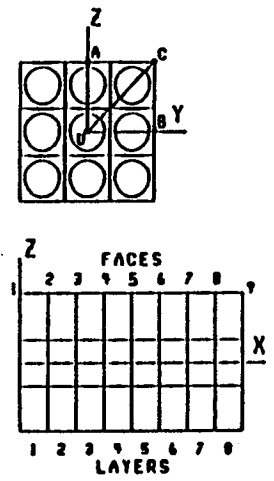
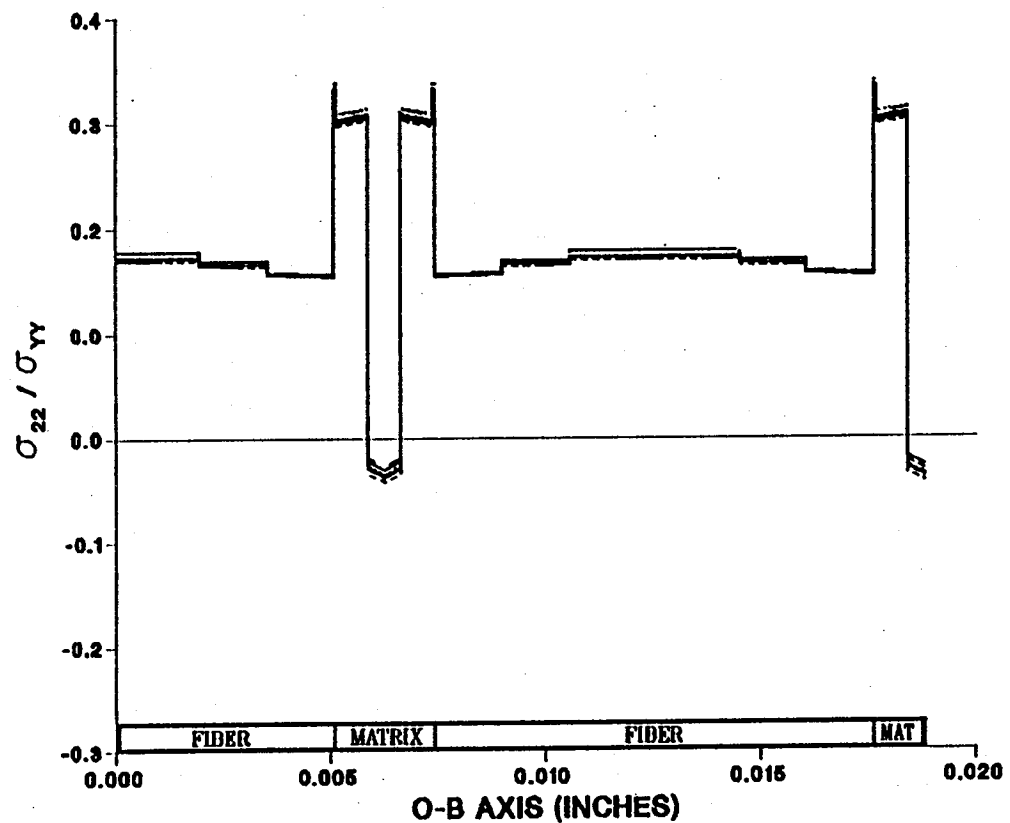
Figure 7.30 - σ_{22} Normalized Microstresses, O-A Direction, 11.11% Debonding, σ_{yy}^e Loading

carried by the neighboring fibers. Note that when the center fiber is completely debonded it still shows a small stress level at the first face of grid points (figure 7.30). This is a result of keeping these points attached to the matrix so as not to remove the fiber-matrix connectivity altogether, thus avoiding singularities in the finite element analysis. At this level of debonding, the transverse stresses on all the other faces of the center fiber are virtually zero.

Figures 7.31 to 7.33 portray the transverse microstresses in the O-B direction due to a transverse enforced displacement. In these figures the matrix material between the fibers contains compressive stresses as a result of the large $\frac{E}{E_{f22}^m}$ ratio. This produces a sharp stress gradient through this area. Even though the stress levels shown here are not large (note scale in figures 7.31 to 7.33), this large gradient from tension to compression may be significant in the failure of the matrix. As center fiber debonding increases, a increase in this compressive stress can be seen. At the same time, each debonded face of the center fiber approaches a zero transverse stress state. Only small changes in the stress levels of the neighboring fibers are witnessed.

In figures 7.34 to 7.36 the transverse microstresses along the direction of the line segment O-C as resulting from the loading conditions described above are plotted at varying levels of center fiber debonding. As in the plots in the O-A direction, the stress levels in the fibers are small compared to the stresses in the matrix material. Therefore, center fiber debonding has little effect on the stress levels of the rest of the composite. Since $\frac{E}{E_{f22}^m}$ is large, most of the transverse straining of the composite takes place in the fiber and most of the load

EFFECT OF 0.0% FIBER LENGTH DEBONDING ON CONSTITUENT MICROSTRESSES (σ_{22}) DUE TO A LOAD IN THE YY-DIRECTION



- FACE 1
- FACE 2
- FACE 3
- FACE 4
- FACE 5
- FACE 6
- FACE 7
- FACE 8
- FACE 9

Figure 7.31 - σ_{22} Normalized Microstresses, O-B Direction, 0.0% Debonding, σ_{yy}^e Loading

EFFECT OF 5.56% FIBER LENGTH DEBONDING ON CONSTITUENT MICROSTRESSES (σ_{22}) DUE TO A LOAD IN THE YY-DIRECTION

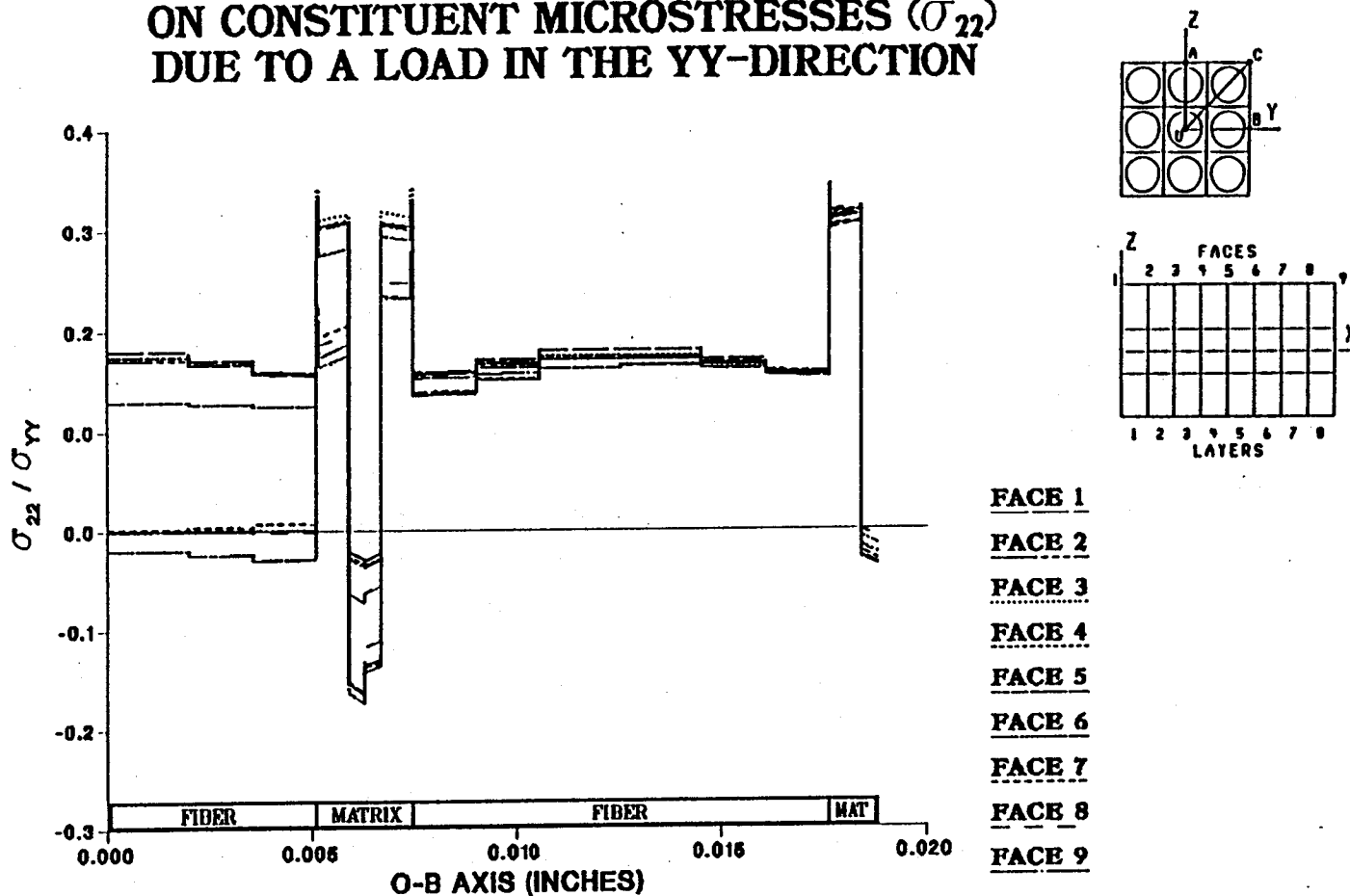


Figure 7.32 - σ_{22} Normalized Microstresses, O-B Direction, 5.56% Debonding, σ_{yy}^e Loading

EFFECT OF 11.11% FIBER LENGTH DEBONDING ON CONSTITUENT MICROSTRESSES (σ_{22}) DUE TO A LOAD IN THE YY-DIRECTION

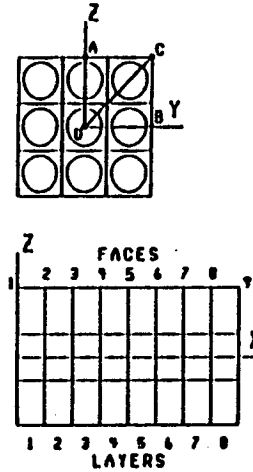
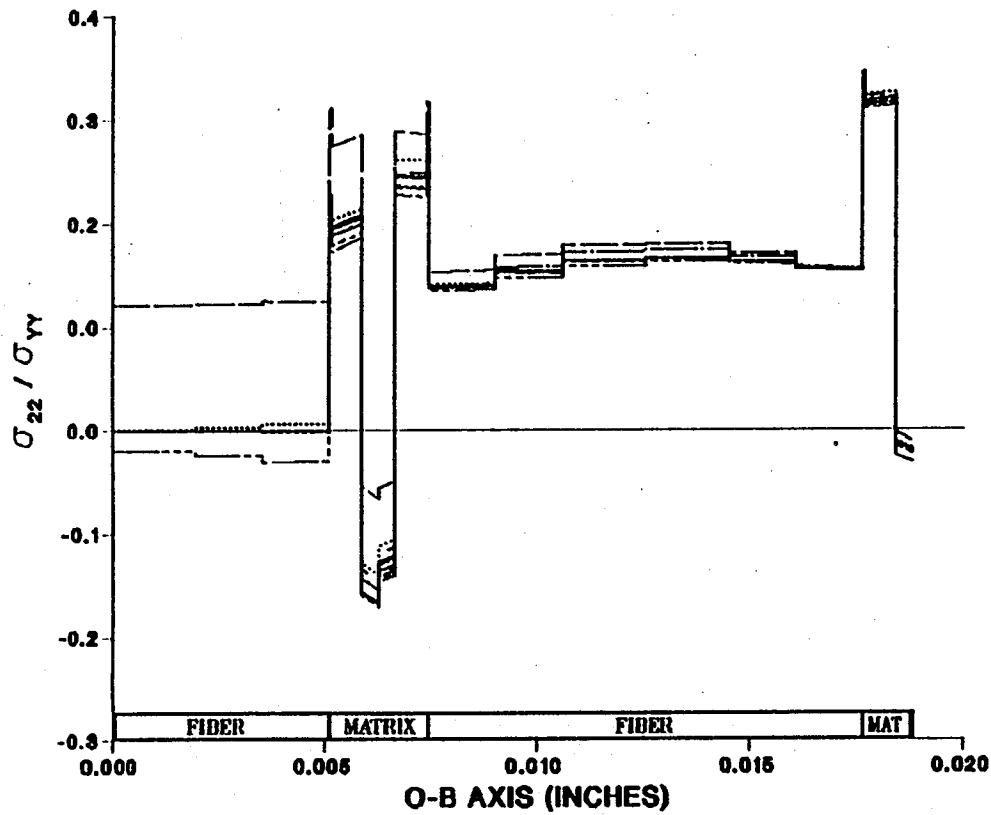


Figure 7.33 - σ_{22} Normalized Microstresses, O-B Direction, 11.11% Debonding, σ_{yy}^e Loading

EFFECT OF 0.0% FIBER LENGTH DEBONDING ON CONSTITUENT MICROSTRESSES (σ_{22}) DUE TO A LOAD IN THE YY-DIRECTION

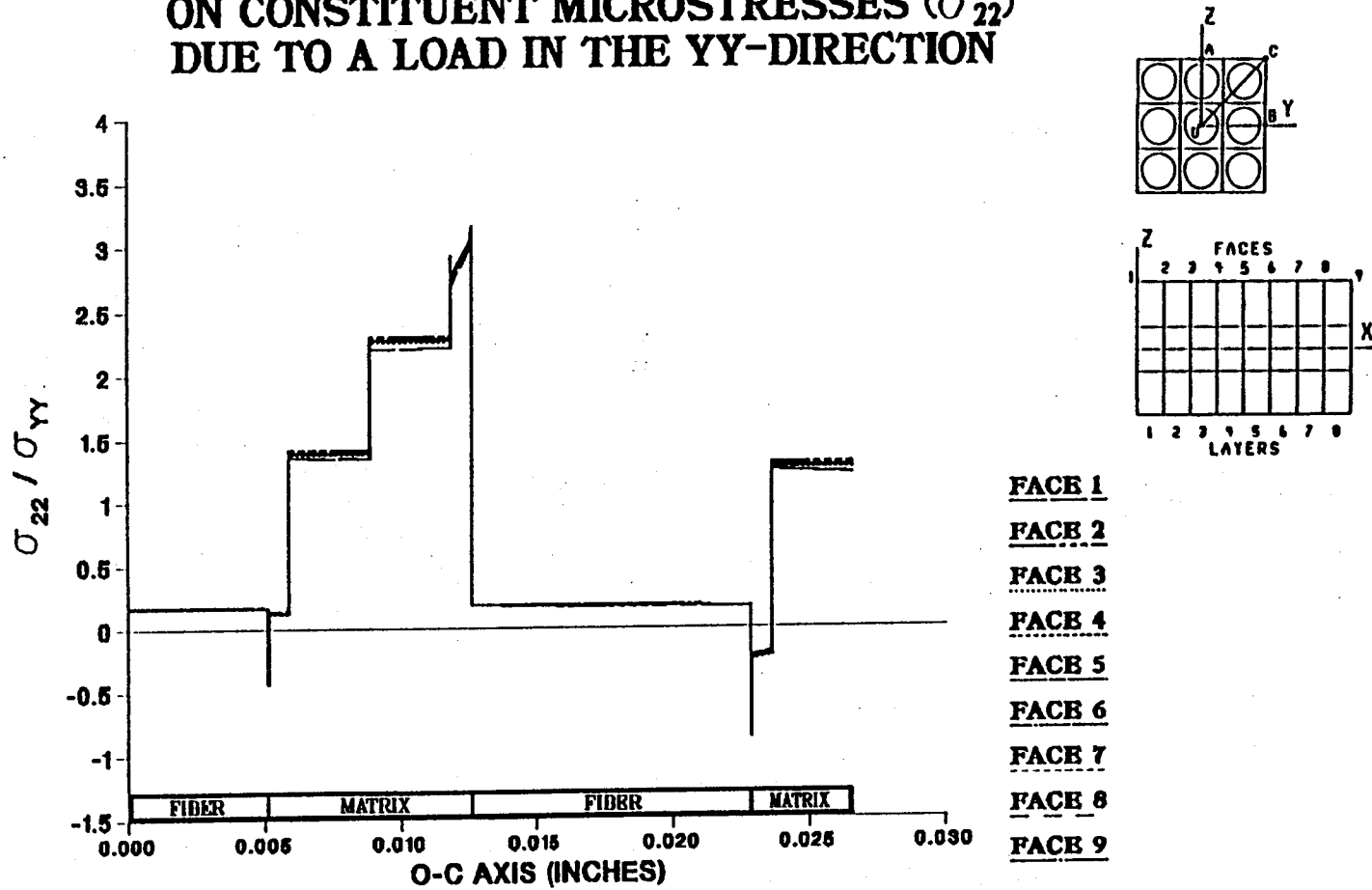


Figure 7.34 - σ_{22} Normalized Microstresses, O-C Direction, 0.0% Debonding, σ_{yy}^e Loading

EFFECT OF 5.56% FIBER LENGTH DEBONDING ON CONSTITUENT MICROSTRESSES (σ_{22}) DUE TO A LOAD IN THE YY-DIRECTION

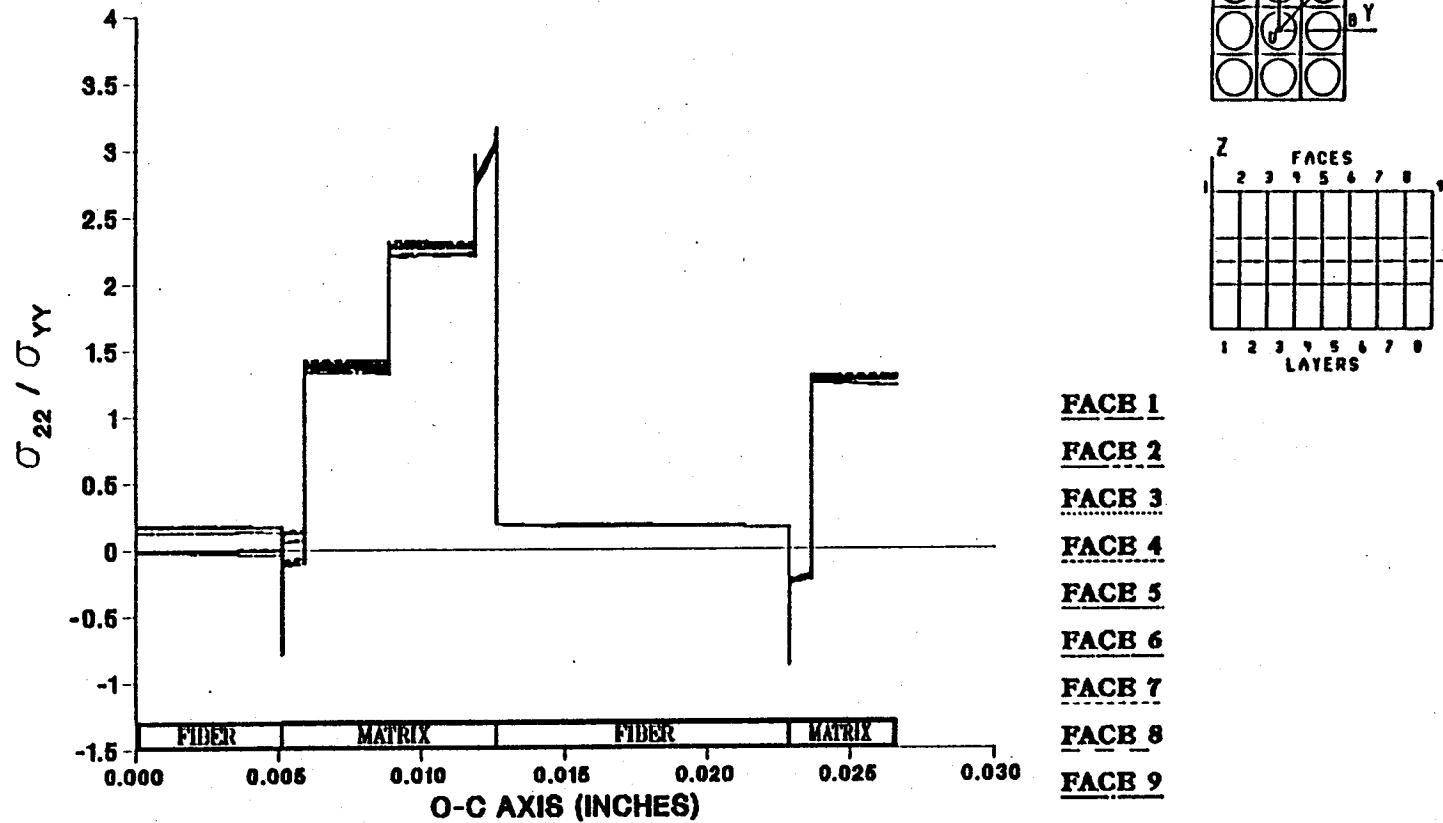


Figure 7.35 — σ_{22} Normalized Microstresses, O-C Direction, 5.56% Debonding, σ_{yy}^e Loading

EFFECT OF 11.11% FIBER LENGTH DEBONDING ON CONSTITUENT MICROSTRESSES (σ_{22}) DUE TO A LOAD IN THE YY-DIRECTION

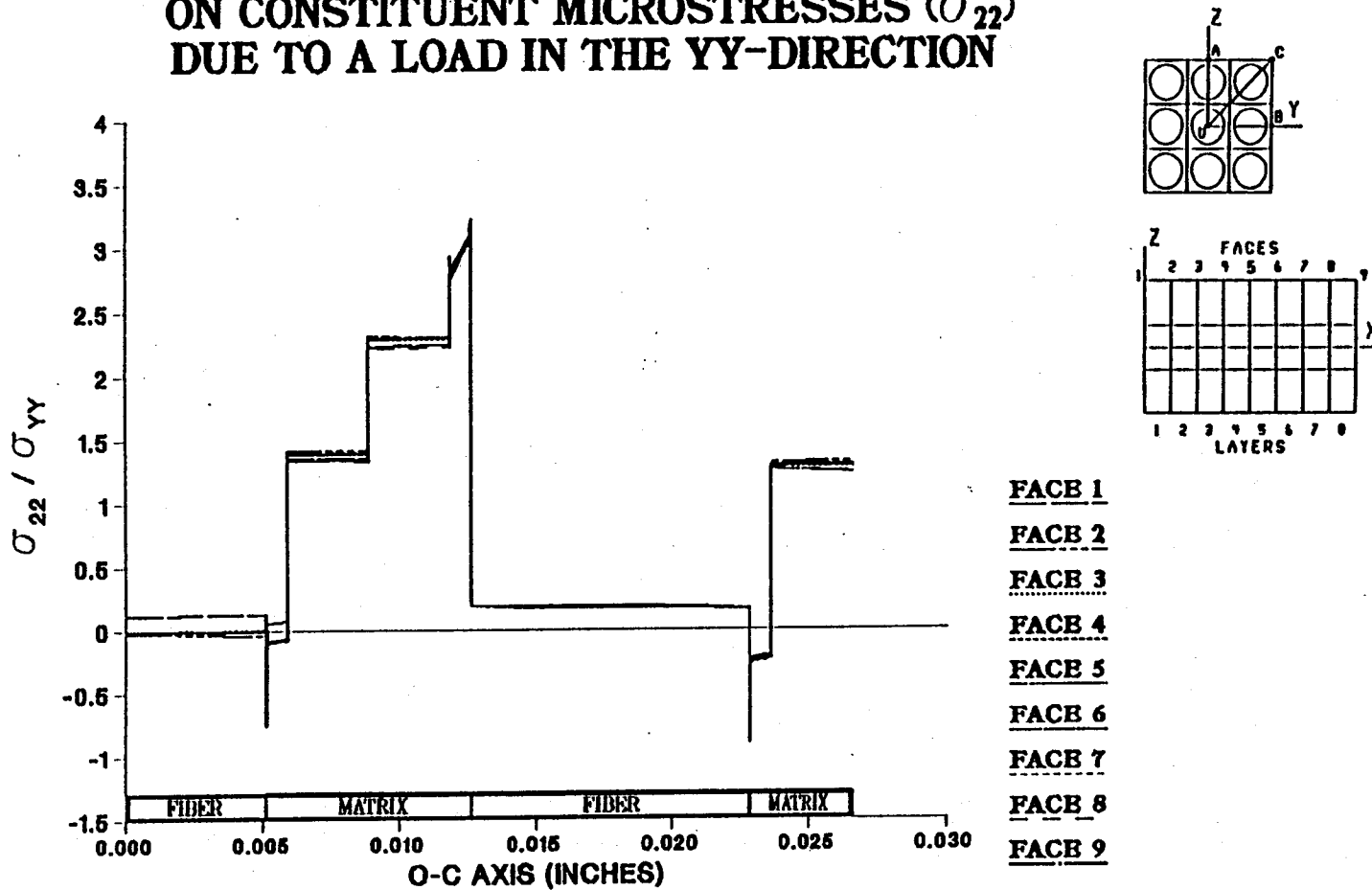


Figure 7.36 — σ_{22} Normalized Microstresses, O-C Direction, 11.11% Debonding, σ_{yy}^e Loading

is carried by the matrix. The step-like increases of stress seen in the matrix material are a result of the stress field around the more transversely straining fibers.

Figures 7.37 through 7.39 are the graphical representations of the constituent microstresses in the 11 direction plotted along a line defined by the O-A line segment with varying degrees of center fiber debonding. These microstresses are due to a transverse enforced displacement as described earlier. Before fiber debonding is initiated, each pair of faces that are an equal distance from the center of the model have the same stress state, as demonstrated by the coincident lines for faces 1 and 9, 2 and 8, 3 and 7, and 4 and 6 (figure 7.37). These faces are referred to as sister faces. Face 5 is in the plane of symmetry at the center of the model and, therefore, has no sister face. In the 11 direction, the fiber is in compression and the matrix is in tension. This is due to the large $\frac{E}{E_{f22}^m}$ ratio, the small $\frac{E}{E_{f11}^m}$ ratio, and the difference in the Poisson's ratios of the fiber and the matrix. As fiber debonding begins the sister faces no longer have the same stress profiles. With increasing fiber debonding, stress levels in the center fiber begin to drop as well as those in the neighboring matrix material of the debonded faces. For faces where the matrix is still bonded to the center fiber, nominal stress risers can be seen forming on the edge of the neighboring fiber and in the matrix areas nearest the debonded fiber (figure 7.38). When the center fiber is totally debonded, these edges of the matrix and the neighboring fibers show signs of local stress concentrations due to the absence of the center fiber

EFFECT OF 0.0% FIBER LENGTH DEBONDING ON CONSTITUENT MICROSTRESSES (σ_{11}) DUE TO A LOAD IN THE YY-DIRECTION

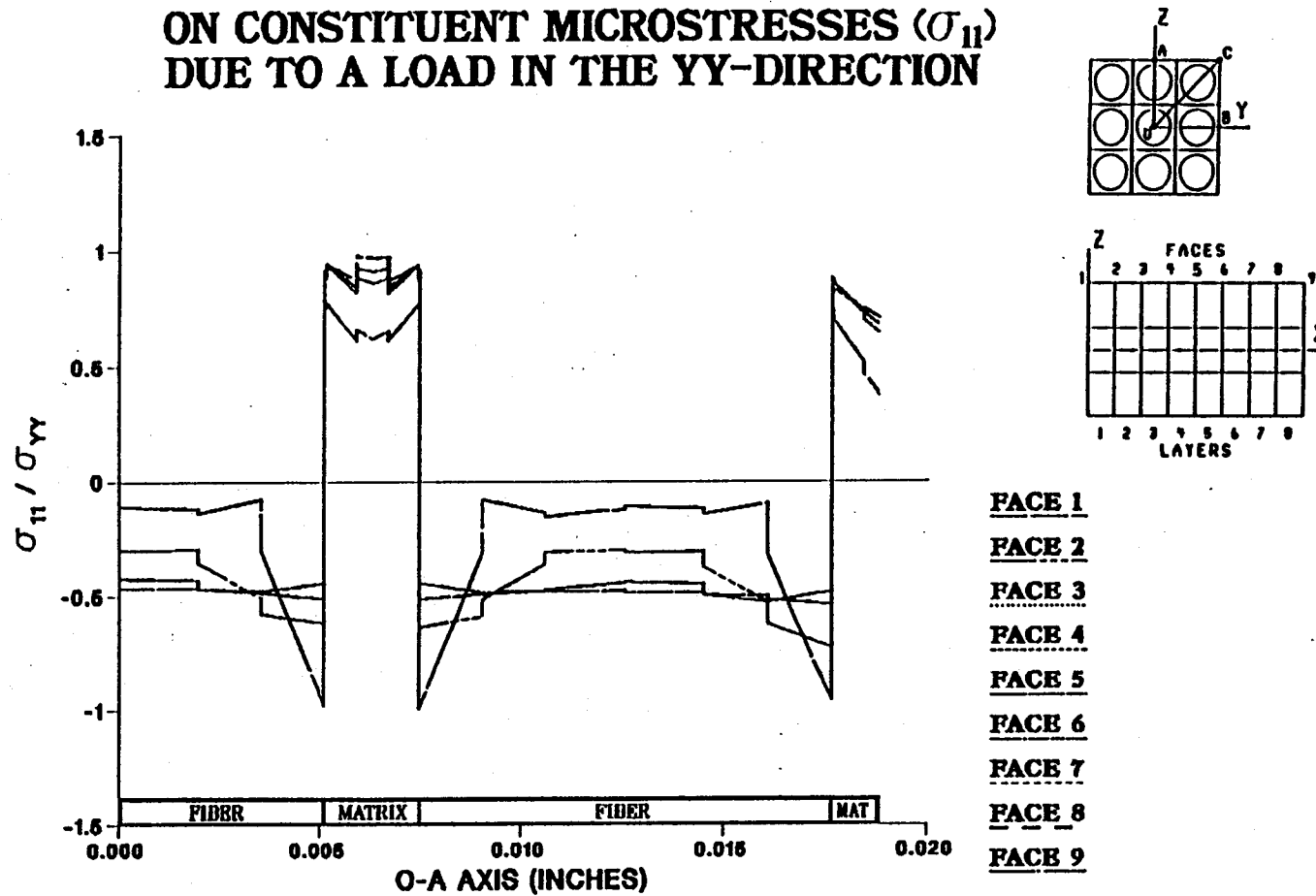


Figure 7.37 - σ_{11} Normalized Microstresses, O-A Direction, 0.0% Debonding, σ_{yy}^e Loading

EFFECT OF 5.56% FIBER LENGTH DEBONDING ON CONSTITUENT MICROSTRESSES (σ_{11}) DUE TO A LOAD IN THE YY-DIRECTION

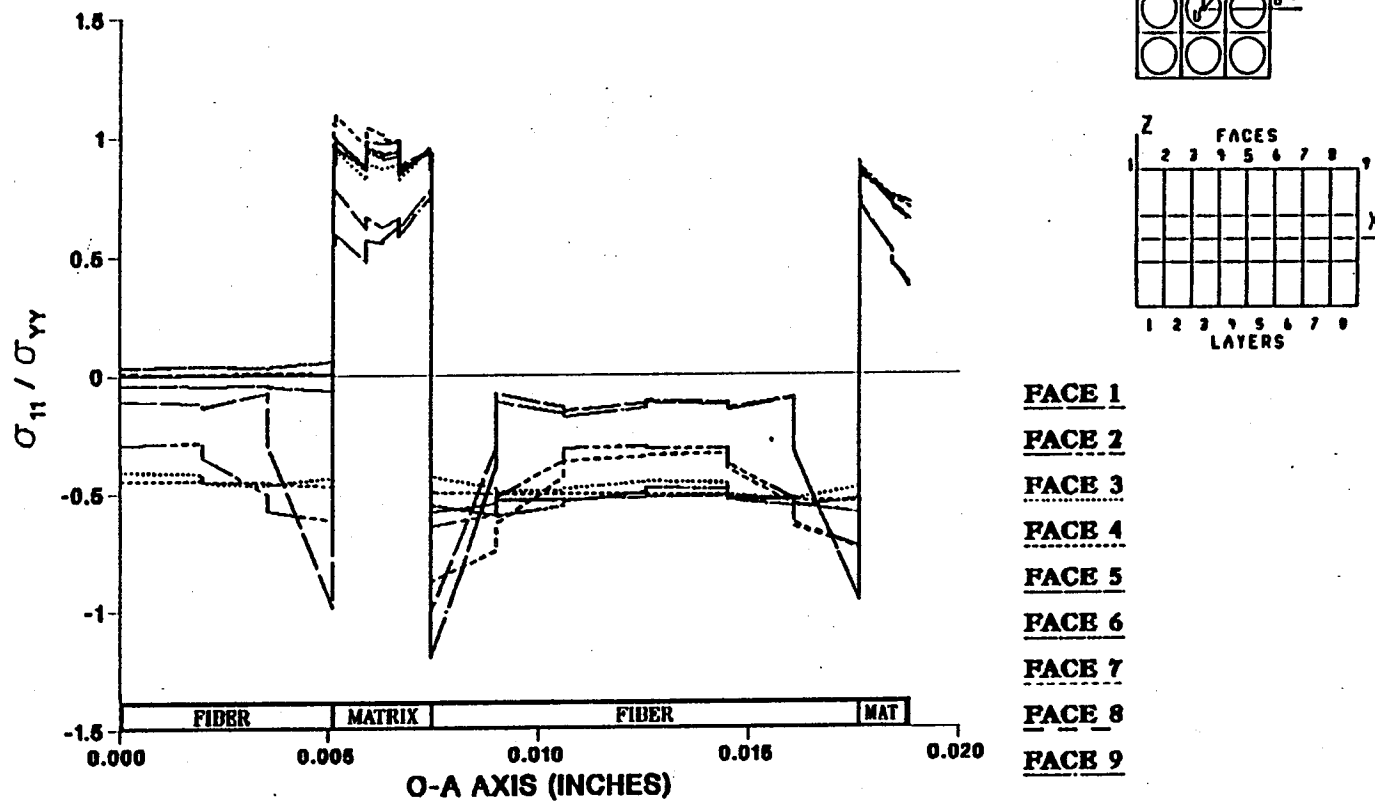


Figure 7.38 - σ_{11} Normalized Microstresses, O-A Direction, 5.56% Debonding, σ_{yy}^e Loading

EFFECT OF 11.1% FIBER LENGTH DEBONDING ON CONSTITUENT MICROSTRESSES (σ_{11}) DUE TO A LOAD IN THE YY-DIRECTION

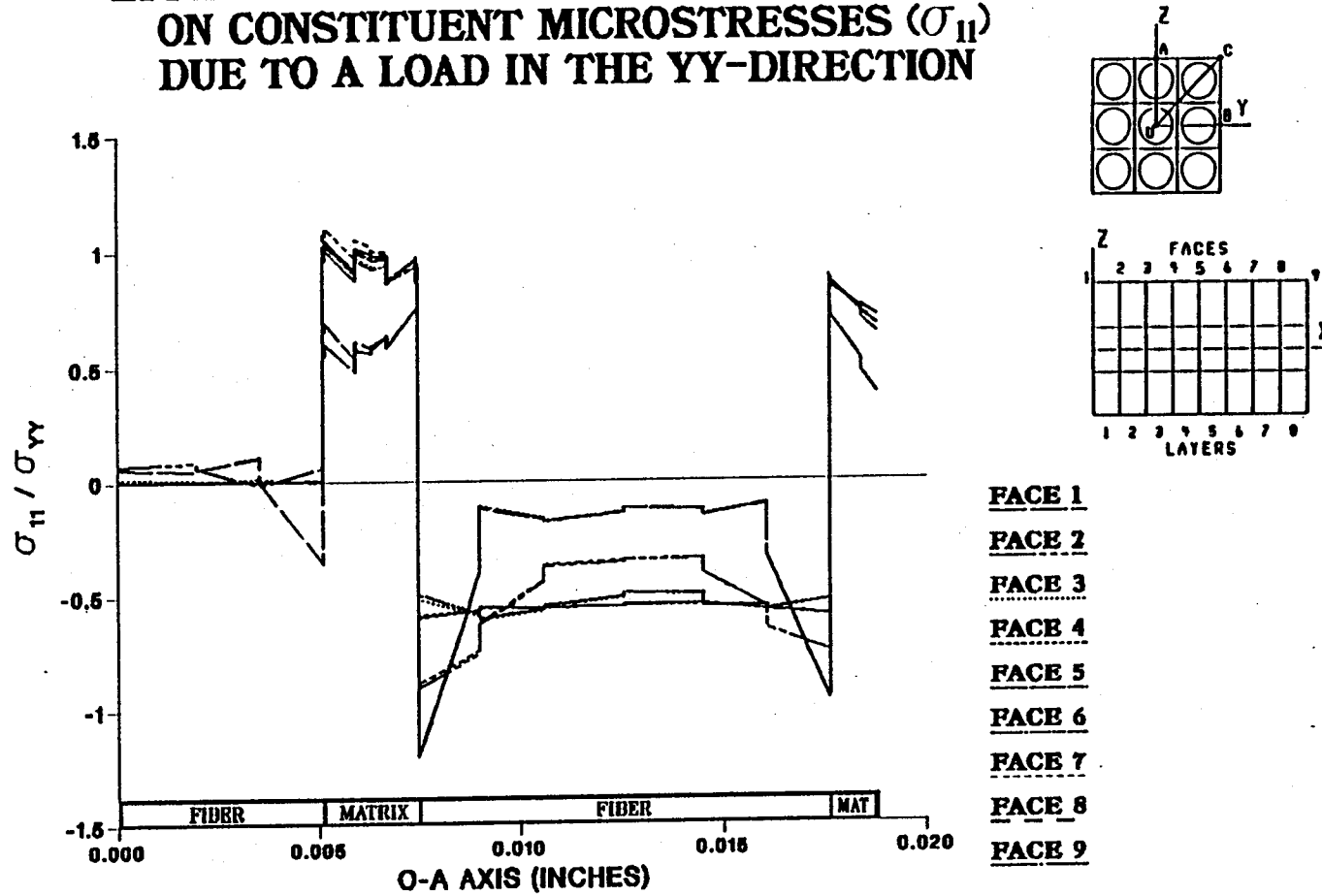


Figure 7.39 - σ_{11} Normalized Microstresses, O-A Direction, 11.1% Debonding, σ_{yy}^e Loading

(figure 7.39). This increase in stress is not distributed across the area of the matrix or the area of the fiber but is manifested in the form of local stress risers in each.

Normalized constituent microstresses in the 11 direction are again displayed in figures 7.40 through 7.48 but in these figures the stresses are plotted along a direction defined by line segment O-B. Again, these stresses are a result of a transverse enforced displacement. Initially, all stresses are compressive and sister faces, as described above, maintain consistent stress profiles (figure 7.40). With the first layer of elements debonded (1.39% fiber debonding), a sharp stress riser appears in tension in face 9 and the stress profiles of the sister faces diverge (figure 7.41). As the next layer of elements is allowed to debond, the stress riser in the center fiber is diminished. As before, stress risers develop at the edges of the neighboring fibers and in the matrix. The stress concentrations in the neighboring fibers dominate (figure 7.42). When the fiber is completely debonded, the stress level in the center fiber approaches zero and the resulting stress concentrations are seen as local effects at the edges of the fiber and matrix (figure 7.48).

Figures 7.49 through 7.51 depict the stress (σ_{11}) profiles along a line defined by O-C due to the load condition discussed above with varying levels of center fiber debonding. Again, for the case of no fiber debonding, stress profiles of each pair of sister faces closely correlate with each other. With increasing center fiber debonding, the stress levels of the surrounding matrix and fiber materials are not significantly affected. Some drop in the tensile stress level in the neighboring matrix material can be seen along with some increase in the compressive stress level of the neighboring fiber, neither of which are very

EFFECT OF 0.0% FIBER LENGTH DEBONDING ON CONSTITUENT MICROSTRESSES (σ_{11}) DUE TO A LOAD IN THE YY-DIRECTION

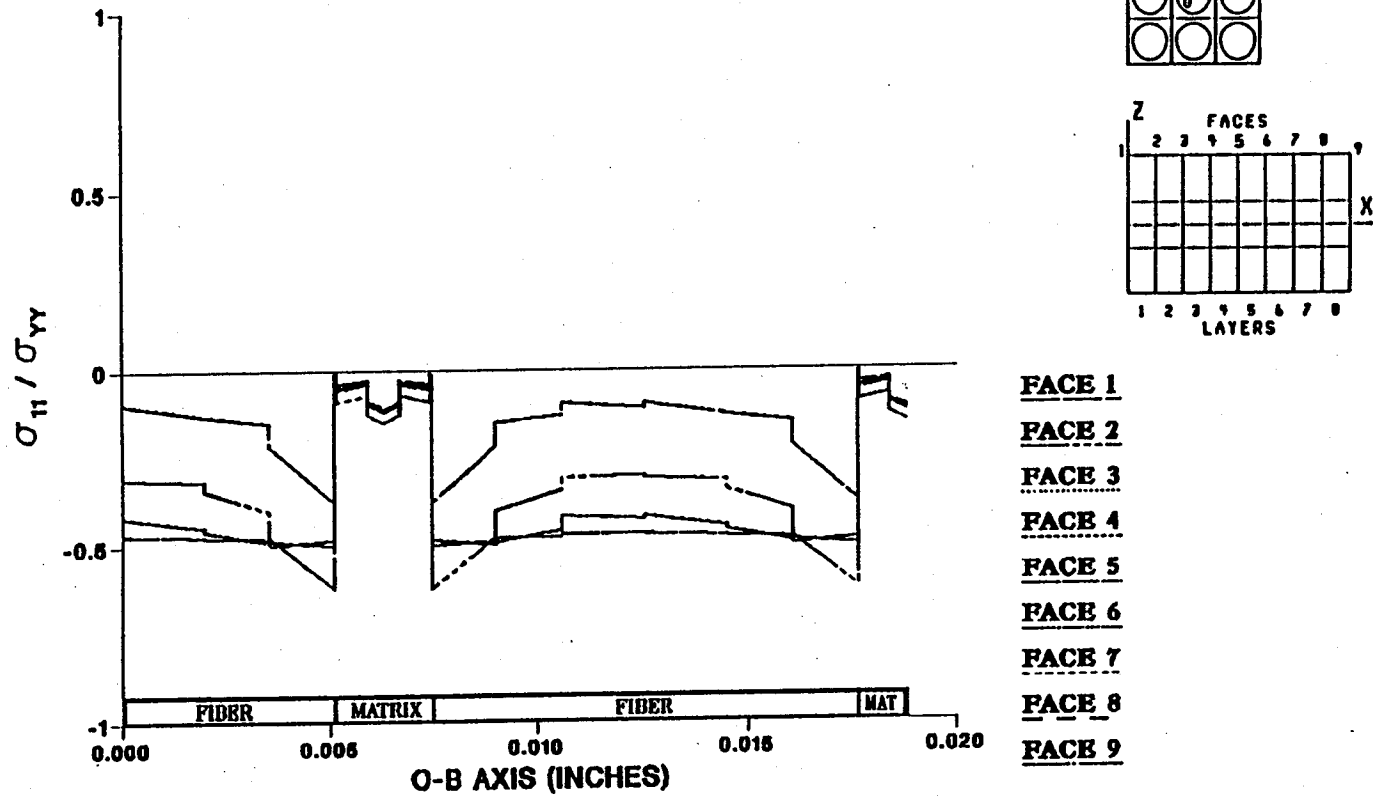


Figure 7.40 - σ_{11} Normalized Microstresses, O-B Direction, 0.0% Debonding, σ_{yy}^e Loading

EFFECT OF 1.39% FIBER LENGTH DEBONDING ON CONSTITUENT MICROSTRESSES (σ_{11}) DUE TO A LOAD IN THE YY-DIRECTION

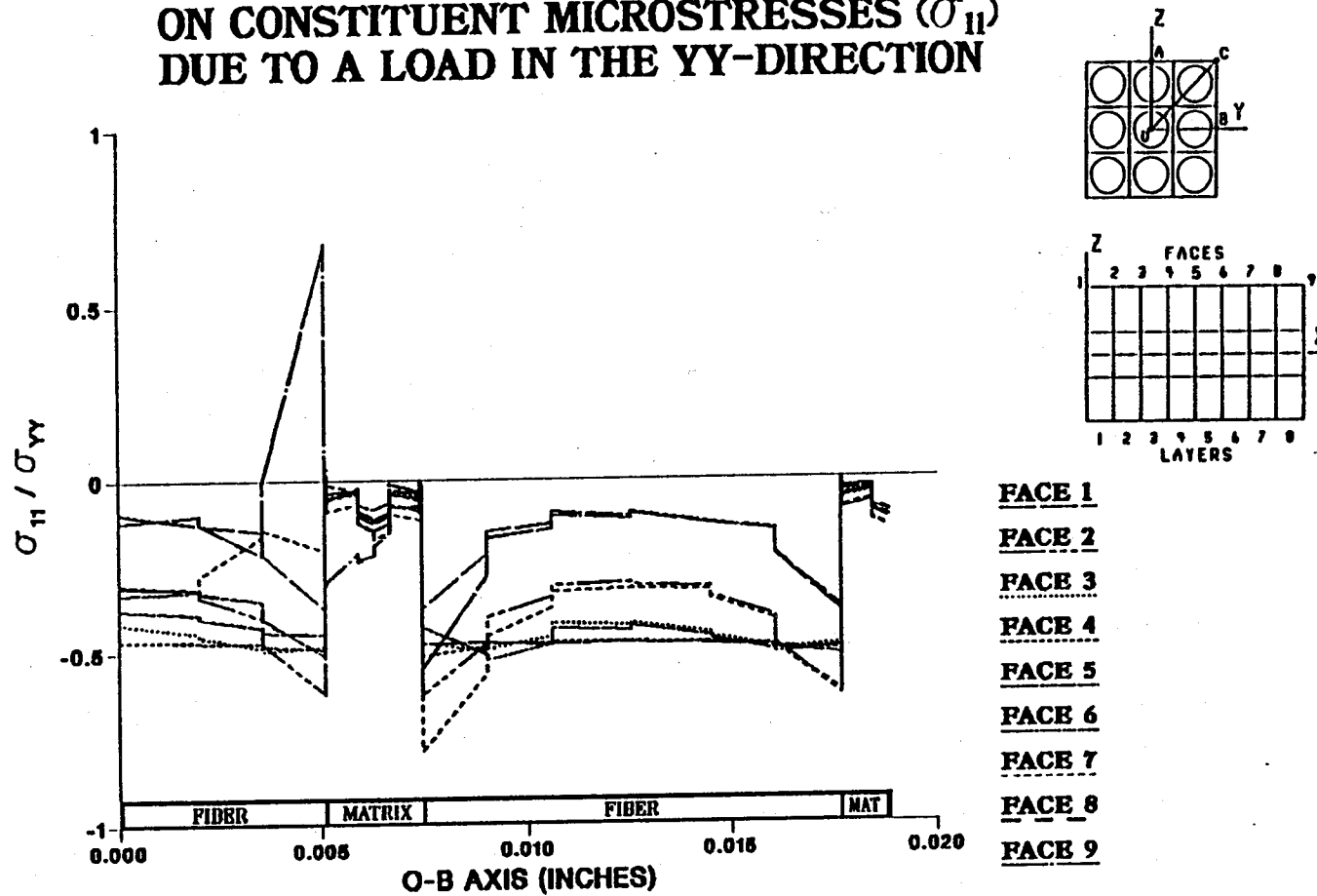


Figure 7.41 - σ_{11} Normalized Microstresses, O-B Direction, 1.39% Debonding, σ_{yy}^e Loading

EFFECT OF 2.78% FIBER LENGTH DEBONDING ON CONSTITUENT MICROSTRESSES (σ_{11}) DUE TO A LOAD IN THE YY-DIRECTION

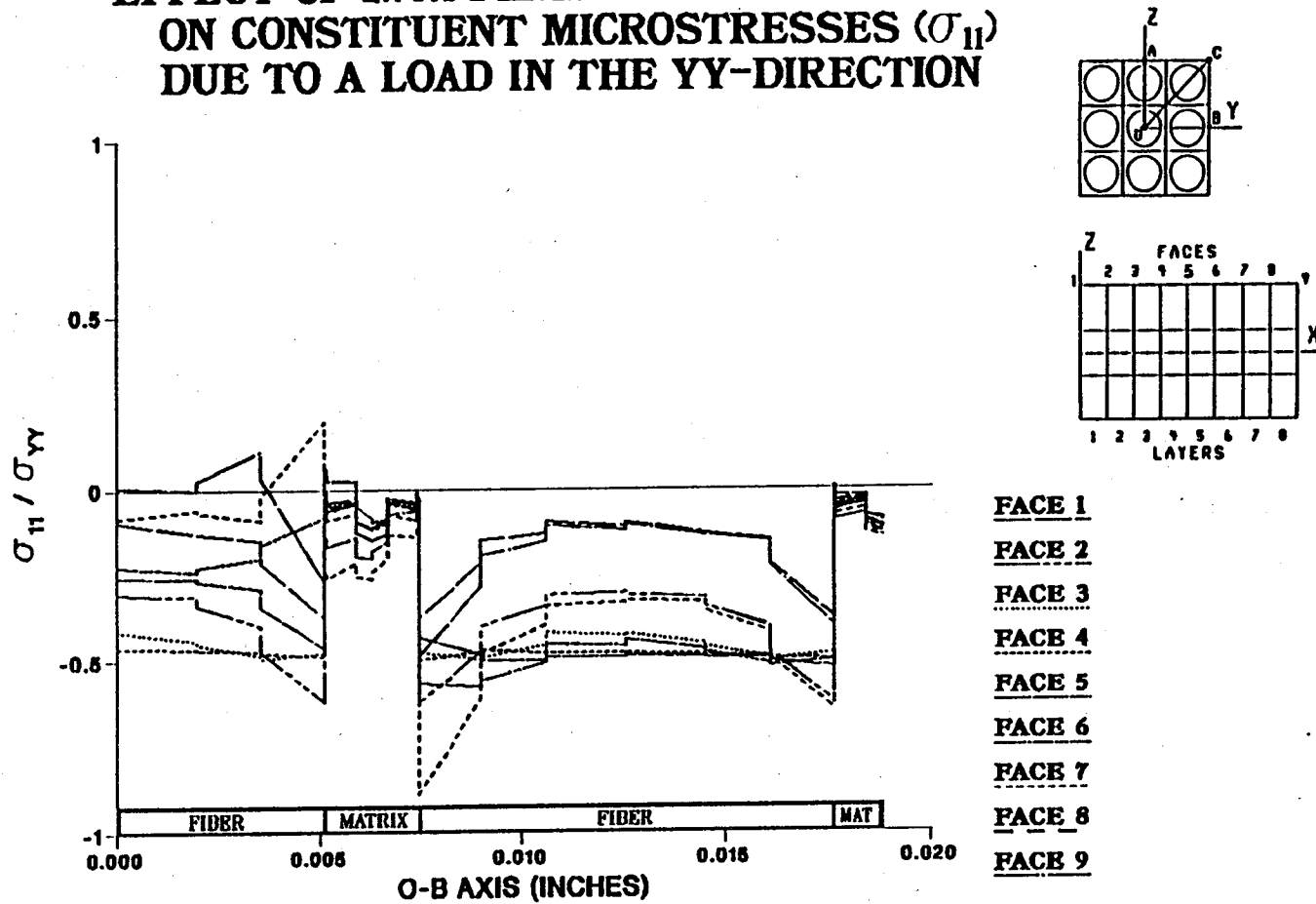


Figure 7.42 - σ_{11} Normalized Microstresses, O-B Direction, 2.78% Debonding, σ_{yy}^e Loading

EFFECT OF 4.17% FIBER LENGTH DEBONDING ON CONSTITUENT MICROSTRESSES (σ_{11}) DUE TO A LOAD IN THE YY-DIRECTION

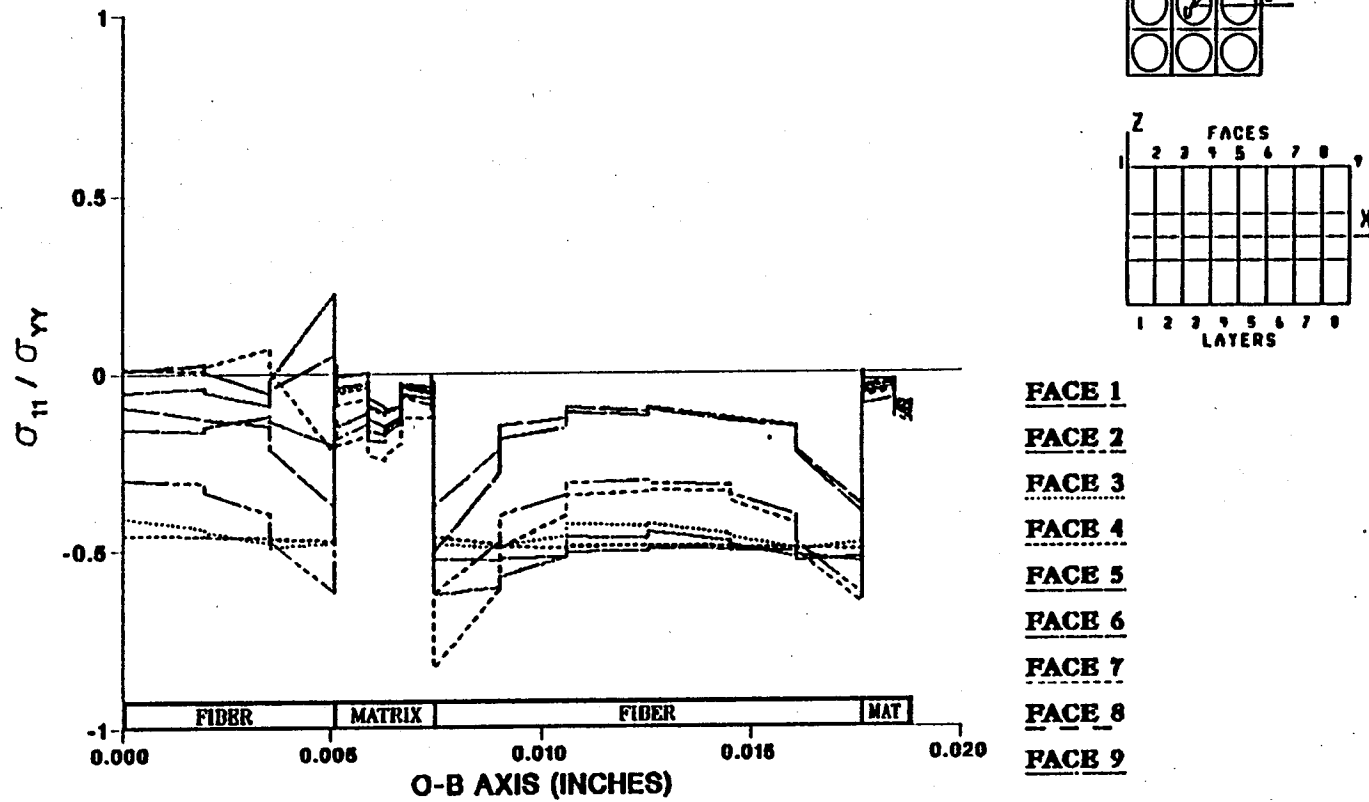


Figure 7.43 - σ_{11} Normalized Microstresses, O-B Direction, 4.17% Debonding, σ_{yy}^e Loading

EFFECT OF 5.56% FIBER LENGTH DEBONDING ON CONSTITUENT MICROSTRESSES (σ_{11}) DUE TO A LOAD IN THE YY-DIRECTION

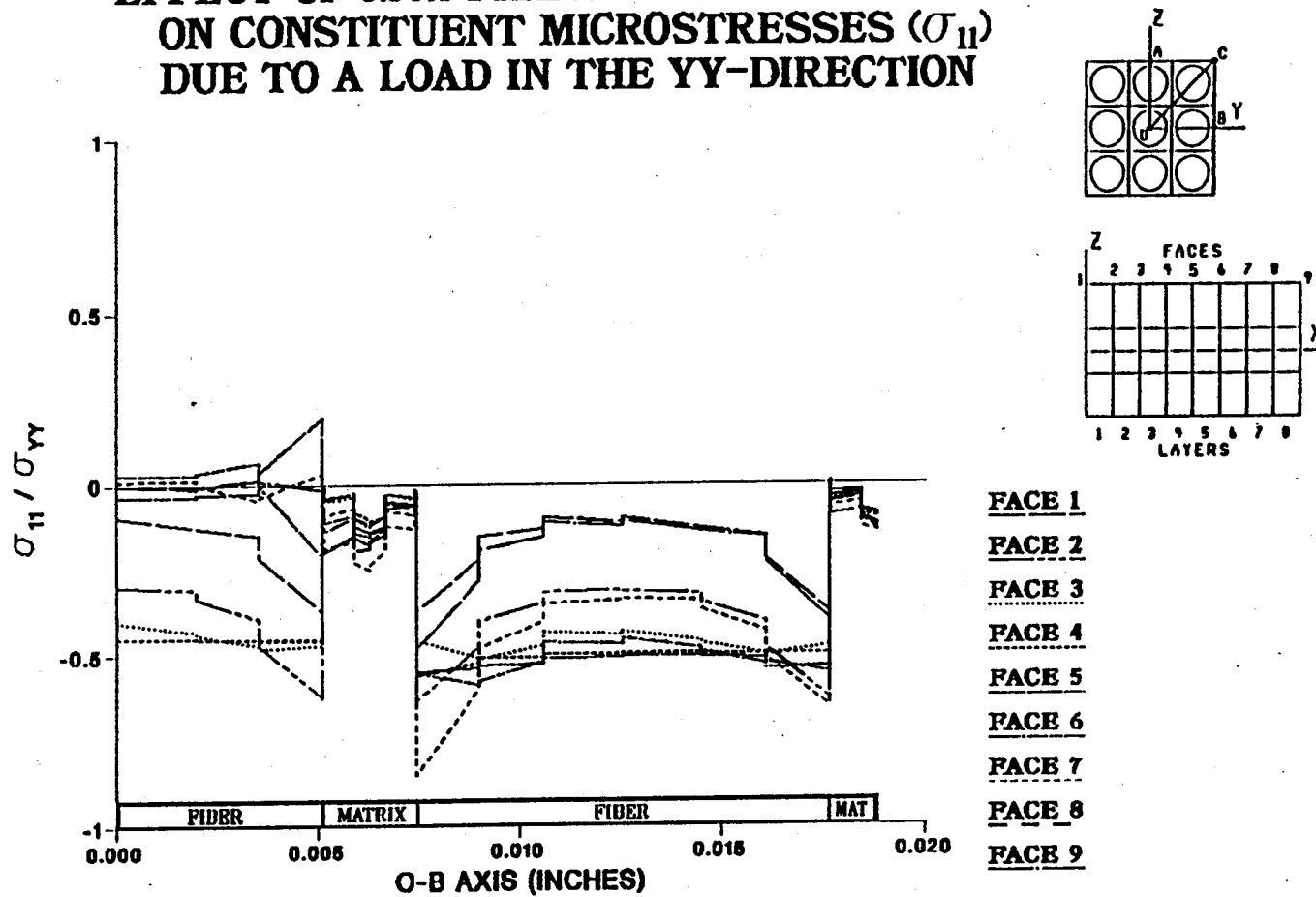


Figure 7.44 — σ_{11} Normalized Microstresses, O-B Direction, 5.56% Debonding, σ_{yy}^e Loading

EFFECT OF 6.94% FIBER LENGTH DEBONDING ON CONSTITUENT MICROSTRESSES (σ_{11}) DUE TO A LOAD IN THE YY-DIRECTION

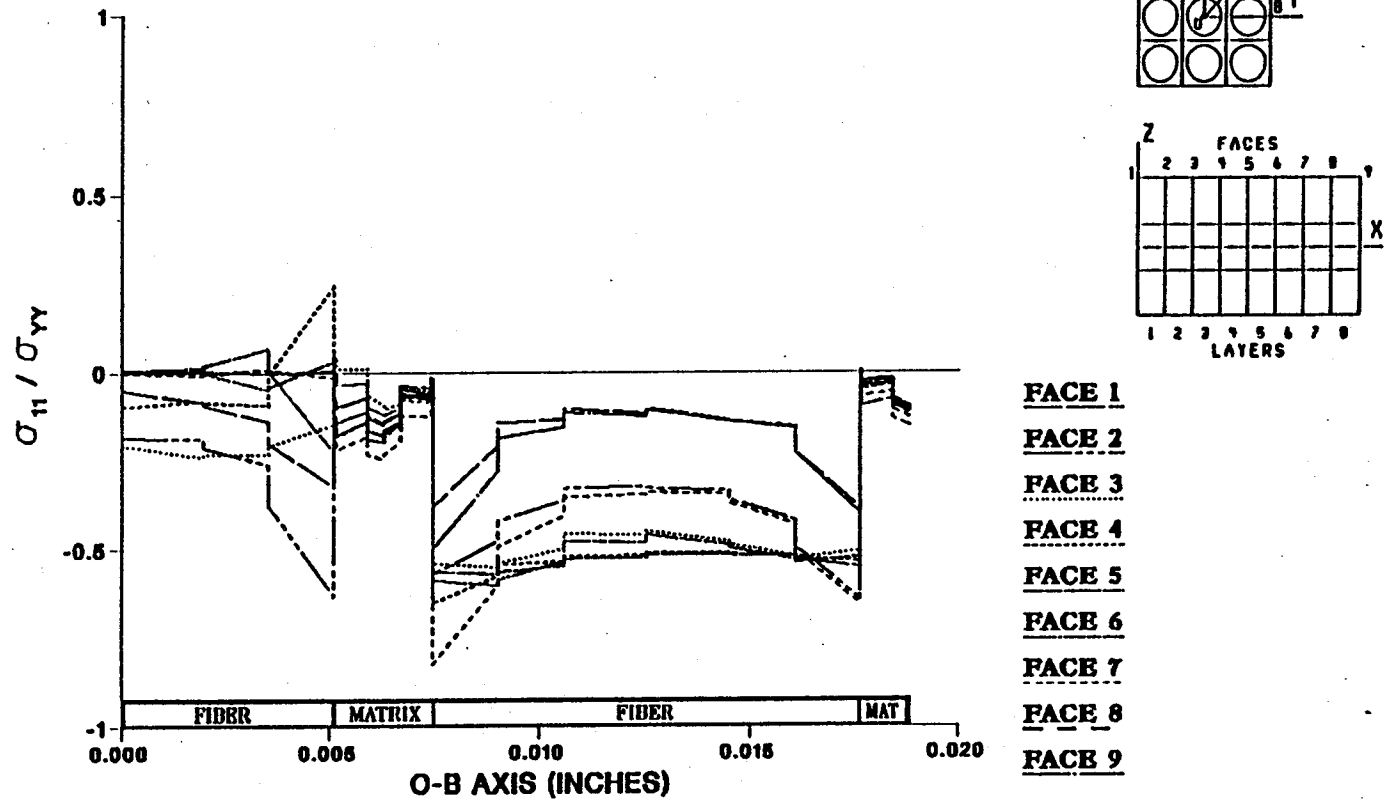


Figure 7.45 - σ_{11} Normalized Microstresses, O-B Direction, 6.94% Debonding, σ_{yy}^e Loading

EFFECT OF 8.33% FIBER LENGTH DEBONDING ON CONSTITUENT MICROSTRESSES (σ_{11}) DUE TO A LOAD IN THE YY-DIRECTION

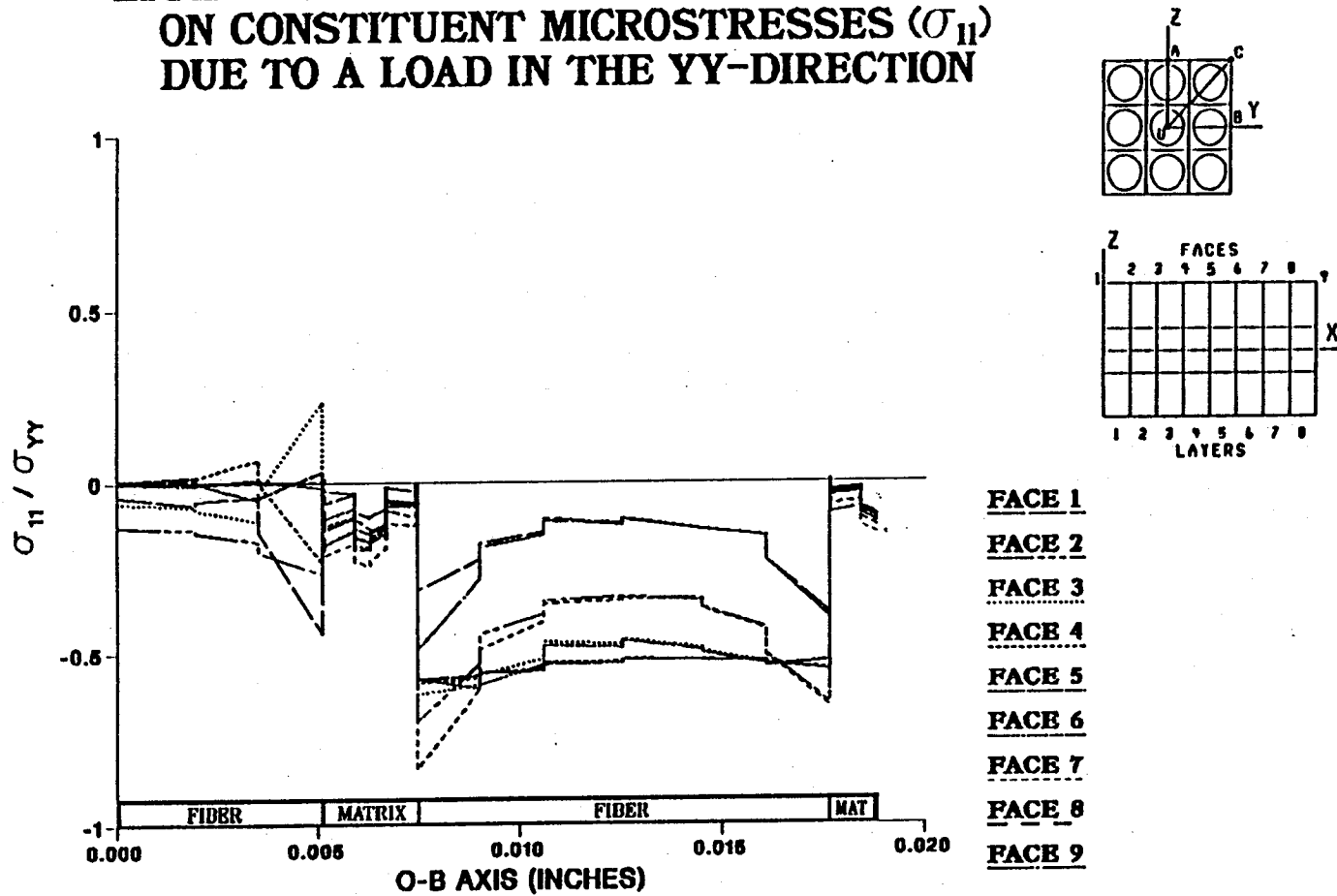


Figure 7.46 - σ_{11} Normalized Microstresses, O-B Direction, 8.33% Debonding, σ_{yy}^e Loading

EFFECT OF 9.72% FIBER LENGTH DEBONDING ON CONSTITUENT MICROSTRESSES (σ_{11}) DUE TO A LOAD IN THE YY-DIRECTION

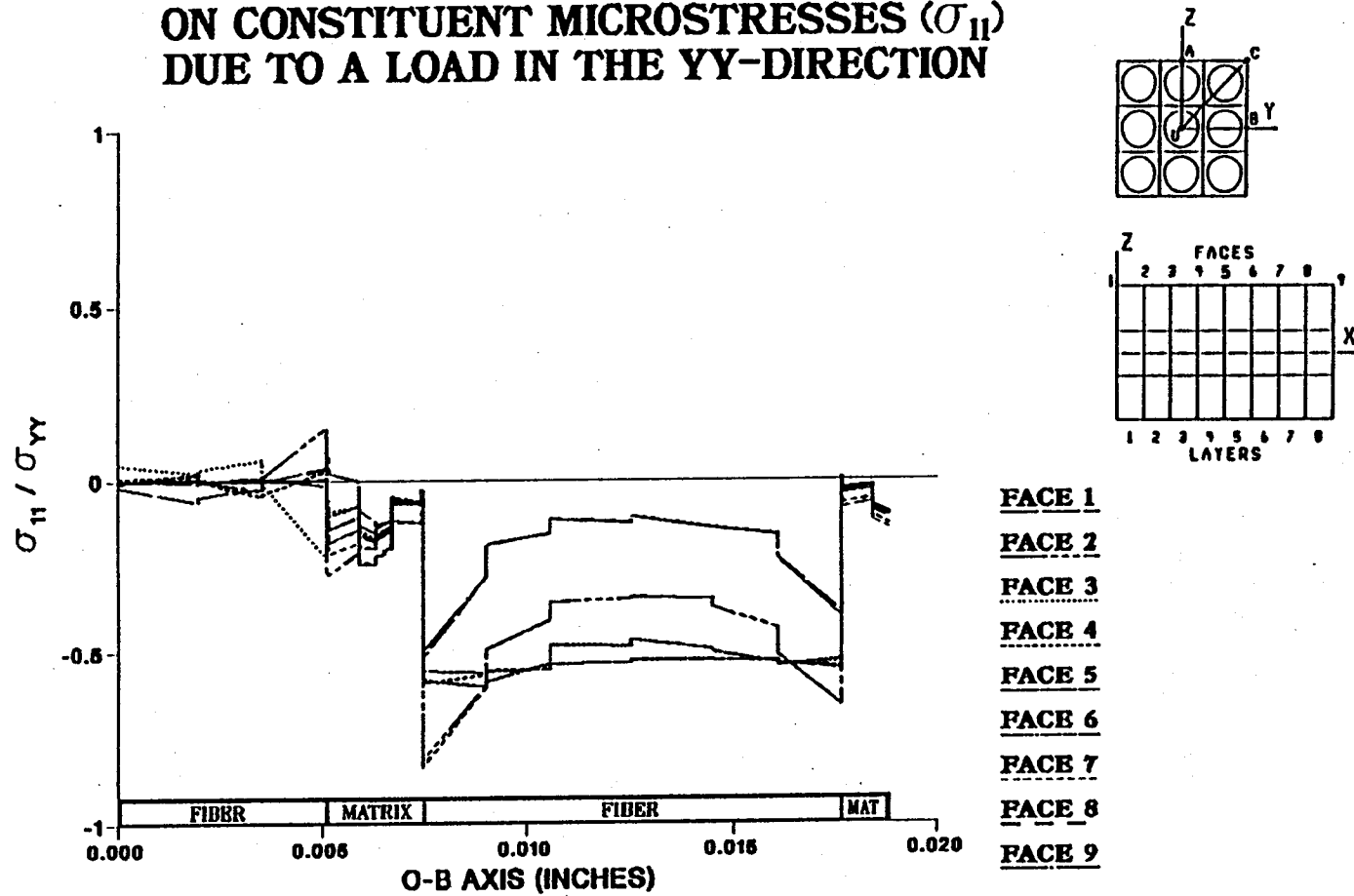


Figure 7.47 - σ_{11} Normalized Microstresses, O-B Direction, 9.72% Debonding, σ_{yy}^e Loading

EFFECT OF 11.11% FIBER LENGTH DEBONDING ON CONSTITUENT MICROSTRESSES (σ_{11}) DUE TO A LOAD IN THE YY-DIRECTION

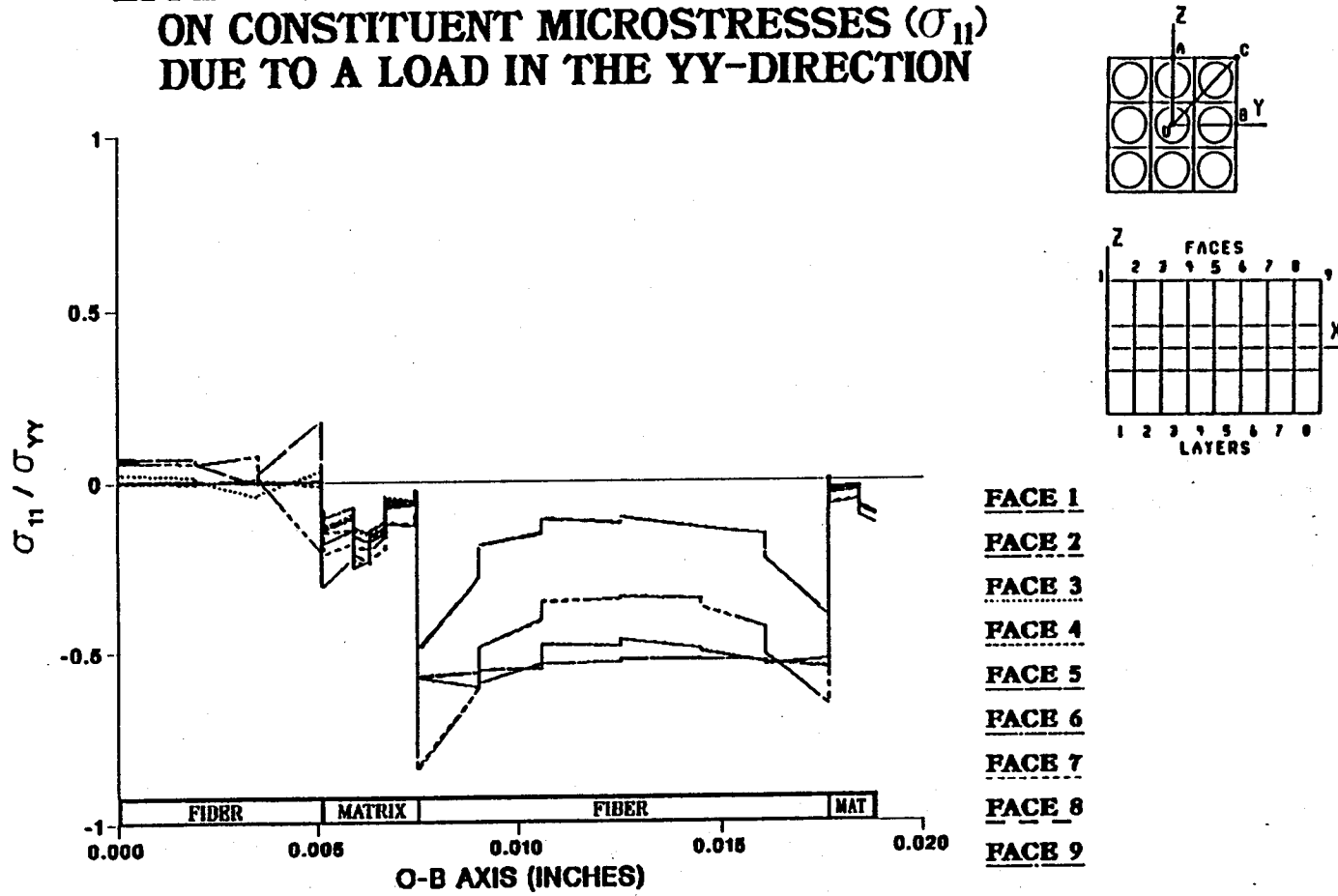
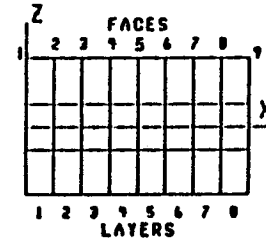
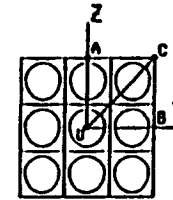
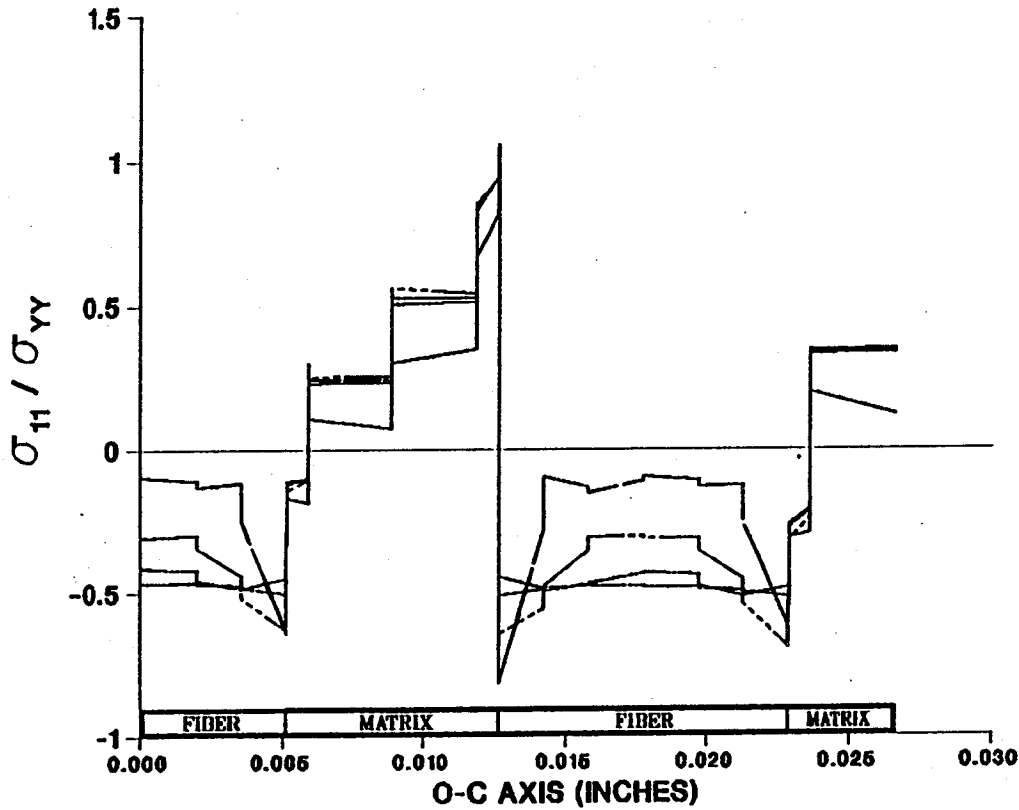


Figure 7.48 - σ_{11} Normalized Microstresses, O-B Direction, 11.11% Debonding, σ_{yy}^e Loading

EFFECT OF 0.0% FIBER LENGTH DEBONDING ON CONSTITUENT MICROSTRESSES (σ_{11}) DUE TO A LOAD IN THE YY-DIRECTION



- FACE 1
- FACE 2
- FACE 3
- FACE 4
- FACE 5
- FACE 6
- FACE 7
- FACE 8
- FACE 9

Figure 7.49 - σ_{11} Normalized Microstresses, O-C Direction, 0.0% Debonding, σ_{yy}^e Loading

EFFECT OF 5.56% FIBER LENGTH DEBONDING ON CONSTITUENT MICROSTRESSES (σ_{11}) DUE TO A LOAD IN THE YY-DIRECTION

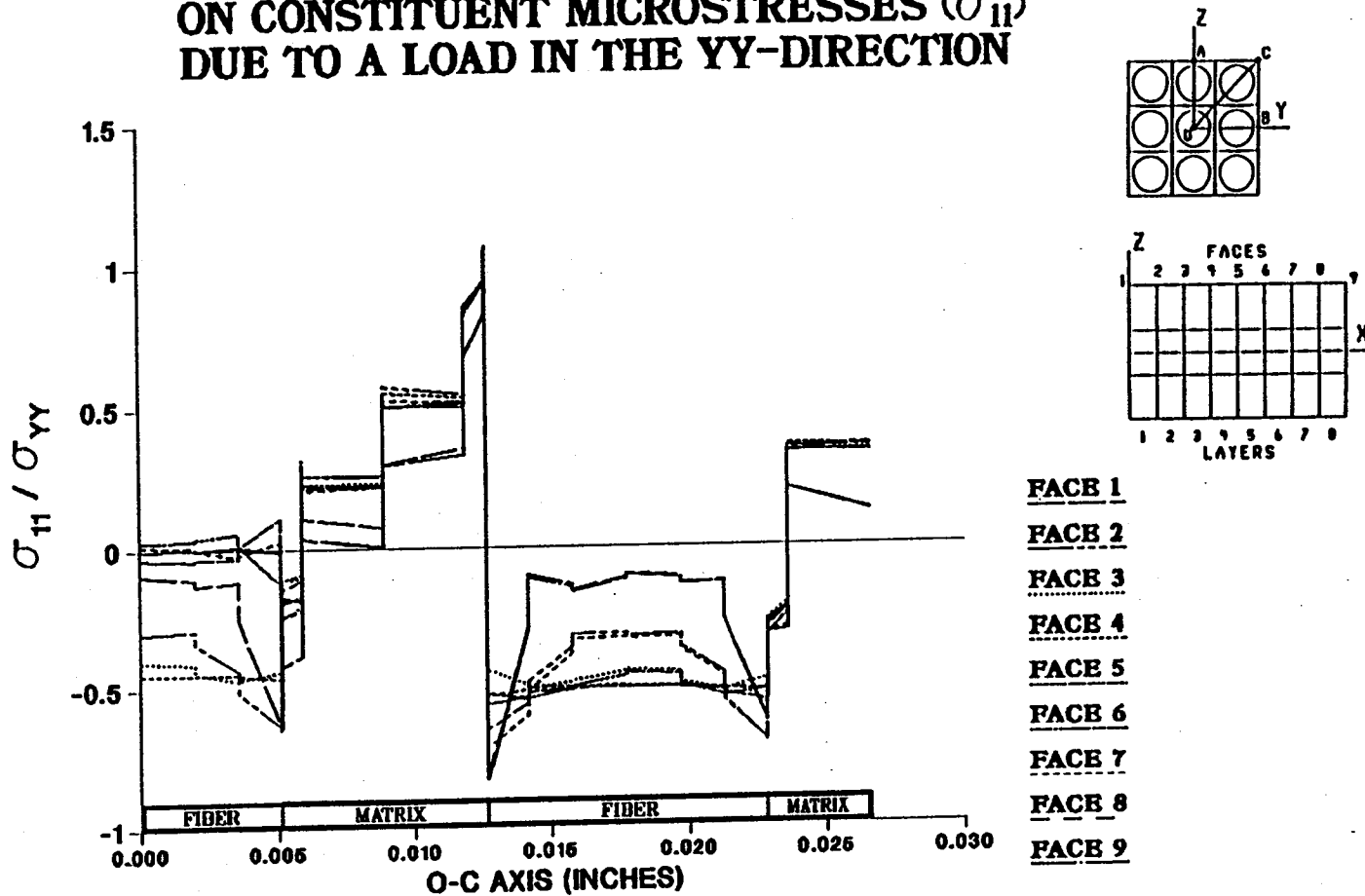


Figure 7.50 - σ_{11} Normalized Microstresses, O-C Direction, 5.56% Debonding, σ_{yy}^e Loading

EFFECT OF 11.11% FIBER LENGTH DEBONDING ON CONSTITUENT MICROSTRESSES (σ_{11}) DUE TO A LOAD IN THE YY-DIRECTION

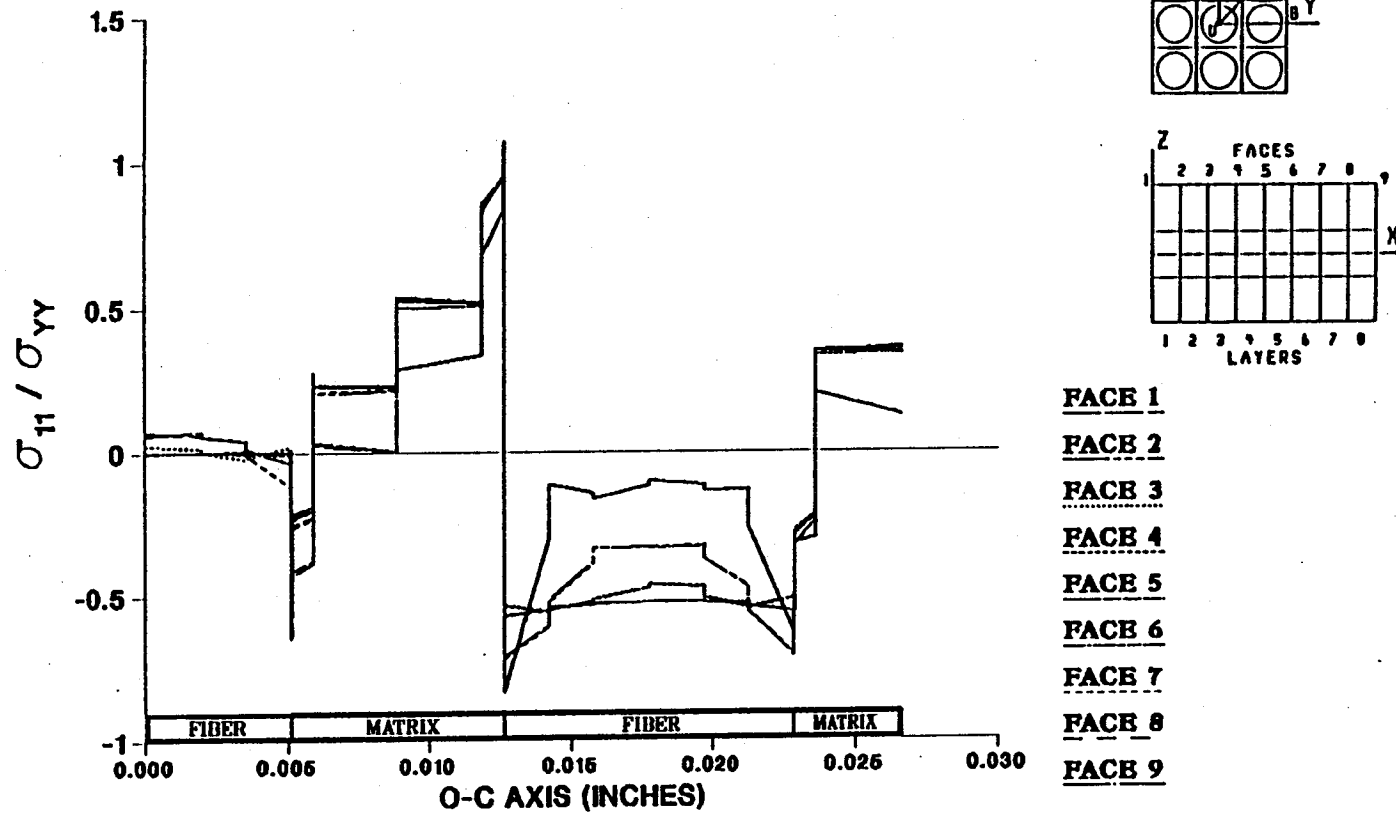


Figure 7.51 - σ_{11} Normalized Microstresses, O-C Direction, 11.11% Debonding, σ_{yy}^e Loading

dramatic. When the center fiber is at 100% disbond the stresses in the center fiber have diminished but no significant change has taken place in the stress profiles of the rest of the composite.

Figures 7.52 to 7.54 depict the microstresses in the 33 direction (σ_{33}) due to a transverse load, σ_{yy} . They are plotted along the O-B direction for various degrees of center fiber debonding. The most dramatic level of stress is at the interface between fiber and matrix. As the center fiber is debonded, these spikes of compressive stress increase as the stress state in the center fiber is relaxed. The drop in the stress state of the center fiber is minimal. Virtually no increase in the stress level of the neighboring fiber is seen, even when the center fiber is totally debonded (figure 7.54). The result of the debonding is a localized increase in compressive stress in the matrix material bordering on the debonded fiber.

Figures 7.55, 7.56, and 7.57 depict the transverse shear microstresses, σ_{23} , developed in the composite as the result of a transverse enforced displacement. These microstresses are plotted along lines in the O-A, O-B, and O-C directions, respectively. No significant change in the stress profiles shown in these figures takes place with the onset of center fiber debonding. The majority of the shear stresses occur in the matrix regions, therefore, the debonding of the center fiber does not significantly effect the stress levels in the rest of the composite.

EFFECT OF 0.0% FIBER LENGTH DEBONDING ON CONSTITUENT MICROSTRESSES (σ_{33}) DUE TO A LOAD IN THE YY-DIRECTION

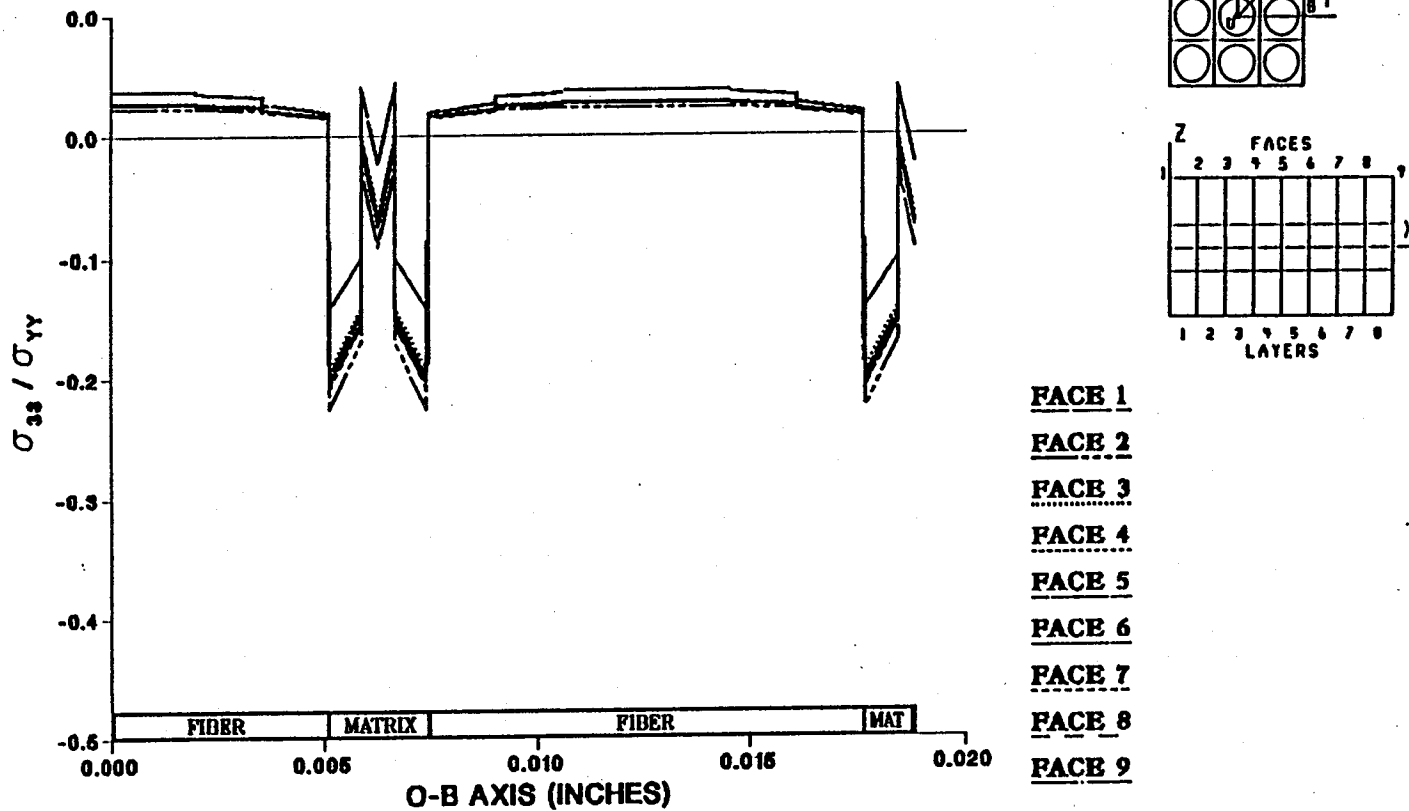
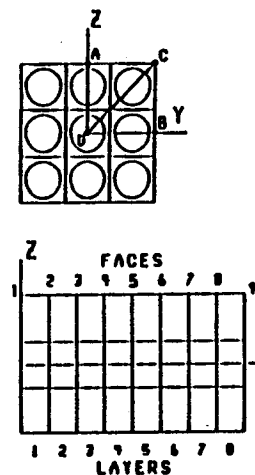
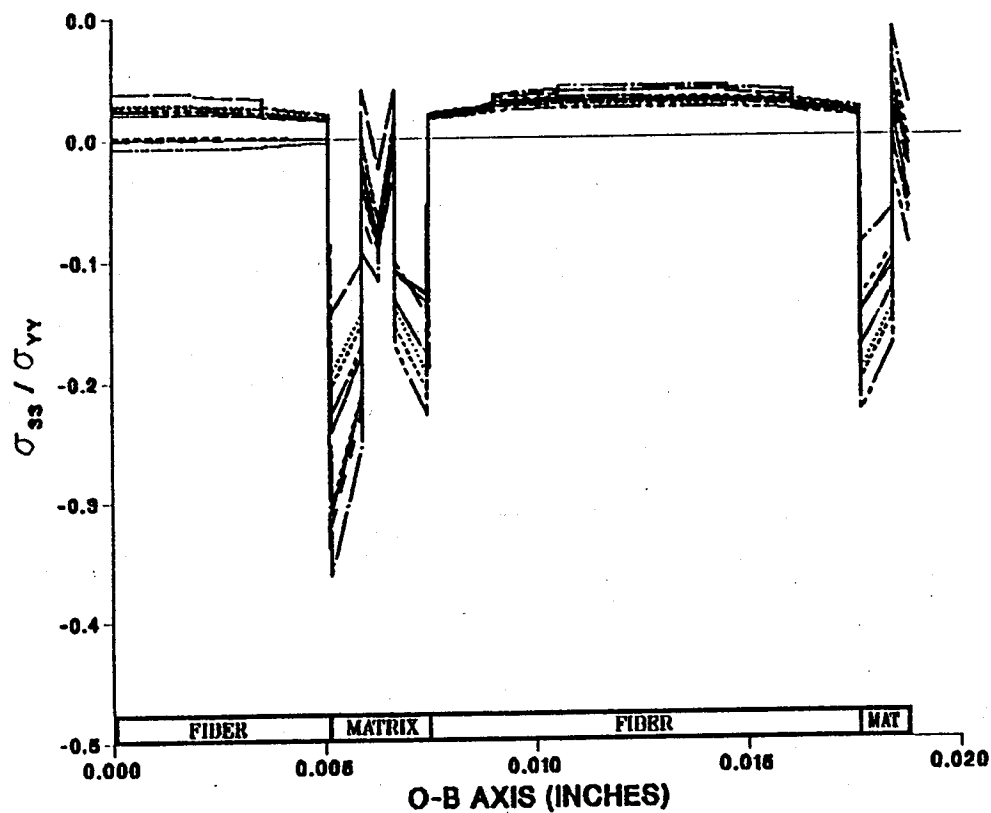


Figure 7.52 - σ_{33} Normalized Microstresses, O-B Direction, 0.0% Debonding, σ_{yy}^e Loading

EFFECT OF 5.56% FIBER LENGTH DEBONDING ON CONSTITUENT MICROSTRESSES (σ_{33}) DUE TO A LOAD IN THE YY-DIRECTION



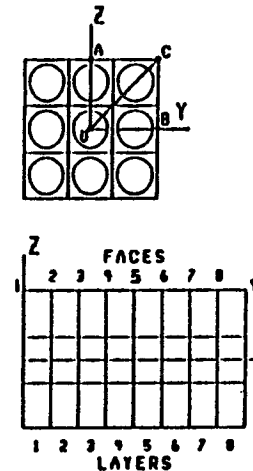
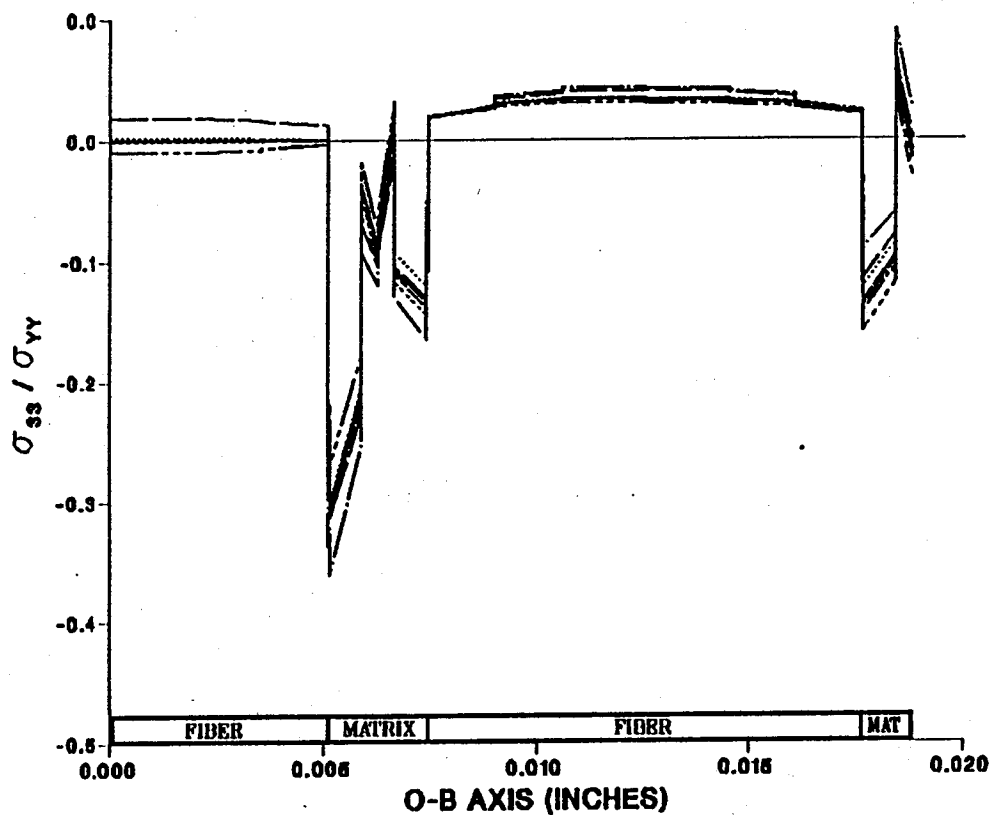
130



- FACE 1
- FACE 2
- FACE 3
- FACE 4
- FACE 5
- FACE 6
- FACE 7
- FACE 8
- FACE 9

Figure 7.53 — σ_{33} Normalized Microstresses, O-B Direction, 5.56% Debonding, σ_{yy}^e Loading

EFFECT OF 11.1% FIBER LENGTH DEBONDING ON CONSTITUENT MICROSTRESSES (σ_{33}) DUE TO A LOAD IN THE YY-DIRECTION



- FACE 1
- FACE 2
- FACE 3
- FACE 4
- FACE 5
- FACE 6
- FACE 7
- FACE 8
- FACE 9

Figure 7.54 — σ_{33} Normalized Microstresses, O-B Direction, 11.1% Debonding, σ_{yy}^e Loading

EFFECT OF 0.0% FIBER LENGTH DEBONDING ON CONSTITUENT MICROSTRESSES (σ_{23}) DUE TO A LOAD IN THE YY-DIRECTION

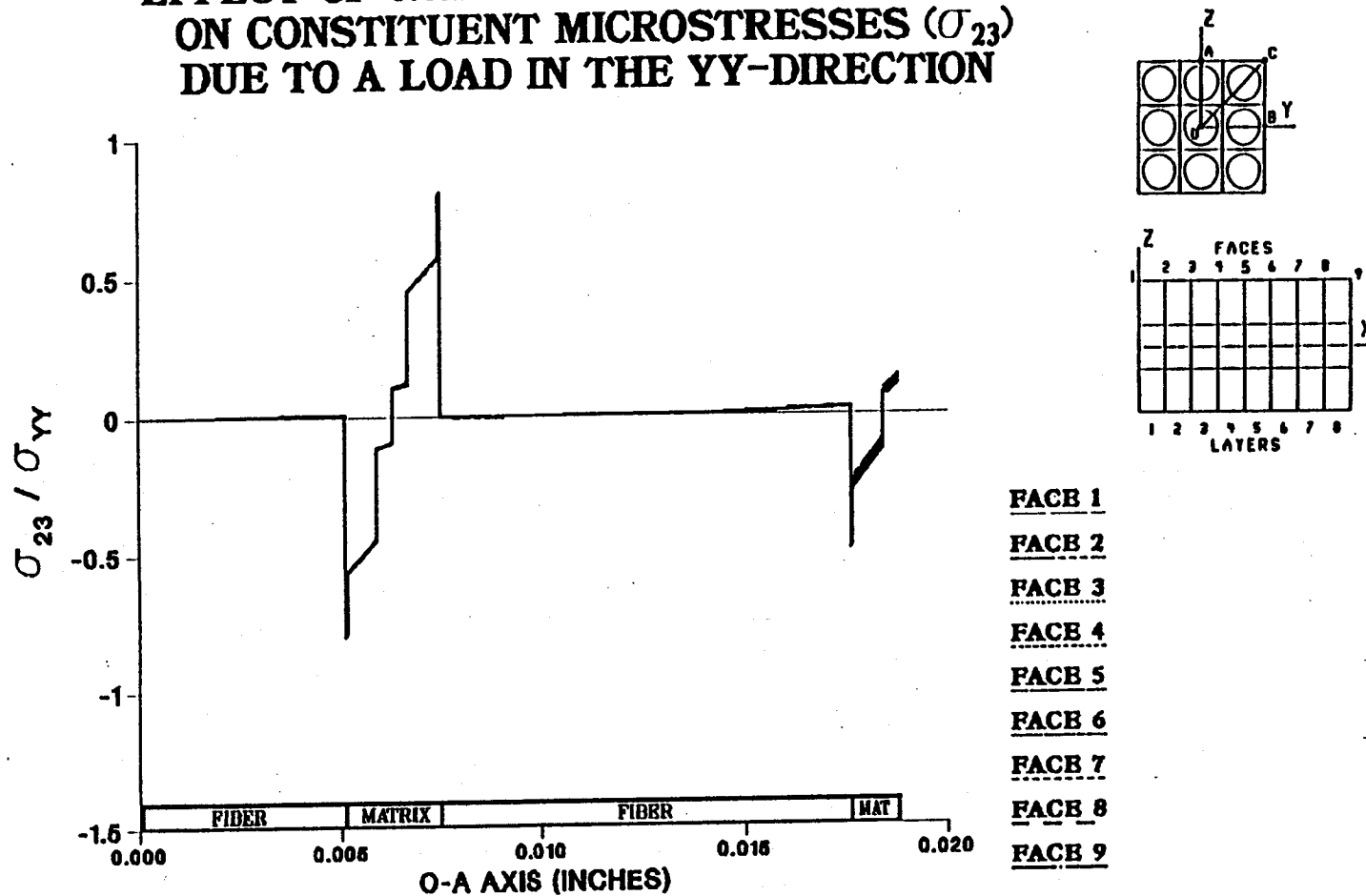
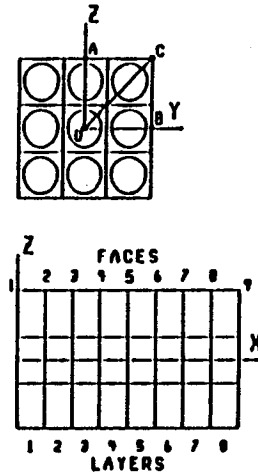
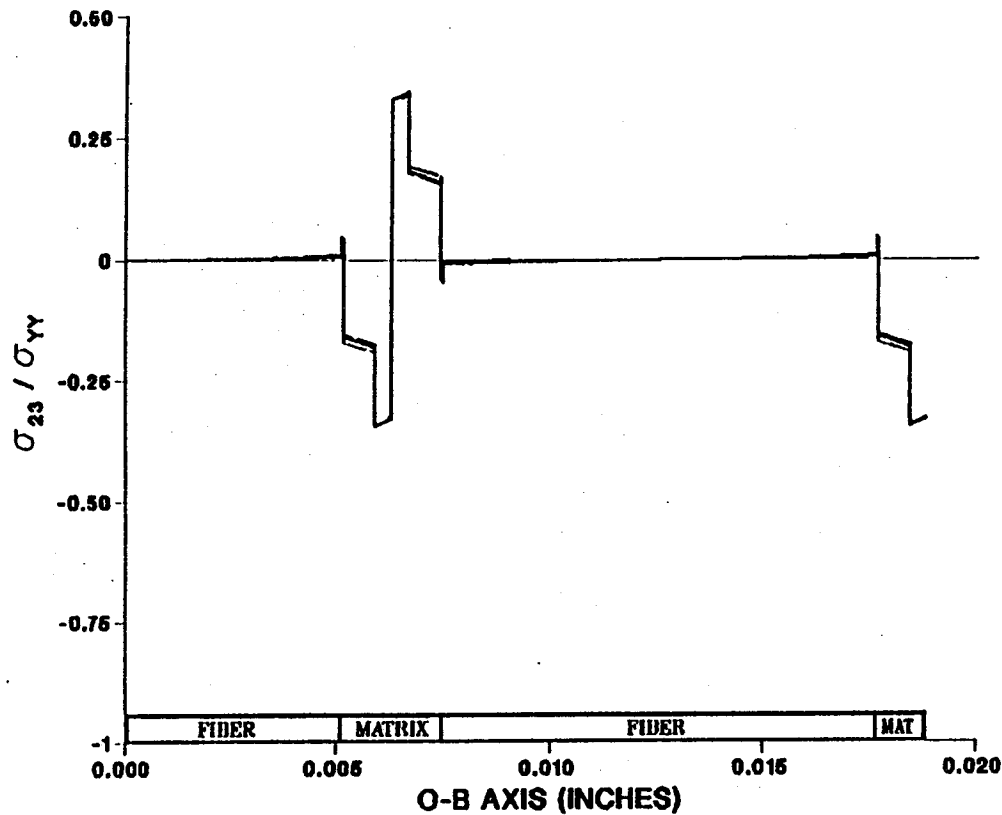


Figure 7.55 - σ_{23} Normalized Microstresses, O-A Direction, 0.0% Debonding, σ_{yy}^e Loading

EFFECT OF 0.0% FIBER LENGTH DEBONDING ON CONSTITUENT MICROSTRESSES (σ_{23}) DUE TO A LOAD IN THE YY-DIRECTION

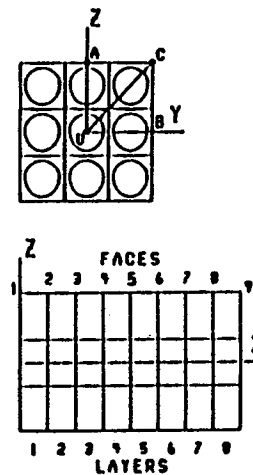
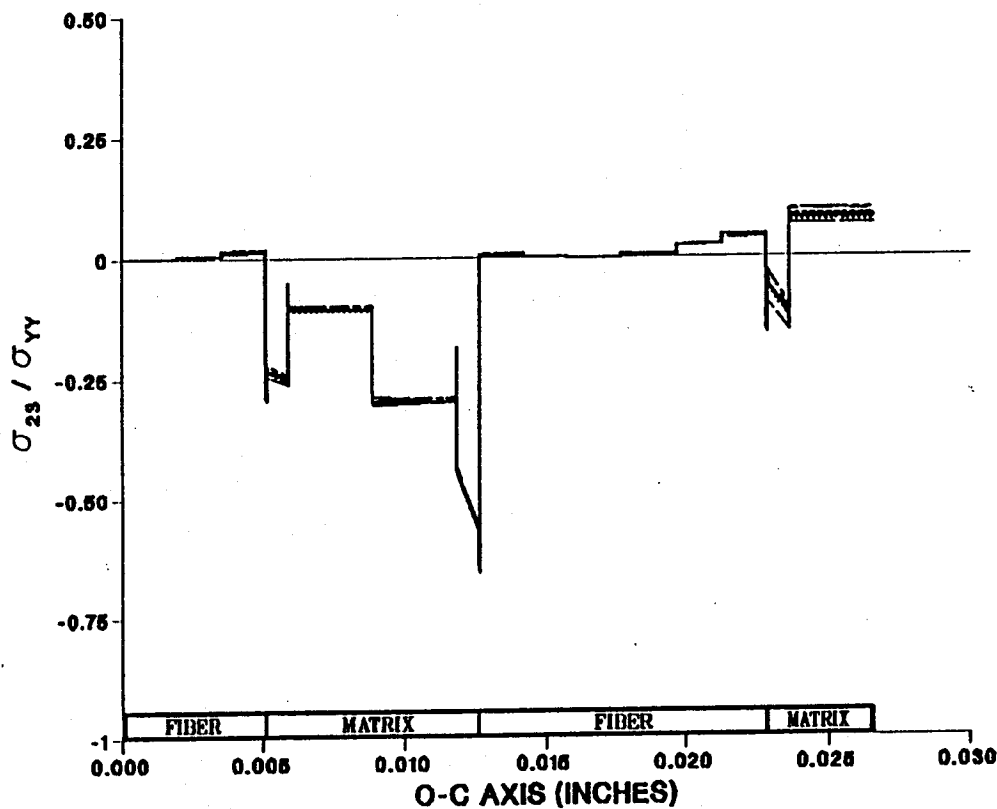


- FACE 1
- FACE 2
- FACE 3
- FACE 4
- FACE 5
- FACE 6
- FACE 7
- FACE 8
- FACE 9

Figure 7.56 - σ_{23} Normalized Microstresses, O-B Direction, 0.0% Debonding, σ_{yy}^e Loading

EFFECT OF 0.0% FIBER LENGTH DEBONDING ON CONSTITUENT MICROSTRESSES (σ_{23}) DUE TO A LOAD IN THE YY-DIRECTION

134



- FACE 1
- FACE 2
- FACE 3
- FACE 4
- FACE 5
- FACE 6
- FACE 7
- FACE 8
- FACE 9

Figure 7.57 - σ_{23} Normalized Microstresses, O-C Direction, 0.0% Debonding, σ_{yy}^e Loading

7.3) Loading: σ_{yx}^e

In figures 7.58 through 7.60 the constituent microstresses (σ_{12}) due to an enforced displacement in the YX direction are plotted for increasing levels of center fiber debonding along a line in the direction defined by the line segment O-A. The matrix portion of the composite is stressed to a greater degree than the fiber. This is expected because of the large $\frac{G}{G_{f12}^m}$ ratio $\left[\frac{G}{G_{f12}^m} \approx 6 \right]$. As each layer of elements in the center fiber is released from the matrix, the stress level in that fiber layer approaches zero and an increase in the stress level of the matrix material at that point is evident. Little change in the stress profile of the neighboring fiber can be seen, even at total center fiber debonding (figure 7.60). The change in the stress state, due to the debonding of the center fiber, manifests itself in the form of a local shear stress riser in the matrix material at the edge of the debonded fiber with little evidence of the increased stress level being distributed to the community of surrounding fibers. This is evident when figure 7.58 is compared to figure 7.60.

Figures 7.61 to 7.63 are shown to reflect the effect of center fiber debonding on constituent microstresses (σ_{12}) along a line in the O-B direction. These stresses result from an enforced shear displacement in the YX. Center fiber debonding produces the most significant changes in the stress profile in the matrix at the point of debonding and, as expected, in the center fiber. These areas decrease in their level of stress as the center fiber is increasingly debonded.

EFFECT OF 0.0% FIBER LENGTH DEBONDING ON CONSTITUENT MICROSTRESSES (σ_{12}) DUE TO A LOAD IN THE YX-DIRECTION

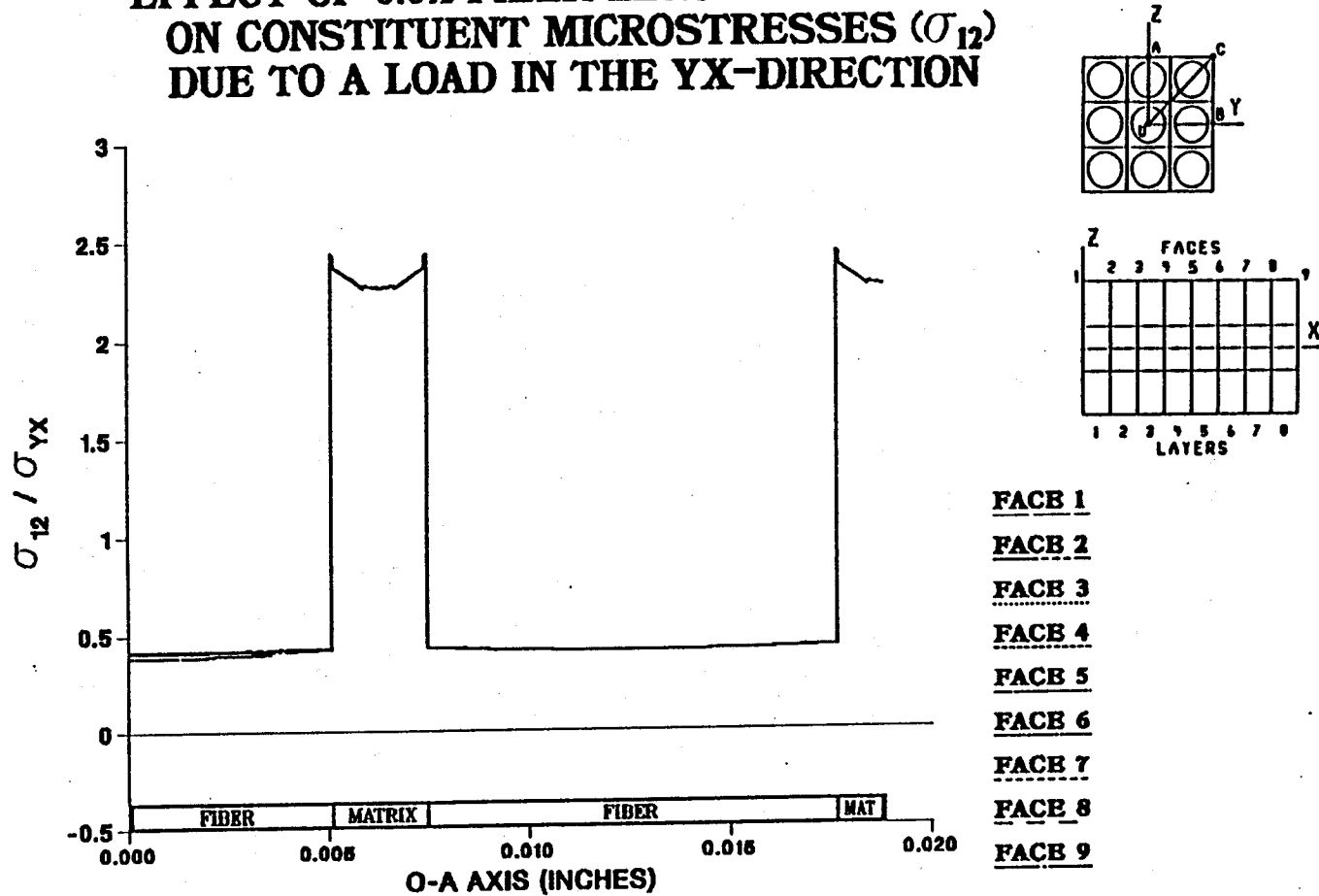


Figure 7.58 — σ_{12} Normalized Microstresses, O-A Direction, 0.0% Debonding, σ_{yx}^e Loading

EFFECT OF 5.56% FIBER LENGTH DEBONDING ON CONSTITUENT MICROSTRESSES (σ_{12}) DUE TO A LOAD IN THE YX-DIRECTION

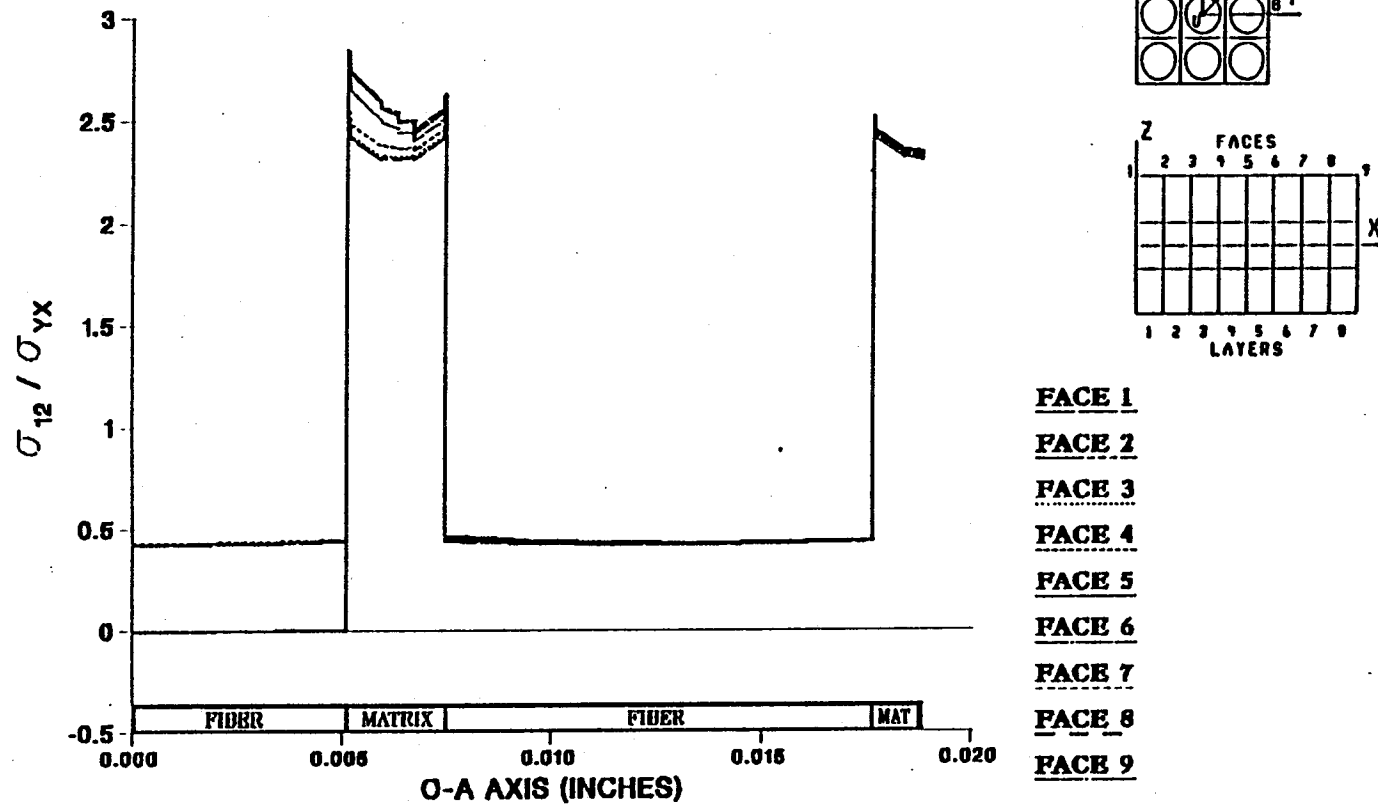


Figure 7.59 - σ_{12} Normalized Microstresses, O-A Direction, 5.56% Debonding, σ_{yx}^e Loading

EFFECT OF 11.1% FIBER LENGTH DEBONDING ON CONSTITUENT MICROSTRESSES (σ_{12}) DUE TO A LOAD IN THE YX-DIRECTION

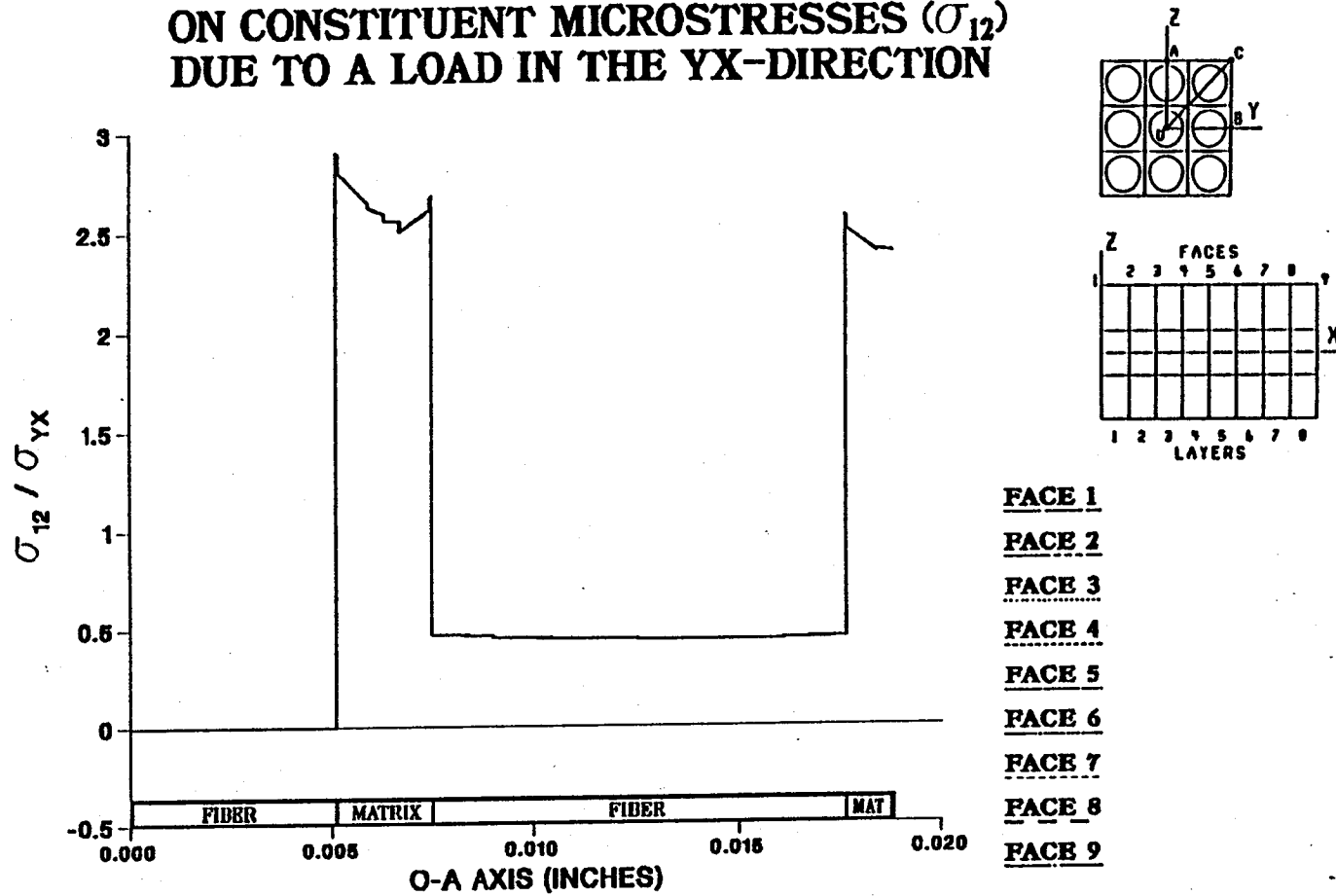
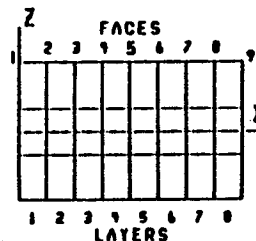
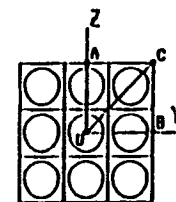
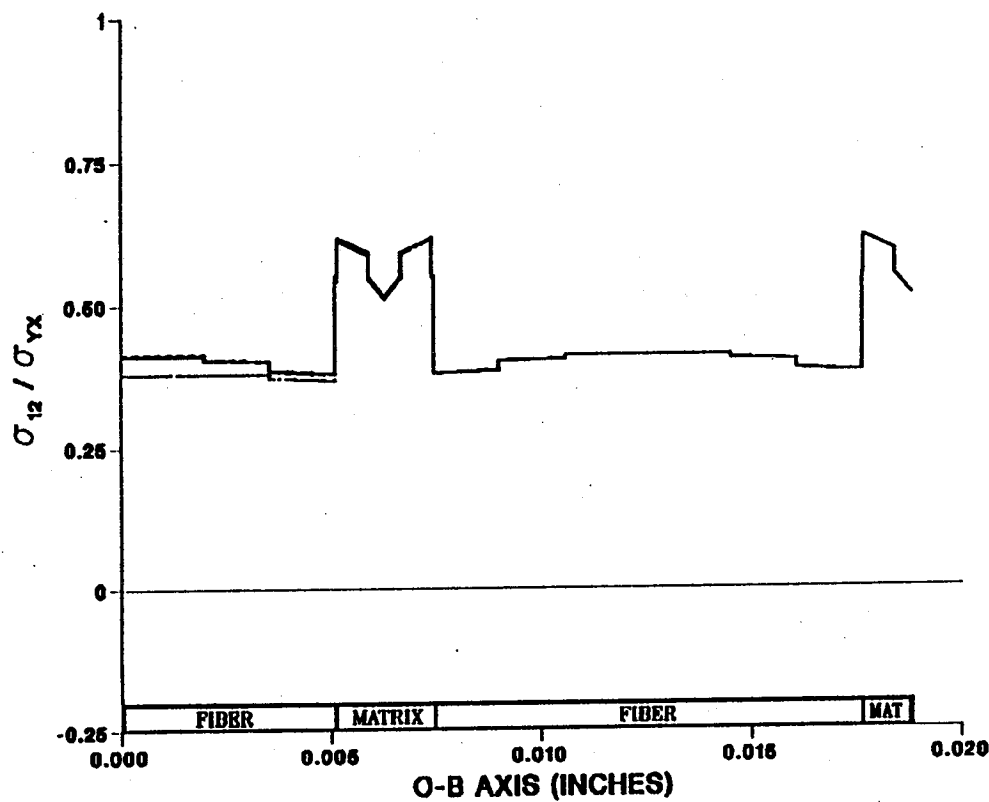


Figure 7.60 - σ_{12} Normalized Microstresses, O-A Direction, 11.1% Debonding, σ_{yx}^e Loading

EFFECT OF 0.0% FIBER LENGTH DEBONDING ON CONSTITUENT MICROSTRESSES (σ_{12}) DUE TO A LOAD IN THE YX-DIRECTION



- FACE 1
- FACE 2
- FACE 3
- FACE 4
- FACE 5
- FACE 6
- FACE 7
- FACE 8
- FACE 9

Figure 7.61 - σ_{12} Normalized Microstresses, O-B Direction, 0.0% Debonding, σ_{yx}^e Loading

EFFECT OF 5.56% FIBER LENGTH DEBONDING ON CONSTITUENT MICROSTRESSES (σ_{12}) DUE TO A LOAD IN THE YX-DIRECTION

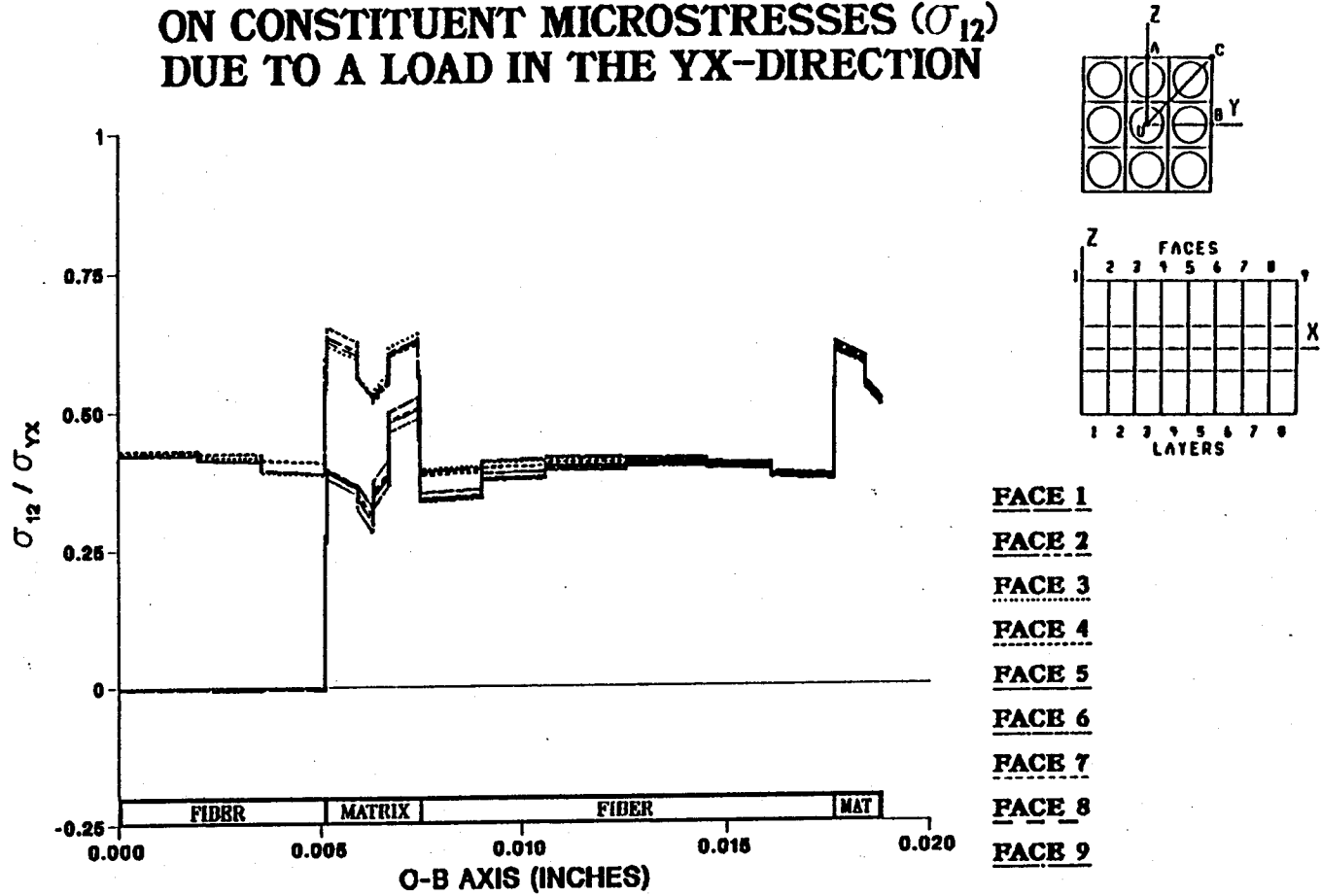


Figure 7.62 - σ_{12} Normalized Microstresses, O-B Direction, 5.56% Debonding, σ_{yx}^e Loading

EFFECT OF 11.11% FIBER LENGTH DEBONDING ON CONSTITUENT MICROSTRESSES (σ_{12}) DUE TO A LOAD IN THE YX-DIRECTION

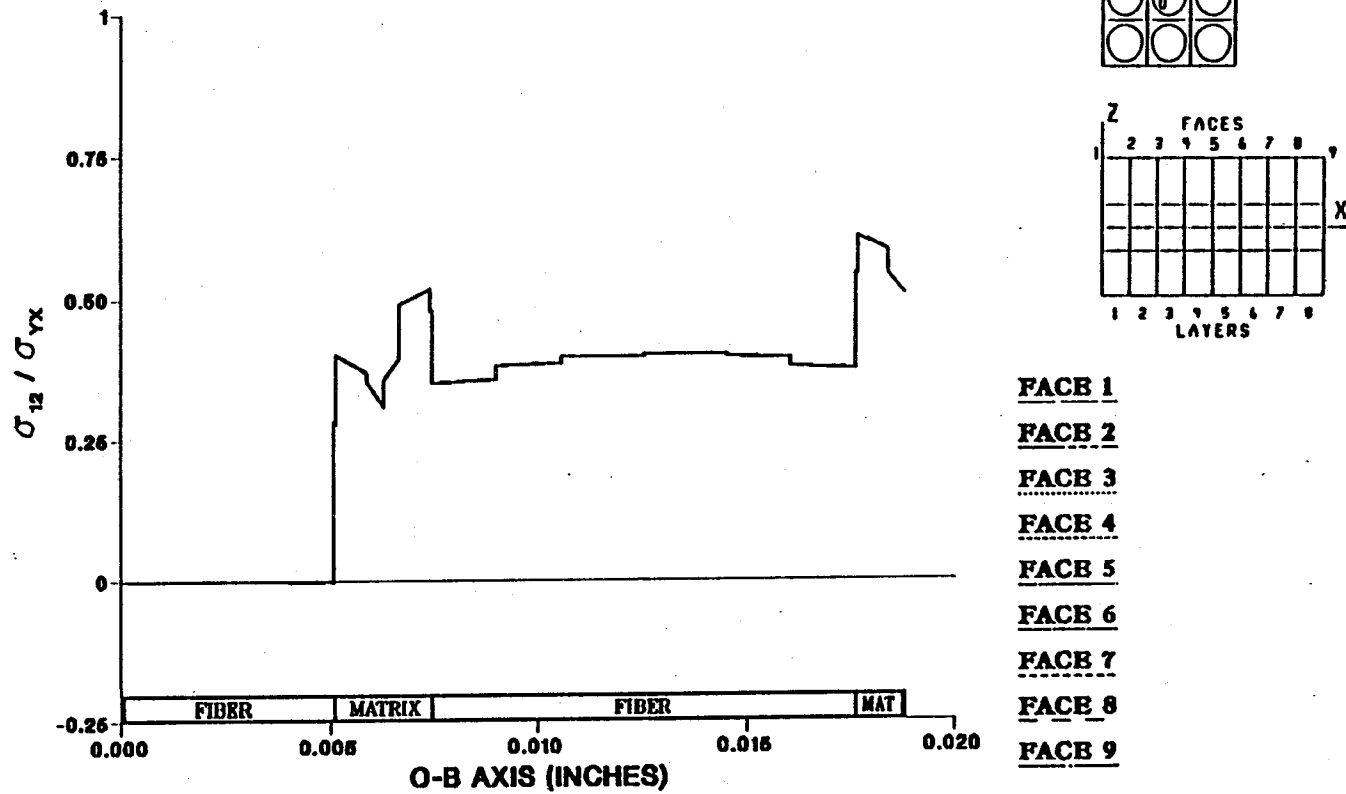


Figure 7.63 — σ_{12} Normalized Microstresses, O-B Direction, 11.11% Debonding, σ_{yx}^e Loading

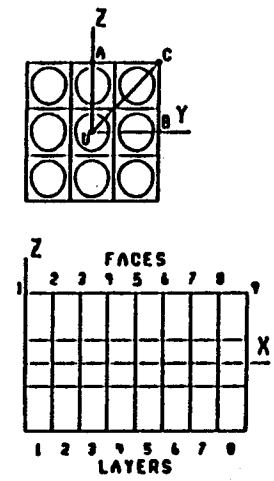
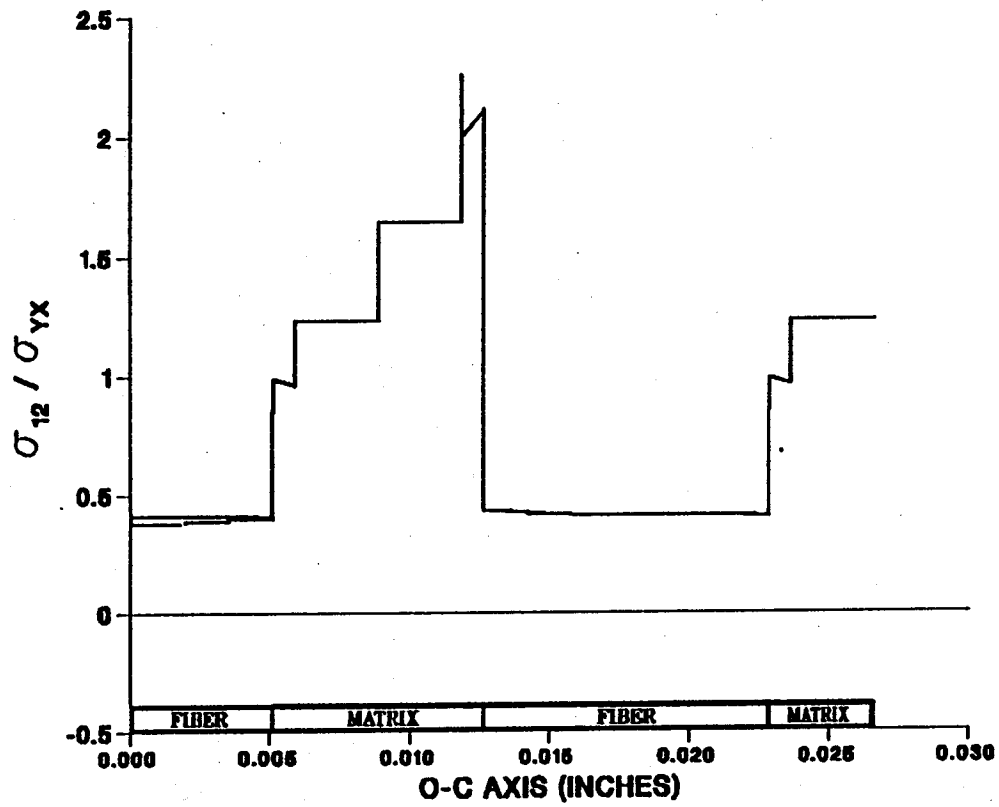
Some stress relaxation can be seen in the fiber that is not being debonded, though this change in the fiber's stress state is quite small (note scale in figures 7.61 through 7.63).

By the use of figures 7.64 to 7.66 an attempt has been made to show the effect of center fiber debonding on σ_{12} microstresses. These figures represent the microstresses occurring when an enforced shear displacement in the YX has been applied to the composite model. They are plotted along a line defined by the line segment O—C. Center fiber debonding causes the stress levels to drop on faces of the center fiber that have been debonded. On these same grid faces, the stresses in the matrix next to the debonding fiber decrease, but not as dramatically as those in the center fiber. Stress profiles of the neighboring fiber remain virtually unchanged as the percent disbond increases. Little shear stress sharing takes place among fibers in the composite because most of the σ_{12} shear stress is carried by the matrix. The decrease in the stress level created by the debonding of the center fiber is manifested as local stress reductions at the edge of the matrix material nearest the debonding fiber.

7.4) Loading: σ_{yz}^e

Figures 7.67 to 7.69 depict the effect of center fiber debonding on the σ_{23} microstress profiles, plotted in the O—A direction, resulting from an applied shear in the YZ direction. The σ_{23} shear stress is mostly carried by the matrix material in the P100—Graphite/Copper composite. As debonding is modeled, the stress level of the center fiber decreases as each face of grids in the fiber is released from the matrix. The stress level in the matrix material local to the

EFFECT OF 0.0% FIBER LENGTH DEBONDING ON CONSTITUENT MICROSTRESSES (σ_{12}) DUE TO A LOAD IN THE YX-DIRECTION



- FACE 1
- FACE 2
- FACE 3
- FACE 4
- FACE 5
- FACE 6
- FACE 7
- FACE 8
- FACE 9

Figure 7.64 – σ_{12} Normalized Microstresses, O–C Direction, 0.0% Debonding, σ_{yx}^e Loading

EFFECT OF 5.56% FIBER LENGTH DEBONDING ON CONSTITUENT MICROSTRESSES (σ_{12}) DUE TO A LOAD IN THE YX-DIRECTION

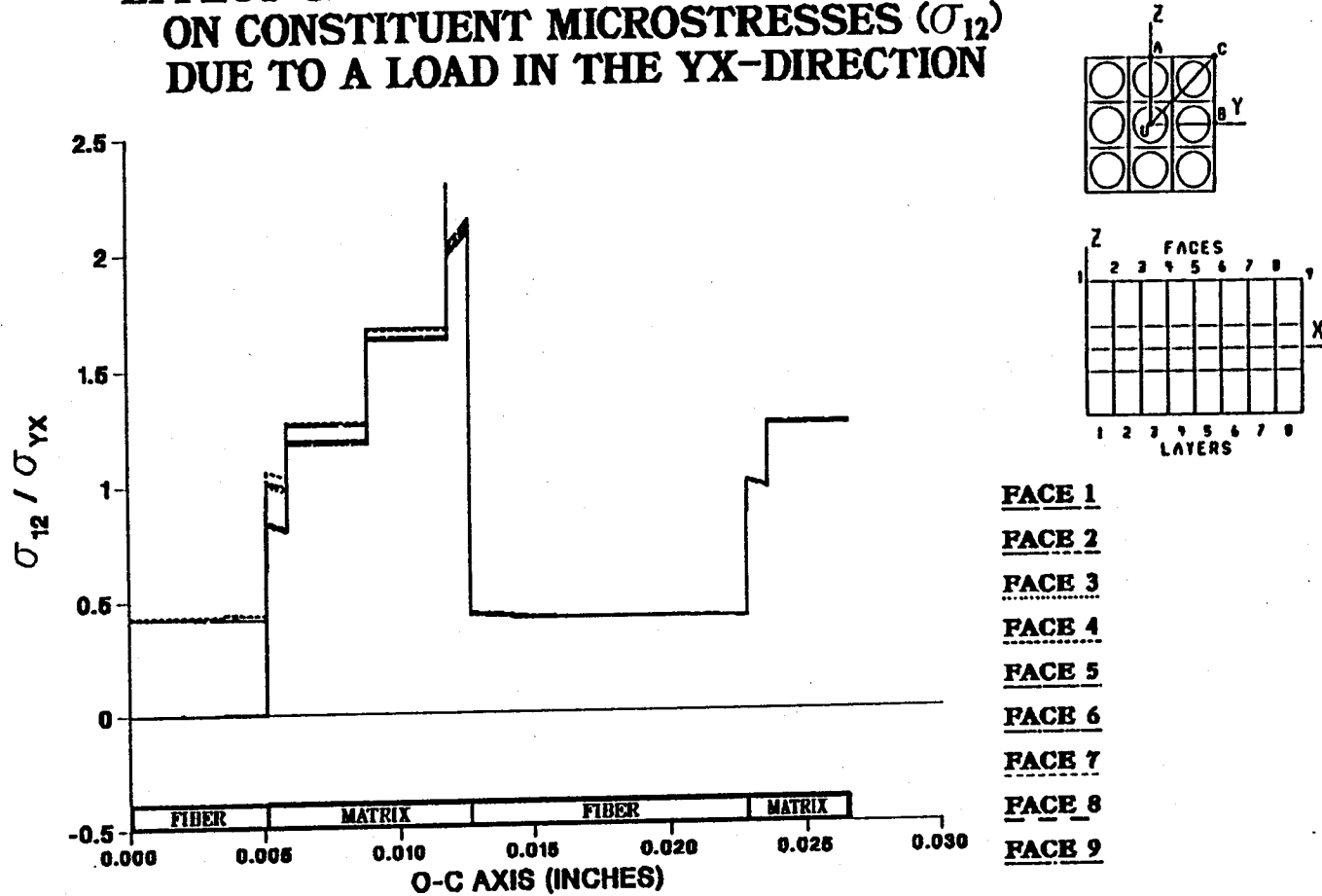
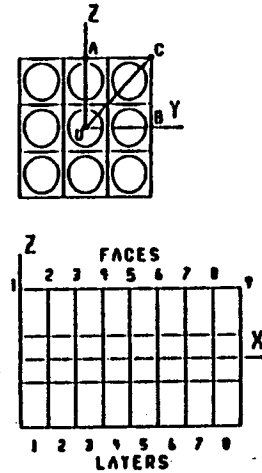
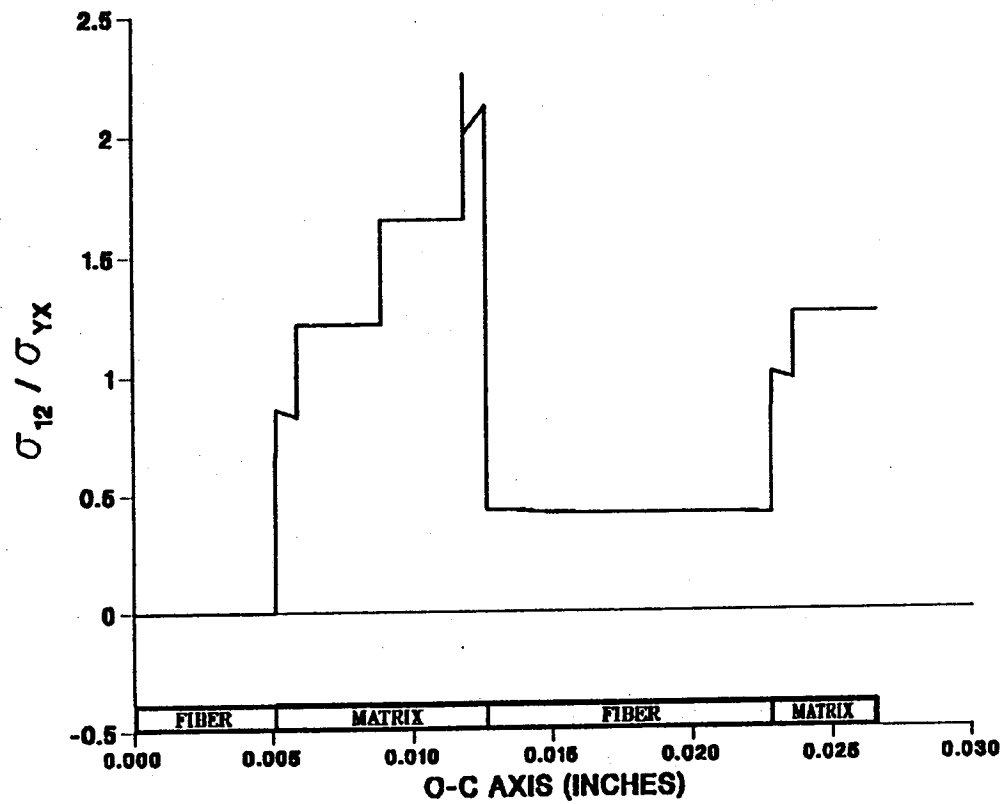


Figure 7.65 – σ_{12} Normalized Microstresses, O–C Direction, 5.56% Debonding, σ_{yx}^e Loading

EFFECT OF 11.11% FIBER LENGTH DEBONDING ON CONSTITUENT MICROSTRESSES (σ_{12}) DUE TO A LOAD IN THE YX-DIRECTION



- FACE 1
- FACE 2
- FACE 3
- FACE 4
- FACE 5
- FACE 6
- FACE 7
- FACE 8
- FACE 9

Figure 7.66 - σ_{12} Normalized Microstresses, O-C Direction, 11.11% Debonding, σ_{yx}^e Loading

EFFECT OF 0.0% FIBER LENGTH DEBONDING ON CONSTITUENT MICROSTRESSES (σ_{23}) DUE TO A LOAD IN THE YZ-DIRECTION

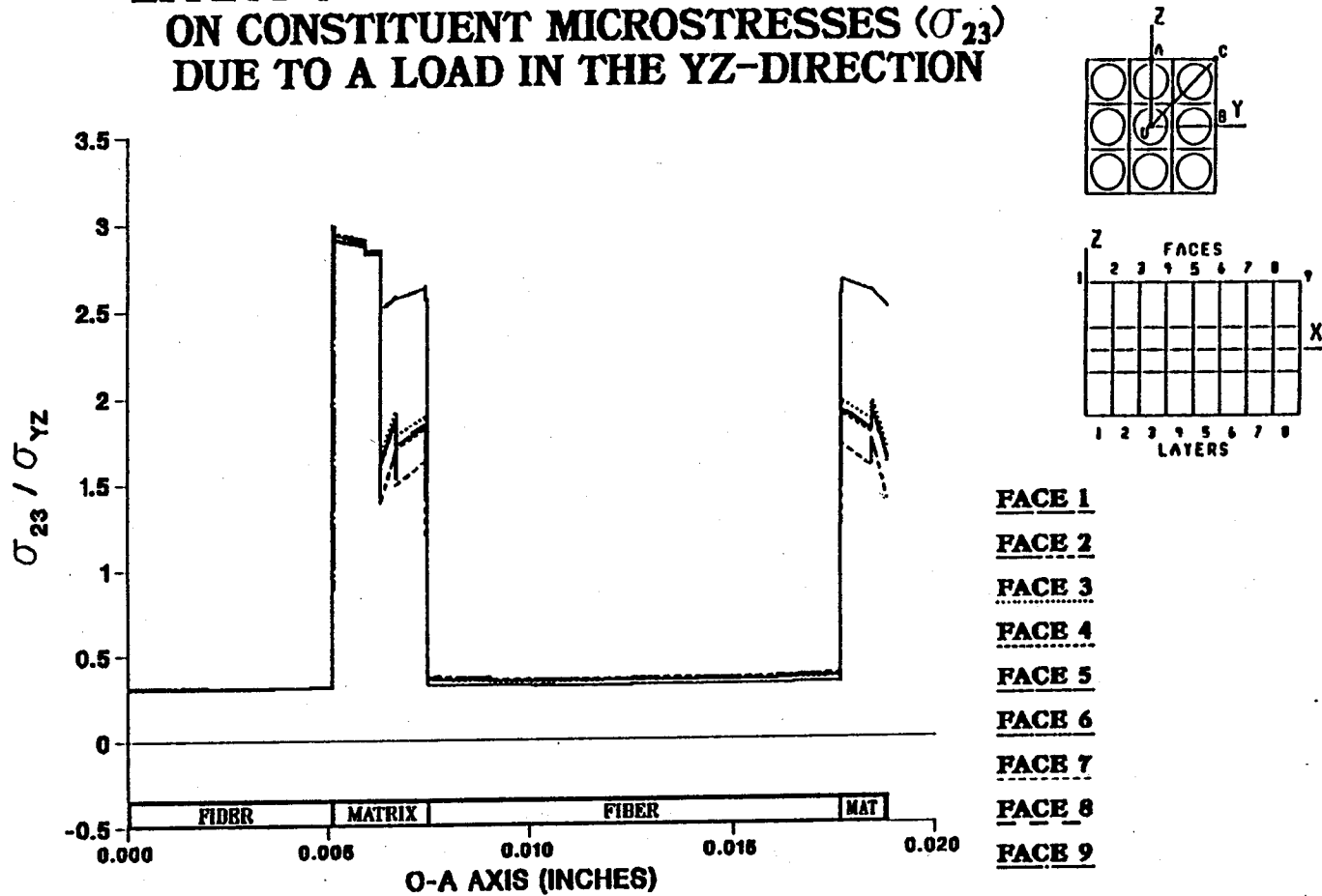
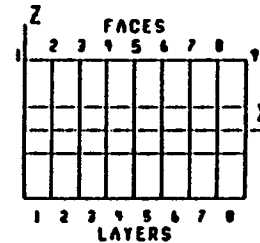
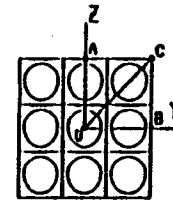
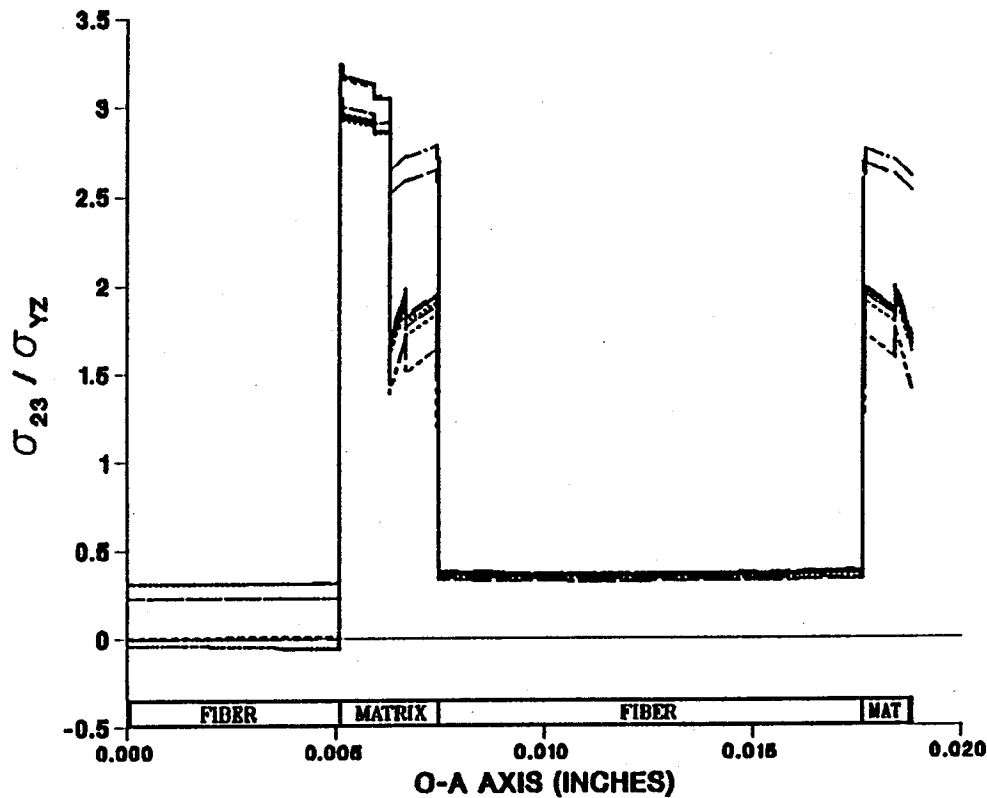


Figure 7.67 - σ_{23} Normalized Microstresses, O-A Direction, 0.0% Debonding, σ_{yz}^e Loading

EFFECT OF 5.56% FIBER LENGTH DEBONDING ON CONSTITUENT MICROSTRESSES (σ_{23}) DUE TO A LOAD IN THE YZ-DIRECTION



- FACE 1
- FACE 2
- FACE 3
- FACE 4
- FACE 5
- FACE 6
- FACE 7
- FACE 8
- FACE 9

Figure 7.68 -- σ_{23} Normalized Microstresses, O-A Direction, 5.56% Debonding, σ_{yz}^e Loading



EFFECT OF 5.56% FIBER LENGTH DEBONDING ON CONSTITUENT MICROSTRESSES (σ_{23}) DUE TO A LOAD IN THE YZ-DIRECTION

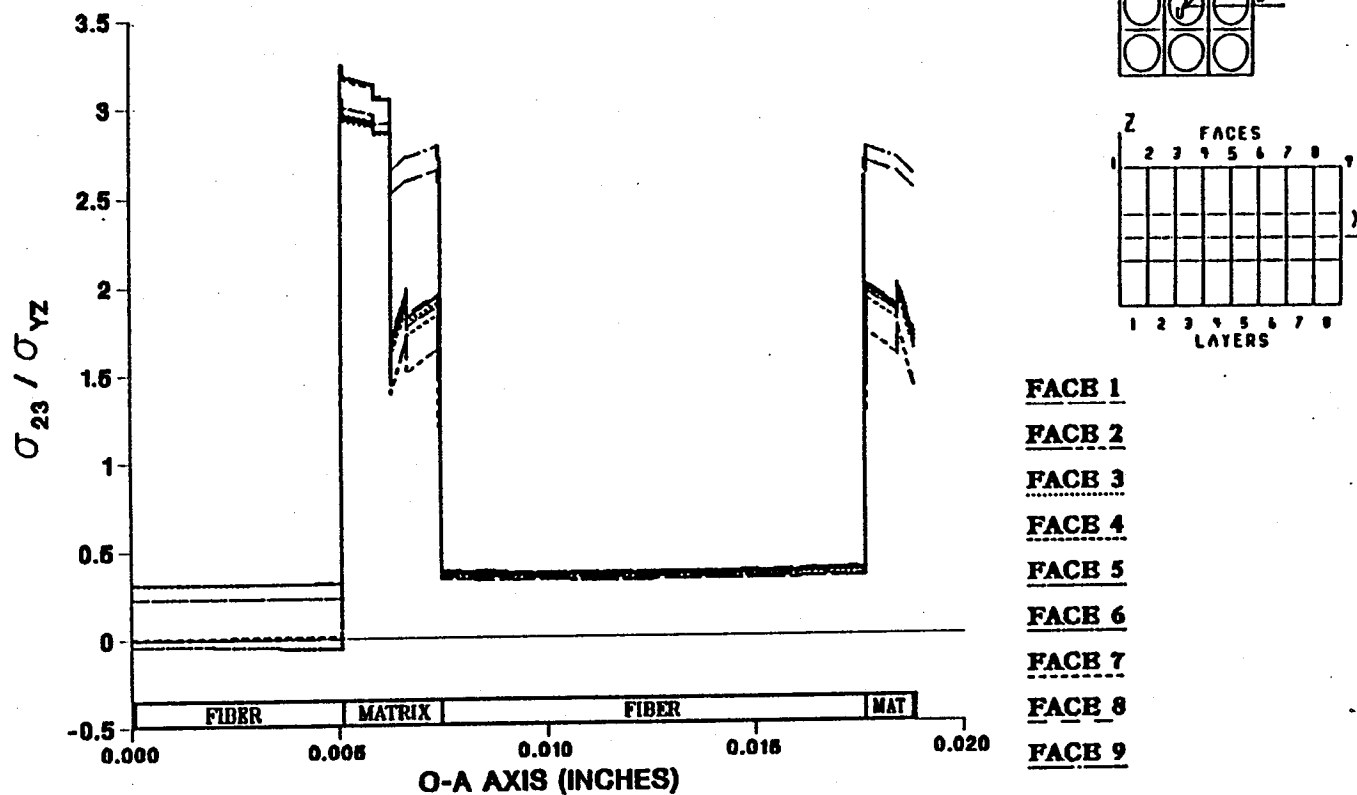


Figure 7.68 — σ_{23} Normalized Microstresses, O-A Direction, 5.56% Debonding, σ_{yz}^e Loading

EFFECT OF 11.1% FIBER LENGTH DEBONDING ON CONSTITUENT MICROSTRESSES (σ_{23}) DUE TO A LOAD IN THE YZ-DIRECTION

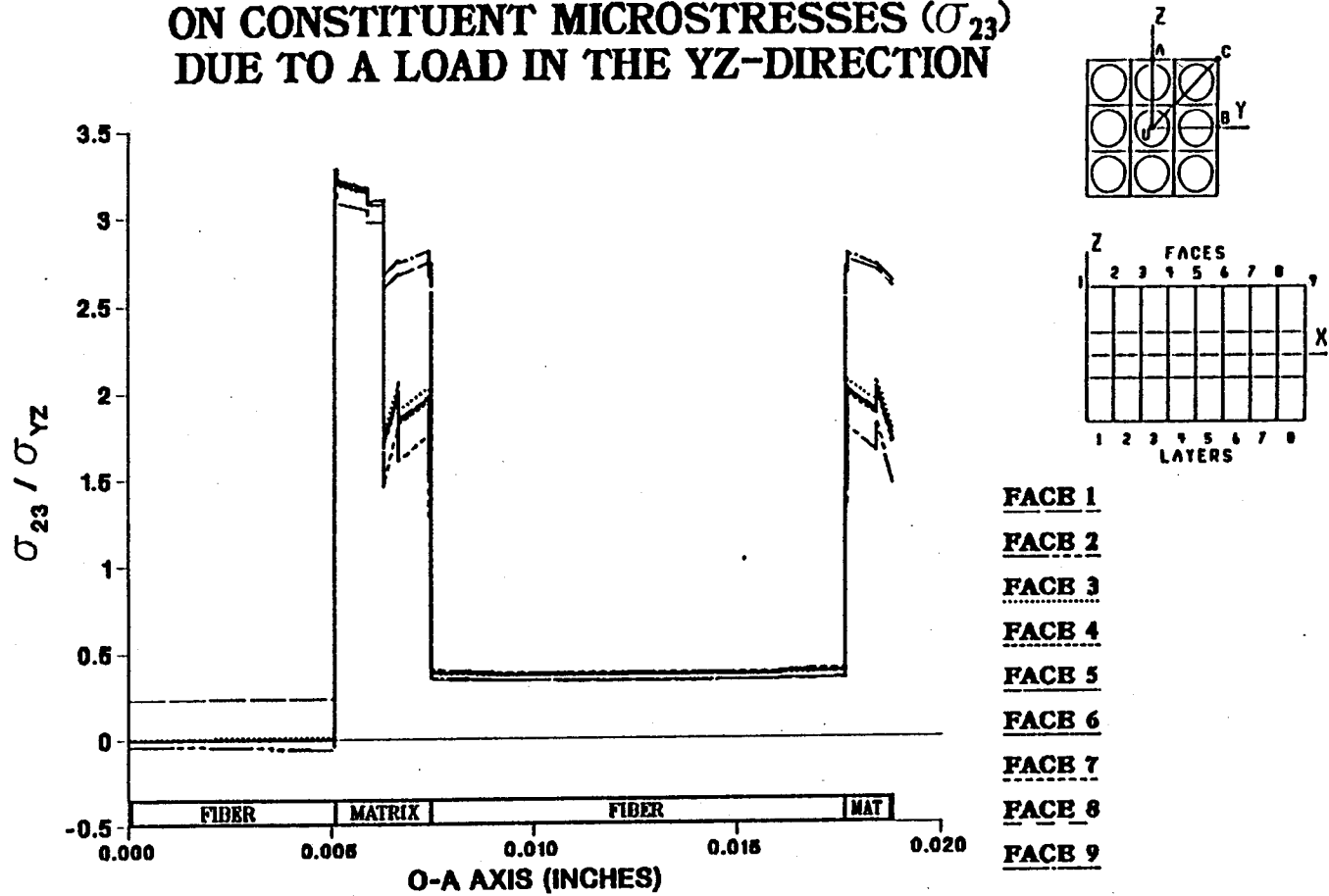


Figure 7.69 – σ_{23} Normalized Microstresses, O–A Direction, 11.1% Debonding, σ_{yz}^e Loading

debonding interface also drops, but not as significantly as in the center fiber. Little change can be seen in the stress profiles of the grid faces in the neighboring fiber. This suggests that, since the matrix is structurally dominate in shear, little change in the shear stress state of the other fibers will be evident.

In figures 7.70 to 7.72 the same load and microstresses are considered, but here they are plotted along a line defined by the O-B line segment. The trend here is very similar to that stated above except that the stress levels in the matrix material are not as great as before. Debonding produces a slight reduction in the local matrix stress state, and little change is seen in the stress profile of the other fiber.

Figures 7.73 through 7.75 are σ_{23} microstress plots in the O-C direction resulting from a YZ shear at increasing levels of center fiber debonding. As before, only a slight decrease in the stress level of the interfacial matrix material can be seen as the result of the center fiber debonding. Virtually no change in the stress level of the other fiber can be seen as center fiber debonding is propagated. Again, the dominate shear modulus of the matrix masks the effects of the debonding from the other fibers.

7.5) Loading: Temperature Load

The effect of center fiber debonding on longitudinal thermal microstresses (σ_{11}) along a line in the direction of the O-A line segment is given in figures 7.76 through 7.84. Figure 7.76 shows the stress profile before fiber debonding. Note the effect of the large α mismatch between fiber and matrix.

EFFECT OF 0.0% FIBER LENGTH DEBONDING ON CONSTITUENT MICROSTRESSES (σ_{23}) DUE TO A LOAD IN THE YZ-DIRECTION

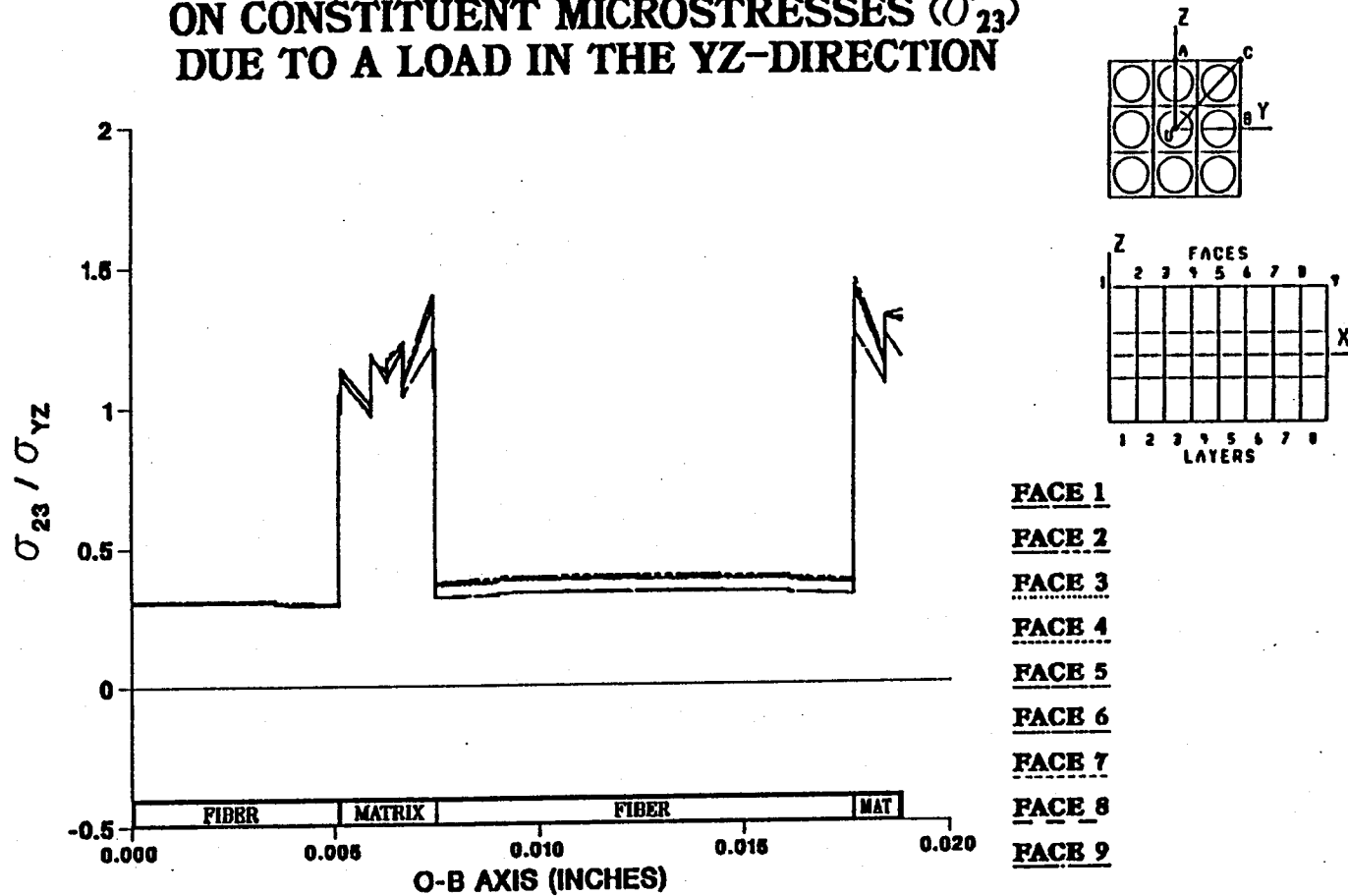


Figure 7.70 - σ_{23} Normalized Microstresses, O-B Direction, 0.0% Debonding, σ_{yz}^e Loading

EFFECT OF 5.56% FIBER LENGTH DEBONDING ON CONSTITUENT MICROSTRESSES (σ_{23}) DUE TO A LOAD IN THE YZ-DIRECTION

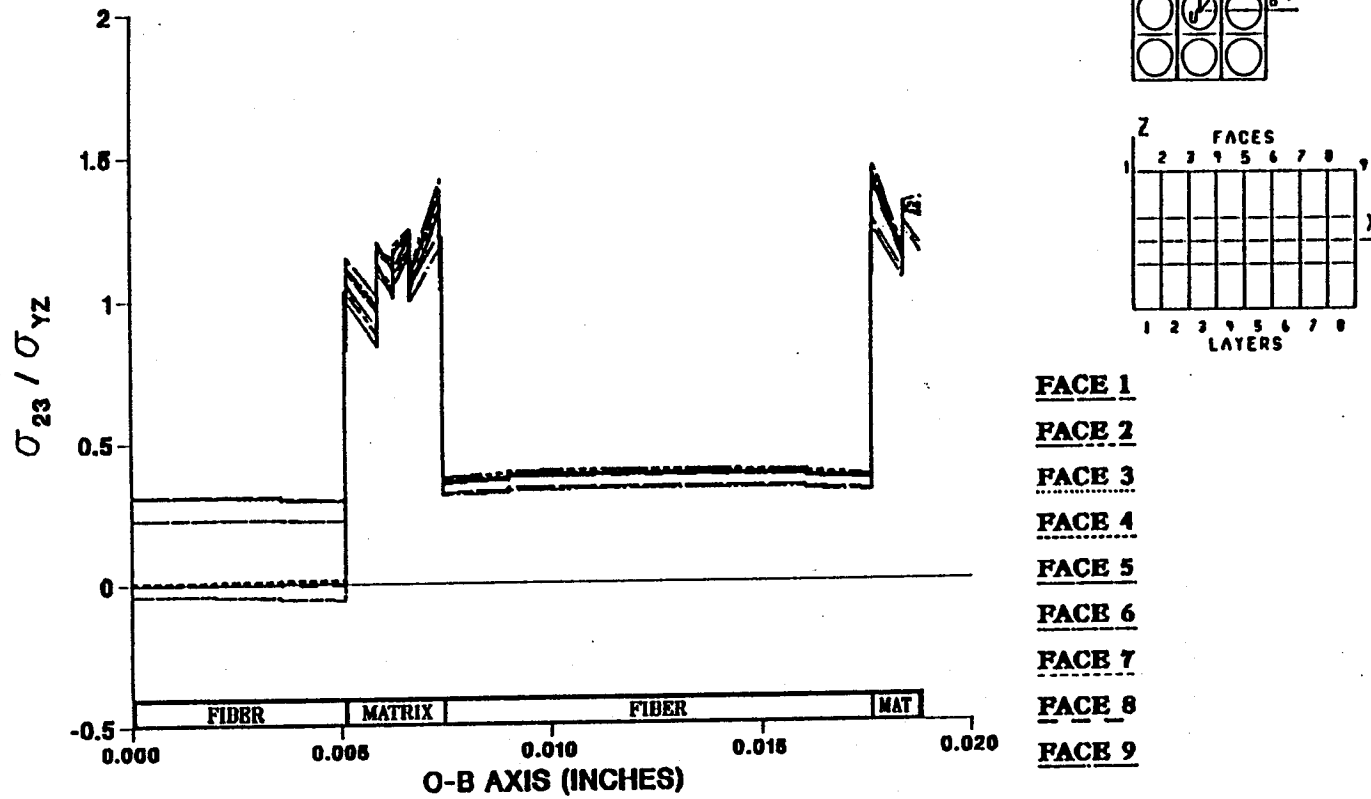


Figure 7.71 - σ_{23} Normalized Microstresses, O-B Direction, 5.56% Debonding, σ_{yz}^e Loading

EFFECT OF 11.1% FIBER LENGTH DEBONDING ON CONSTITUENT MICROSTRESSES (σ_{23}) DUE TO A LOAD IN THE YZ-DIRECTION

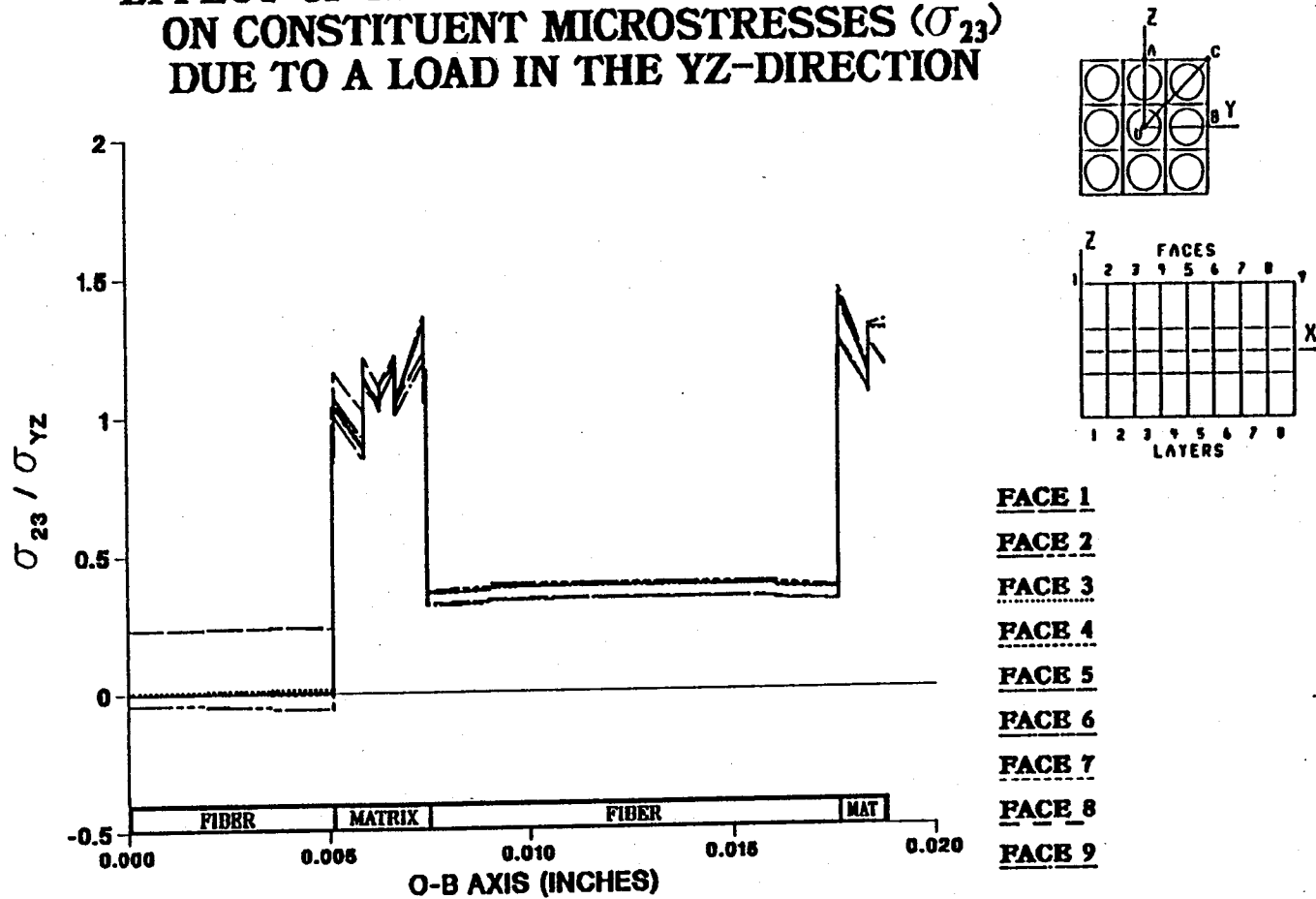


Figure 7.72 - σ_{23} Normalized Microstresses, O-B Direction, 11.1% Debonding, σ_{yz}^e Loading

EFFECT OF 0.0% FIBER LENGTH DEBONDING ON CONSTITUENT MICROSTRESSES (σ_{23}) DUE TO A LOAD IN THE YZ-DIRECTION

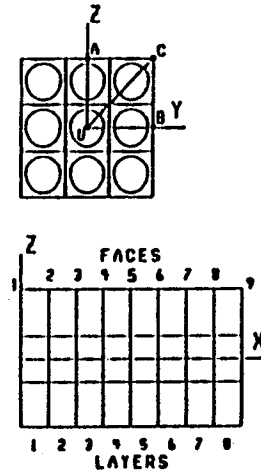
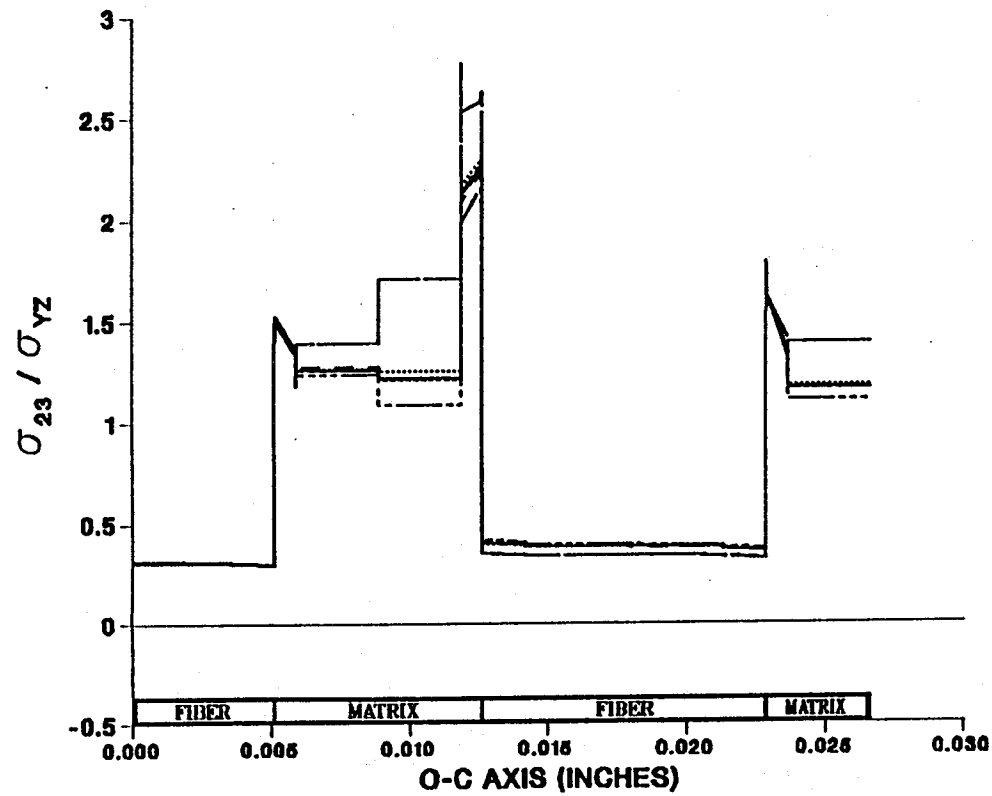


Figure 7.73 - σ_{23} Normalized Microstresses, O-C Direction, 0.0% Debonding, σ_{yz}^e Loading

EFFECT OF 5.56% FIBER LENGTH DEBONDING ON CONSTITUENT MICROSTRESSES (σ_{23}) DUE TO A LOAD IN THE YZ-DIRECTION

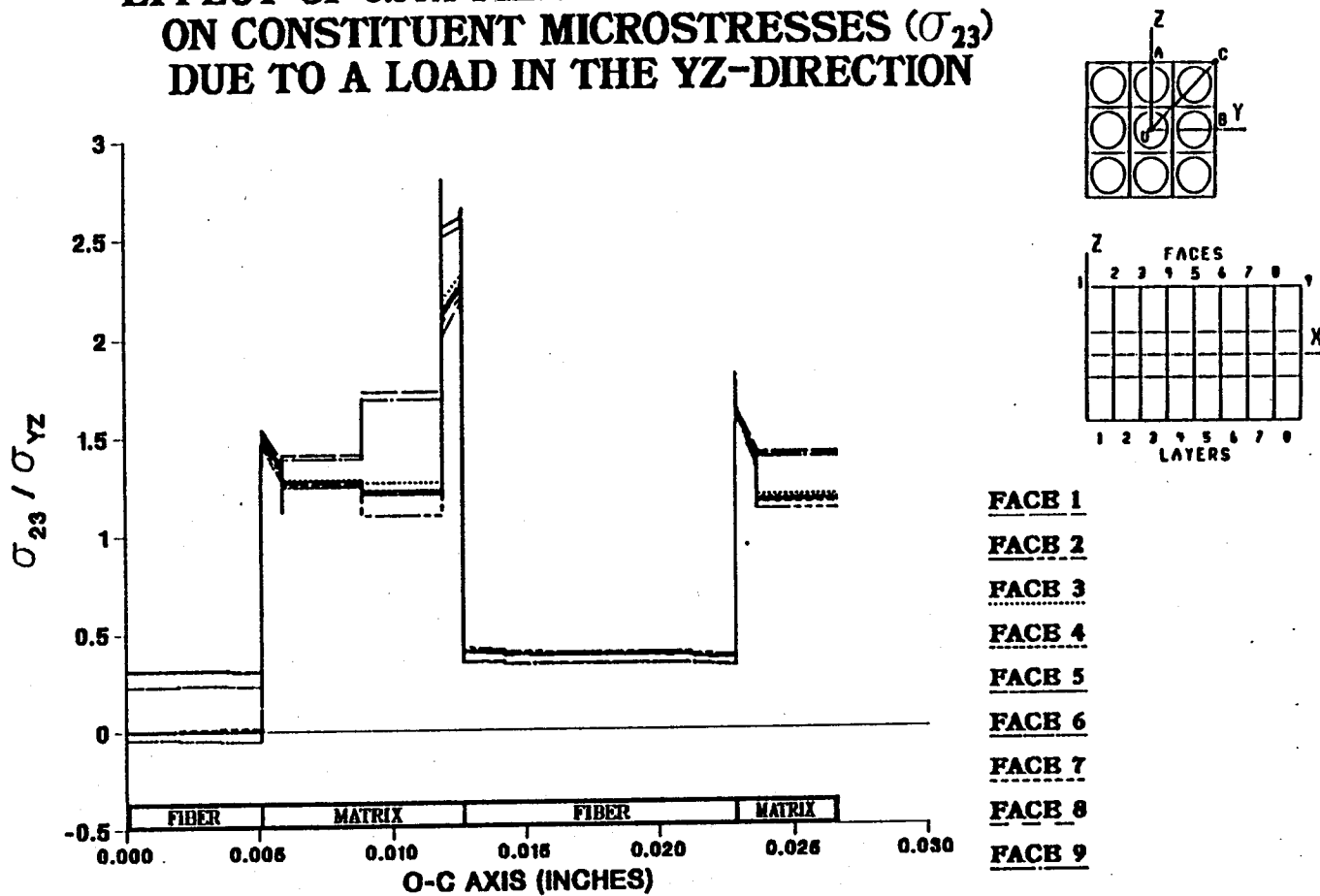
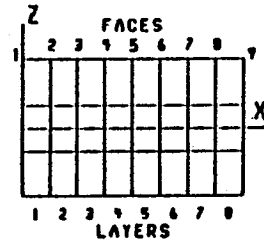
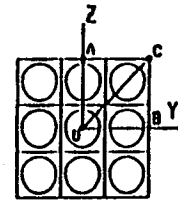
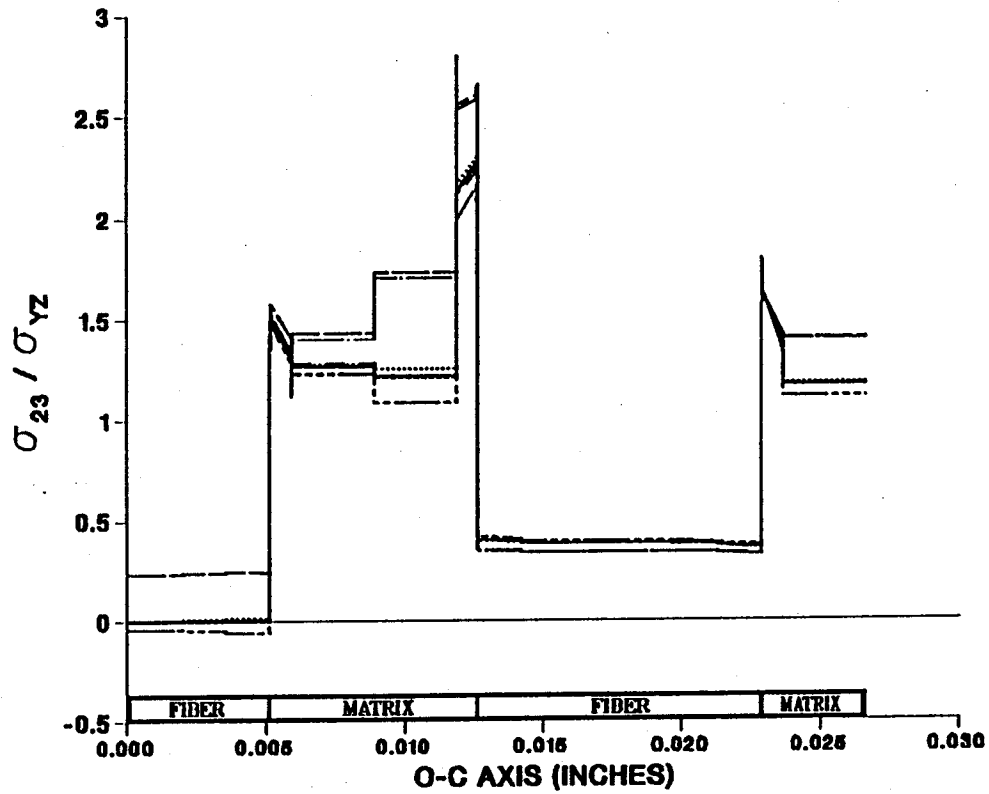


Figure 7.74 - σ_{23} Normalized Microstresses, O-C Direction, 5.56% Debonding, σ_{yz}^e Loading

EFFECT OF 11.11% FIBER LENGTH DEBONDING ON CONSTITUENT MICROSTRESSES (σ_{23}) DUE TO A LOAD IN THE YZ-DIRECTION



- FACE 1
- FACE 2
- FACE 3
- FACE 4
- FACE 5
- FACE 6
- FACE 7
- FACE 8
- FACE 9

Figure 7.75 - σ_{23} Normalized Microstresses, O-C Direction, 11.11% Debonding, σ_{yz}^e Loading

EFFECT OF 0.0% FIBER LENGTH DEBONDING ON CONSTITUENT MICROSTRESSES (σ_{11}) DUE TO AN APPLIED THERMAL LOAD

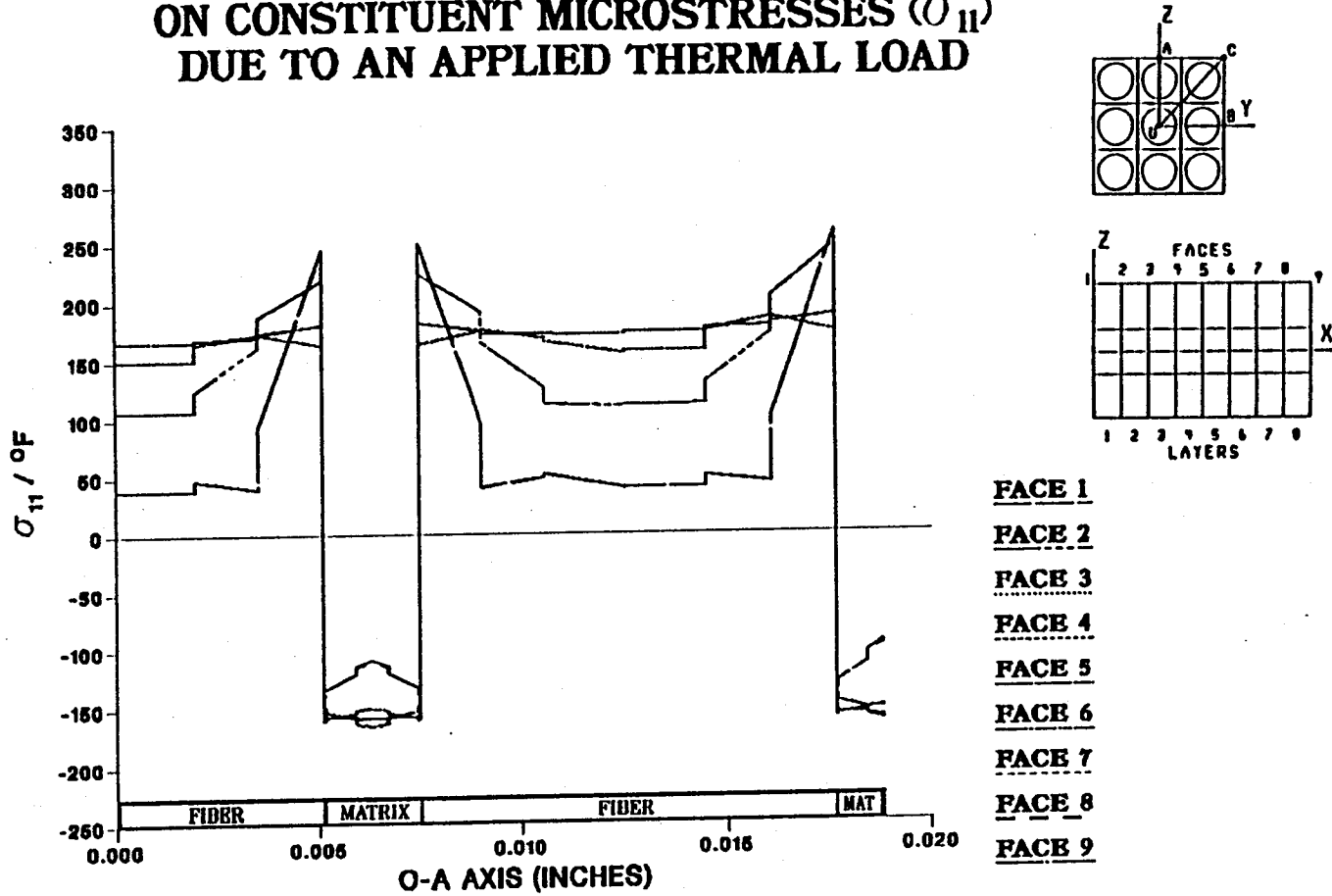


Figure 7.76 - σ_{11} Normalized Microstresses, O-A Direction, 0.0% Debonding, Thermal Loading

EFFECT OF 1.39% FIBER LENGTH DEBONDING ON CONSTITUENT MICROSTRESSES (σ_{11}) DUE TO AN APPLIED THERMAL LOAD

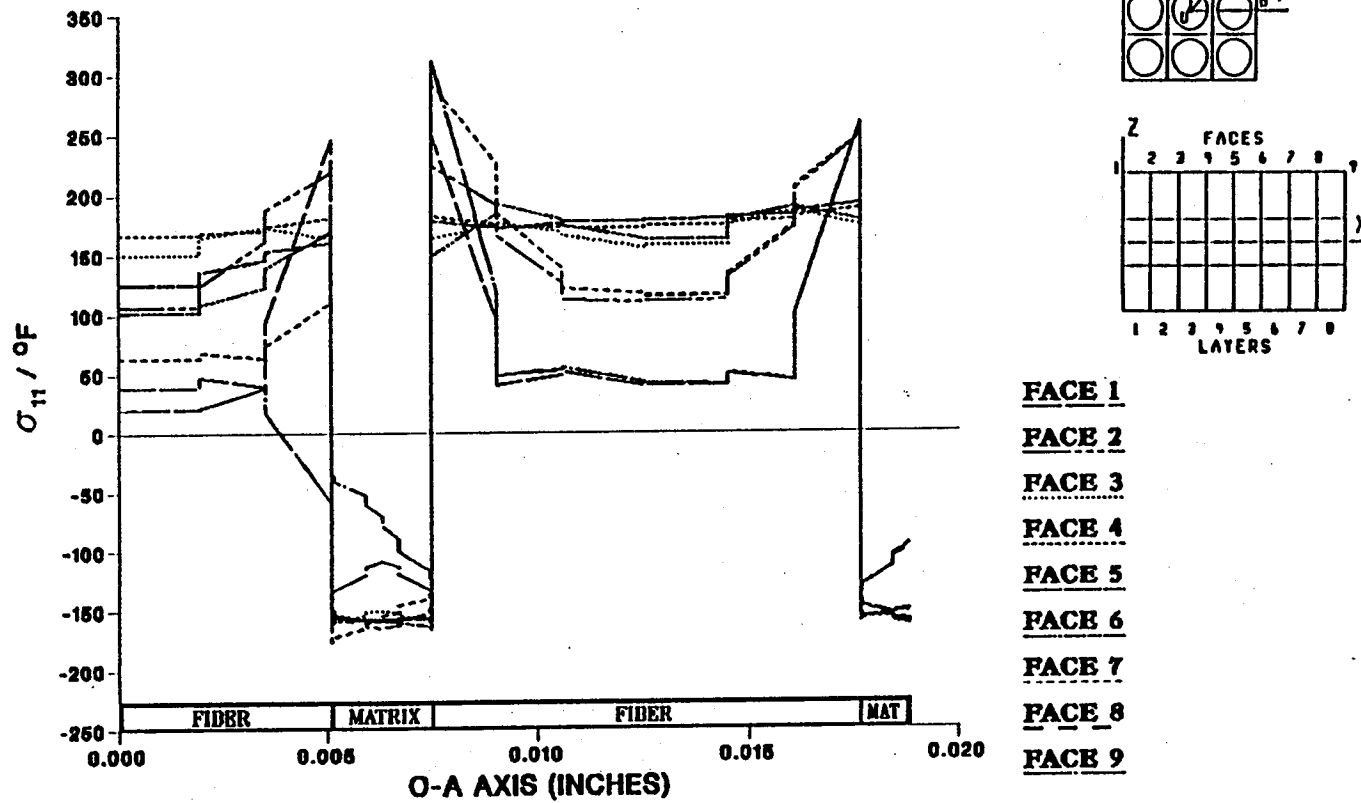


Figure 7.77 - σ_{11} Normalized Microstresses, O-A Direction, 1.39% Debonding, Thermal Loading

EFFECT OF 2.78% FIBER LENGTH DEBONDING ON CONSTITUENT MICROSTRESSES (σ_{11}) DUE TO AN APPLIED THERMAL LOAD

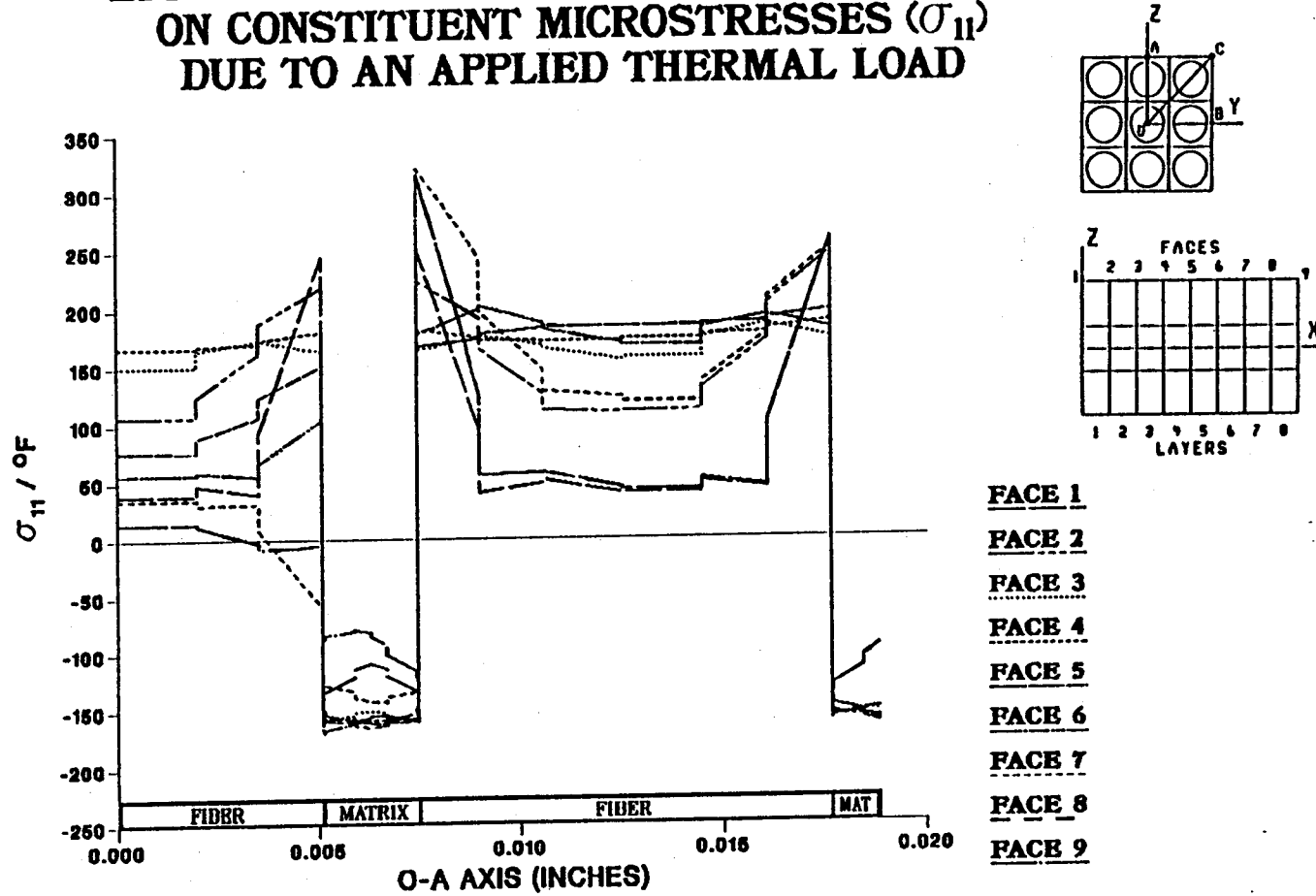


Figure 7.78 - σ_{11} Normalized Microstresses, O-A Direction, 2.78% Debonding, Thermal Loading

EFFECT OF 4.17% FIBER LENGTH DEBONDING ON CONSTITUENT MICROSTRESSES (σ_{11}) DUE TO AN APPLIED THERMAL LOAD

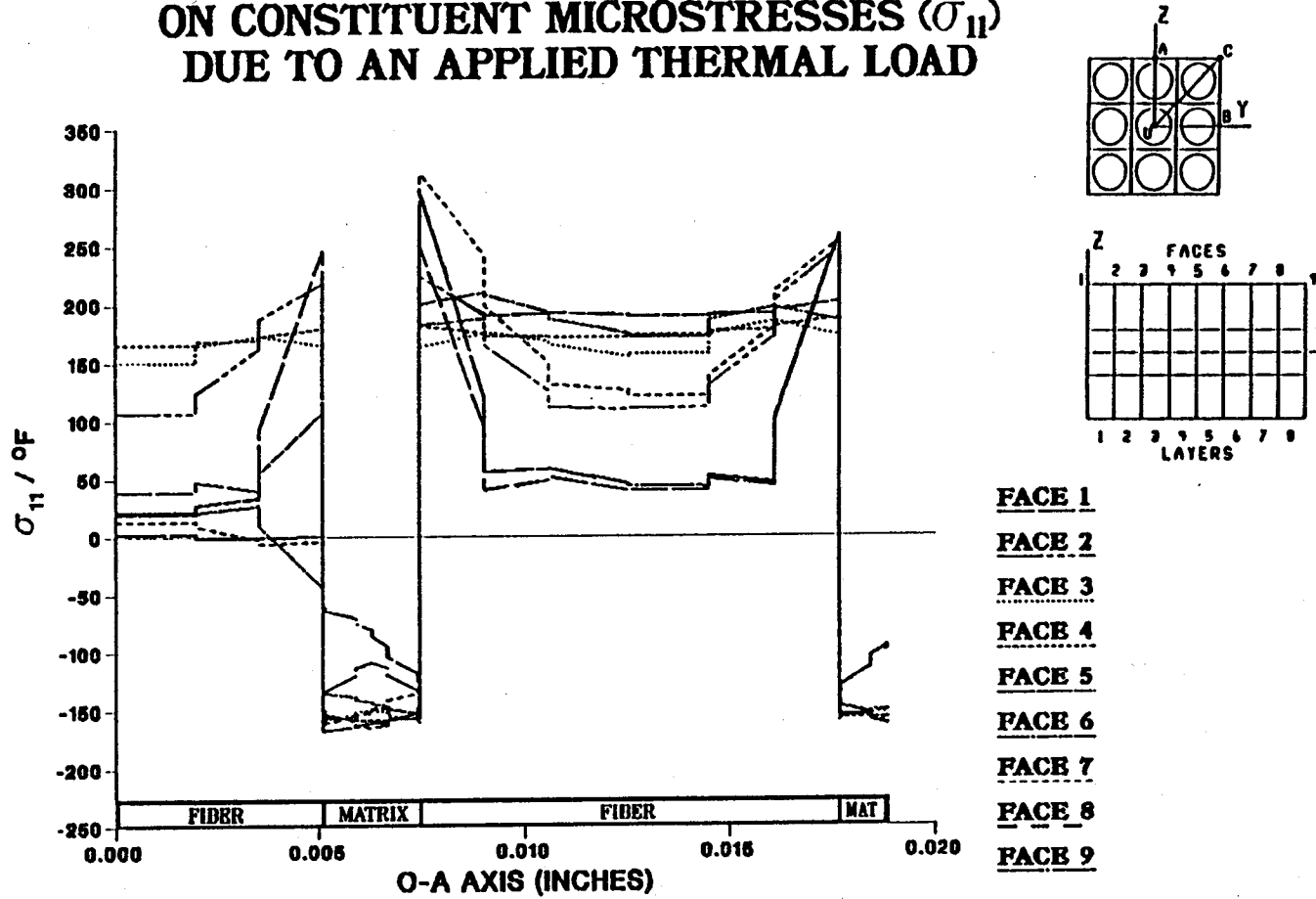


Figure 7.79 - σ_{11} Normalized Microstresses, O-A Direction, 4.17% Debonding, Thermal Loading

EFFECT OF 5.56% FIBER LENGTH DEBONDING ON CONSTITUENT MICROSTRESSES (σ_{11}) DUE TO AN APPLIED THERMAL LOAD

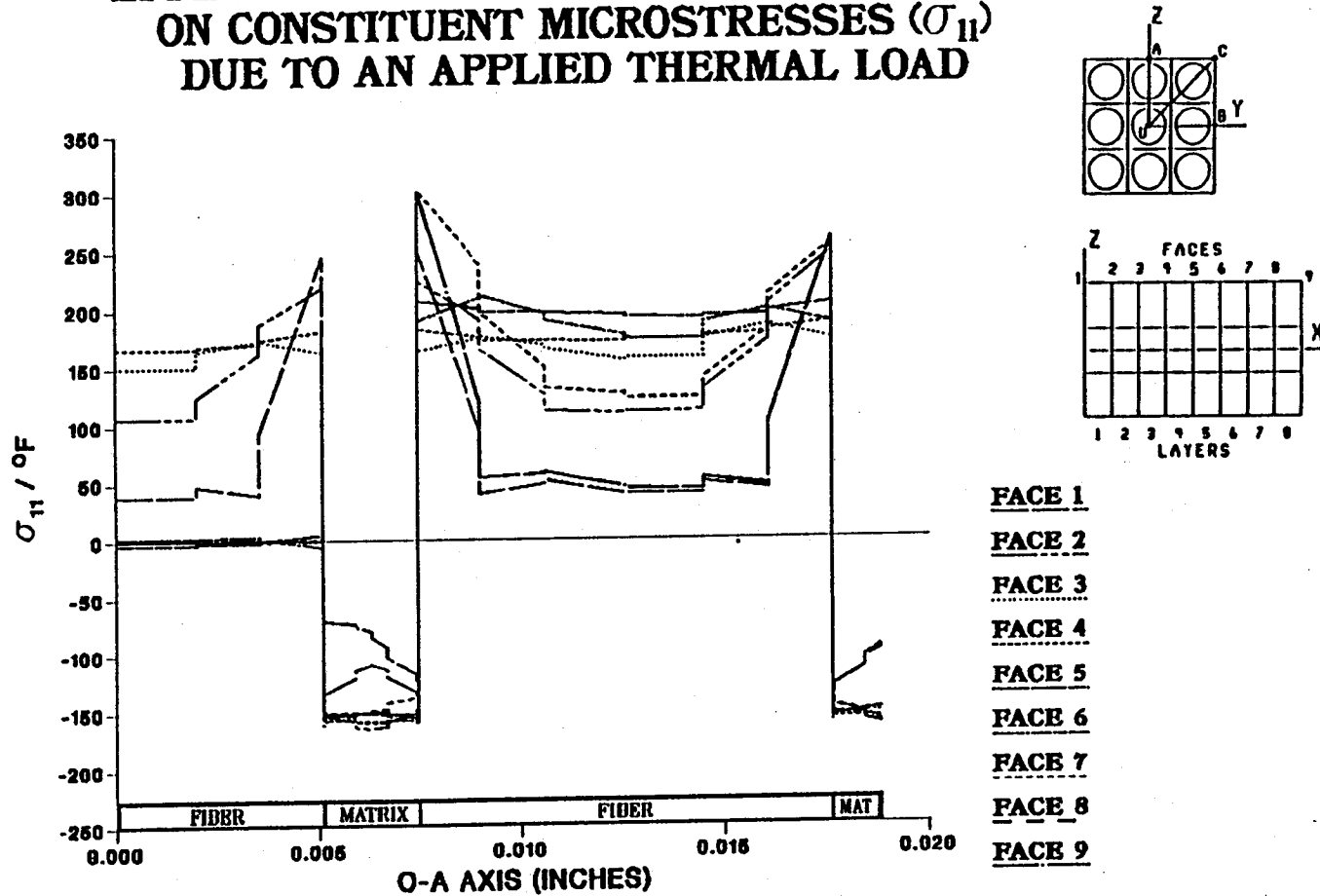


Figure 7.80 - σ_{11} Normalized Microstresses, O-A Direction, 5.56% Debonding, Thermal Loading

EFFECT OF 6.94% FIBER LENGTH DEBONDING ON CONSTITUENT MICROSTRESSES (σ_{11}) DUE TO AN APPLIED THERMAL LOAD

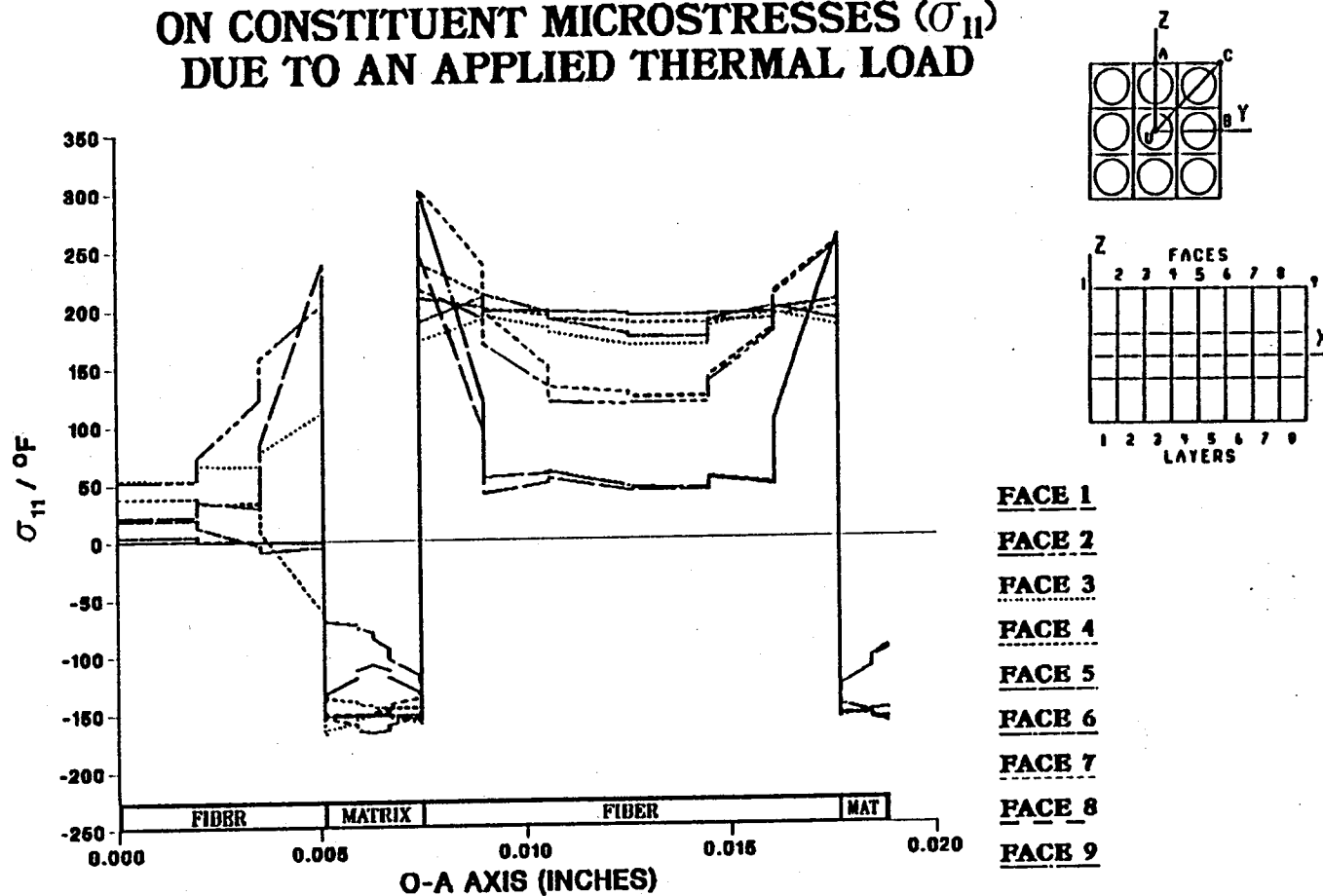


Figure 7.81 - σ_{11} Normalized Microstresses, O-A Direction, 6.94% Debonding, Thermal Loading

EFFECT OF 8.33% FIBER LENGTH DEBONDING ON CONSTITUENT MICROSTRESSES (σ_{11}) DUE TO AN APPLIED THERMAL LOAD

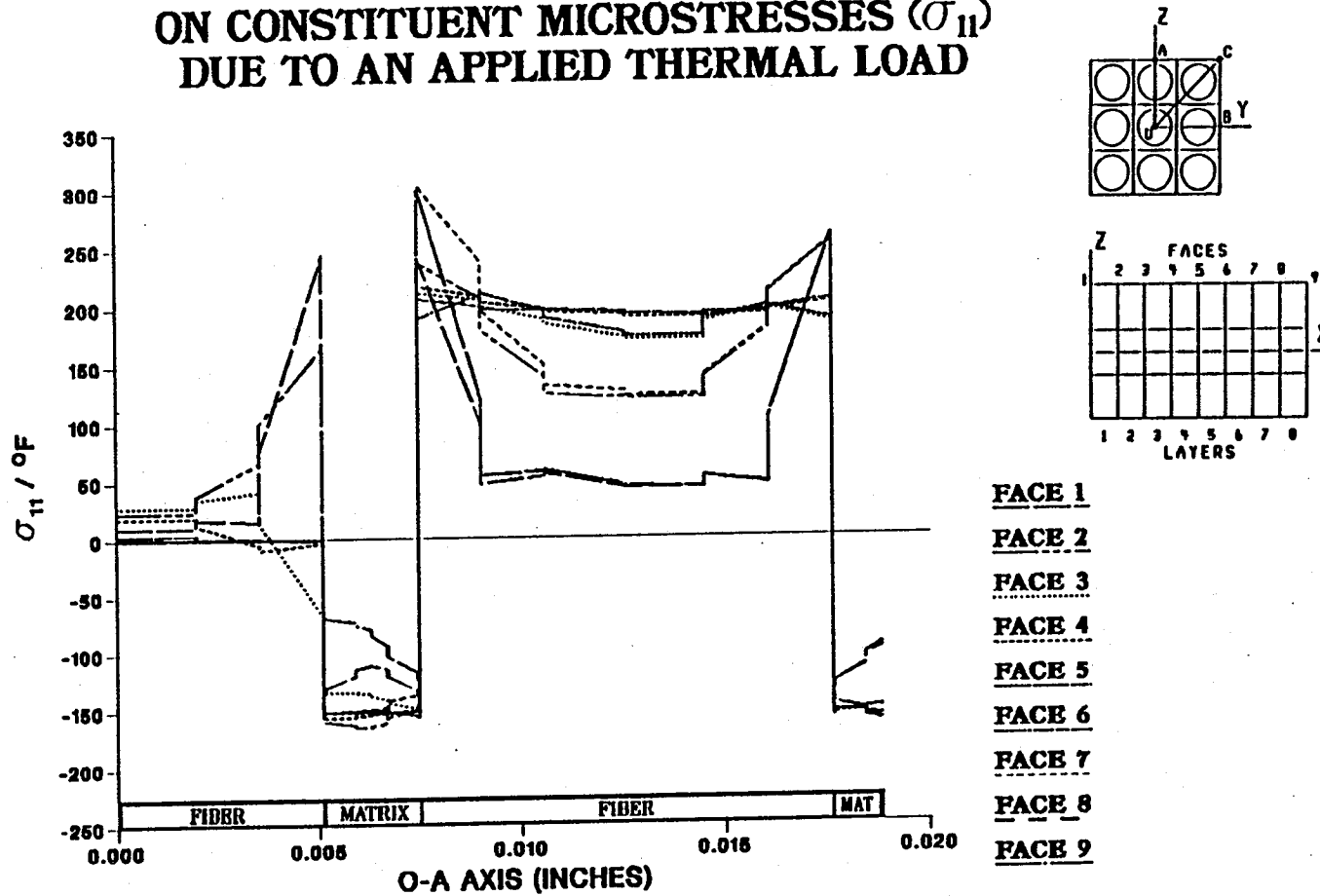


Figure 7.82 - σ_{11} Normalized Microstresses, O-A Direction, 8.33% Debonding, Thermal Loading

EFFECT OF 9.72% FIBER LENGTH DEBONDING ON CONSTITUENT MICROSTRESSES (σ_{11}) DUE TO AN APPLIED THERMAL LOAD

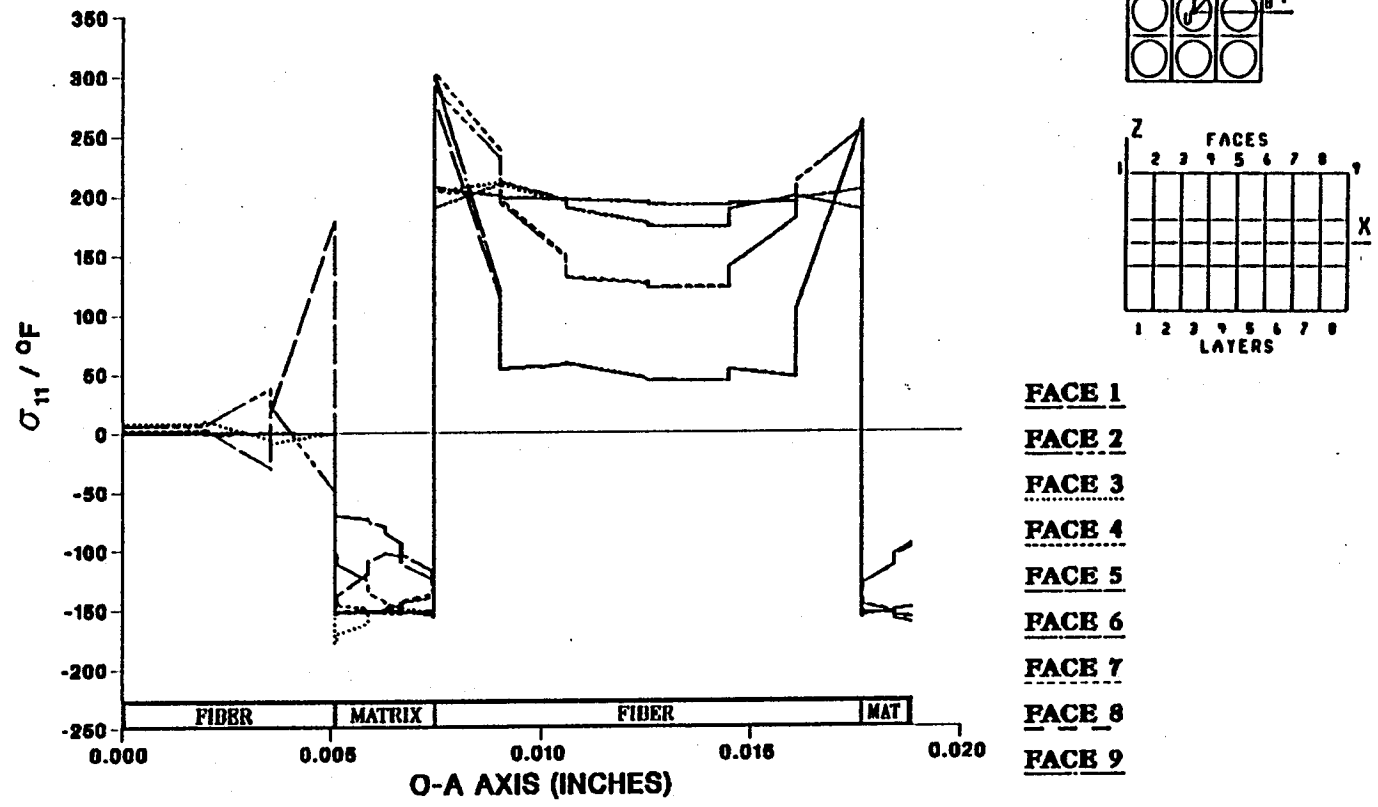


Figure 7.83 - σ_{11} Normalized Microstresses, O-A Direction, 9.72% Debonding, Thermal Loading

EFFECT OF 11.1% FIBER LENGTH DEBONDING ON CONSTITUENT MICROSTRESSES (σ_{11}) DUE TO AN APPLIED THERMAL LOAD

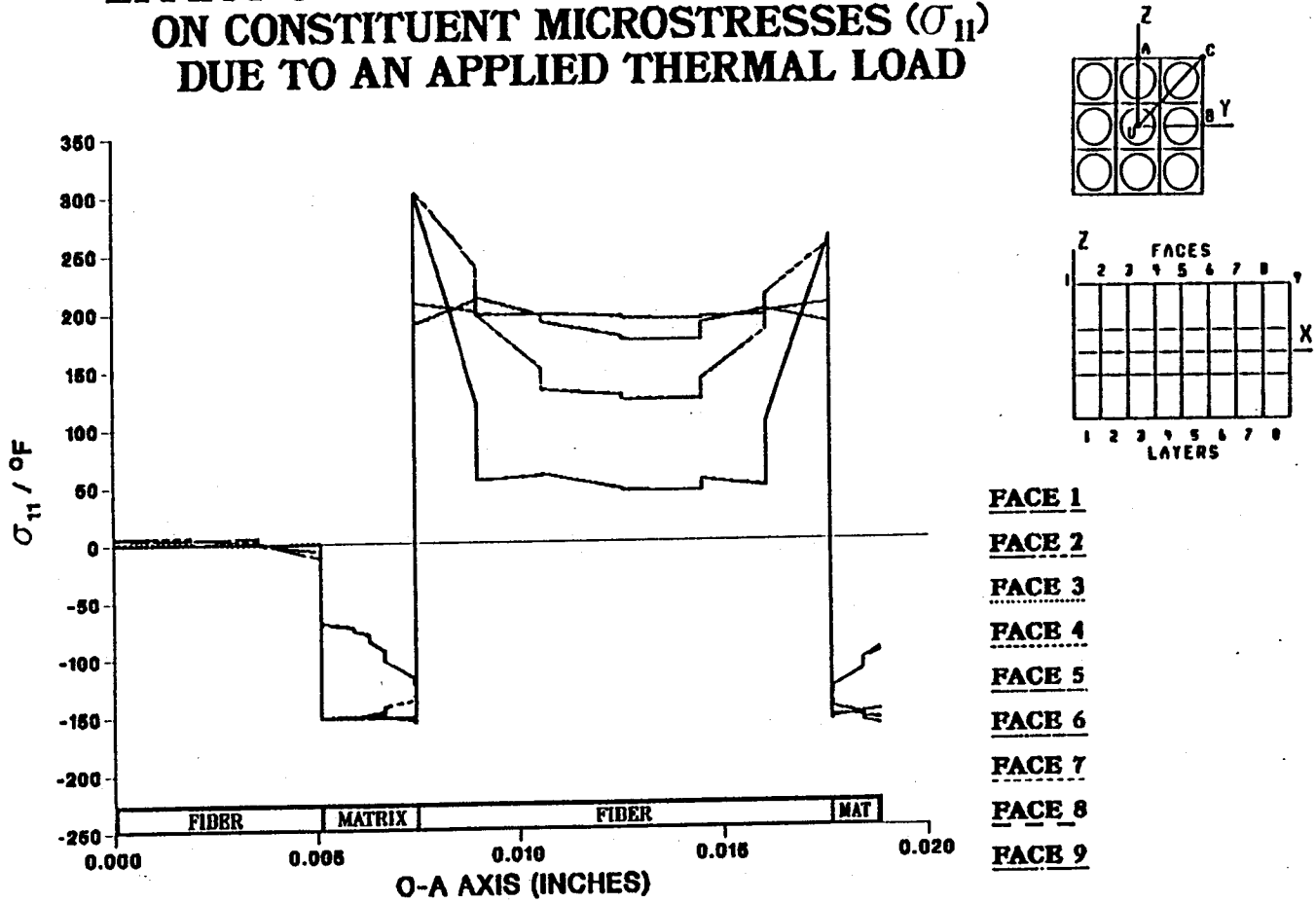


Figure 7.84 - σ_{11} Normalized Microstresses, O-A Direction, 11.1% Debonding, Thermal Loading

The matrix is in compression while the fiber is in tension. This produces large stress gradients at the fiber-matrix interface. In this thermal loading case, the composite is fixed in the center so it displaces symmetrically. Therefore, each line describing the stress state of a given face is coincident with the line describing the stress state in its sister face. Fiber debonding is not implemented symmetrically. Therefore, lines describing the stress state of each sister face diverge with debonding of the center fiber (figure 7.77).

As debonding progresses, as seen in figures 7.78 through 7.83, stresses in the center fiber decrease, particularly those in the middle of the fiber. Stresses in the neighboring fibers increase, particularly in the area nearest the debonding fiber. When the center fiber is totally debonded, all longitudinal stresses in the fiber are virtually eliminated and the load it was carrying has been transferred to the surrounding fibers (figure 7.84). Consider that a similar event took place in the debonding of the axial loaded composite. The surrounding fibers inherited the center fiber's load when it was debonded. In the thermal loaded case the resulting increase in stress in the neighboring fibers is seen more as a local stress concentration at the edge of the fibers nearest the center fiber. In the case of the axially loaded composite the added load is distributed evenly across the entire area of the neighboring fibers (figure 7.9). This difference can be attributed to the large difference in the thermal expansion coefficients of the fiber and the matrix. Figures 7.85 to 7.87 depict similar results but along the direction defined by the line segment O-C. In figure 7.87 the effect of fiber debonding on local stress increases in the neighboring fiber is not as significant due to the greater distance from the debonding fiber.

EFFECT OF 0.0% FIBER LENGTH DEBONDING ON CONSTITUENT MICROSTRESSES (σ_{11}) DUE TO AN APPLIED THERMAL LOAD

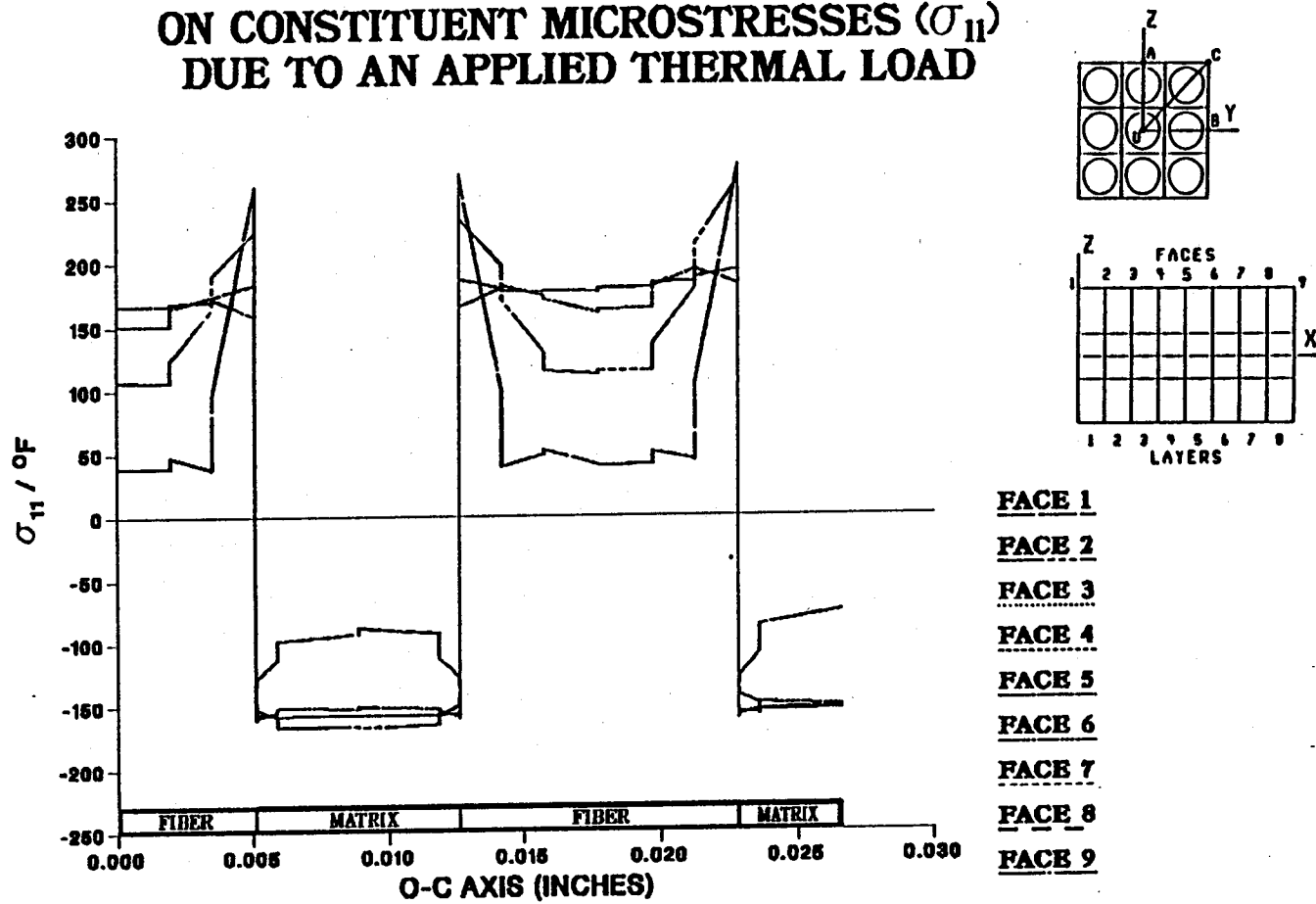


Figure 7.85 – σ_{11} Normalized Microstresses, O-C Direction, 0.0% Debonding, Thermal Loading

EFFECT OF 5.56% FIBER LENGTH DEBONDING ON CONSTITUENT MICROSTRESSES (σ_{11}) DUE TO AN APPLIED THERMAL LOAD

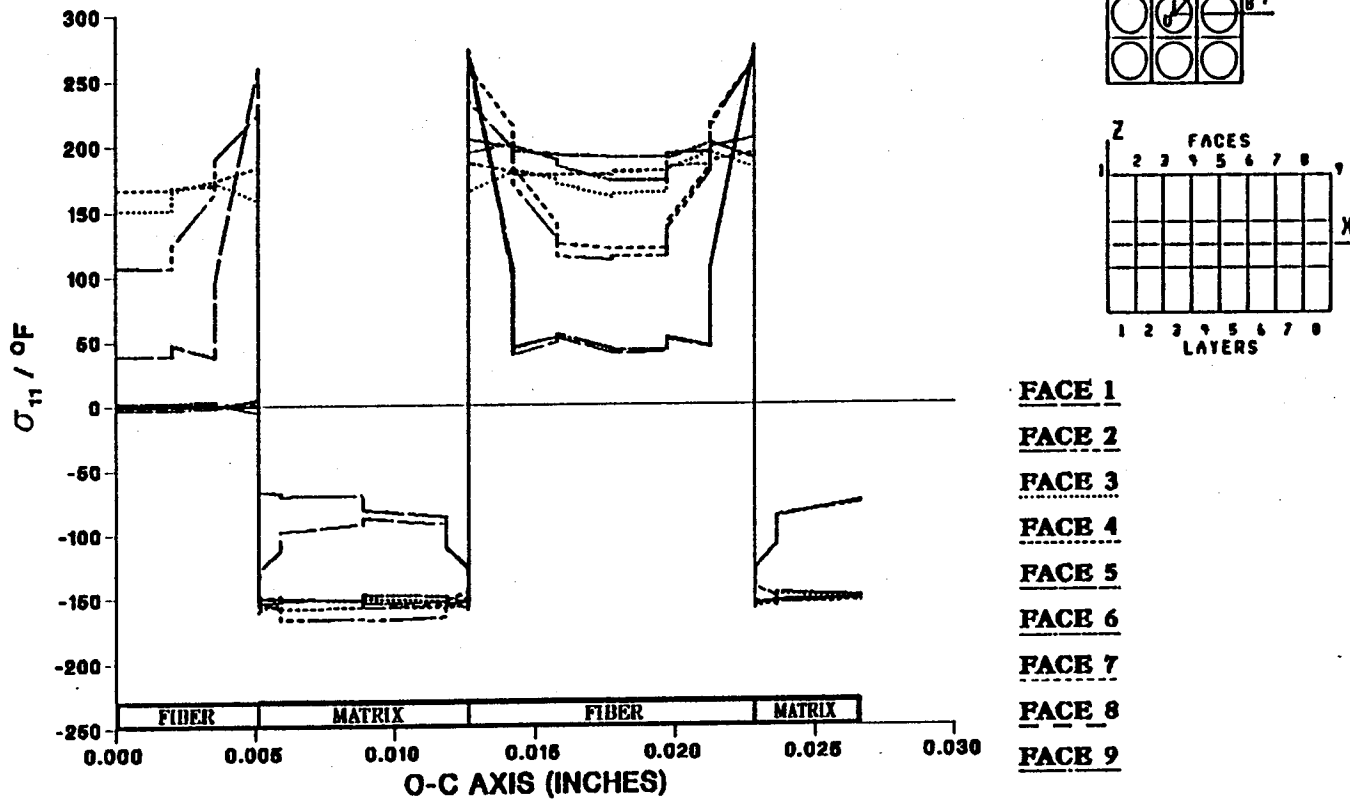


Figure 7.86 – σ_{11} Normalized Microstresses, O-C Direction, 5.56% Debonding, Thermal Loading

EFFECT OF 11.11% FIBER LENGTH DEBONDING ON CONSTITUENT MICROSTRESSES (σ_{11}) DUE TO AN APPLIED THERMAL LOAD

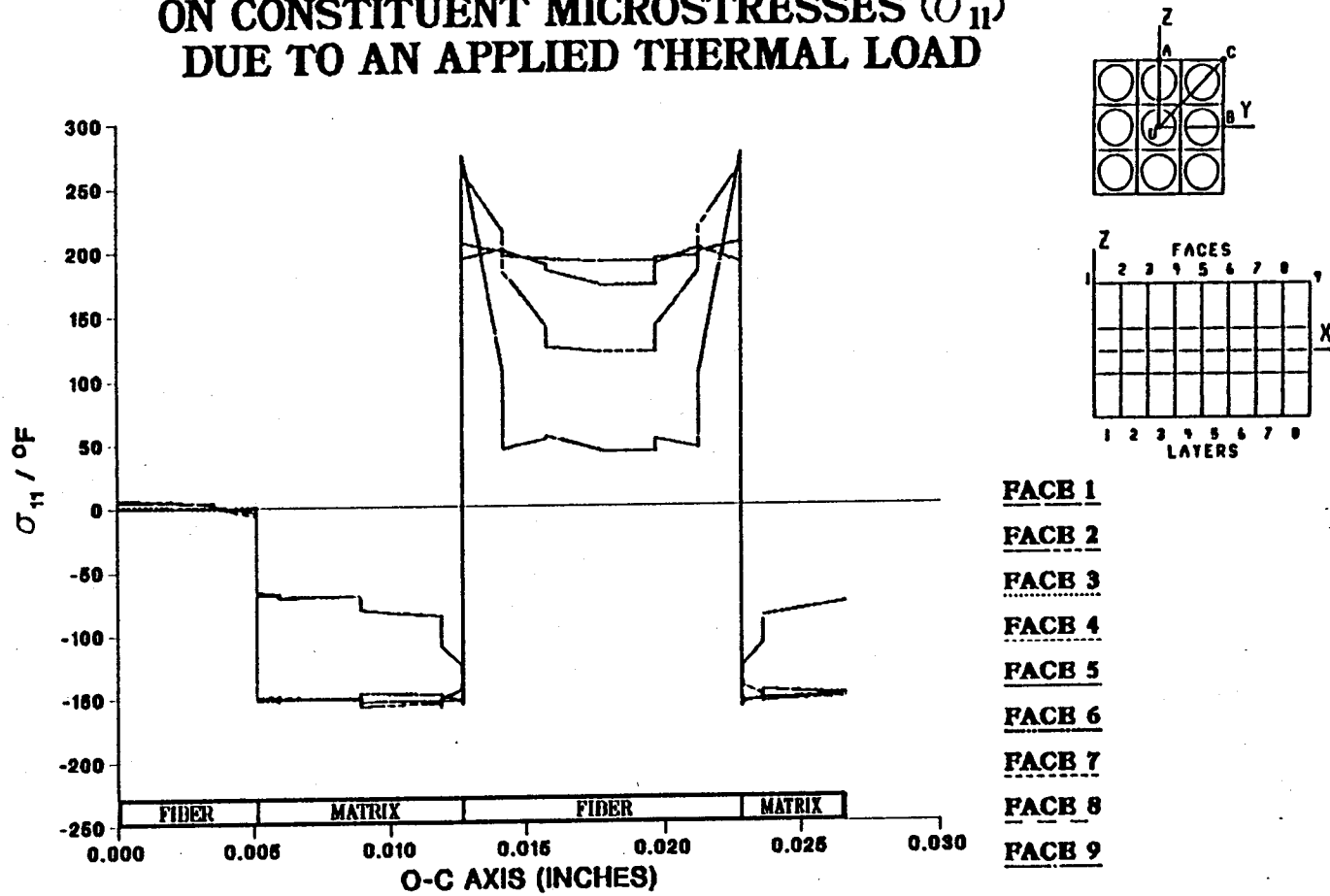


Figure 7.87 — σ_{11} Normalized Microstresses, O-C Direction, 11.11% Debonding, Thermal Loading

Figures 7.88 to 7.90 and 7.91 to 7.93 depict the effect of fiber debonding on longitudinal shear microstresses (σ_{13}) due to a thermal load and are plotted in the directions defined by the line segments O-A and O-C, respectively. These figures provided a graphic representation of the high shear stresses between fiber and matrix due to the large difference in thermal expansion coefficients of the fiber and the matrix. The areas of high shear stress are at the interface between the fiber and matrix materials which corresponds to the location of the large gradient of axial stresses mentioned earlier. This suggests load transfer between fiber and matrix by means of shear stresses. With increasing fiber disbond, the stresses in the center fiber are relaxed and the center fiber becomes structurally inactive.

Figures 7.94 through 7.96 also show the effect of fiber debonding on longitudinal shear microstresses (σ_{12}) due to a thermal load and are plotted in the directions defined by the line segment O-A. These results are similar to those described above.

It is of interest to note that any loading case which caused the cylindrical "holes" left by the debonding fibers to decrease in diameter would in actuality cause a compressive stress on the disbonded fiber. This compressive stress would induce friction between fiber and matrix and increase the global stiffness of the composite. In turn, these effects would change the stress profiles discussed above.

EFFECT OF 0.0% FIBER LENGTH DEBONDING ON CONSTITUENT MICROSTRESSES (σ_{31}) DUE TO AN APPLIED THERMAL LOAD

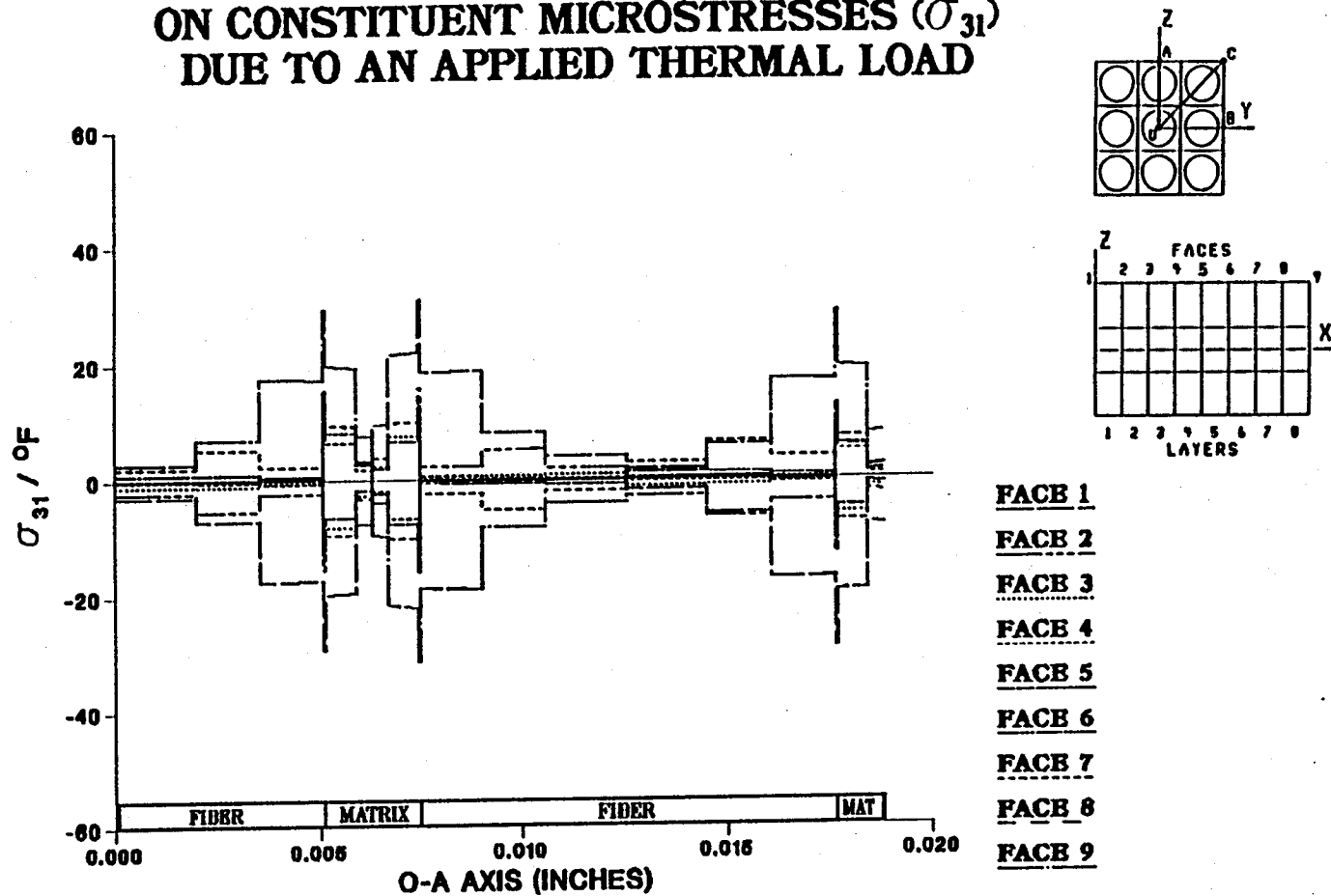


Figure 7.88 - σ_{31} Normalized Microstresses, O-A Direction, 0.0% Debonding, Thermal Loading

EFFECT OF 5.56% FIBER LENGTH DEBONDING ON CONSTITUENT MICROSTRESSES (σ_{31}) DUE TO AN APPLIED THERMAL LOAD

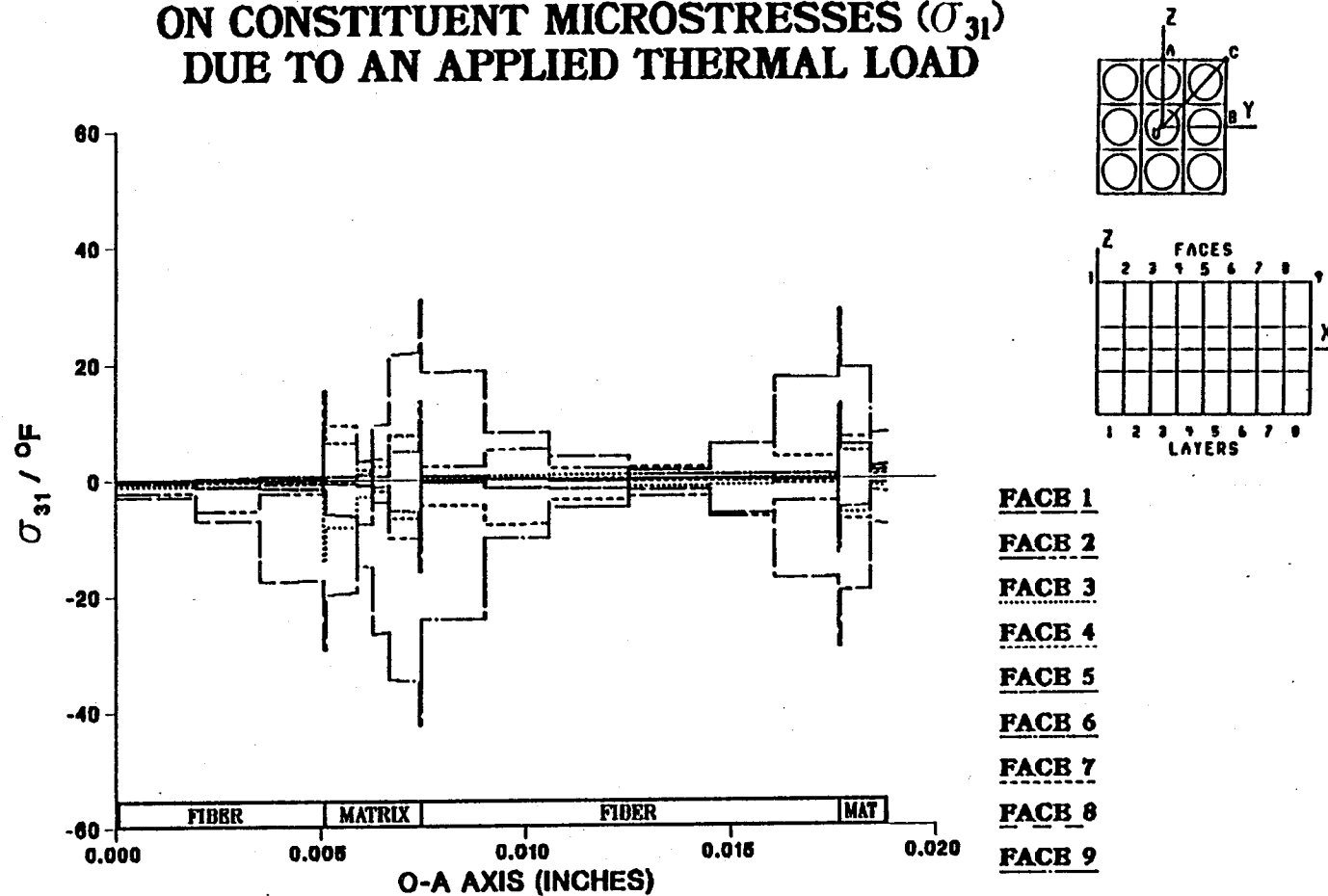
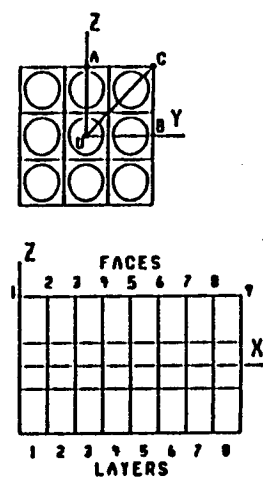


Figure 7.89 — σ_{31} Normalized Microstresses, O-A Direction, 5.56% Debonding, Thermal Loading

EFFECT OF 11.11% FIBER LENGTH DEBONDING ON CONSTITUENT MICROSTRESSES (σ_{31}) DUE TO AN APPLIED THERMAL LOAD



172

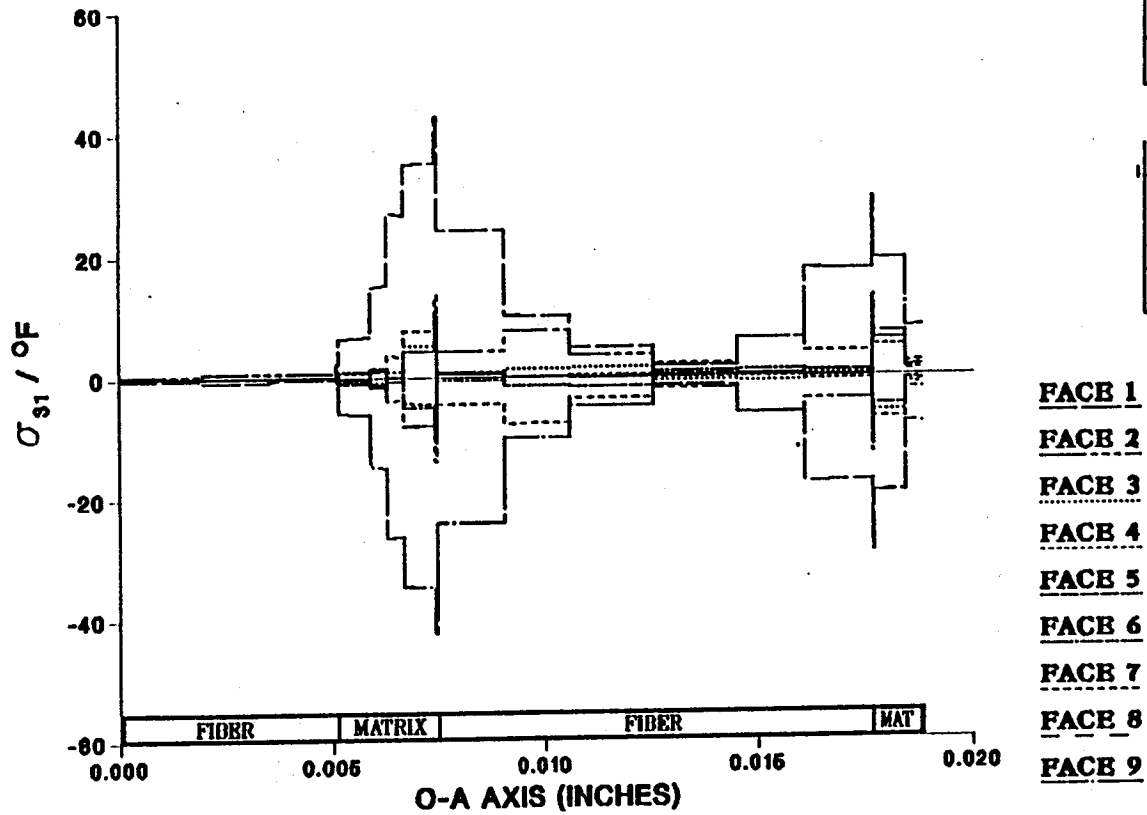


Figure 7.90 - σ_{31} Normalized Microstresses, O-A Direction, 11.11% Debonding, Thermal Loading

EFFECT OF 0.0% FIBER LENGTH DEBONDING ON CONSTITUENT MICROSTRESSES (σ_{31}) DUE TO AN APPLIED THERMAL LOAD

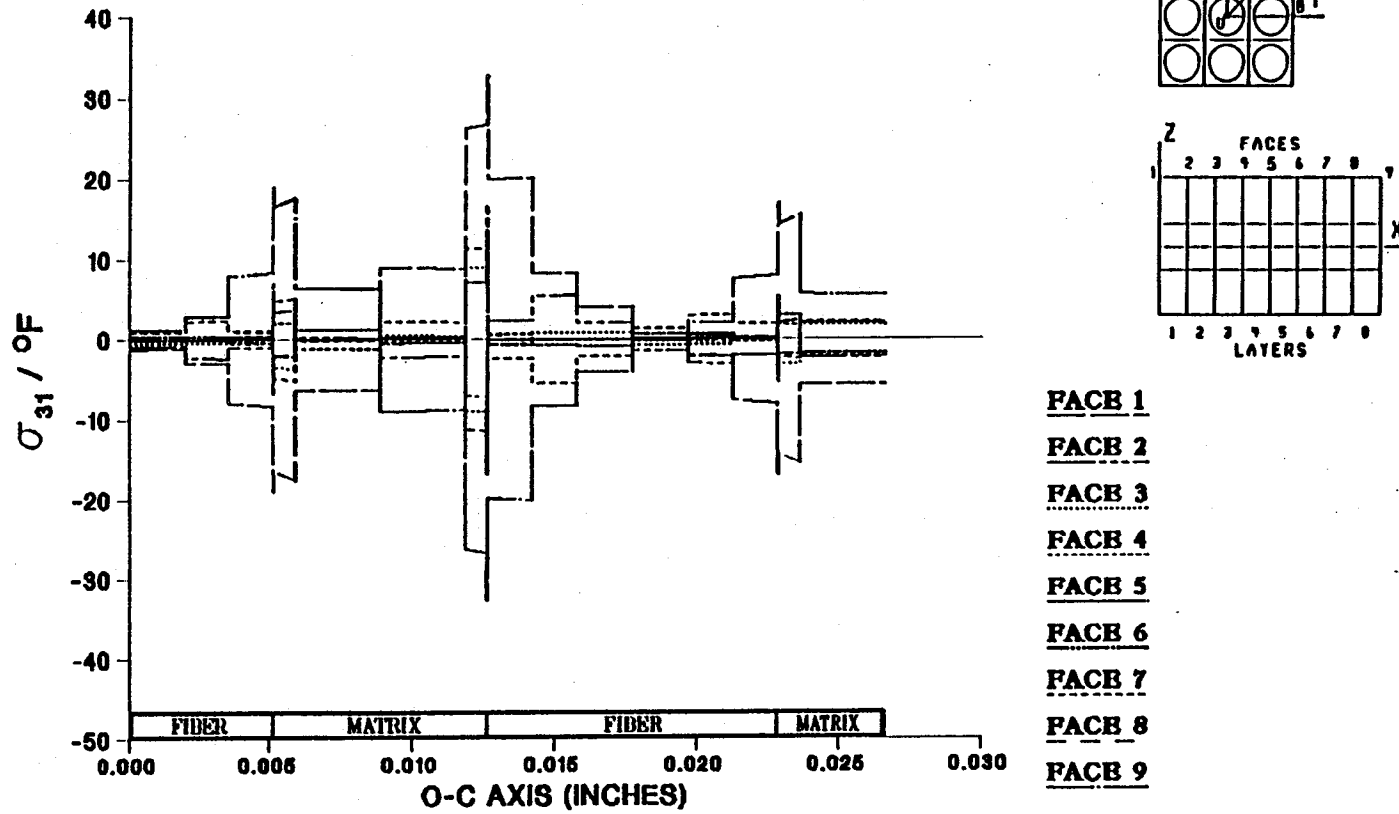


Figure 7.91 - σ_{31} Normalized Microstresses, O-C Direction, 0.0% Debonding, Thermal Loading

EFFECT OF 5.56% FIBER LENGTH DEBONDING ON CONSTITUENT MICROSTRESSES (σ_{31}) DUE TO AN APPLIED THERMAL LOAD

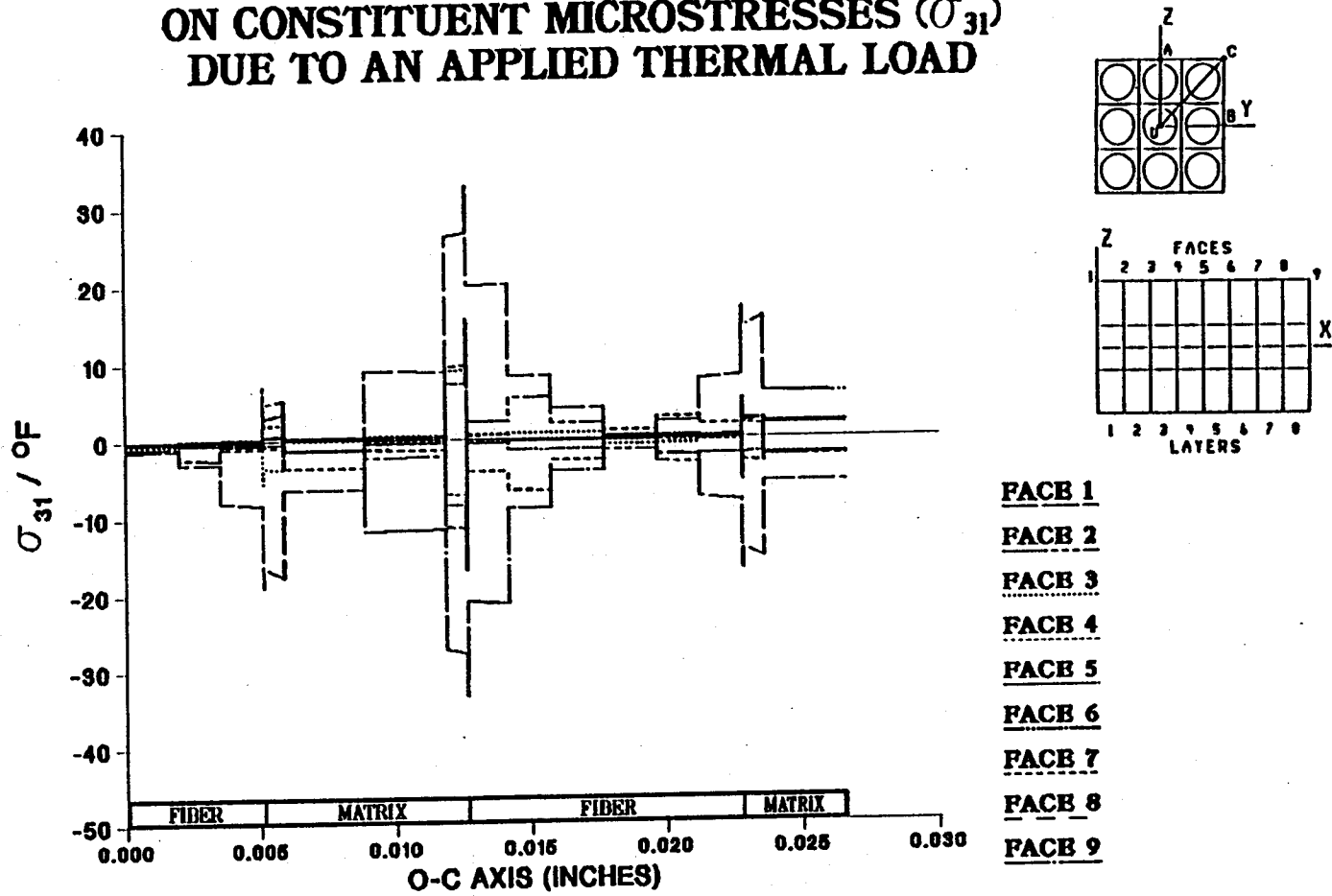


Figure 7.92 - σ_{31} Normalized Microstresses, O-C Direction, 5.56% Debonding, Thermal Loading

**EFFECT OF 11.11% FIBER LENGTH DEBONDING
ON CONSTITUENT MICROSTRESSES (σ_{31})
DUE TO AN APPLIED THERMAL LOAD**

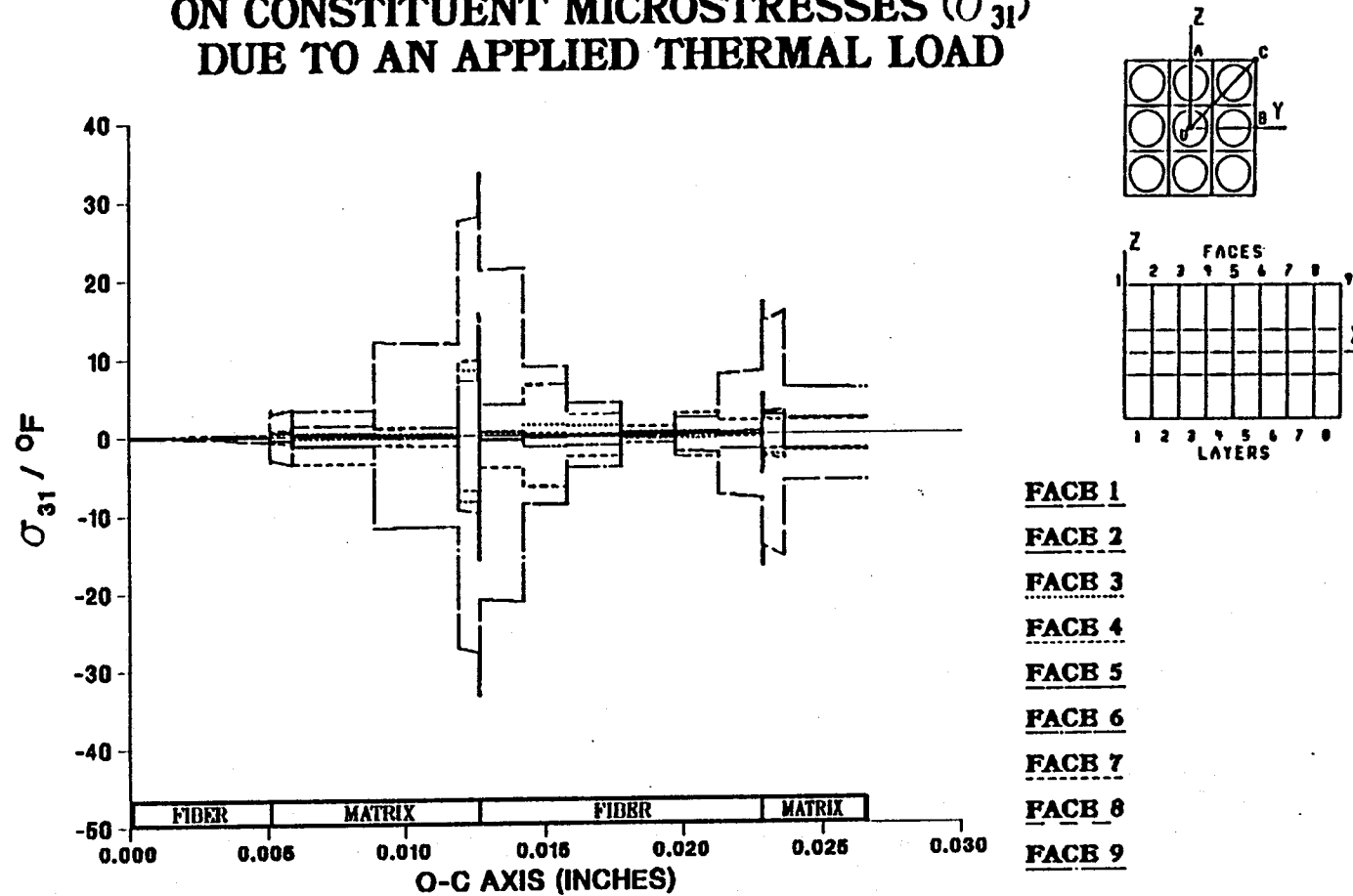
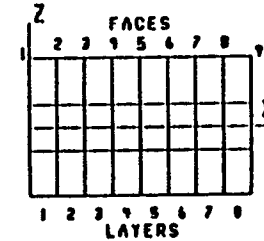
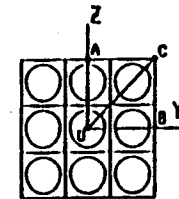
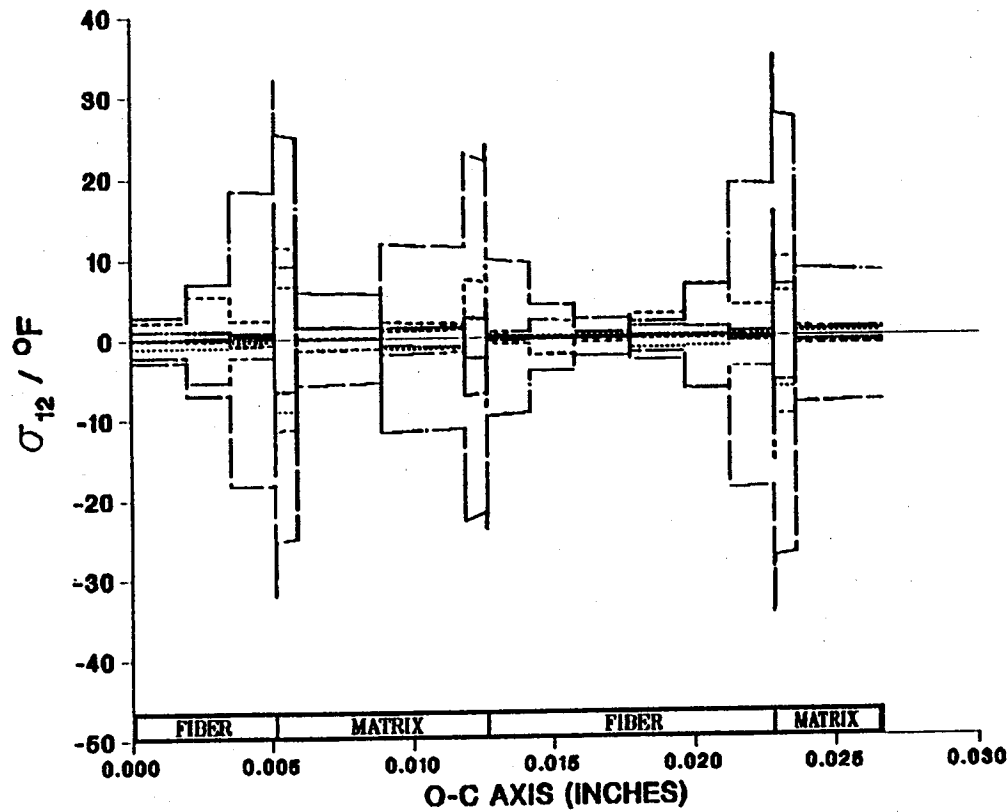


Figure 7.93 - σ_{31} Normalized Microstresses, O-C Direction, 11.11% Debonding, Thermal Loading

EFFECT OF 0.0% FIBER LENGTH DEBONDING ON CONSTITUENT MICROSTRESSES (σ_{12}) DUE TO AN APPLIED THERMAL LOAD



- FACE 1
- FACE 2
- FACE 3
- FACE 4
- FACE 5
- FACE 6
- FACE 7
- FACE 8
- FACE 9

Figure 7.94 - σ_{12} Normalized Microstresses, O-A Direction, 0.0% Debonding, Thermal Loading

EFFECT OF 5.56% FIBER LENGTH DEBONDING ON CONSTITUENT MICROSTRESSES (σ_{12}) DUE TO AN APPLIED THERMAL LOAD

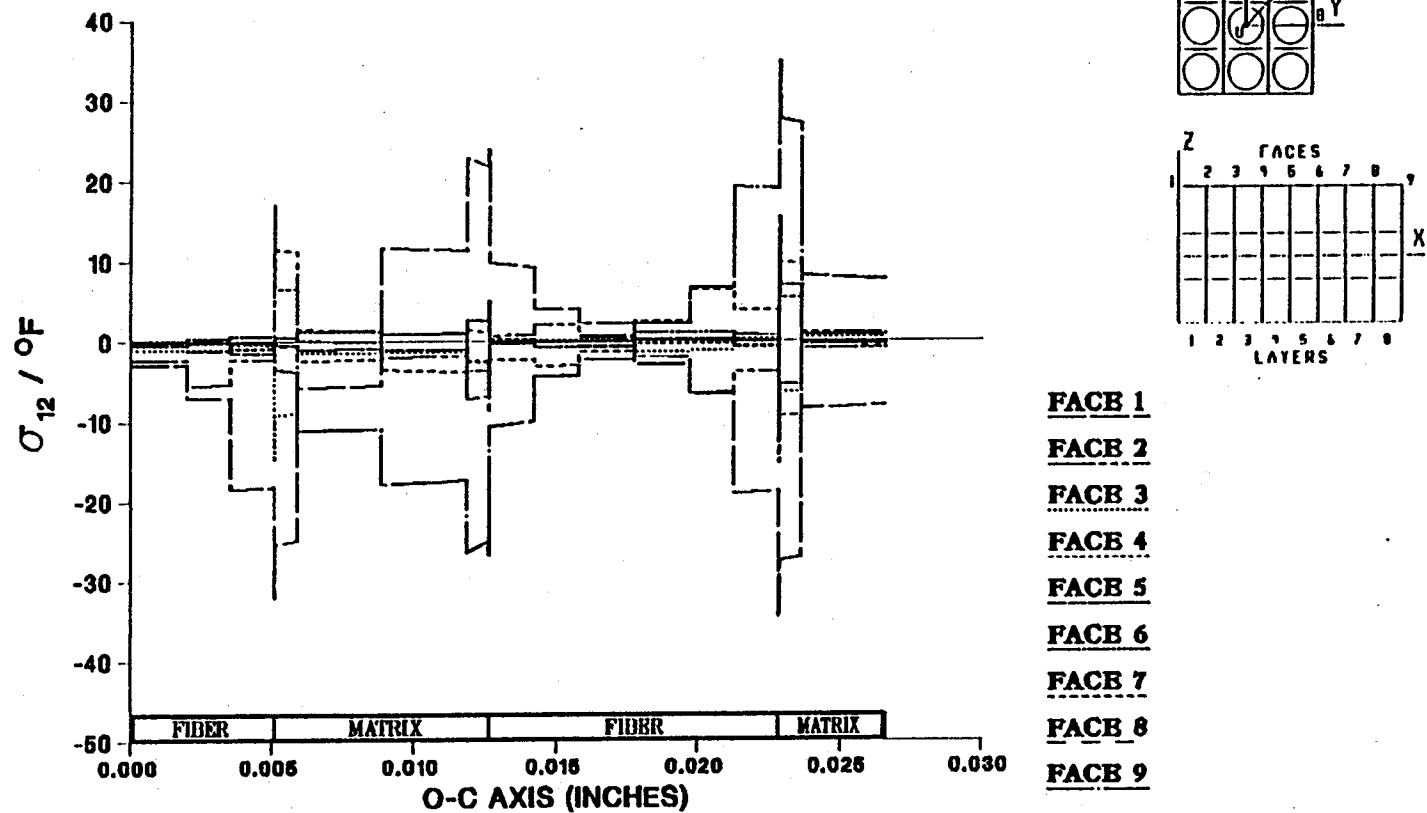


Figure 7.95 - σ_{12} Normalized Microstresses, O-A Direction, 5.56% Debonding, Thermal Loading

EFFECT OF 11.11% FIBER LENGTH DEBONDING ON CONSTITUENT MICROSTRESSES (σ_{12}) DUE TO AN APPLIED THERMAL LOAD

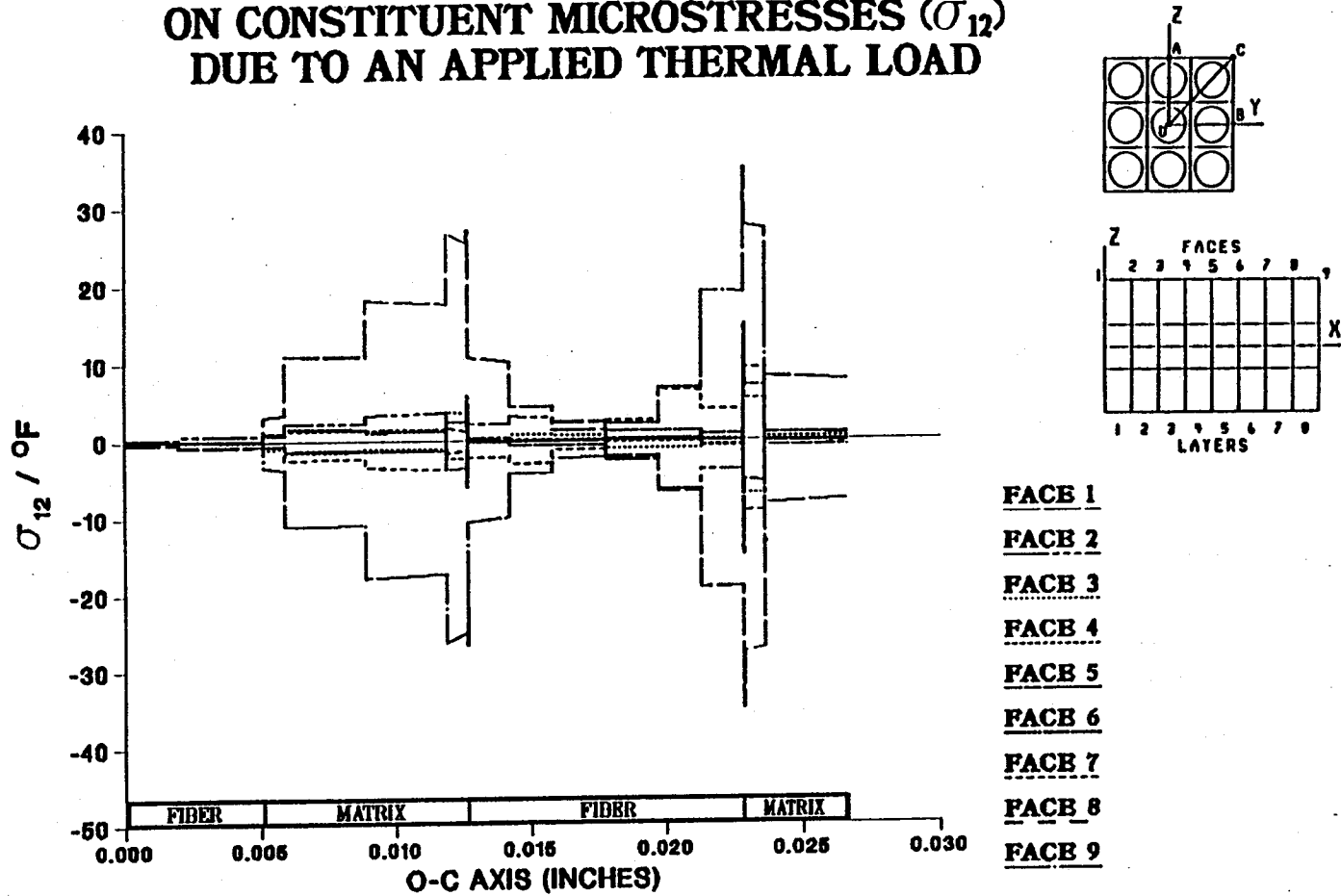


Figure 7.96 - σ_{12} Normalized Microstresses, O-A Direction, 11.11% Debonding, Thermal Loading

CHAPTER 8

CONCLUSIONS

From the results of the material property degradation analysis it can be seen that, in general, a rule of mixtures based on active fiber volume is not a viable method in determining the composite's material properties. Of the material properties considered, the longitudinal thermal expansion coefficient seems to be the most sensitive to fiber debonding. This sensitivity of α_{111} makes it a good indicator of the level of debonding in a composite. If α_{111} is above predicted values then the suspicion of the presence of debonding may be justified and the degree of debonding may be approximated by one of the plots in this report.

For small amounts of debonding composite material properties did not change significantly. High temperature results indicate a shift in the value of the material properties while maintaining the same rate of degradation as in the room temperature results.

When all the fibers were debonded, resulting in a higher percent disbond, more significant changes in the material's properties were observed. The longitudinal modulus, E_{111} , and ν_{112} both show nonlinear degradation at these higher levels of fiber debonding. Again, high temperature results show a shift in the value of the material properties while maintaining the same rate of degradation as in the room temperature results.

In the plots of the normalized microstresses the effects of debonding the center fiber are considered. In general, the changes in the internal stress state of the composite are manifested in two ways: 1) by stress risers local to the debonding area and 2) by the neighboring fibers sharing the increased level of stress. Varied amounts of each of these effects can be seen in the stress plots. The amount of each is dependant on the loading conditions and the composite's constituent material properties. An example of the local stress riser effect is seen in the σ_{23} microstresses generated by an applied YX displacement (figures 7.58 – 7.60). The distribution of the additional stress to the other fibers can be seen in figures 7.1 through 7.9. These figures depict the microstresses in the 11 direction produced by a longitudinal enforced displacement. Other examples are discussed in the previous chapter.

In cases where the microstresses in the fibers are small, fiber debonding had little effect. An example would be the σ_{23} microstresses resulting from a displacement transverse to the fiber direction (figures 7.55 – 7.57).

CHAPTER 9

SUMMARY

This work has shown that the greatest effect of fiber debonding on composite material properties occurs when neighboring fibers are debonded and all load must be carried by the matrix material. This method of finding material properties of debonded composites is a viable one yet the amount of required computer time is very costly. Some of the extra cost in computer time can be attributed to the use of superelements. While they are convenient to use in a modular finite element mesh such as this, they are also computer intensive and can lead to high analysis cost. The ability to do restarts using the saved database did alleviate some computer overhead on the runs where only the boundary conditions changed and not the mesh itself.

Some of the stress plots have large jumps in stress due to the presence of a ring of elements with large aspect ratios around each fiber. Where this does not significantly effect the material property calculations, it may appear conspicuous when considering the stress states in the fiber and the matrix.

To achieve the results described here, over 230 large MSC NASTRAN superelement computer runs were made. This alone is stifling for the average computer installation. Many supporting FORTRAN programs were written and utilized to aid in the data reduction, material property calculations,

least-squares approximations, microstress normalization, and plotting. Each of these programs consume additional computer time. This inordinate amount of computer utilization suggests that, while yielding consistent results, this form of investigation into fiber debonding is very time consuming and expensive.

The modeling of debonding of composite materials using the finite element method provides the ability to obtain the stresses internal to the composite. These microstresses can not be attained by experimental methods. This method provides unique insight into the mechanics of load transfer between fiber and matrix.

REFERENCES

1. M. A. Gockel, ed., MSC/NASTRAN: Handbook for Superelement Analysis: MSC/NASTRAN Version 61 (Los Angeles: The MacNeal-Schwendler Corporation, 1982), p. 1.1-1.
2. *ibid.*, p. 2.1-4.
3. Bhagwan D. Agarwal and Lawrence J. Broutman, Analysis and Performance of Fiber Composites (New York: John Wiley and Sons, Inc., 1980), p. 19.
4. Brian C. Hoskin and Alan A. Baker, eds., Composite Materials for Aircraft Structures (New York: American Institute of Aeronautics and Astronautics, Inc., 1986), pp. 12-21.
5. Lawrence H. VanVlack, Elements of Material Science and Engineering (Reading, Massachusetts: Addison-Wesley Publishing Company, 1985), pp. 122-125, 177-188.
6. Bhagwan D. Agarwal and Lawrence J. Broutman, pp. 110-113.
7. James A. Cornie, *et al*, "Processing of Metal and Ceramic Matrix Composites", Ceramic Bulletin, vol. 65, no. 2, 1986. pp. 293-303.
8. John L. Kardos, "Composite Interfaces: Myths, Mechanisms and Modifications", Chemtech, July 1984 pp. 430-434.
9. Brian C. Hoskin and Alan A. Baker, eds., pp. 12-21.
10. John J. Caruso, Application to Finite Element Substructuring to Composite Micromechanics (NASA Technical Memorandum 83729, August 1984), pp. 22-37.
11. M. A. Gockel, ed., p. 2.2-2 - 2.2-5.
12. O. C. Zienkiewicz, The Finite Element Method (London: McGraw-Hill Book Company (UK) Limited, 1985), pp. 162-164.
13. John C. Muskvitch, MSC/NASTRAN Superelement Analysis (Rockville, Maryland: The MacNeal-Schwendler Corporation, 1987), pp. 1-2 - 1-4.

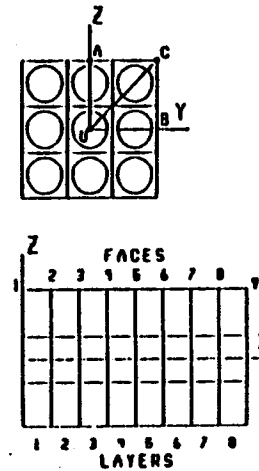
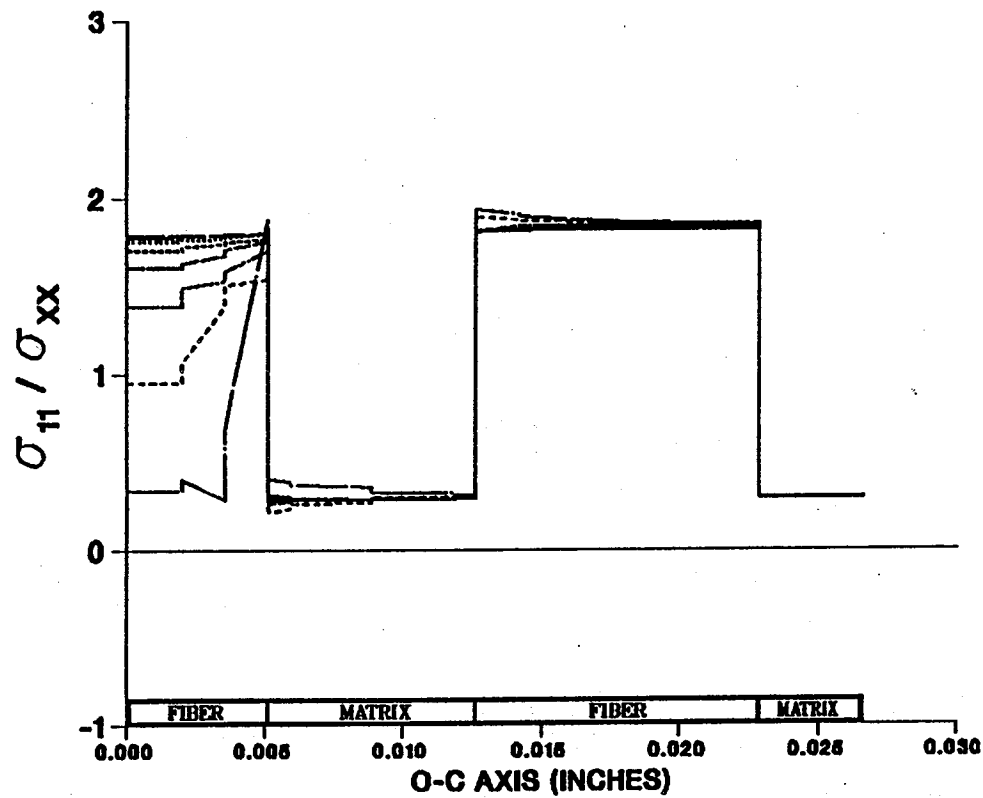
14. John C. Caruso and Christos C. Chamis, "Superelement Methods Applications to Micromechanics of High Temperature Metal Matrix Composites", AIAA'88 29th Structures, Structural Dynamics, and Materials (AIAA-88-2390, Washington D. C.: American Institute of Aeronautics and Astronautics, April 1988), pp 1392-1397.
15. Dale A. Hopkins and Christos C. Chamis, A Unique Set of Micromechanics Equations for High Temperature Metal Matrix Composites (NASA Technical Memorandum 87154, November 1985), pp. 15-17.
16. Robert W. Horbeck, Numerical Methods (New York: Quantum Publishers, Inc., 1975), pp.121-125.
17. Dale A. Hopkins and Pappu L. N. Murthy, "METCAN - The Metal Matrix Composite Analyzer", Lewis Structures Technology - 1988, Volume 2 - Structural Mechanics (NASA Conference Publication 3003, May 1988), pp. 2-141 - 2-156.
18. Dale A. Hopkins and Christos C. Chamis, p. 16.

APPENDIX

APPENDIX

The following pages contain additional microstress plots. These provide the ability to analyze the internal stresses state at each level of fiber debonding. These normalized microstress plots have been include to complete the descriptions of the stress states described in the body of this paper.

EFFECT OF 0.0% FIBER LENGTH DEBONDING ON CONSTITUENT MICROSTRESSES (σ_{11}) DUE TO A LOAD IN THE XX-DIRECTION



- FACE 1
- FACE 2
- FACE 3
- FACE 4
- FACE 5
- FACE 6
- FACE 7
- FACE 8
- FACE 9

Figure A.1 - σ_{11} Normalized Microstresses, O-C Direction, 0.0% Debonding, σ_{xx}^e Loading

**EFFECT OF 1.39% FIBER LENGTH DEBONDING
ON CONSTITUENT MICROSTRESSES (σ_{11})
DUE TO A LOAD IN THE XX-DIRECTION**

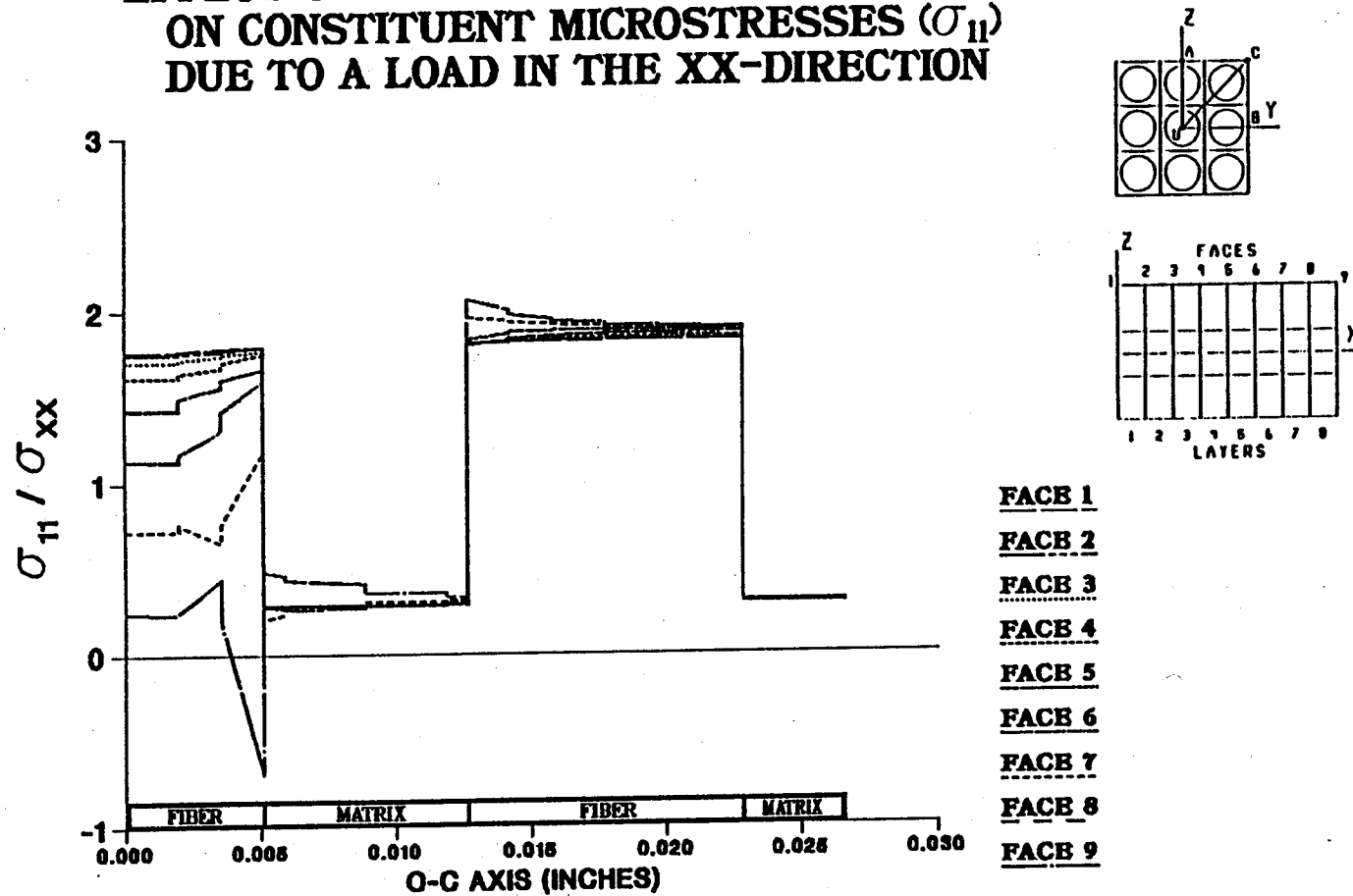


Figure A.2 - σ_{11} Normalized Microstresses, O-C Direction, 1.39% Debonding, σ_{xx}^e Loading

EFFECT OF 2.78% FIBER LENGTH DEBONDING ON CONSTITUENT MICROSTRESSES (σ_{11}) DUE TO A LOAD IN THE XX-DIRECTION

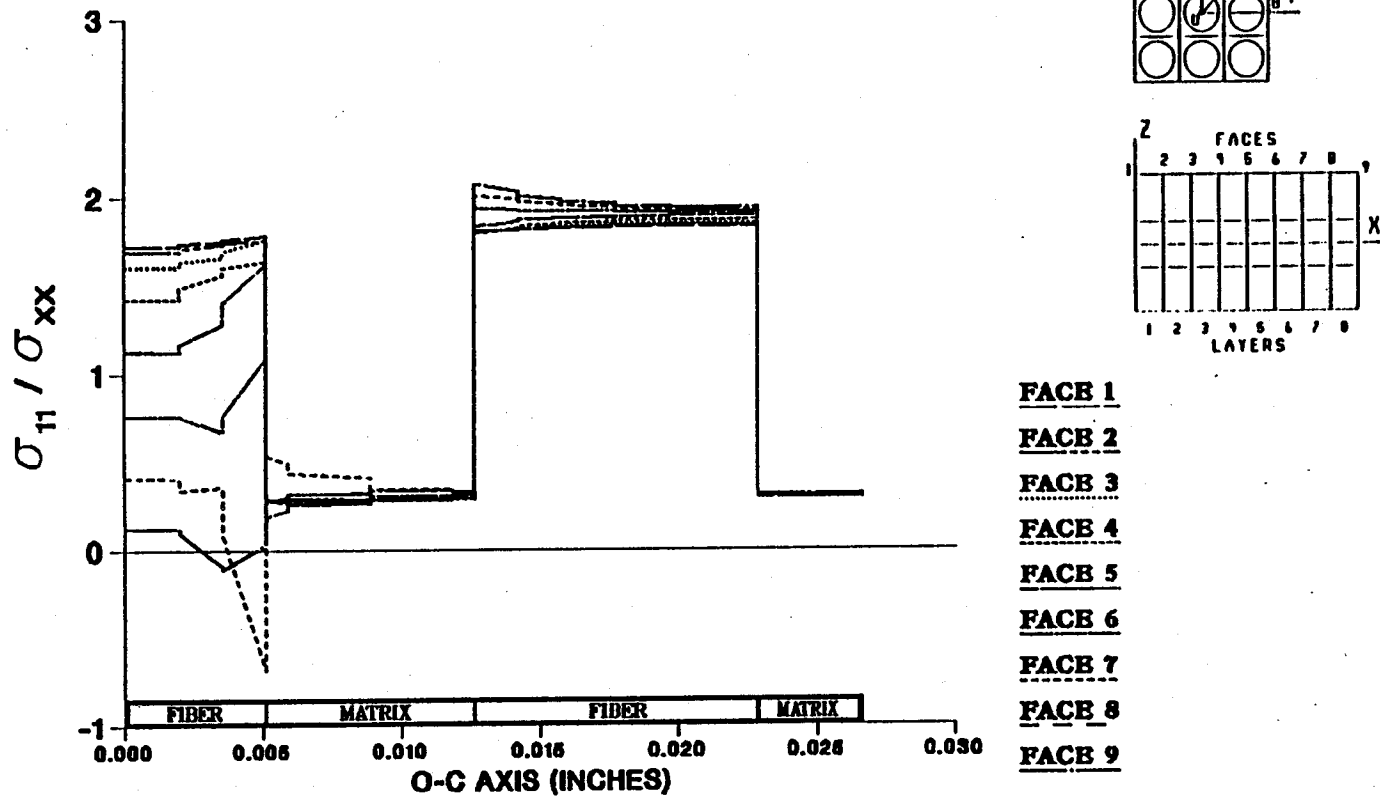


Figure A.3 - σ_{11} Normalized Microstresses, O-C Direction, 2.78% Debonding, σ_{xx}^e Loading

EFFECT OF 4.17% FIBER LENGTH DEBONDING ON CONSTITUENT MICROSTRESSES (σ_{11}) DUE TO A LOAD IN THE XX-DIRECTION

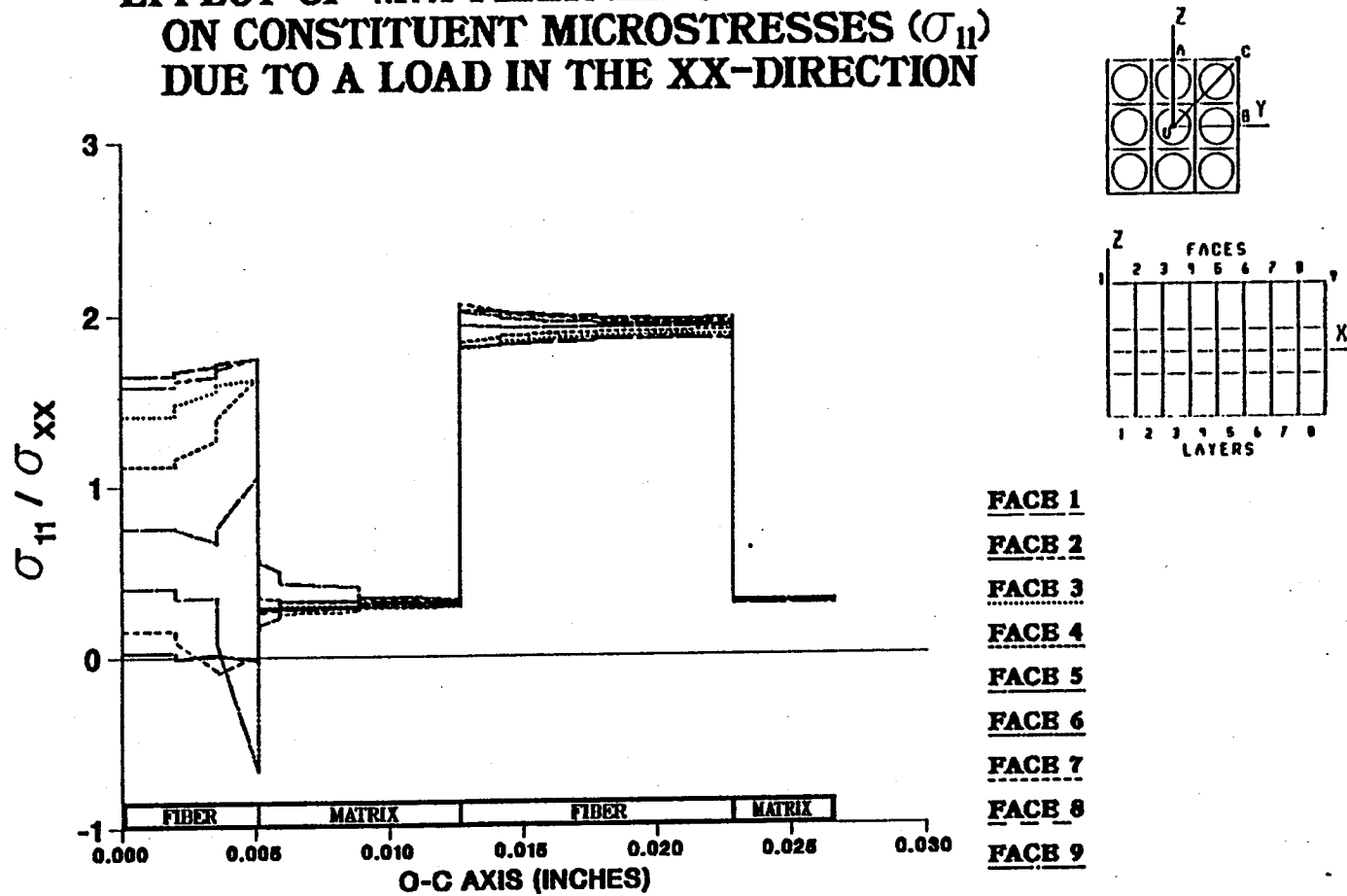


Figure A.4 – σ_{11} Normalized Microstresses, O-C Direction, 4.17% Debonding, σ_{xx}^0 Loading

EFFECT OF 5.56% FIBER LENGTH DEBONDING ON CONSTITUENT MICROSTRESSES (σ_{11}) DUE TO A LOAD IN THE XX-DIRECTION

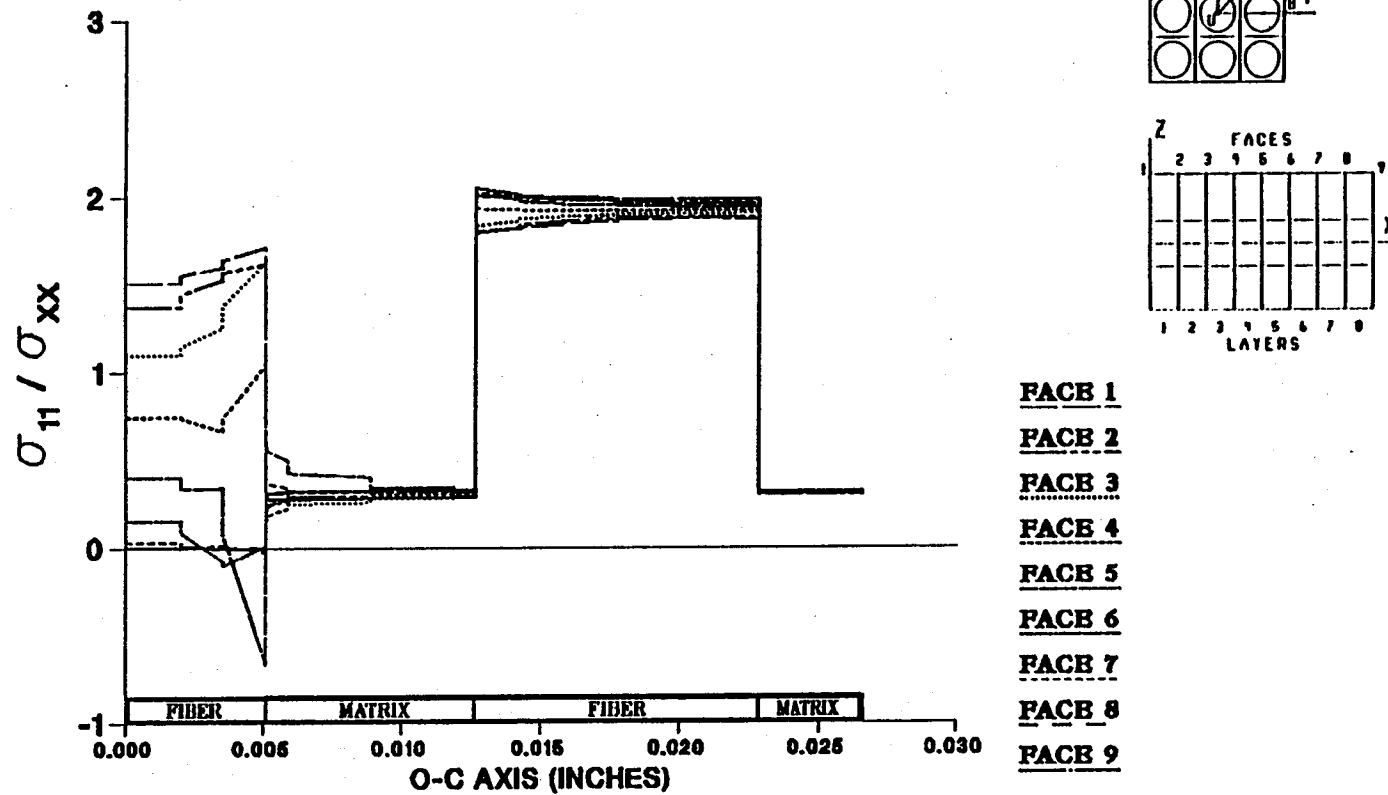


Figure A.5 - σ_{11} Normalized Microstresses, O-C Direction, 5.56% Debonding, σ_{xx}^e Loading

EFFECT OF 6.94% FIBER LENGTH DEBONDING ON CONSTITUENT MICROSTRESSES (σ_{11}) DUE TO A LOAD IN THE XX-DIRECTION

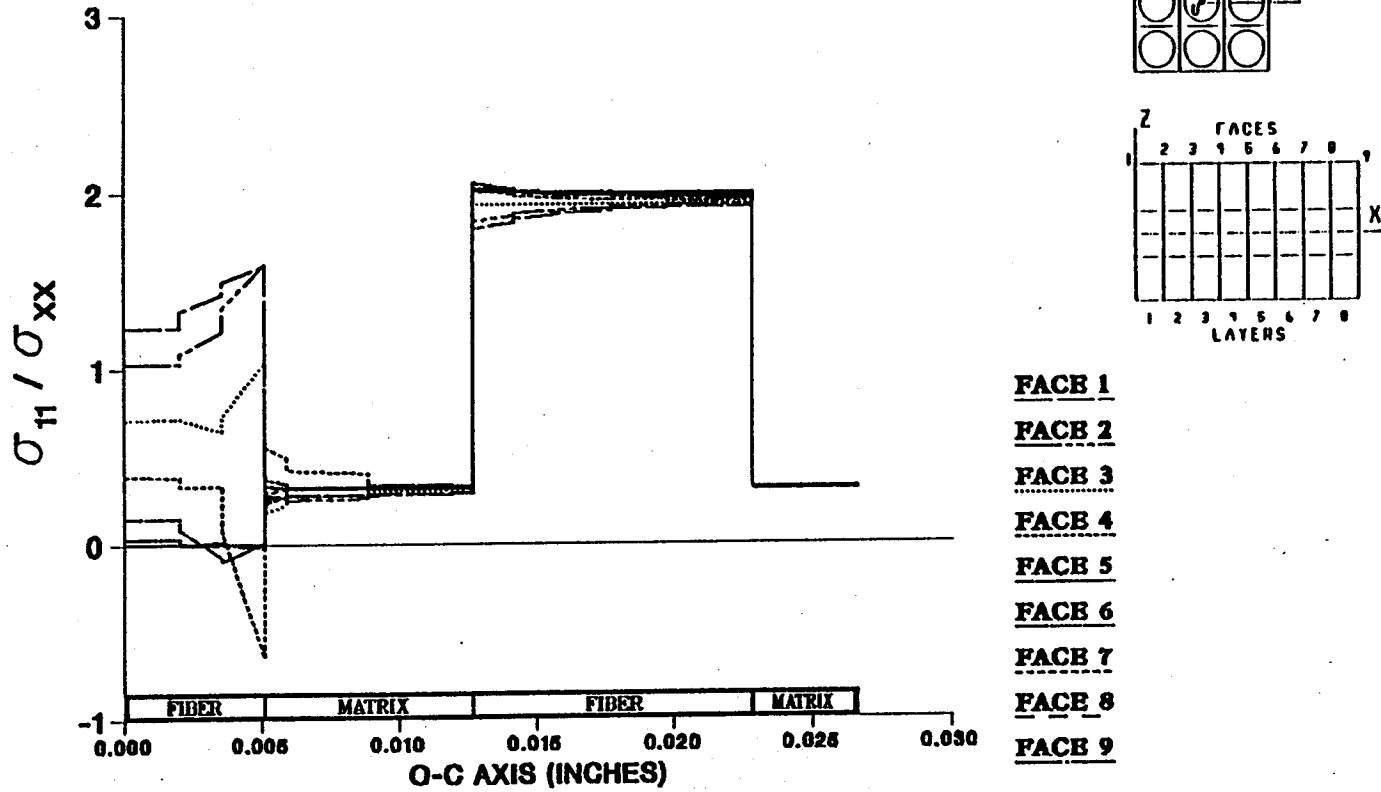


Figure A.6 - σ_{11} Normalized Microstresses, O-C Direction, 6.94% Debonding, σ_{xx}^e Loading

**EFFECT OF 8.33% FIBER LENGTH DEBONDING
ON CONSTITUENT MICROSTRESSES (σ_{11})
DUE TO A LOAD IN THE XX-DIRECTION**

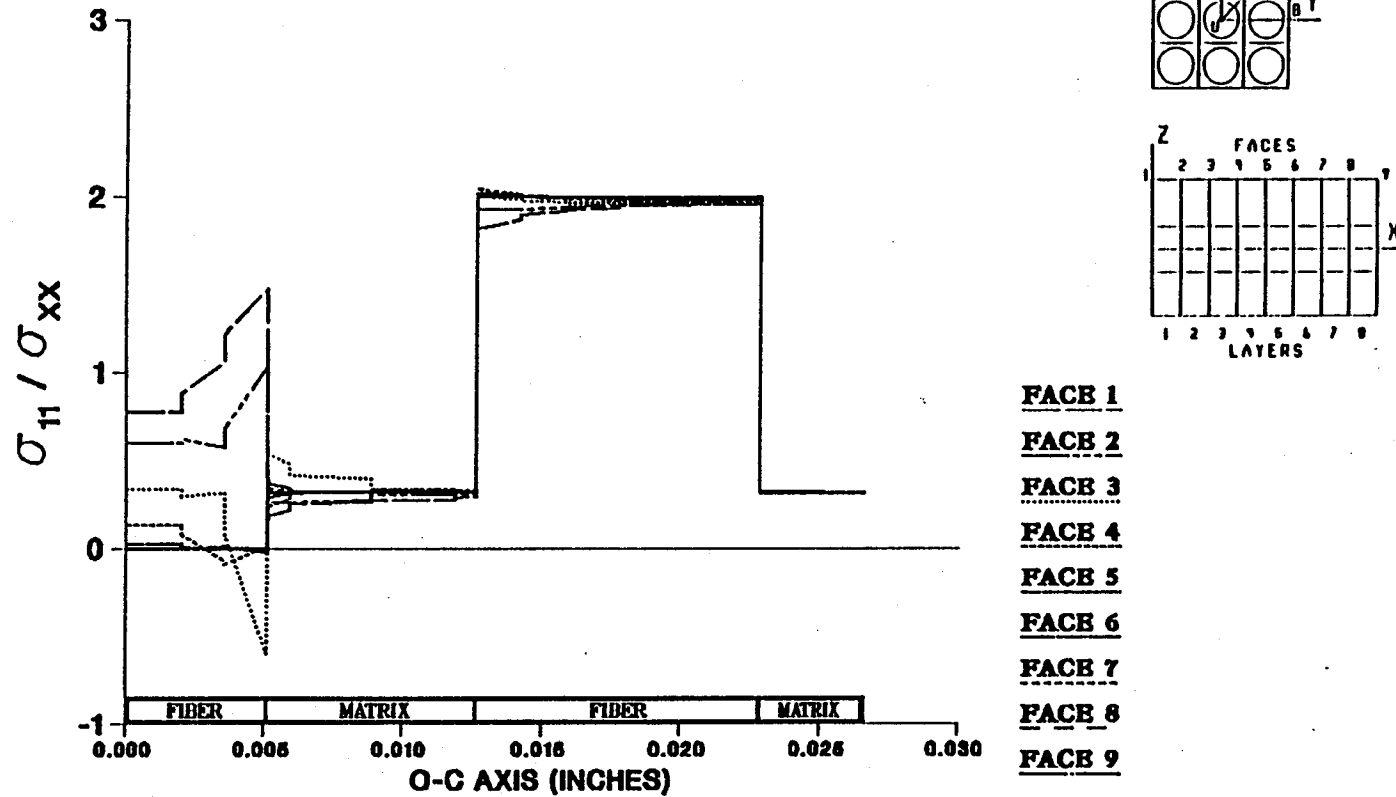
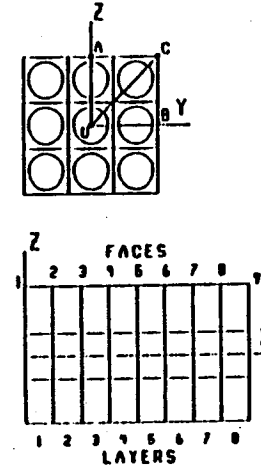
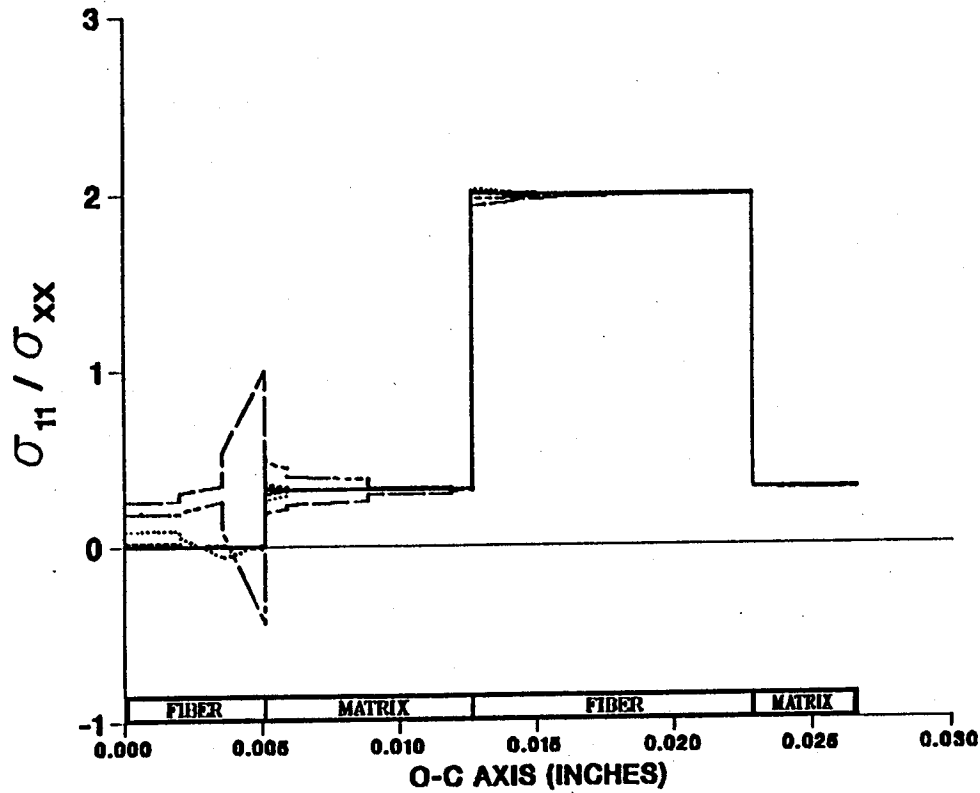


Figure A.7 - σ_{11} Normalized Microstresses, O-C Direction, 8.33% Debonding, σ_{xx}^e Loading

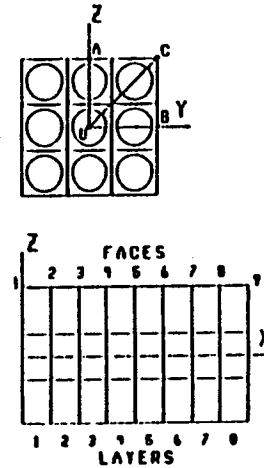
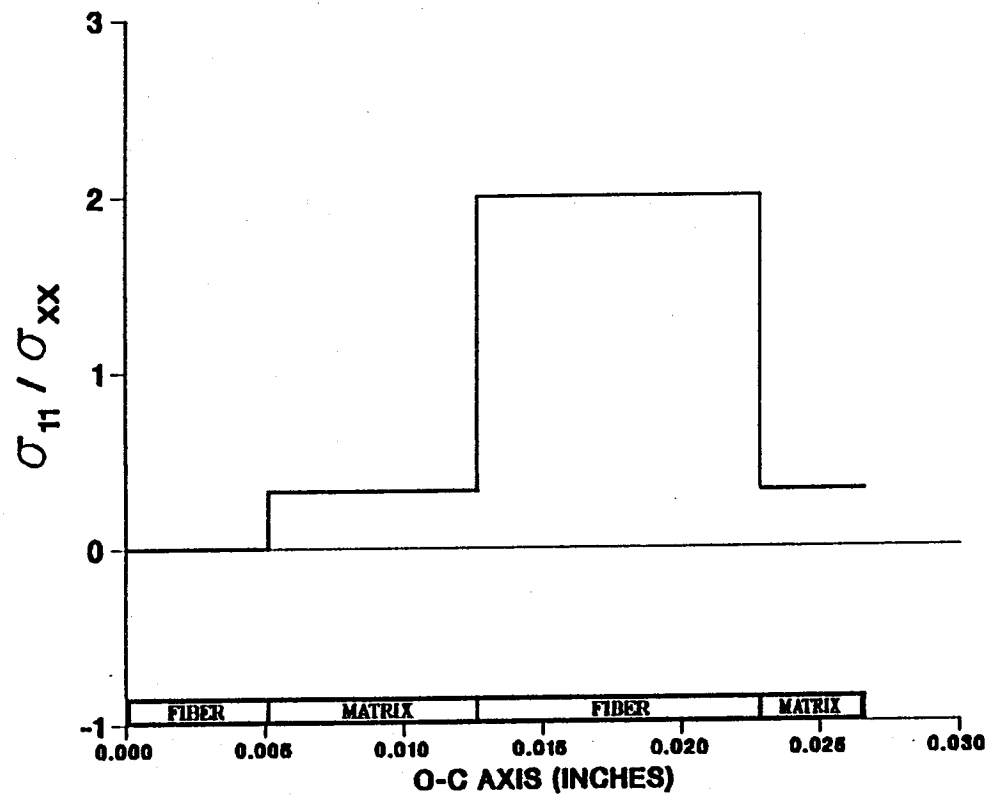
EFFECT OF 9.72% FIBER LENGTH DEBONDING ON CONSTITUENT MICROSTRESSES (σ_{11}) DUE TO A LOAD IN THE XX-DIRECTION



- FACE 1
- FACE 2
- FACE 3
- FACE 4
- FACE 5
- FACE 6
- FACE 7
- FACE 8
- FACE 9

Figure A.8 — σ_{11} Normalized Microstresses, O-C Direction, 9.72% Debonding, σ_{xx}^e Loading

EFFECT OF 11.1% FIBER LENGTH DEBONDING ON CONSTITUENT MICROSTRESSES (σ_{11}) DUE TO A LOAD IN THE XX-DIRECTION



- FACE 1
- FACE 2
- FACE 3
- FACE 4
- FACE 5
- FACE 6
- FACE 7
- FACE 8
- FACE 9

Figure A.9 - σ_{11} Normalized Microstresses, O-C Direction, 11.1% Debonding, σ_{xx}^e Loading

EFFECT OF 0.0% FIBER LENGTH DEBONDING ON CONSTITUENT MICROSTRESSES (σ_{31}) DUE TO A LOAD IN THE XX-DIRECTION

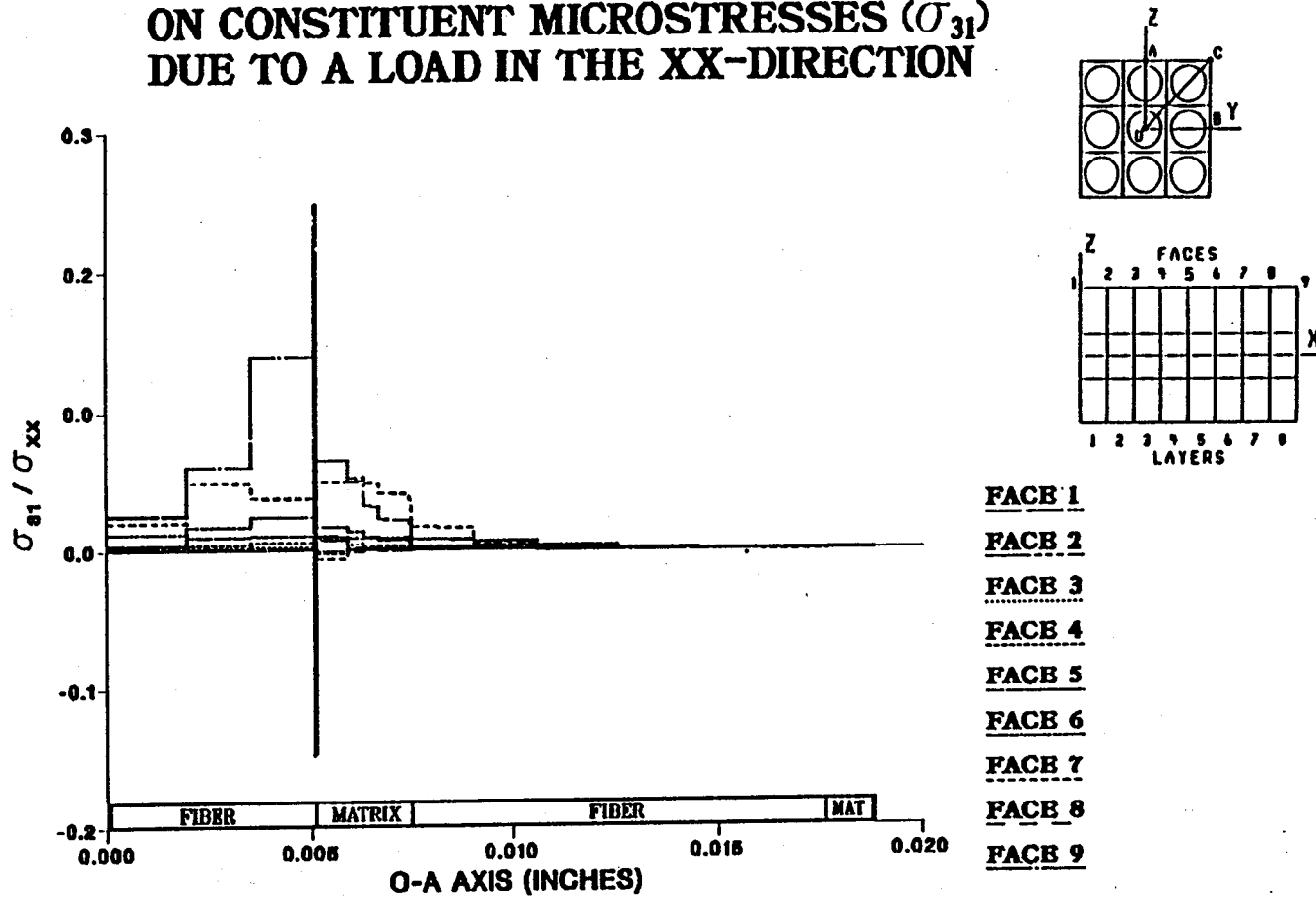
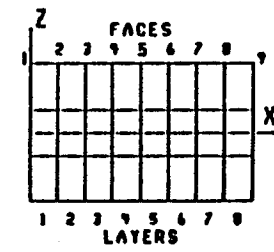
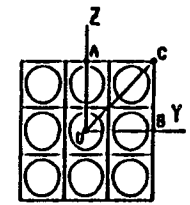
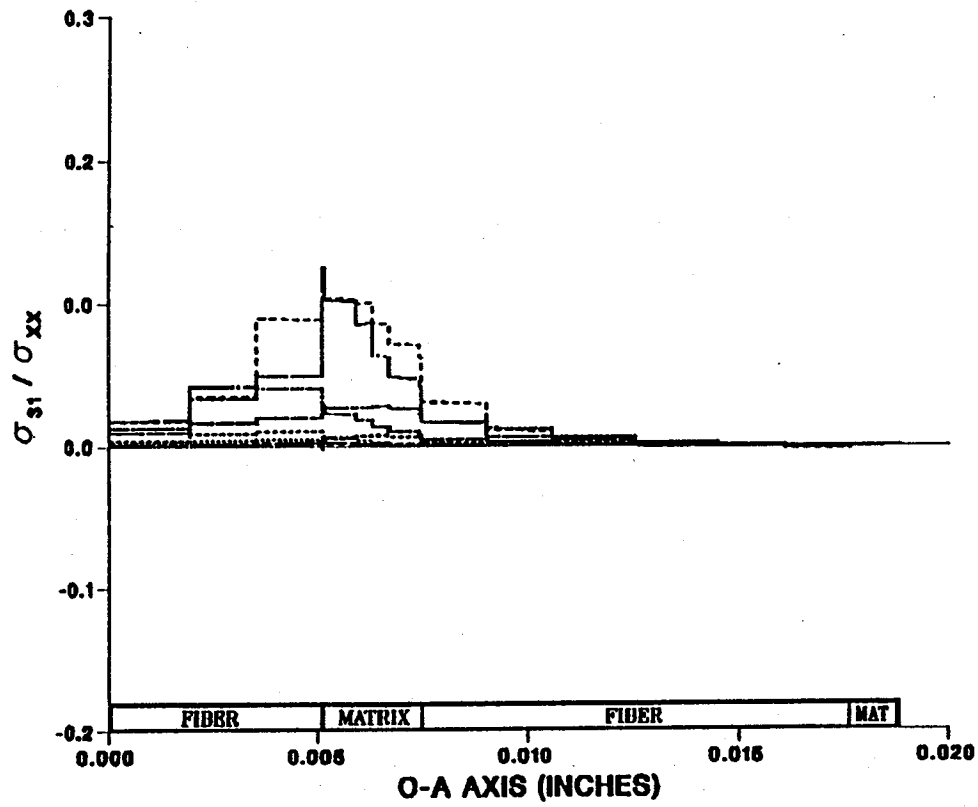


Figure A.10 - σ_{31} Normalized Microstresses, O-A Direction, 0.0% Debonding, σ_{xx}^e Loading

EFFECT OF 1.39% FIBER LENGTH DEBONDING ON CONSTITUENT MICROSTRESSES (σ_{31}) DUE TO A LOAD IN THE XX-DIRECTION



- FACE 1
- FACE 2
- FACE 3
- FACE 4
- FACE 5
- FACE 6
- FACE 7
- FACE 8
- FACE 9

Figure A.11 - σ_{31} Normalized Microstresses, O-A Direction, 1.39% Debonding, σ_{xx}^e Loading

EFFECT OF 2.78% FIBER LENGTH DEBONDING ON CONSTITUENT MICROSTRESSES (σ_{31}) DUE TO A LOAD IN THE XX-DIRECTION

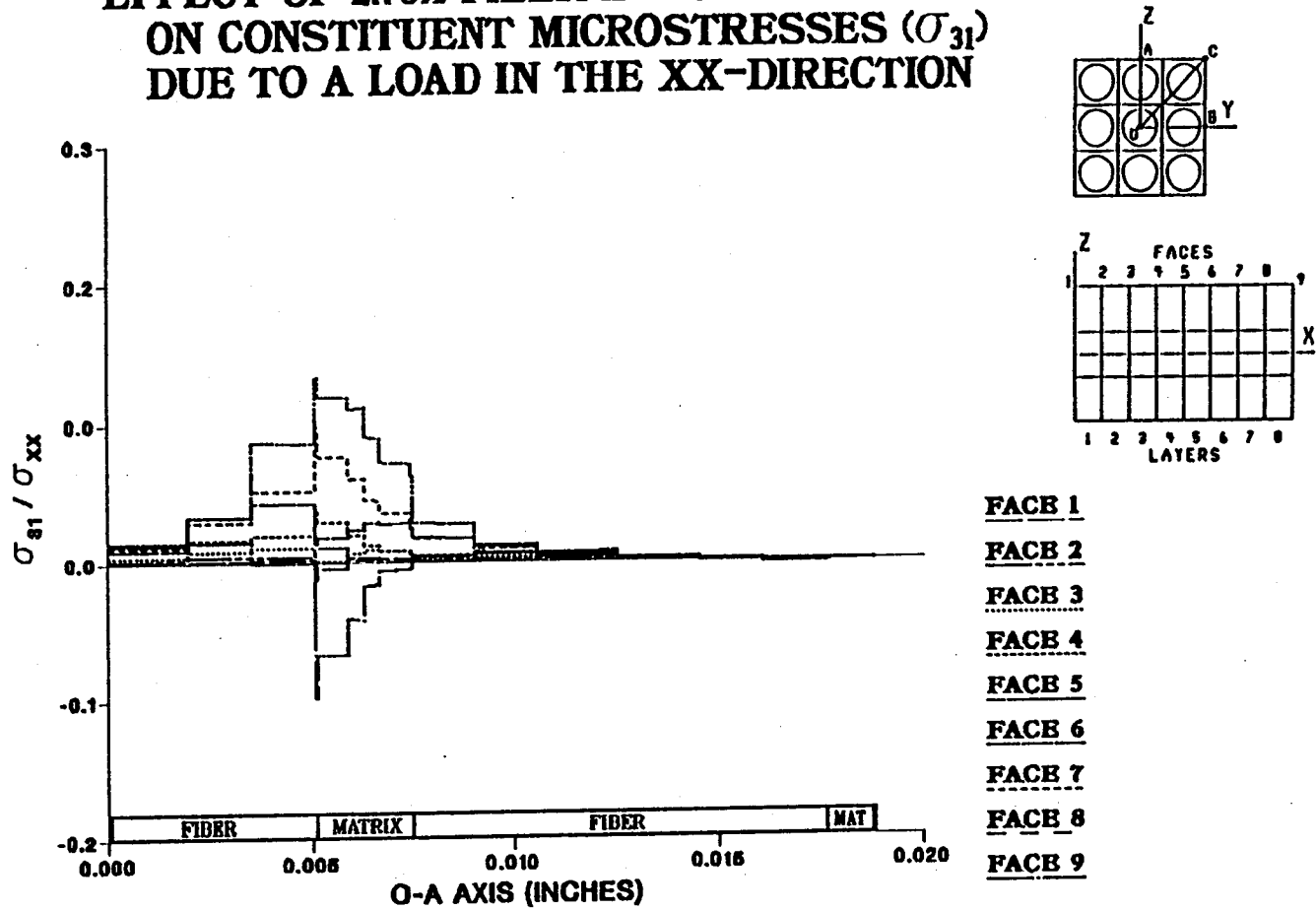


Figure A.12 — σ_{31} Normalized Microstresses, O-A Direction, 2.78% Debonding, σ_{xx}^e Loading

EFFECT OF 4.17% FIBER LENGTH DEBONDING ON CONSTITUENT MICROSTRESSES (σ_{31}) DUE TO A LOAD IN THE XX-DIRECTION

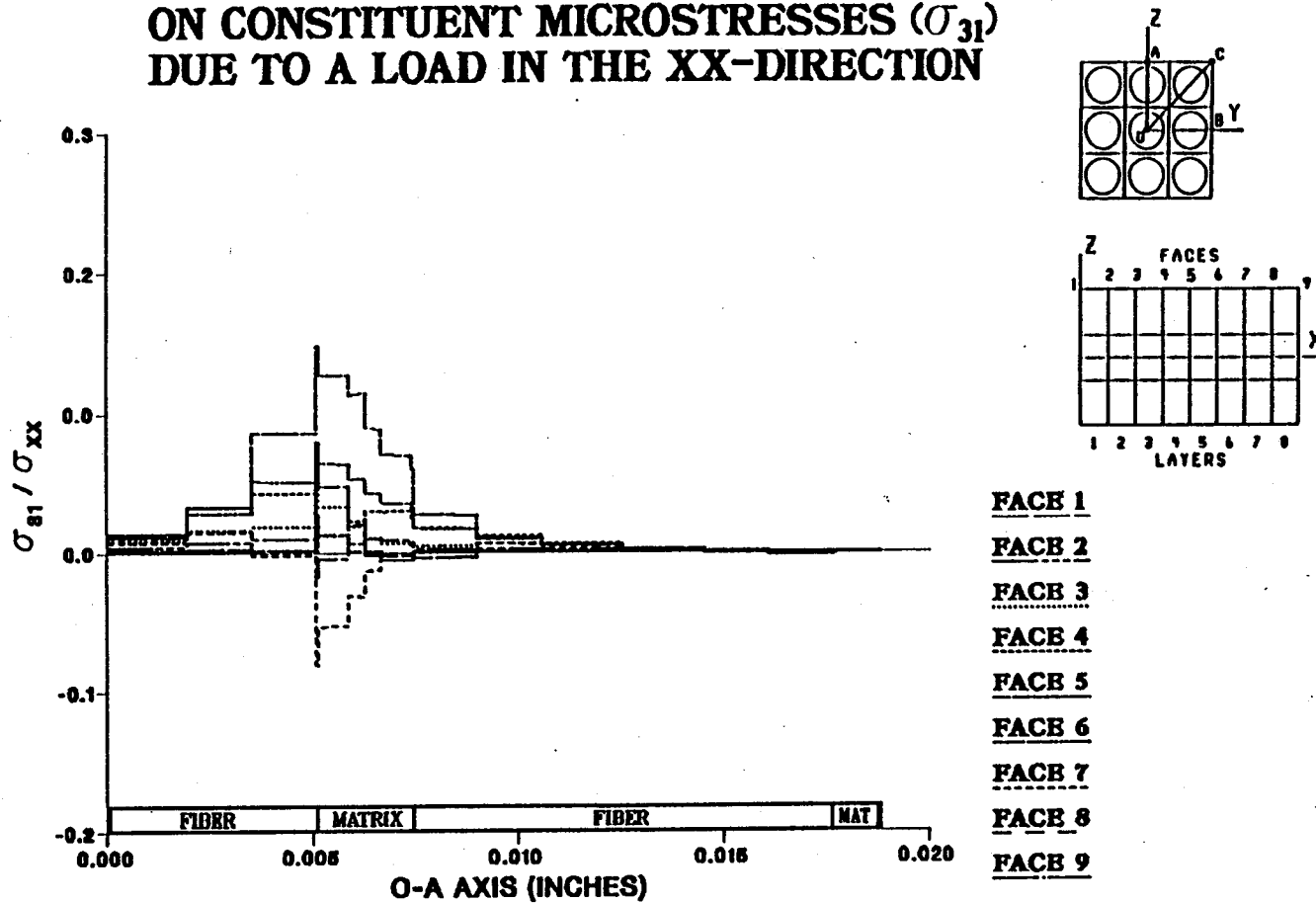
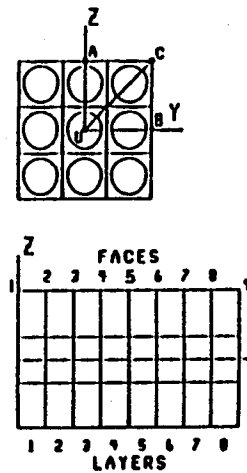
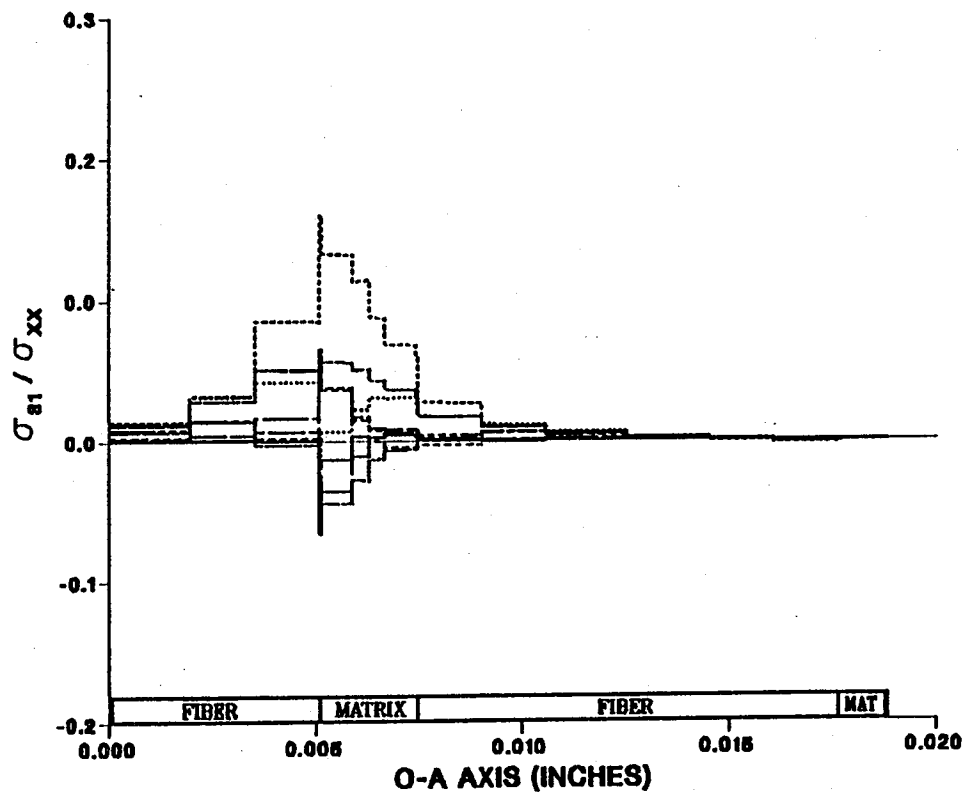


Figure A.13 – σ_{31} Normalized Microstresses, O–A Direction, 4.17% Debonding, σ_{xx}^e Loading

EFFECT OF 5.56% FIBER LENGTH DEBONDING ON CONSTITUENT MICROSTRESSES (σ_{31}) DUE TO A LOAD IN THE XX-DIRECTION



- FACE 1
- FACE 2
- FACE 3
- FACE 4
- FACE 5
- FACE 6
- FACE 7
- FACE 8
- FACE 9

Figure A.14 - σ_{31} Normalized Microstresses, O-A Direction, 5.56% Debonding, σ_{xx}^e Loading

EFFECT OF 6.94% FIBER LENGTH DEBONDING ON CONSTITUENT MICROSTRESSES (σ_{31}) DUE TO A LOAD IN THE XX-DIRECTION

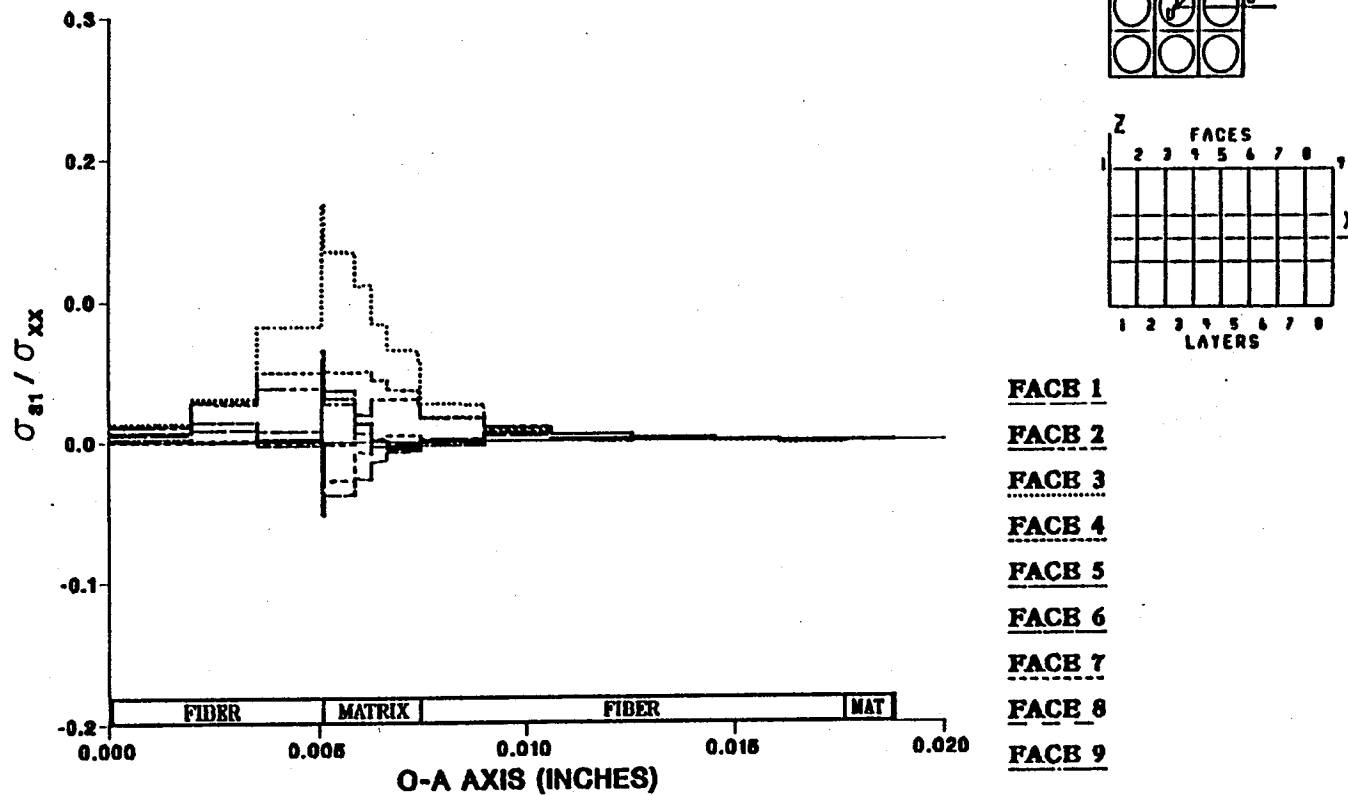


Figure A.15 - σ_{31} Normalized Microstresses, O-A Direction, 6.94% Debonding, σ_{xx}^e Loading

EFFECT OF 8.33% FIBER LENGTH DEBONDING ON CONSTITUENT MICROSTRESSES (σ_{31}) DUE TO A LOAD IN THE XX-DIRECTION

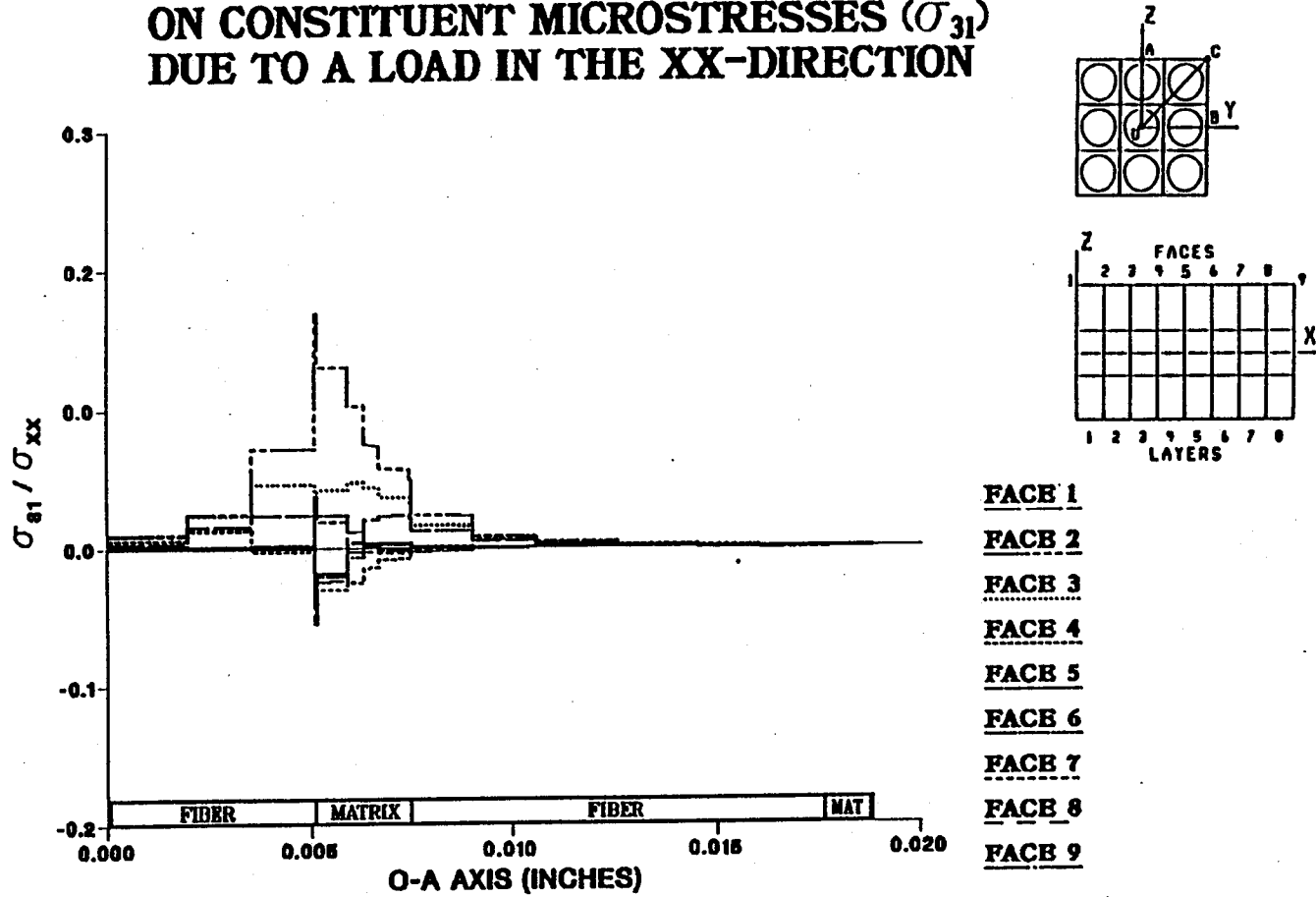
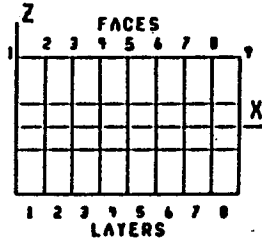
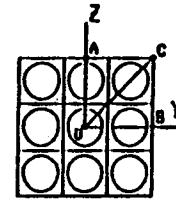
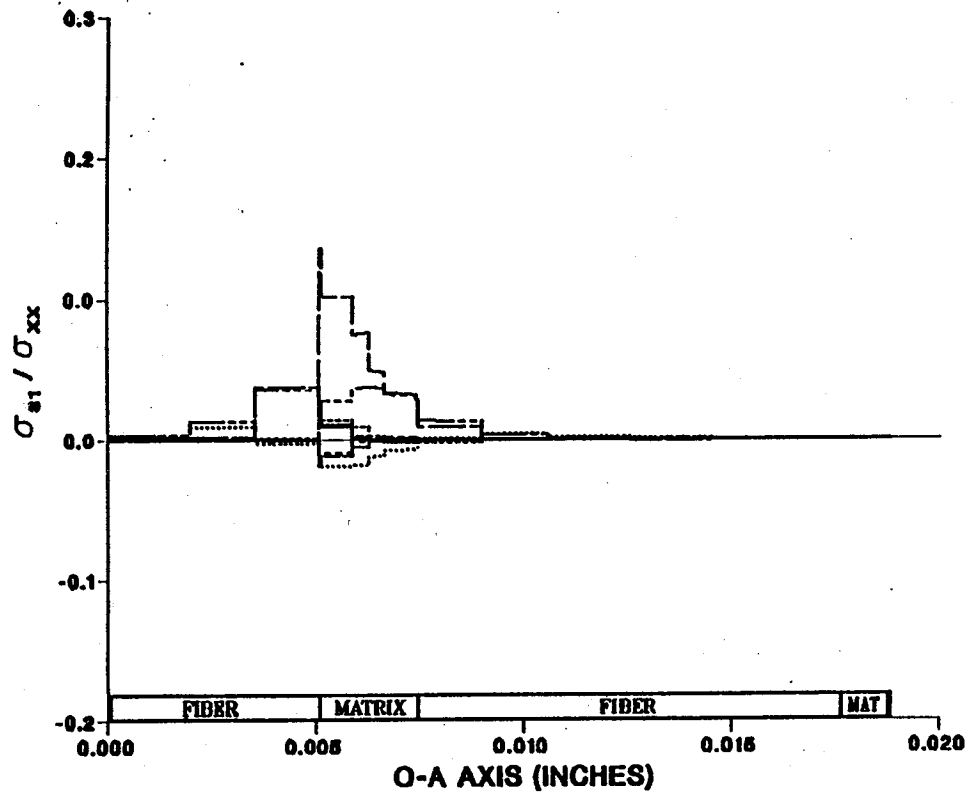


Figure A.16 – σ_{31} Normalized Microstresses, O–A Direction, 8.33% Debonding, σ_{xx}^e Loading

EFFECT OF 9.72% FIBER LENGTH DEBONDING ON CONSTITUENT MICROSTRESSES (σ_{31}) DUE TO A LOAD IN THE XX-DIRECTION



- FACE 1
- FACE 2
- FACE 3
- FACE 4
- FACE 5
- FACE 6
- FACE 7
- FACE 8
- FACE 9

Figure A.17 - σ_{31} Normalized Microstresses, O-A Direction, 9.72% Debonding, σ_{xx}^e Loading

EFFECT OF 11.11% FIBER LENGTH DEBONDING ON CONSTITUENT MICROSTRESSES (σ_{31}) DUE TO A LOAD IN THE XX-DIRECTION

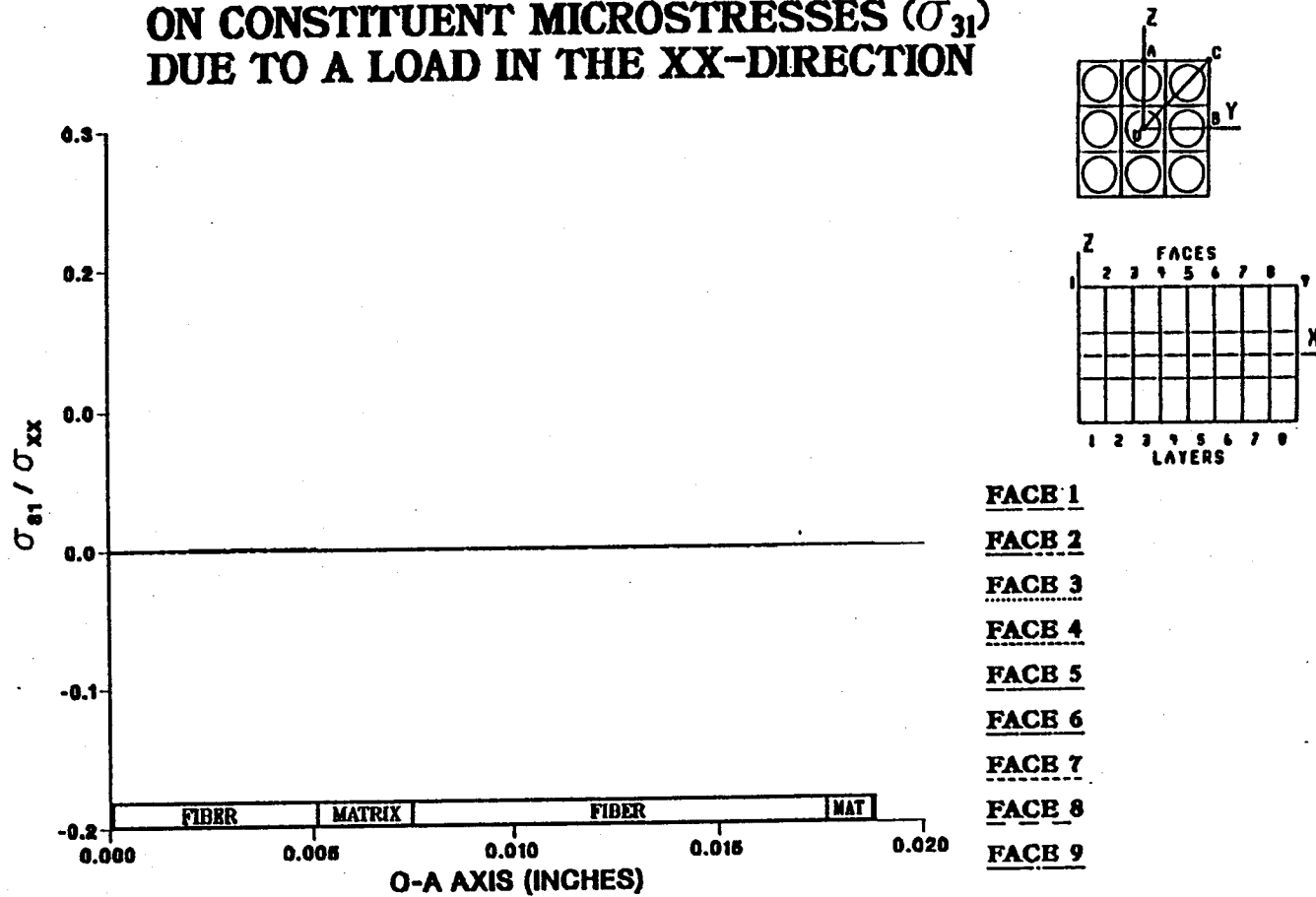


Figure A.18 - σ_{31} Normalized Microstresses, O-A Direction, 11.11% Debonding, σ_{xx}^e Loading

EFFECT OF 0.0% FIBER LENGTH DEBONDING ON CONSTITUENT MICROSTRESSES (σ_{31}) DUE TO A LOAD IN THE XX-DIRECTION

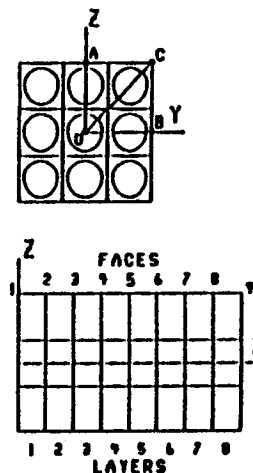
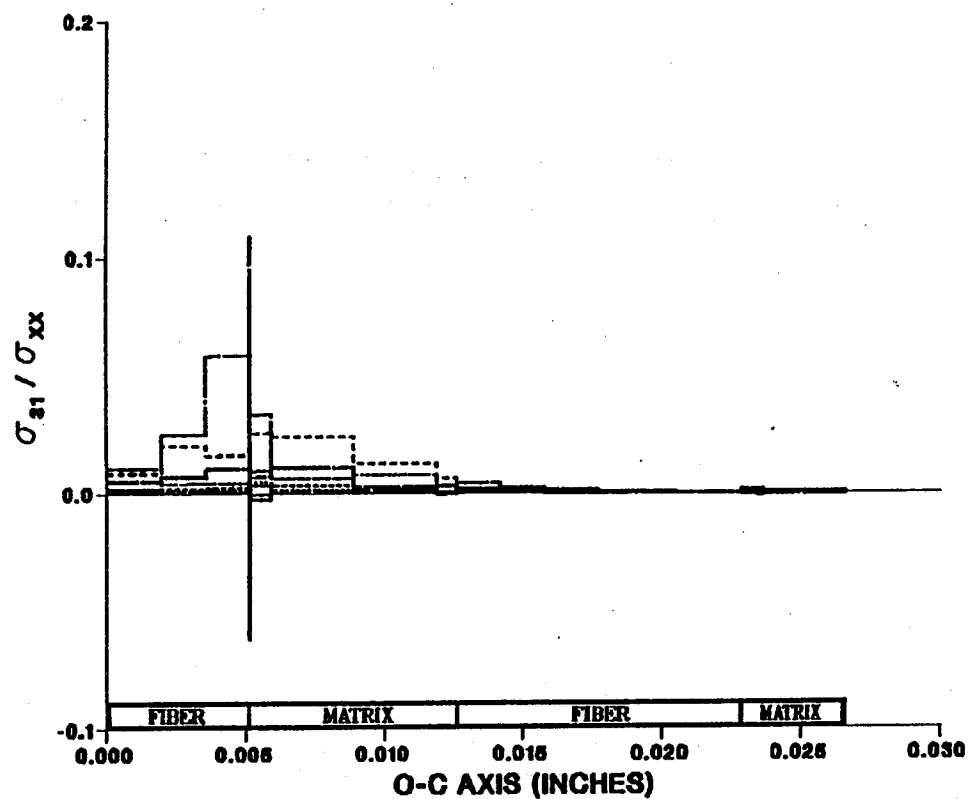


Figure A.19 - σ_{31} Normalized Microstresses, O-C Direction, 0.0% Debonding, σ_{xx}^e Loading

EFFECT OF 1.39% FIBER LENGTH DEBONDING ON CONSTITUENT MICROSTRESSES (σ_{31}) DUE TO A LOAD IN THE XX-DIRECTION

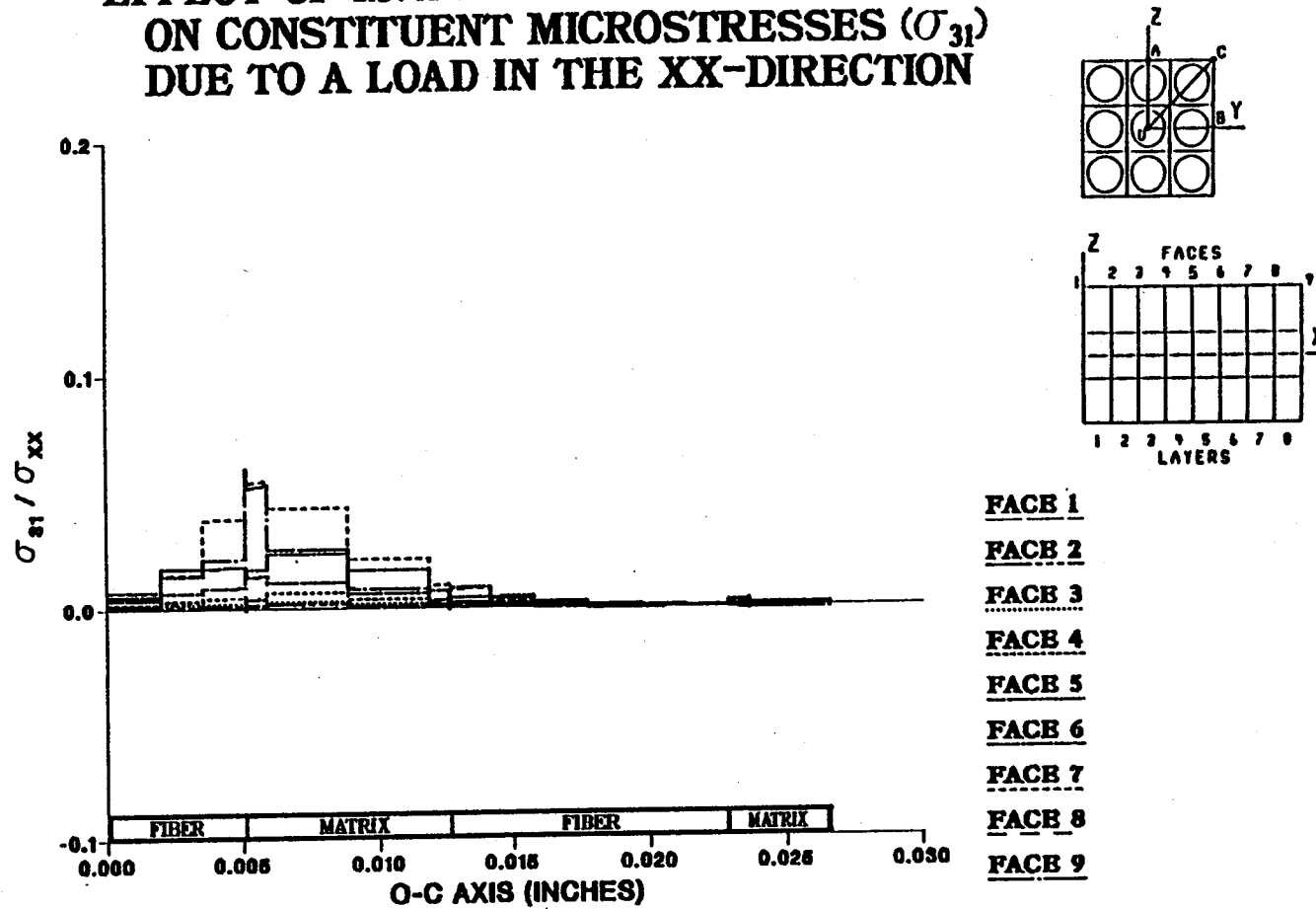
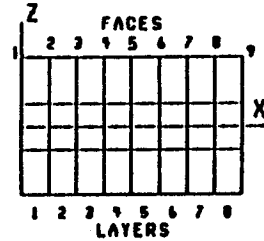
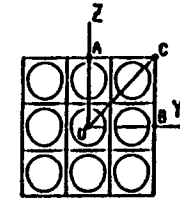
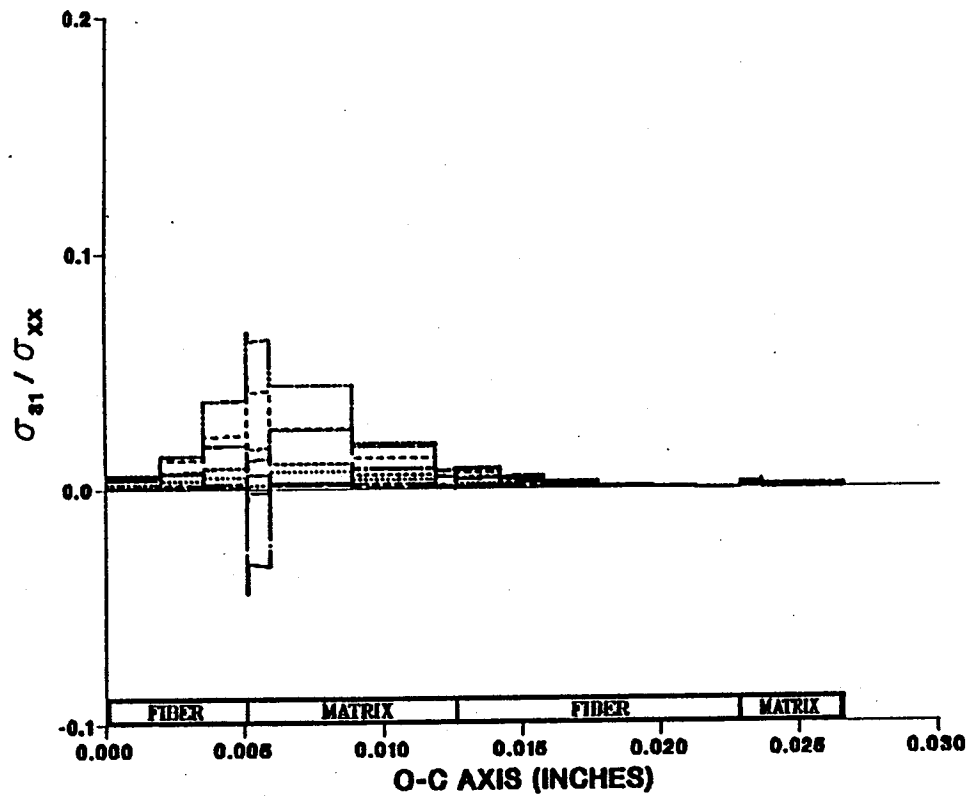


Figure A.20 - σ_{31} Normalized Microstresses, O-C Direction, 1.39% Debonding, σ_{xx}^e Loading

EFFECT OF 2.78% FIBER LENGTH DEBONDING ON CONSTITUENT MICROSTRESSES (σ_{31}) DUE TO A LOAD IN THE XX-DIRECTION



- FACE 1
- FACE 2
- FACE 3
- FACE 4
- FACE 5
- FACE 6
- FACE 7
- FACE 8
- FACE 9

Figure A.21 – σ_{31} Normalized Microstresses, O–C Direction, 2.78% Debonding, σ_{xx}^e Loading

EFFECT OF 4.17% FIBER LENGTH DEBONDING ON CONSTITUENT MICROSTRESSES (σ_{31}) DUE TO A LOAD IN THE XX-DIRECTION

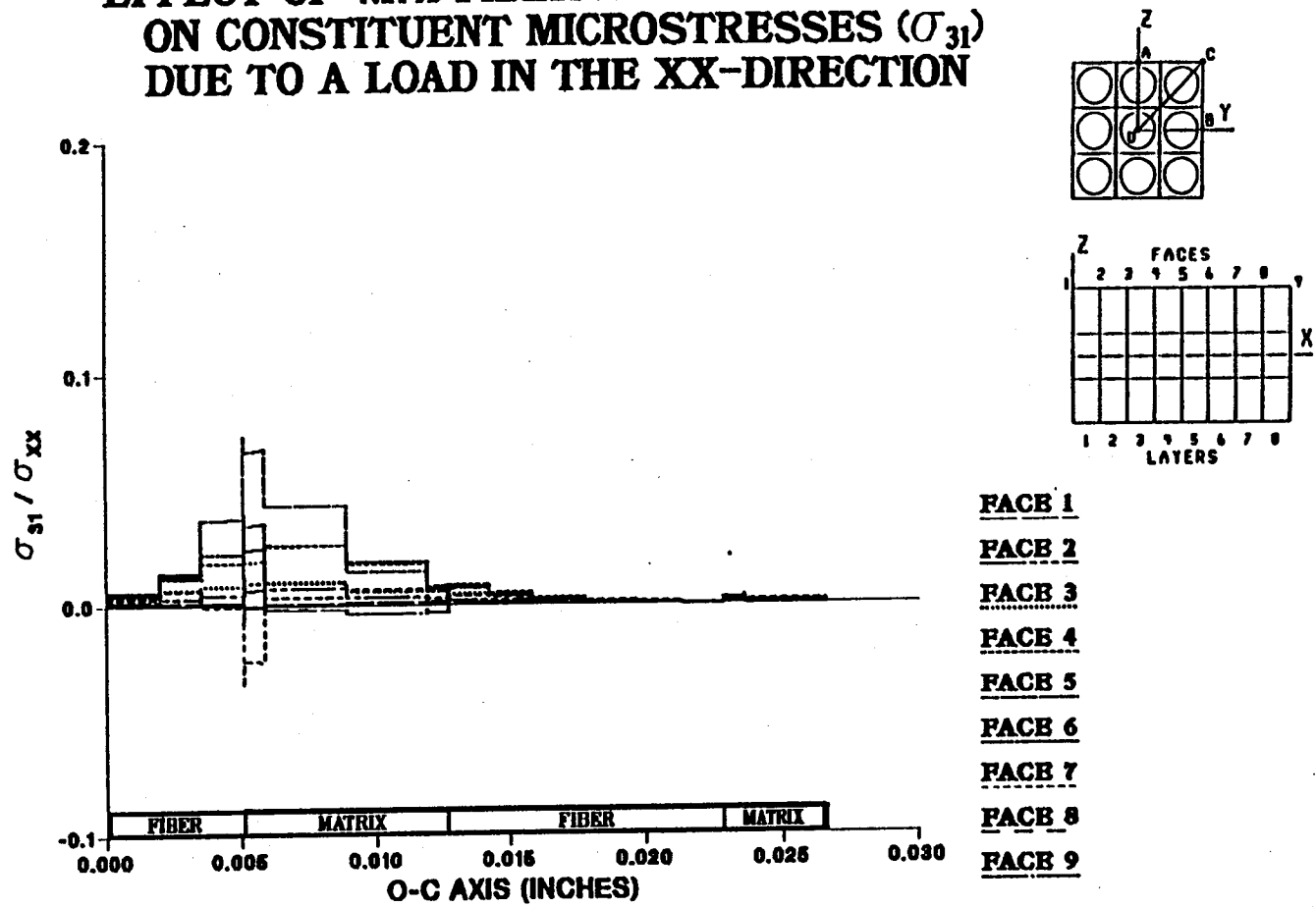


Figure A.22 — σ_{31} Normalized Microstresses, O—C Direction, 4.17% Debonding, σ_{xx}^e Loading

EFFECT OF 5.56% FIBER LENGTH DEBONDING ON CONSTITUENT MICROSTRESSES (σ_{31}) DUE TO A LOAD IN THE XX-DIRECTION

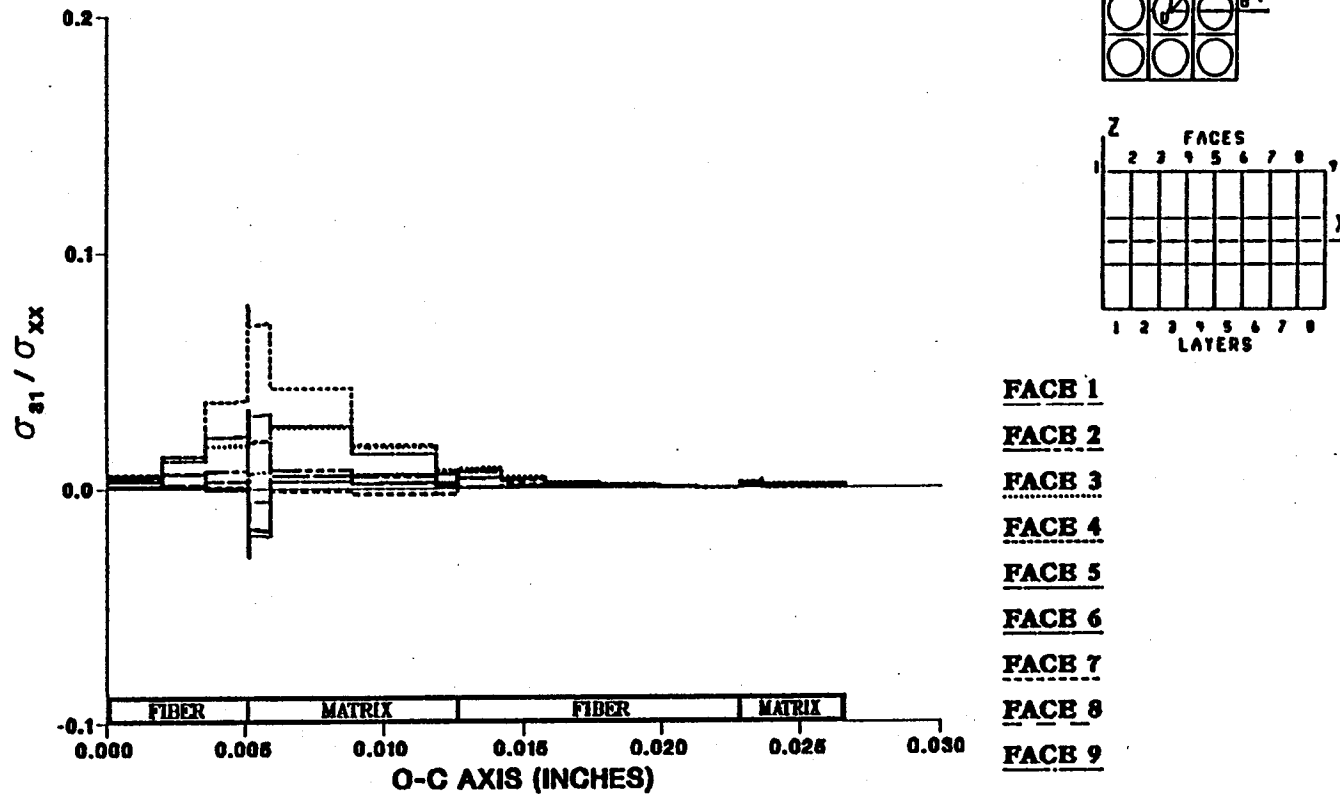


Figure A.23 - σ_{31} Normalized Microstresses, O-C Direction, 5.56% Debonding, σ_{xx}^e Loading

EFFECT OF 6.94% FIBER LENGTH DEBONDING ON CONSTITUENT MICROSTRESSES (σ_{31}) DUE TO A LOAD IN THE XX-DIRECTION

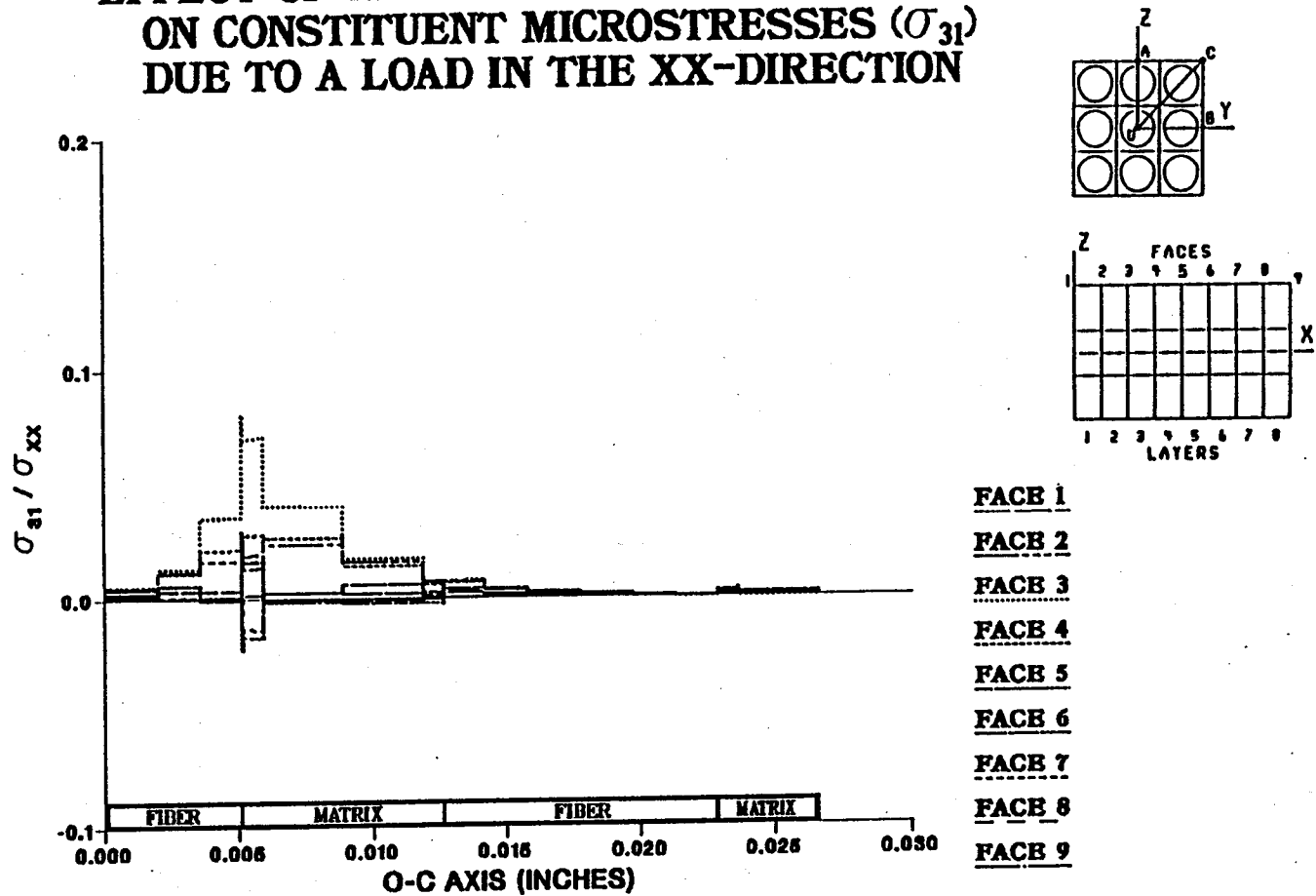


Figure A.24 - σ_{31} Normalized Microstresses, O-C Direction, 6.94% Debonding, σ_{xx}^e Loading

EFFECT OF 8.33% FIBER LENGTH DEBONDING ON CONSTITUENT MICROSTRESSES (σ_{31}) DUE TO A LOAD IN THE XX-DIRECTION

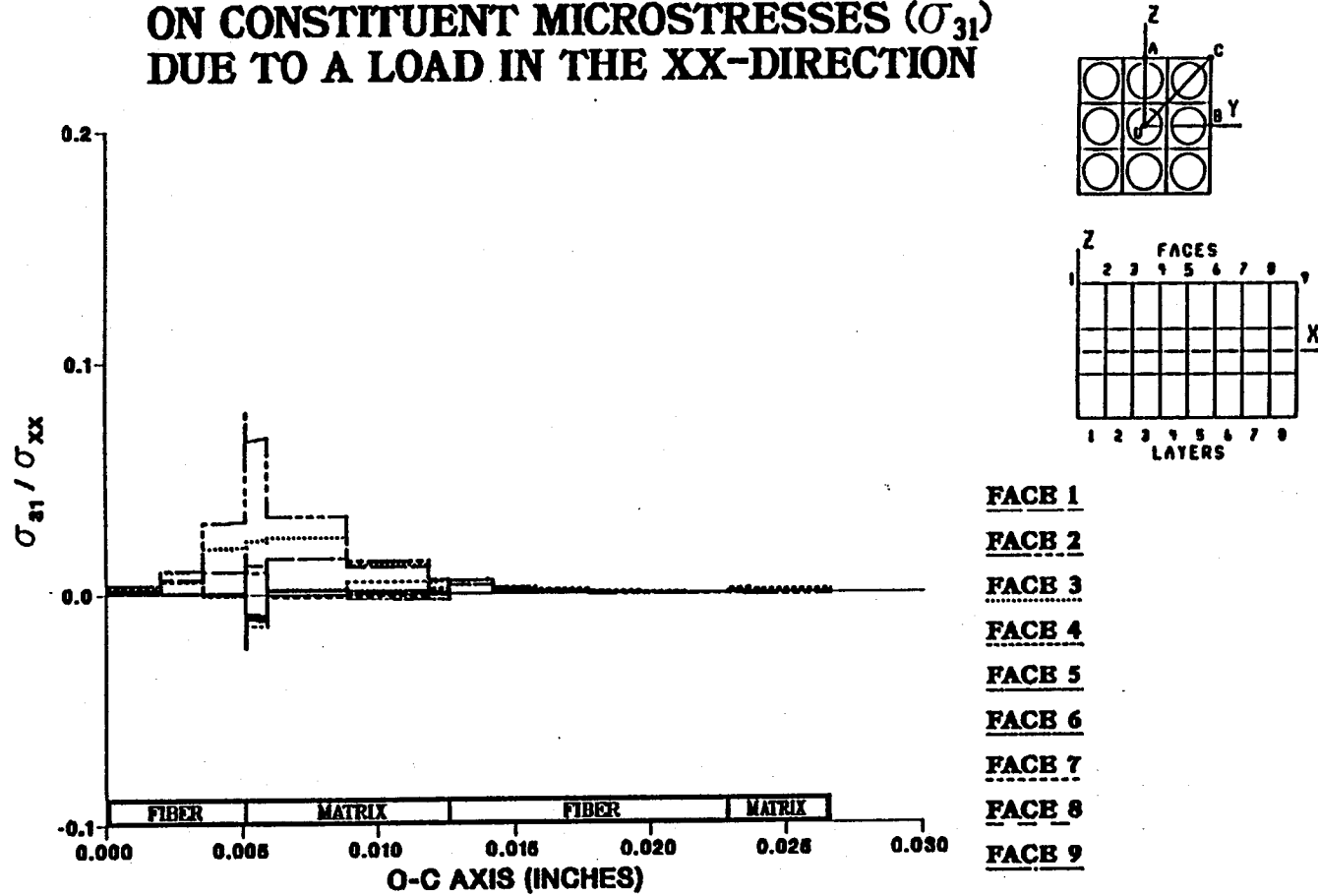


Figure A.25 - σ_{31} Normalized Microstresses, O-C Direction, 8.33% Debonding, σ_{xx}^e Loading

EFFECT OF 9.72% FIBER LENGTH DEBONDING ON CONSTITUENT MICROSTRESSES (σ_{31}) DUE TO A LOAD IN THE XX-DIRECTION

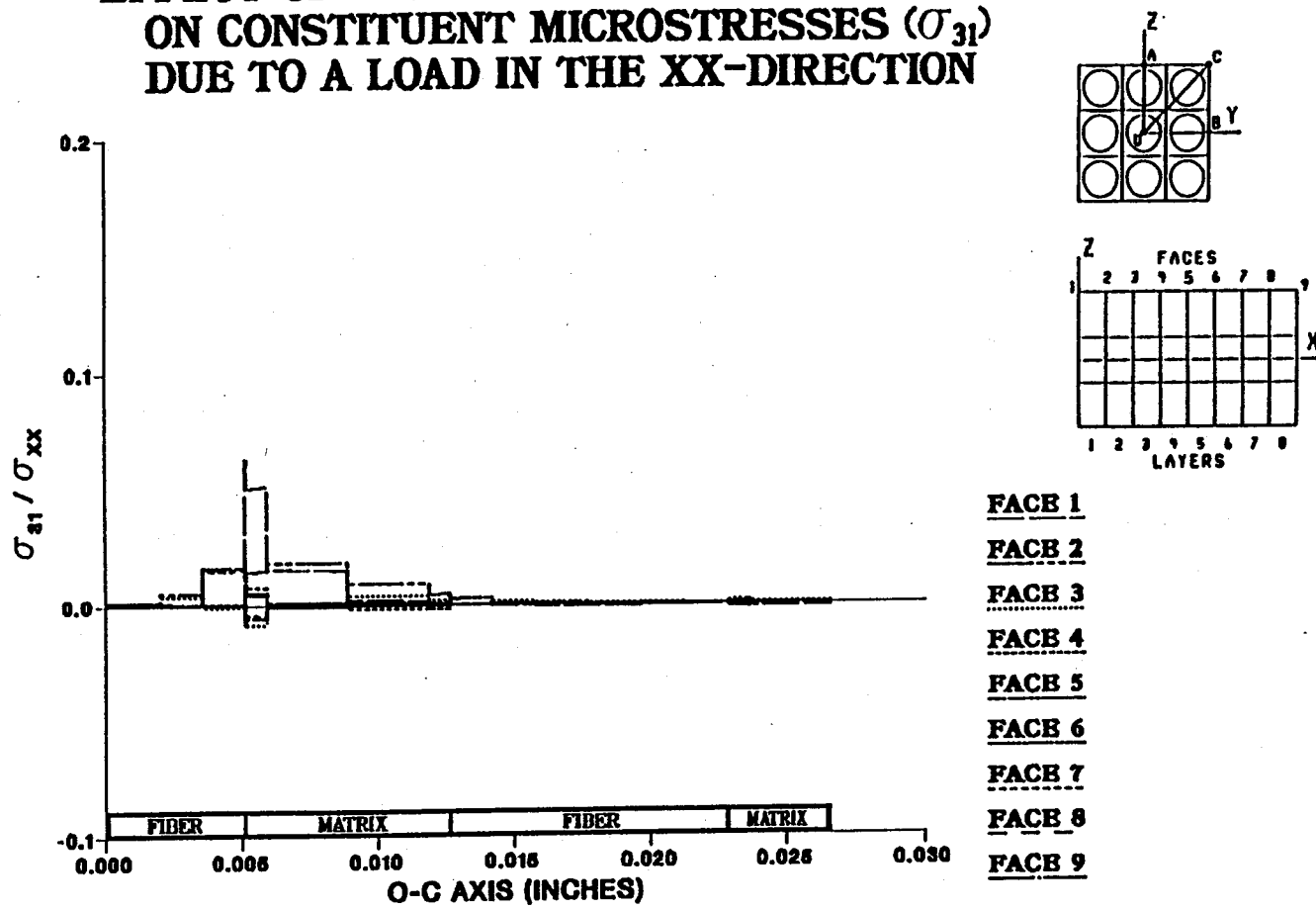


Figure A.26 - σ_{31} Normalized Microstresses, O-C Direction, 9.72% Debonding, σ_{xx}^e Loading

EFFECT OF 11.1% FIBER LENGTH DEBONDING ON CONSTITUENT MICROSTRESSES (σ_{31}) DUE TO A LOAD IN THE XX-DIRECTION

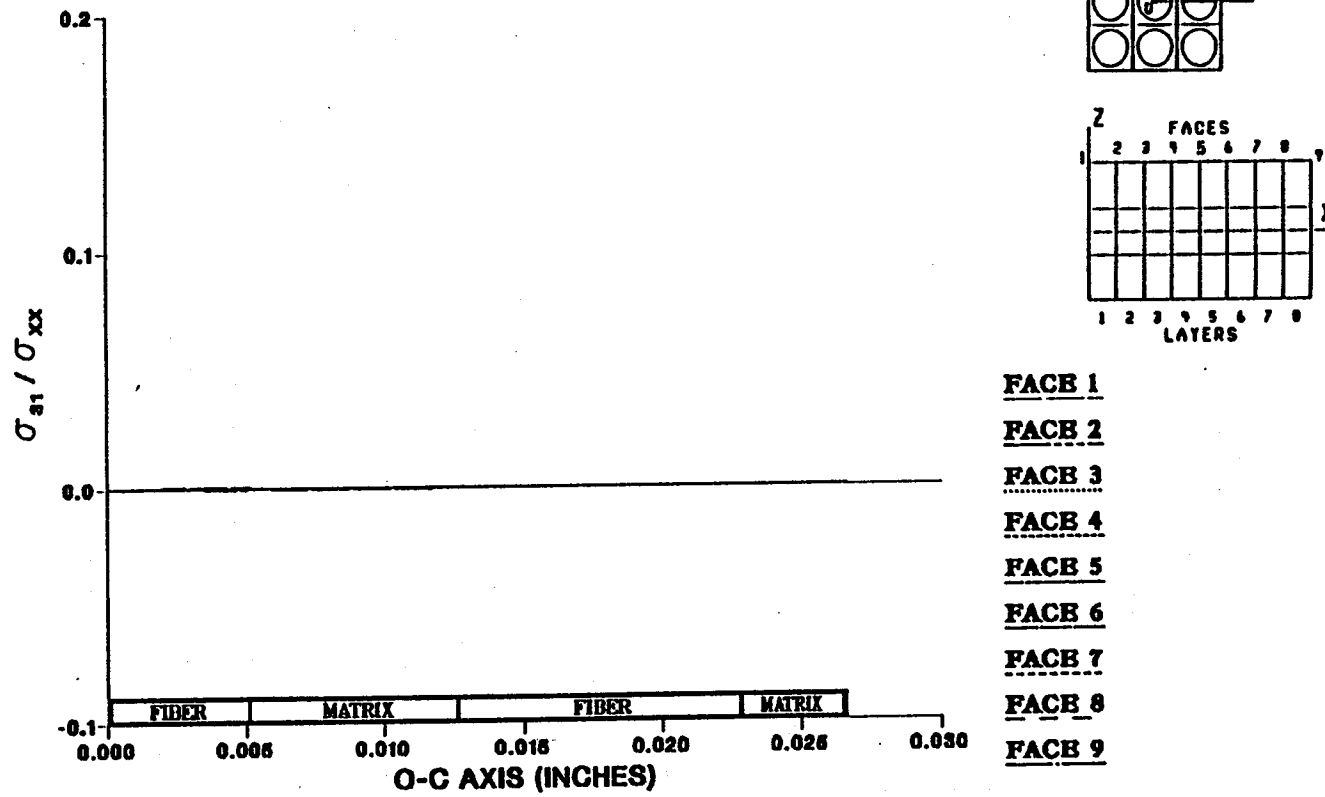
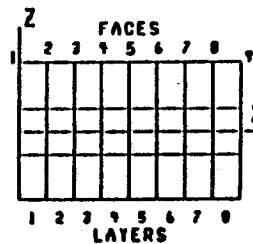
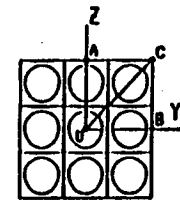
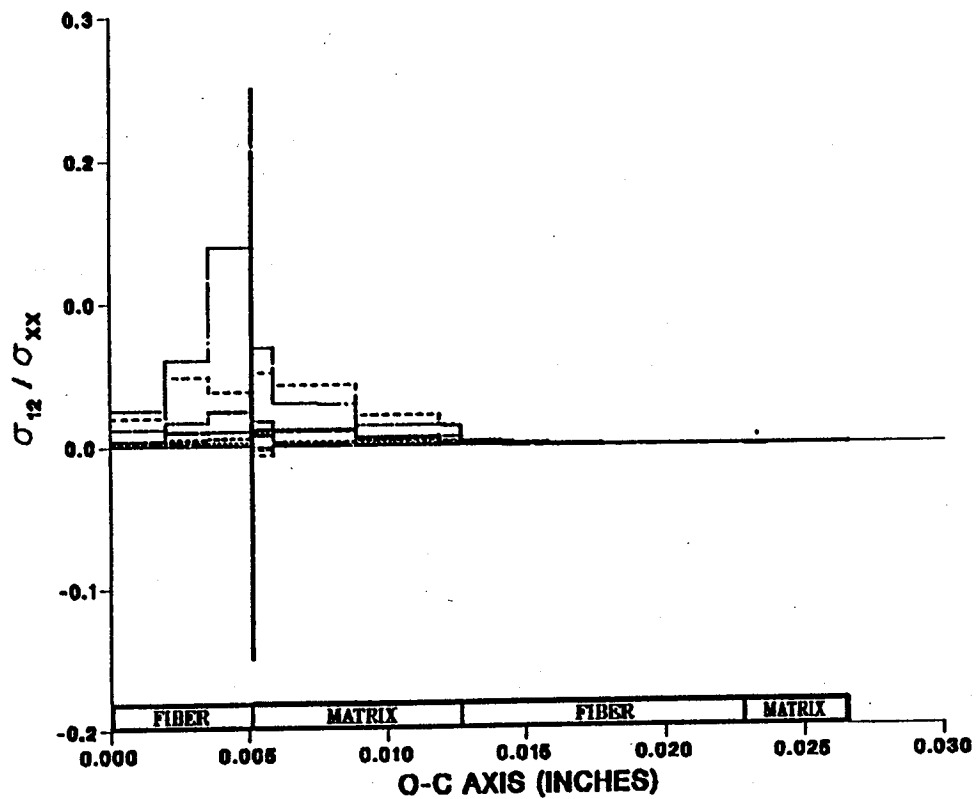


Figure A.27 - σ_{31} Normalized Microstresses, O-C Direction, 11.1% Debonding, σ_{xx}^e Loading

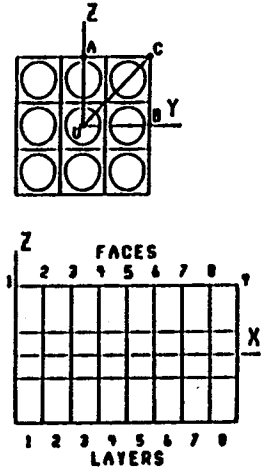
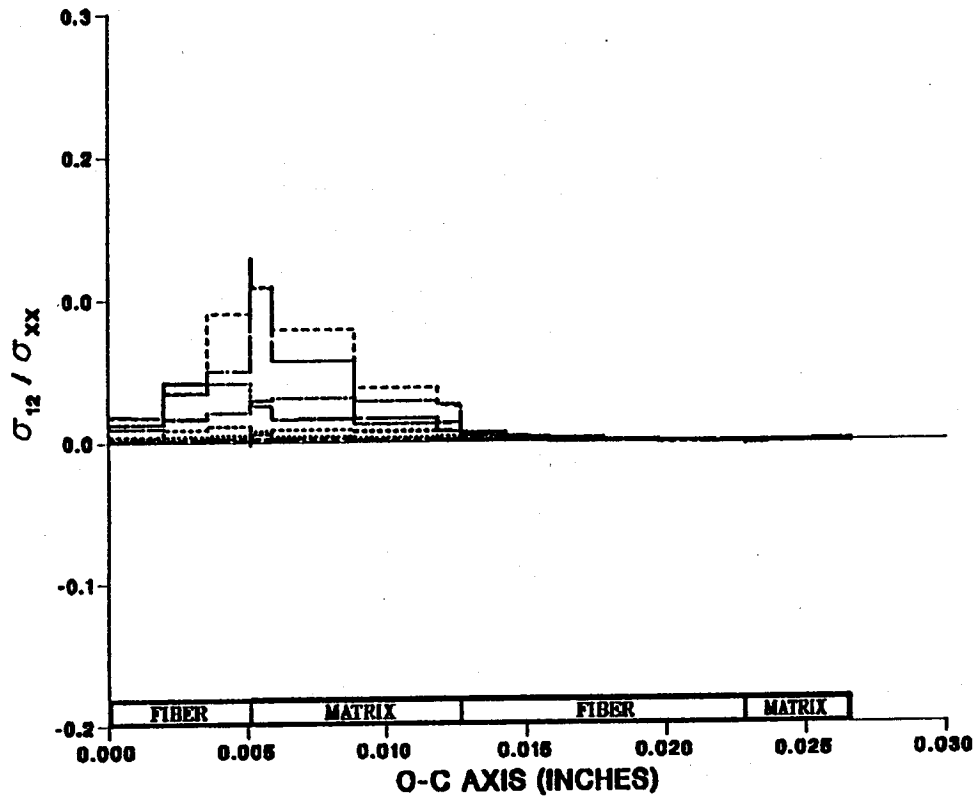
EFFECT OF 0.0% FIBER LENGTH DEBONDING ON CONSTITUENT MICROSTRESSES (σ_{12}) DUE TO A LOAD IN THE XX-DIRECTION



- FACE 1
- FACE 2
- FACE 3
- FACE 4
- FACE 5
- FACE 6
- FACE 7
- FACE 8
- FACE 9

Figure A.28 - σ_{12} Normalized Microstresses, O-C Direction, 0.0% Debonding, σ_{xx}^e Loading

EFFECT OF 1.39% FIBER LENGTH DEBONDING ON CONSTITUENT MICROSTRESSES (σ_{12}) DUE TO A LOAD IN THE XX-DIRECTION



- FACE 1
- FACE 2
- FACE 3
- FACE 4
- FACE 5
- FACE 6
- FACE 7
- FACE 8
- FACE 9

Figure A.29 - σ_{12} Normalized Microstresses, O-C Direction, 1.39% Debonding, σ_{xx}^e Loading

EFFECT OF 2.78% FIBER LENGTH DEBONDING ON CONSTITUENT MICROSTRESSES (σ_{12}) DUE TO A LOAD IN THE XX-DIRECTION

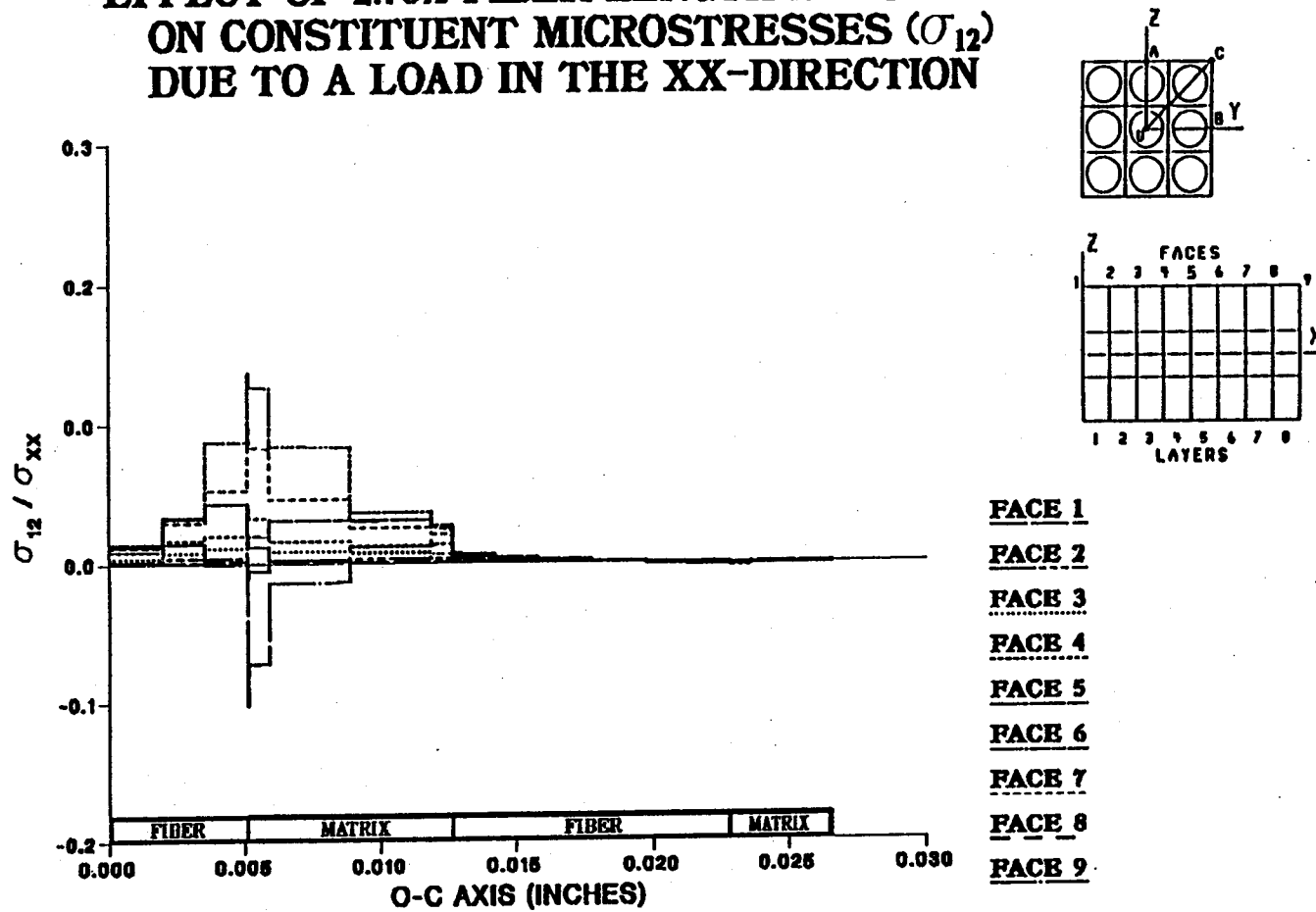


Figure A.30 - σ_{12} Normalized Microstresses, O-C Direction, 2.78% Debonding, σ_{xx}^e Loading

EFFECT OF 4.17% FIBER LENGTH DEBONDING ON CONSTITUENT MICROSTRESSES (σ_{12}) DUE TO A LOAD IN THE XX-DIRECTION

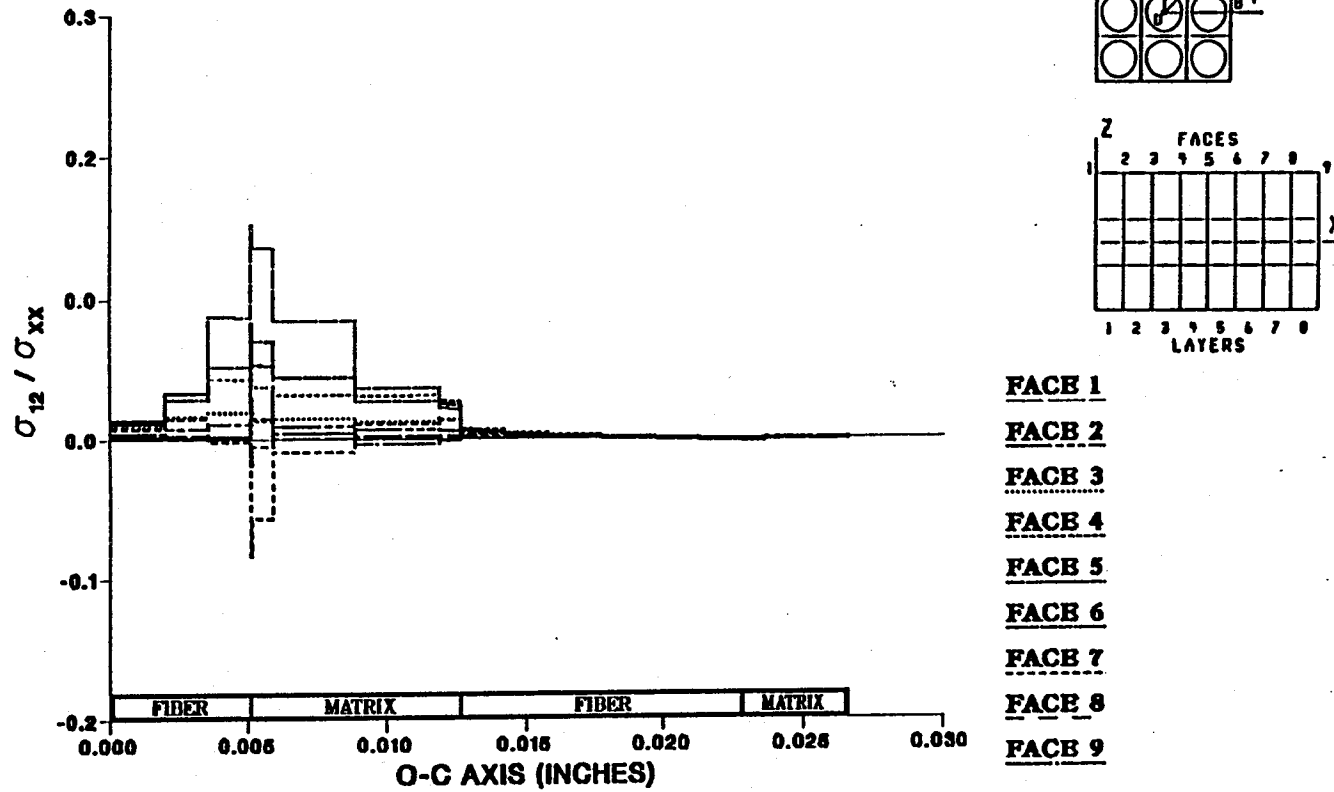


Figure A.31 - σ_{12} Normalized Microstresses, O-C Direction, 4.17% Debonding, σ_{xx}^e Loading

**EFFECT OF 5.56% FIBER LENGTH DEBONDING
ON CONSTITUENT MICROSTRESSES (σ_{12})
DUE TO A LOAD IN THE XX-DIRECTION**

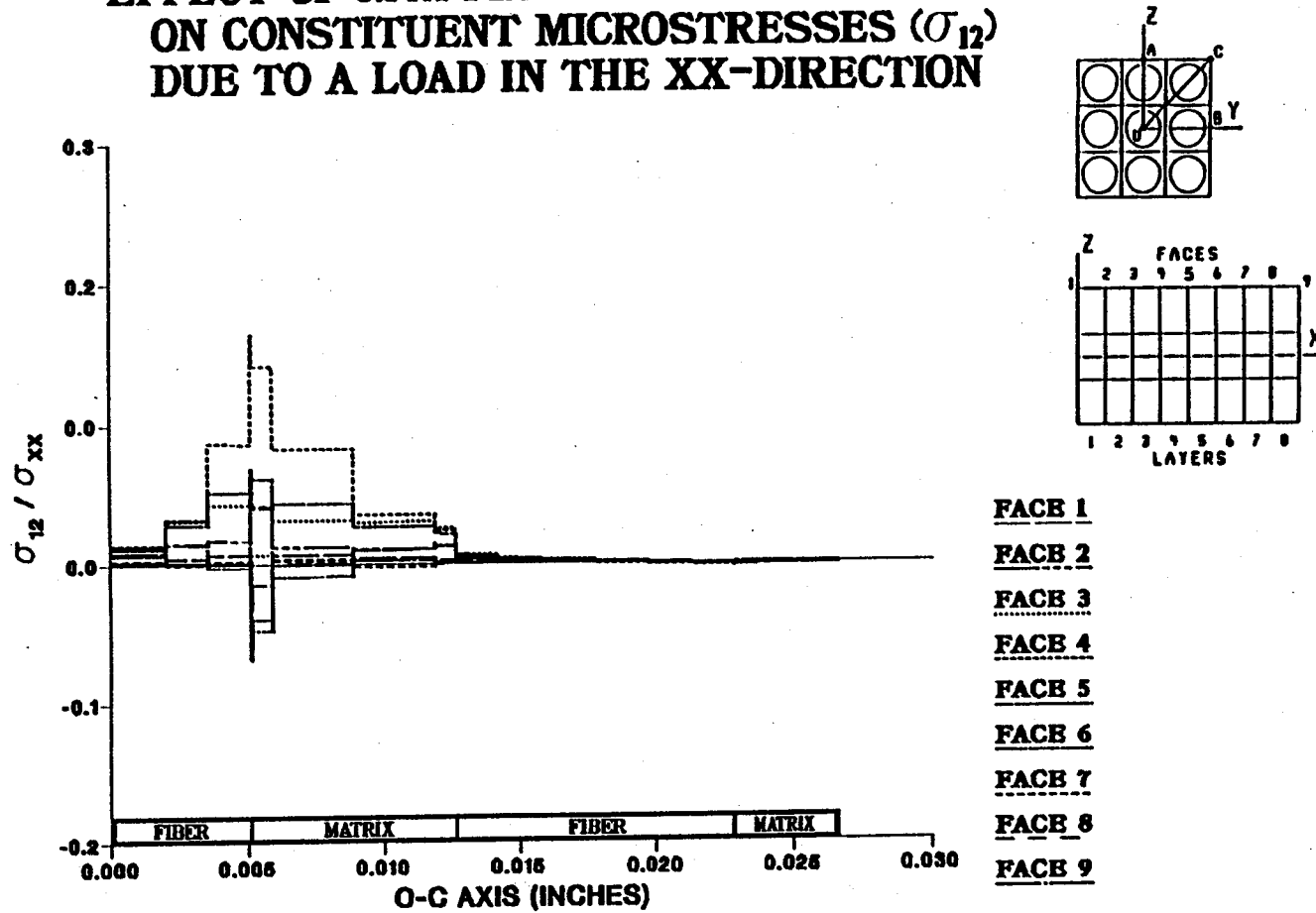
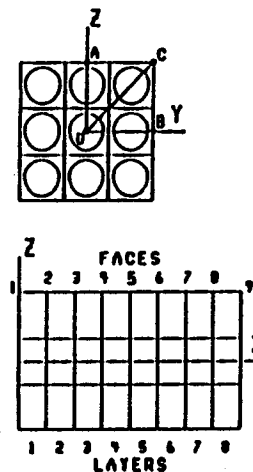
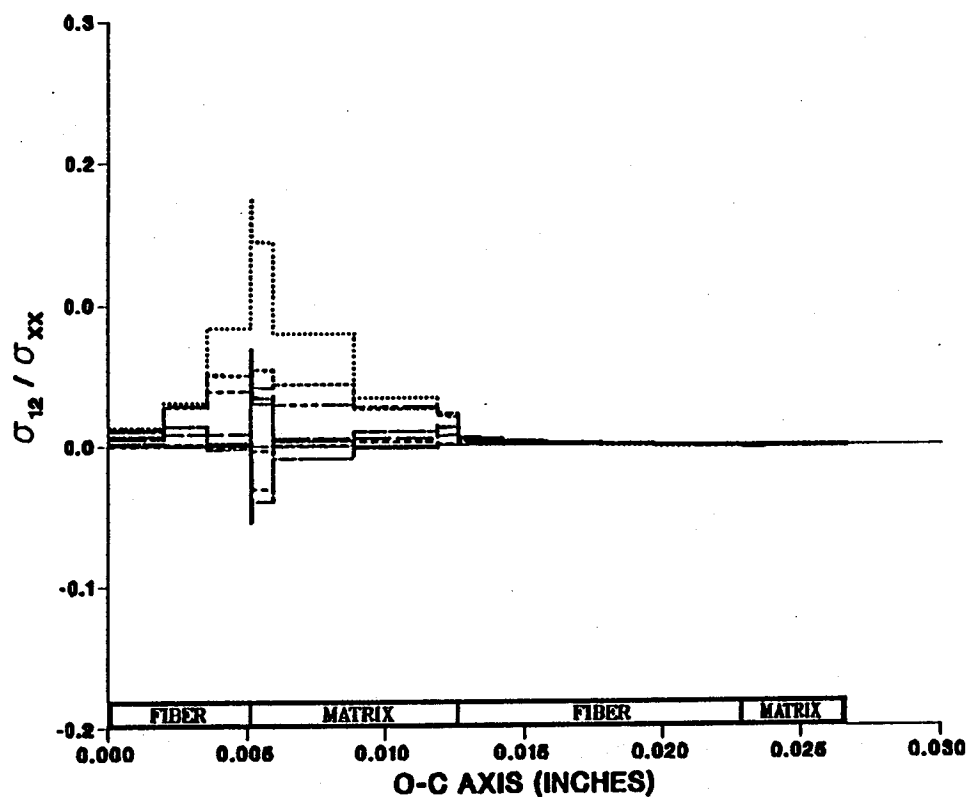


Figure A.32 - σ_{12} Normalized Microstresses, O-C Direction, 5.56% Debonding, σ_{xx}^e Loading

EFFECT OF 6.94% FIBER LENGTH DEBONDING ON CONSTITUENT MICROSTRESSES (σ_{12}) DUE TO A LOAD IN THE XX-DIRECTION



- FACE 1
- FACE 2
- FACE 3
- FACE 4
- FACE 5
- FACE 6
- FACE 7
- FACE 8
- FACE 9

Figure A.33 – σ_{12} Normalized Microstresses, O–C Direction, 6.94% Debonding, σ_{xx}^e Loading

EFFECT OF 8.33% FIBER LENGTH DEBONDING ON CONSTITUENT MICROSTRESSES (σ_{12}) DUE TO A LOAD IN THE XX-DIRECTION

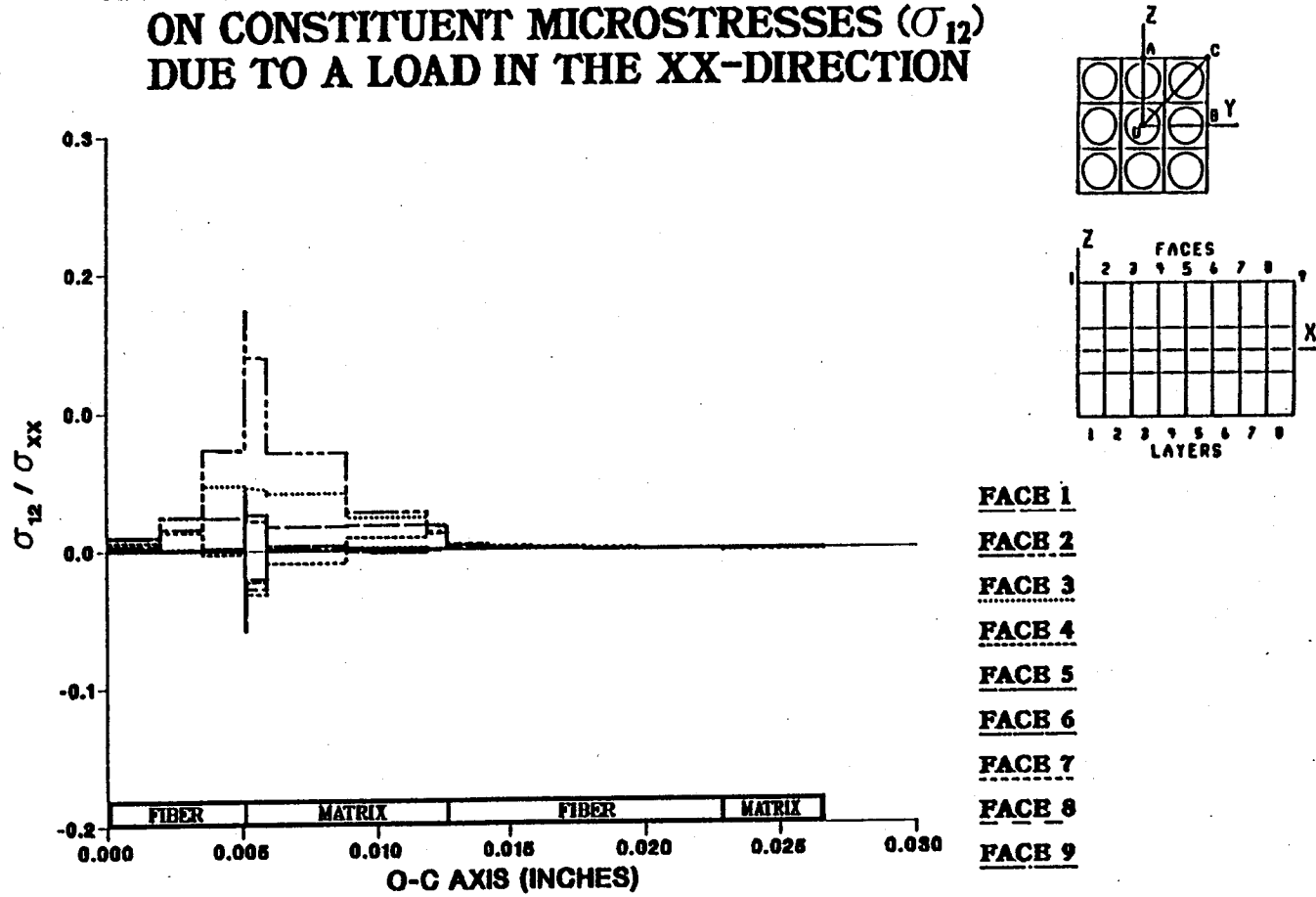
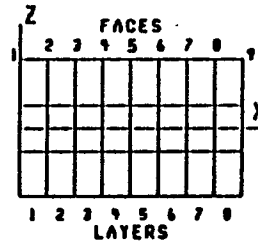
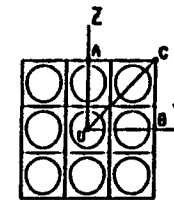
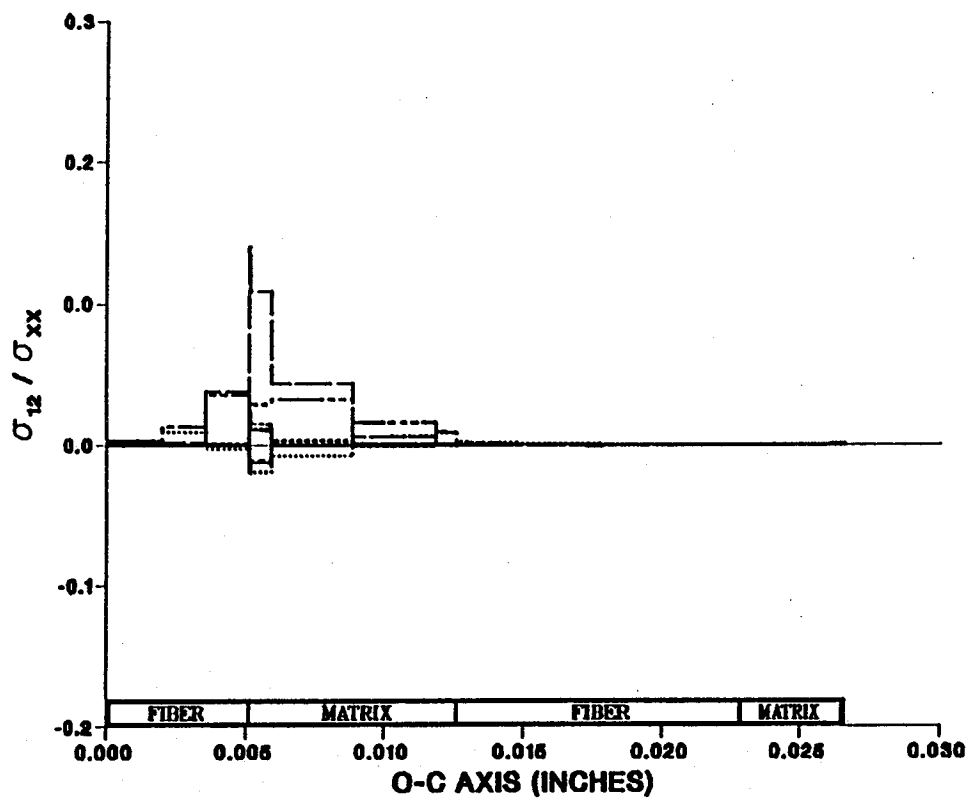


Figure A.34 - σ_{12} Normalized Microstresses, O-C Direction, 8.33% Debonding, σ_{xx}^e Loading

EFFECT OF 9.72% FIBER LENGTH DEBONDING ON CONSTITUENT MICROSTRESSES (σ_{12}) DUE TO A LOAD IN THE XX-DIRECTION



- FACE 1
- FACE 2
- FACE 3
- FACE 4
- FACE 5
- FACE 6
- FACE 7
- FACE 8
- FACE 9

Figure A.35 – σ_{12} Normalized Microstresses, O–C Direction, 9.72% Debonding, σ_{xx}^e Loading

EFFECT OF 11.11% FIBER LENGTH DEBONDING ON CONSTITUENT MICROSTRESSES (σ_{12}) DUE TO A LOAD IN THE XX-DIRECTION

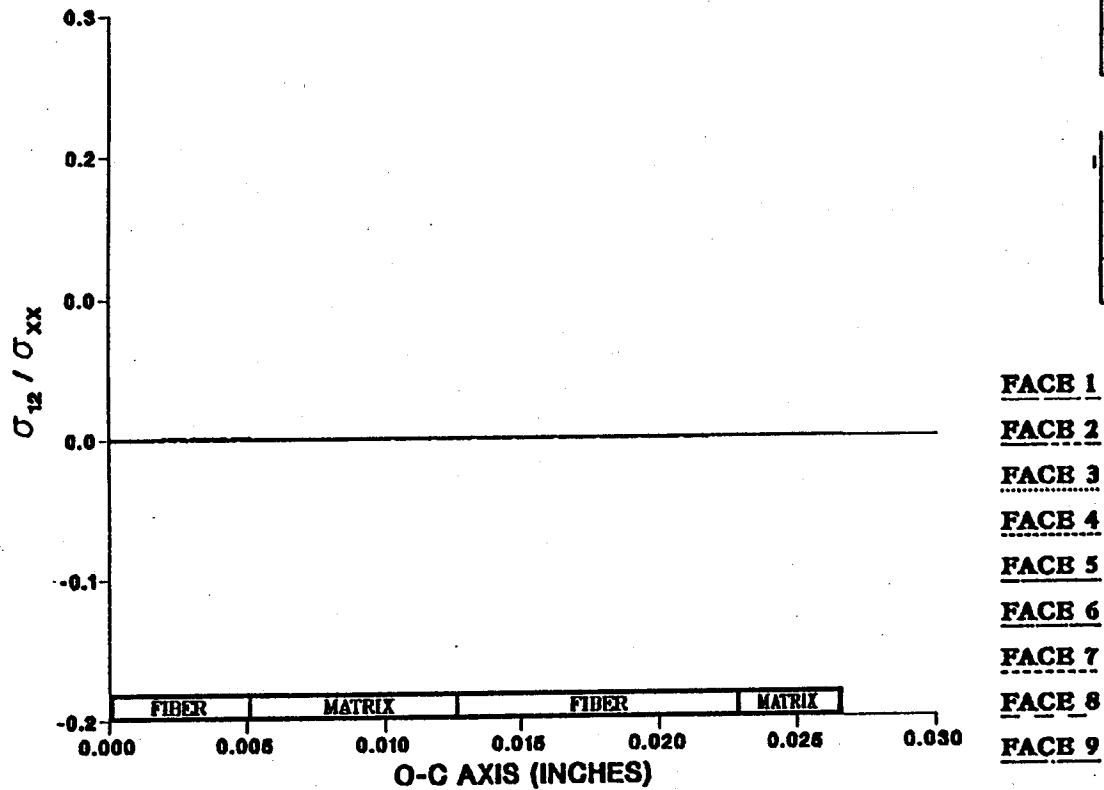
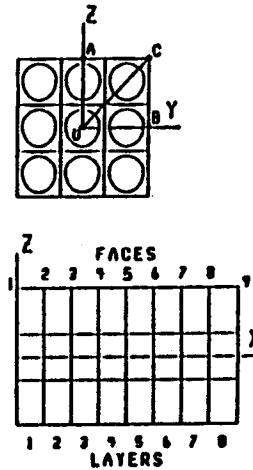


Figure A.36 - σ_{12} Normalized Microstresses, O-C Direction, 11.11% Debonding, σ_{xx}^e Loading

EFFECT OF 0.0% FIBER LENGTH DEBONDING ON CONSTITUENT MICROSTRESSES (σ_{22}) DUE TO A LOAD IN THE YY-DIRECTION

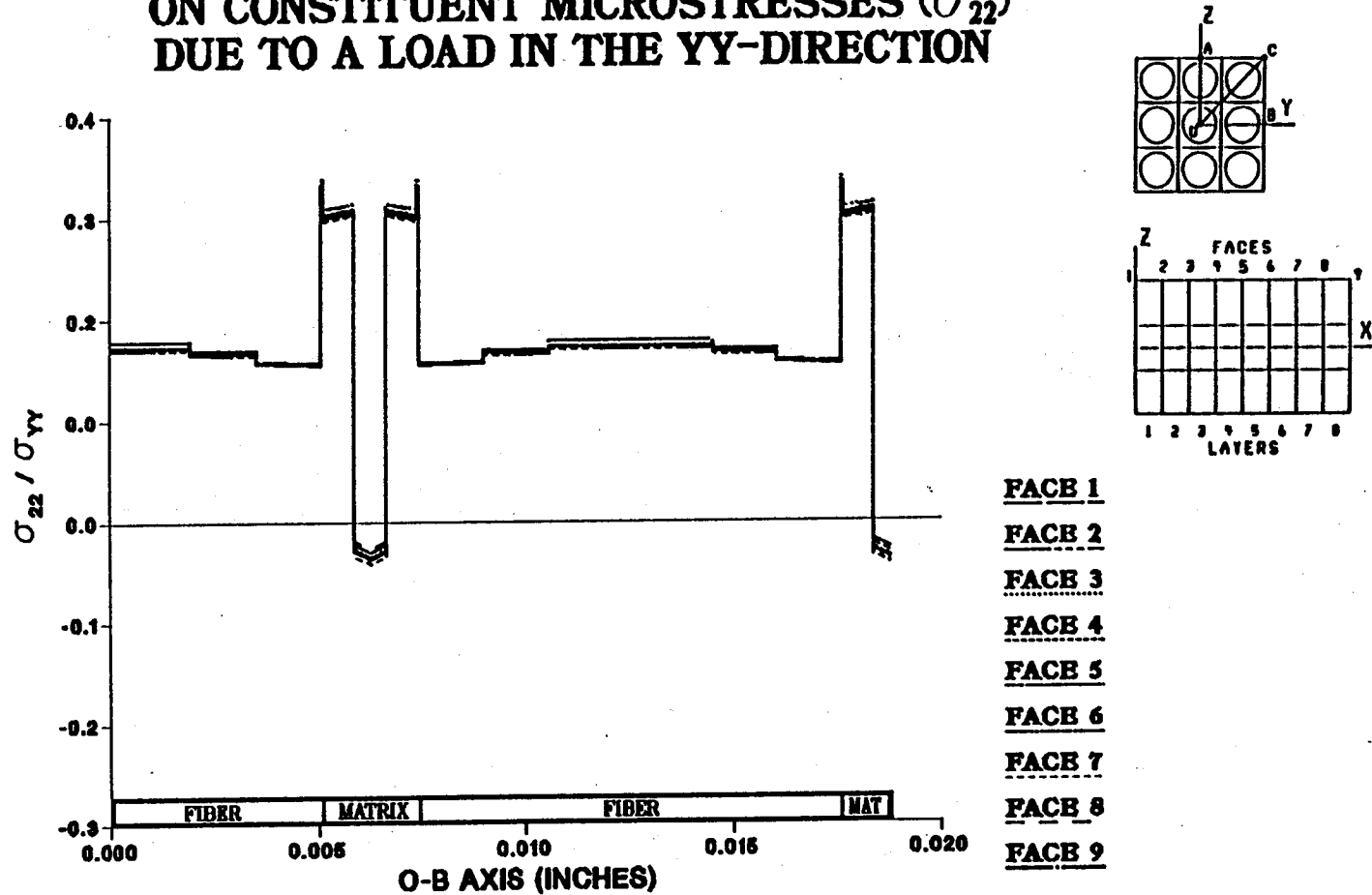
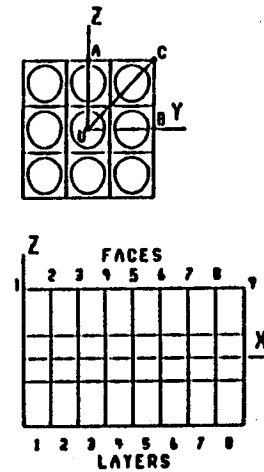
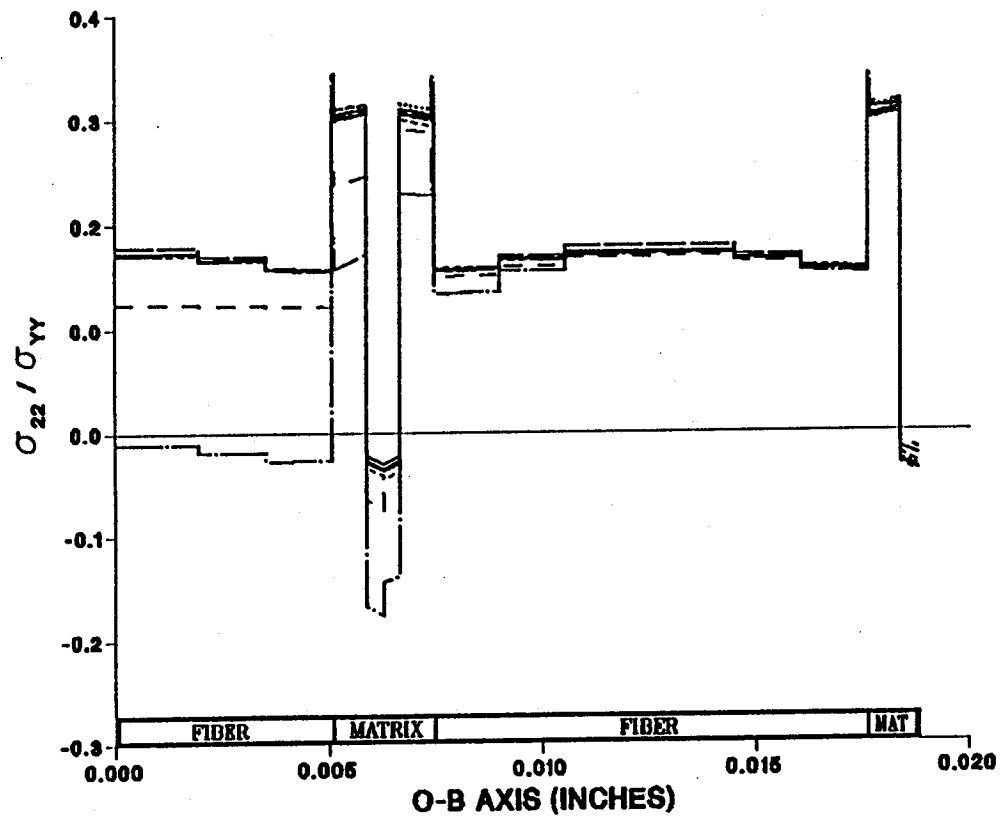


Figure A.37 - σ_{22} Normalized Microstresses, O-B Direction, 0.0% Debonding, σ_{yy}^e Loading

EFFECT OF 1.39% FIBER LENGTH DEBONDING ON CONSTITUENT MICROSTRESSES (σ_{22}) DUE TO A LOAD IN THE YY-DIRECTION



- FACB 1
- FACB 2
- FACB 3
- FACB 4
- FACB 5
- FACB 6
- FACB 7
- FACB 8
- FACB 9

Figure A.38 — σ_{22} Normalized Microstresses, O-B Direction, 1.39% Debonding, σ_{yy}^e Loading

EFFECT OF 2.78% FIBER LENGTH DEBONDING ON CONSTITUENT MICROSTRESSES (σ_{22}) DUE TO A LOAD IN THE YY-DIRECTION

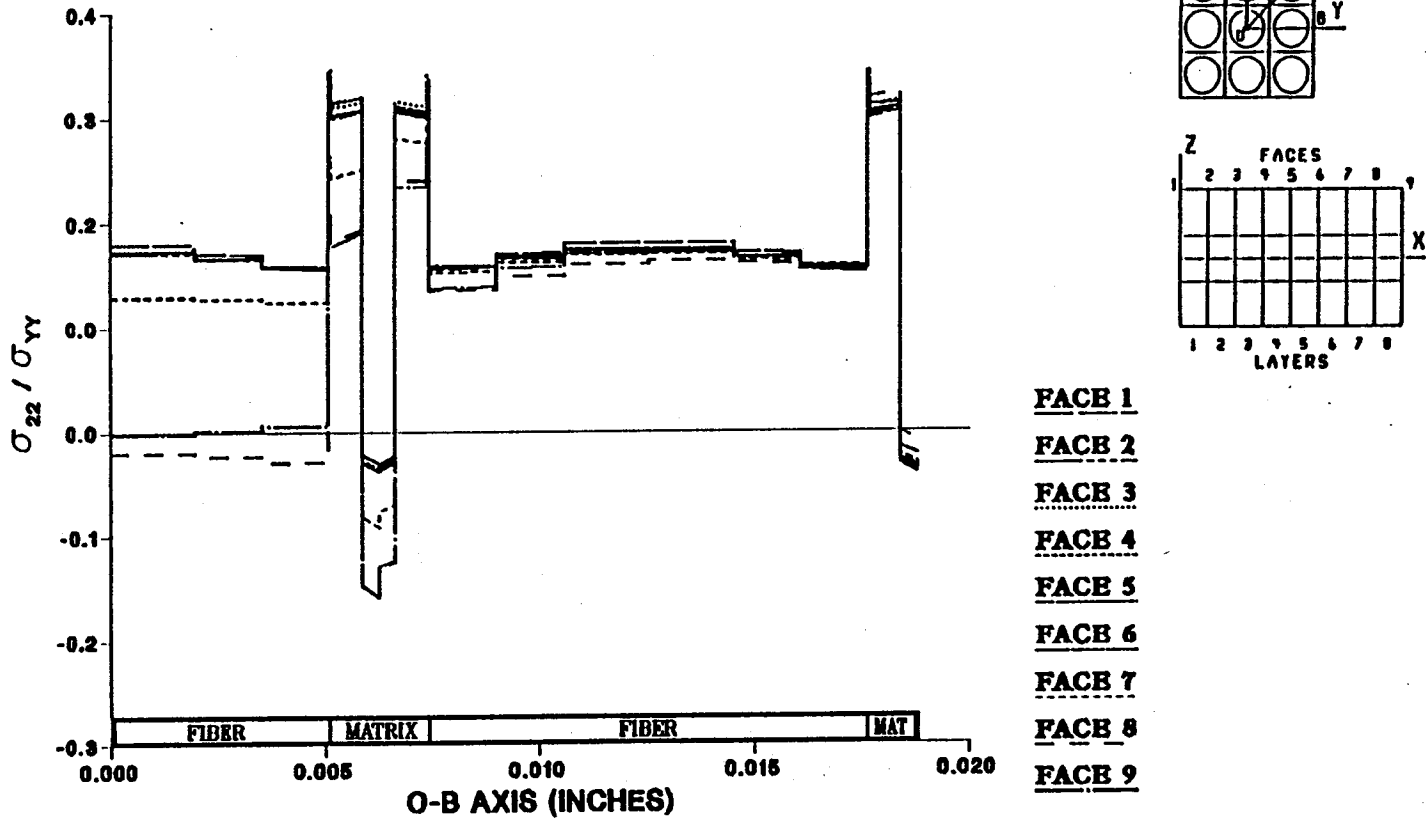


Figure A.39 – σ_{22} Normalized Microstresses, O–B Direction, 2.78% Debonding, σ_{yy}^e Loading

EFFECT OF 4.17% FIBER LENGTH DEBONDING ON CONSTITUENT MICROSTRESSES (σ_{22}) DUE TO A LOAD IN THE YY-DIRECTION

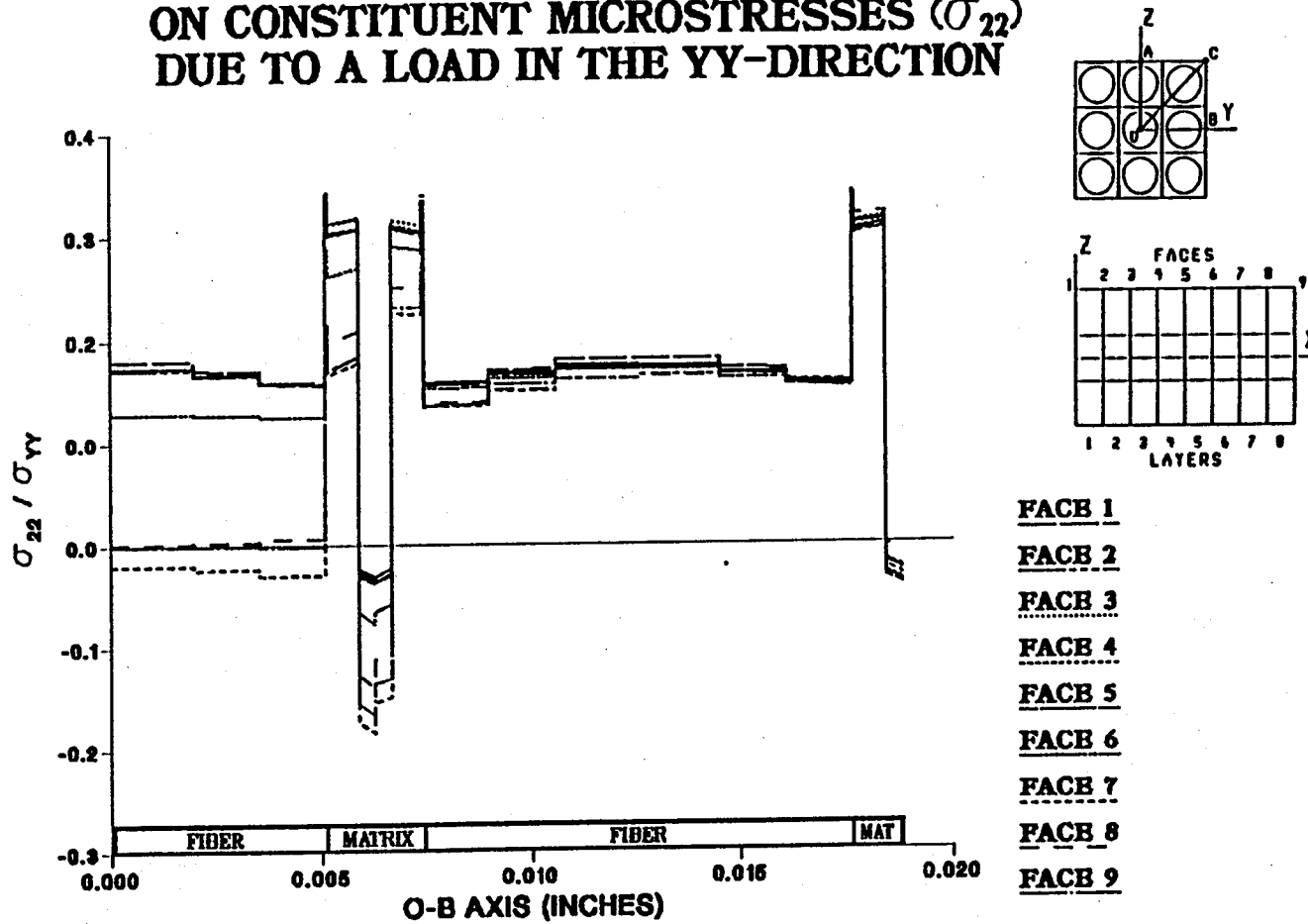


Figure A.40 – σ_{22} Normalized Microstresses, O–B Direction, 4.17% Debonding, σ_{yy}^e Loading

EFFECT OF 5.56% FIBER LENGTH DEBONDING ON CONSTITUENT MICROSTRESSES (σ_{22}) DUE TO A LOAD IN THE YY-DIRECTION

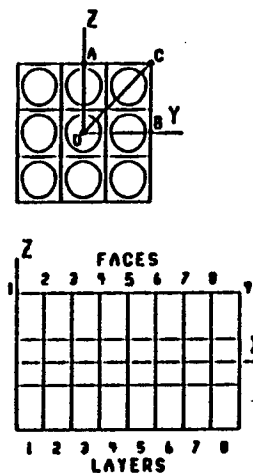
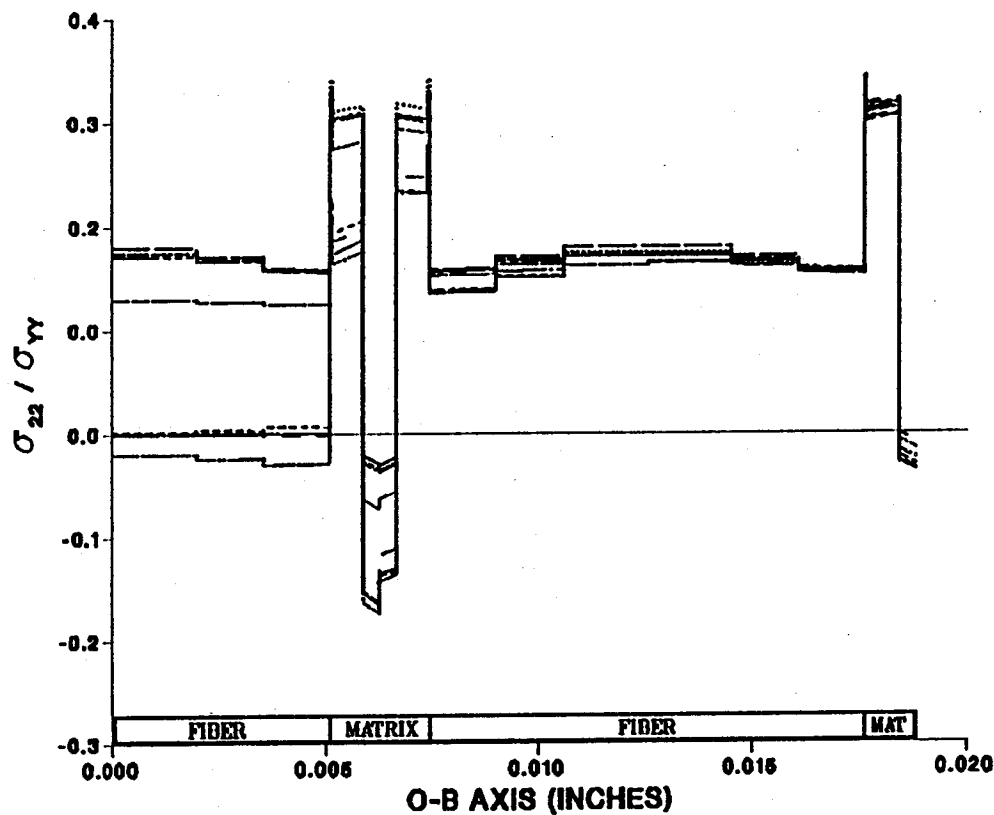


Figure A.41 - σ_{22} Normalized Microstresses, O-B Direction, 5.56% Debonding, σ_{yy}^e Loading

EFFECT OF 6.94% FIBER LENGTH DEBONDING ON CONSTITUENT MICROSTRESSES (σ_{22}) DUE TO A LOAD IN THE YY-DIRECTION

228

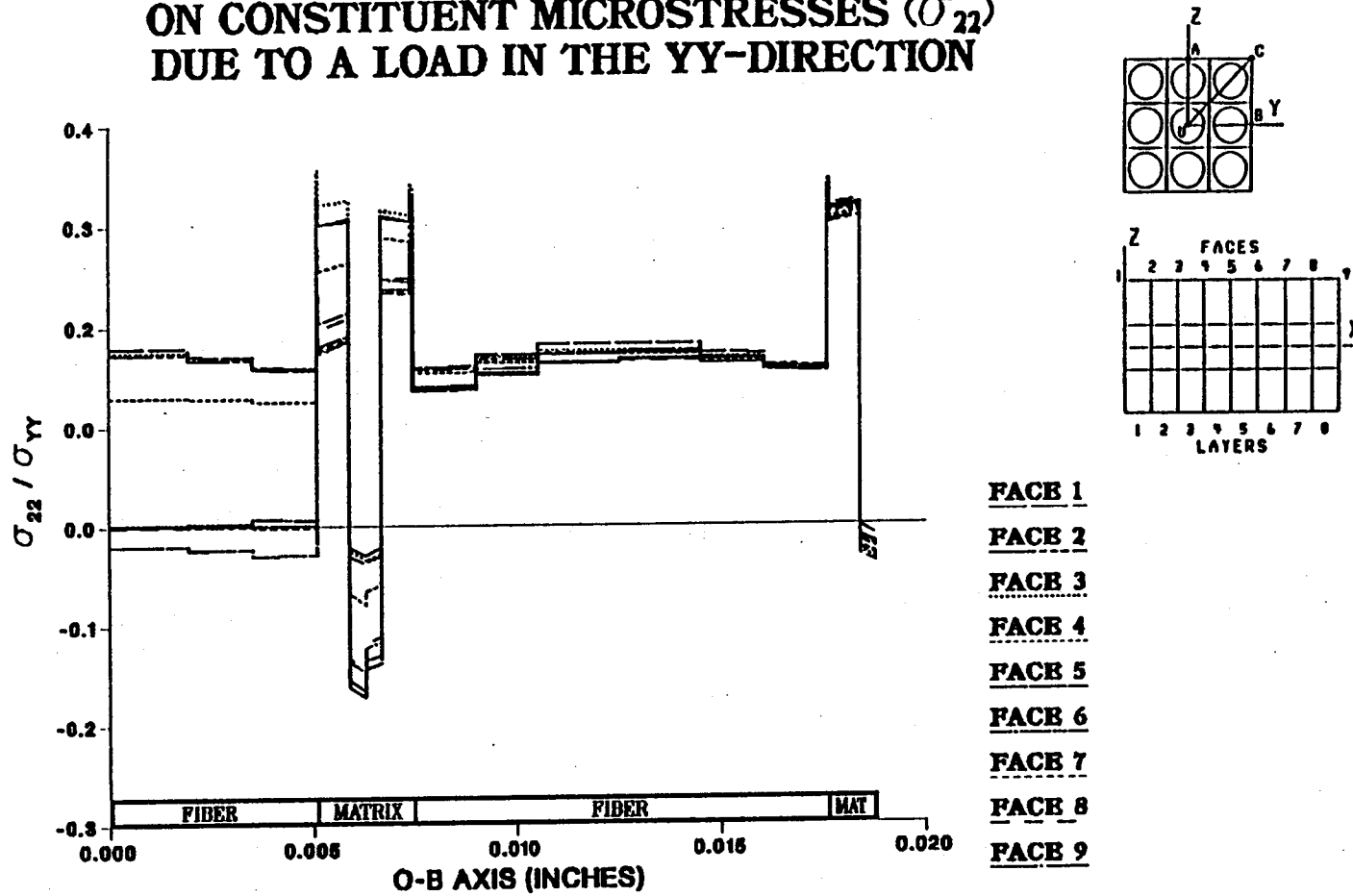
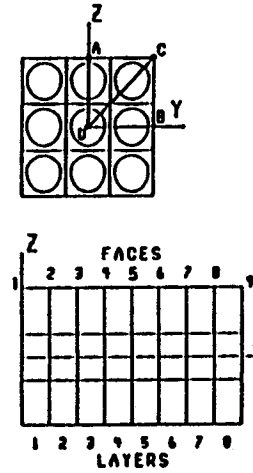
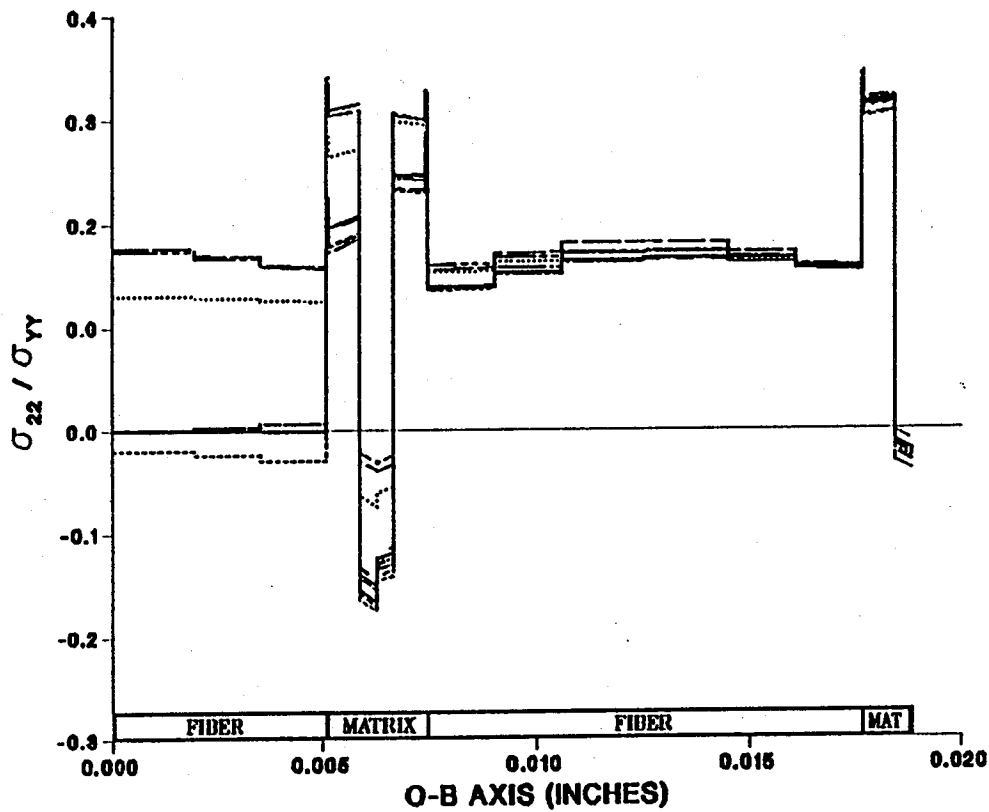


Figure A.42 – σ_{22} Normalized Microstresses, O–B Direction, 6.94% Debonding, σ_{yy}^e Loading

EFFECT OF 8.33% FIBER LENGTH DEBONDING ON CONSTITUENT MICROSTRESSES (σ_{22}) DUE TO A LOAD IN THE YY-DIRECTION



- FACE 1
- FACE 2
- FACE 3
- FACE 4
- FACE 5
- FACE 6
- FACE 7
- FACE 8
- FACE 9

Figure A.43 - σ_{22} Normalized Microstresses, O-B Direction, 8.33% Debonding, σ_{yy}^e Loading

EFFECT OF 9.72% FIBER LENGTH DEBONDING ON CONSTITUENT MICROSTRESSES (σ_{22}) DUE TO A LOAD IN THE YY-DIRECTION

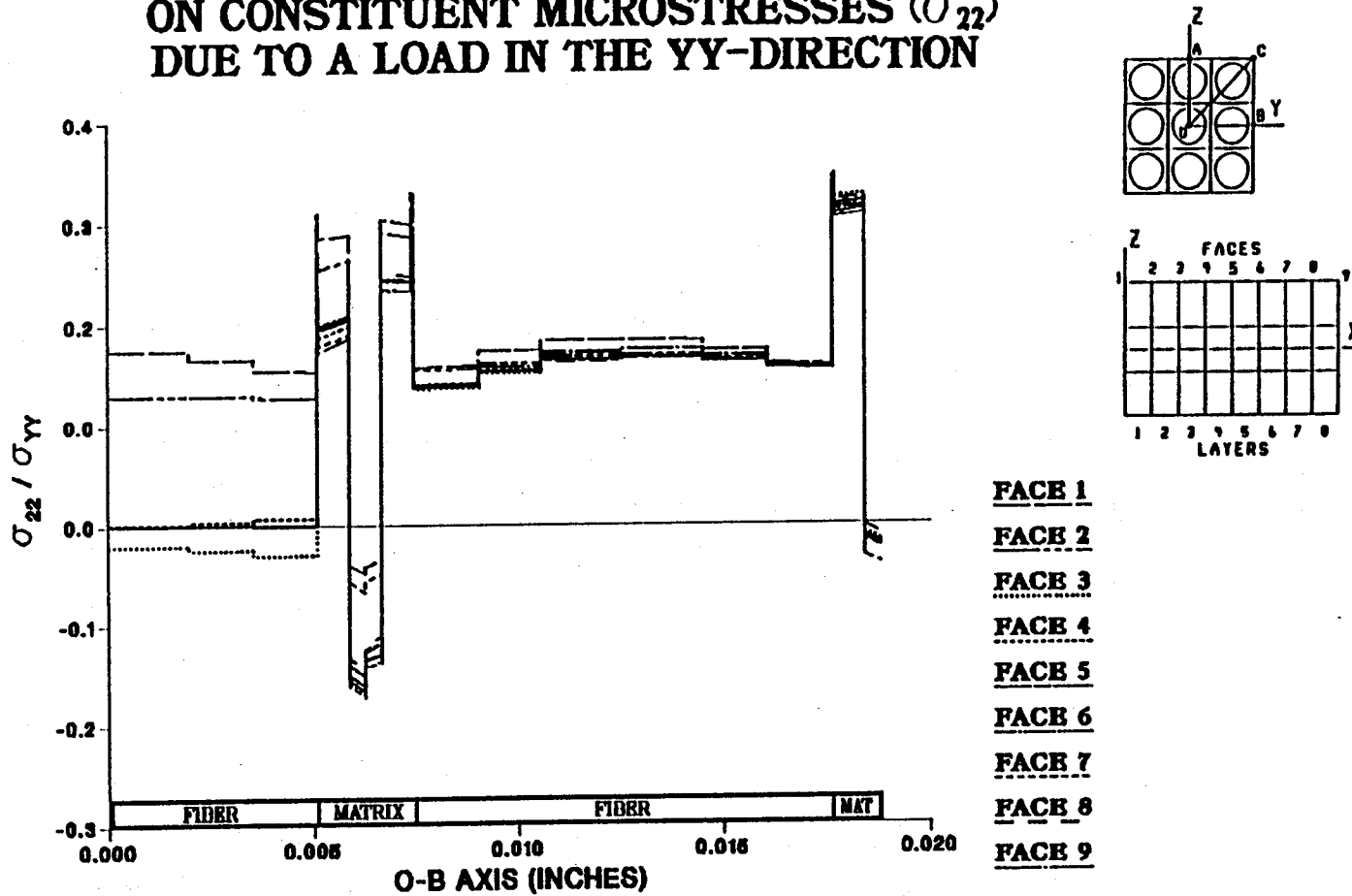


Figure A.44 - σ_{22} Normalized Microstresses, O-B Direction, 9.72% Debonding, σ_{yy}^e Loading

EFFECT OF 11.1% FIBER LENGTH DEBONDING ON CONSTITUENT MICROSTRESSES (σ_{22}) DUE TO A LOAD IN THE YY-DIRECTION

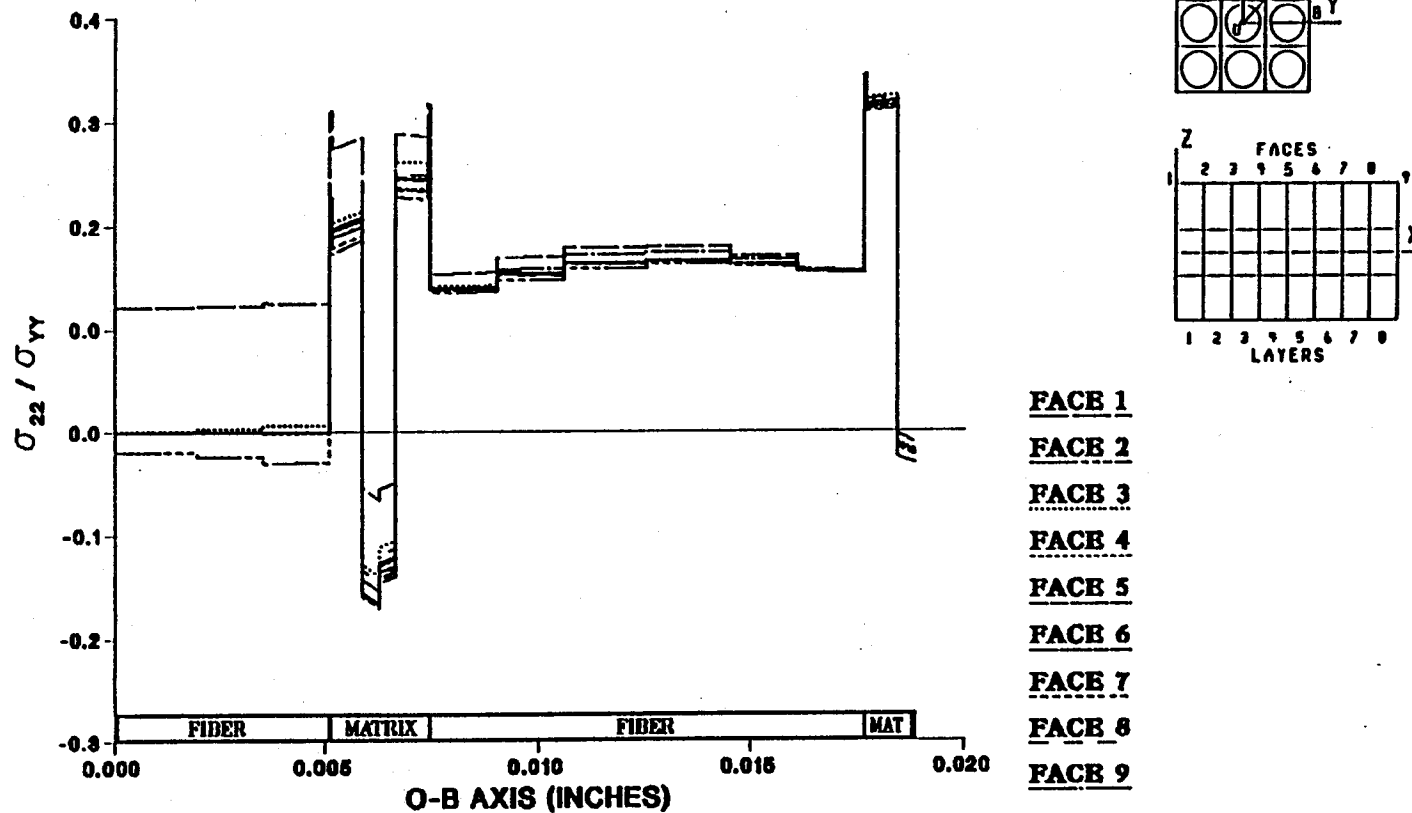


Figure A.45 — σ_{22} Normalized Microstresses, O-B Direction, 11.1% Debonding, σ_{yy}^e Loading

EFFECT OF 0.0% FIBER LENGTH DEBONDING ON CONSTITUENT MICROSTRESSES (σ_{22}) DUE TO A LOAD IN THE YY-DIRECTION

232

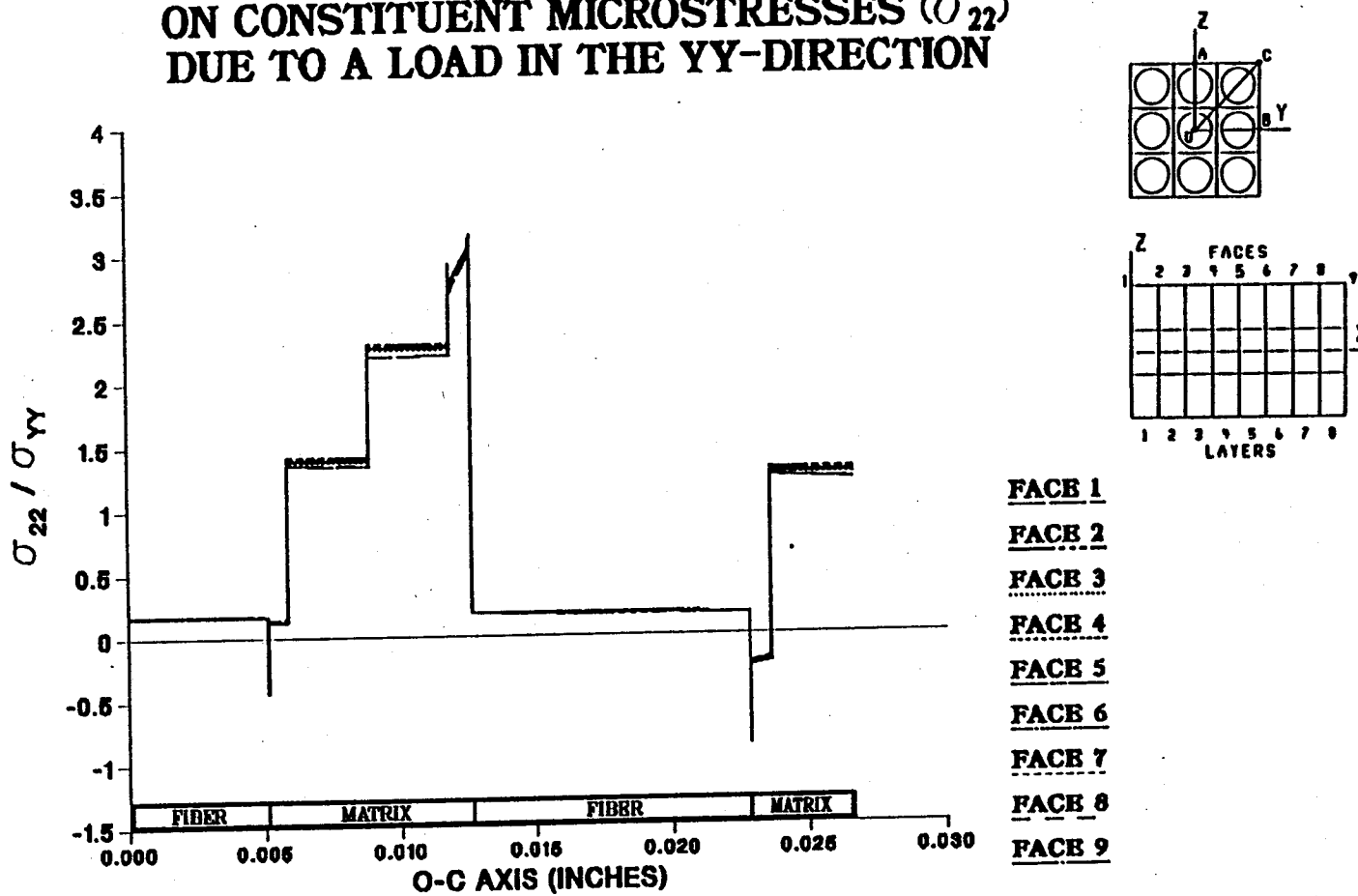


Figure A.46 - σ_{22} Normalized Microstresses, O-C Direction, 0.0% Debonding, σ_{yy}^e Loading

EFFECT OF 1.39% FIBER LENGTH DEBONDING ON CONSTITUENT MICROSTRESSES (σ_{22}) DUE TO A LOAD IN THE YY-DIRECTION

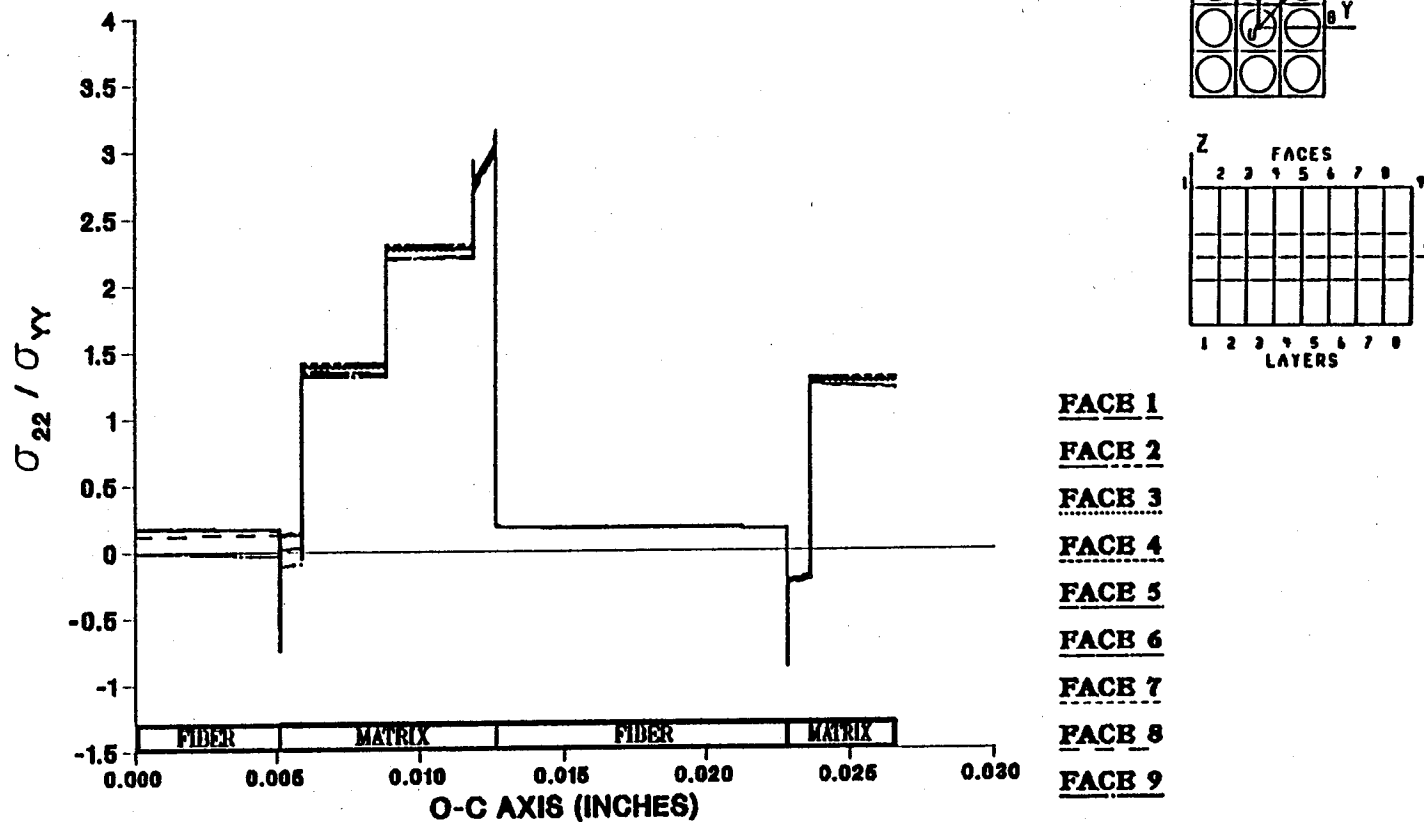


Figure A.47 – σ_{22} Normalized Microstresses, O–C Direction, 1.39% Debonding, σ_{yy}^e Loading

EFFECT OF 2.78% FIBER LENGTH DEBONDING ON CONSTITUENT MICROSTRESSES (σ_{22}) DUE TO A LOAD IN THE YY-DIRECTION

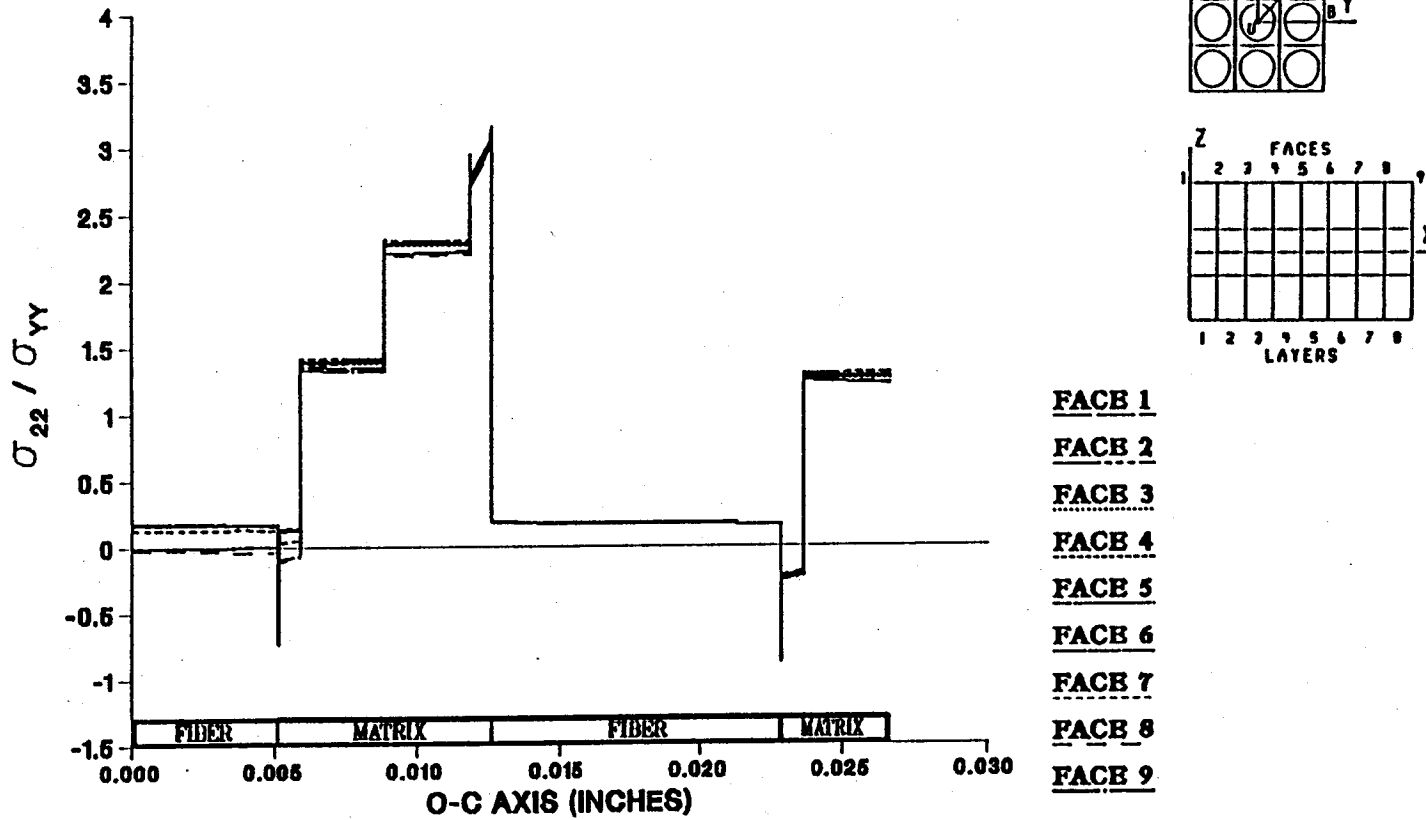


Figure A.48 - σ_{22} Normalized Microstresses, O-C Direction, 2.78% Debonding, σ_{yy}^e Loading

EFFECT OF 4.17% FIBER LENGTH DEBONDING ON CONSTITUENT MICROSTRESSES (σ_{22}) DUE TO A LOAD IN THE YY-DIRECTION

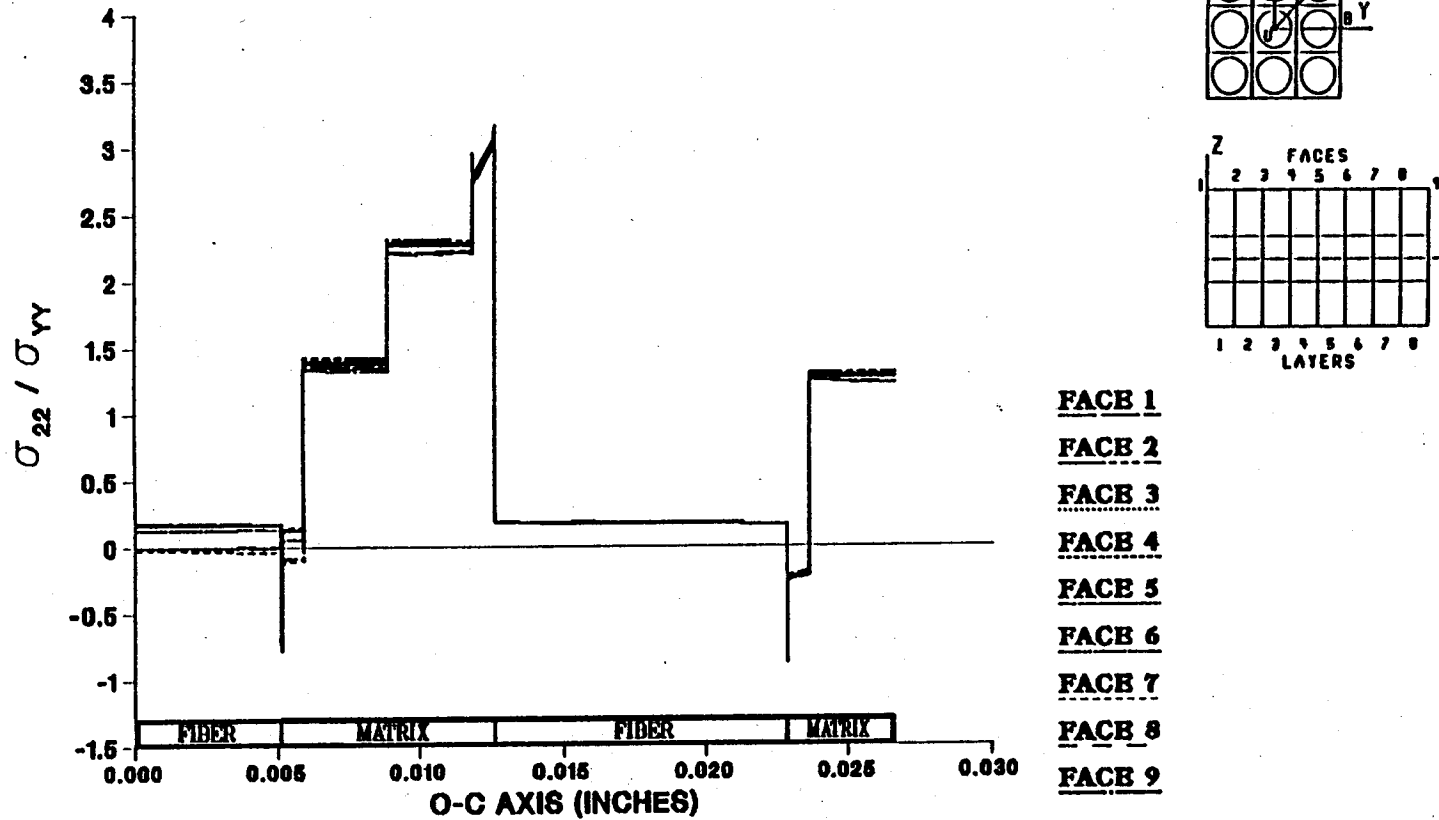


Figure A.49 — σ_{22} Normalized Microstresses, O-C Direction, 4.17% Debonding, σ_{yy}^e Loading

EFFECT OF 5.56% FIBER LENGTH DEBONDING ON CONSTITUENT MICROSTRESSES (σ_{22}) DUE TO A LOAD IN THE YY-DIRECTION

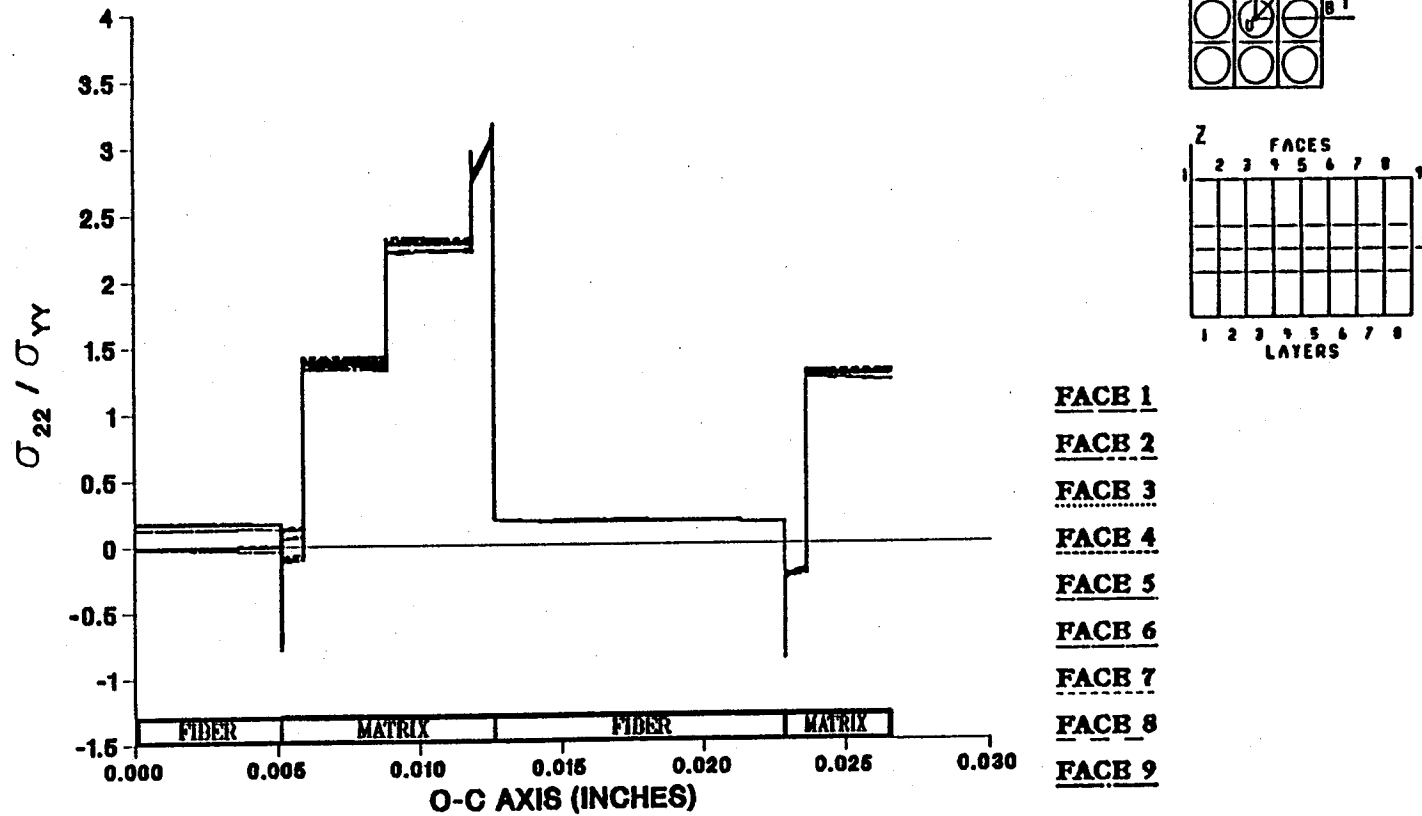


Figure A.50 — σ_{22} Normalized Microstresses, O-C Direction, 5.56% Debonding, σ_{yy}^e Loading

EFFECT OF 6.94% FIBER LENGTH DEBONDING ON CONSTITUENT MICROSTRESSES (σ_{22}) DUE TO A LOAD IN THE YY-DIRECTION

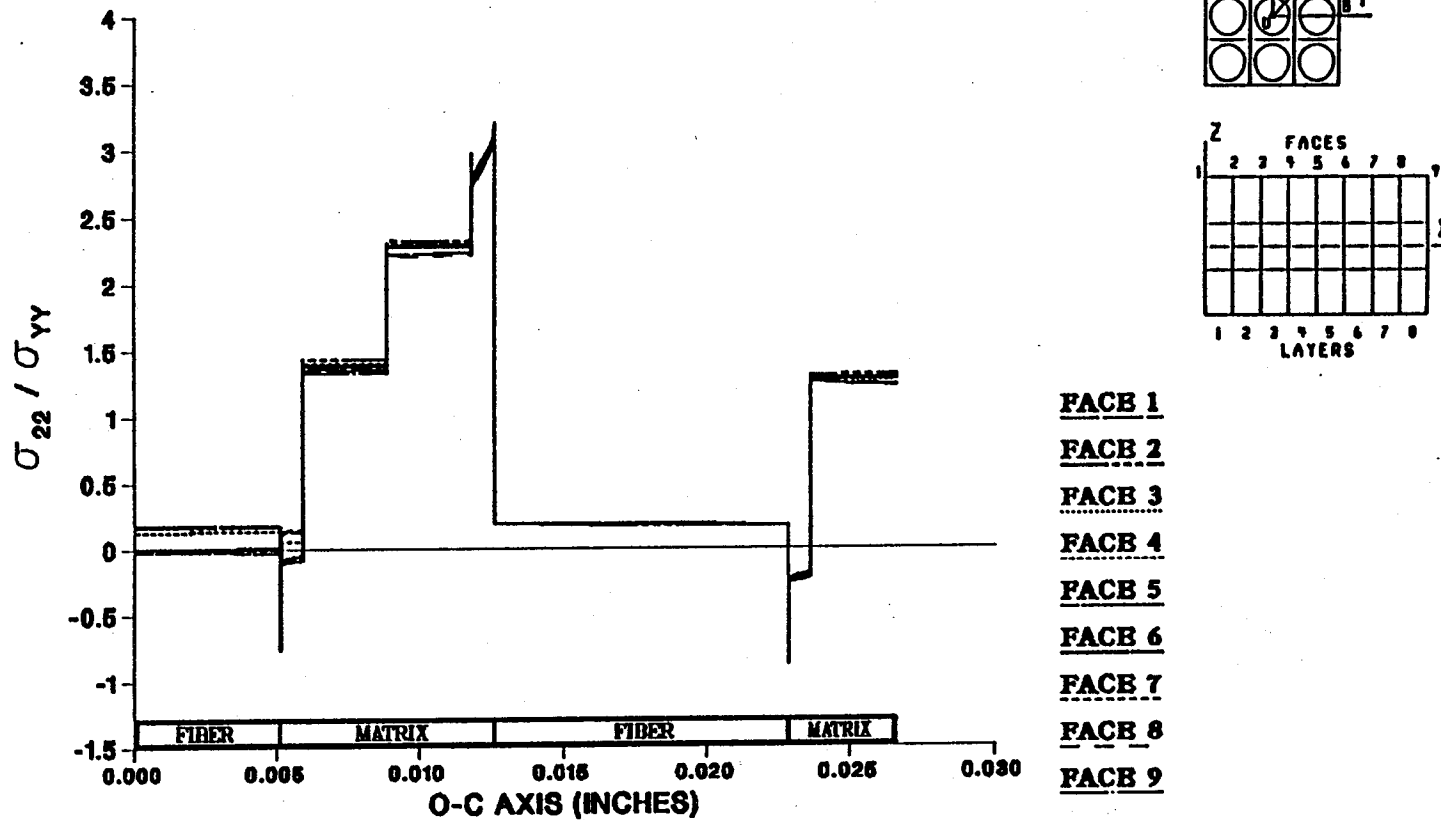


Figure A.51 - σ_{22} Normalized Microstresses, O-C Direction, 6.94% Debonding, σ_{yy}^e Loading

EFFECT OF 8.33% FIBER LENGTH DEBONDING ON CONSTITUENT MICROSTRESSES (σ_{22}) DUE TO A LOAD IN THE YY-DIRECTION

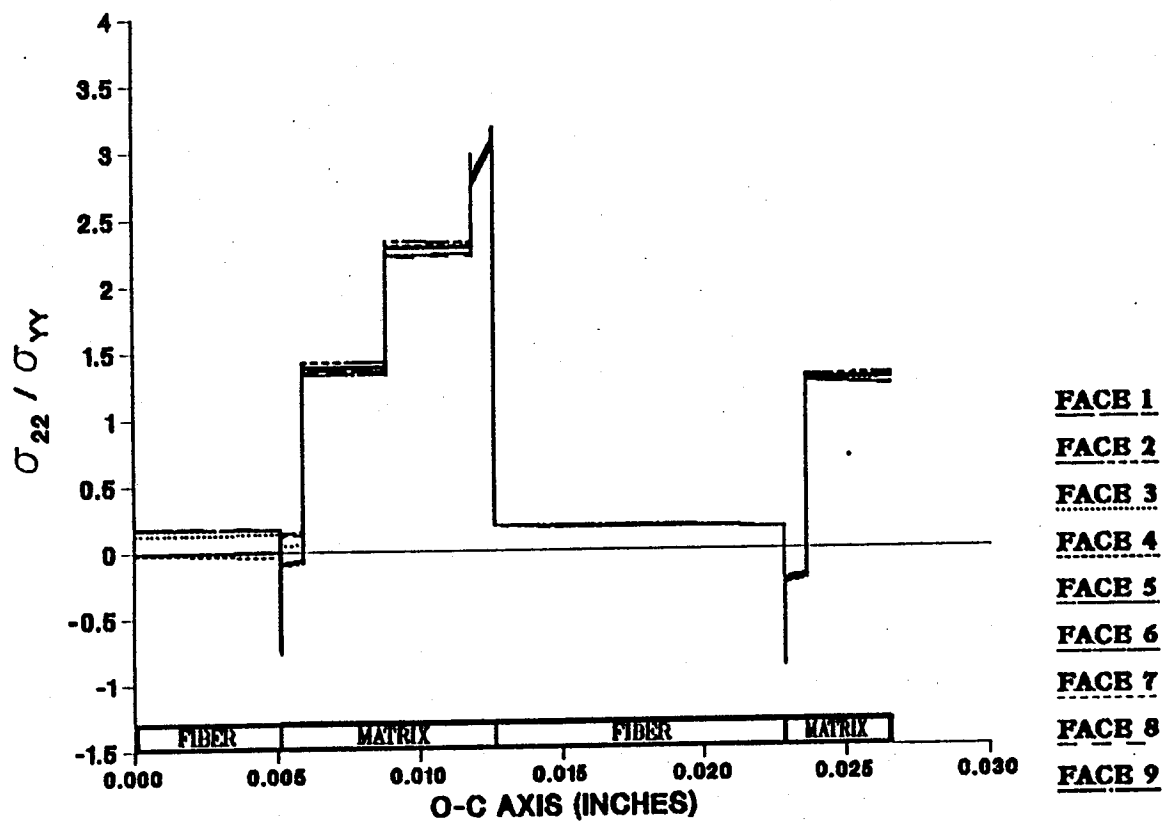
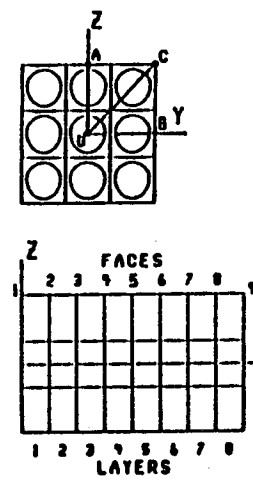


Figure A.52 — σ_{22} Normalized Microstresses, O-C Direction, 8.33% Debonding, σ_{yy}^e Loading

EFFECT OF 9.72% FIBER LENGTH DEBONDING ON CONSTITUENT MICROSTRESSES (σ_{22}) DUE TO A LOAD IN THE YY-DIRECTION

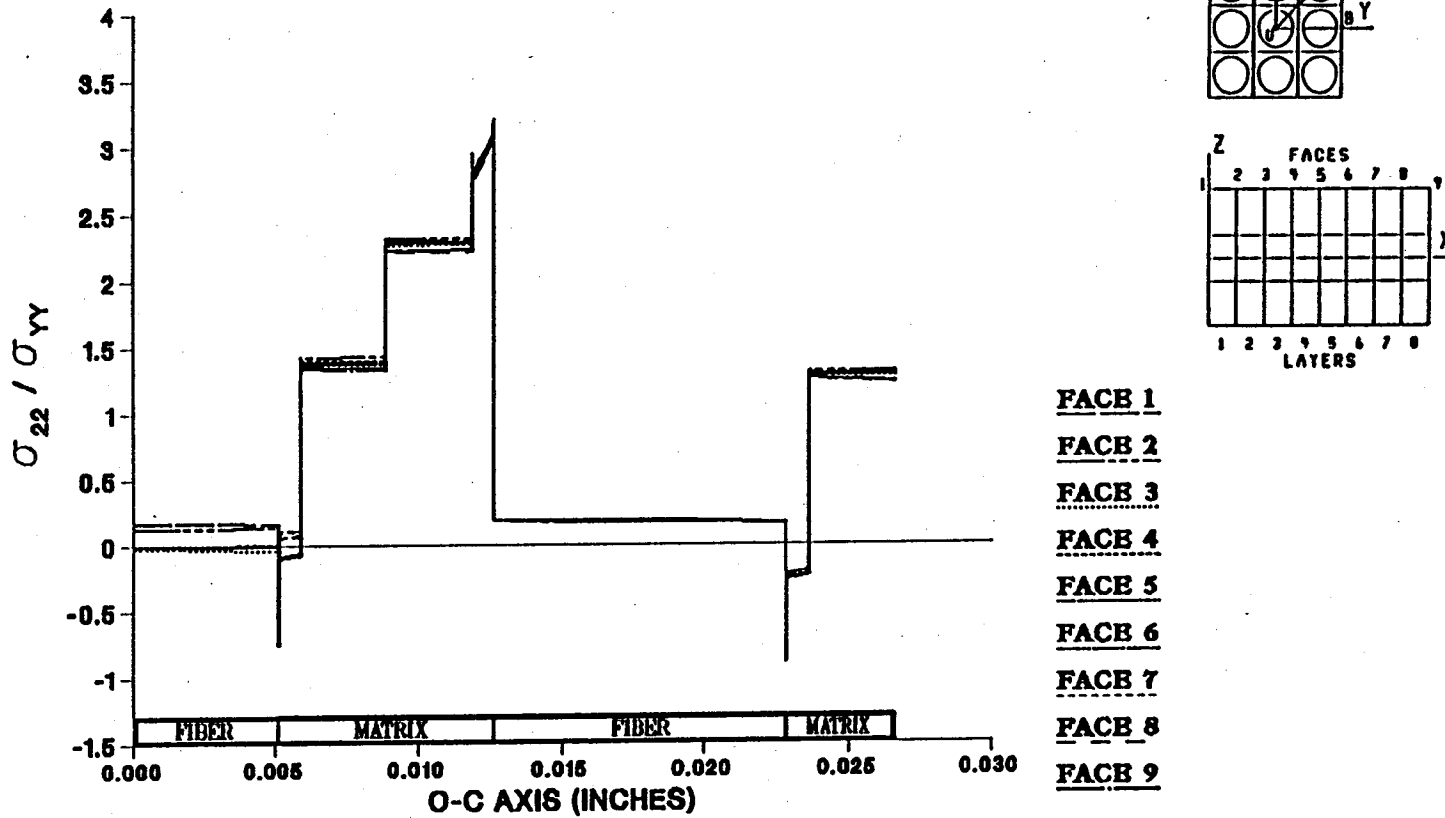


Figure A.53 – σ_{22} Normalized Microstresses, O–C Direction, 9.72% Debonding, σ_{yy}^e Loading

EFFECT OF 11.11% FIBER LENGTH DEBONDING ON CONSTITUENT MICROSTRESSES (σ_{22}) DUE TO A LOAD IN THE YY-DIRECTION

240

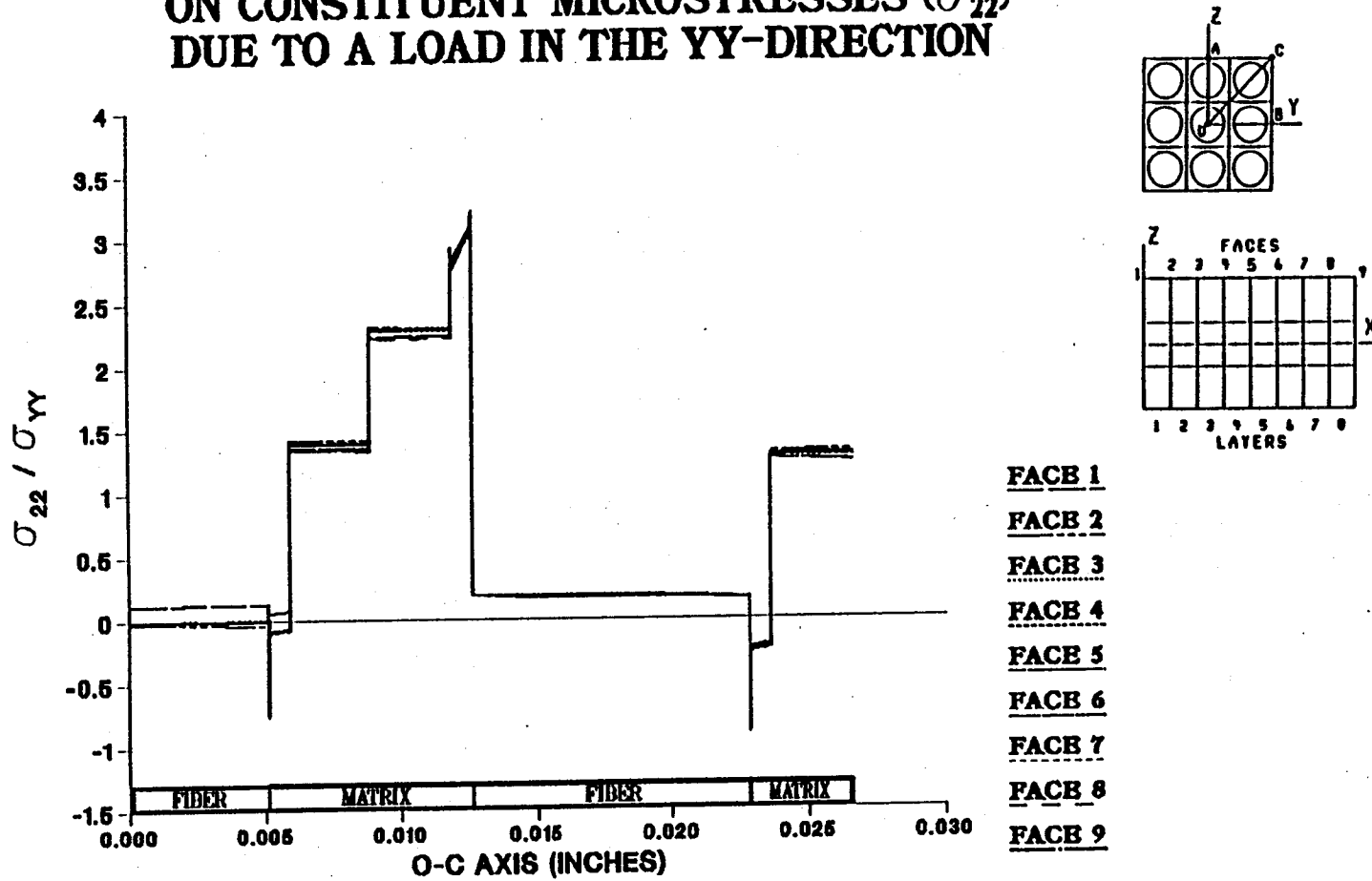


Figure A.54 - σ_{22} Normalized Microstresses, O-C Direction, 11.11% Debonding, σ_{yy}^e Loading

EFFECT OF 0.0% FIBER LENGTH DEBONDING ON CONSTITUENT MICROSTRESSES (σ_{11}) DUE TO A LOAD IN THE YY-DIRECTION

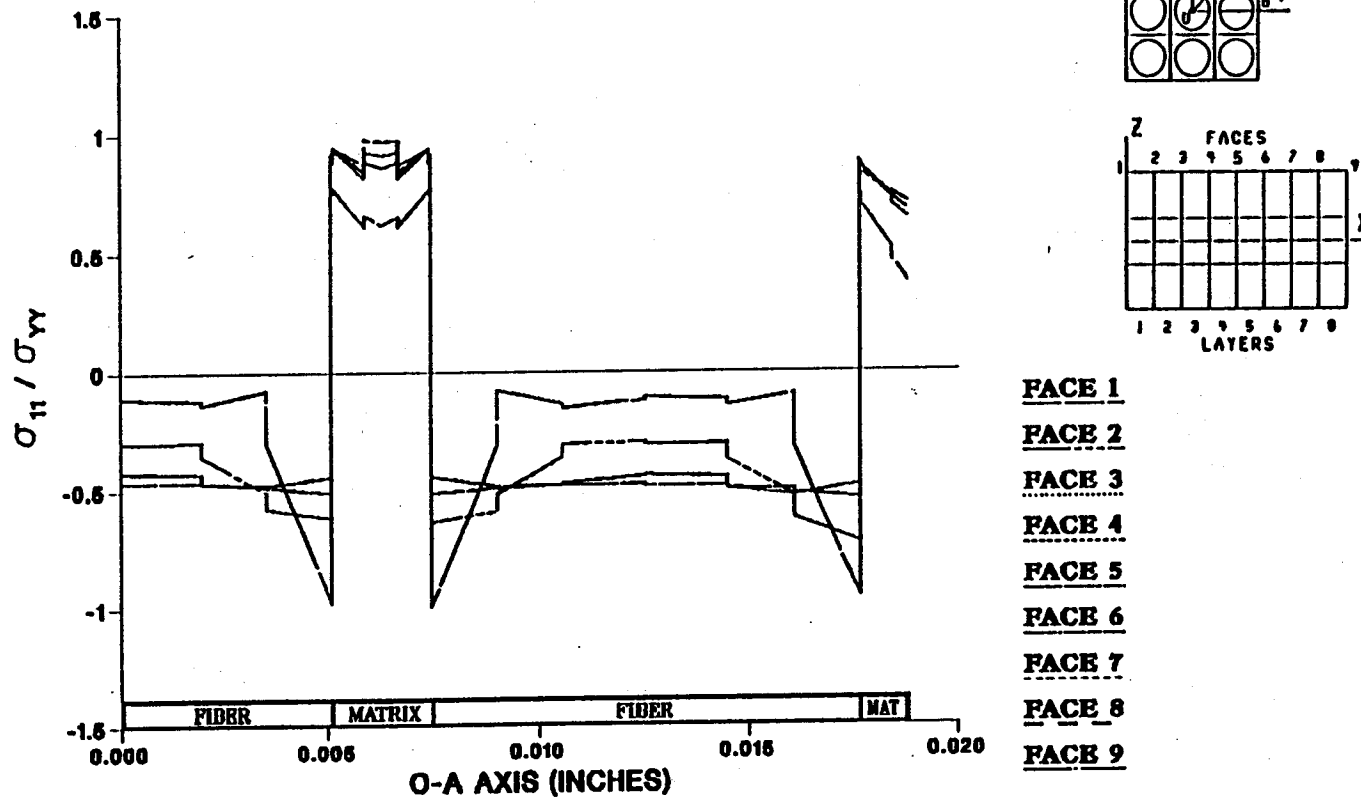


Figure A.55 - σ_{11} Normalized Microstresses, O-A Direction, 0.0% Debonding, σ_{yy}^e Loading

EFFECT OF 1.39% FIBER LENGTH DEBONDING ON CONSTITUENT MICROSTRESSES (σ_{11}) DUE TO A LOAD IN THE YY-DIRECTION

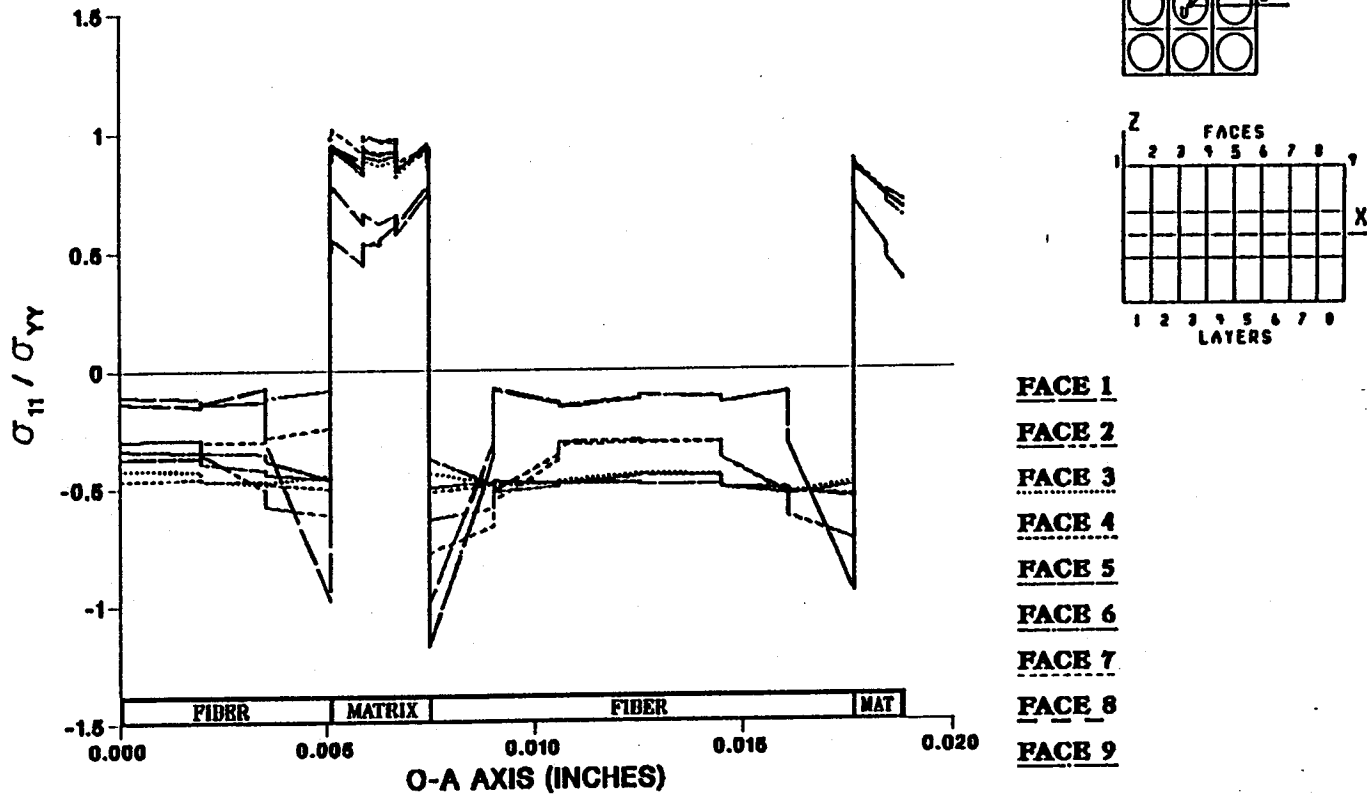


Figure A.56 - σ_{11} Normalized Microstresses, O-A Direction, 1.39% Debonding, σ_{yy}^e Loading

EFFECT OF 2.78% FIBER LENGTH DEBONDING ON CONSTITUENT MICROSTRESSES (σ_{11}) DUE TO A LOAD IN THE YY-DIRECTION

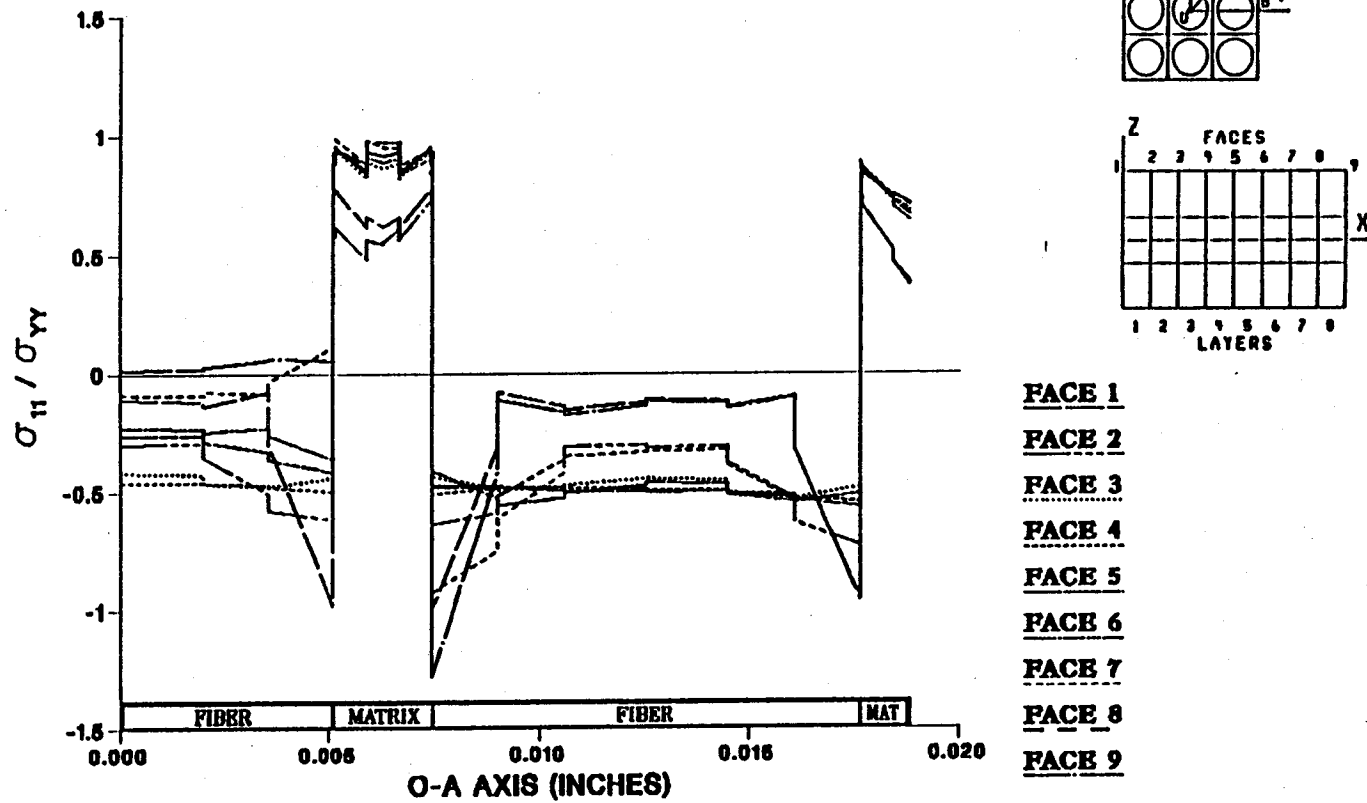


Figure A.57 - σ_{11} Normalized Microstresses, O-A Direction, 2.78% Debonding, σ_{yy}^e Loading

EFFECT OF 4.17% FIBER LENGTH DEBONDING ON CONSTITUENT MICROSTRESSES (σ_{11}) DUE TO A LOAD IN THE YY-DIRECTION

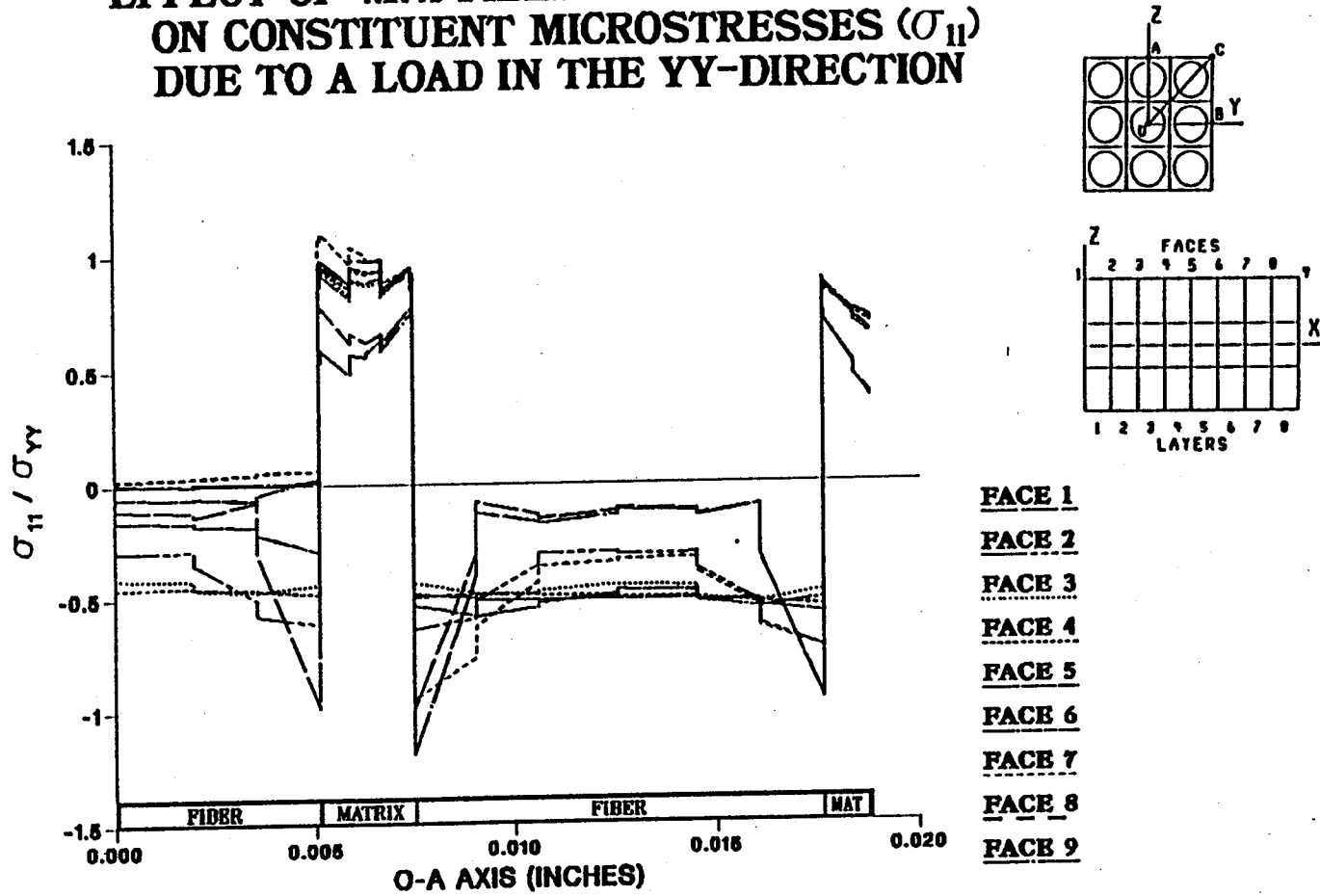
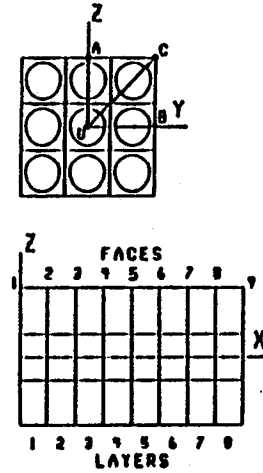
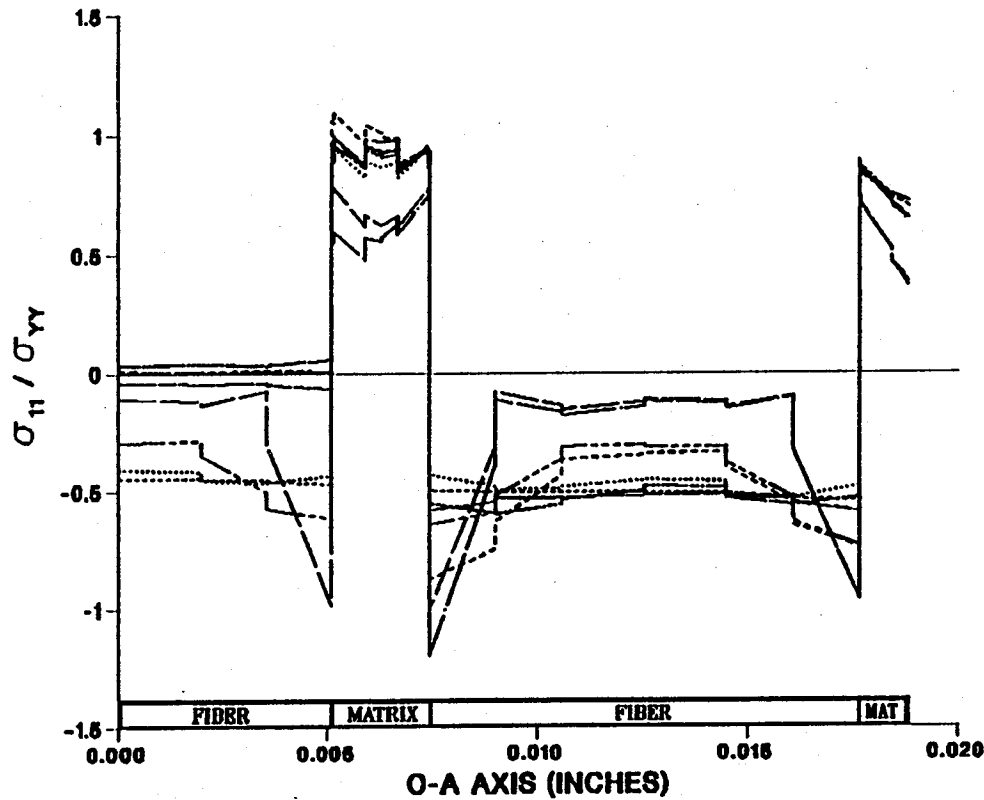


Figure A.58 - σ_{11} Normalized Microstresses, O-A Direction, 4.17% Debonding, σ_{yy}^e Loading

EFFECT OF 5.56% FIBER LENGTH DEBONDING ON CONSTITUENT MICROSTRESSES (σ_{11}) DUE TO A LOAD IN THE YY-DIRECTION



- FACE 1
- FACE 2
- FACE 3
- FACE 4
- FACE 5
- FACE 6
- FACE 7
- FACE 8
- FACE 9

Figure A.59 – σ_{11} Normalized Microstresses, O–A Direction, 5.56% Debonding, σ_{yy}^e Loading

EFFECT OF 6.94% FIBER LENGTH DEBONDING ON CONSTITUENT MICROSTRESSES (σ_{11}) DUE TO A LOAD IN THE YY-DIRECTION

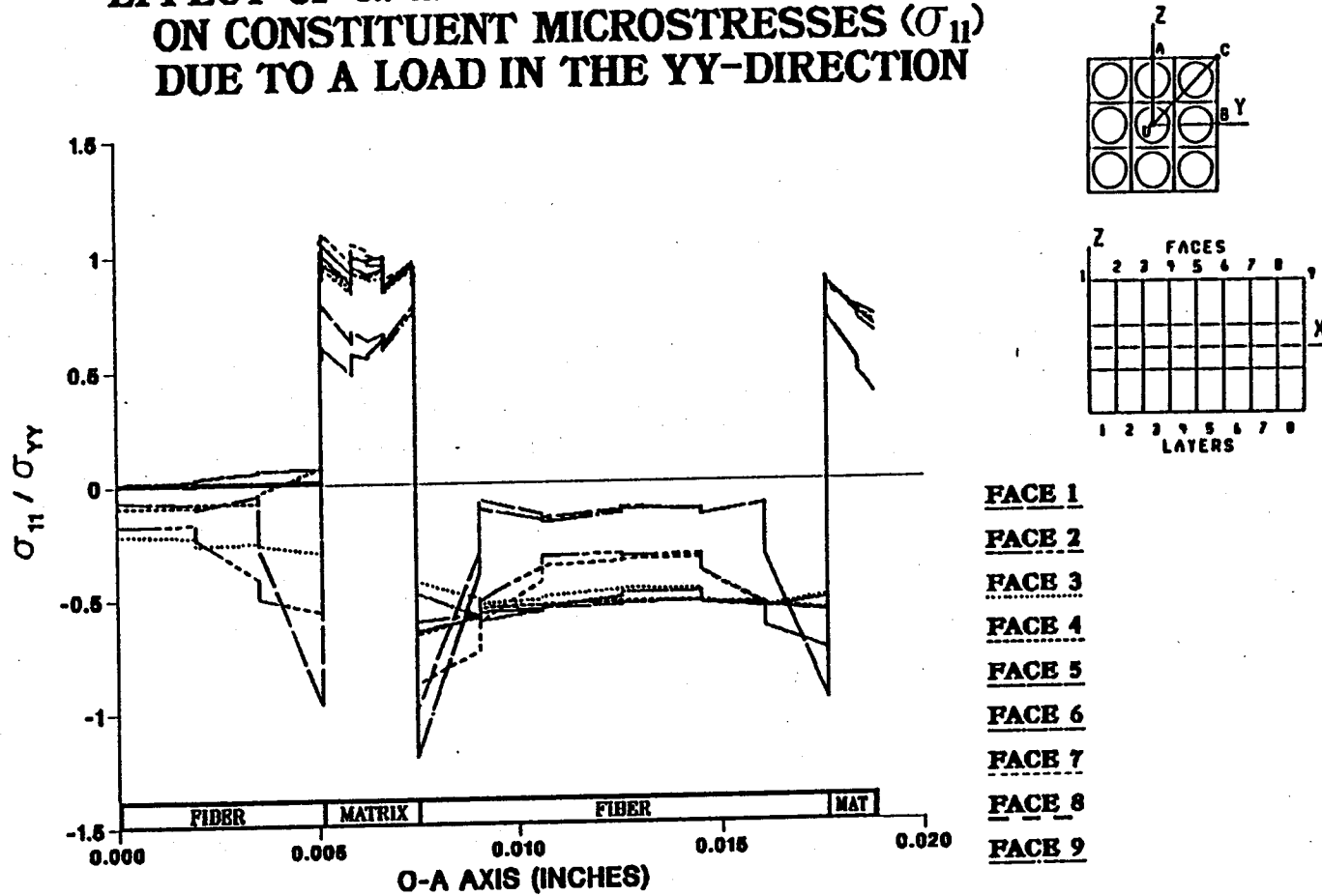
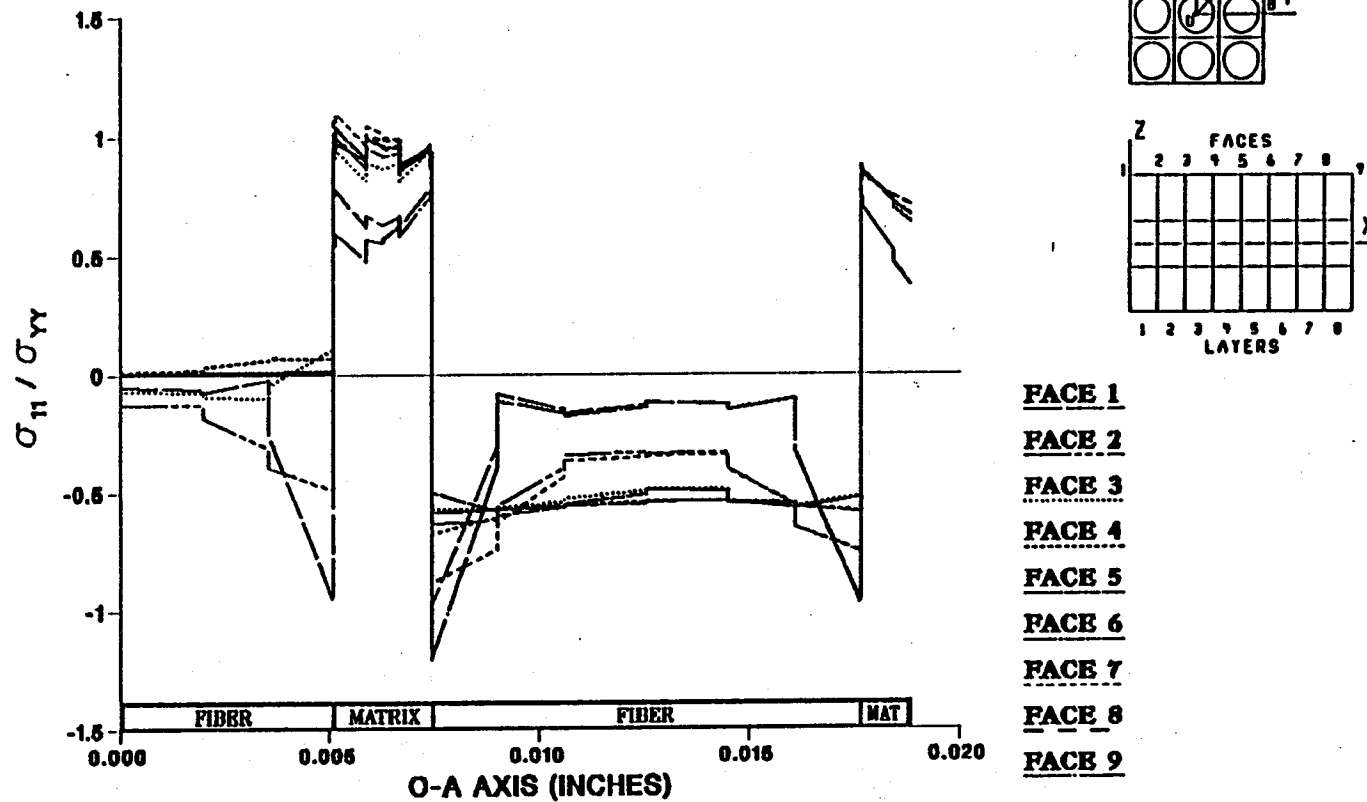


Figure A.60 - σ_{11} Normalized Microstresses, O-A Direction, 6.94% Debonding, σ_{yy}^e Loading

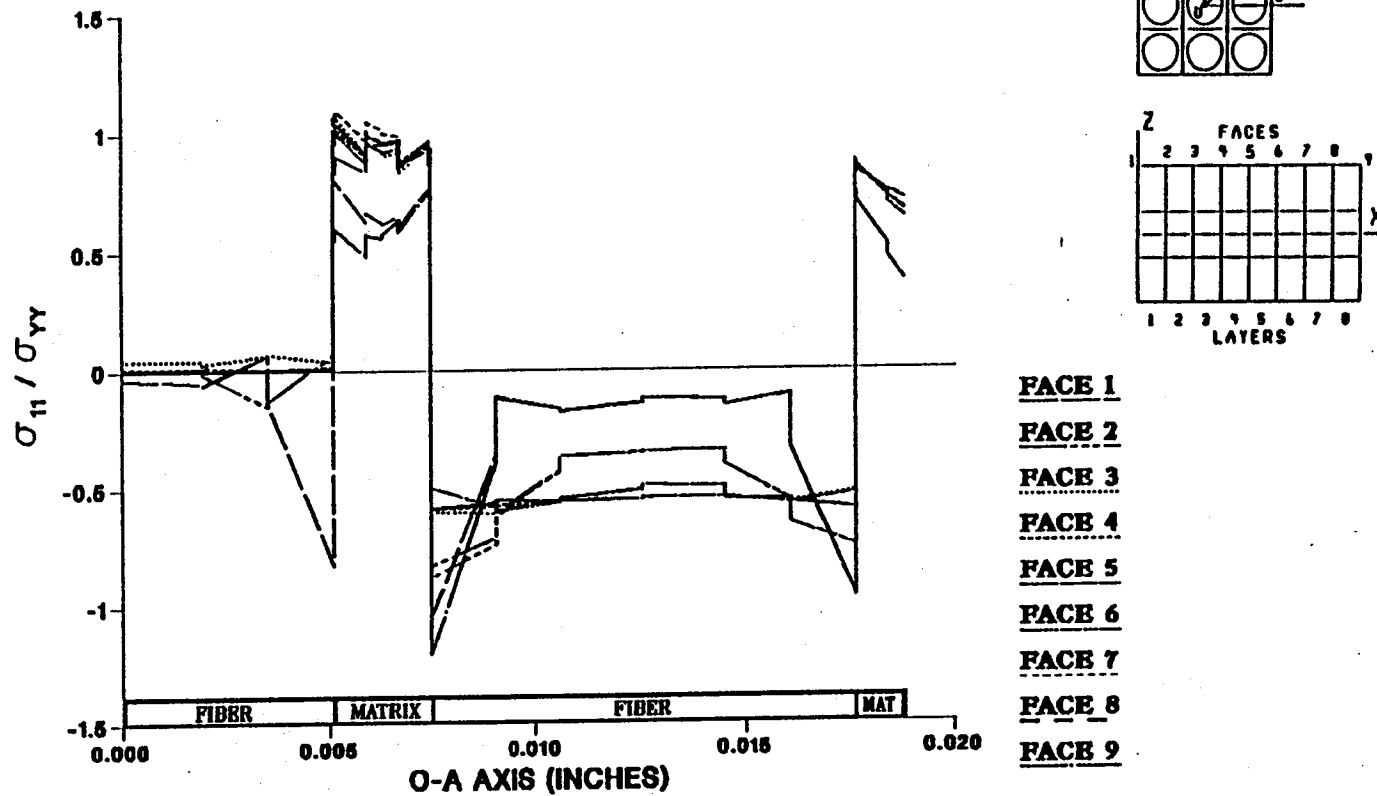
EFFECT OF 8.33% FIBER LENGTH DEBONDING ON CONSTITUENT MICROSTRESSES (σ_{11}) DUE TO A LOAD IN THE YY-DIRECTION



- FACE 1
- FACE 2
- FACE 3
- FACE 4
- FACE 5
- FACE 6
- FACE 7
- FACE 8
- FACE 9

Figure A.61 - σ_{11} Normalized Microstresses, O-A Direction, 8.33% Debonding, σ_{yy}^e Loading

EFFECT OF 9.72% FIBER LENGTH DEBONDING ON CONSTITUENT MICROSTRESSES (σ_{11}) DUE TO A LOAD IN THE YY-DIRECTION



- FACE 1
- FACE 2
- FACE 3
- FACE 4
- FACE 5
- FACE 6
- FACE 7
- FACE 8
- FACE 9

Figure A.62 - σ_{11} Normalized Microstresses, O-A Direction, 9.72% Debonding, σ_{yy}^e Loading

EFFECT OF 11.11% FIBER LENGTH DEBONDING ON CONSTITUENT MICROSTRESSES (σ_{11}) DUE TO A LOAD IN THE YY-DIRECTION

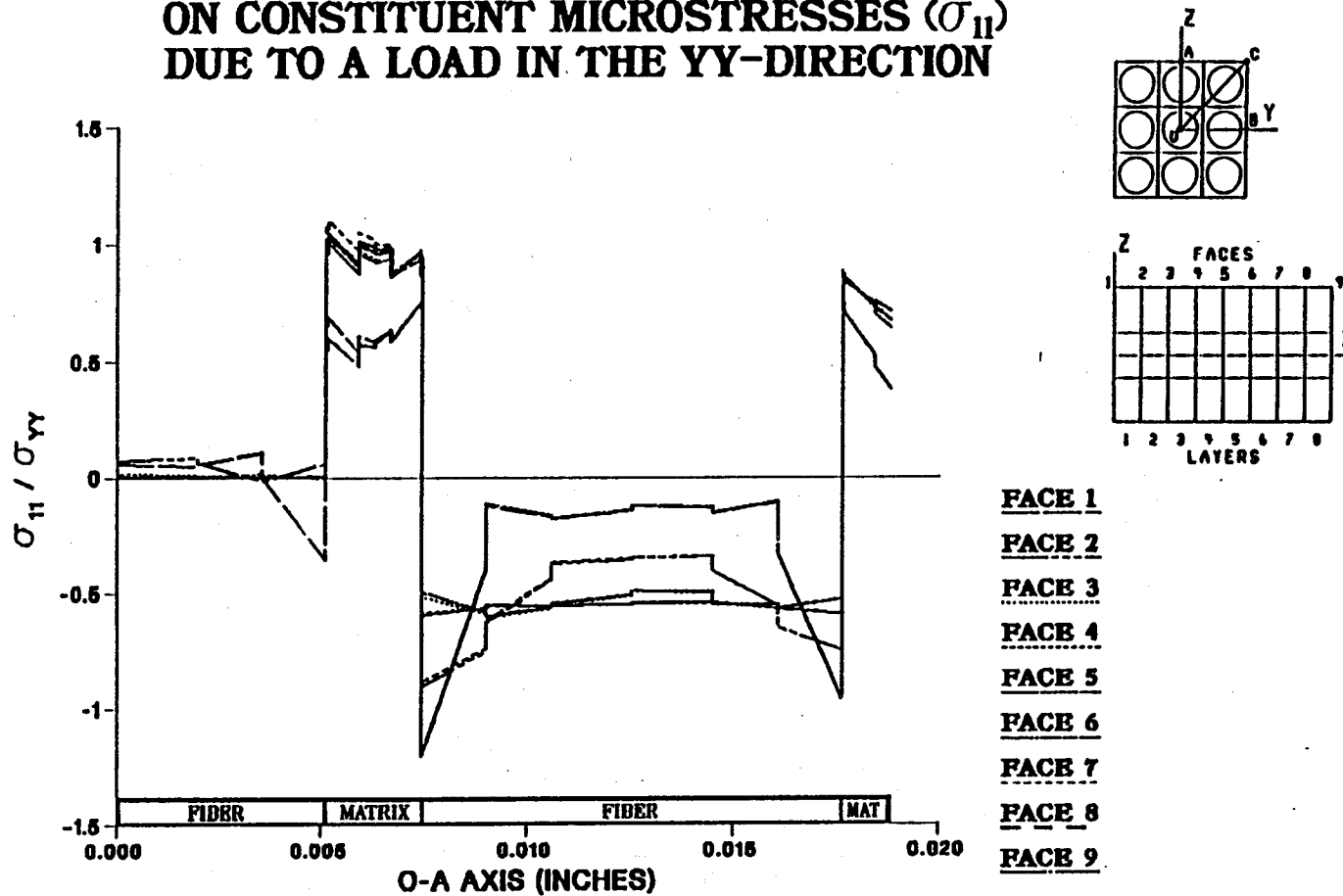


Figure A.63 - σ_{11} Normalized Microstresses, O-A Direction, 11.11% Debonding, σ_{yy}^e Loading

EFFECT OF 0.0% FIBER LENGTH DEBONDING ON CONSTITUENT MICROSTRESSES (σ_{11}) DUE TO A LOAD IN THE YY-DIRECTION

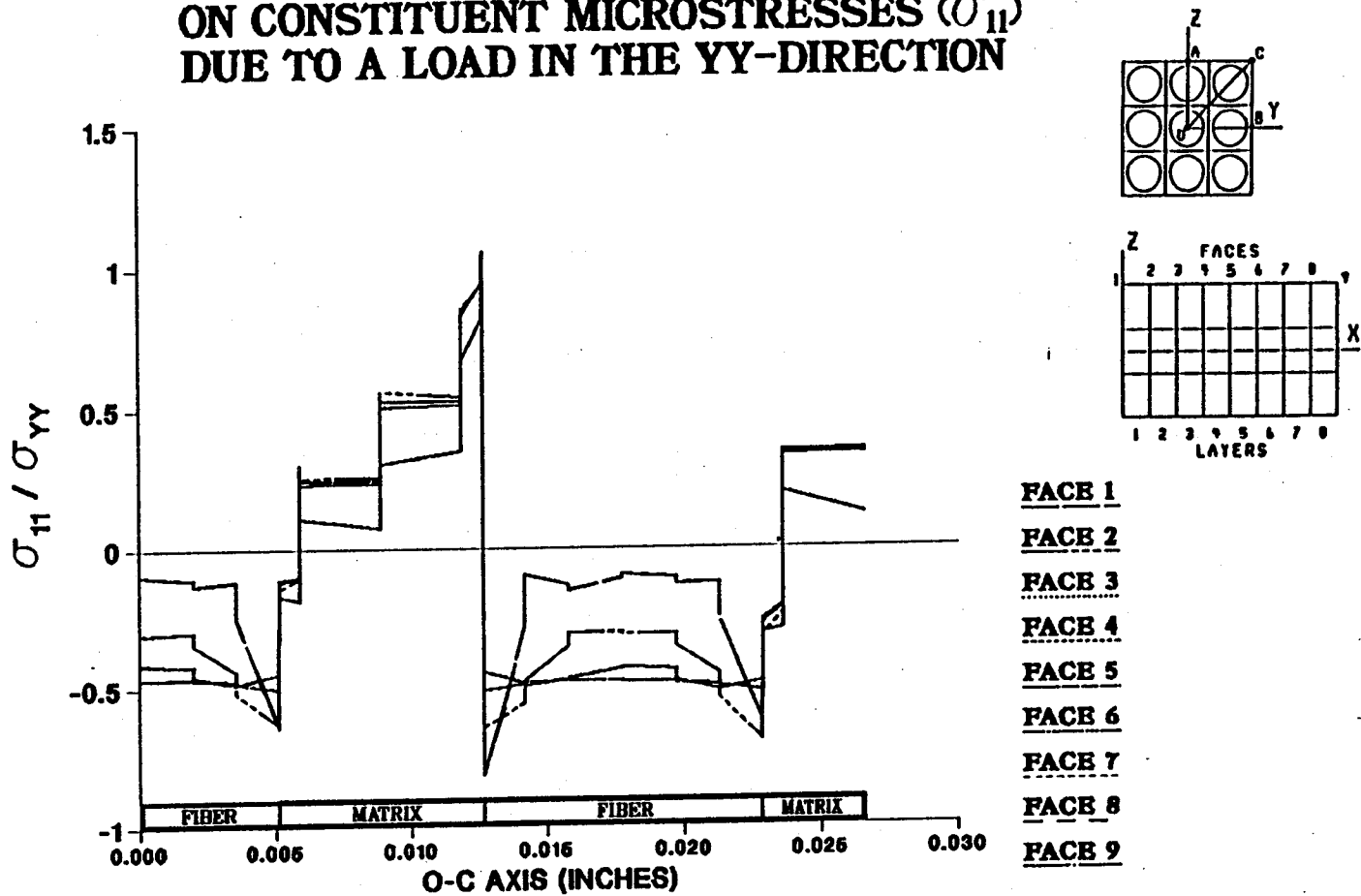


Figure A.64 - σ_{11} Normalized Microstresses, O-C Direction, 0.0% Debonding, σ_{yy}^e Loading

EFFECT OF 1.39% FIBER LENGTH DEBONDING ON CONSTITUENT MICROSTRESSES (σ_{11}) DUE TO A LOAD IN THE YY-DIRECTION

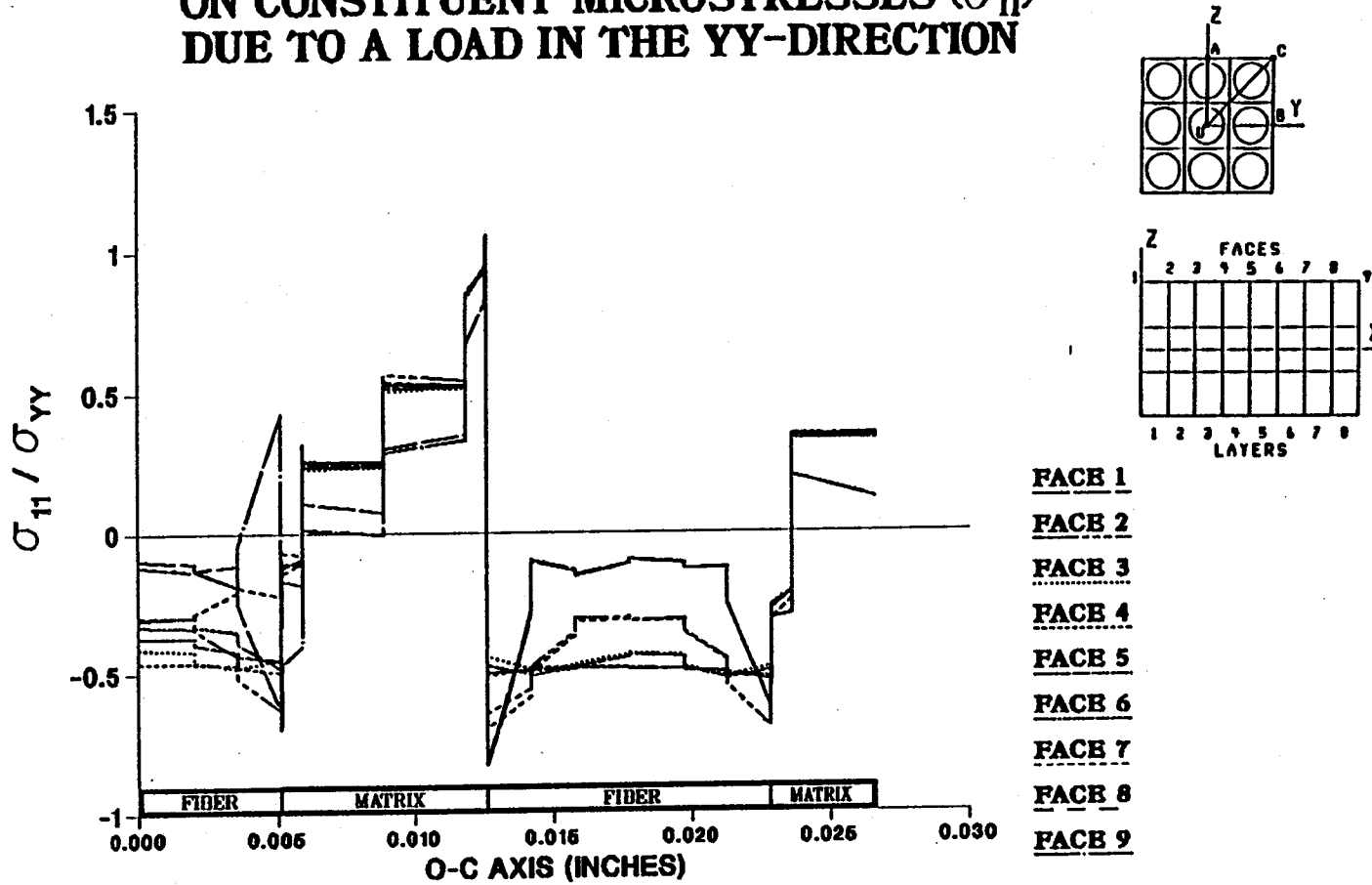
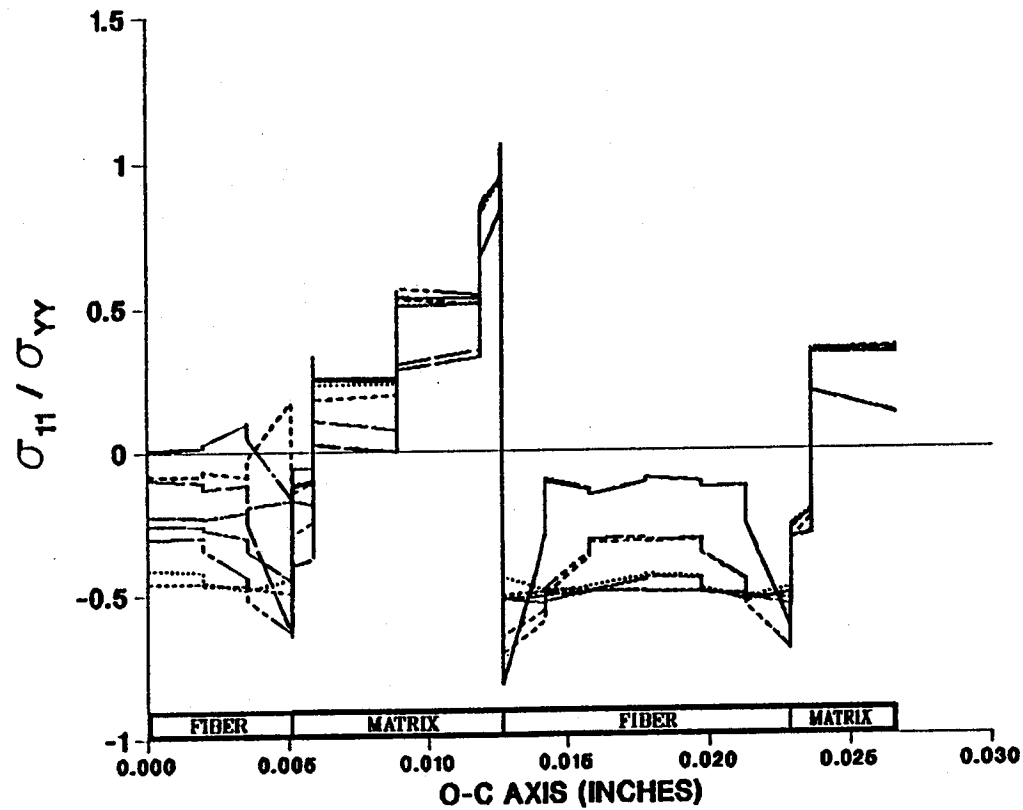
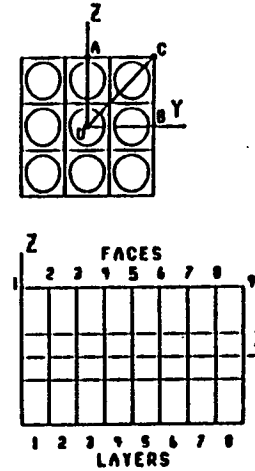


Figure A.65 — σ_{11} Normalized Microstresses, O-C Direction, 1.39% Debonding, σ_{yy}^e Loading

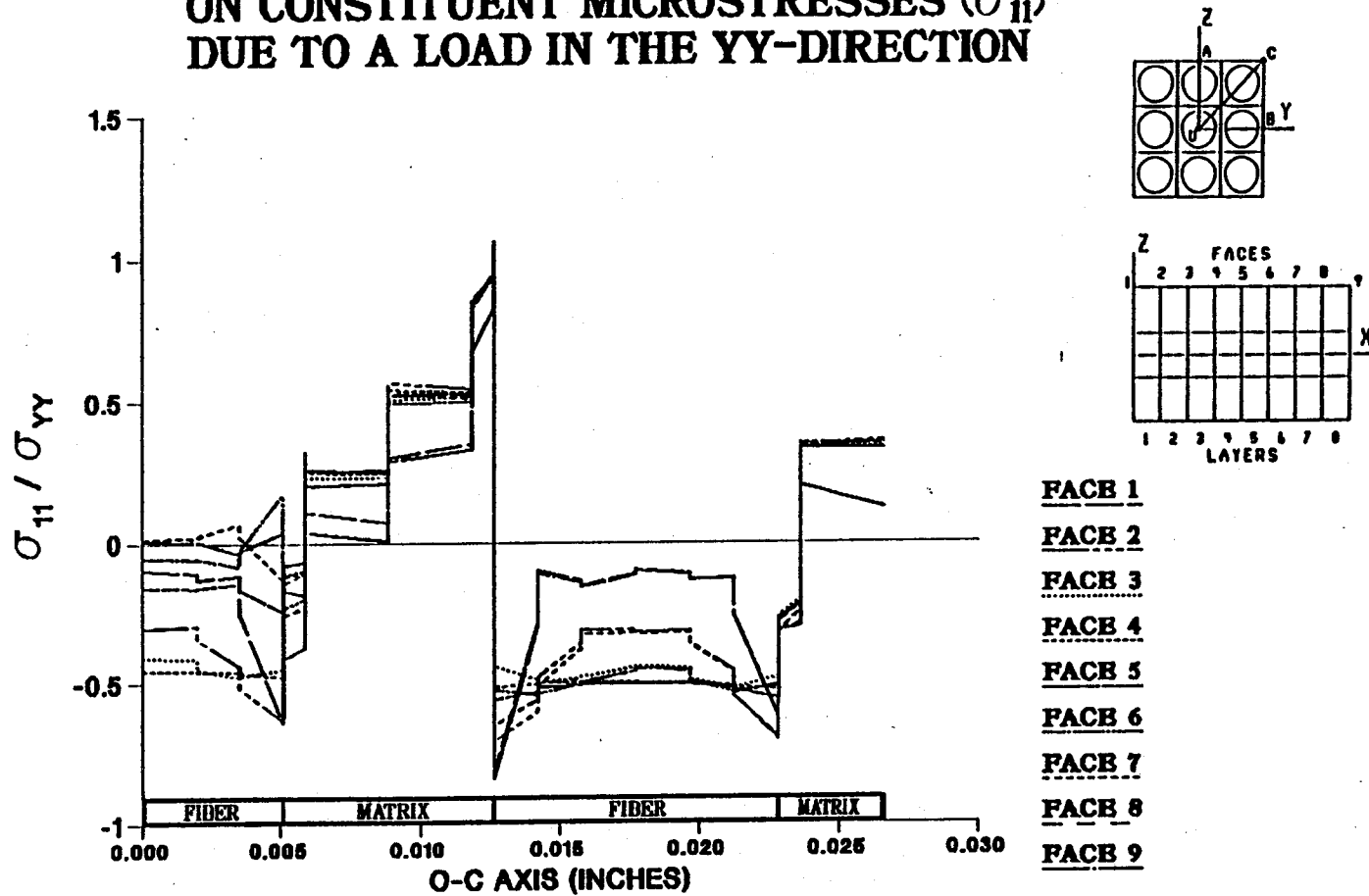
EFFECT OF 2.78% FIBER LENGTH DEBONDING ON CONSTITUENT MICROSTRESSES (σ_{11}) DUE TO A LOAD IN THE YY-DIRECTION



- FACE 1
- FACE 2
- FACE 3
- FACE 4
- FACE 5
- FACE 6
- FACE 7
- FACE 8
- FACE 9

Figure A.66 - σ_{11} Normalized Microstresses, O-C Direction, 2.78% Debonding, σ_{yy}^e Loading

EFFECT OF 4.17% FIBER LENGTH DEBONDING ON CONSTITUENT MICROSTRESSES (σ_{11}) DUE TO A LOAD IN THE YY-DIRECTION



- FACE 1
- FACE 2
- FACE 3
- FACE 4
- FACE 5
- FACE 6
- FACE 7
- FACE 8
- FACE 9

Figure A.67 - σ_{11} Normalized Microstresses, O-C Direction, 4.17% Debonding, σ_{yy}^e Loading

EFFECT OF 5.56% FIBER LENGTH DEBONDING ON CONSTITUENT MICROSTRESSES (σ_{11}) DUE TO A LOAD IN THE YY-DIRECTION

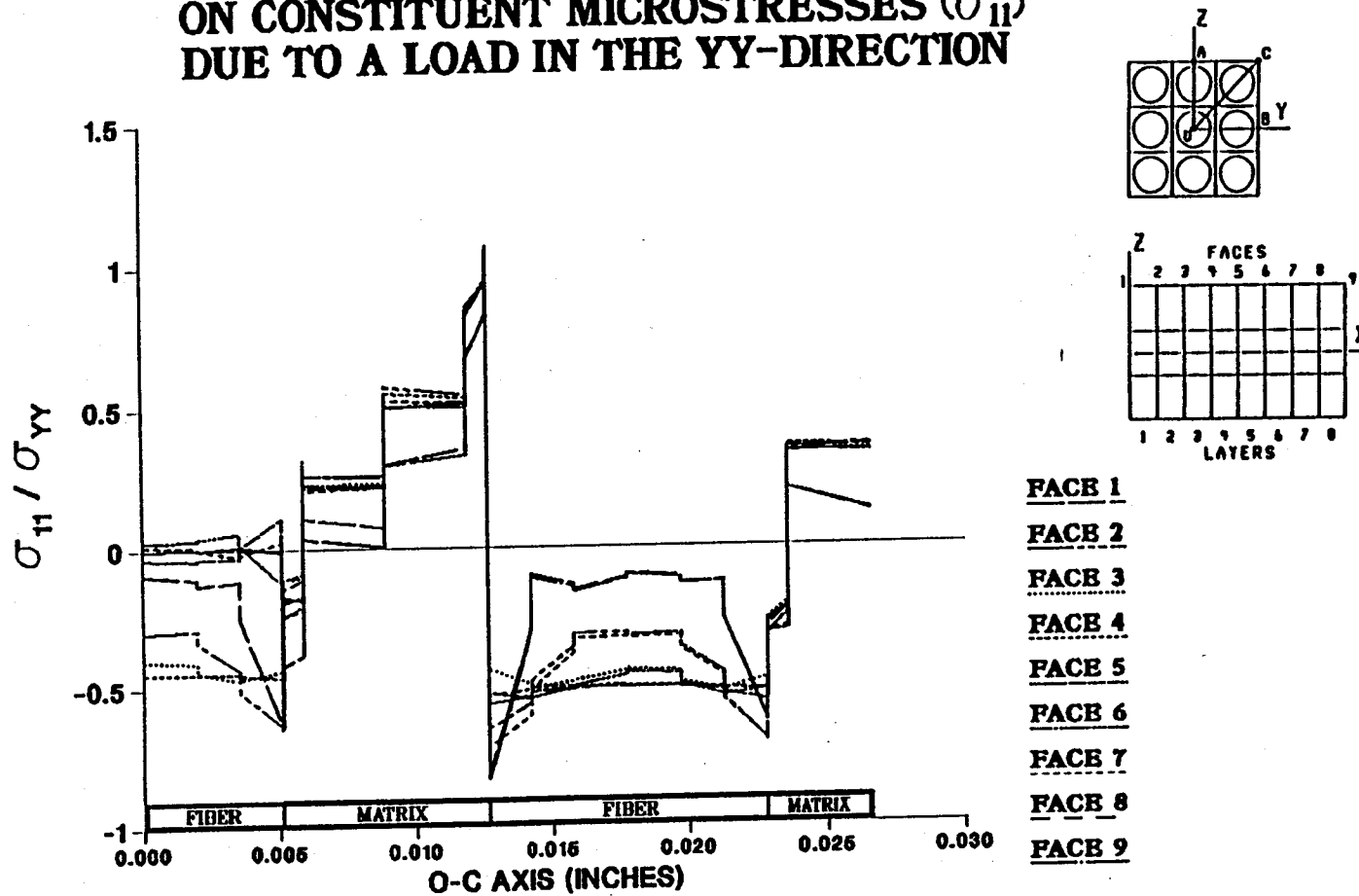


Figure A.68 – σ_{11} Normalized Microstresses, O–C Direction, 5.56% Debonding, σ_{yy}^e Loading

EFFECT OF 6.94% FIBER LENGTH DEBONDING ON CONSTITUENT MICROSTRESSES (σ_{11}) DUE TO A LOAD IN THE YY-DIRECTION

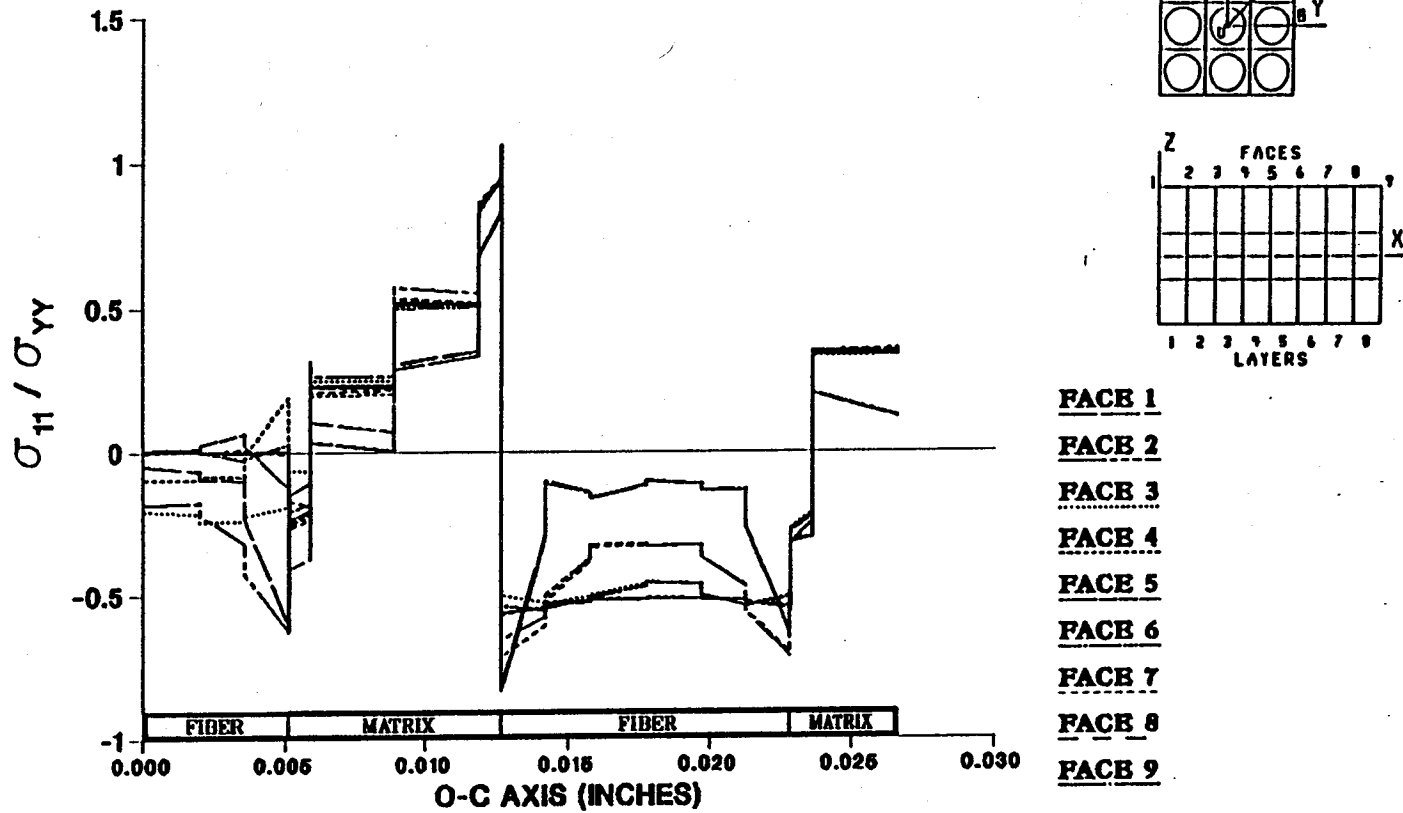


Figure A.69 - σ_{11} Normalized Microstresses, O-C Direction, 6.94% Debonding, σ_{yy}^e Loading

EFFECT OF 8.33% FIBER LENGTH DEBONDING ON CONSTITUENT MICROSTRESSES (σ_{11}) DUE TO A LOAD IN THE YY-DIRECTION

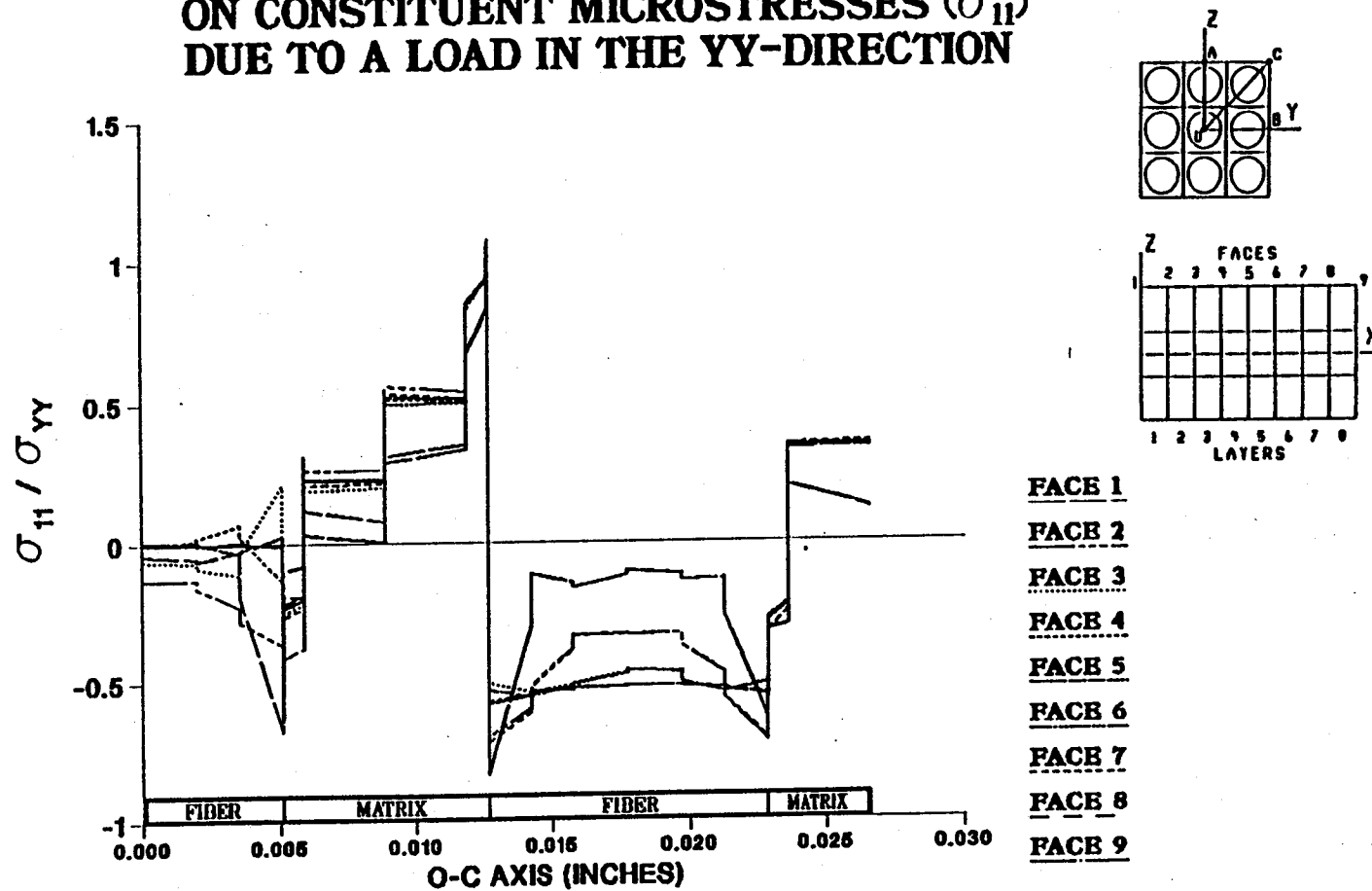


Figure A.70 - σ_{11} Normalized Microstresses, O-C Direction, 8.33% Debonding, σ_{yy}^e Loading

EFFECT OF 9.72% FIBER LENGTH DEBONDING ON CONSTITUENT MICROSTRESSES (σ_{11}) DUE TO A LOAD IN THE YY-DIRECTION

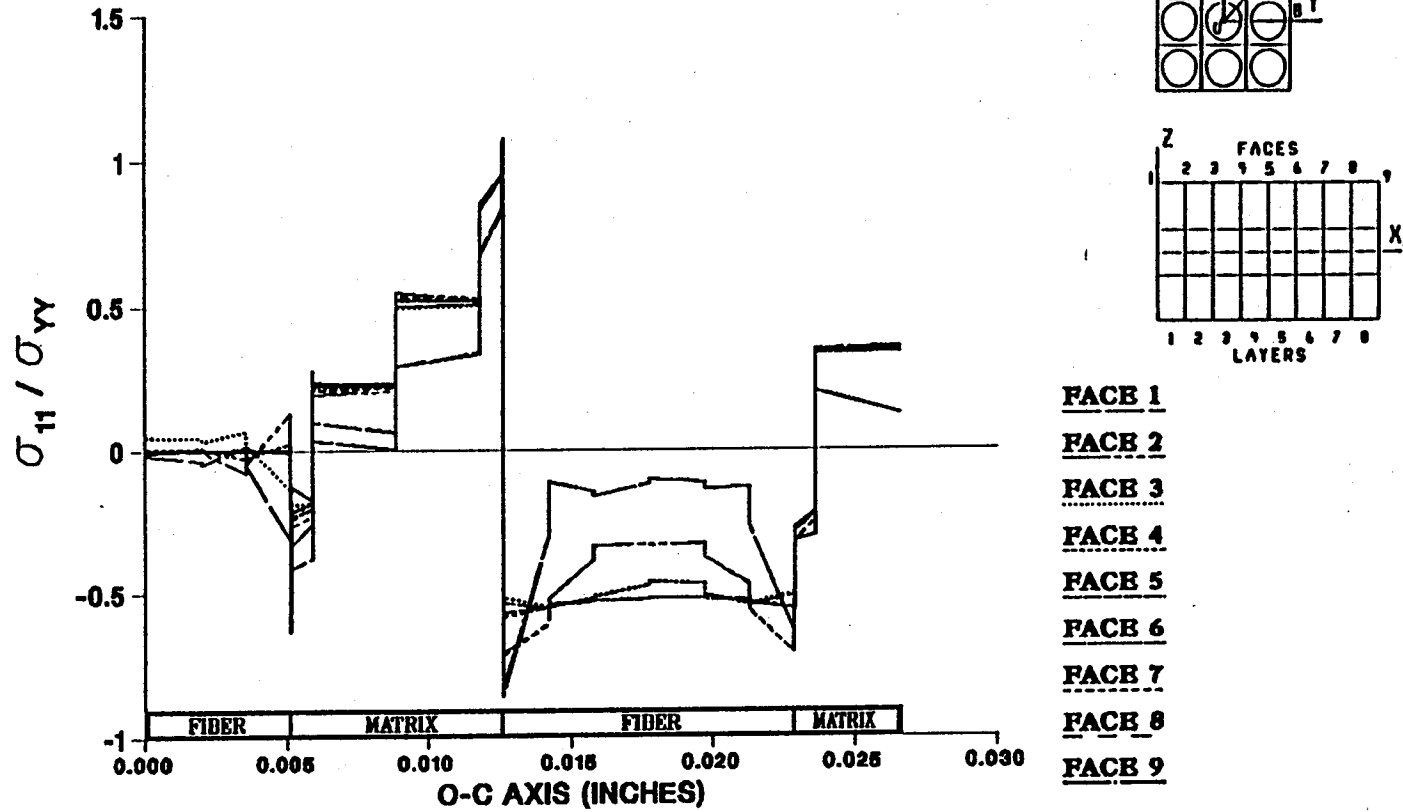
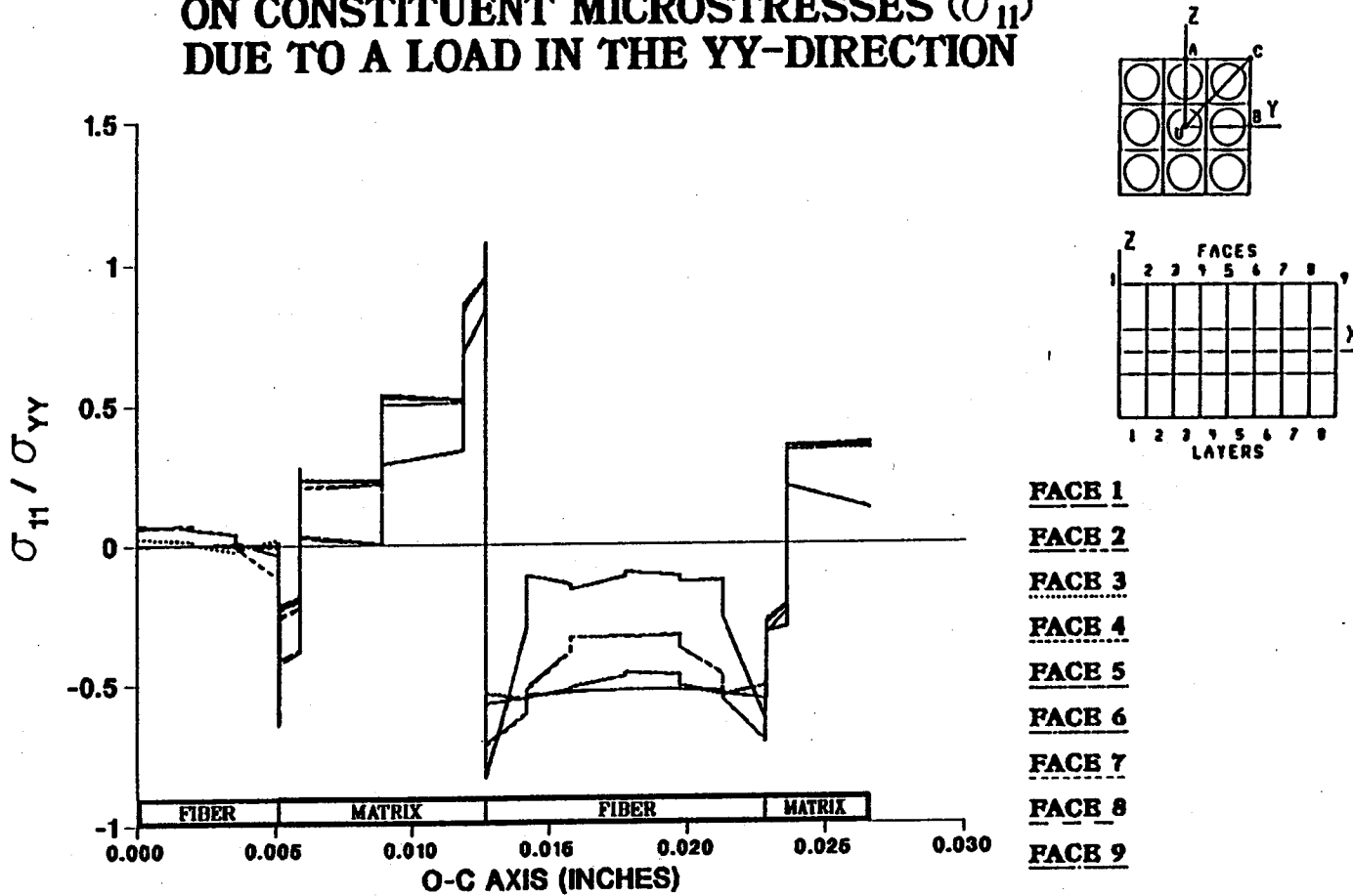


Figure A.71 - σ_{11} Normalized Microstresses, O-C Direction, 9.72% Debonding, σ_{yy}^e Loading

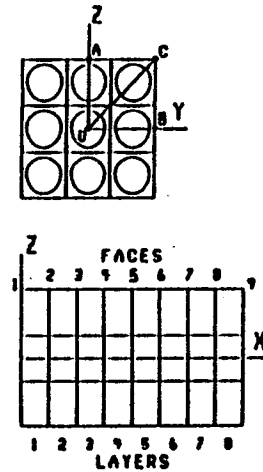
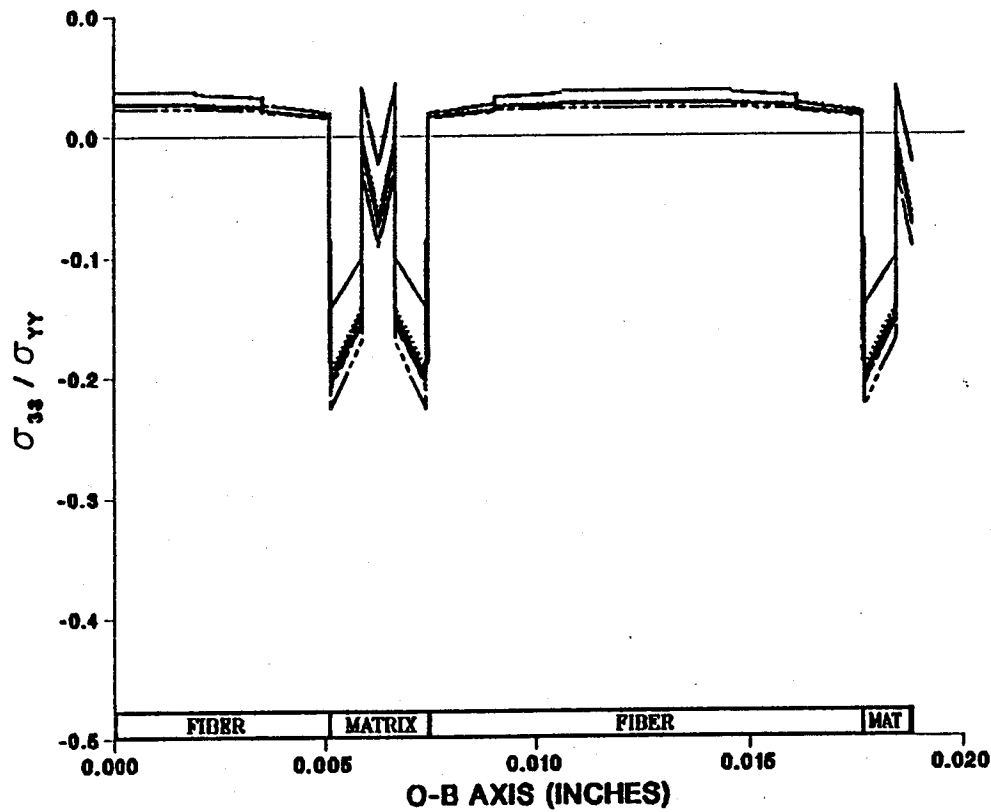
EFFECT OF 11.1% FIBER LENGTH DEBONDING ON CONSTITUENT MICROSTRESSES (σ_{11}) DUE TO A LOAD IN THE YY-DIRECTION



- FACE 1
- FACE 2
- FACE 3
- FACE 4
- FACE 5
- FACE 6
- FACE 7
- FACE 8
- FACE 9

Figure A.72 - σ_{11} Normalized Microstresses, O-C Direction, 11.1% Debonding, σ_{yy}^e Loading

EFFECT OF 0.0% FIBER LENGTH DEBONDING ON CONSTITUENT MICROSTRESSES (σ_{33}) DUE TO A LOAD IN THE YY-DIRECTION



- FACE 1
- FACE 2
- FACE 3
- FACE 4
- FACE 5
- FACE 6
- FACE 7
- FACE 8
- FACE 9

Figure A.73 - σ_{33} Normalized Microstresses, O-B Direction, 0.0% Debonding, σ_{yy}^e Loading

EFFECT OF 1.39% FIBER LENGTH DEBONDING ON CONSTITUENT MICROSTRESSES (σ_{33}) DUE TO A LOAD IN THE YY-DIRECTION

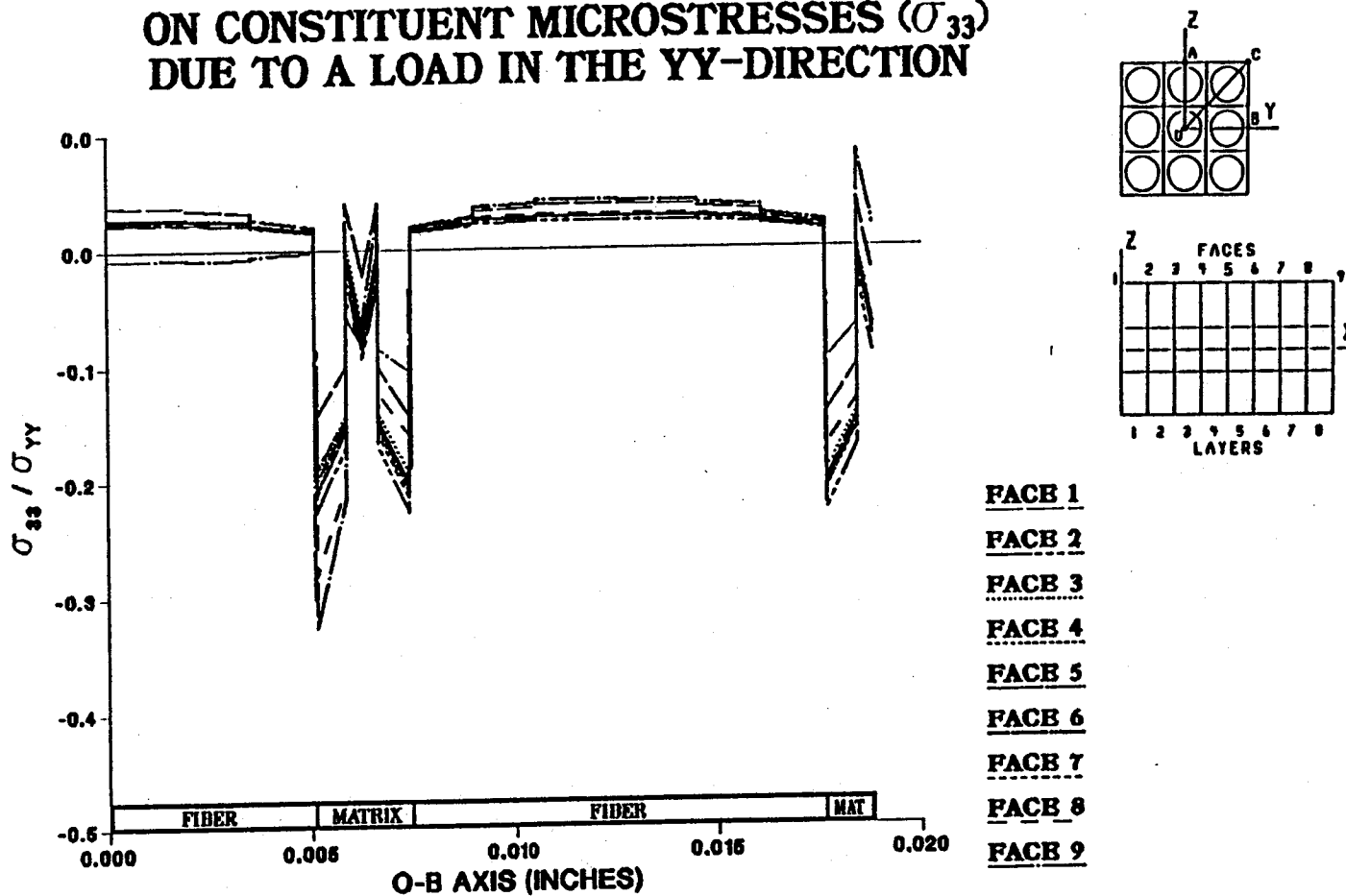
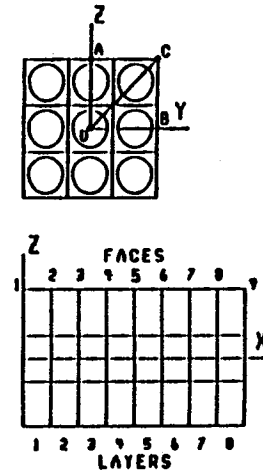
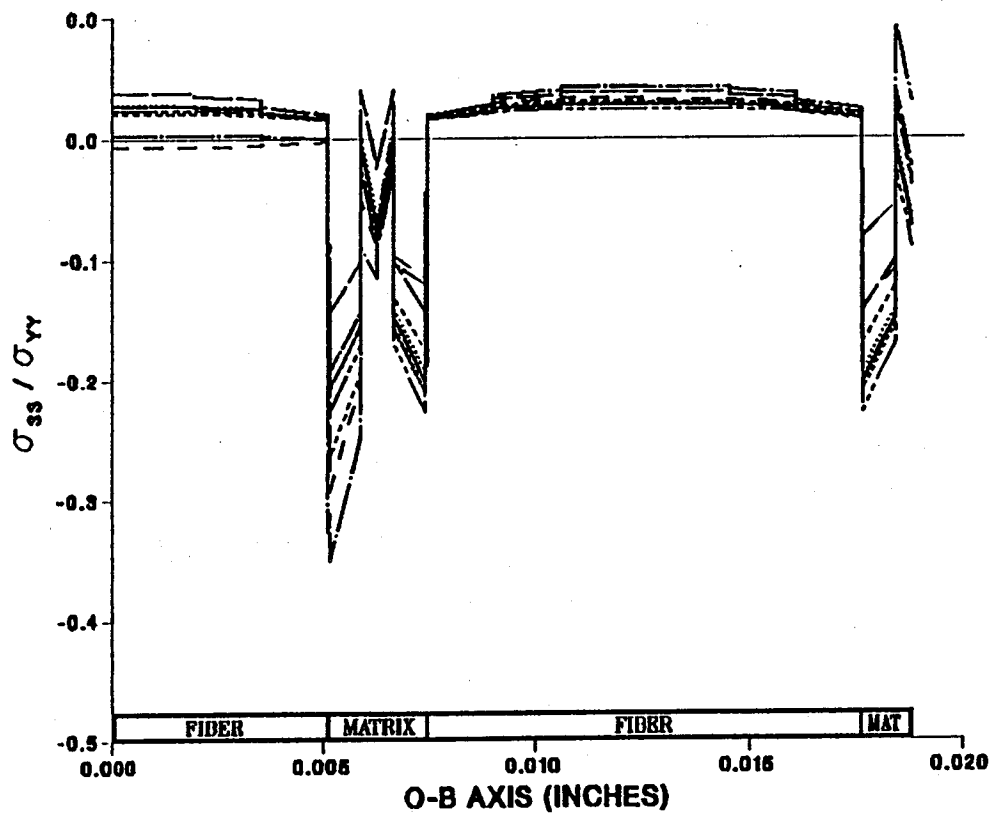


Figure A.74 - σ_{33} Normalized Microstresses, O-B Direction, 1.39% Debonding, σ_{yy}^e Loading

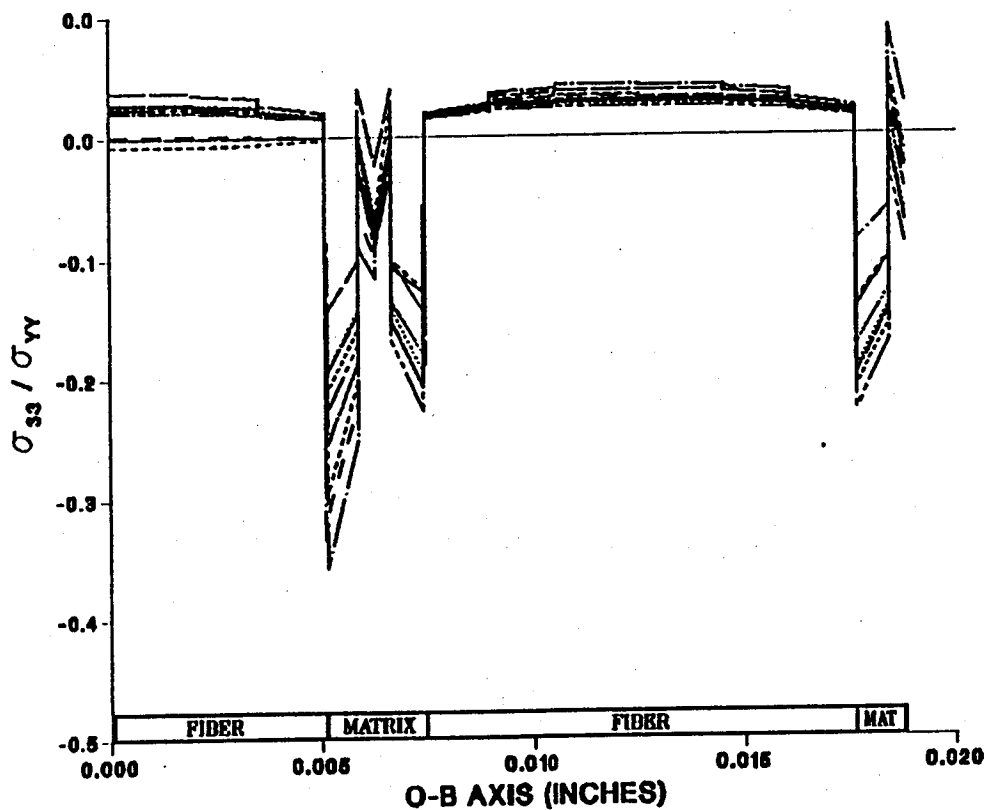
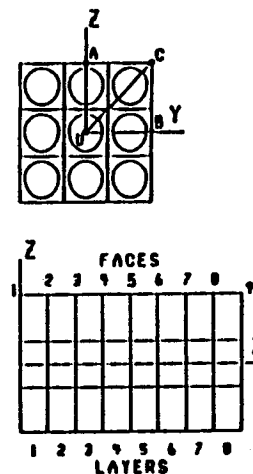
EFFECT OF 2.78% FIBER LENGTH DEBONDING ON CONSTITUENT MICROSTRESSES (σ_{33}) DUE TO A LOAD IN THE YY-DIRECTION



- FACE 1
- FACE 2
- FACE 3
- FACE 4
- FACE 5
- FACE 6
- FACE 7
- FACE 8
- FACE 9

Figure A.75 - σ_{33} Normalized Microstresses, O-B Direction, 2.78% Debonding, σ_{yy}^e Loading

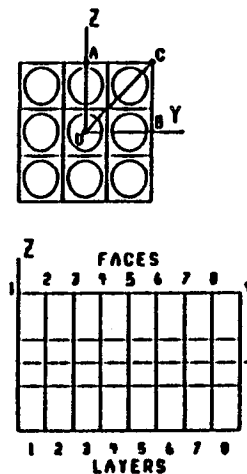
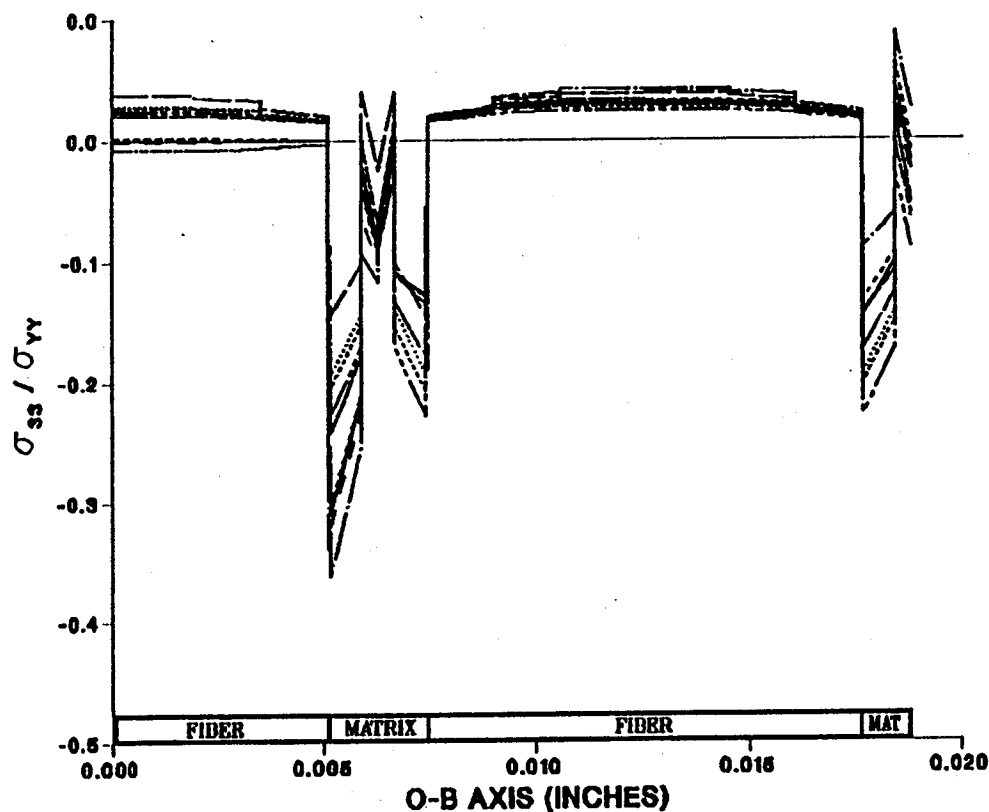
EFFECT OF 4.17% FIBER LENGTH DEBONDING ON CONSTITUENT MICROSTRESSES (σ_{33}) DUE TO A LOAD IN THE YY-DIRECTION



- FACE 1
- FACE 2
- FACE 3
- FACE 4
- FACE 5
- FACE 6
- FACE 7
- FACE 8
- FACE 9

Figure A.76 — σ_{33} Normalized Microstresses, O-B Direction, 4.17% Debonding, σ_{yy}^e Loading

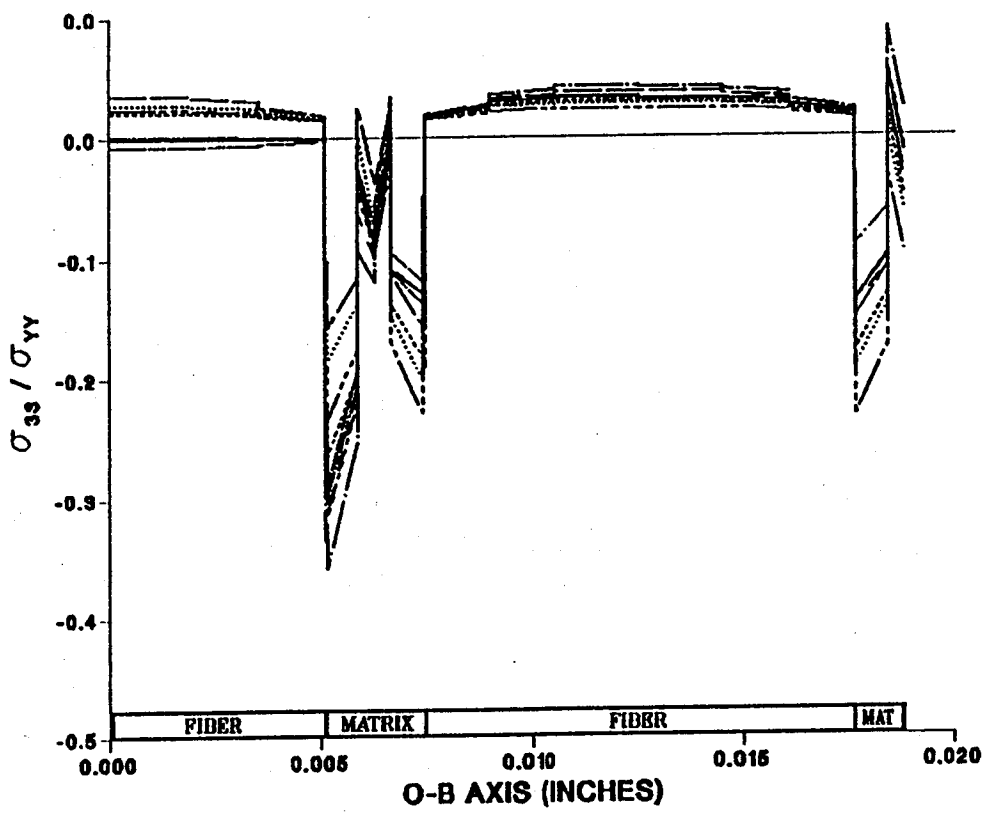
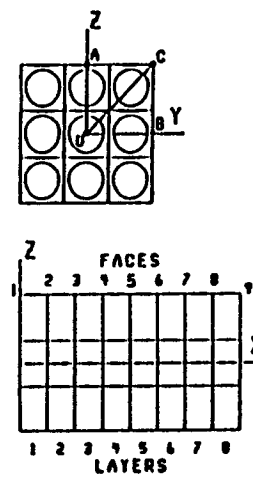
EFFECT OF 5.56% FIBER LENGTH DEBONDING ON CONSTITUENT MICROSTRESSES (σ_{33}) DUE TO A LOAD IN THE YY-DIRECTION



- FACE 1
- FACE 2
- FACE 3
- FACE 4
- FACE 5
- FACE 6
- FACE 7
- FACE 8
- FACE 9

Figure A.77 - σ_{33} Normalized Microstresses, O-B Direction, 5.56% Debonding, σ_{yy}^e Loading

EFFECT OF 6.94% FIBER LENGTH DEBONDING ON CONSTITUENT MICROSTRESSES (σ_{33}) DUE TO A LOAD IN THE YY-DIRECTION

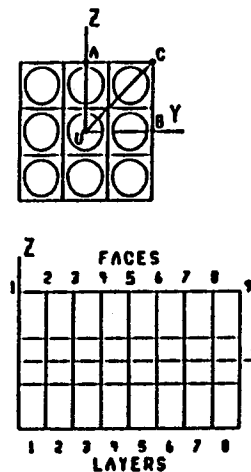
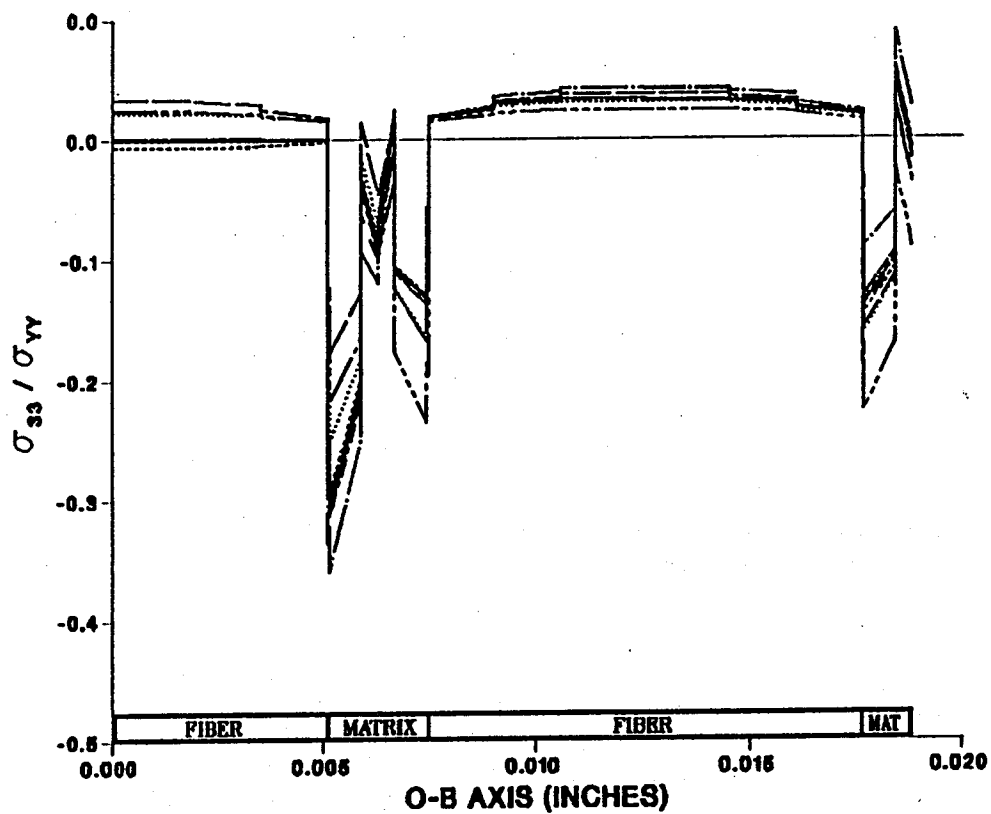


- FACE 1
- FACE 2
- FACE 3
- FACE 4
- FACE 5
- FACE 6
- FACE 7
- FACE 8
- FACE 9

264

Figure A.78 - σ_{33} Normalized Microstresses, O-B Direction, 6.94% Debonding, σ_{yy}^e Loading

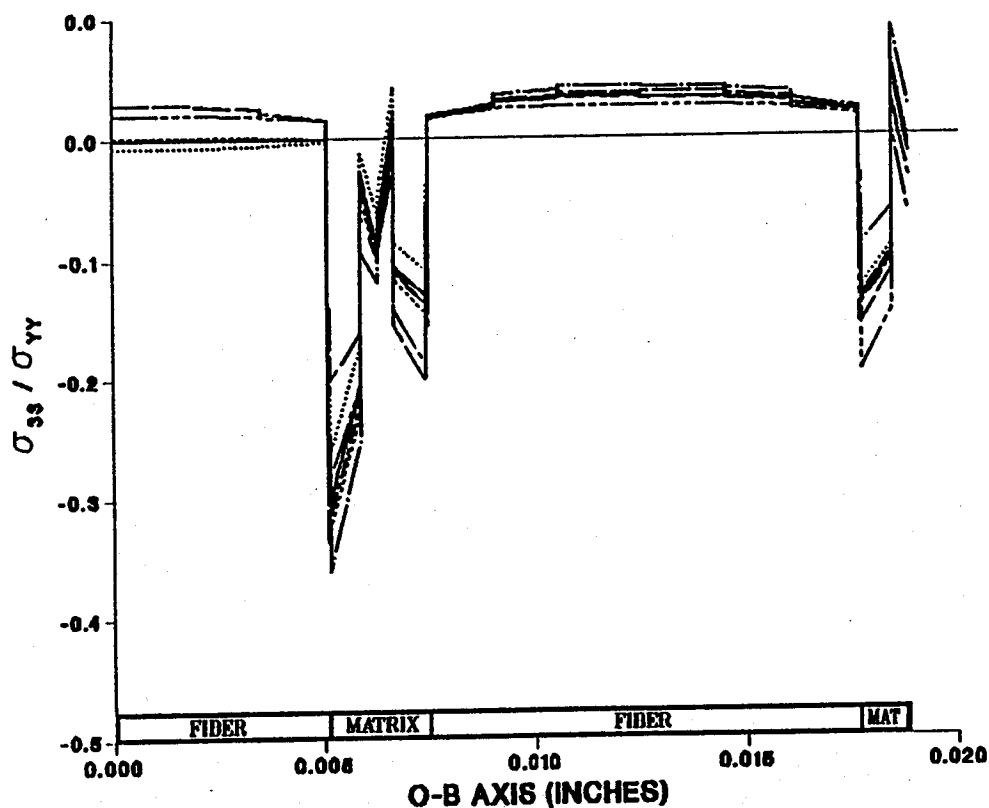
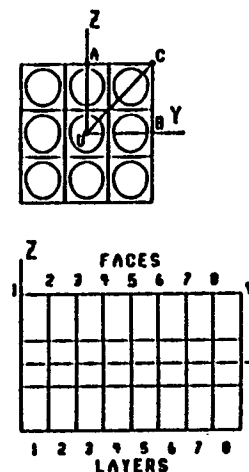
EFFECT OF 8.33% FIBER LENGTH DEBONDING ON CONSTITUENT MICROSTRESSES (σ_{33}) DUE TO A LOAD IN THE YY-DIRECTION



- FACE 1
- FACE 2
- FACE 3
- FACE 4
- FACE 5
- FACE 6
- FACE 7
- FACE 8
- FACE 9

Figure A.79 -- σ_{33} Normalized Microstresses, O-B Direction, 8.33% Debonding, σ_{yy}^e Loading

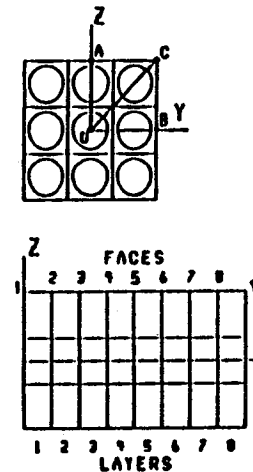
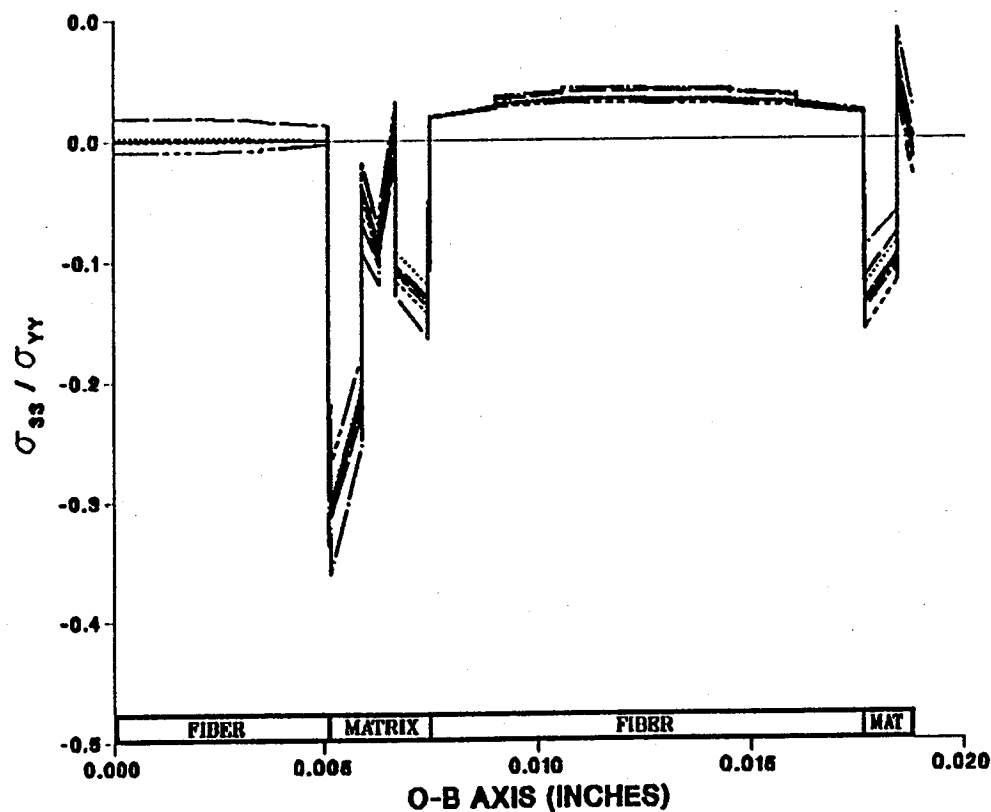
EFFECT OF 9.72% FIBER LENGTH DEBONDING ON CONSTITUENT MICROSTRESSES (σ_{33}) DUE TO A LOAD IN THE YY-DIRECTION



- FACE 1
- FACE 2
- FACE 3
- FACE 4
- FACE 5
- FACE 6
- FACE 7
- FACE 8
- FACE 9

Figure A.80 - σ_{33} Normalized Microstresses, O-B Direction, 9.72% Debonding, σ_{yy}^e Loading

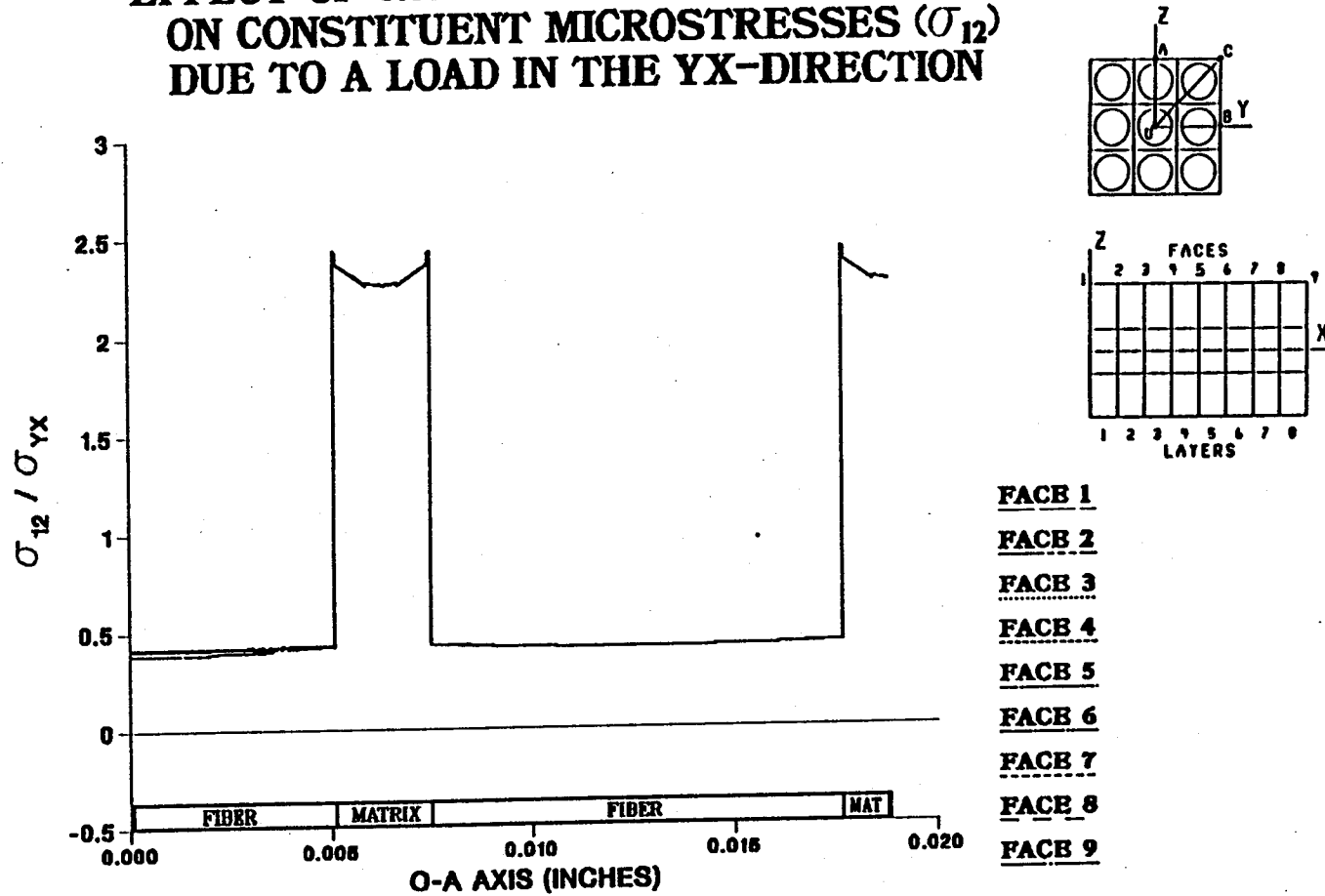
EFFECT OF 11.1% FIBER LENGTH DEBONDING ON CONSTITUENT MICROSTRESSES (σ_{33}) DUE TO A LOAD IN THE YY-DIRECTION



- FACE 1
- FACE 2
- FACE 3
- FACE 4
- FACE 5
- FACE 6
- FACE 7
- FACE 8
- FACE 9

Figure A.81 - σ_{33} Normalized Microstresses, O-B Direction, 11.1% Debonding, σ_{yy}^e Loading

EFFECT OF 0.0% FIBER LENGTH DEBONDING ON CONSTITUENT MICROSTRESSES (σ_{12}) DUE TO A LOAD IN THE YX-DIRECTION



- FACE 1
- FACE 2
- FACE 3
- FACE 4
- FACE 5
- FACE 6
- FACE 7
- FACE 8
- FACE 9

Figure A.82 - σ_{12} Normalized Microstresses, O-A Direction, 0.0% Debonding, σ_{yx}^e Loading

EFFECT OF 1.39% FIBER LENGTH DEBONDING ON CONSTITUENT MICROSTRESSES (σ_{12}) DUE TO A LOAD IN THE YX-DIRECTION

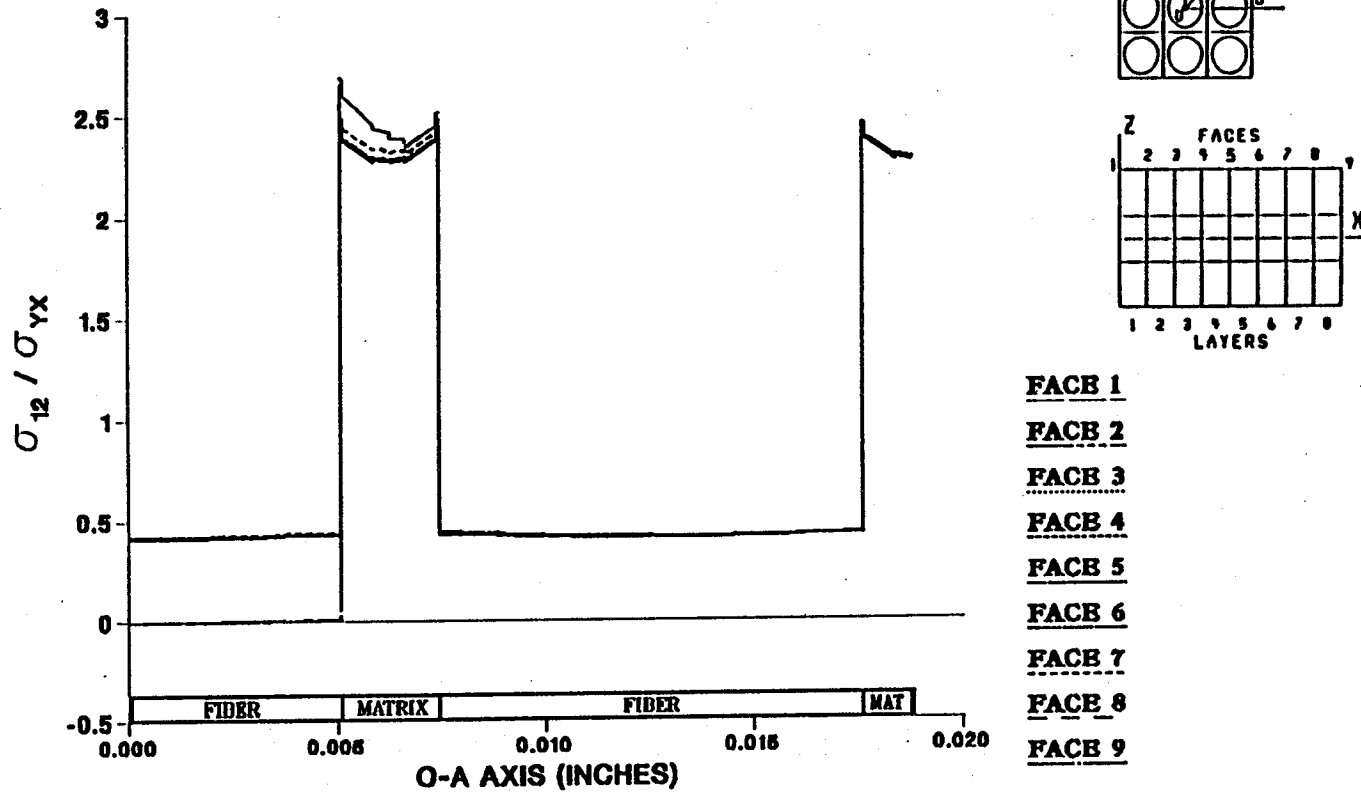


Figure A.83 - σ_{12} Normalized Microstresses, O-A Direction, 1.39% Debonding, σ_{yx}^e Loading

EFFECT OF 2.78% FIBER LENGTH DEBONDING ON CONSTITUENT MICROSTRESSES (σ_{12}) DUE TO A LOAD IN THE YX-DIRECTION

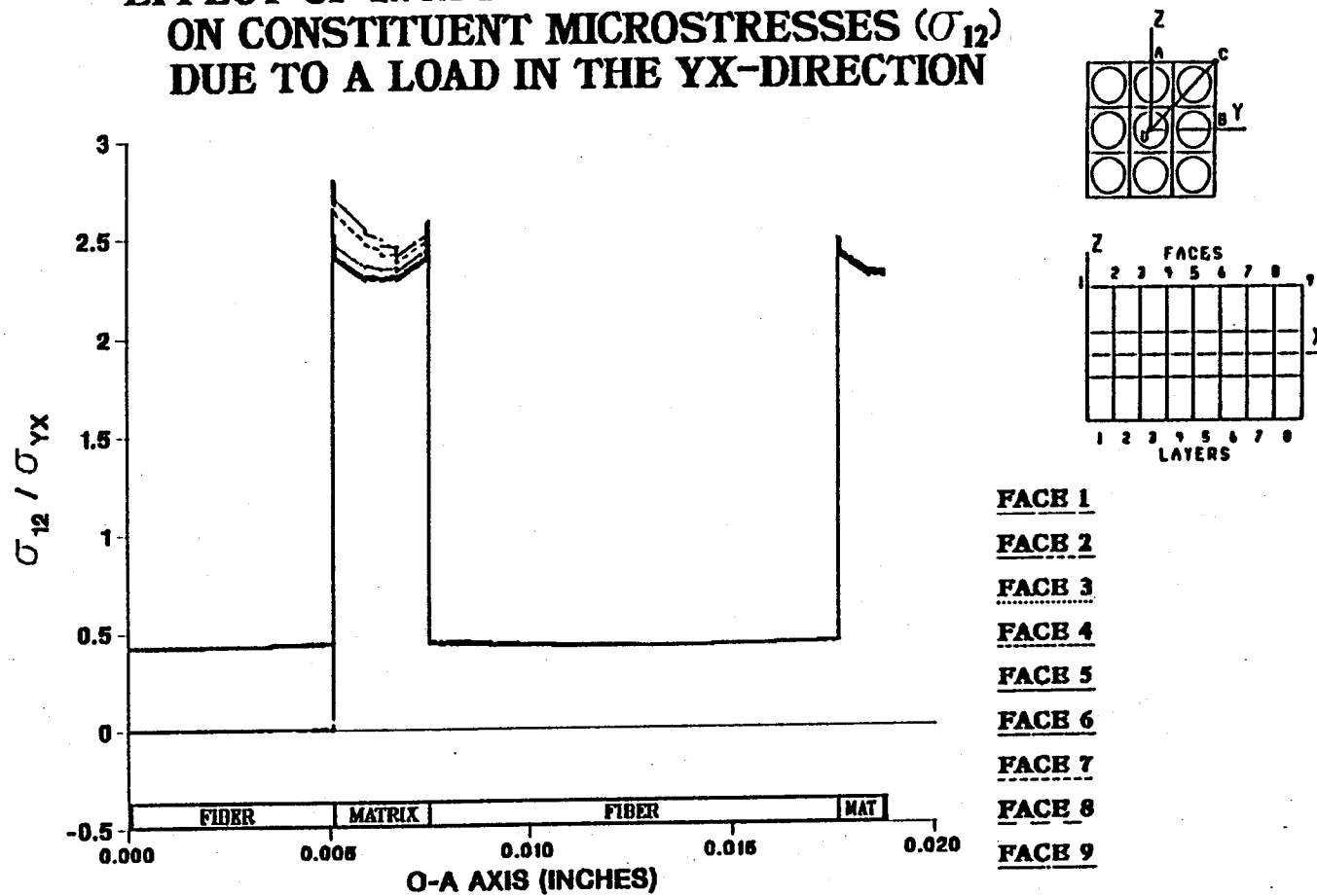


Figure A.84 — σ_{12} Normalized Microstresses, O-A Direction, 2.78% Debonding, σ_{yx}^e Loading

EFFECT OF 4.17% FIBER LENGTH DEBONDING ON CONSTITUENT MICROSTRESSES (σ_{12}) DUE TO A LOAD IN THE YX-DIRECTION

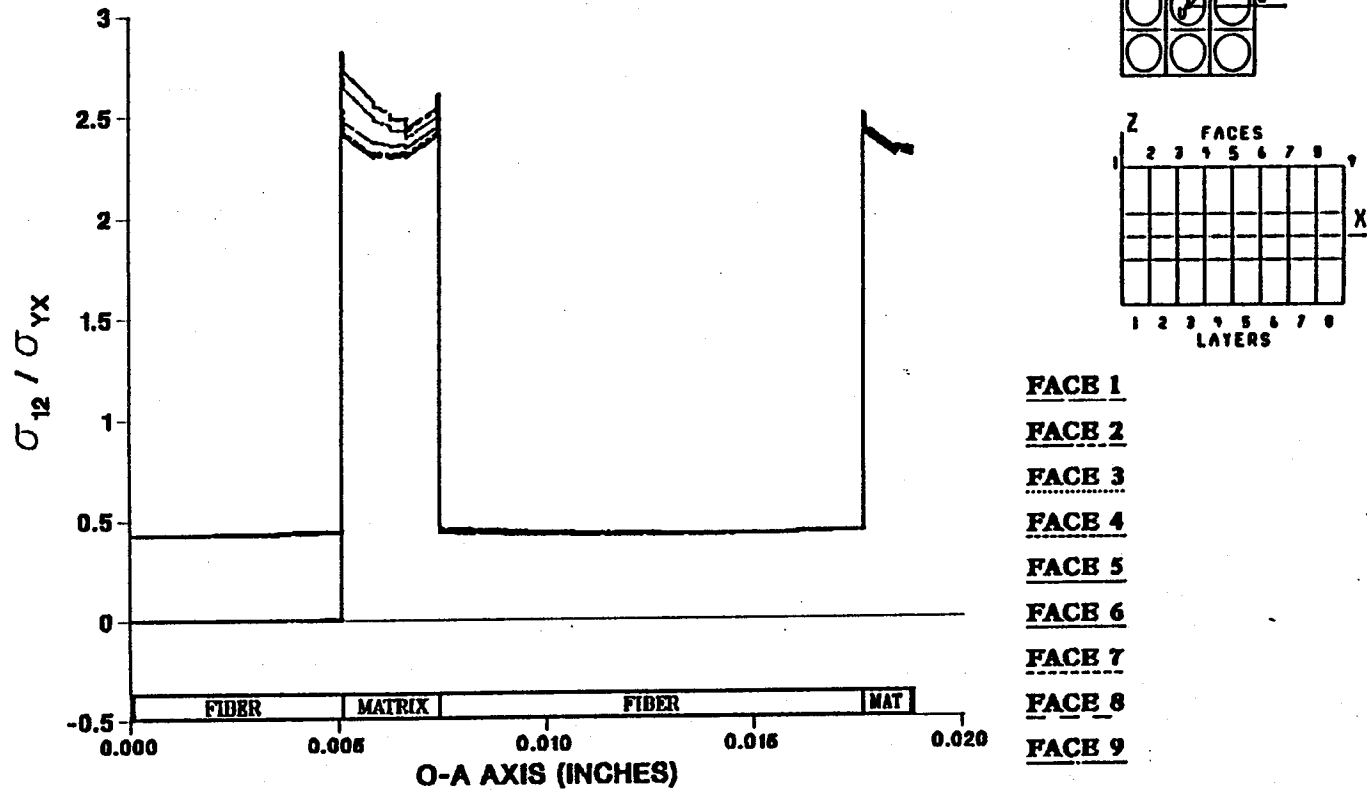


Figure A.85 — σ_{12} Normalized Microstresses, O-A Direction, 4.17% Debonding, σ_{yx}^c Loading

EFFECT OF 5.56% FIBER LENGTH DEBONDING ON CONSTITUENT MICROSTRESSES (σ_{12}) DUE TO A LOAD IN THE YX-DIRECTION

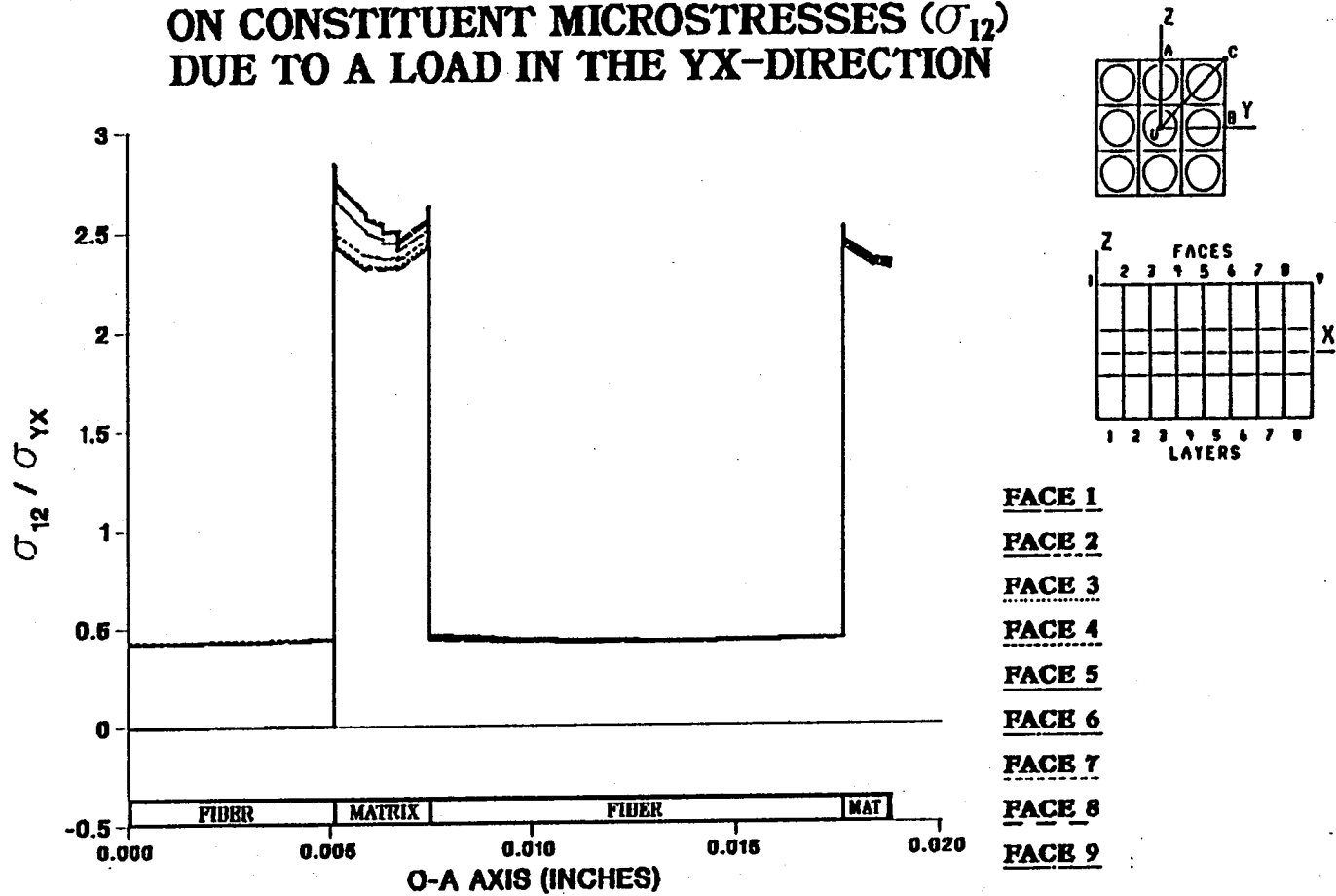
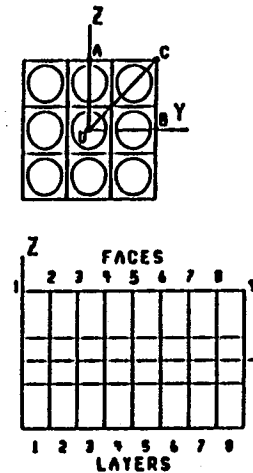
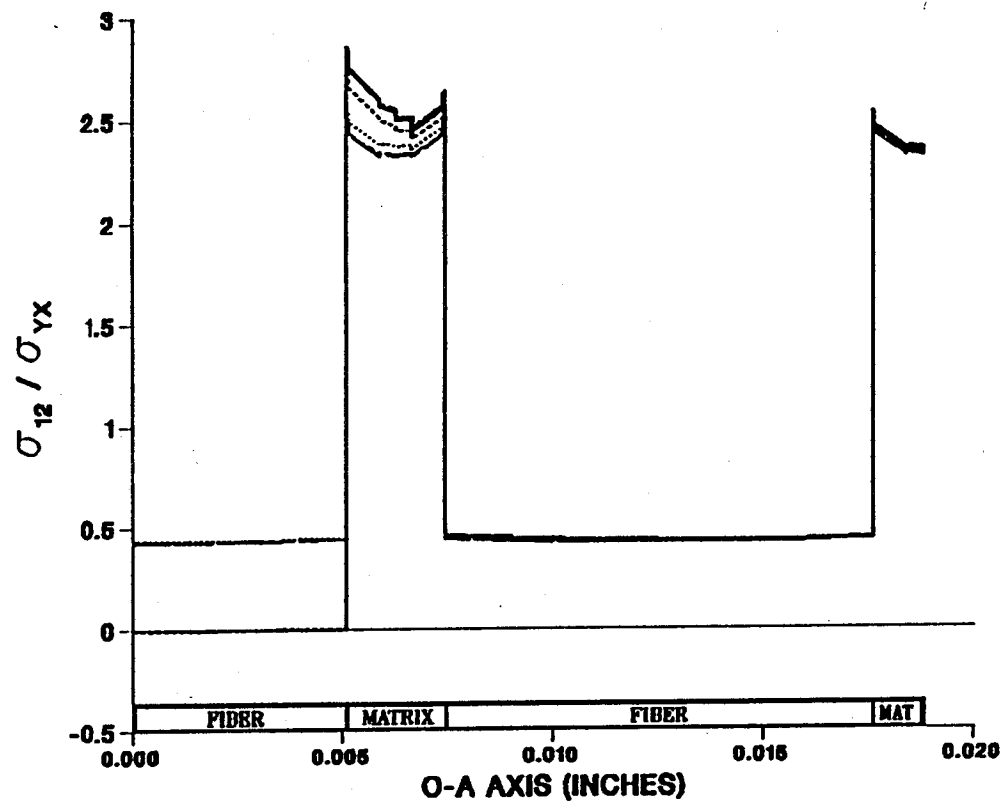


Figure A.86 - σ_{12} Normalized Microstresses, O-A Direction, 5.56% Debonding, σ_{yx}^e Loading

EFFECT OF 6.94% FIBER LENGTH DEBONDING ON CONSTITUENT MICROSTRESSES (σ_{12}) DUE TO A LOAD IN THE YX-DIRECTION



- FACE 1
- FACE 2
- FACE 3
- FACE 4
- FACE 5
- FACE 6
- FACE 7
- FACE 8
- FACE 9

Figure A.87 - σ_{12} Normalized Microstresses, O-A Direction, 6.94% Debonding, σ_{yx}^e Loading

EFFECT OF 8.33% FIBER LENGTH DEBONDING ON CONSTITUENT MICROSTRESSES (σ_{12}) DUE TO A LOAD IN THE YX-DIRECTION

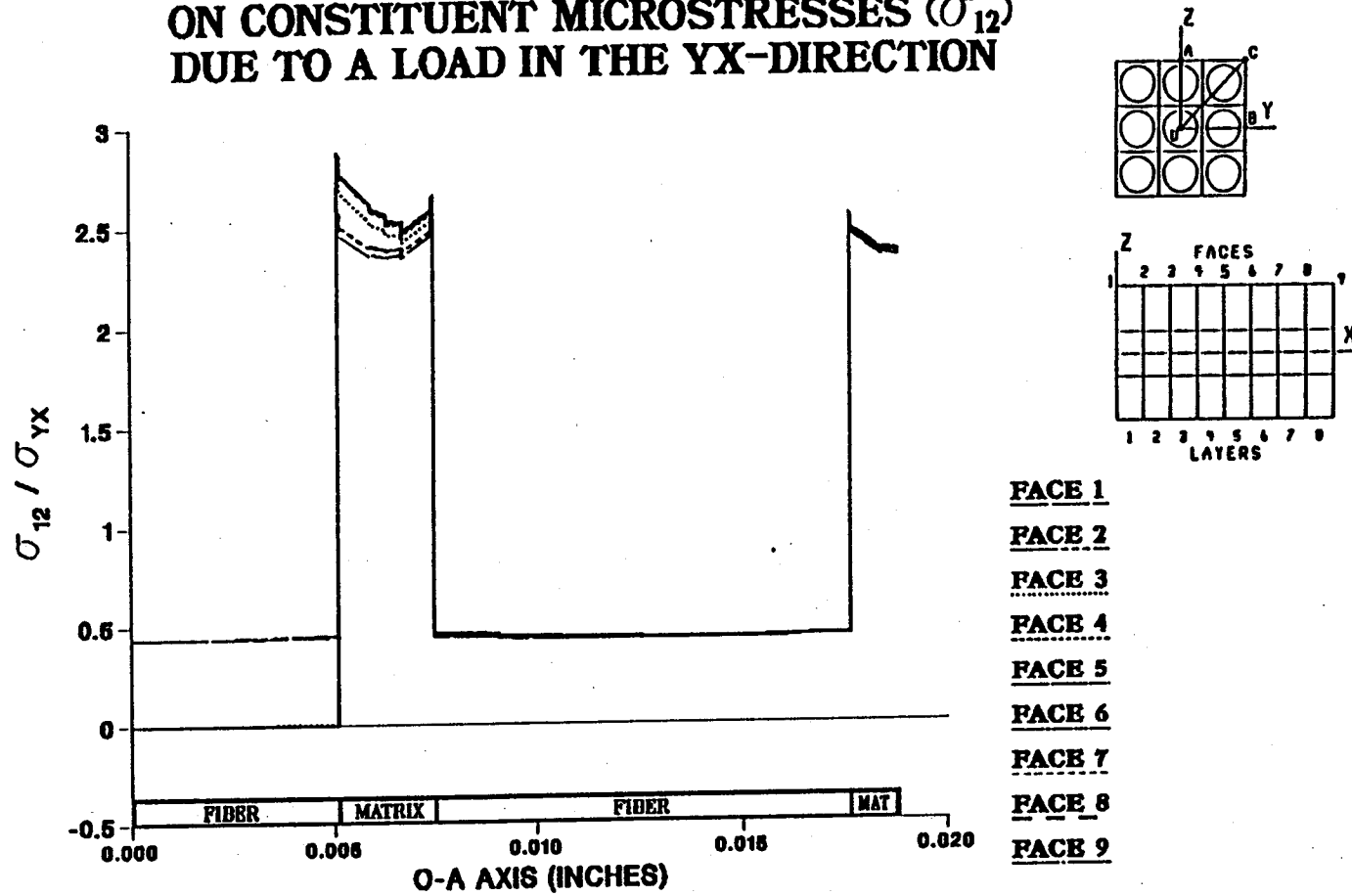


Figure A.88 - σ_{12} Normalized Microstresses, O-A Direction, 8.33% Debonding, σ_{yx}^e Loading

EFFECT OF 9.72% FIBER LENGTH DEBONDING ON CONSTITUENT MICROSTRESSES (σ_{12}) DUE TO A LOAD IN THE YX-DIRECTION

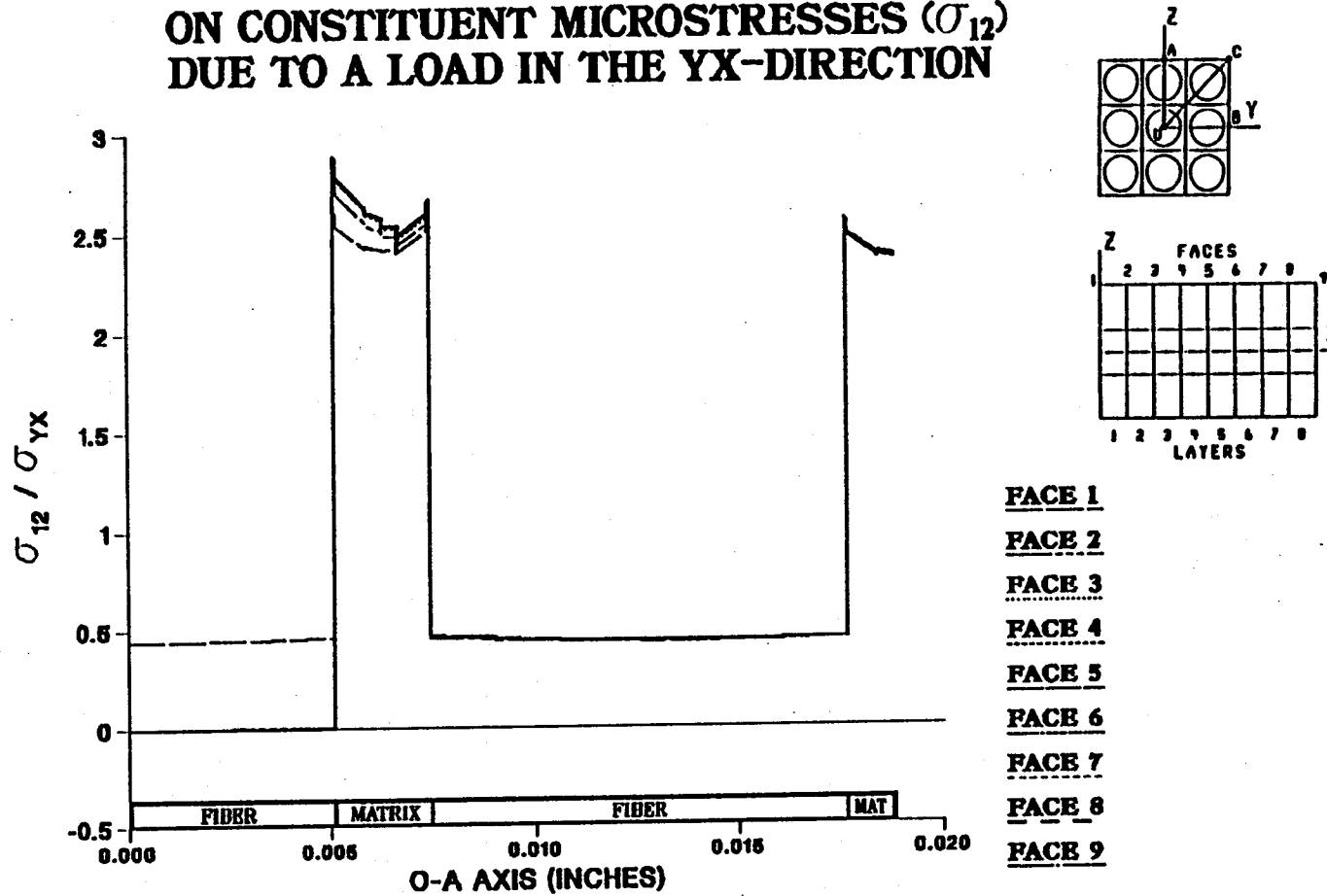


Figure A.89 - σ_{12} Normalized Microstresses, O-A Direction, 9.72% Debonding, σ_{yx}^e Loading

EFFECT OF 11.11% FIBER LENGTH DEBONDING ON CONSTITUENT MICROSTRESSES (σ_{12}) DUE TO A LOAD IN THE YX-DIRECTION

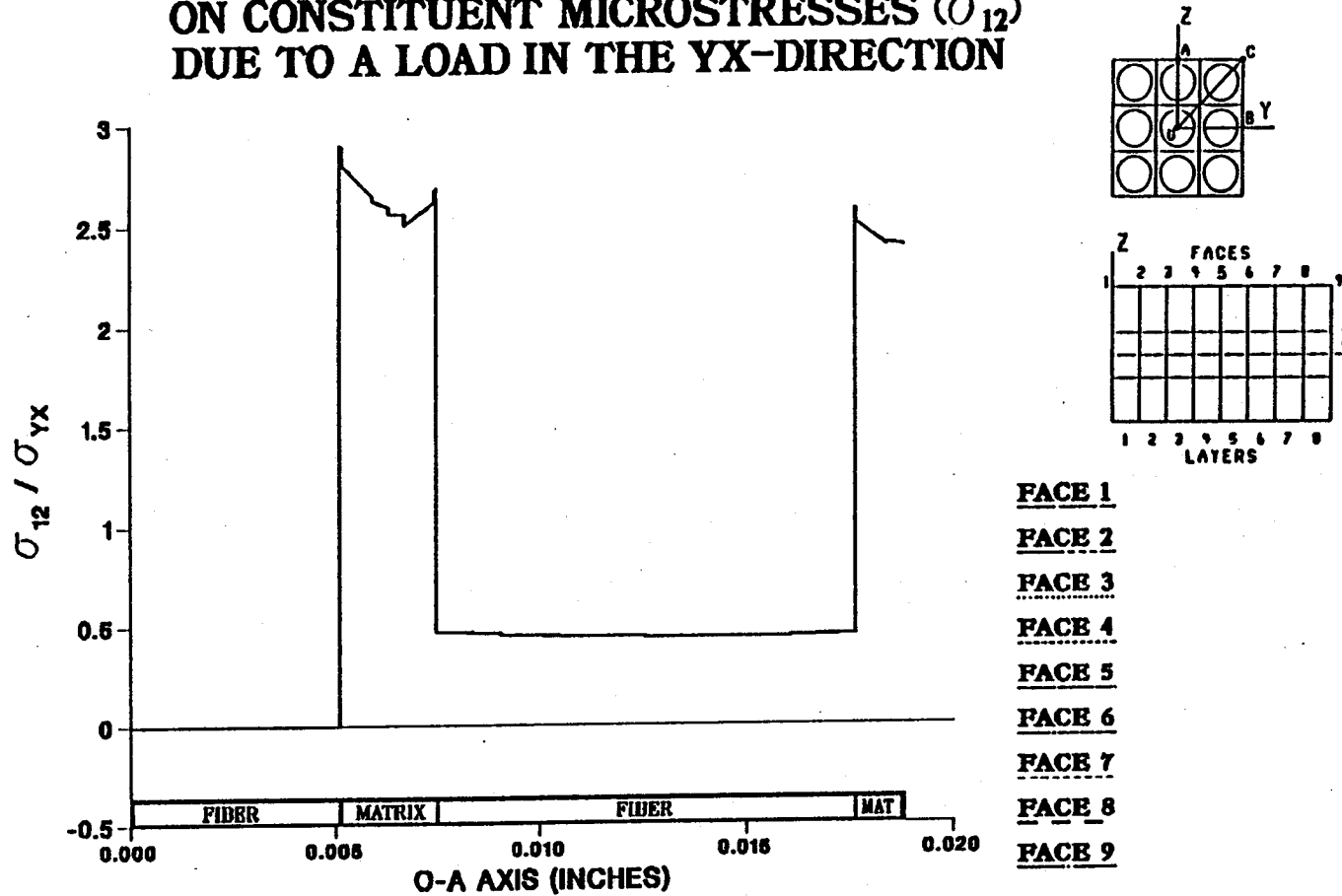
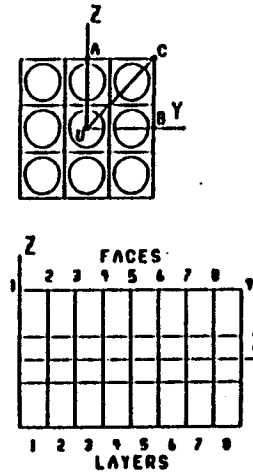
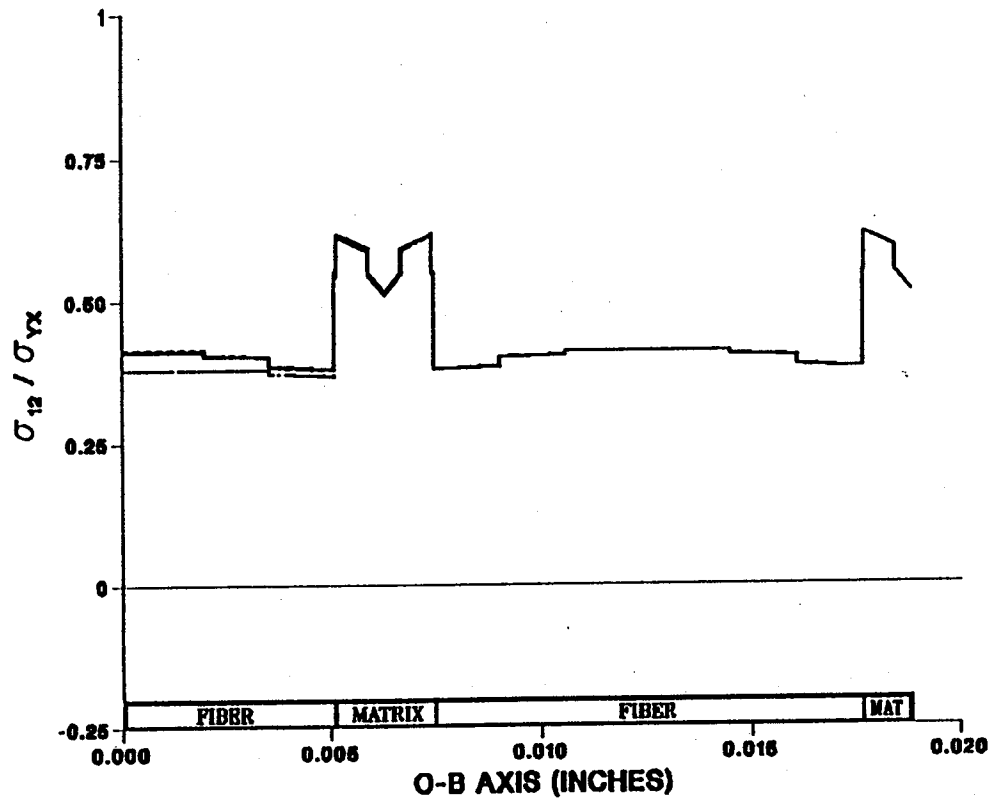


Figure A.90 - σ_{12} Normalized Microstresses, O-A Direction, 11.11% Debonding, σ_{yx}^e Loading

EFFECT OF 0.0% FIBER LENGTH DEBONDING ON CONSTITUENT MICROSTRESSES (σ_{12}) DUE TO A LOAD IN THE YX-DIRECTION



- FACE 1
- FACE 2
- FACE 3
- FACE 4
- FACE 5
- FACE 6
- FACE 7
- FACE 8
- FACE 9

Figure A.91 - σ_{12} Normalized Microstresses, O-B Direction, 0.0% Debonding, σ_{yx}^e Loading

EFFECT OF 1.39% FIBER LENGTH DEBONDING ON CONSTITUENT MICROSTRESSES (σ_{12}) DUE TO A LOAD IN THE YX-DIRECTION

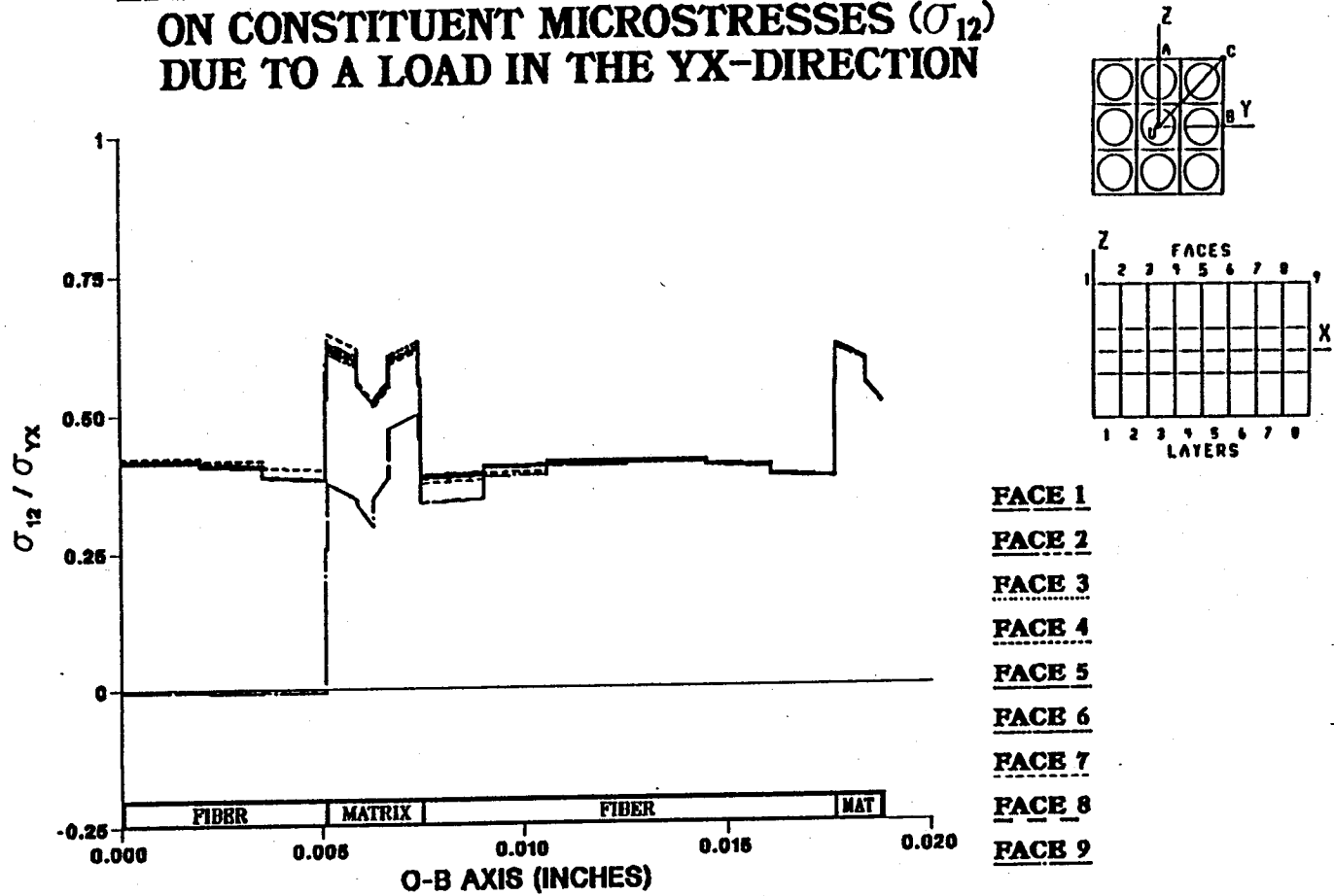
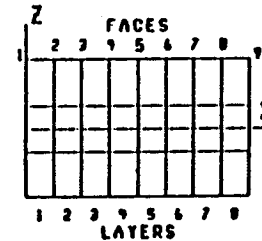
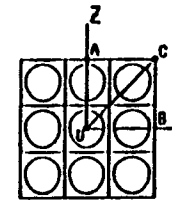
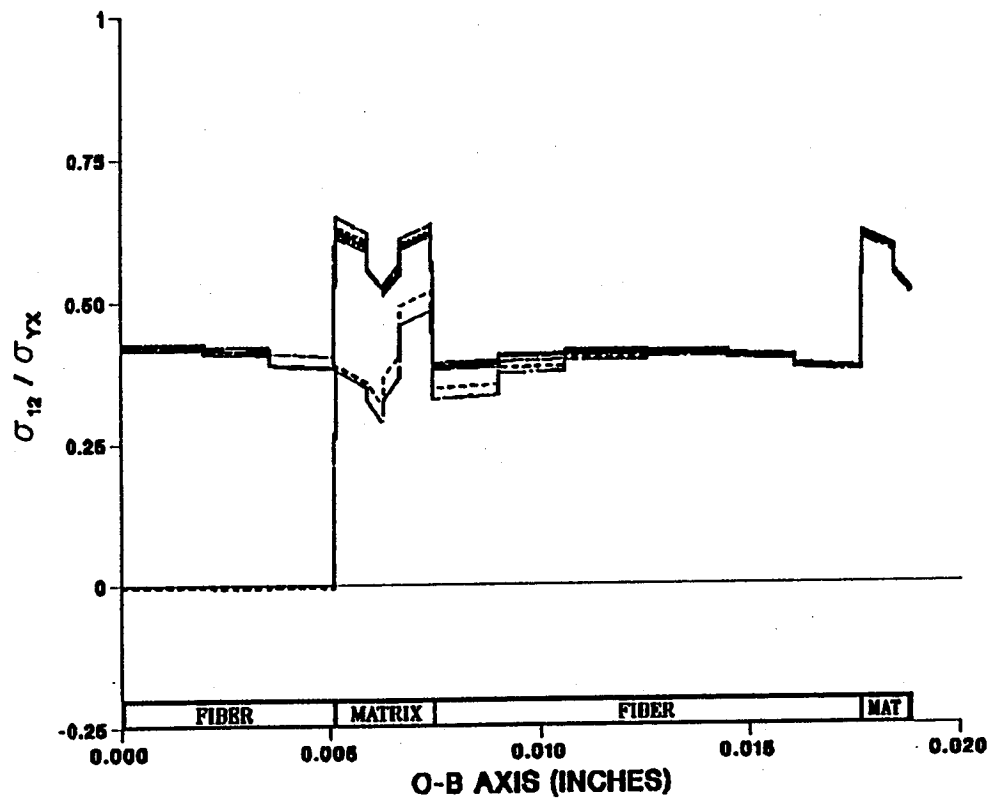


Figure A.92 – σ_{12} Normalized Microstresses, O–B Direction, 1.39% Debonding, σ_{yx}^e Loading

**EFFECT OF 2.78% FIBER LENGTH DEBONDING
ON CONSTITUENT MICROSTRESSES (σ_{12})
DUE TO A LOAD IN THE YX-DIRECTION**



FACE 1
FACE 2
FACE 3
FACE 4
FACE 5
FACE 6
FACE 7
FACE 8
FACE 9

Figure A.93 - σ_{12} Normalized Microstresses, O-B Direction, 2.78% Debonding, σ_{yx}^e Loading

EFFECT OF 4.17% FIBER LENGTH DEBONDING ON CONSTITUENT MICROSTRESSES (σ_{12}) DUE TO A LOAD IN THE YX-DIRECTION

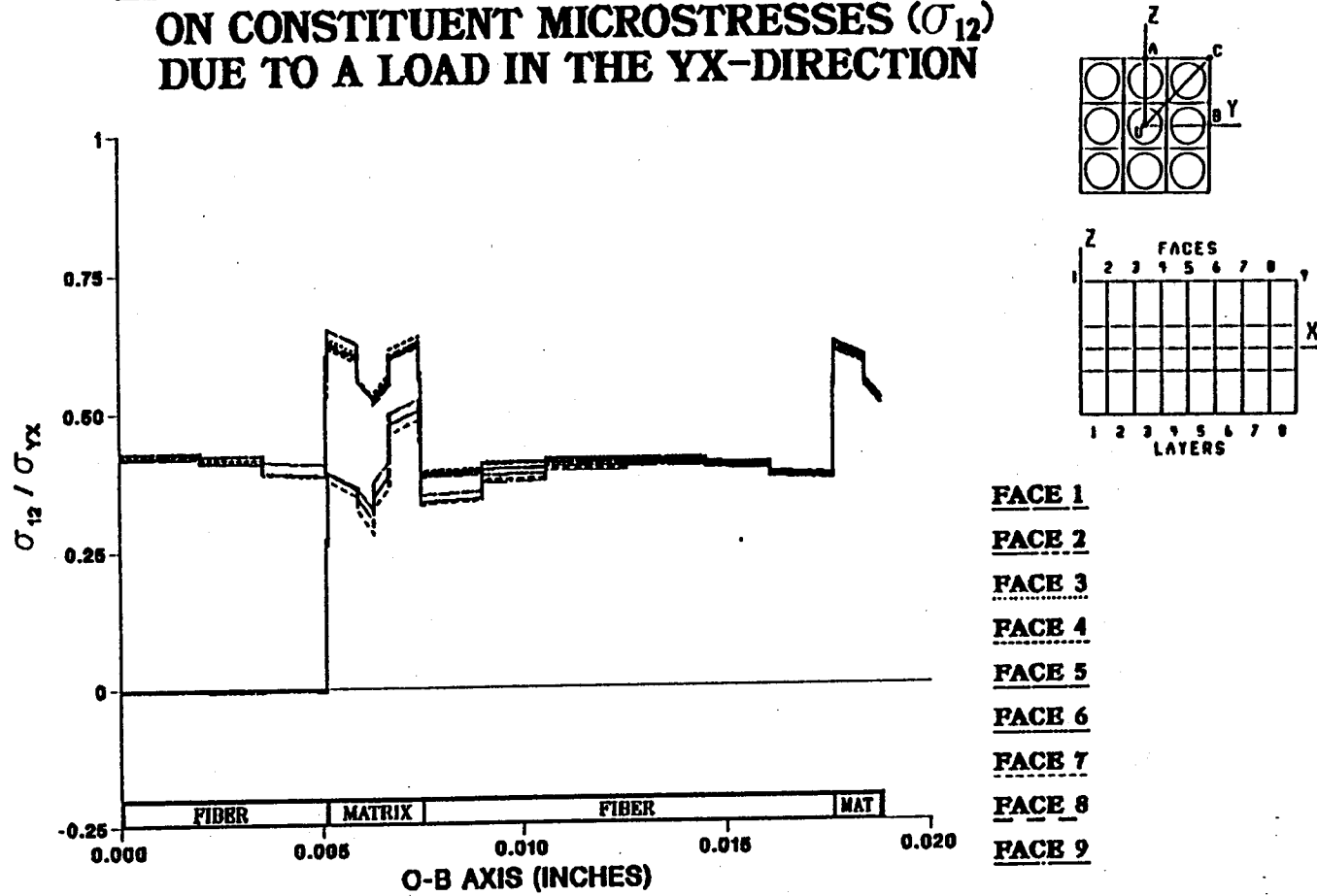


Figure A.94 — σ_{12} Normalized Microstresses, O-B Direction, 4.17% Debonding, σ_{yx}^e Loading

EFFECT OF 5.56% FIBER LENGTH DEBONDING ON CONSTITUENT MICROSTRESSES (σ_{12}) DUE TO A LOAD IN THE YX-DIRECTION

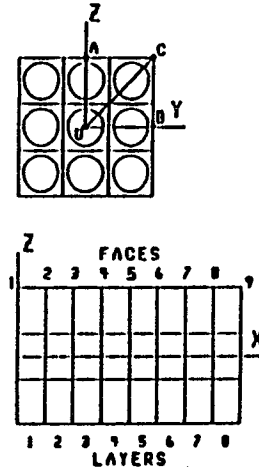
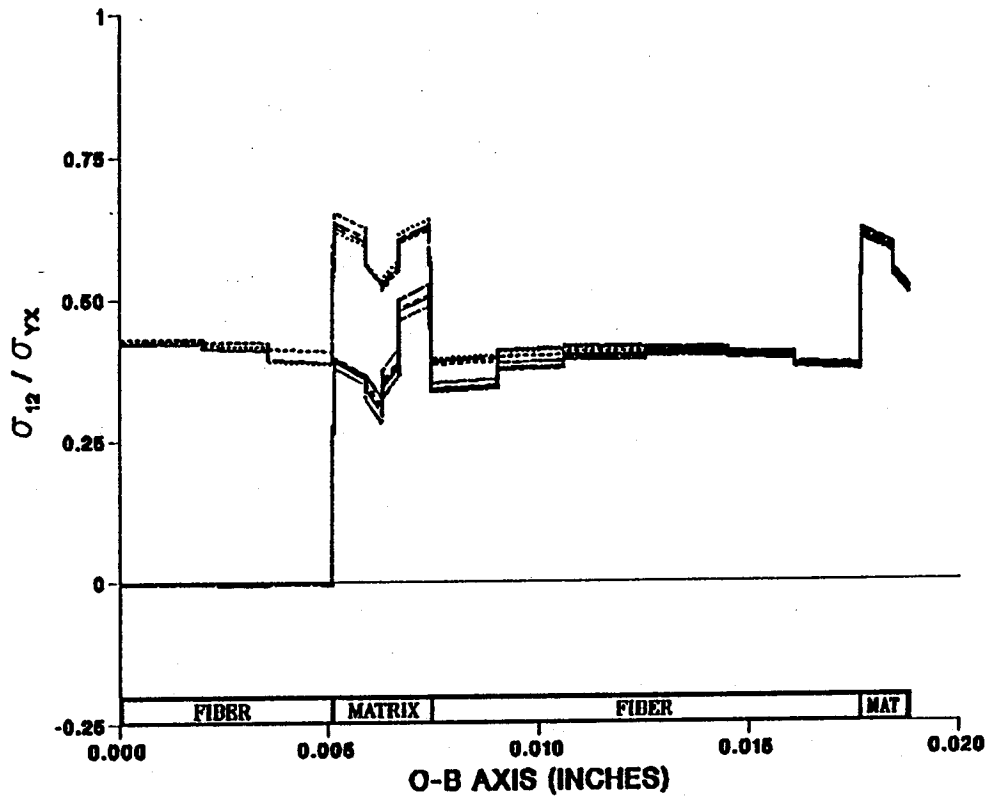


Figure A.95 - σ_{12} Normalized Microstresses, O-B Direction, 5.56% Debonding, σ_{yx}^e Loading

EFFECT OF 6.94% FIBER LENGTH DEBONDING ON CONSTITUENT MICROSTRESSES (σ_{12}) DUE TO A LOAD IN THE YX-DIRECTION

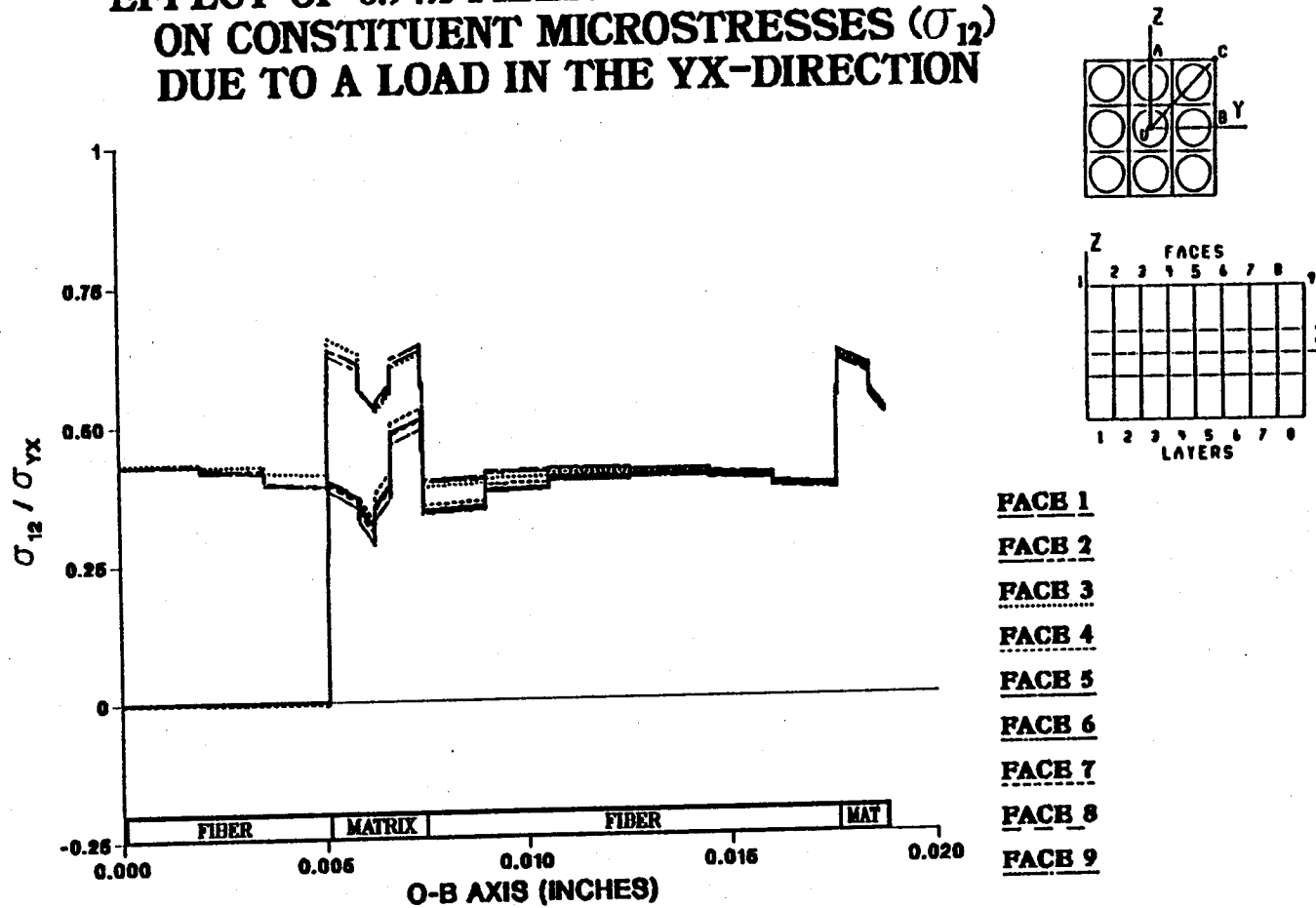


Figure A.96 - σ_{12} Normalized Microstresses, O-B Direction, 6.94% Debonding, σ_{yx}^e Loading

EFFECT OF 8.33% FIBER LENGTH DEBONDING ON CONSTITUENT MICROSTRESSES (σ_{12}) DUE TO A LOAD IN THE YX-DIRECTION

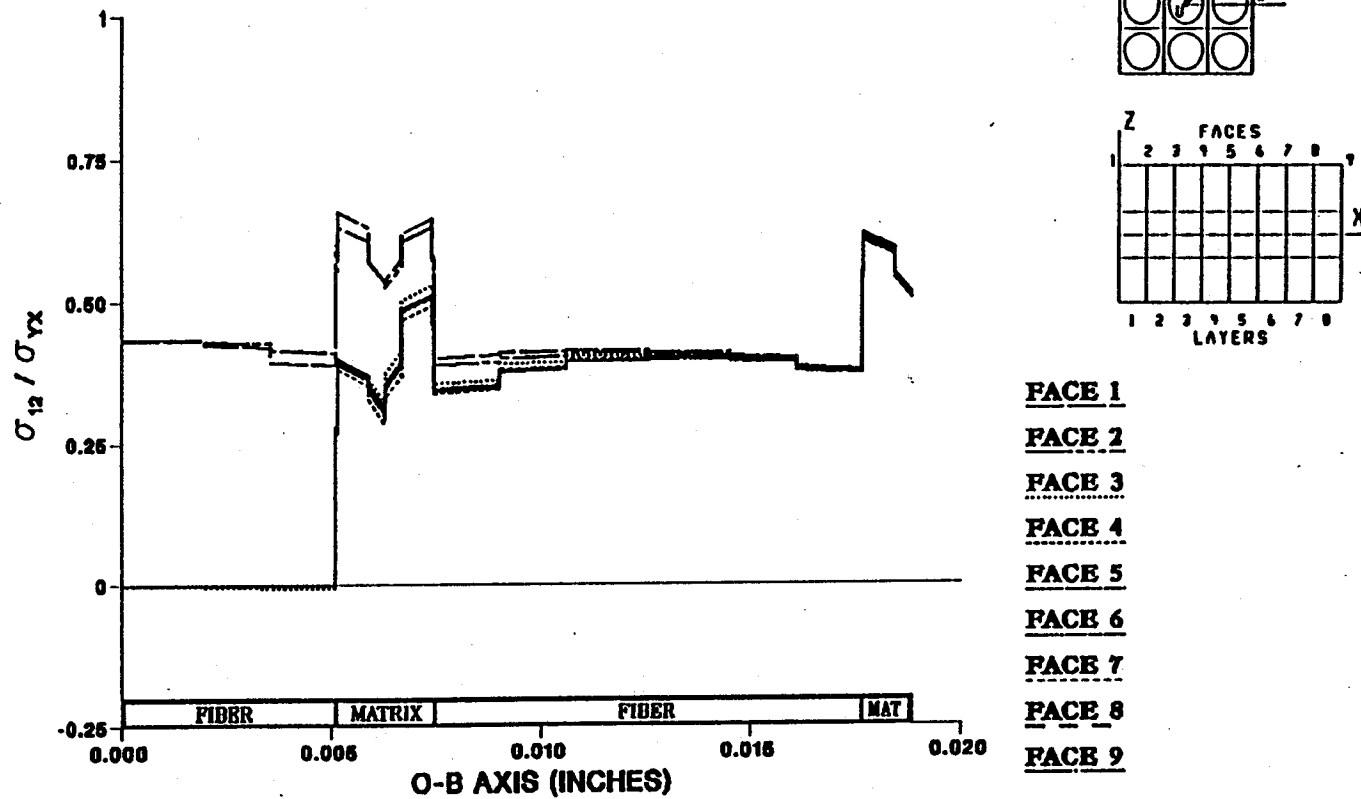


Figure A.97 - σ_{12} Normalized Microstresses, O-B Direction, 8.33% Debonding, σ_{yx}^e Loading

EFFECT OF 9.72% FIBER LENGTH DEBONDING ON CONSTITUENT MICROSTRESSES (σ_{12}) DUE TO A LOAD IN THE YX-DIRECTION

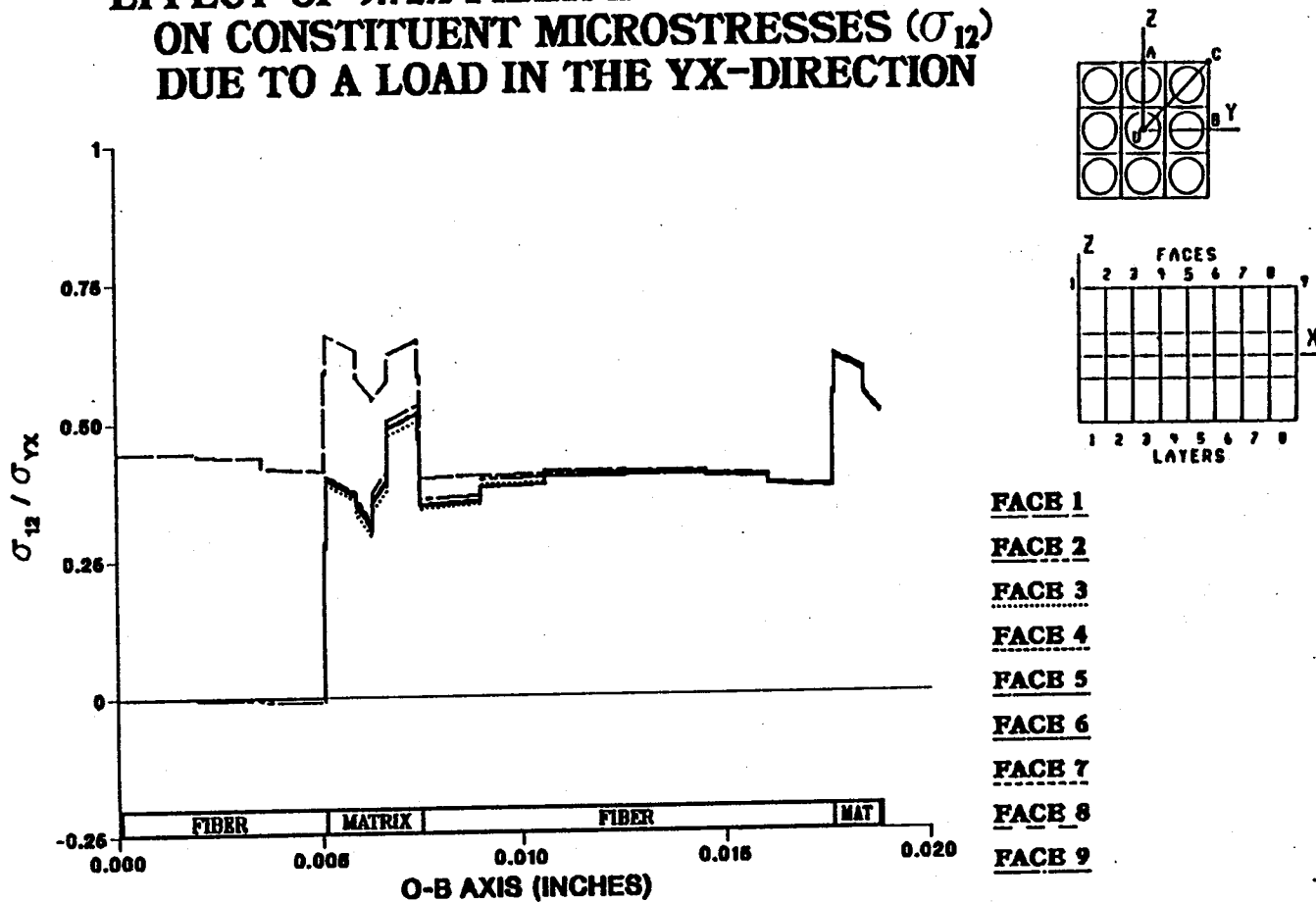
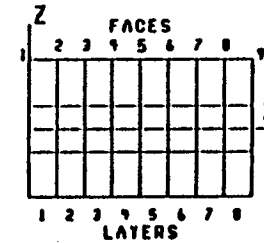
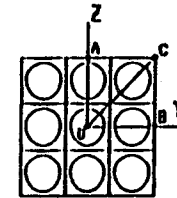
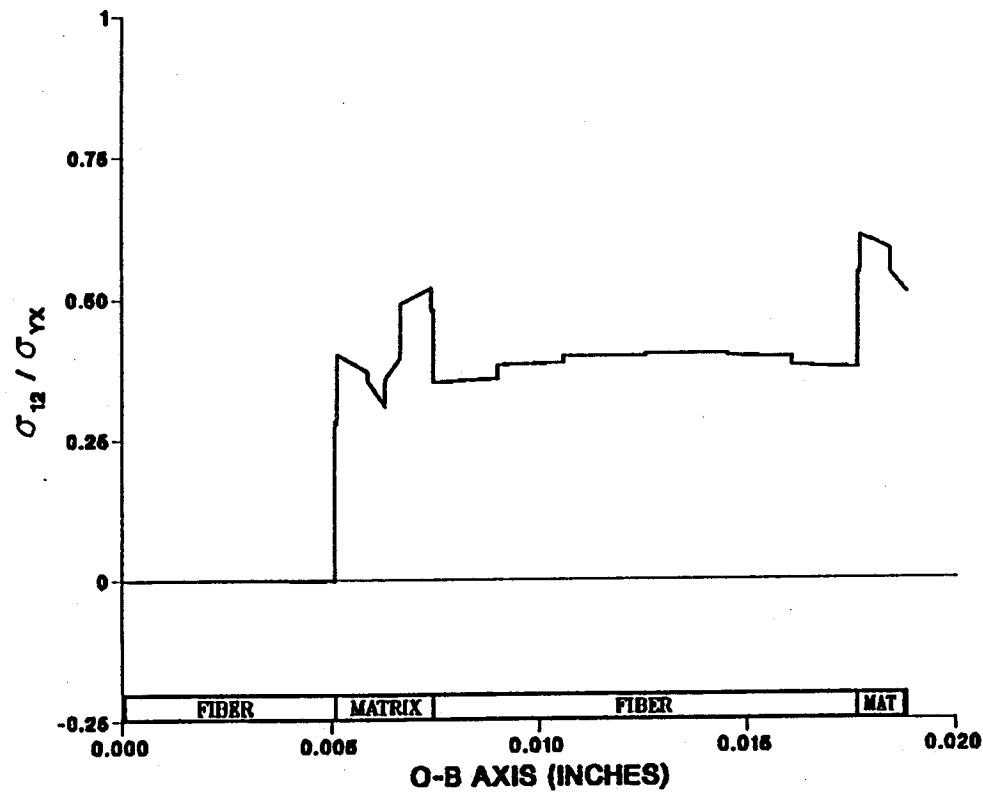


Figure A.98 — σ_{12} Normalized Microstresses, O-B Direction, 9.72% Debonding, σ_{yx}^e Loading

EFFECT OF 11.11% FIBER LENGTH DEBONDING ON CONSTITUENT MICROSTRESSES (σ_{12}) DUE TO A LOAD IN THE YX-DIRECTION



- FACE 1
- FACE 2
- FACE 3
- FACE 4
- FACE 5
- FACE 6
- FACE 7
- FACE 8
- FACE 9

Figure A.99 - σ_{12} Normalized Microstresses, O-B Direction, 11.11% Debonding, σ_{yx}^e Loading

EFFECT OF 0.0% FIBER LENGTH DEBONDING ON CONSTITUENT MICROSTRESSES (σ_{12}) DUE TO A LOAD IN THE YX-DIRECTION

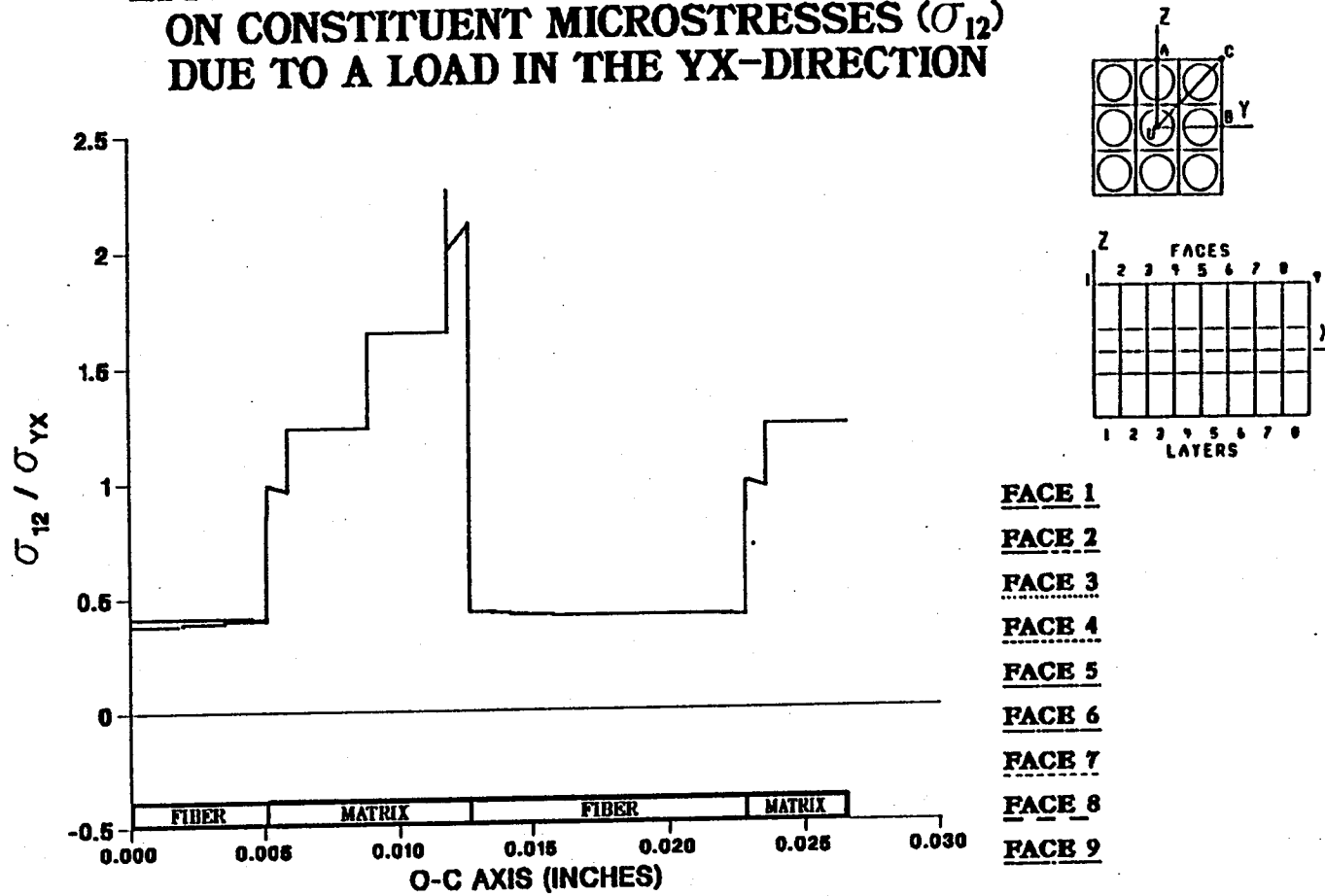


Figure A.100 - σ_{12} Normalized Microstresses, O-C Direction, 0.0% Debonding, σ_{yx}^e Loading

EFFECT OF 1.39% FIBER LENGTH DEBONDING ON CONSTITUENT MICROSTRESSES (σ_{12}) DUE TO A LOAD IN THE YX-DIRECTION

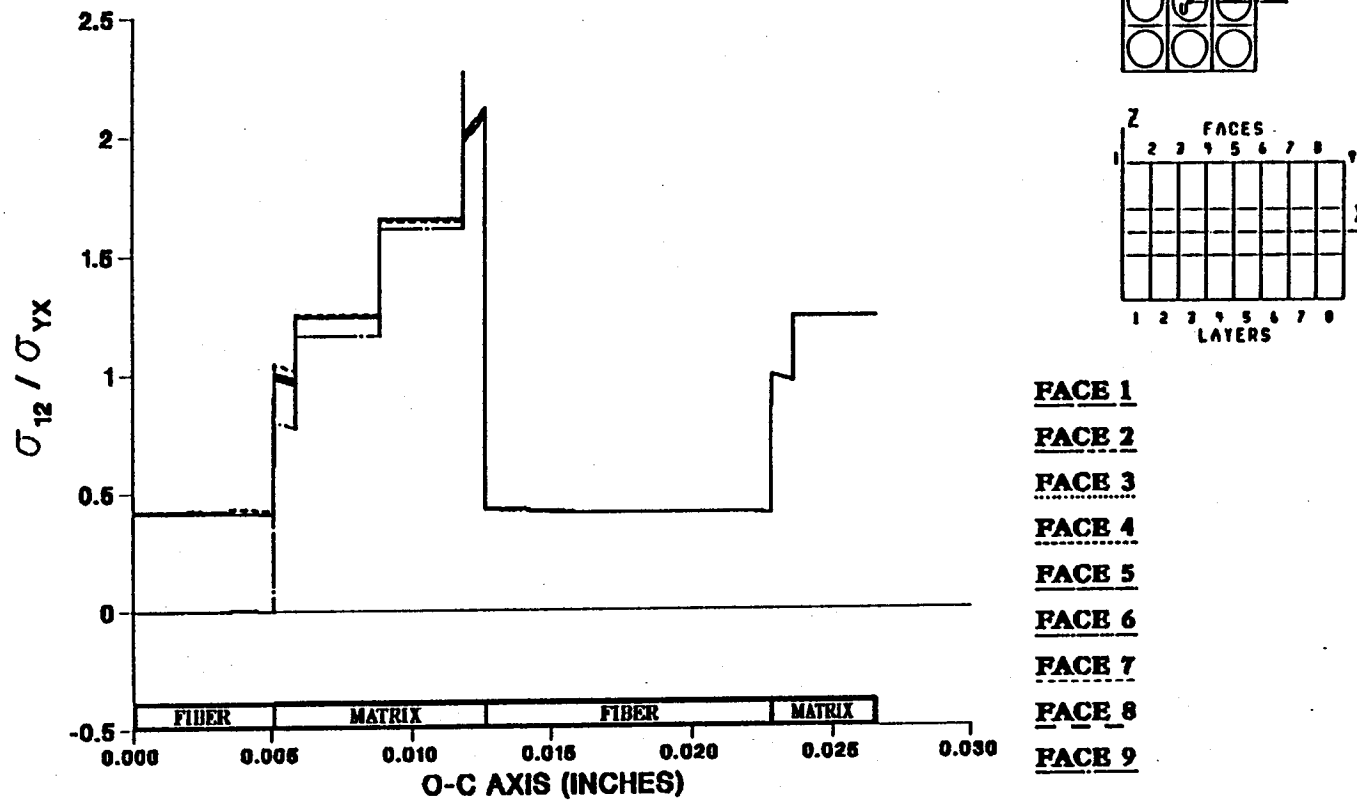


Figure A.101 - σ_{12} Normalized Microstresses, O-C Direction, 1.39% Debonding, σ_{yx}^e Loading

EFFECT OF 2.78% FIBER LENGTH DEBONDING ON CONSTITUENT MICROSTRESSES (σ_{12}) DUE TO A LOAD IN THE YX-DIRECTION

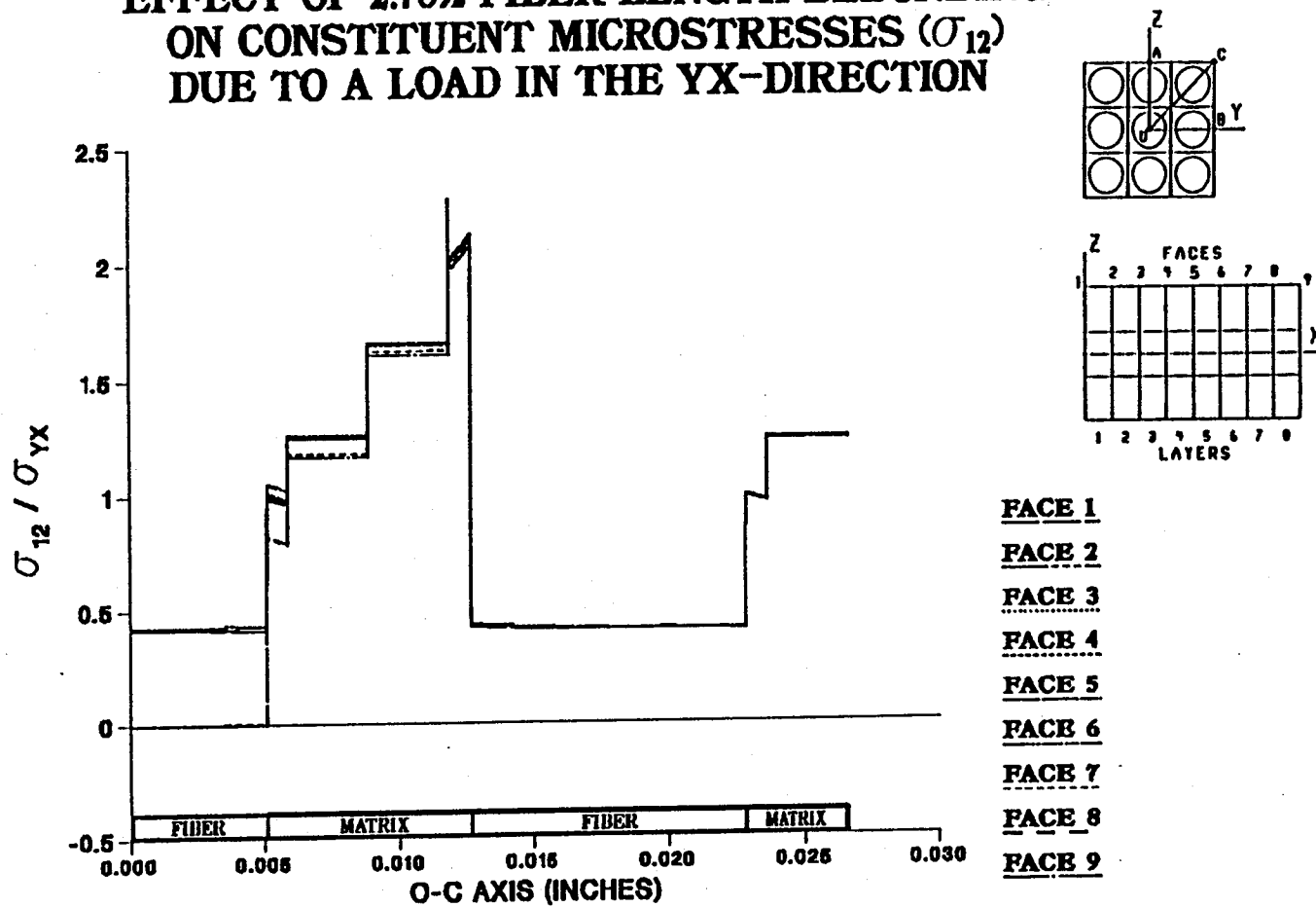


Figure A.102 — σ_{12} Normalized Microstresses, O-C Direction, 2.78% Debonding, σ_{yx}^e Loading

EFFECT OF 4.17% FIBER LENGTH DEBONDING ON CONSTITUENT MICROSTRESSES (σ_{12}) DUE TO A LOAD IN THE YX-DIRECTION

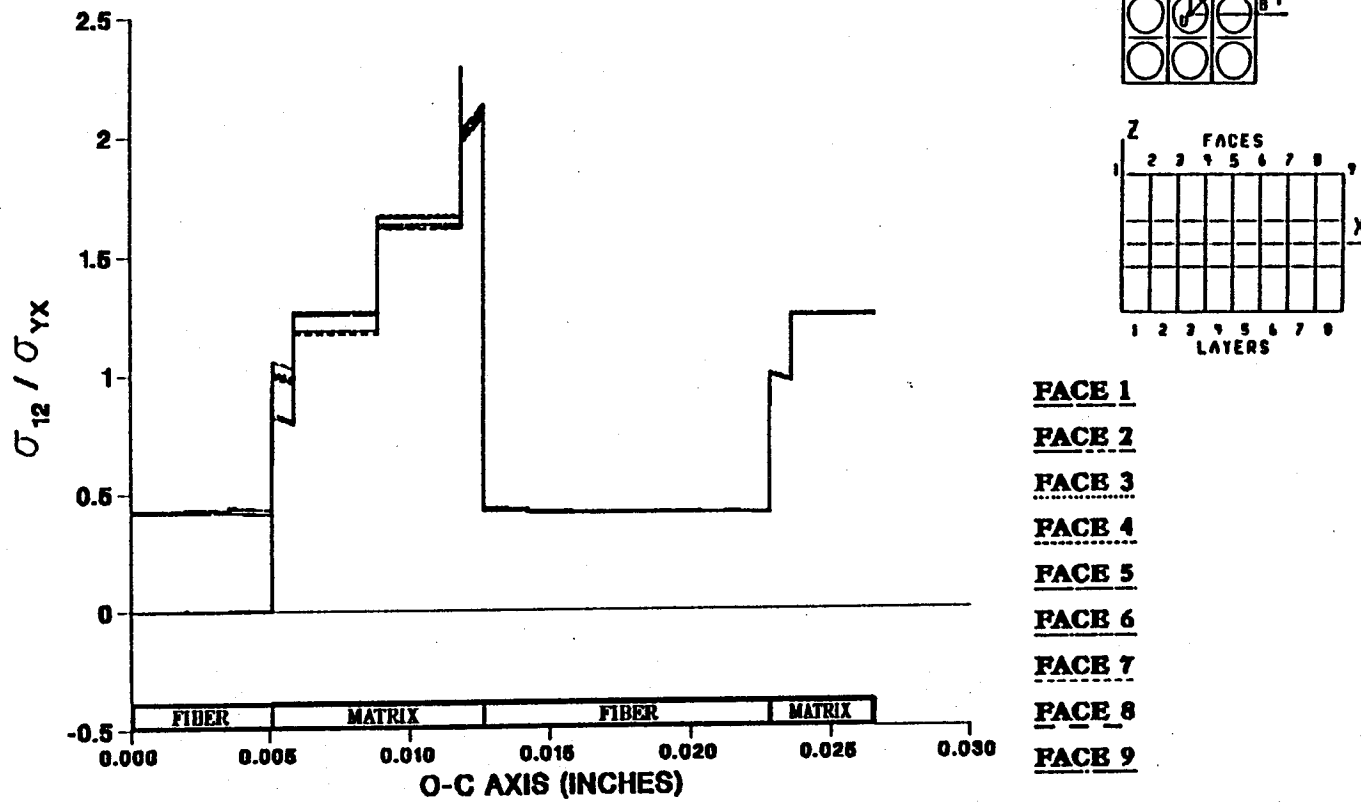
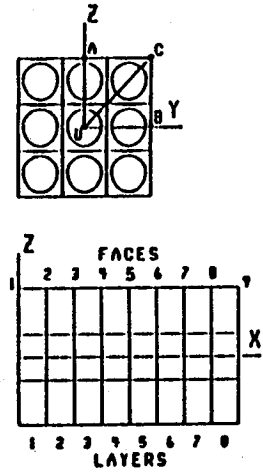
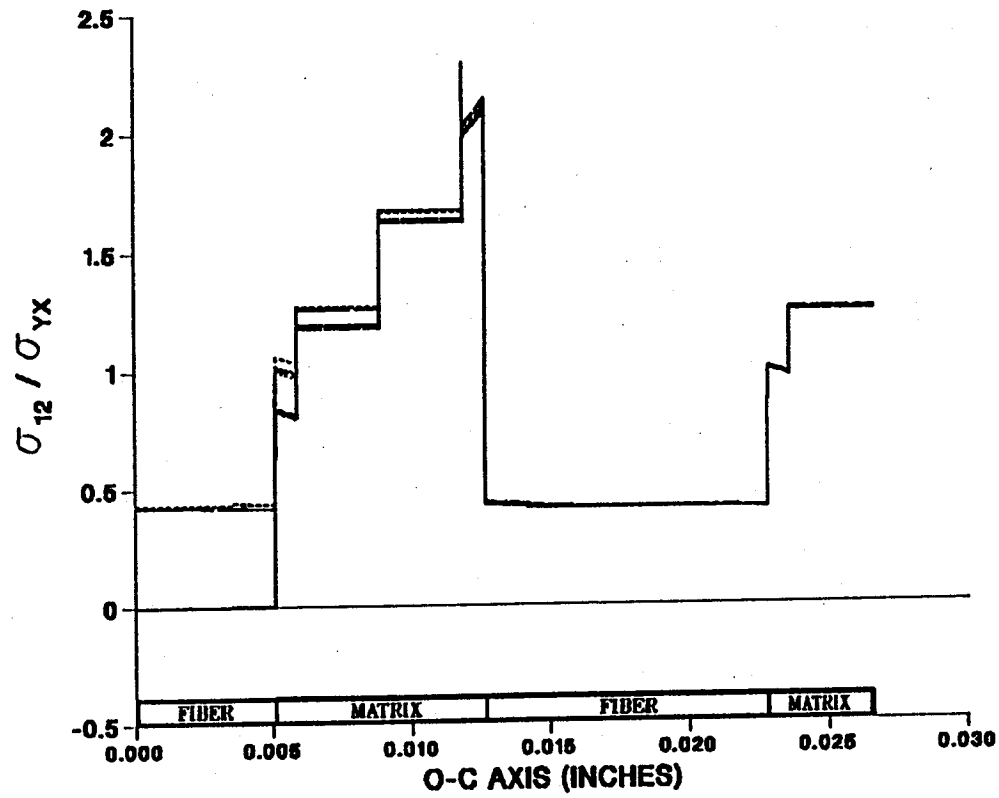


Figure A.103 - σ_{12} Normalized Microstresses, O-C Direction, 4.17% Debonding, σ_{yx}^e Loading

EFFECT OF 5.56% FIBER LENGTH DEBONDING ON CONSTITUENT MICROSTRESSES (σ_{12}) DUE TO A LOAD IN THE YX-DIRECTION



- FACE 1
- FACE 2
- FACE 3
- FACE 4
- FACE 5
- FACE 6
- FACE 7
- FACE 8
- FACE 9

Figure A.104 - σ_{12} Normalized Microstresses, O-C Direction, 5.56% Debonding, σ_{yx}^e Loading

EFFECT OF 6.94% FIBER LENGTH DEBONDING ON CONSTITUENT MICROSTRESSES (σ_{12}) DUE TO A LOAD IN THE YX-DIRECTION

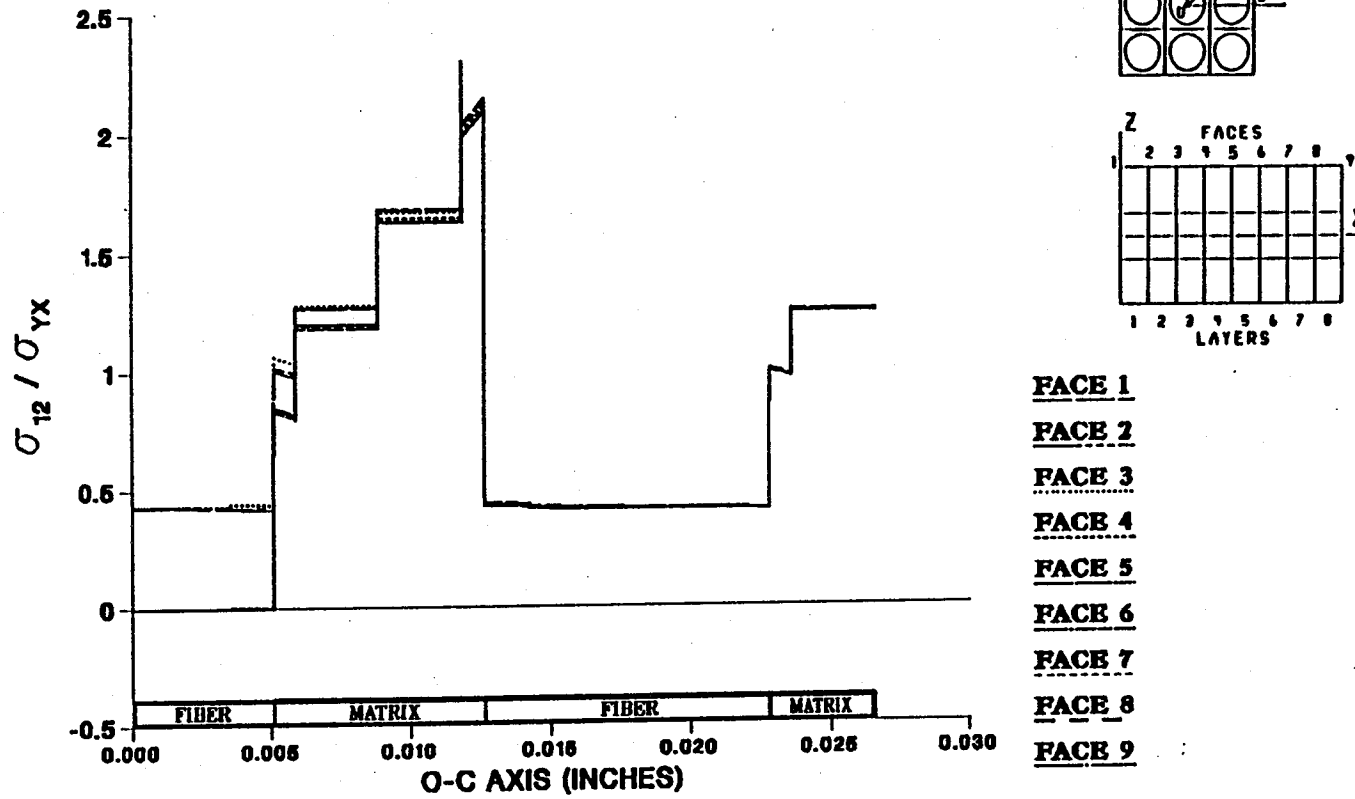


Figure A.105 - σ_{12} Normalized Microstresses, O-C Direction, 6.94% Debonding, σ_{yx}^e Loading

EFFECT OF 8.33% FIBER LENGTH DEBONDING ON CONSTITUENT MICROSTRESSES (σ_{12}) DUE TO A LOAD IN THE YX-DIRECTION

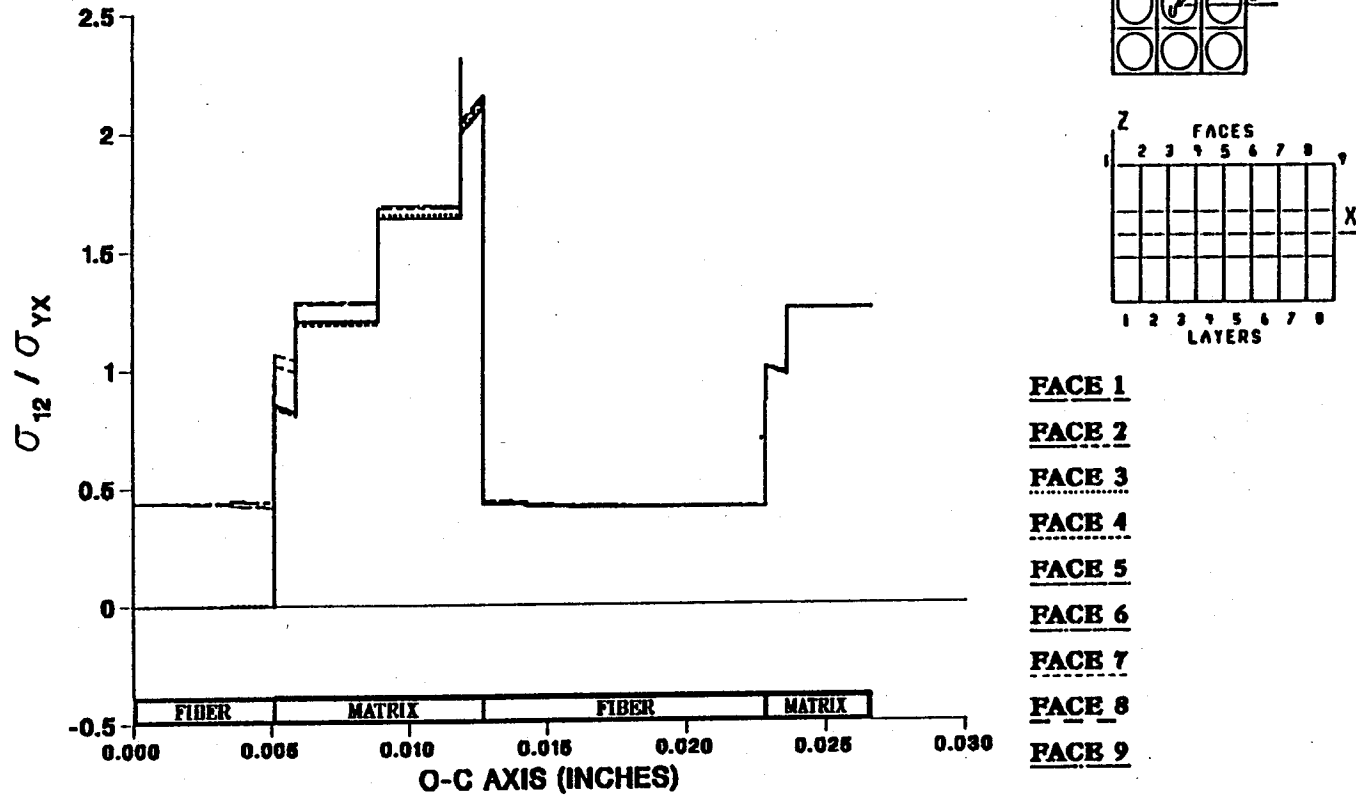
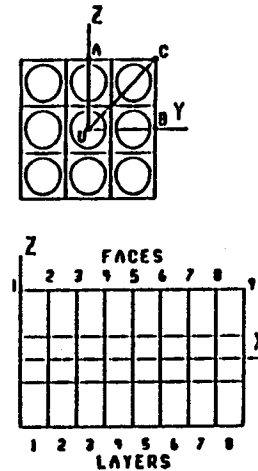
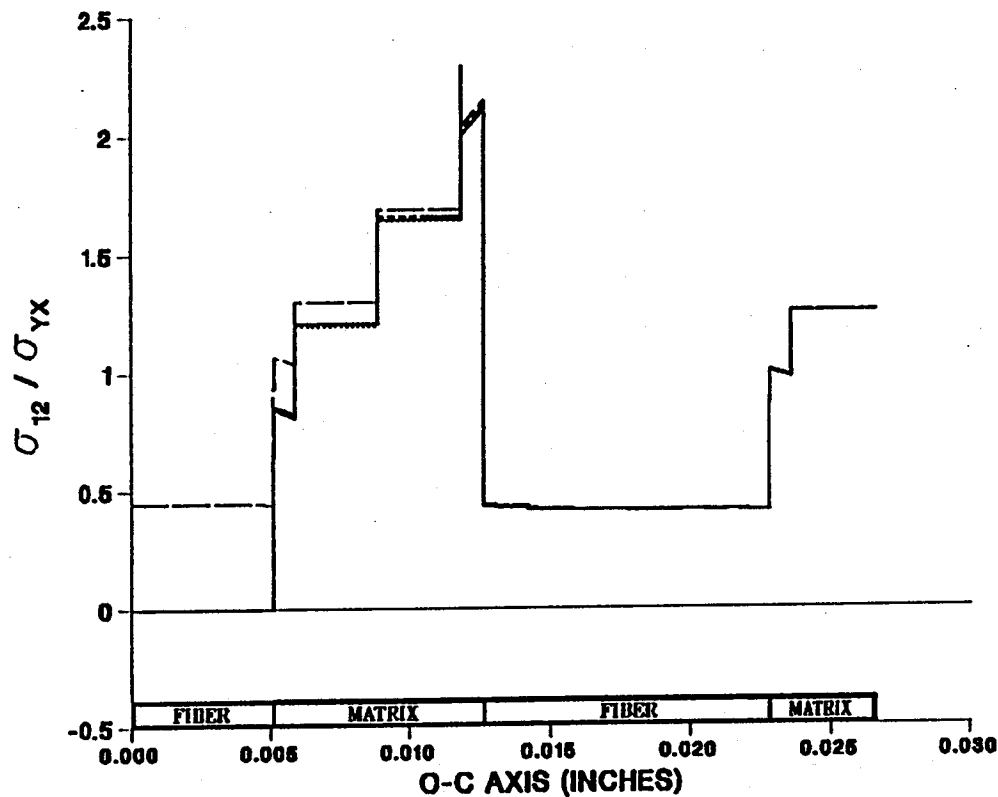


Figure A.106 - σ_{12} Normalized Microstresses, O-C Direction, 8.33% Debonding, σ_{yx}^e Loading

EFFECT OF 9.72% FIBER LENGTH DEBONDING ON CONSTITUENT MICROSTRESSES (σ_{12}) DUE TO A LOAD IN THE YX-DIRECTION



- FACE 1
- FACE 2
- FACE 3
- FACE 4
- FACE 5
- FACE 6
- FACE 7
- FACE 8
- FACE 9

Figure A.107 - σ_{12} Normalized Microstresses, O-C Direction, 9.72% Debonding, σ_{yx}^e Loading

EFFECT OF 11.11% FIBER LENGTH DEBONDING ON CONSTITUENT MICROSTRESSES (σ_{12}) DUE TO A LOAD IN THE YX-DIRECTION

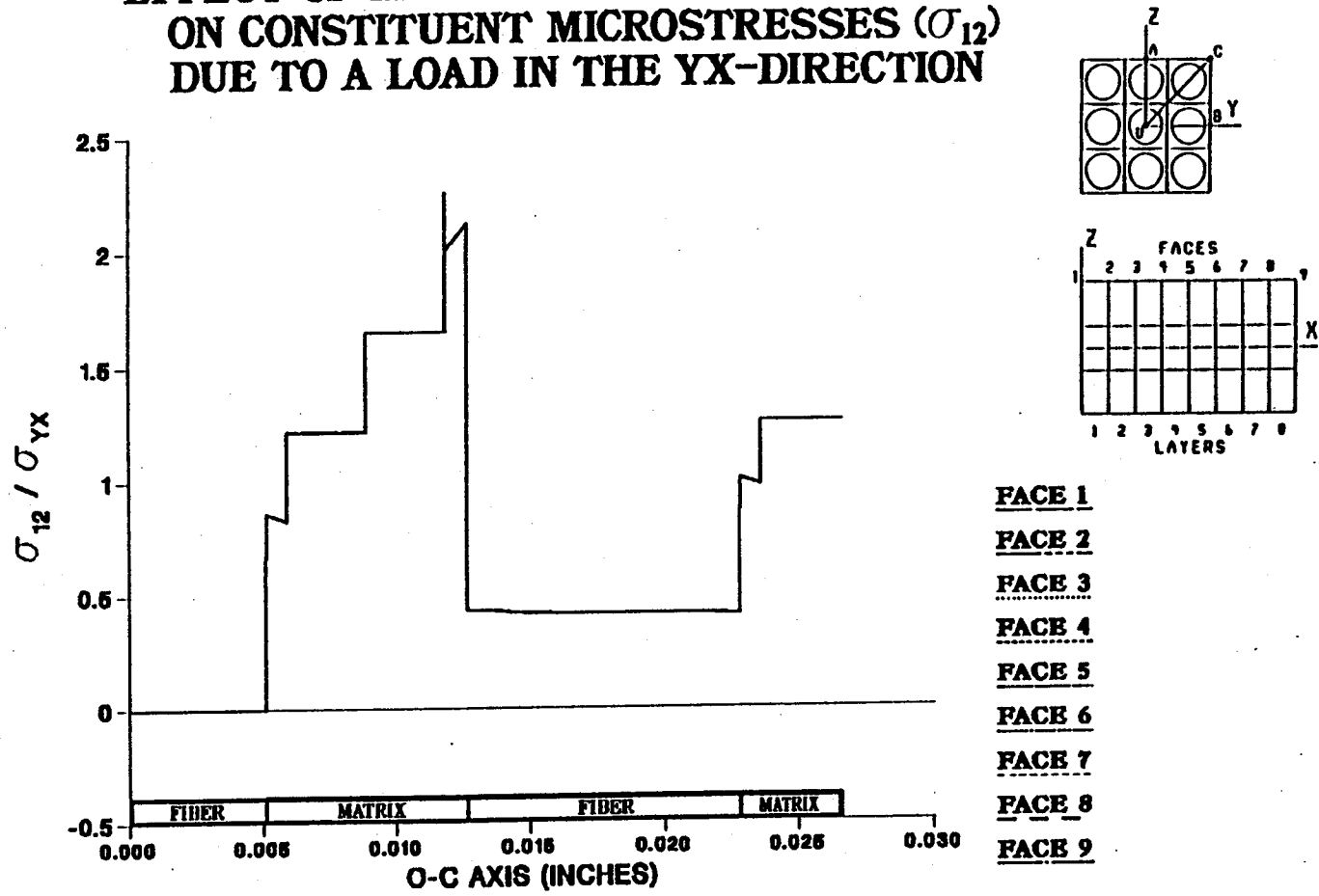


Figure A.108 - σ_{12} Normalized Microstresses, O-C Direction, 11.11% Debonding, σ_{yx}^e Loading

EFFECT OF 0.0% FIBER LENGTH DEBONDING ON CONSTITUENT MICROSTRESSES (σ_{23}) DUE TO A LOAD IN THE YZ-DIRECTION

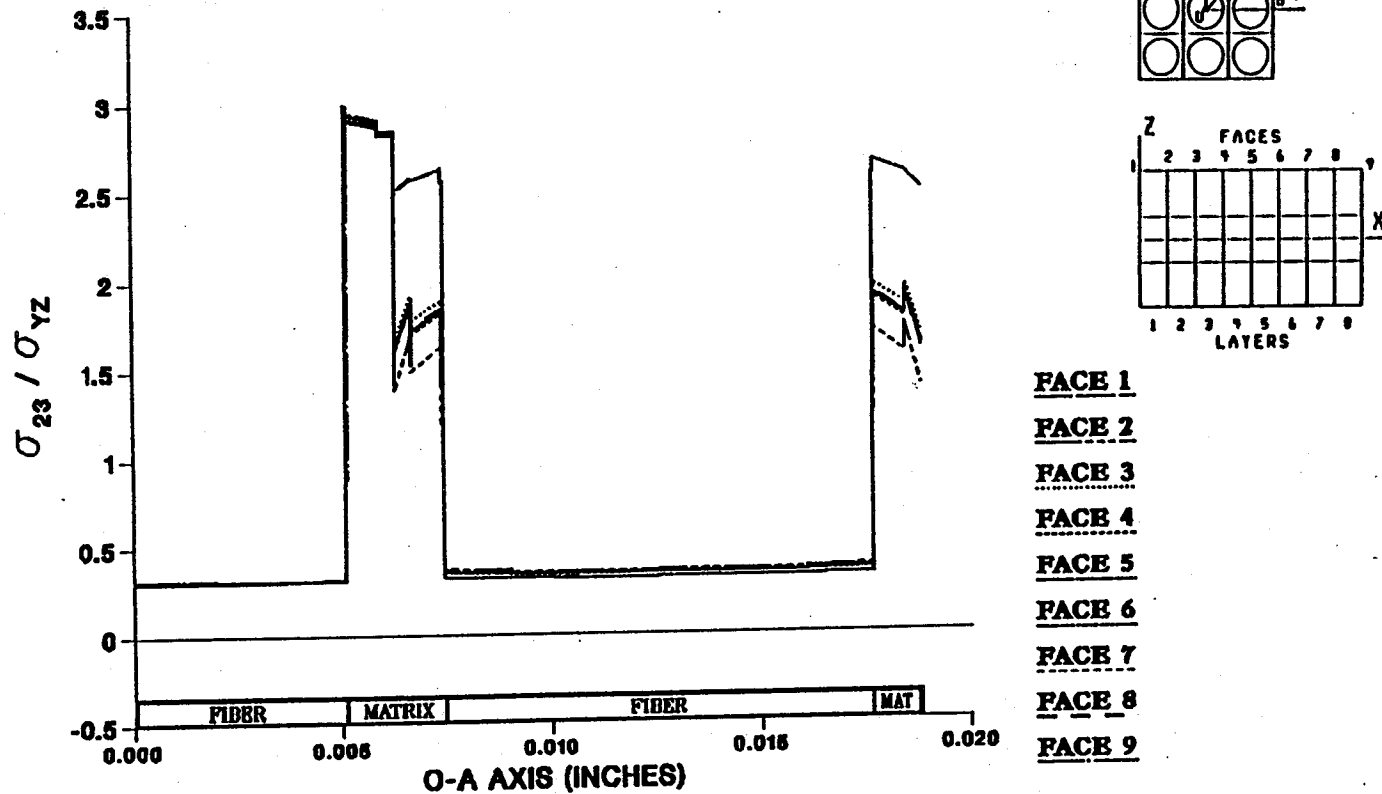


Figure A.109 – σ_{23} Normalized Microstresses, O–A Direction, 0.0% Debonding, σ_{yz}^e Loading

EFFECT OF 1.39% FIBER LENGTH DEBONDING ON CONSTITUENT MICROSTRESSES (σ_{23}) DUE TO A LOAD IN THE YZ-DIRECTION

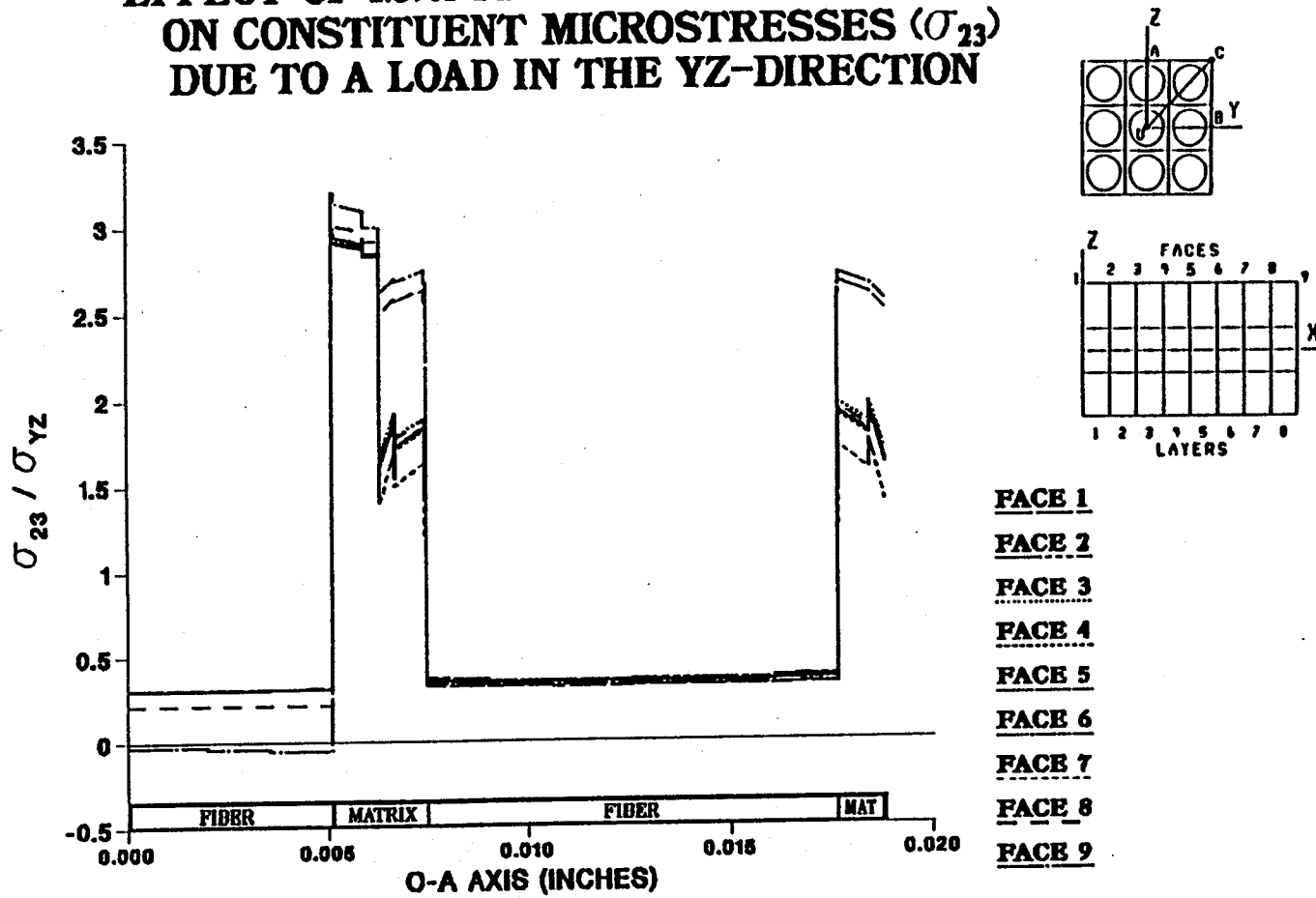


Figure A.110 - σ_{23} Normalized Microstresses, O-A Direction, 1.39% Debonding, σ_{yz}^e Loading

EFFECT OF 2.78% FIBER LENGTH DEBONDING ON CONSTITUENT MICROSTRESSES (σ_{23}) DUE TO A LOAD IN THE YZ-DIRECTION

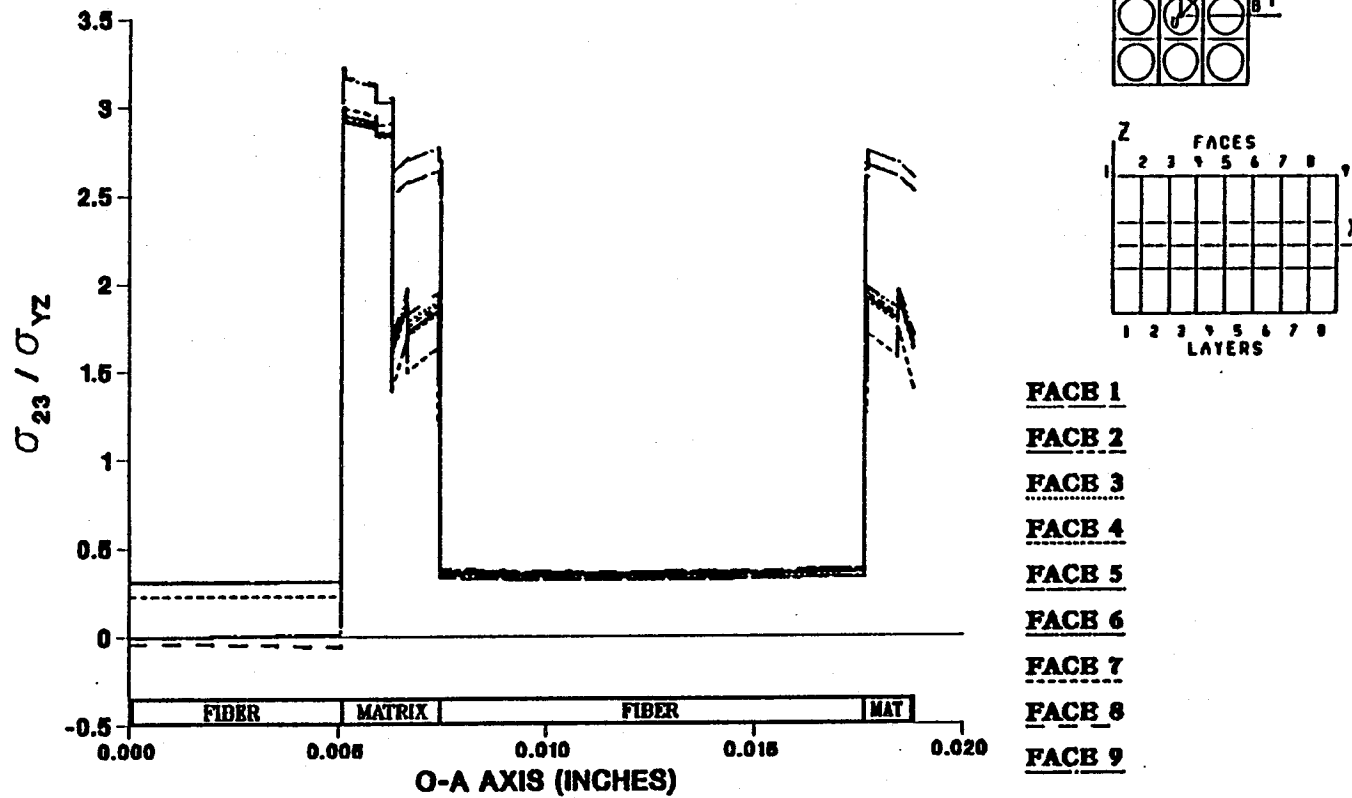


Figure A.111 - σ_{23} Normalized Microstresses, O-A Direction, 2.78% Debonding, σ_{yz}^e Loading

EFFECT OF 4.17% FIBER LENGTH DEBONDING ON CONSTITUENT MICROSTRESSES (σ_{23}) DUE TO A LOAD IN THE YZ-DIRECTION

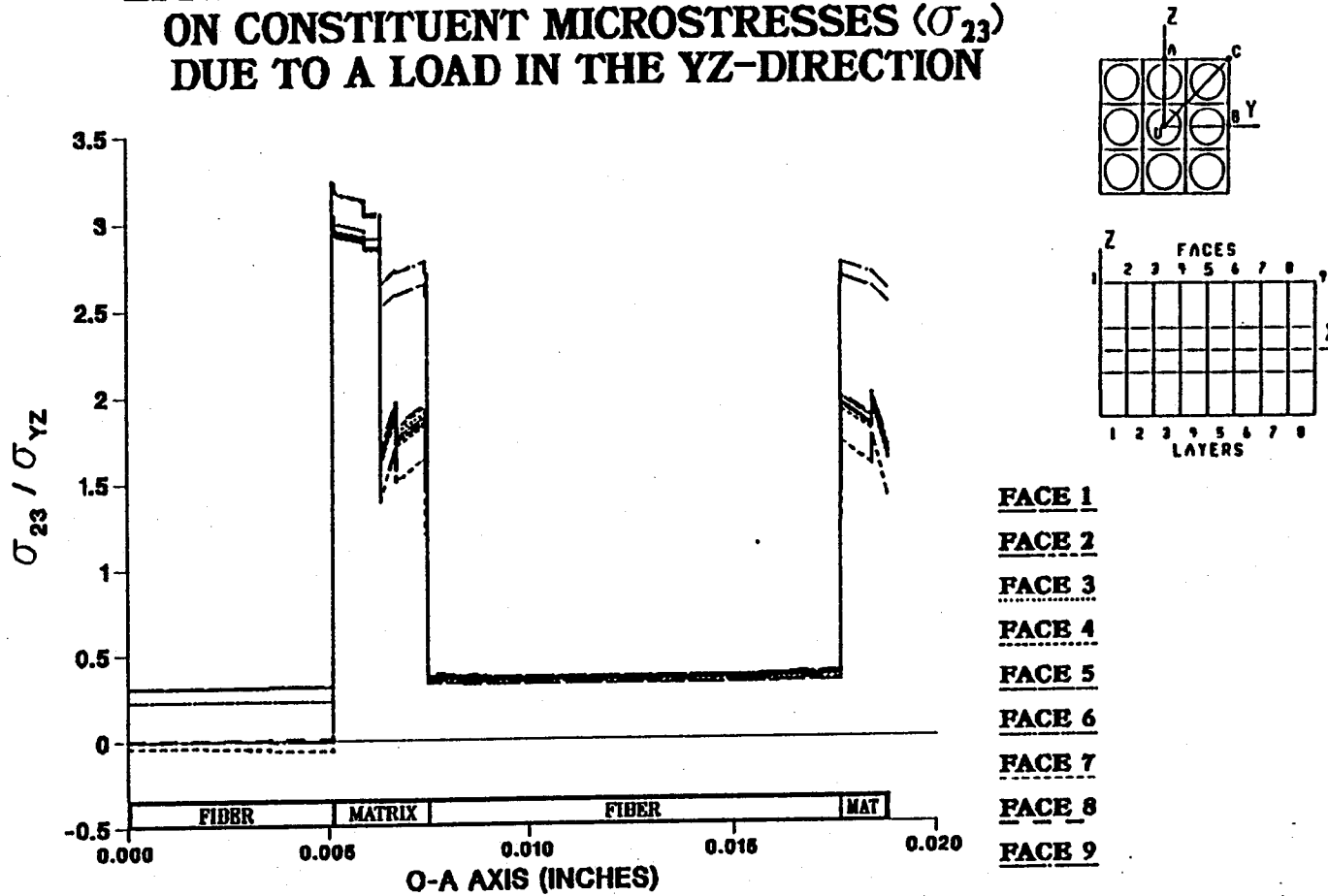


Figure A.112 - σ_{23} Normalized Microstresses, O-A Direction, 4.17% Debonding, σ_{yz}^e Loading

EFFECT OF 5.56% FIBER LENGTH DEBONDING ON CONSTITUENT MICROSTRESSES (σ_{23}) DUE TO A LOAD IN THE YZ-DIRECTION

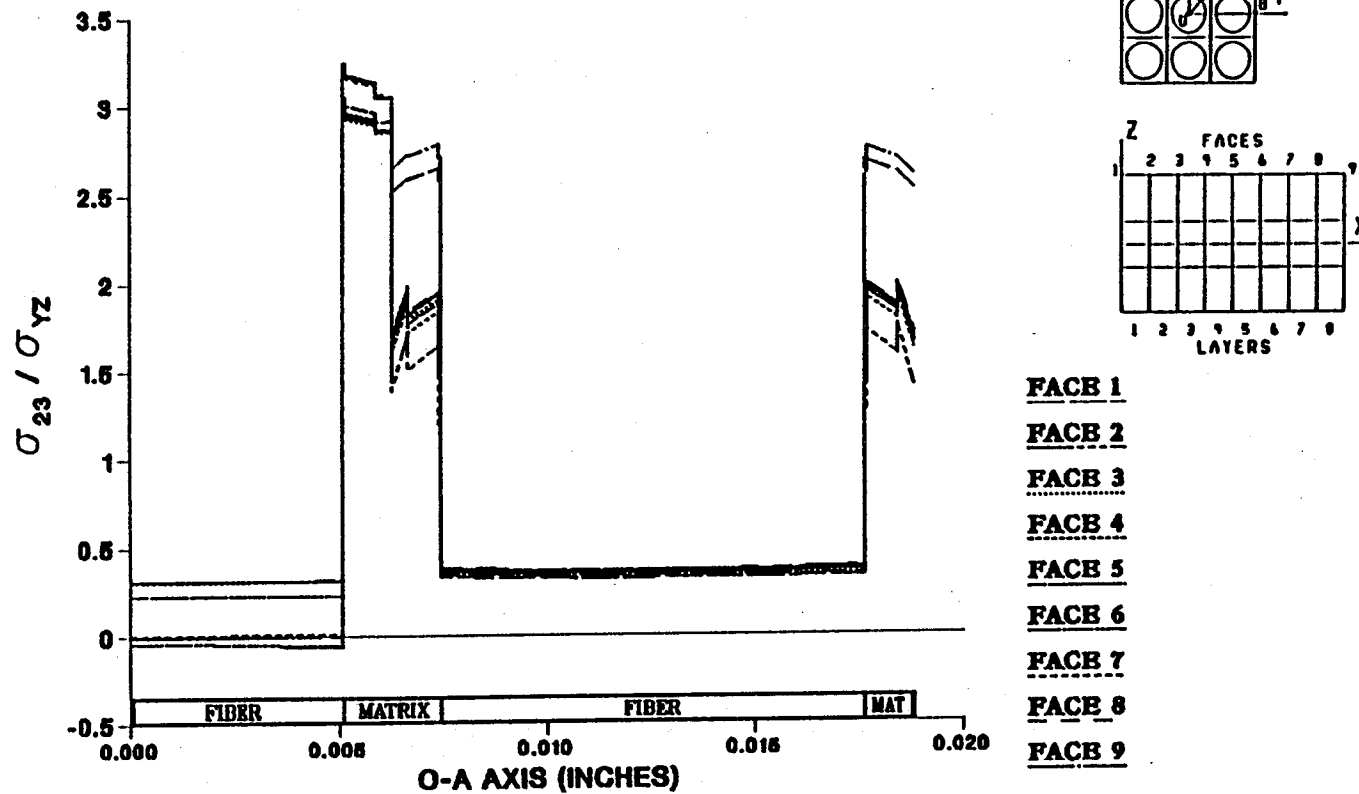


Figure A.113 - σ_{23} Normalized Microstresses, O-A Direction, 5.56% Debonding, σ_{yz}^e Loading

EFFECT OF 6.94% FIBER LENGTH DEBONDING ON CONSTITUENT MICROSTRESSES (σ_{23}) DUE TO A LOAD IN THE YZ-DIRECTION

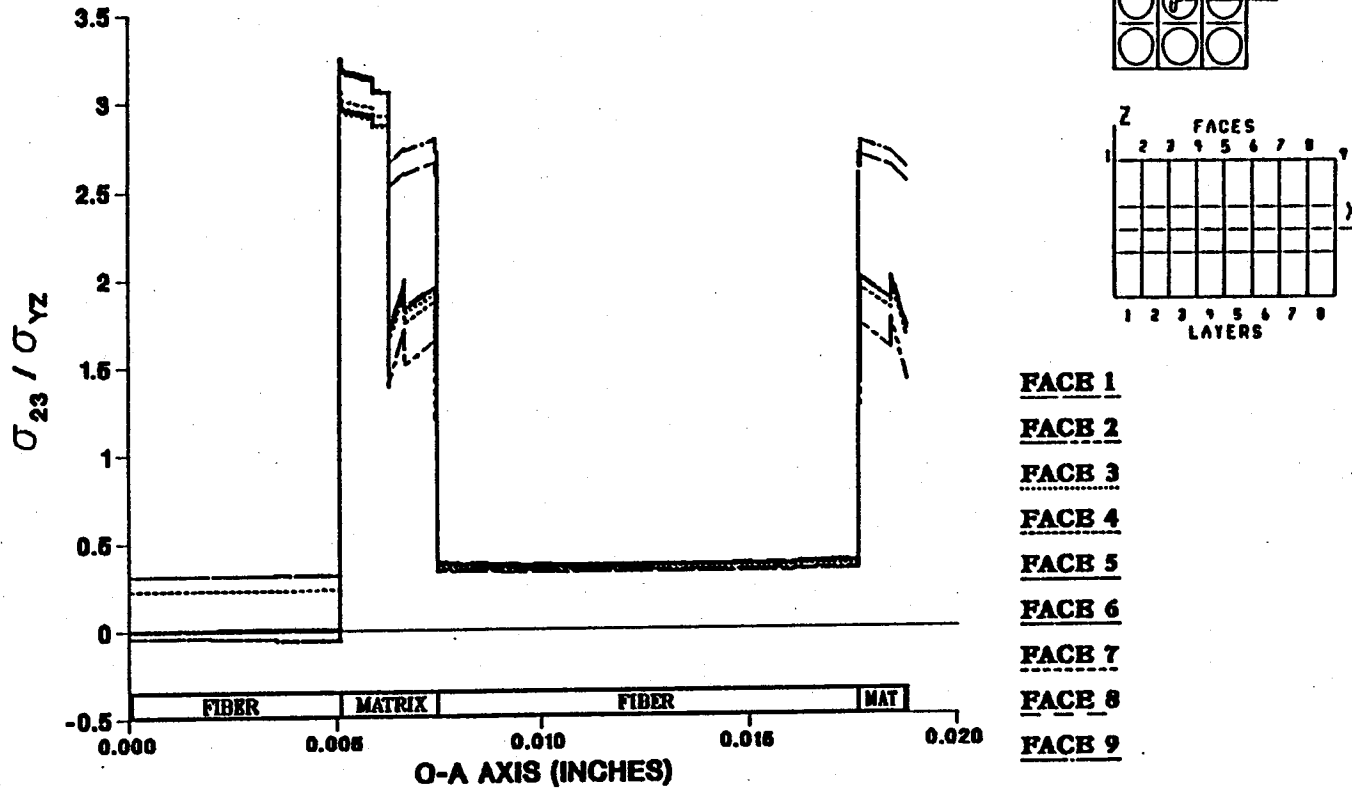


Figure A.114 - σ_{23} Normalized Microstresses, O-A Direction, 6.94% Debonding, σ_{yz}^e Loading

EFFECT OF 8.33% FIBER LENGTH DEBONDING ON CONSTITUENT MICROSTRESSES (σ_{23}) DUE TO A LOAD IN THE YZ-DIRECTION

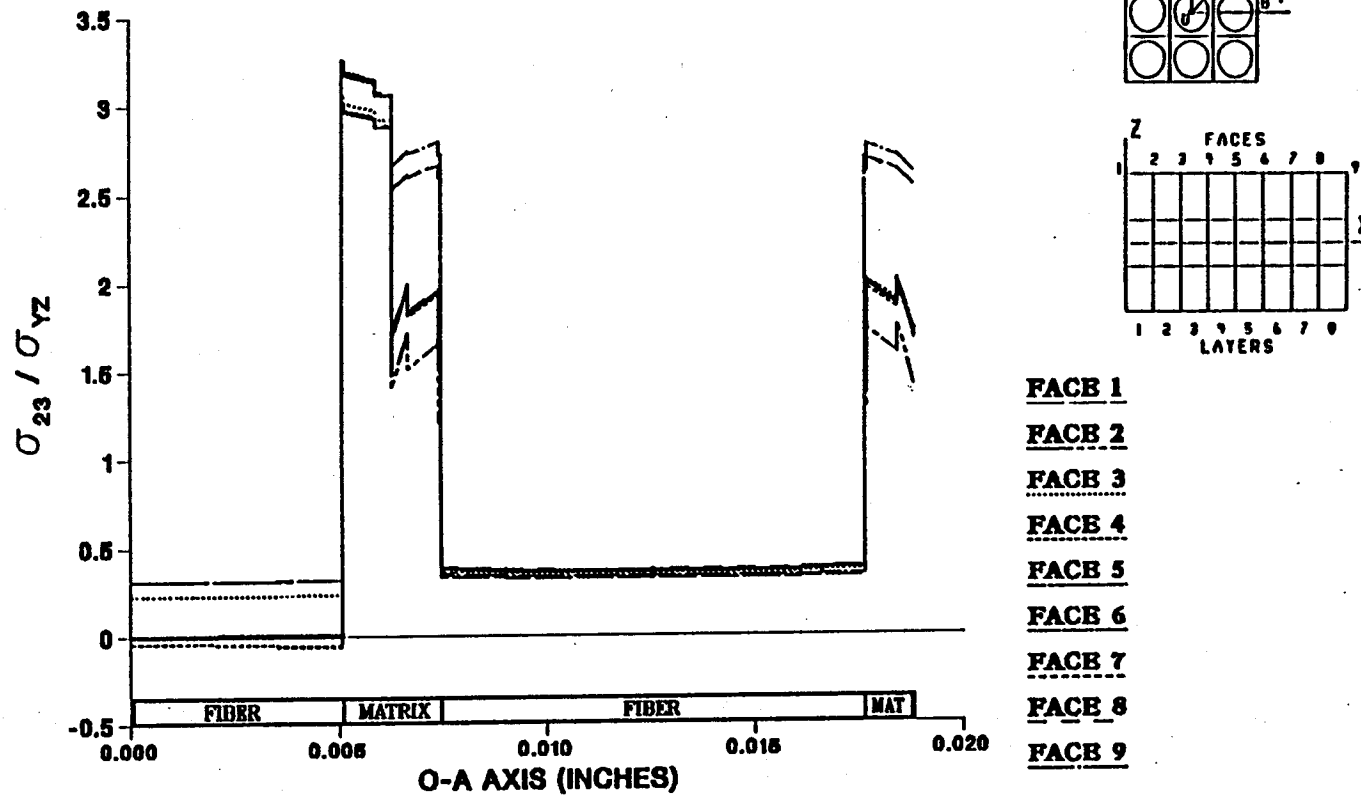
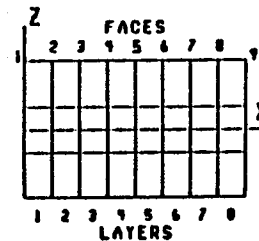
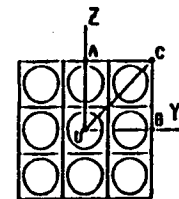
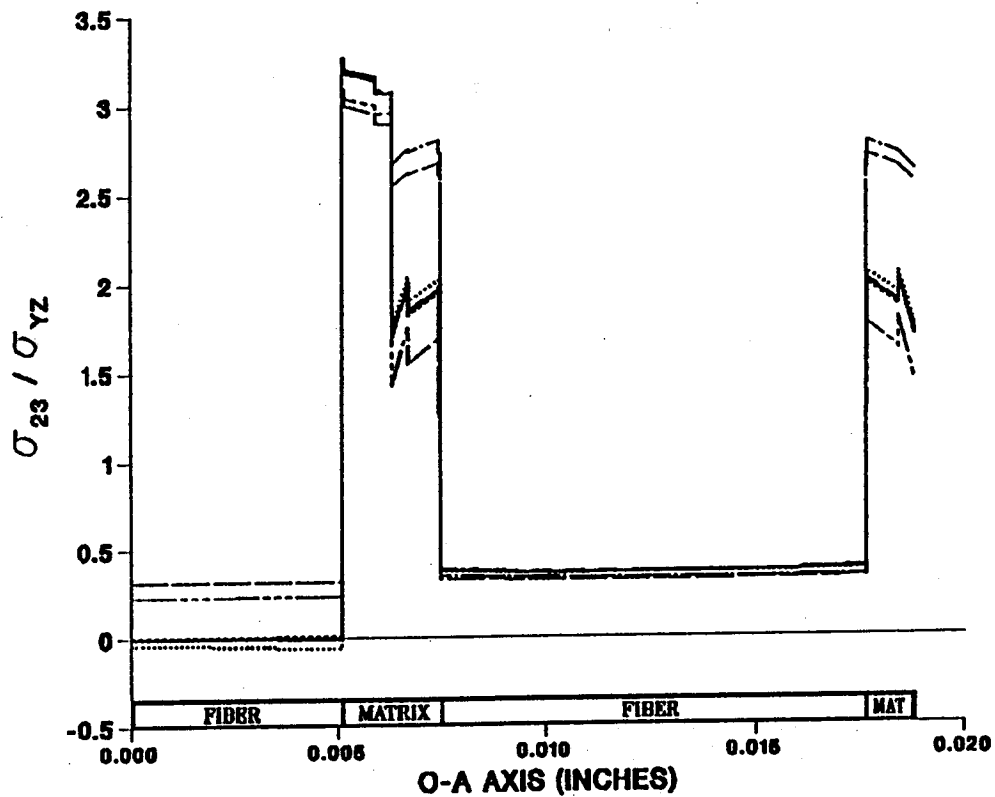


Figure A.115 - σ_{23} Normalized Microstresses, O-A Direction, 8.33% Debonding, σ_{yz}^e Loading

EFFECT OF 9.72% FIBER LENGTH DEBONDING ON CONSTITUENT MICROSTRESSES (σ_{23}) DUE TO A LOAD IN THE YZ-DIRECTION



- FACE 1
- FACE 2
- FACE 3
- FACE 4
- FACE 5
- FACE 6
- FACE 7
- FACE 8
- FACE 9

Figure A.116 - σ_{23} Normalized Microstresses, O-A Direction, 9.72% Debonding, σ_{yz}^e Loading

EFFECT OF 11.1% FIBER LENGTH DEBONDING ON CONSTITUENT MICROSTRESSES (σ_{23}) DUE TO A LOAD IN THE YZ-DIRECTION

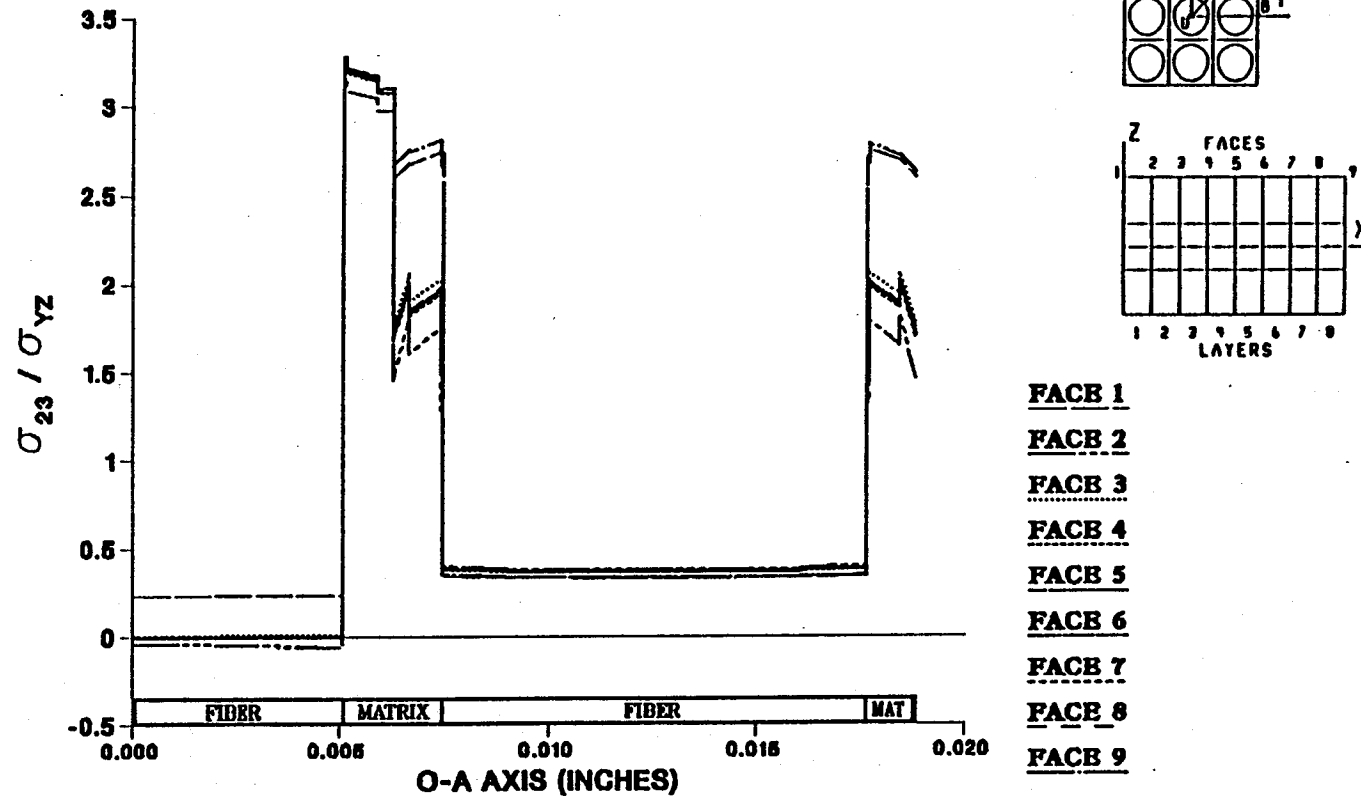


Figure A.117 - σ_{23} Normalized Microstresses, O-A Direction, 11.1% Debonding, σ_{yz}^e Loading

EFFECT OF 0.0% FIBER LENGTH DEBONDING ON CONSTITUENT MICROSTRESSES (σ_{23}) DUE TO A LOAD IN THE YZ-DIRECTION

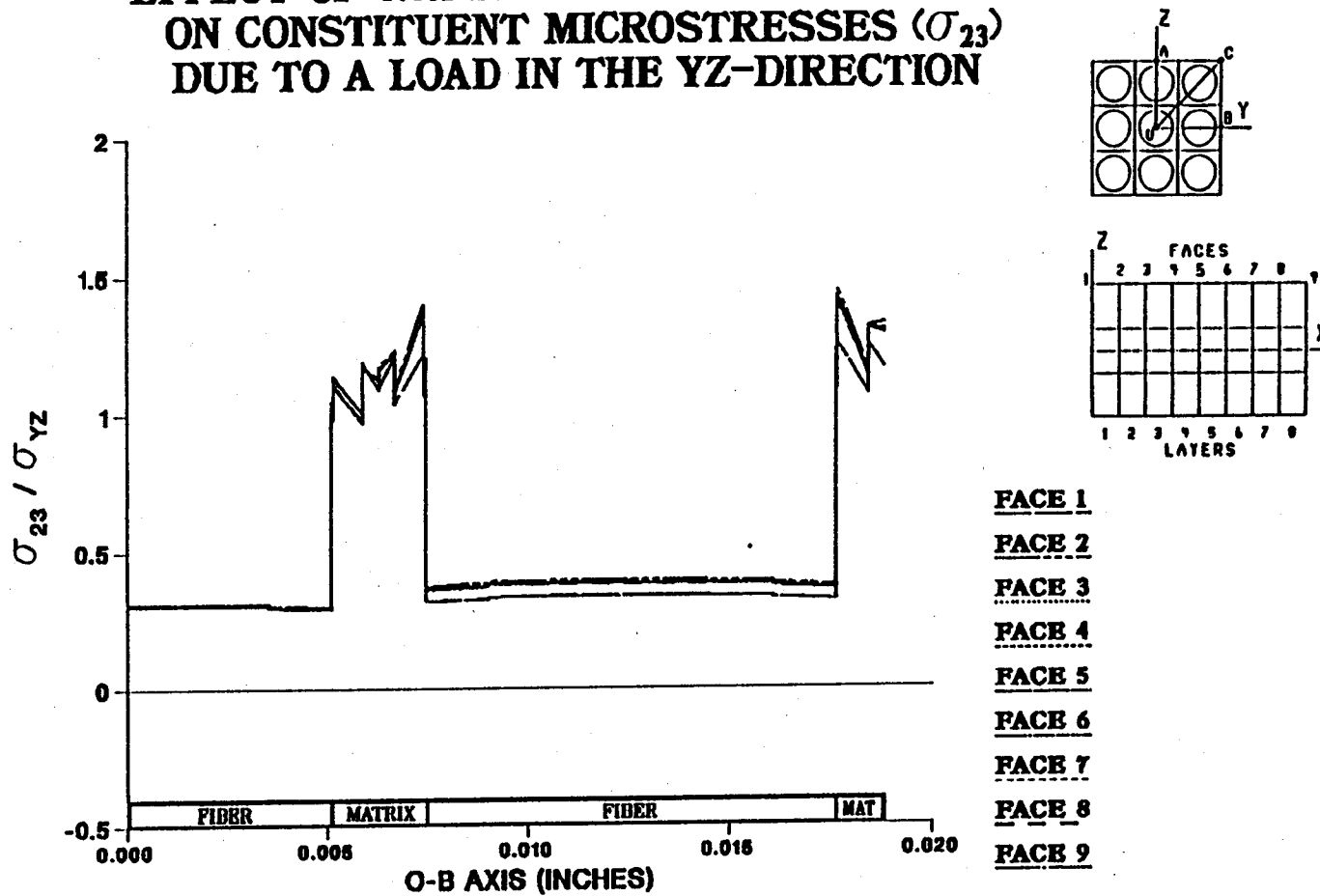


Figure A.118 - σ_{23} Normalized Microstresses, O-B Direction, 0.0% Debonding, σ_{yz}^e Loading

EFFECT OF 1.39% FIBER LENGTH DEBONDING ON CONSTITUENT MICROSTRESSES (σ_{23}) DUE TO A LOAD IN THE YZ-DIRECTION

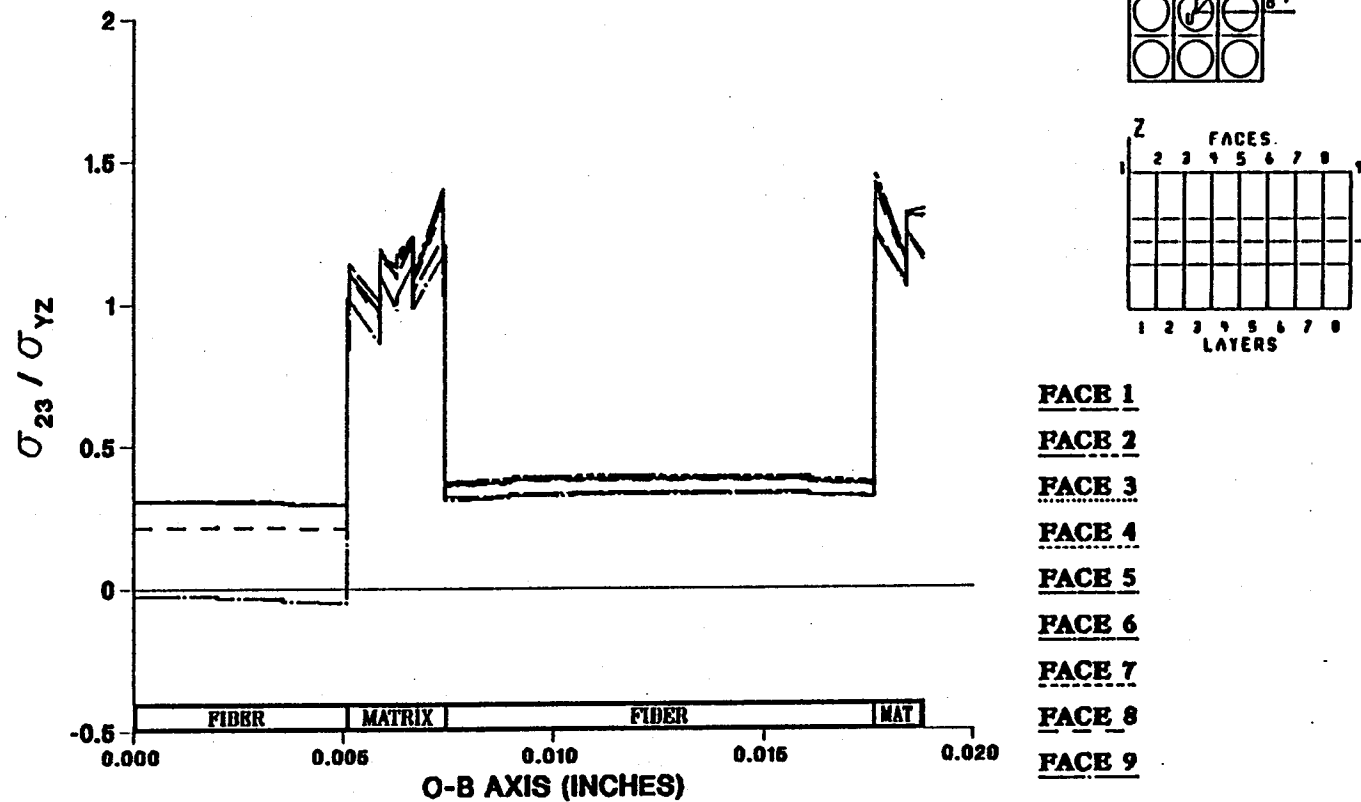


Figure A.119 — σ_{23} Normalized Microstresses, O-B Direction, 1.39% Debonding, σ_{yz}^e Loading

EFFECT OF 2.78% FIBER LENGTH DEBONDING ON CONSTITUENT MICROSTRESSES (σ_{23}) DUE TO A LOAD IN THE YZ-DIRECTION

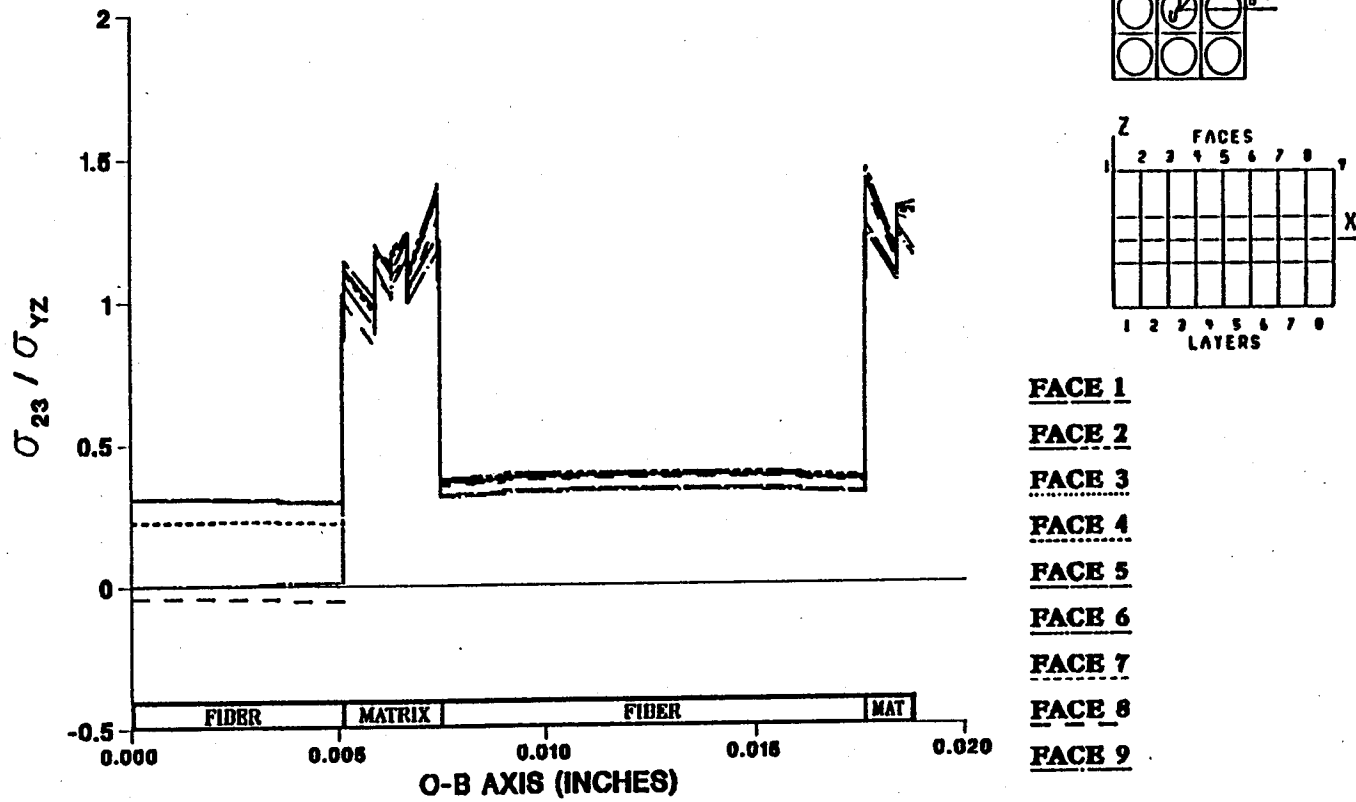


Figure A.120 – σ_{23} Normalized Microstresses, O-B Direction, 2.78% Debonding, σ_{yz}^e Loading

EFFECT OF 4.17% FIBER LENGTH DEBONDING ON CONSTITUENT MICROSTRESSES (σ_{23}) DUE TO A LOAD IN THE YZ-DIRECTION

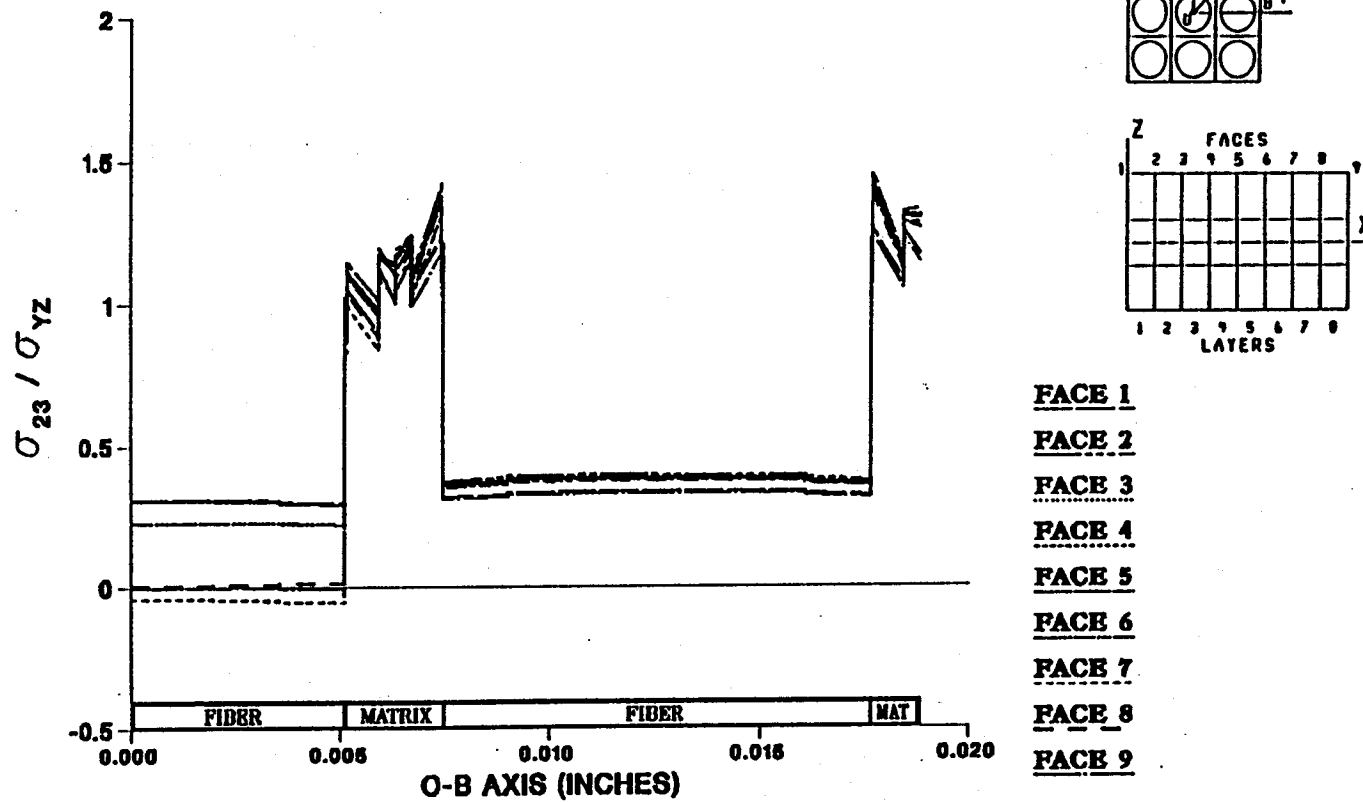


Figure A.121 - σ_{23} Normalized Microstresses, O-B Direction, 4.17% Debonding, σ_{yz}^e Loading

EFFECT OF 5.56% FIBER LENGTH DEBONDING ON CONSTITUENT MICROSTRESSES (σ_{23}) DUE TO A LOAD IN THE YZ-DIRECTION

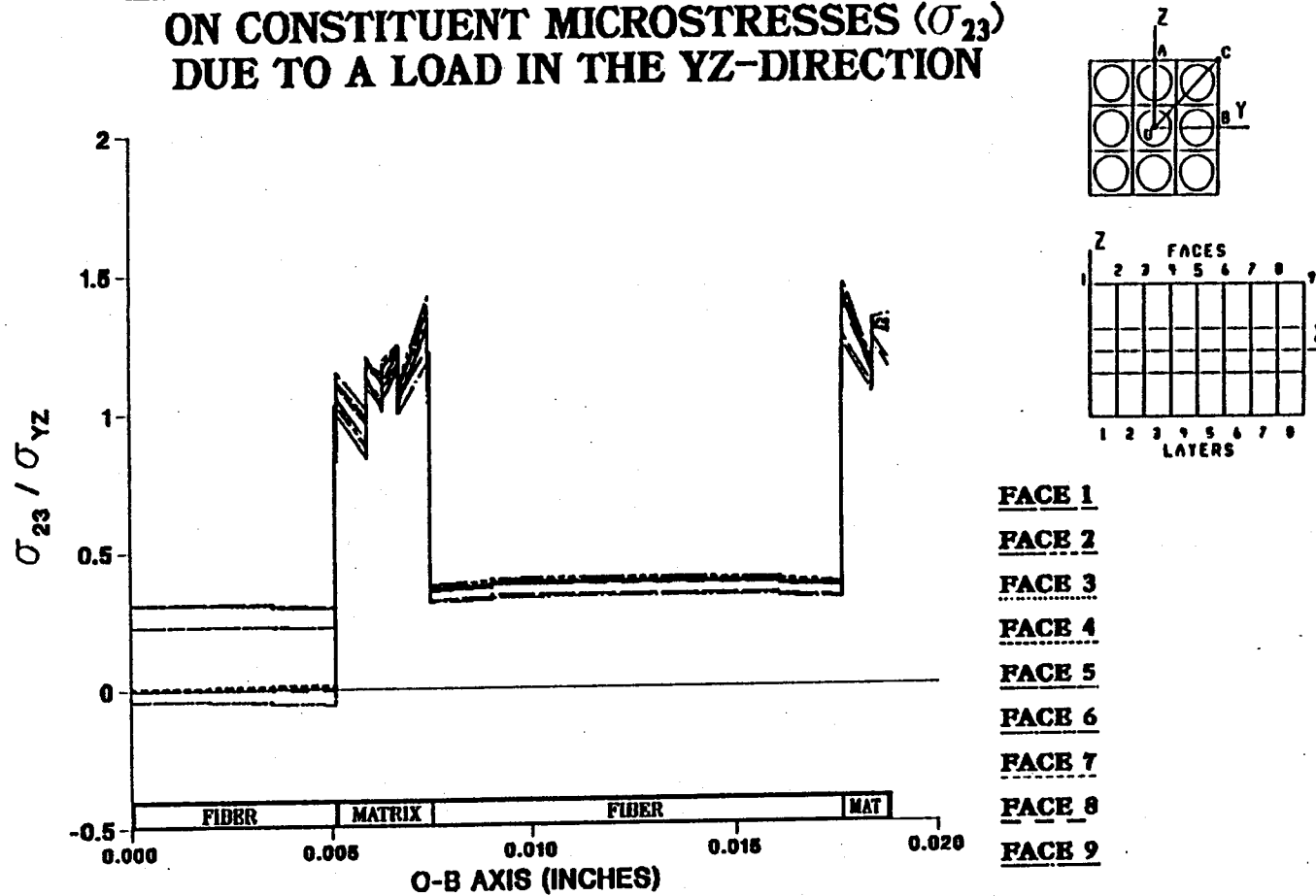


Figure A.122 — σ_{23} Normalized Microstresses, O-B Direction, 5.56% Debonding, σ_{yz}^e Loading

EFFECT OF 6.94% FIBER LENGTH DEBONDING ON CONSTITUENT MICROSTRESSES (σ_{23}) DUE TO A LOAD IN THE YZ-DIRECTION

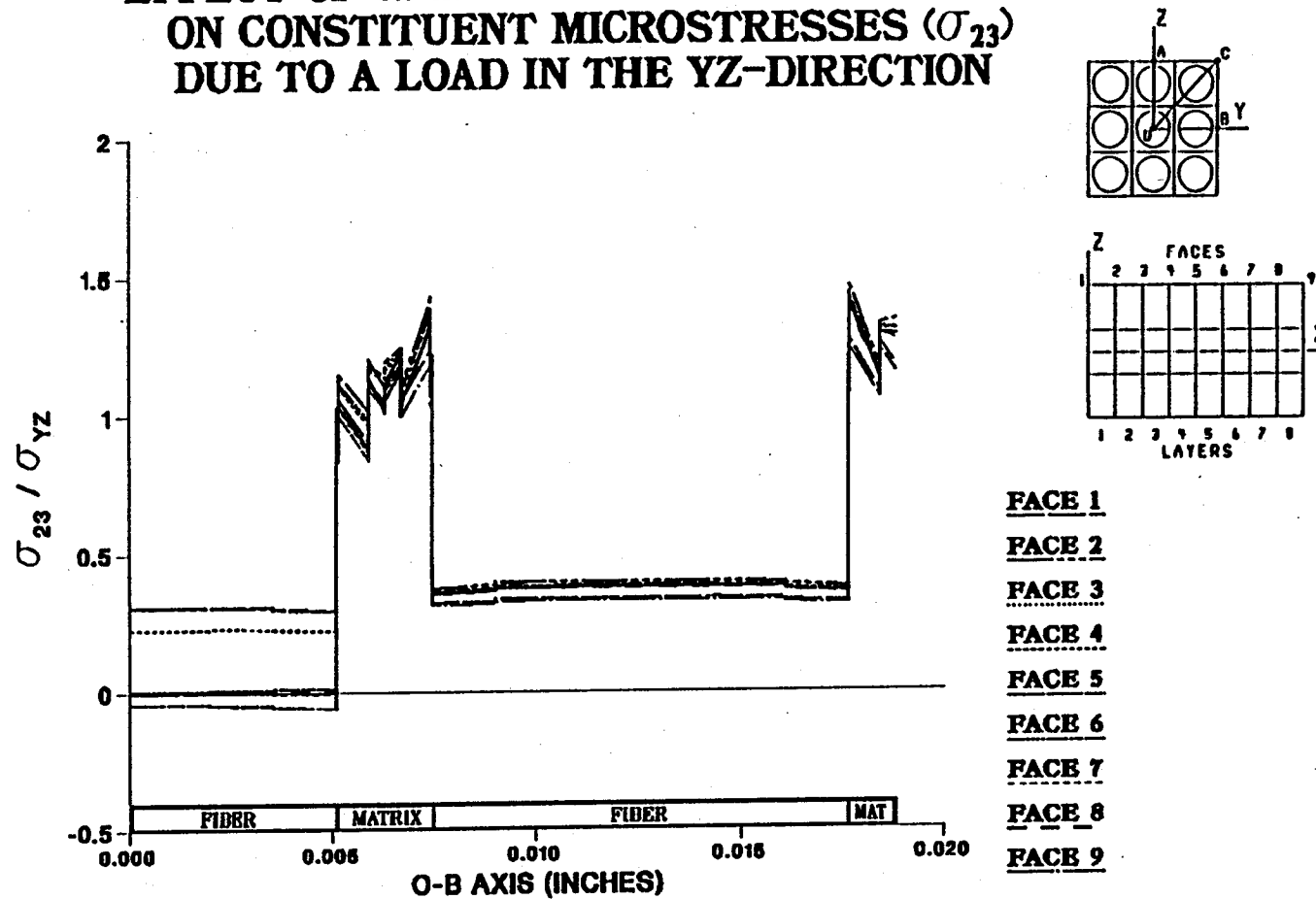


Figure A.123 - σ_{23} Normalized Microstresses, O-B Direction, 6.94% Debonding, σ_{yz}^e Loading

EFFECT OF 8.33% FIBER LENGTH DEBONDING ON CONSTITUENT MICROSTRESSES (σ_{23}) DUE TO A LOAD IN THE YZ-DIRECTION

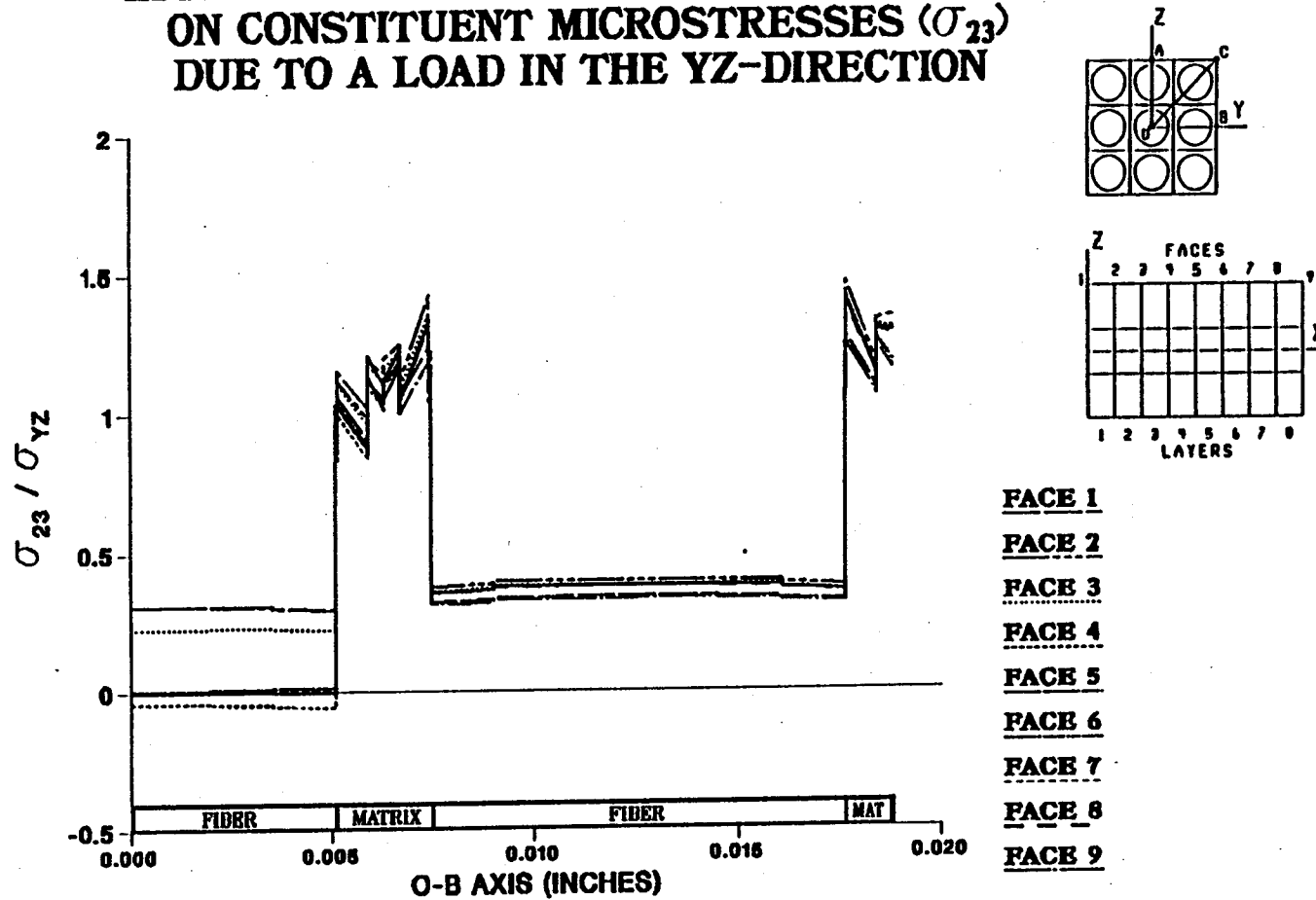


Figure A.124 - σ_{23} Normalized Microstresses, O-B Direction, 8.33% Debonding, σ_{yz}^e Loading

EFFECT OF 9.72% FIBER LENGTH DEBONDING ON CONSTITUENT MICROSTRESSES (σ_{23}) DUE TO A LOAD IN THE YZ-DIRECTION

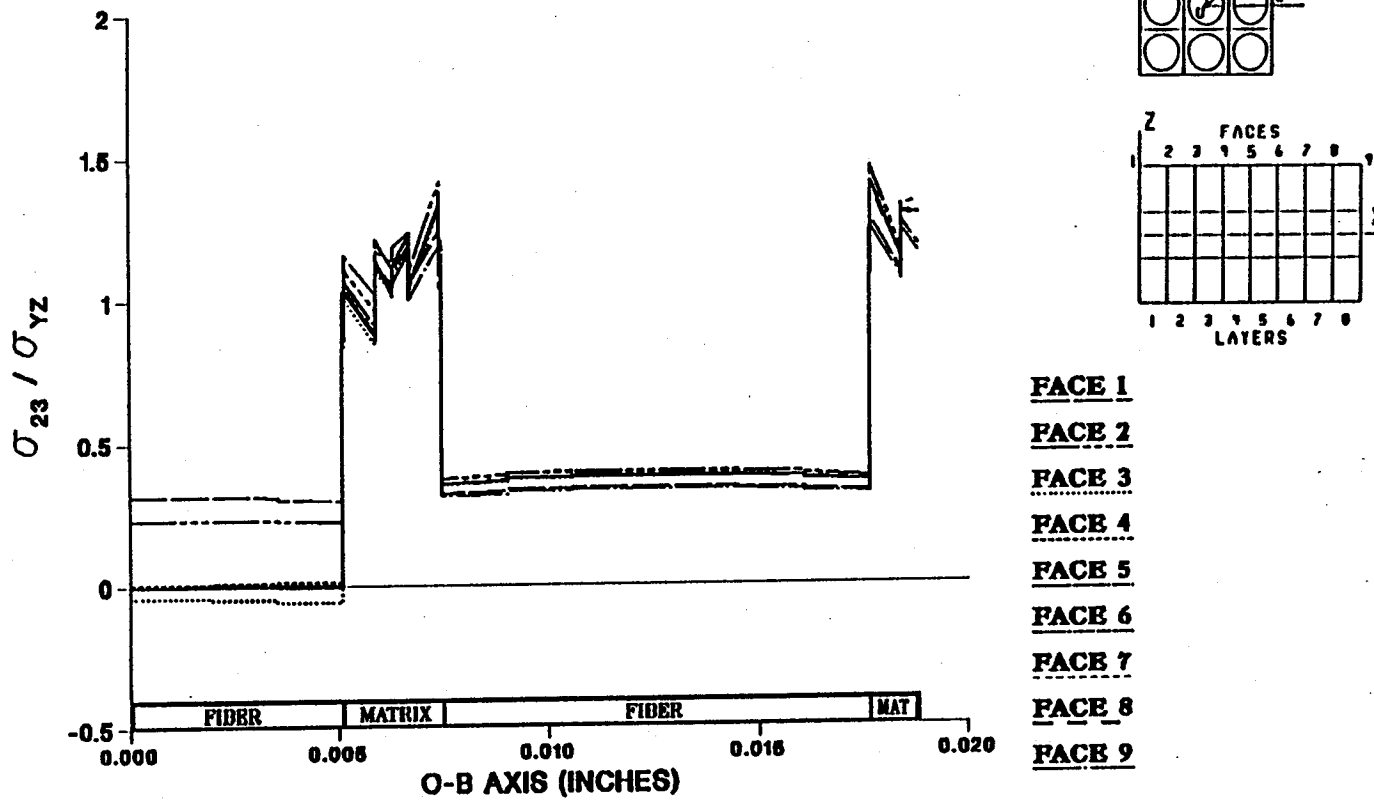


Figure A.125 - σ_{23} Normalized Microstresses, O-B Direction, 9.72% Debonding, σ_{yz}^e Loading

**EFFECT OF 11.11% FIBER LENGTH DEBONDING
ON CONSTITUENT MICROSTRESSES (σ_{23})
DUE TO A LOAD IN THE YZ-DIRECTION**

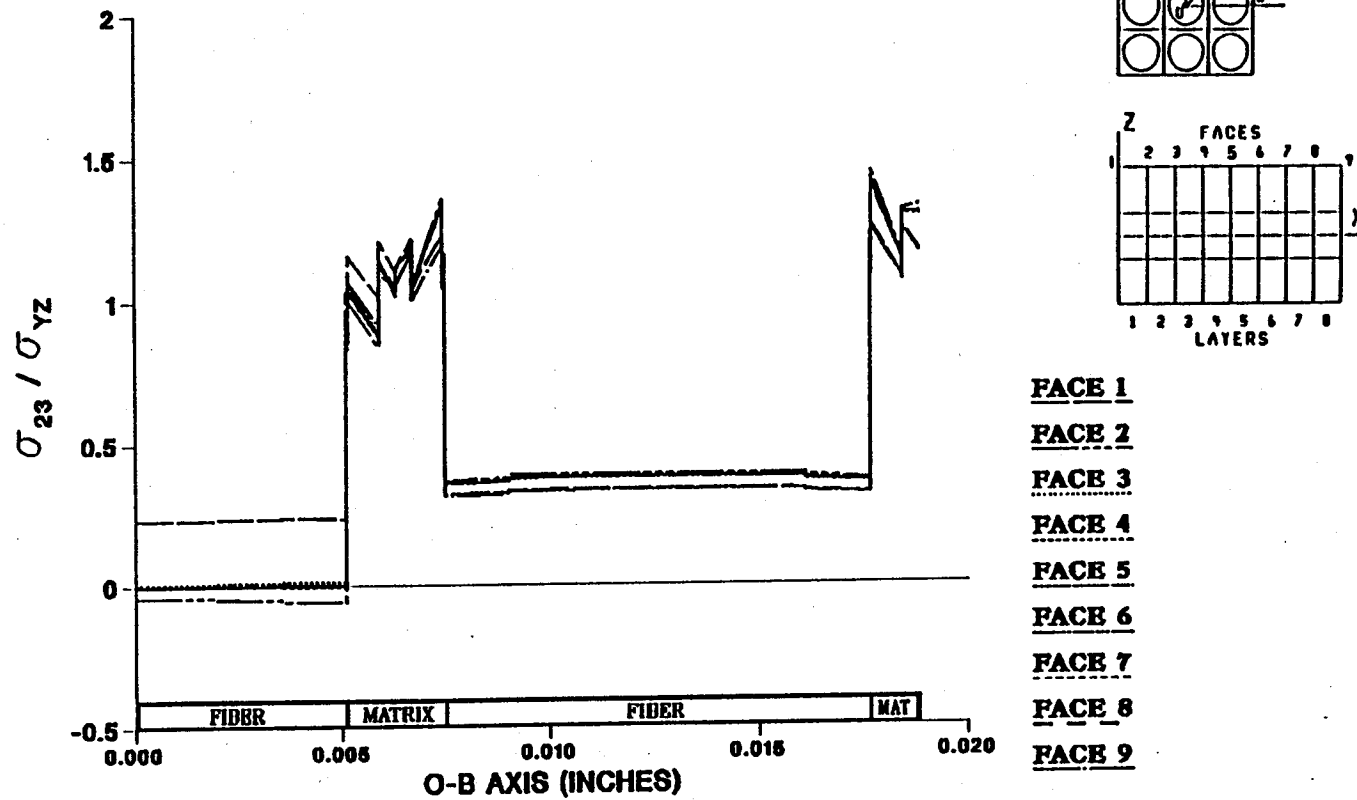
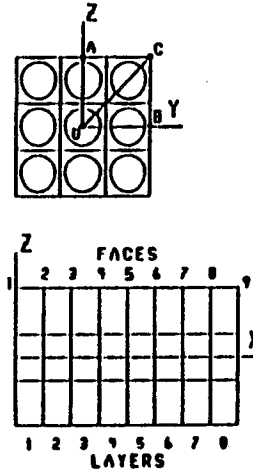
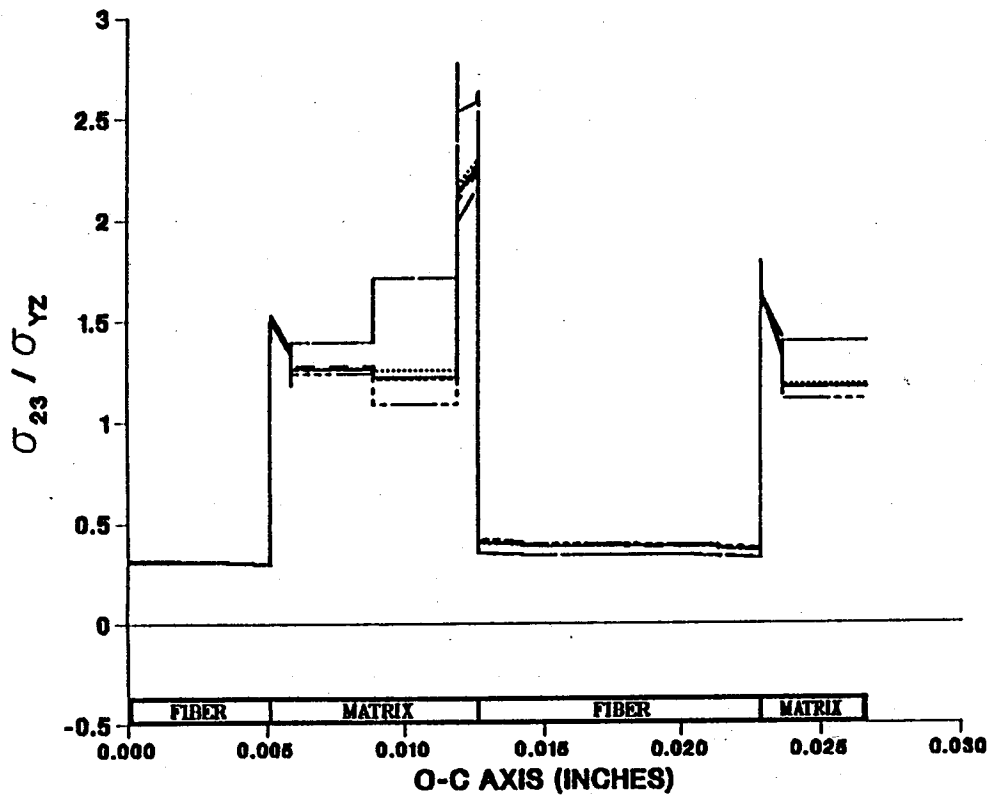


Figure A.126 - σ_{23} Normalized Microstresses, O-B Direction, 11.11% Debonding, σ_{yz}^e Loading

EFFECT OF 0.0% FIBER LENGTH DEBONDING ON CONSTITUENT MICROSTRESSES (σ_{23}) DUE TO A LOAD IN THE YZ-DIRECTION



- FACE 1
- FACE 2
- FACE 3
- FACE 4
- FACE 5
- FACE 6
- FACE 7
- FACE 8
- FACE 9

Figure A.127 - σ_{23} Normalized Microstresses, O-C Direction, 0.0% Debonding, σ_{yz}^e Loading

EFFECT OF 1.39% FIBER LENGTH DEBONDING ON CONSTITUENT MICROSTRESSES (σ_{23}) DUE TO A LOAD IN THE YZ-DIRECTION

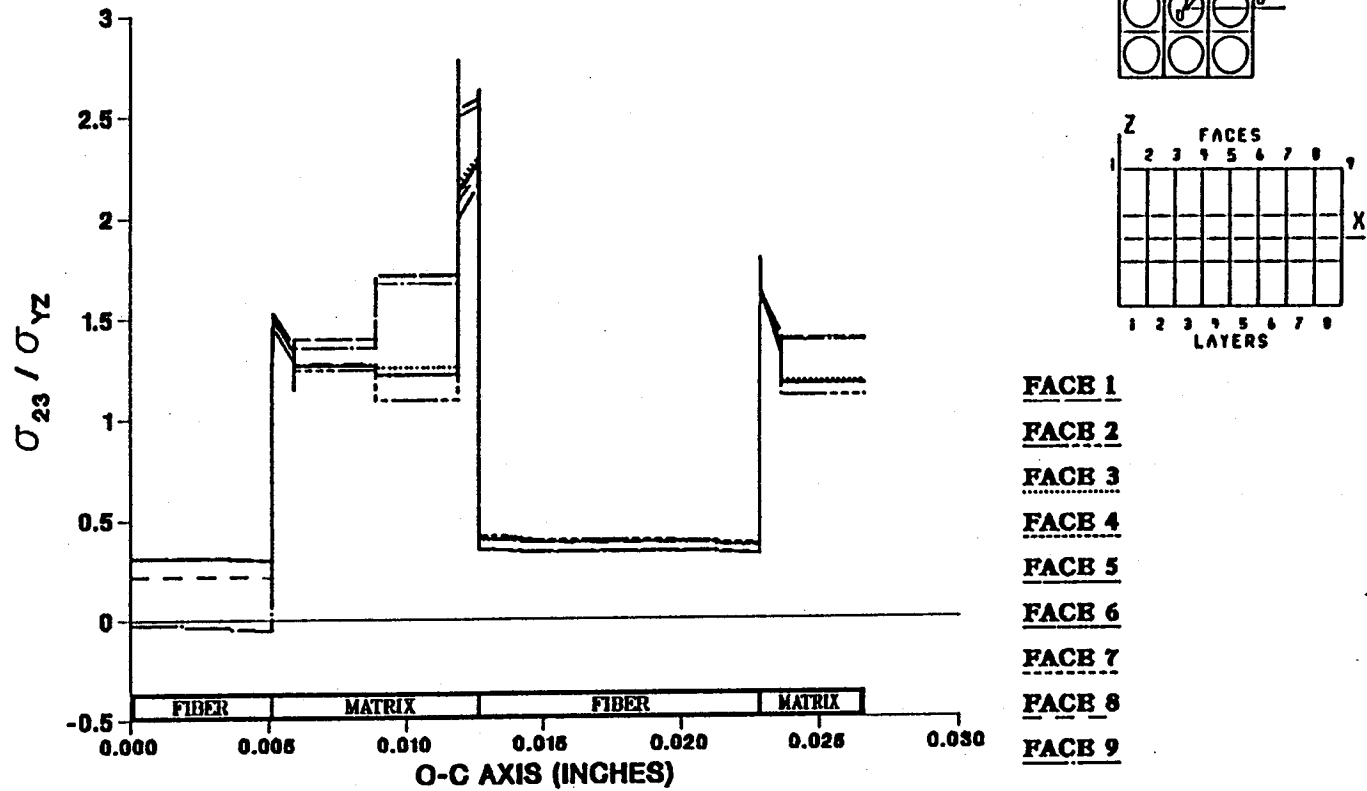


Figure A.128 - σ_{23} Normalized Microstresses, O-C Direction, 1.39% Debonding, σ_{yz}^e Loading

EFFECT OF 2.78% FIBER LENGTH DEBONDING ON CONSTITUENT MICROSTRESSES (σ_{23}) DUE TO A LOAD IN THE YZ-DIRECTION

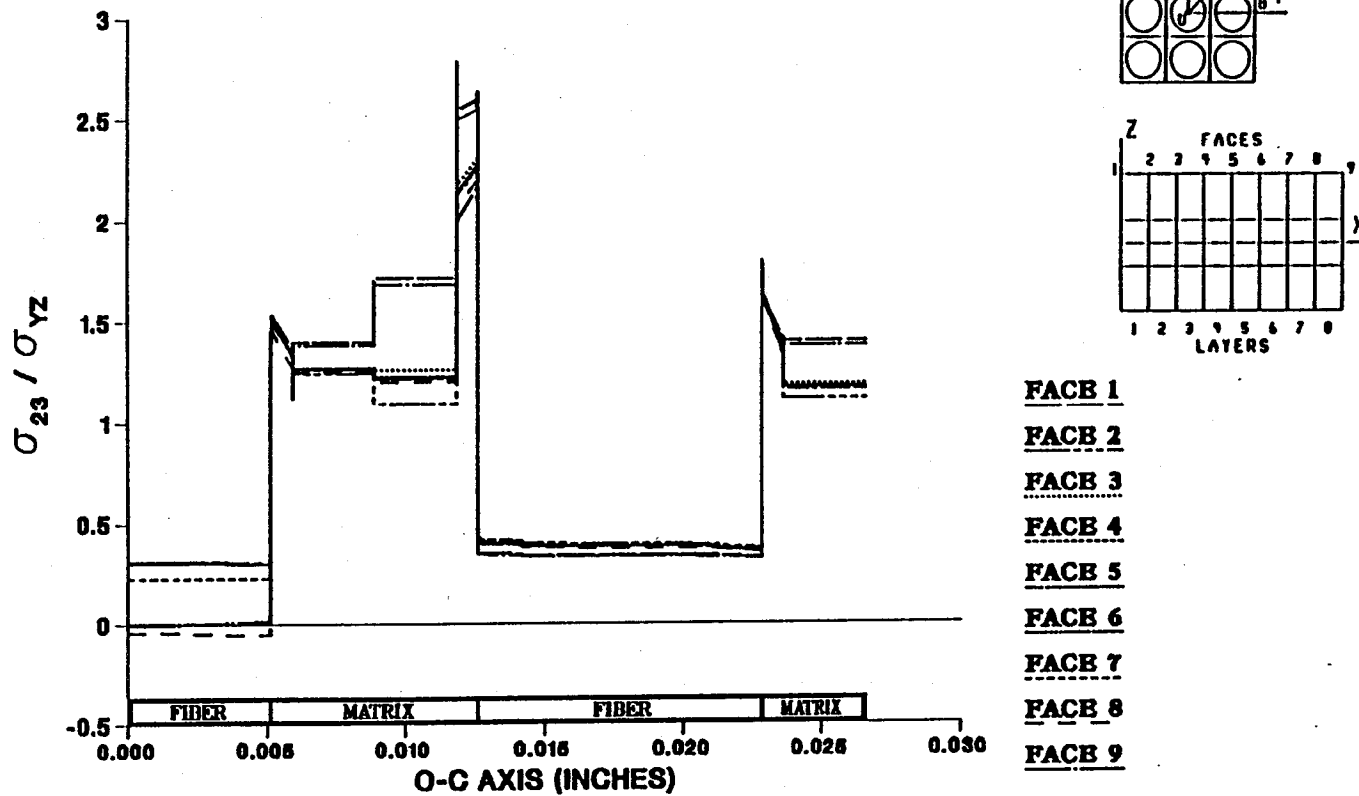


Figure A.129 - σ_{23} Normalized Microstresses, O-C Direction, 2.78% Debonding, σ_{yz}^e Loading

**EFFECT OF 4.17% FIBER LENGTH DEBONDING
ON CONSTITUENT MICROSTRESSES (σ_{23})
DUE TO A LOAD IN THE YZ-DIRECTION**

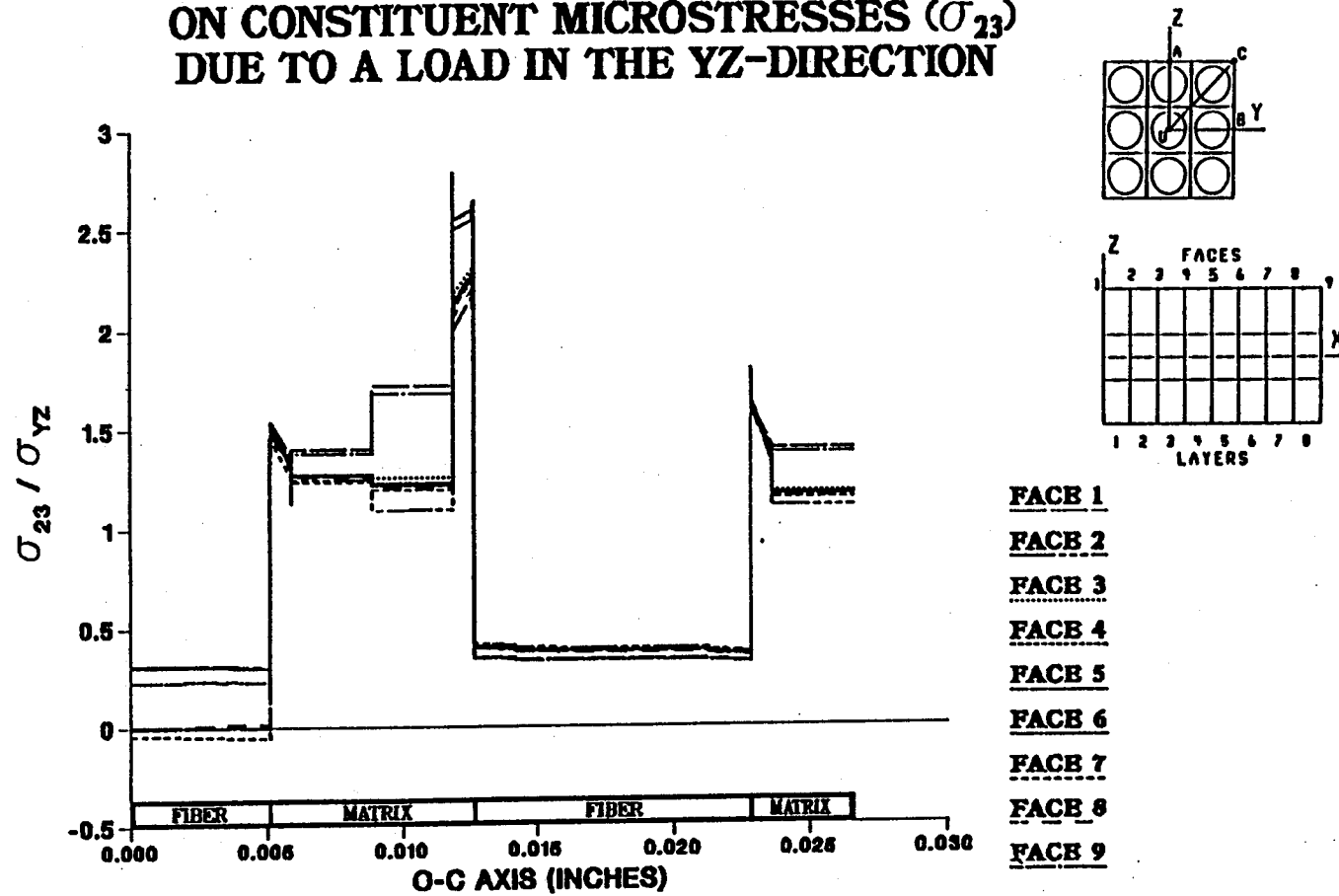


Figure A.130 — σ_{23} Normalized Microstresses, O-C Direction, 4.17% Debonding, σ_{yz}^e Loading

EFFECT OF 5.56% FIBER LENGTH DEBONDING ON CONSTITUENT MICROSTRESSES (σ_{23}) DUE TO A LOAD IN THE YZ-DIRECTION

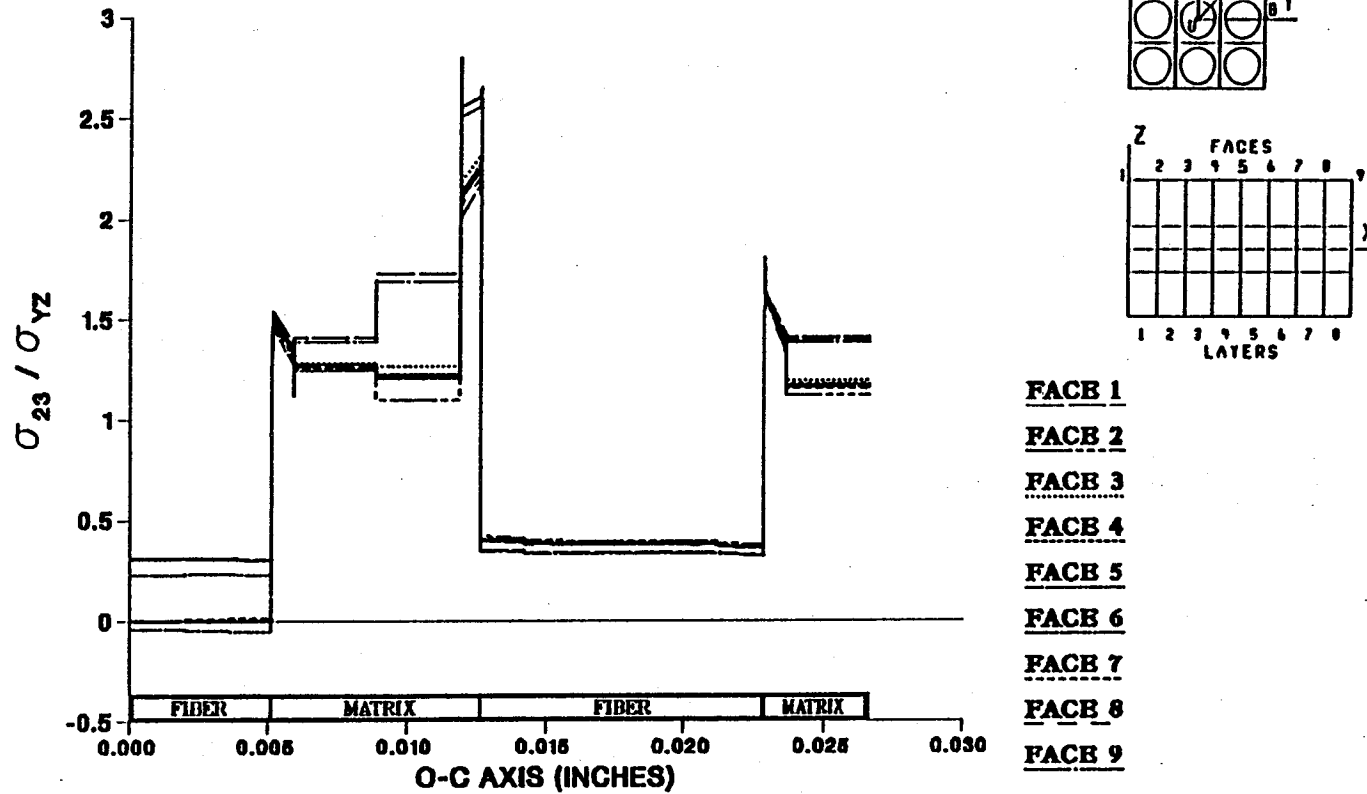


Figure A.131 - σ_{23} Normalized Microstresses, O-C Direction, 5.56% Debonding, σ_{yz}^e Loading

EFFECT OF 6.94% FIBER LENGTH DEBONDING ON CONSTITUENT MICROSTRESSES (σ_{23}) DUE TO A LOAD IN THE YZ-DIRECTION

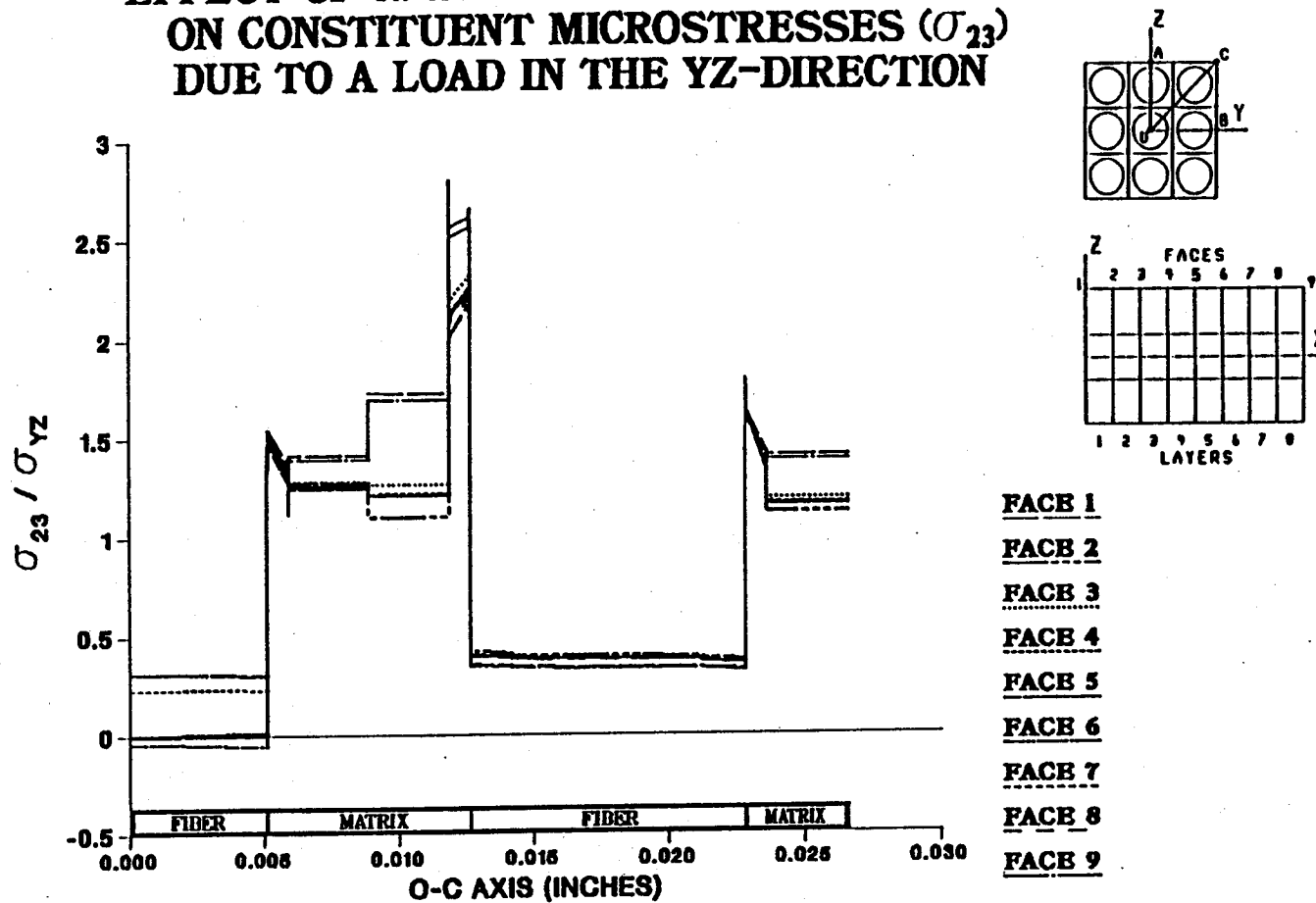


Figure A.132 -- σ_{23} Normalized Microstresses, O-C Direction, 6.94% Debonding, σ_{yz}^e Loading

EFFECT OF 8.33% FIBER LENGTH DEBONDING ON CONSTITUENT MICROSTRESSES (σ_{23}) DUE TO A LOAD IN THE YZ-DIRECTION

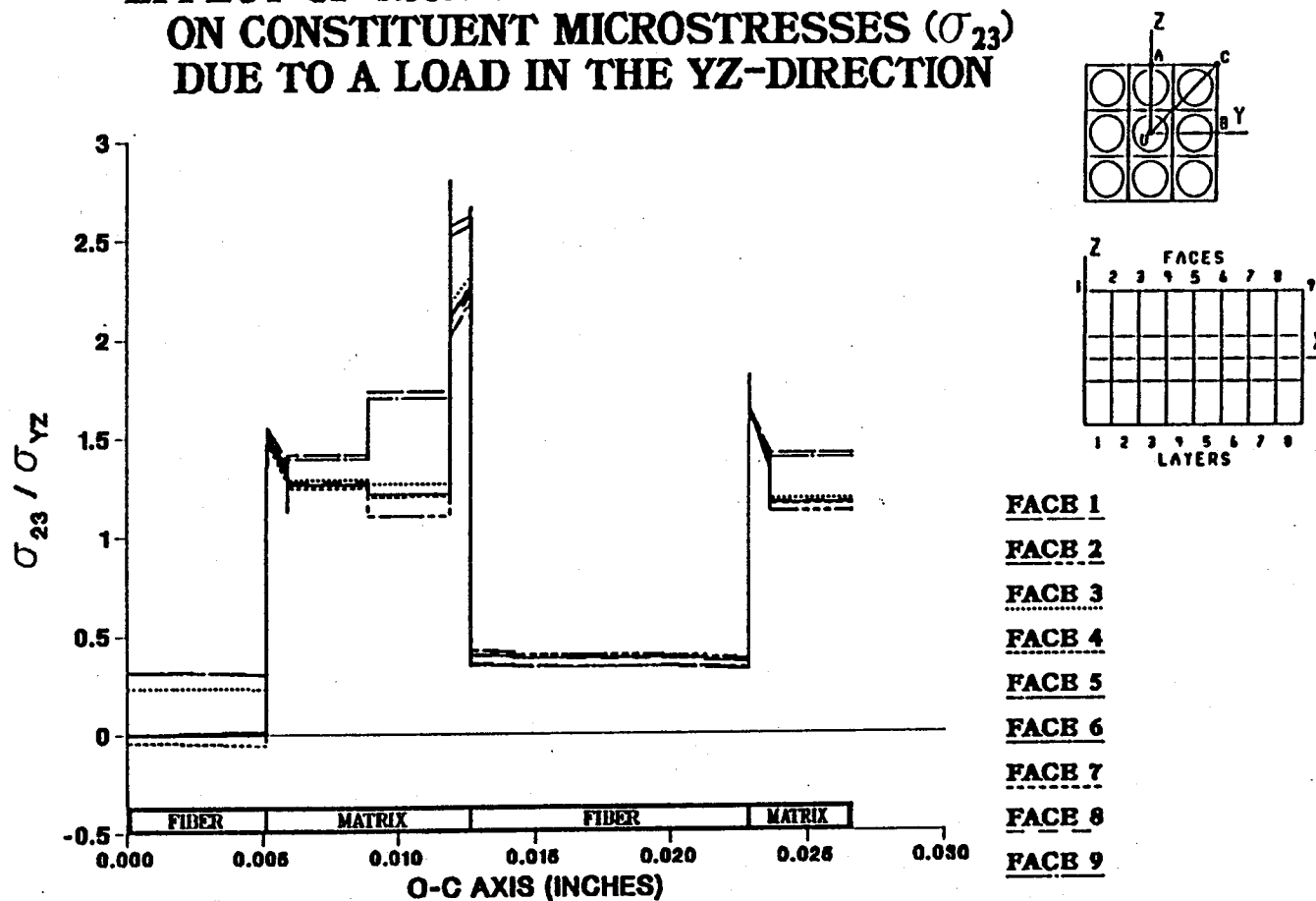


Figure A.133 – σ_{23} Normalized Microstresses, O–C Direction, 8.33% Debonding, σ_{yz}^e Loading

**EFFECT OF 9.72% FIBER LENGTH DEBONDING
ON CONSTITUENT MICROSTRESSES (σ_{23})
DUE TO A LOAD IN THE YZ-DIRECTION**

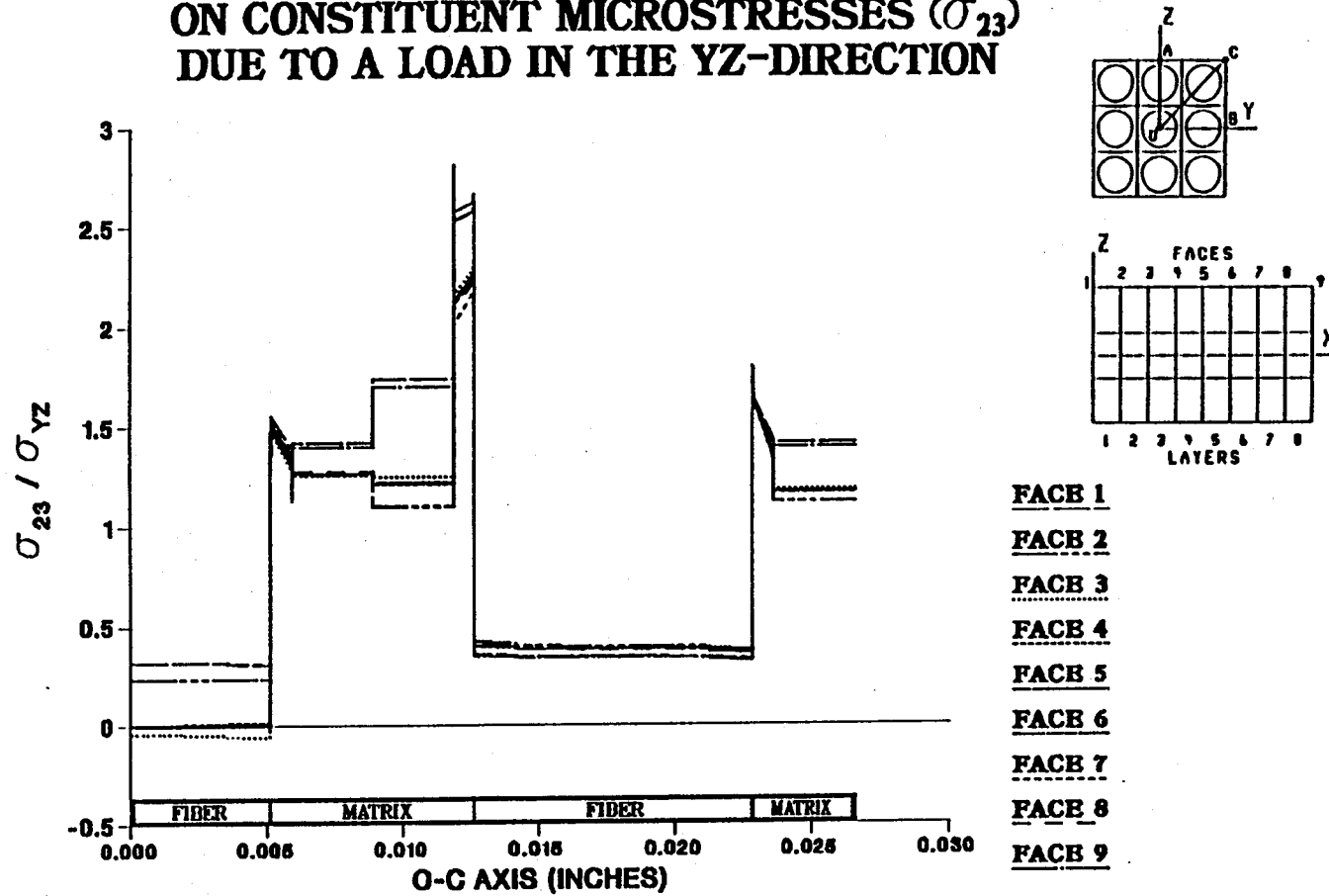


Figure A.134 - σ_{23} Normalized Microstresses, O-C Direction, 9.72% Debonding, σ_{yz}^e Loading

EFFECT OF 11.1% FIBER LENGTH DEBONDING ON CONSTITUENT MICROSTRESSES (σ_{23}) DUE TO A LOAD IN THE YZ-DIRECTION

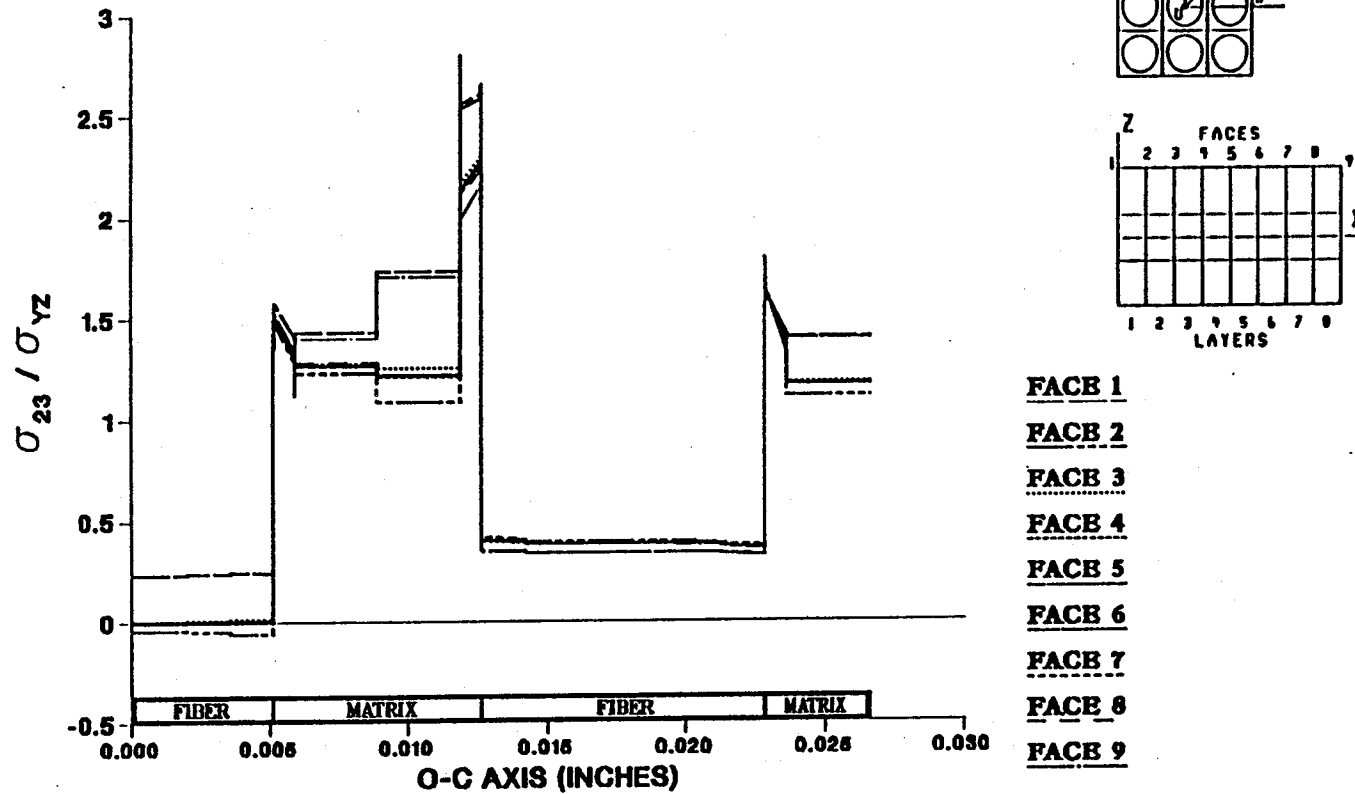


Figure A.135 - σ_{23} Normalized Microstresses, O-C Direction, 11.1% Debonding, σ_{yz}^e Loading

EFFECT OF 0.0% FIBER LENGTH DEBONDING ON CONSTITUENT MICROSTRESSES (σ_{11}) DUE TO AN APPLIED THERMAL LOAD

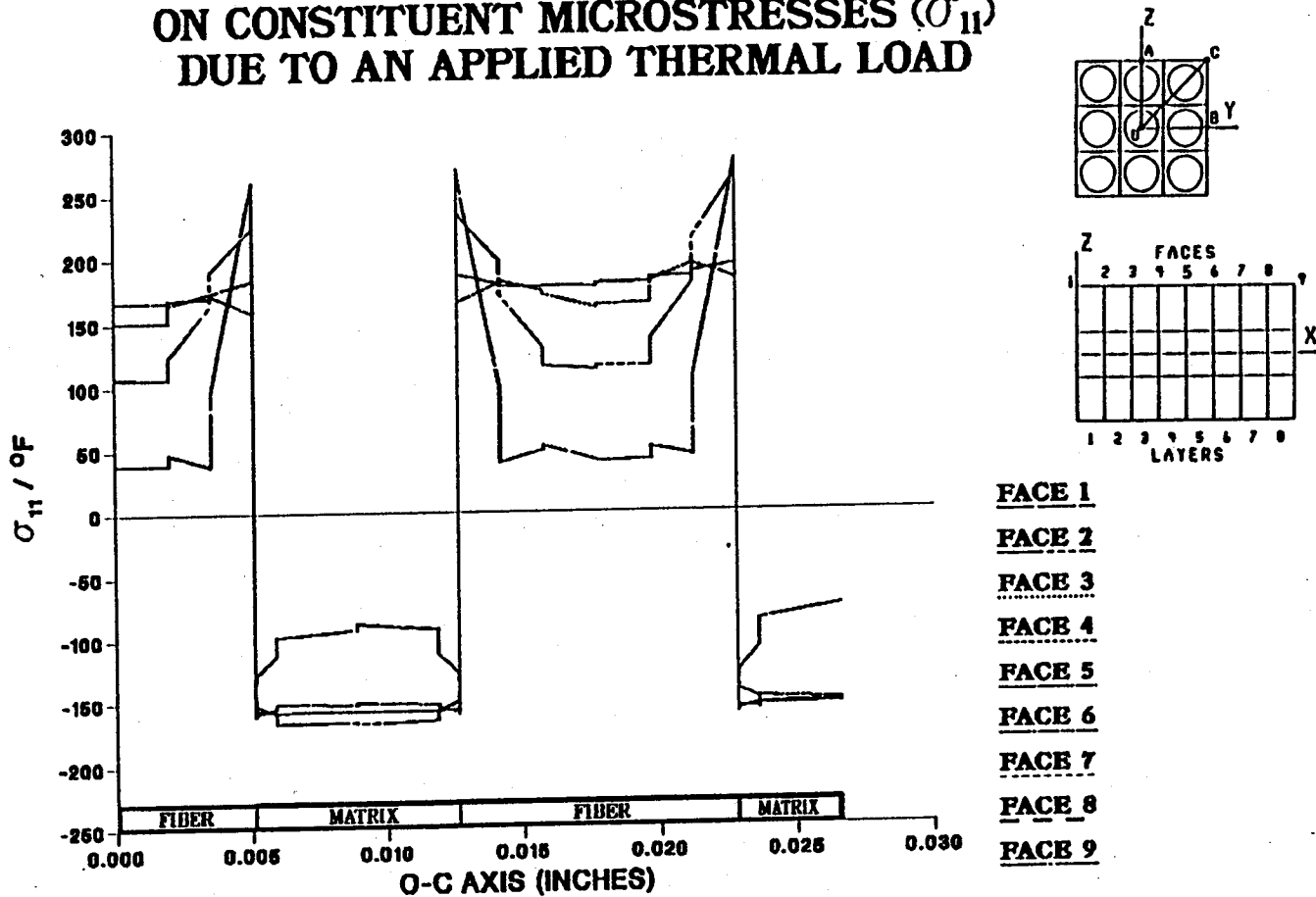
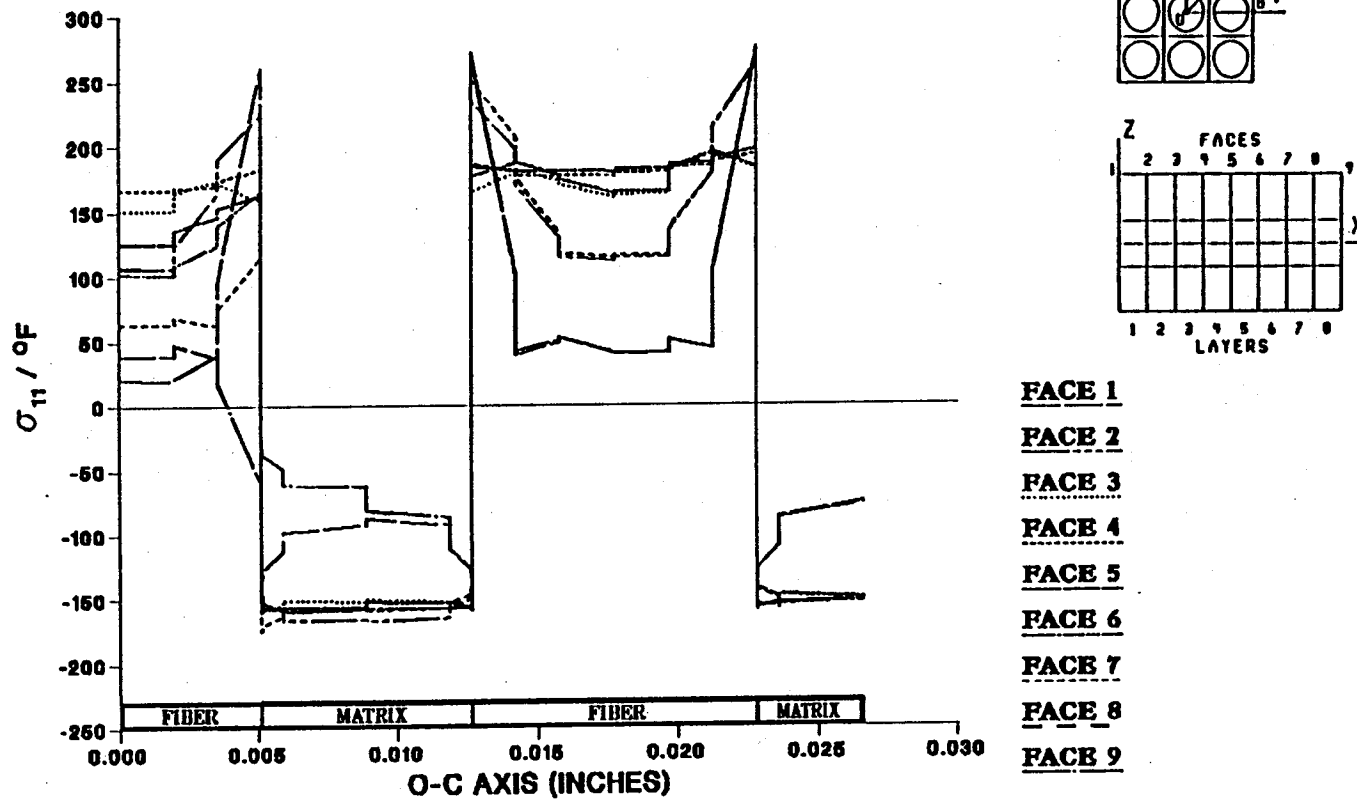


Figure A.136 – σ_{11} Normalized Microstresses, O-C Direction, 0.0% Debonding, Thermal Loading

EFFECT OF 1.39% FIBER LENGTH DEBONDING ON CONSTITUENT MICROSTRESSES (σ_{11}) DUE TO AN APPLIED THERMAL LOAD



- FACE 1
- FACE 2
- FACE 3
- FACE 4
- FACE 5
- FACE 6
- FACE 7
- FACE 8
- FACE 9

Figure A.137 - σ_{11} Normalized Microstresses, O-C Direction, 1.39% Debonding, Thermal Loading

EFFECT OF 2.78% FIBER LENGTH DEBONDING ON CONSTITUENT MICROSTRESSES (σ_{11}) DUE TO AN APPLIED THERMAL LOAD

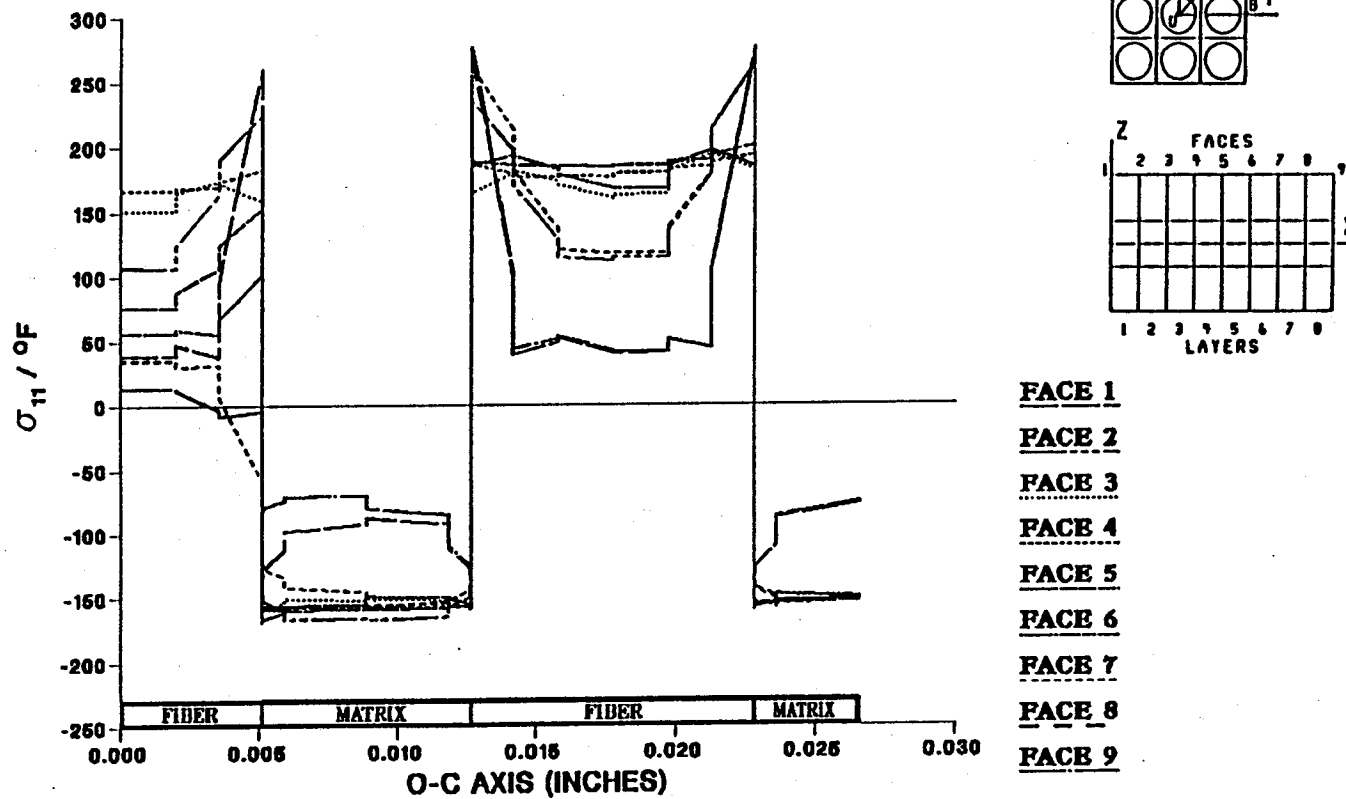


Figure A.138 - σ_{11} Normalized Microstresses, O-C Direction, 2.78% Debonding, Thermal Loading

EFFECT OF 4.17% FIBER LENGTH DEBONDING ON CONSTITUENT MICROSTRESSES (σ_{11}) DUE TO AN APPLIED THERMAL LOAD

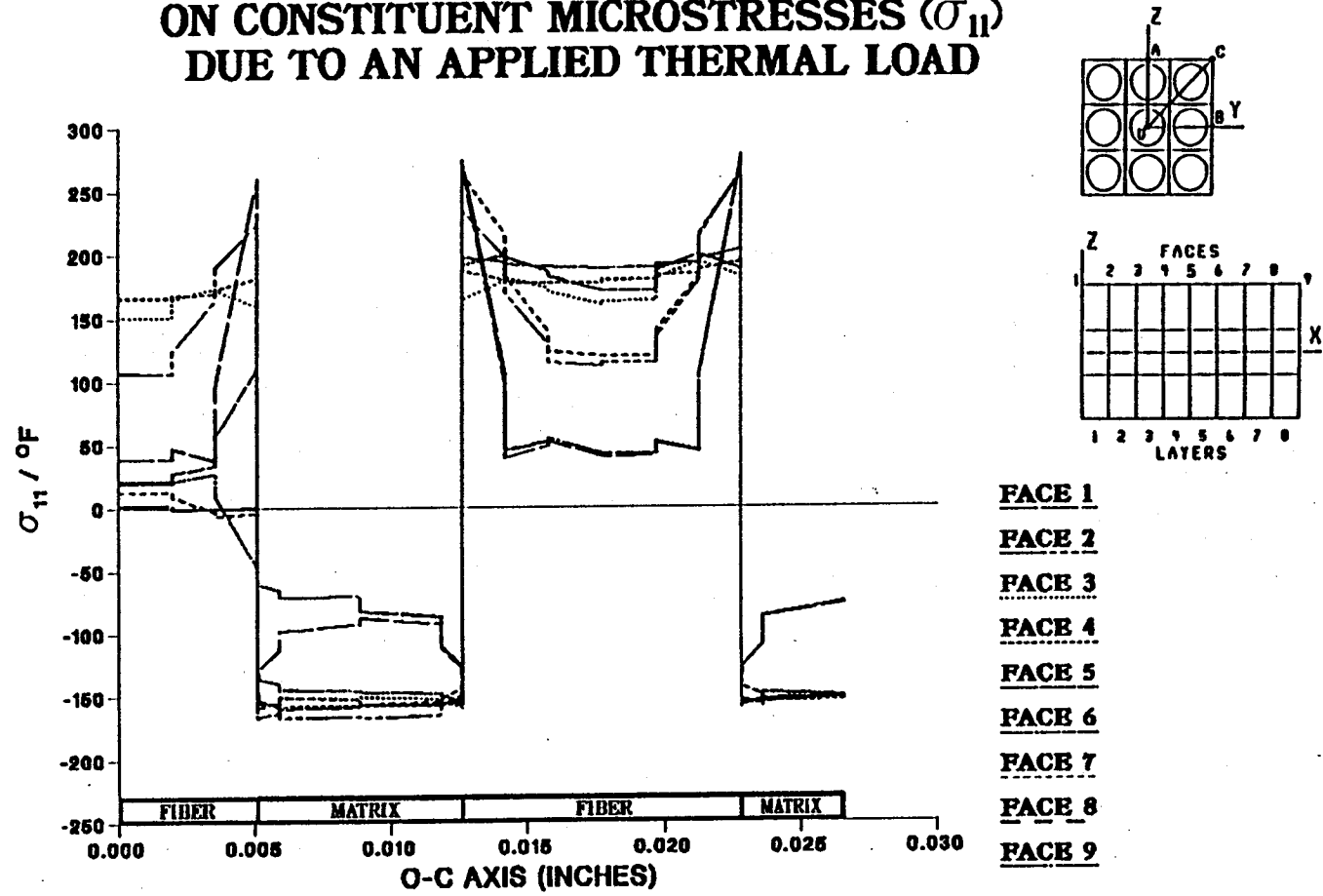


Figure A.139 — σ_{11} Normalized Microstresses, O-C Direction, 4.17% Debonding, Thermal Loading

EFFECT OF 5.56% FIBER LENGTH DEBONDING ON CONSTITUENT MICROSTRESSES (σ_{11}) DUE TO AN APPLIED THERMAL LOAD

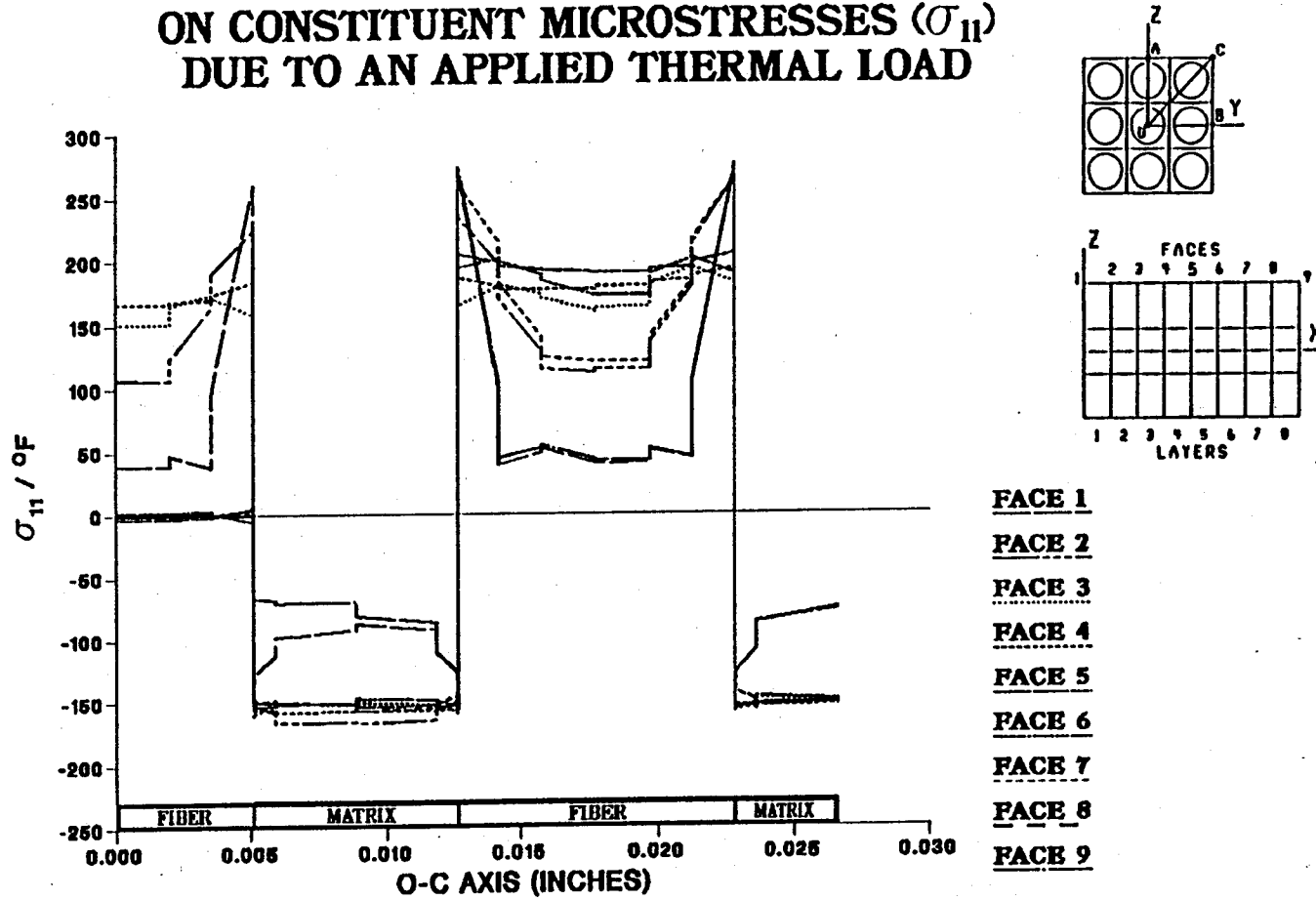


Figure A.140 - σ_{11} Normalized Microstresses, O-C Direction, 5.56% Debonding, Thermal Loading

EFFECT OF 6.94% FIBER LENGTH DEBONDING ON CONSTITUENT MICROSTRESSES (σ_{11}) DUE TO AN APPLIED THERMAL LOAD

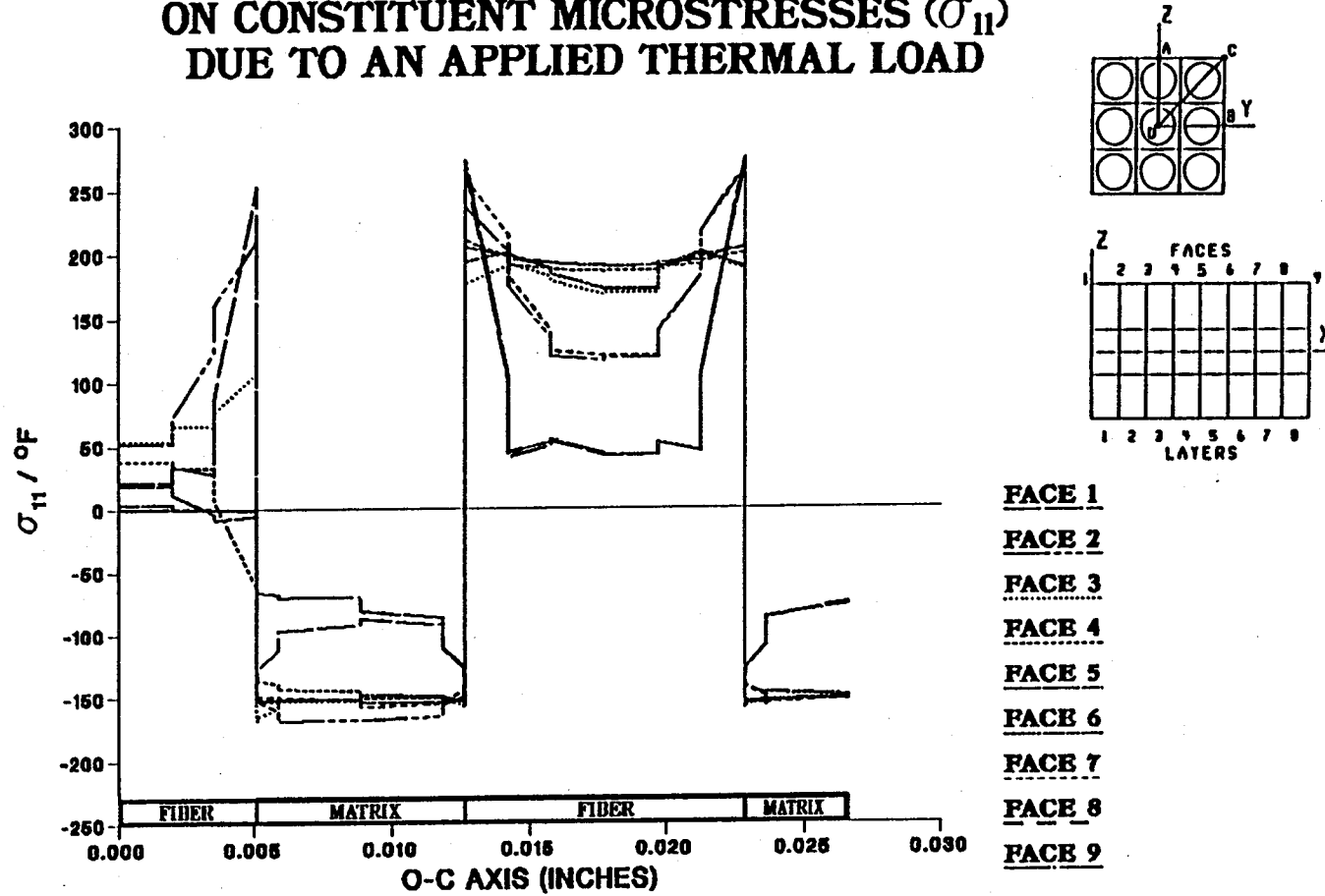


Figure A.141 – σ_{11} Normalized Microstresses, O–C Direction, 6.94% Debonding, Thermal Loading

EFFECT OF 8.33% FIBER LENGTH DEBONDING ON CONSTITUENT MICROSTRESSES (σ_{11}) DUE TO AN APPLIED THERMAL LOAD

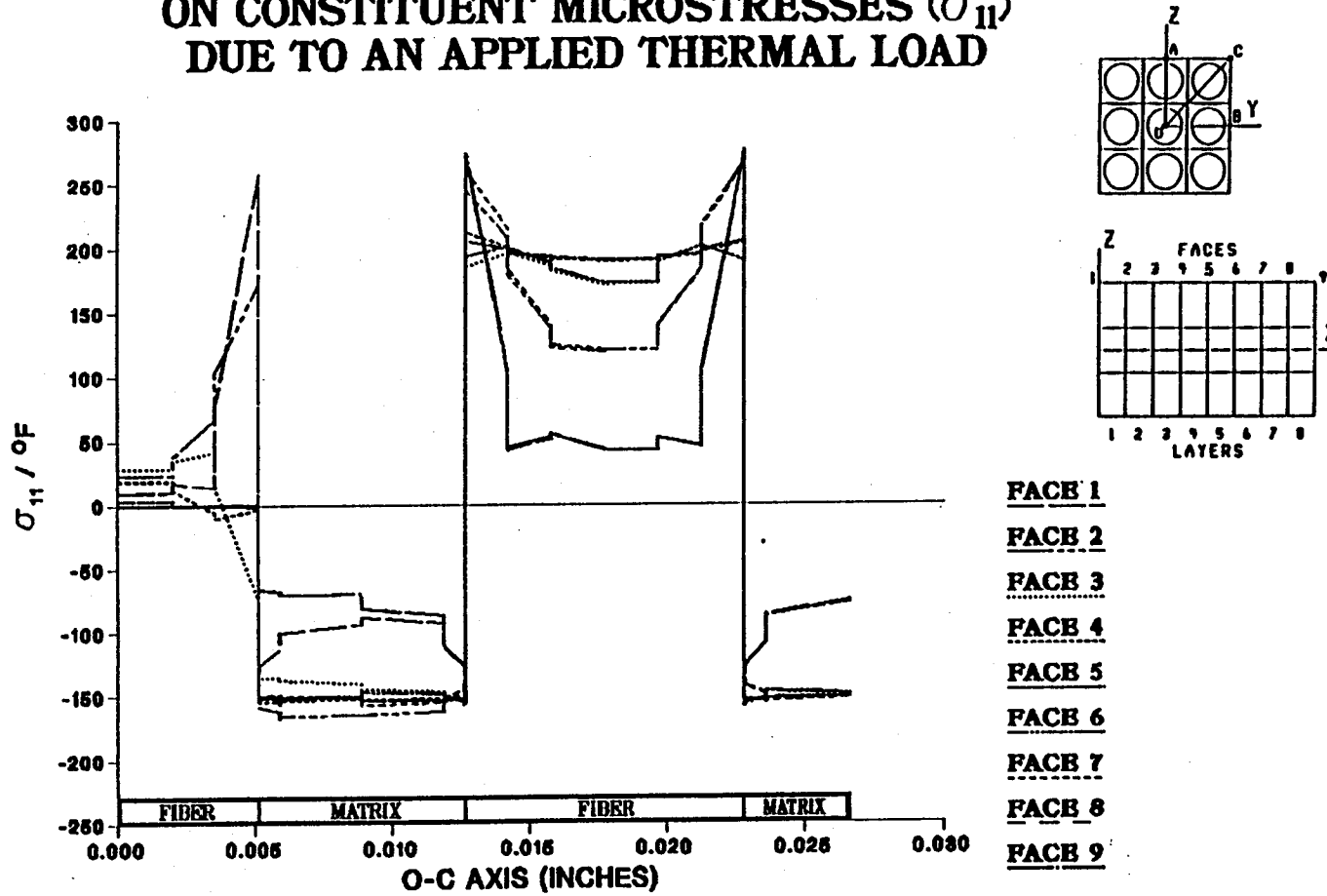


Figure A.142 - σ_{11} Normalized Microstresses, O-C Direction, 8.33% Debonding, Thermal Loading

EFFECT OF 9.72% FIBER LENGTH DEBONDING ON CONSTITUENT MICROSTRESSES (σ_{11}) DUE TO AN APPLIED THERMAL LOAD

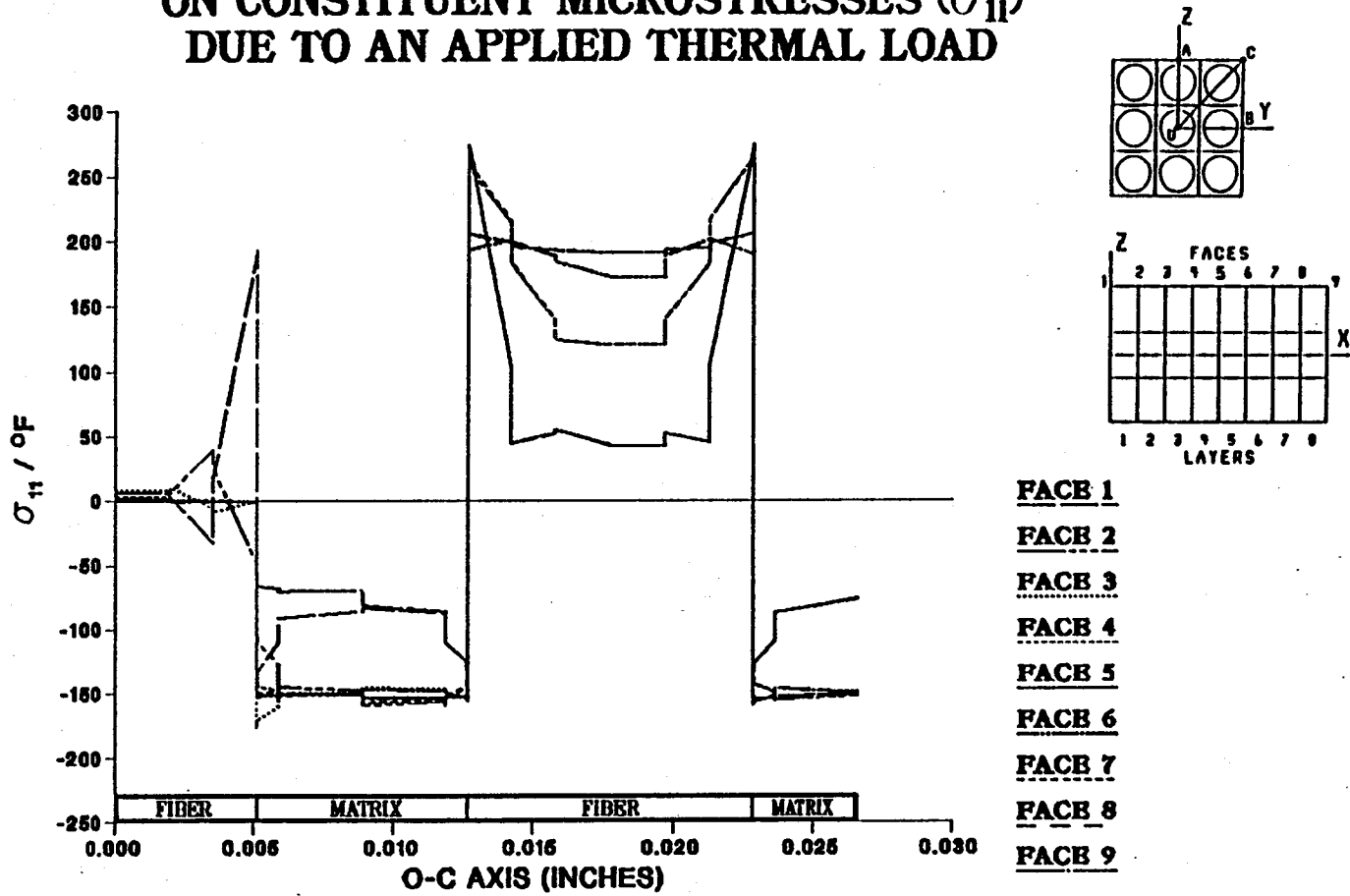


Figure A.143 – σ_{11} Normalized Microstresses, O–C Direction, 9.72% Debonding, Thermal Loading

EFFECT OF 11.11% FIBER LENGTH DEBONDING ON CONSTITUENT MICROSTRESSES (σ_{11}) DUE TO AN APPLIED THERMAL LOAD

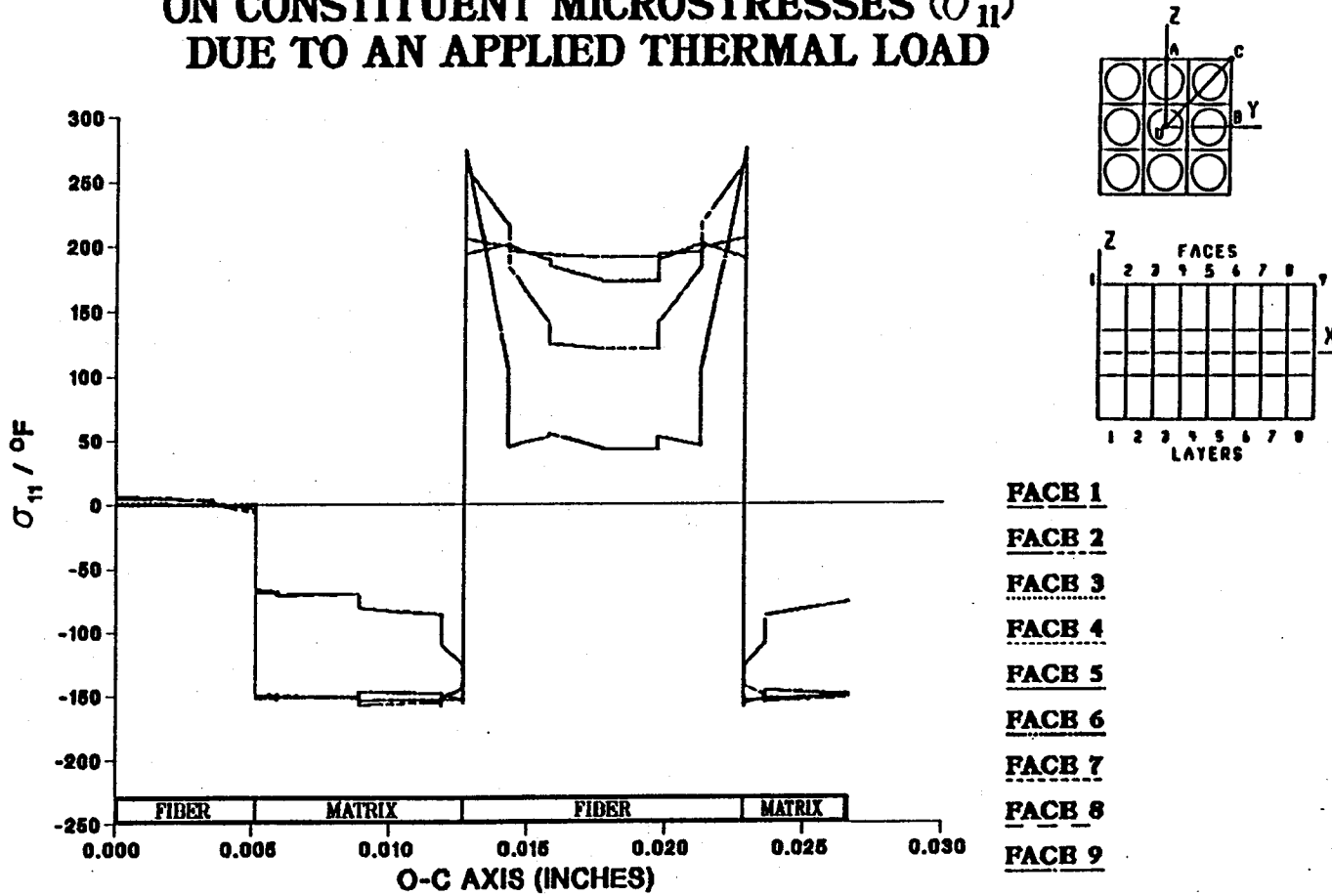


Figure A.144 - σ_{11} Normalized Microstresses, O-C Direction, 11.11% Debonding, Thermal Loading

EFFECT OF 0.0% FIBER LENGTH DEBONDING ON CONSTITUENT MICROSTRESSES (σ_{31}) DUE TO AN APPLIED THERMAL LOAD

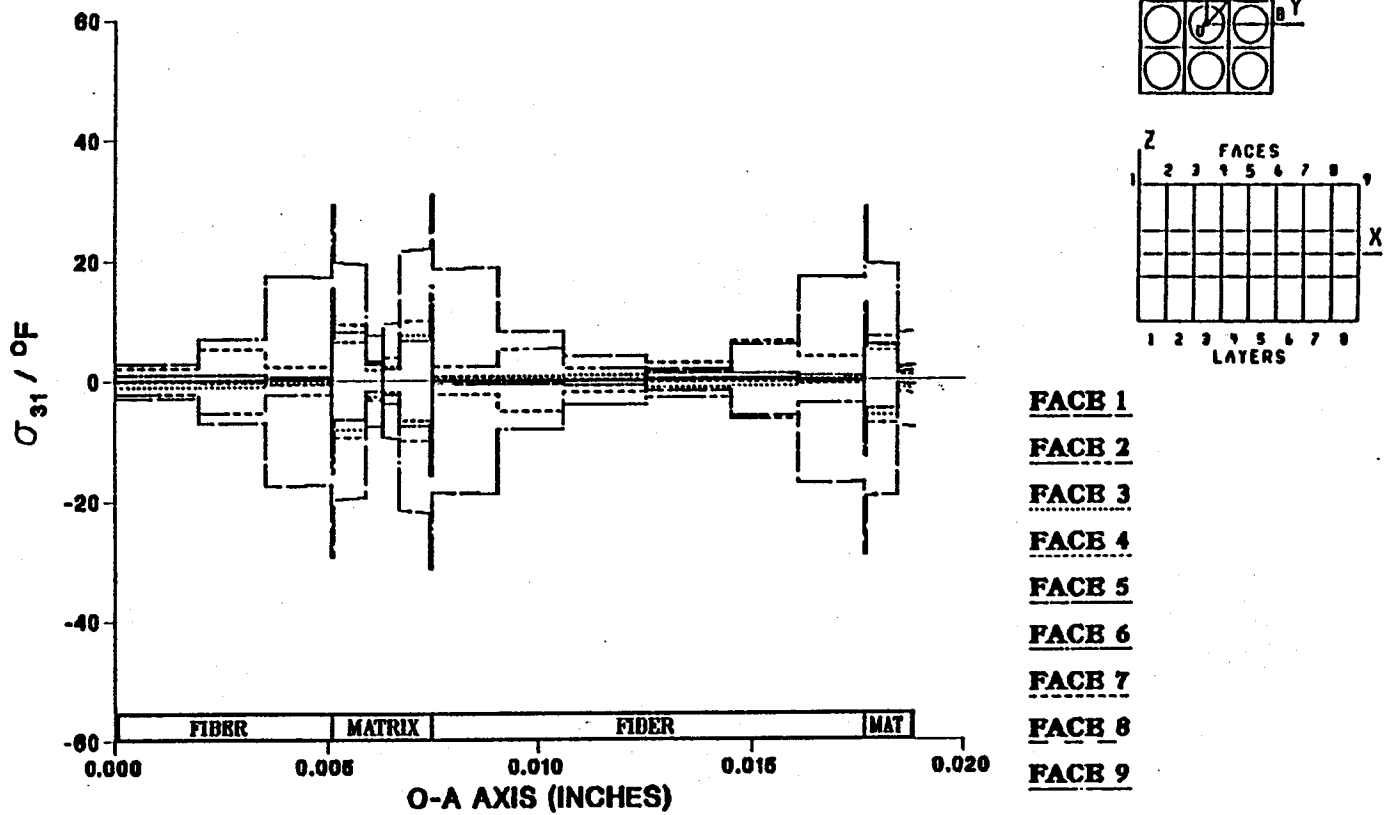
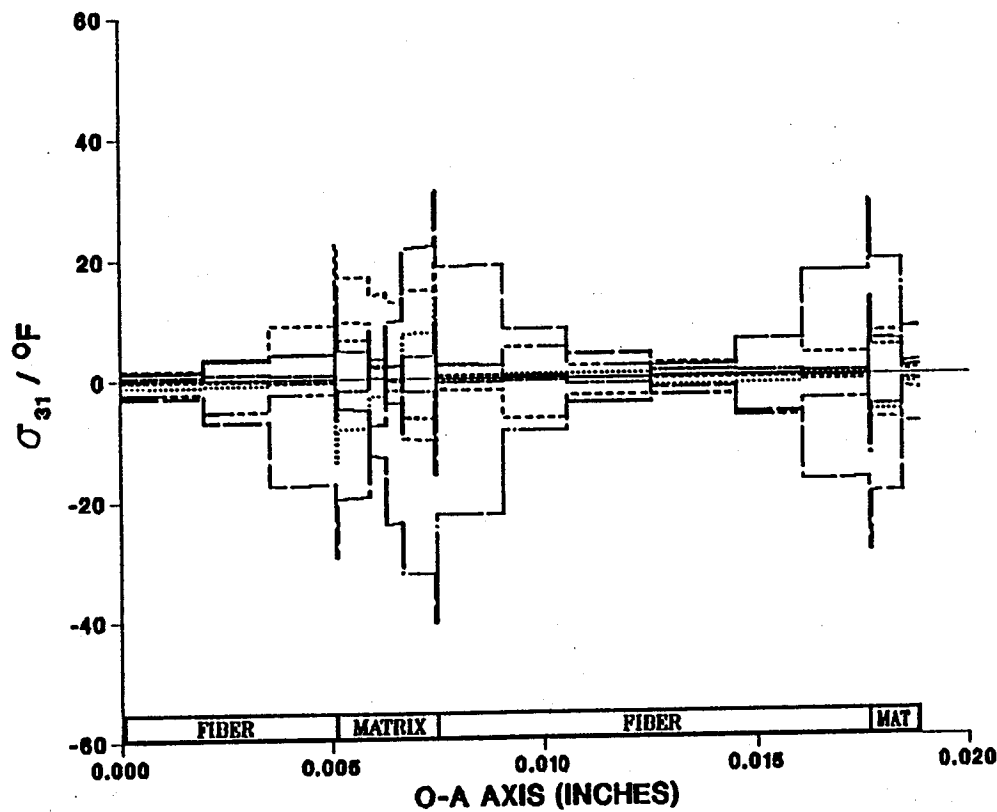
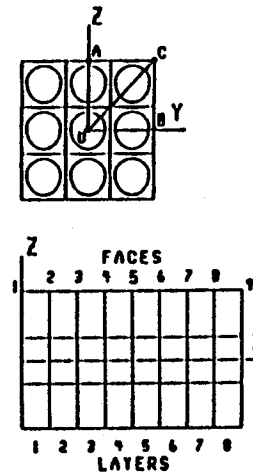


Figure A.145 - σ_{31} Normalized Microstresses, O-A Direction, 0.0% Debonding, Thermal Loading

EFFECT OF 1.39% FIBER LENGTH DEBONDING ON CONSTITUENT MICROSTRESSES (σ_{31}) DUE TO AN APPLIED THERMAL LOAD



- FACE 1
- FACE 2
- FACE 3
- FACE 4
- FACE 5
- FACE 6
- FACE 7
- FACE 8
- FACE 9

Figure A.146 - σ_{31} Normalized Microstresses, O-A Direction, 1.39% Debonding, Thermal Loading

EFFECT OF 2.78% FIBER LENGTH DEBONDING ON CONSTITUENT MICROSTRESSES (σ_{31}) DUE TO AN APPLIED THERMAL LOAD

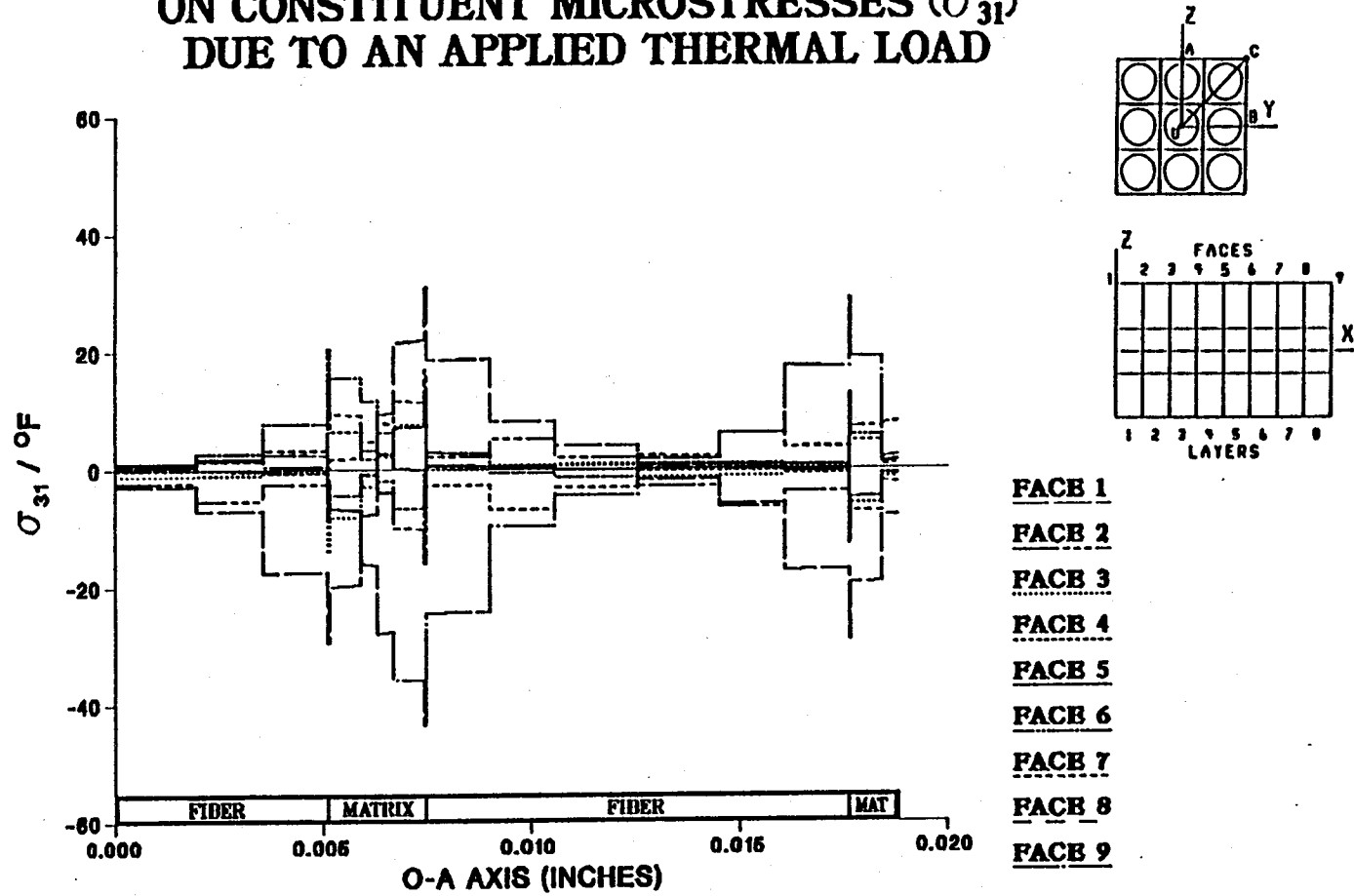


Figure A.147 - σ_{31} Normalized Microstresses, O-A Direction, 2.78% Debonding, Thermal Loading

EFFECT OF 4.17% FIBER LENGTH DEBONDING ON CONSTITUENT MICROSTRESSES (σ_{31}) DUE TO AN APPLIED THERMAL LOAD

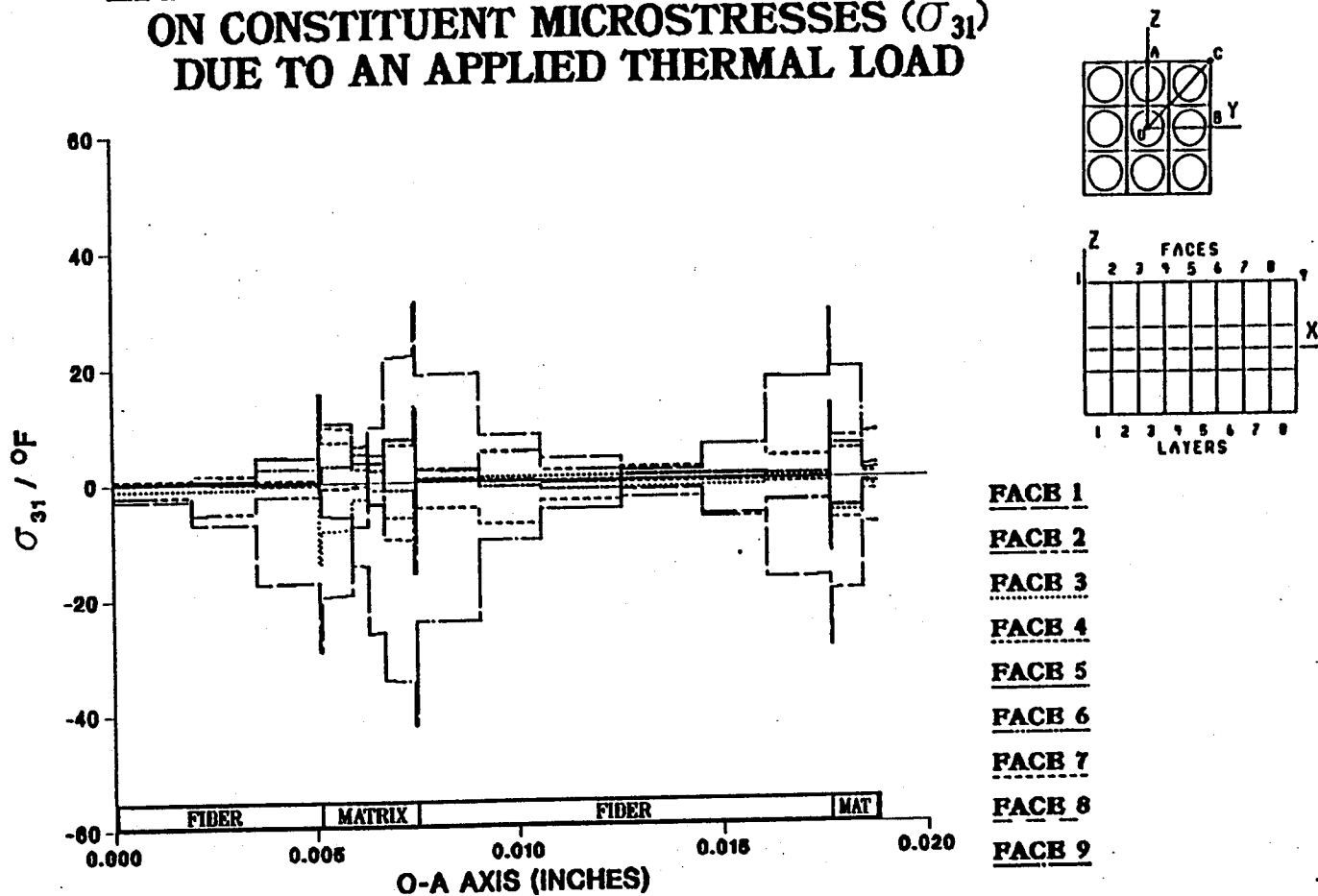


Figure A.148 - σ_{31} Normalized Microstresses, O-A Direction, 4.17% Debonding, Thermal Loading

EFFECT OF 5.56% FIBER LENGTH DEBONDING ON CONSTITUENT MICROSTRESSES (σ_{31}) DUE TO AN APPLIED THERMAL LOAD

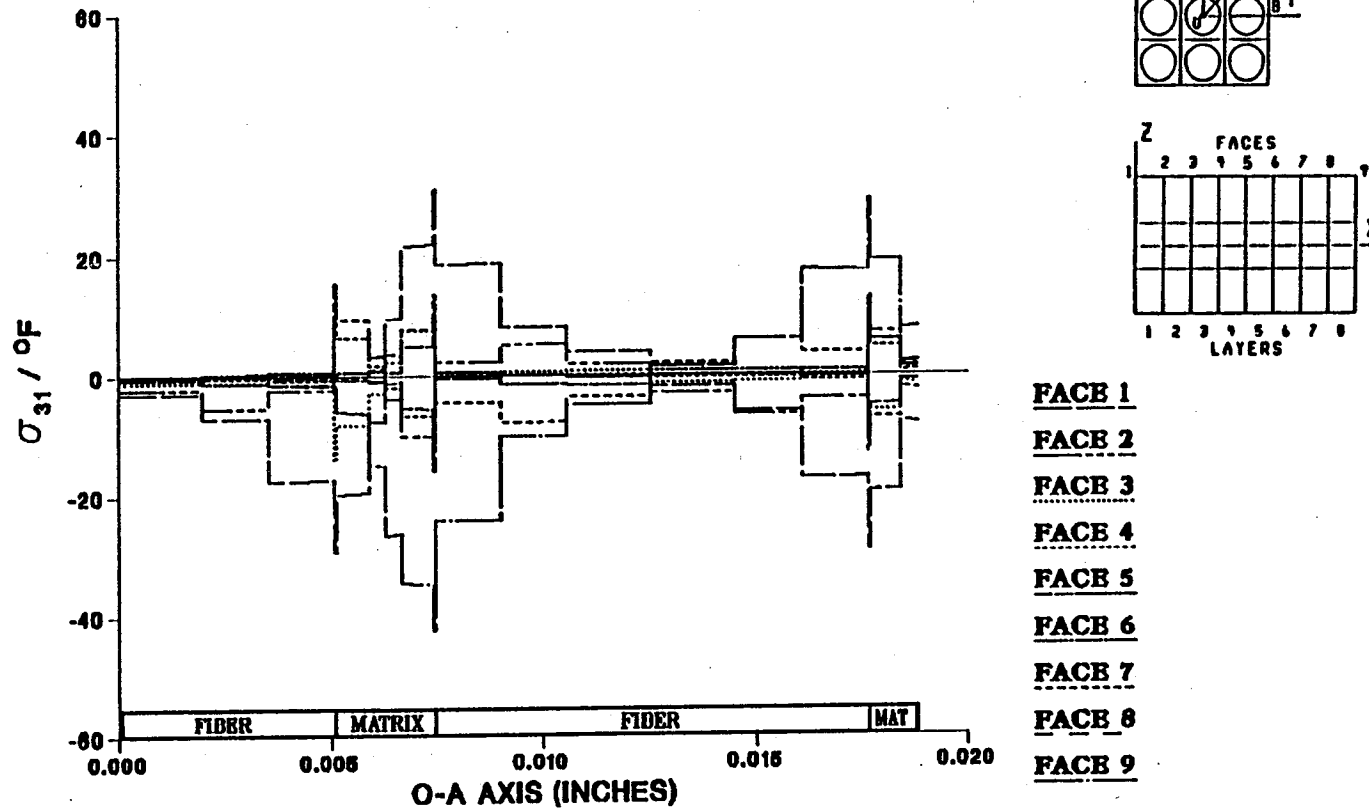


Figure A.149 – σ_{31} Normalized Microstresses, O–A Direction, 5.56% Debonding, Thermal Loading

EFFECT OF 6.94% FIBER LENGTH DEBONDING ON CONSTITUENT MICROSTRESSES (σ_{31}) DUE TO AN APPLIED THERMAL LOAD

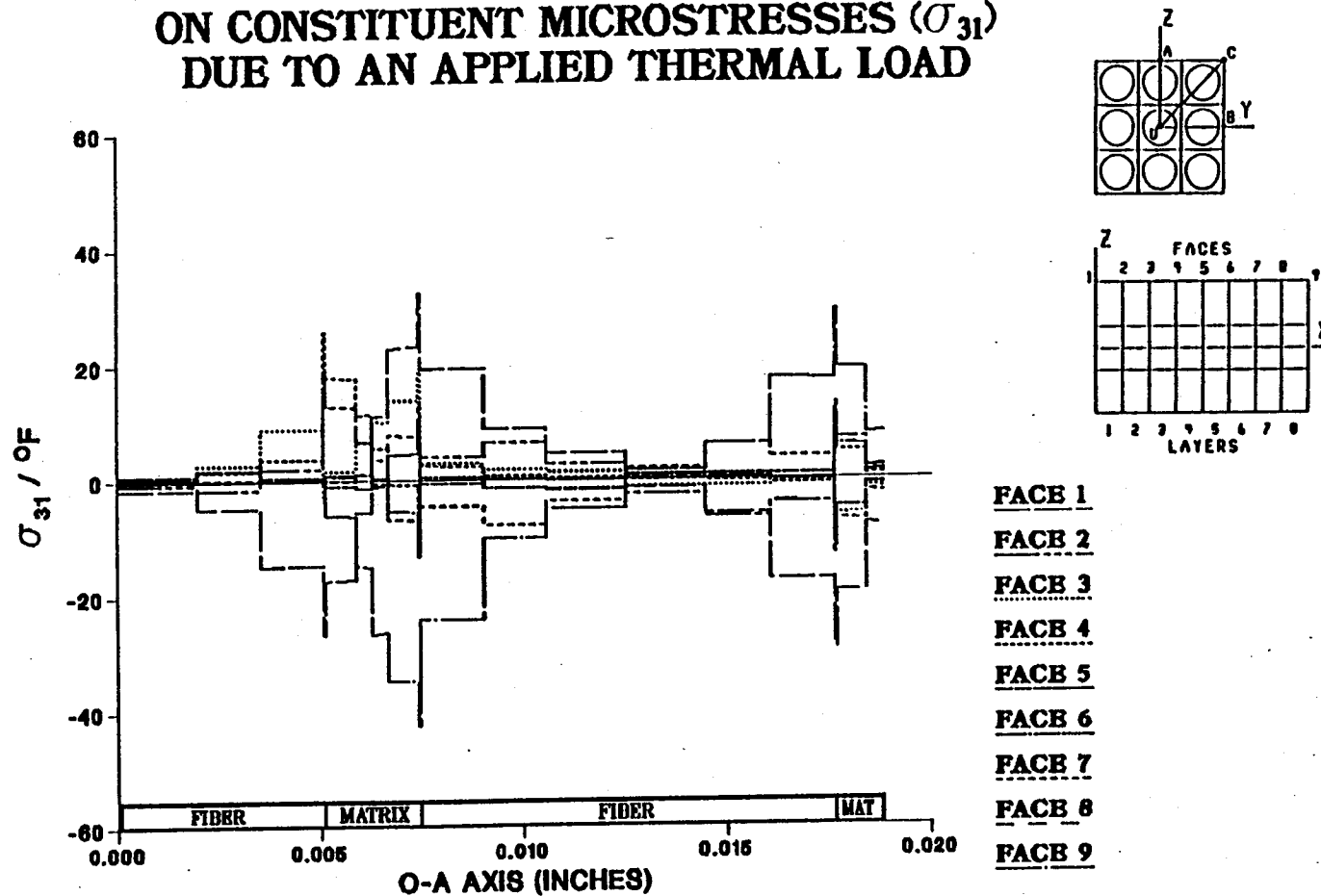


Figure A.150 - σ_{31} Normalized Microstresses, O-A Direction, 6.94% Debonding, Thermal Loading

EFFECT OF 8.33% FIBER LENGTH DEBONDING ON CONSTITUENT MICROSTRESSES (σ_{31}) DUE TO AN APPLIED THERMAL LOAD

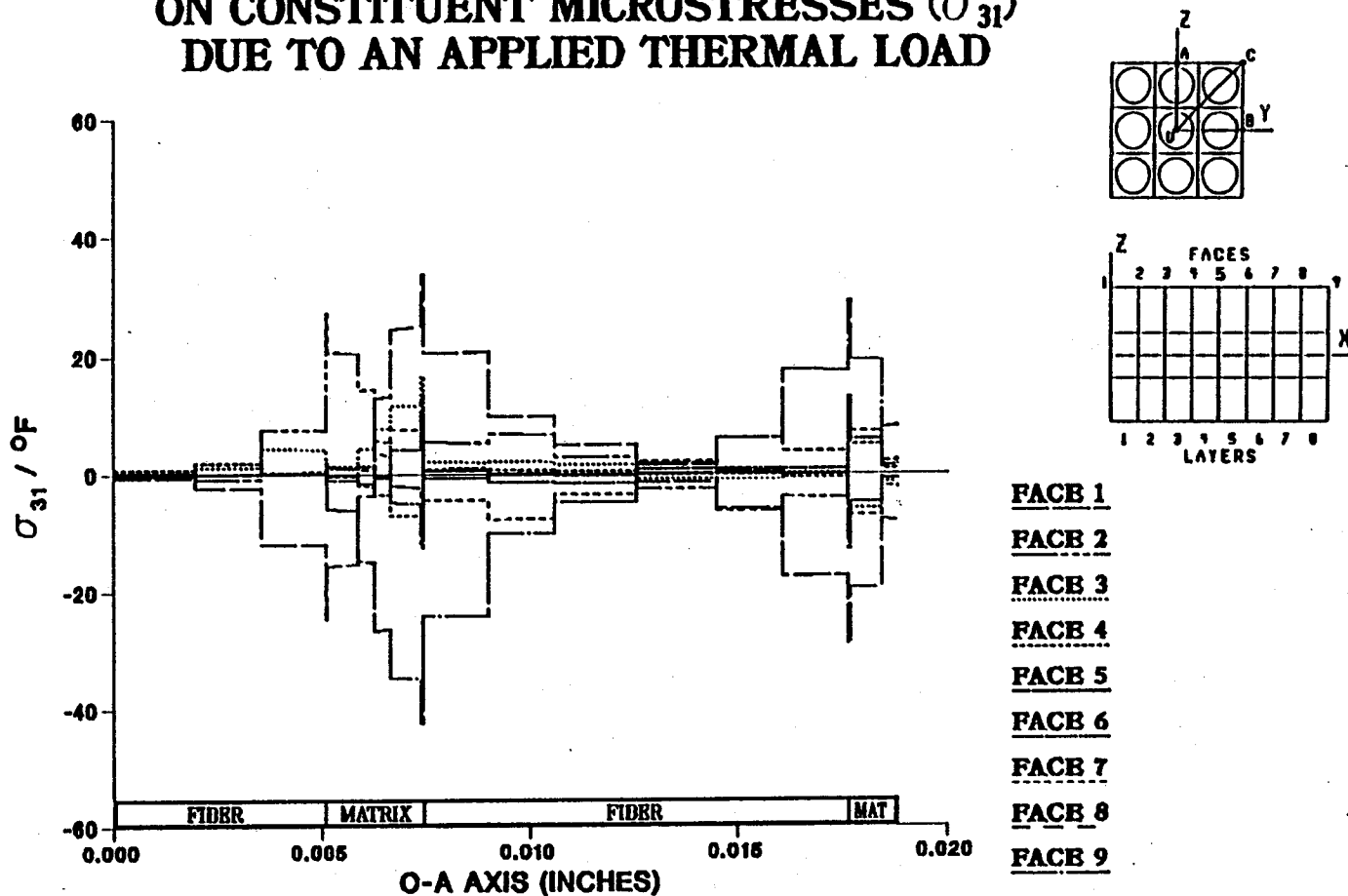


Figure A.151 - σ_{31} Normalized Microstresses, O-A Direction, 8.33% Debonding, Thermal Loading

EFFECT OF 9.72% FIBER LENGTH DEBONDING ON CONSTITUENT MICROSTRESSES (σ_{31}) DUE TO AN APPLIED THERMAL LOAD

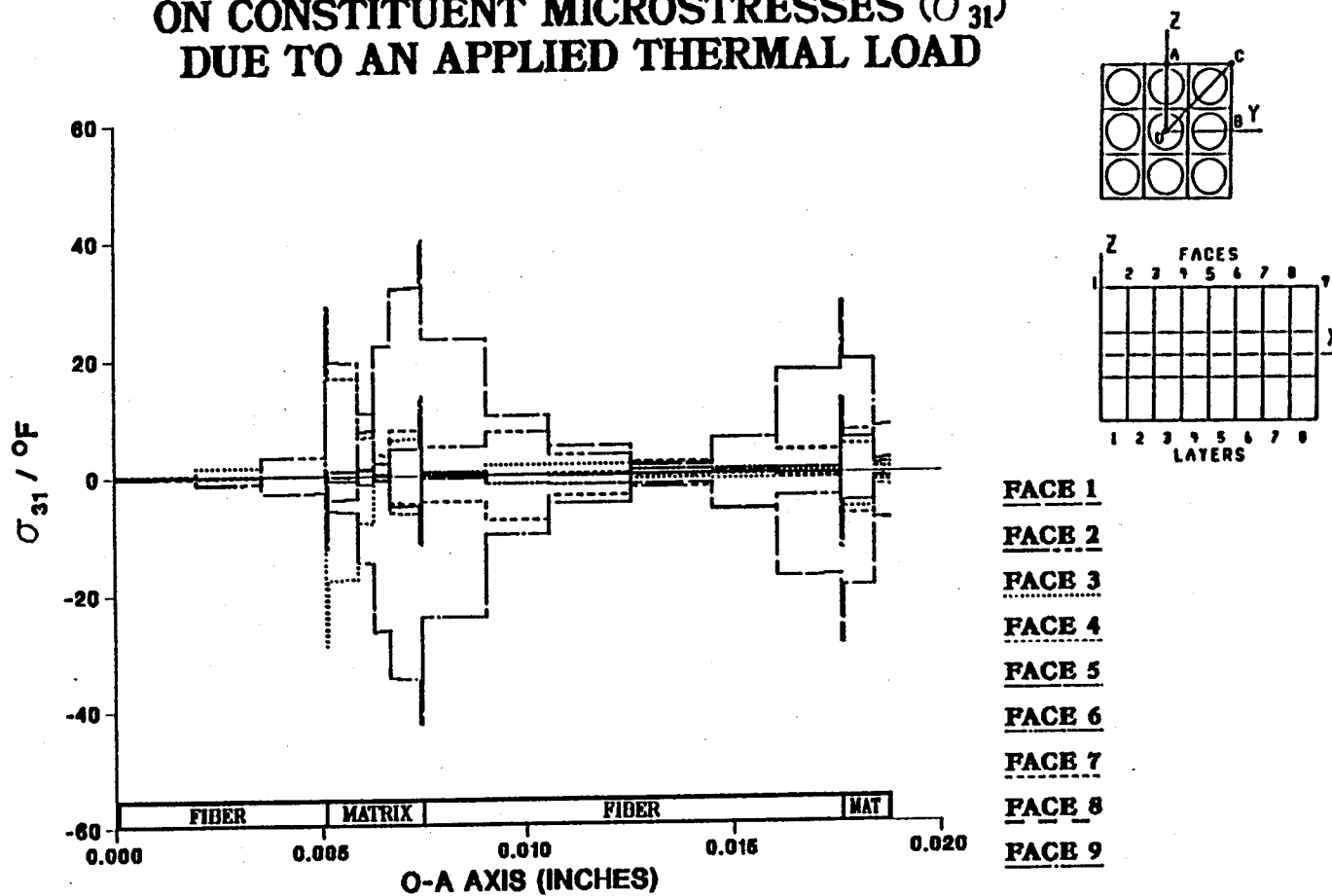


Figure A.152 - σ_{31} Normalized Microstresses, O-A Direction, 9.72% Debonding, Thermal Loading

EFFECT OF 11.1% FIBER LENGTH DEBONDING ON CONSTITUENT MICROSTRESSES (σ_{31}) DUE TO AN APPLIED THERMAL LOAD

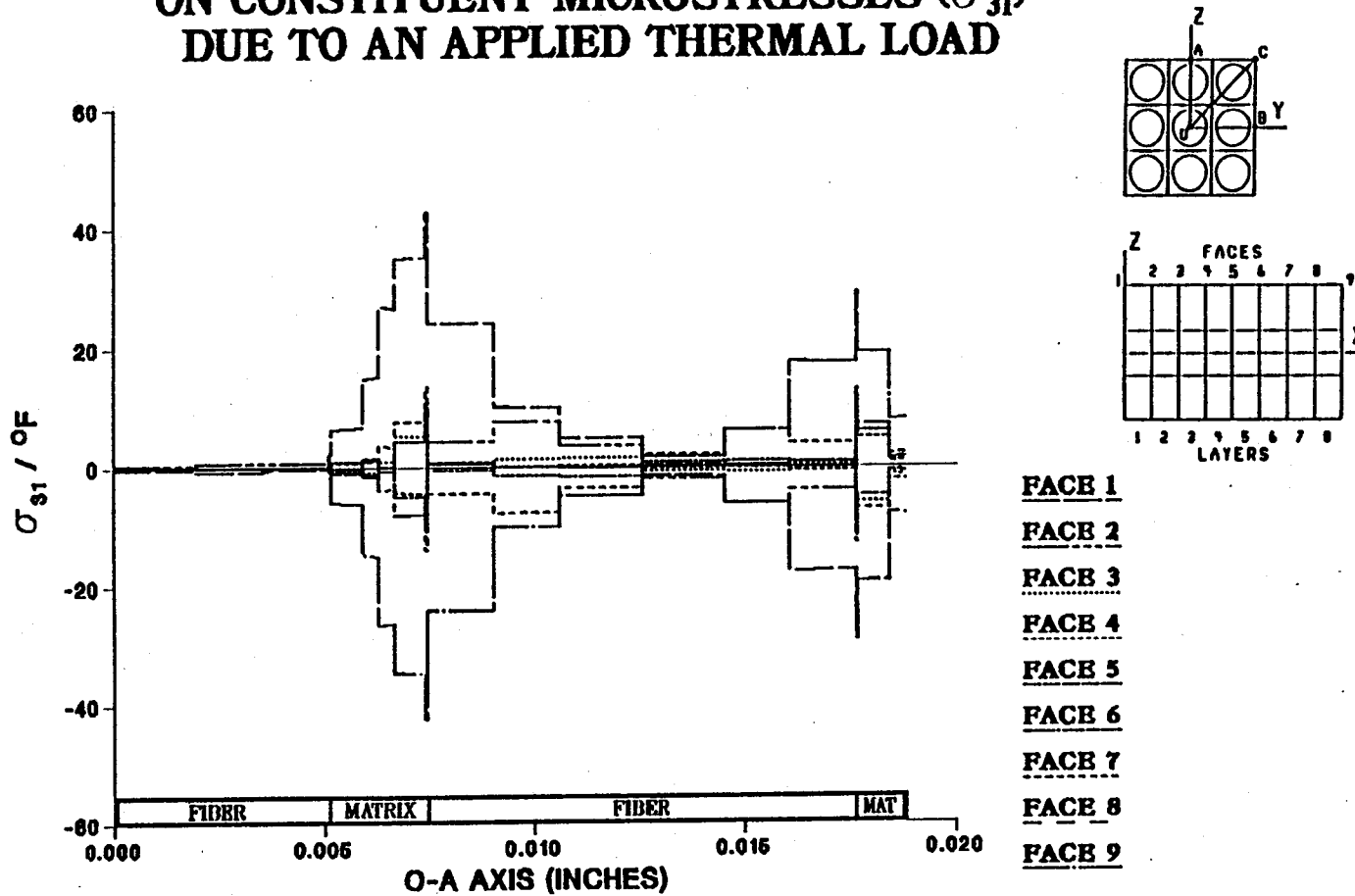
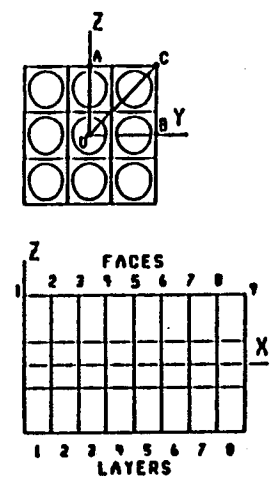
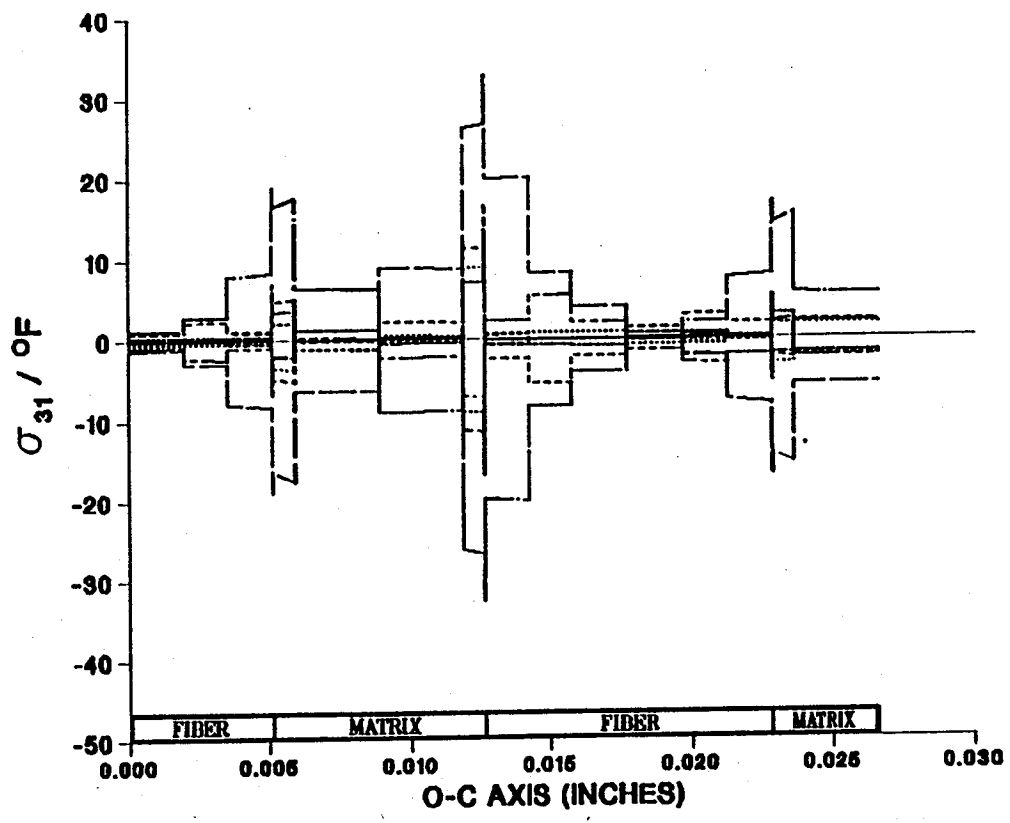


Figure A.153 - σ_{31} Normalized Microstresses, O-A Direction, 11.1% Debonding, Thermal Loading

EFFECT OF 0.0% FIBER LENGTH DEBONDING ON CONSTITUENT MICROSTRESSES (σ_{31}) DUE TO AN APPLIED THERMAL LOAD



- FACE 1
- FACE 2
- FACE 3
- FACE 4
- FACE 5
- FACE 6
- FACE 7
- FACE 8
- FACE 9

Figure A.154 – σ_{31} Normalized Microstresses, O–C Direction, 0.0% Debonding, Thermal Loading

EFFECT OF 1.39% FIBER LENGTH DEBONDING ON CONSTITUENT MICROSTRESSES (σ_{31}) DUE TO AN APPLIED THERMAL LOAD

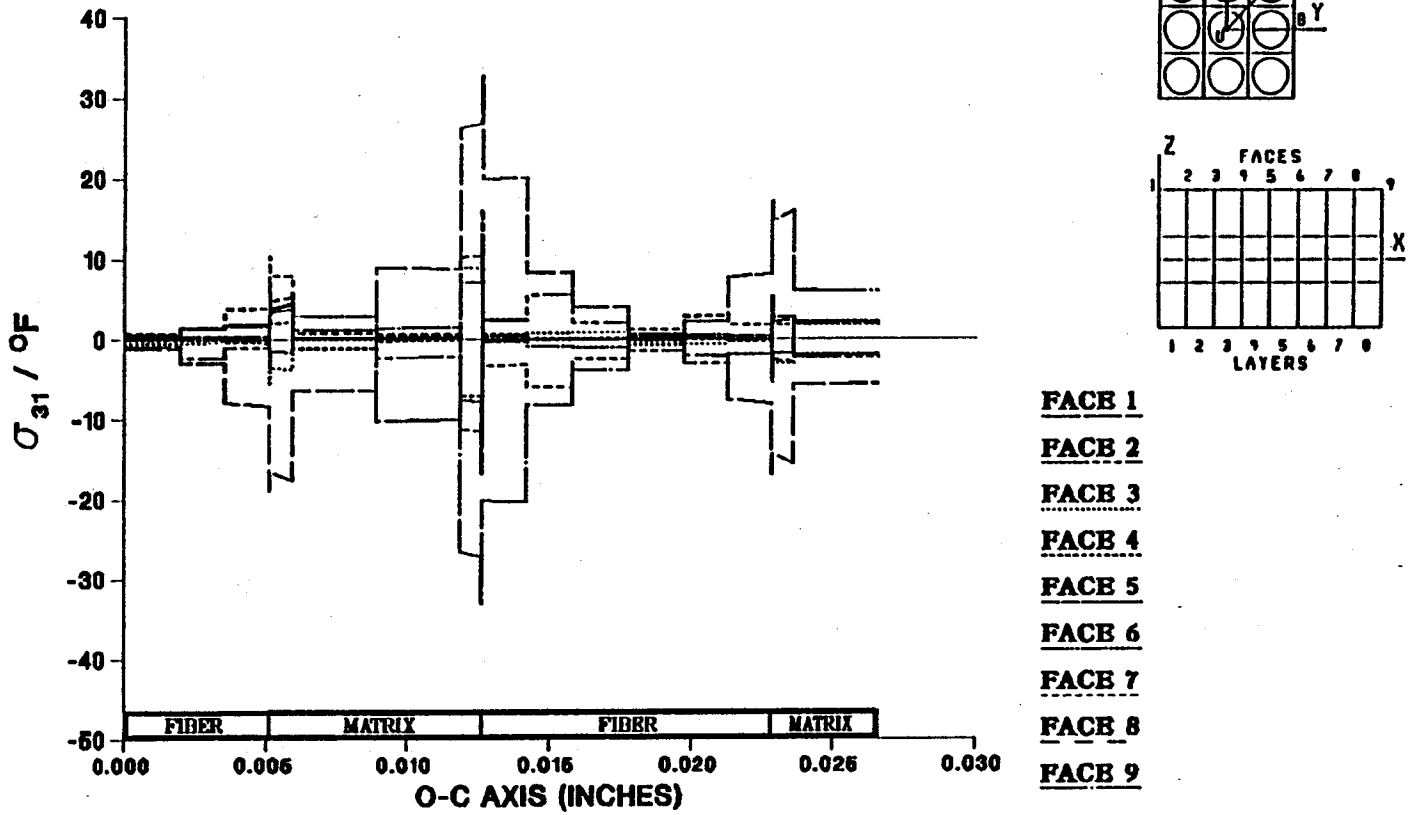


Figure A.155 - σ_{31} Normalized Microstresses, O-C Direction, 1.39% Debonding, Thermal Loading

EFFECT OF 2.78% FIBER LENGTH DEBONDING ON CONSTITUENT MICROSTRESSES (σ_{31}) DUE TO AN APPLIED THERMAL LOAD

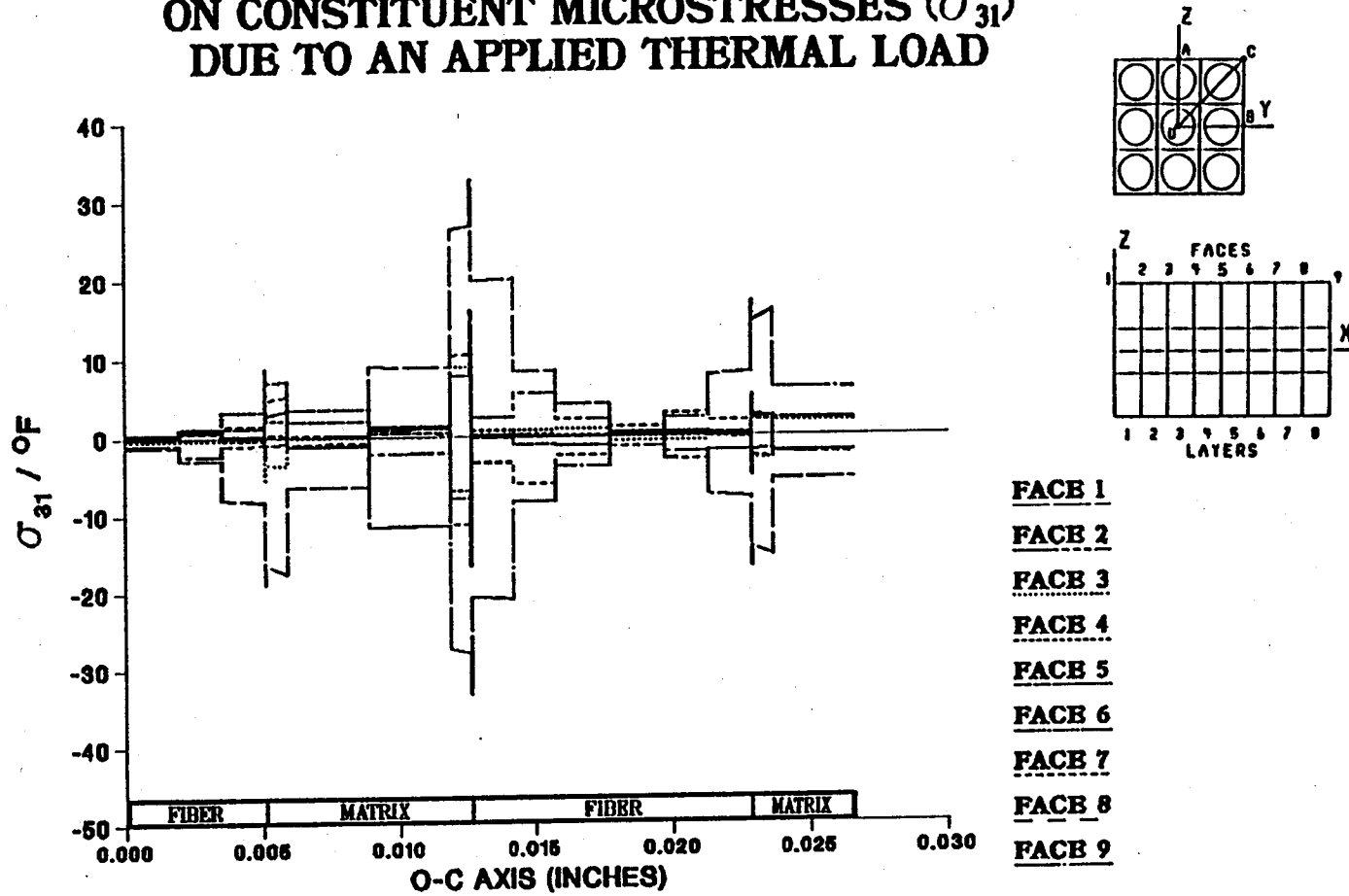


Figure A.156 - σ_{31} Normalized Microstresses, O-C Direction, 2.78% Debonding, Thermal Loading

EFFECT OF 4.17% FIBER LENGTH DEBONDING ON CONSTITUENT MICROSTRESSES (σ_{31}) DUE TO AN APPLIED THERMAL LOAD

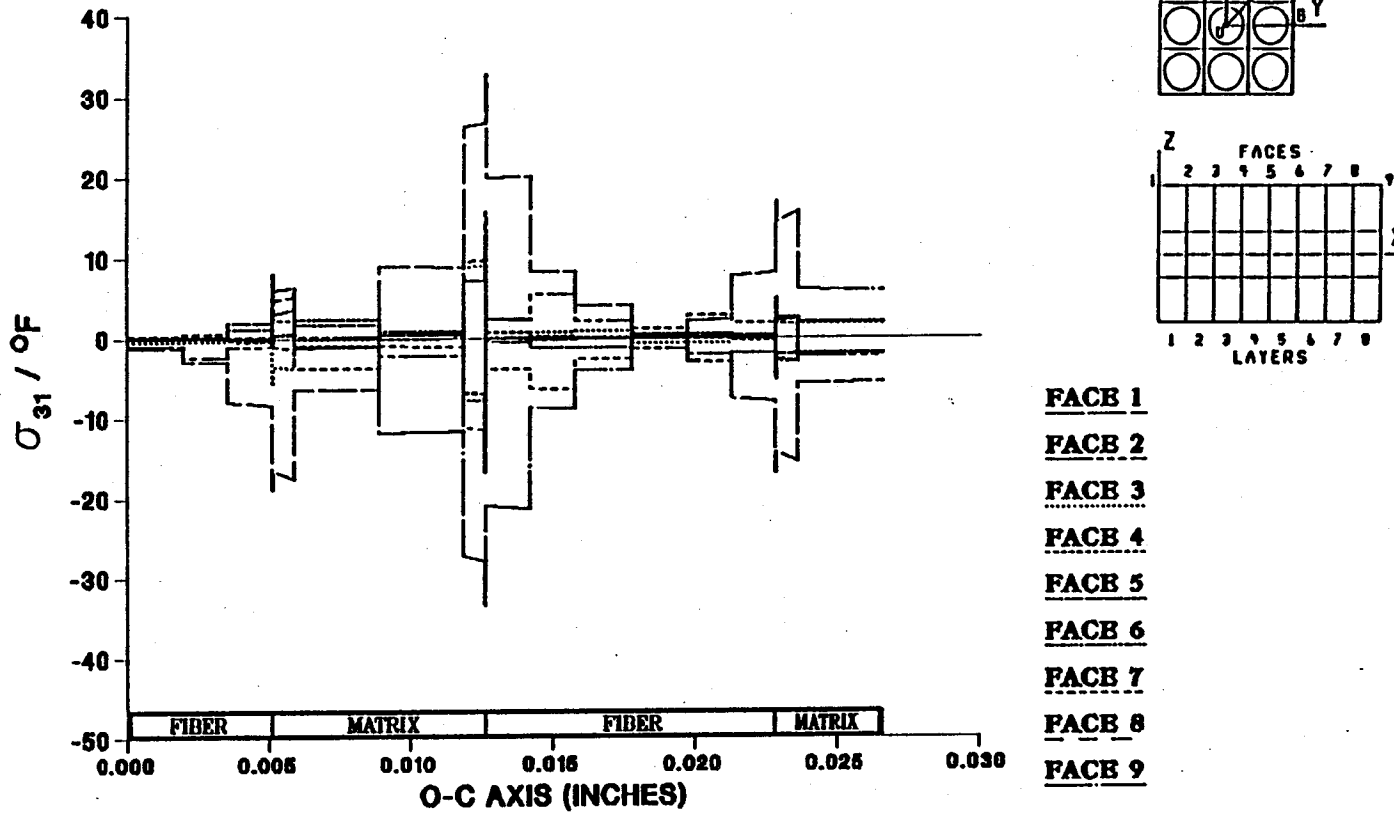


Figure A.157 - σ_{31} Normalized Microstresses, O-C Direction, 4.17% Debonding, Thermal Loading

EFFECT OF 5.56% FIBER LENGTH DEBONDING ON CONSTITUENT MICROSTRESSES (σ_{31}) DUE TO AN APPLIED THERMAL LOAD

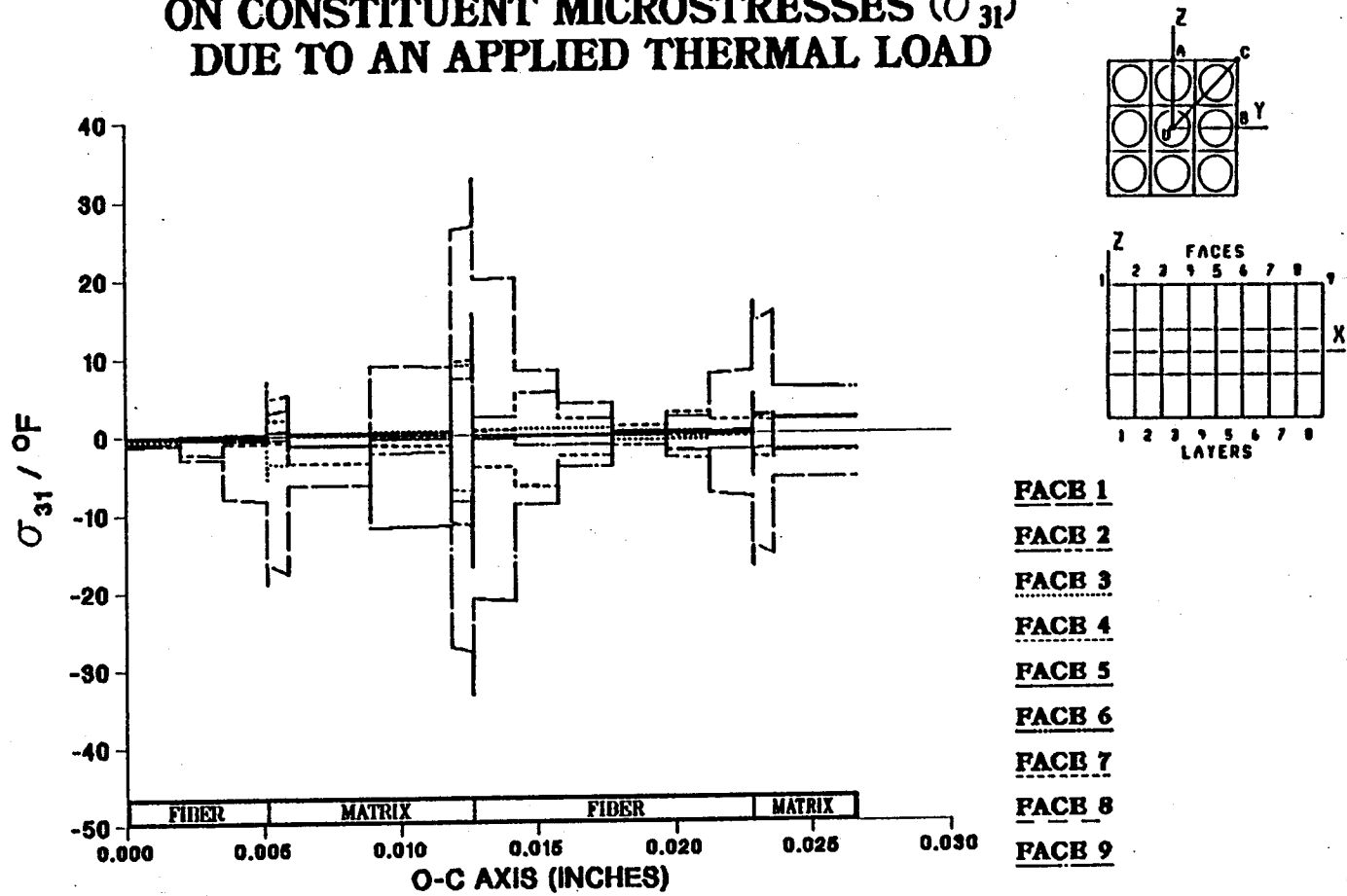


Figure A.158 - σ_{31} Normalized Microstresses, O-C Direction, 5.56% Debonding, Thermal Loading

EFFECT OF 6.94% FIBER LENGTH DEBONDING ON CONSTITUENT MICROSTRESSES (σ_{31}) DUE TO AN APPLIED THERMAL LOAD

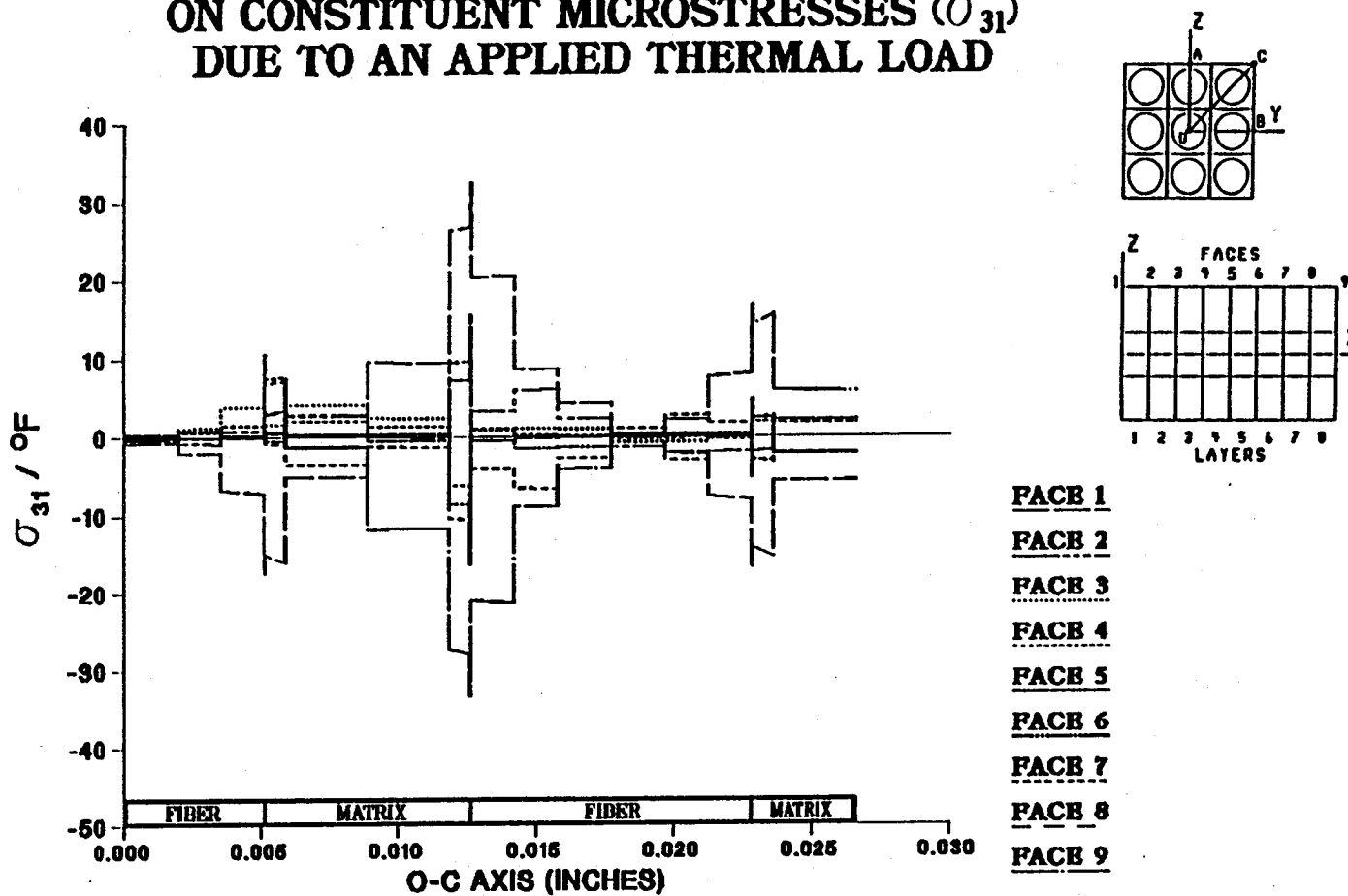


Figure A.159 - σ_{31} Normalized Microstresses, O-C Direction, 6.94% Debonding, Thermal Loading

EFFECT OF 8.33% FIBER LENGTH DEBONDING ON CONSTITUENT MICROSTRESSES (σ_{31}) DUE TO AN APPLIED THERMAL LOAD

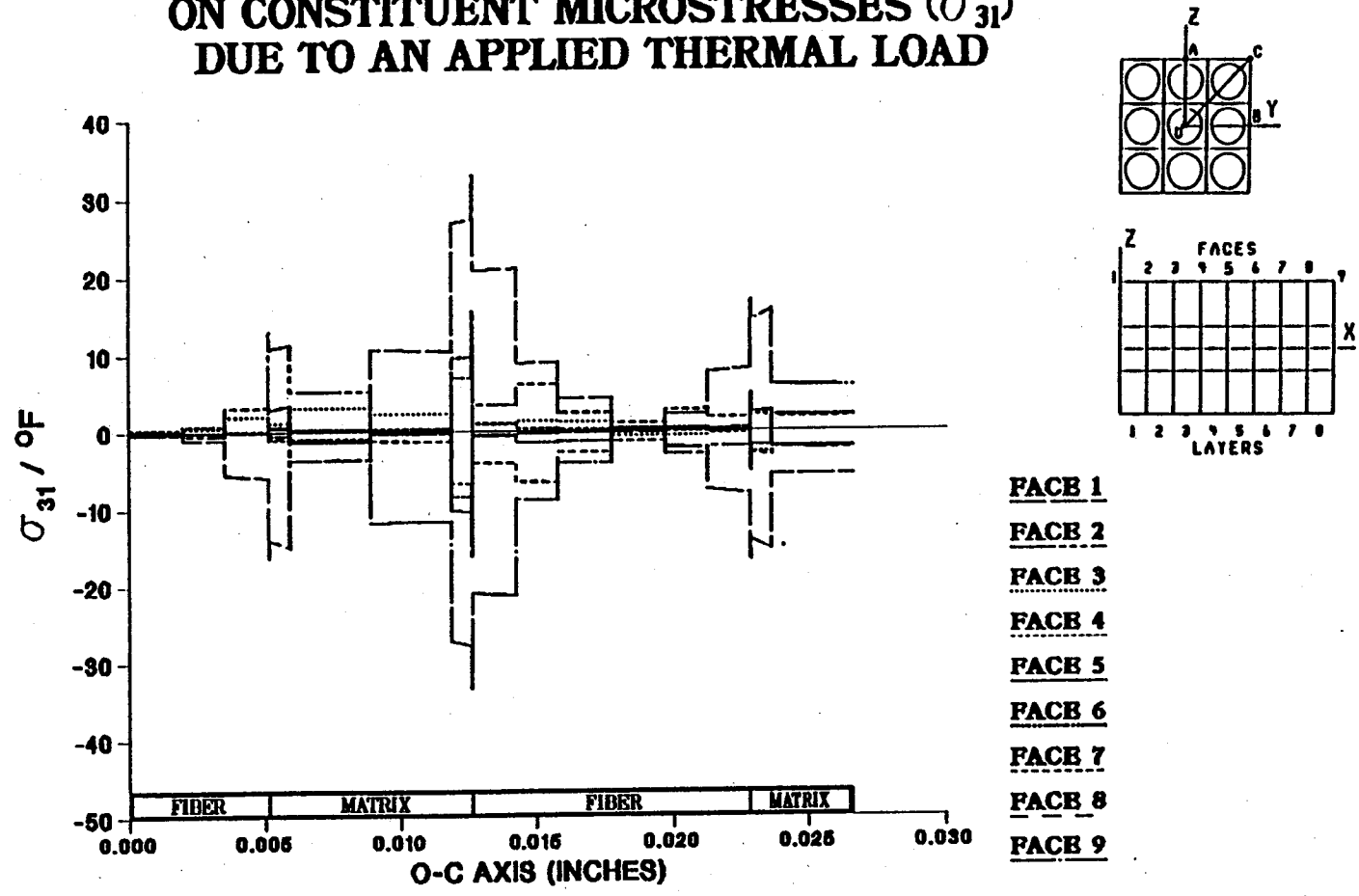


Figure A.160 - σ_{31} Normalized Microstresses, O-C Direction, 8.33% Debonding, Thermal Loading

EFFECT OF 9.72% FIBER LENGTH DEBONDING ON CONSTITUENT MICROSTRESSES (σ_{31}) DUE TO AN APPLIED THERMAL LOAD

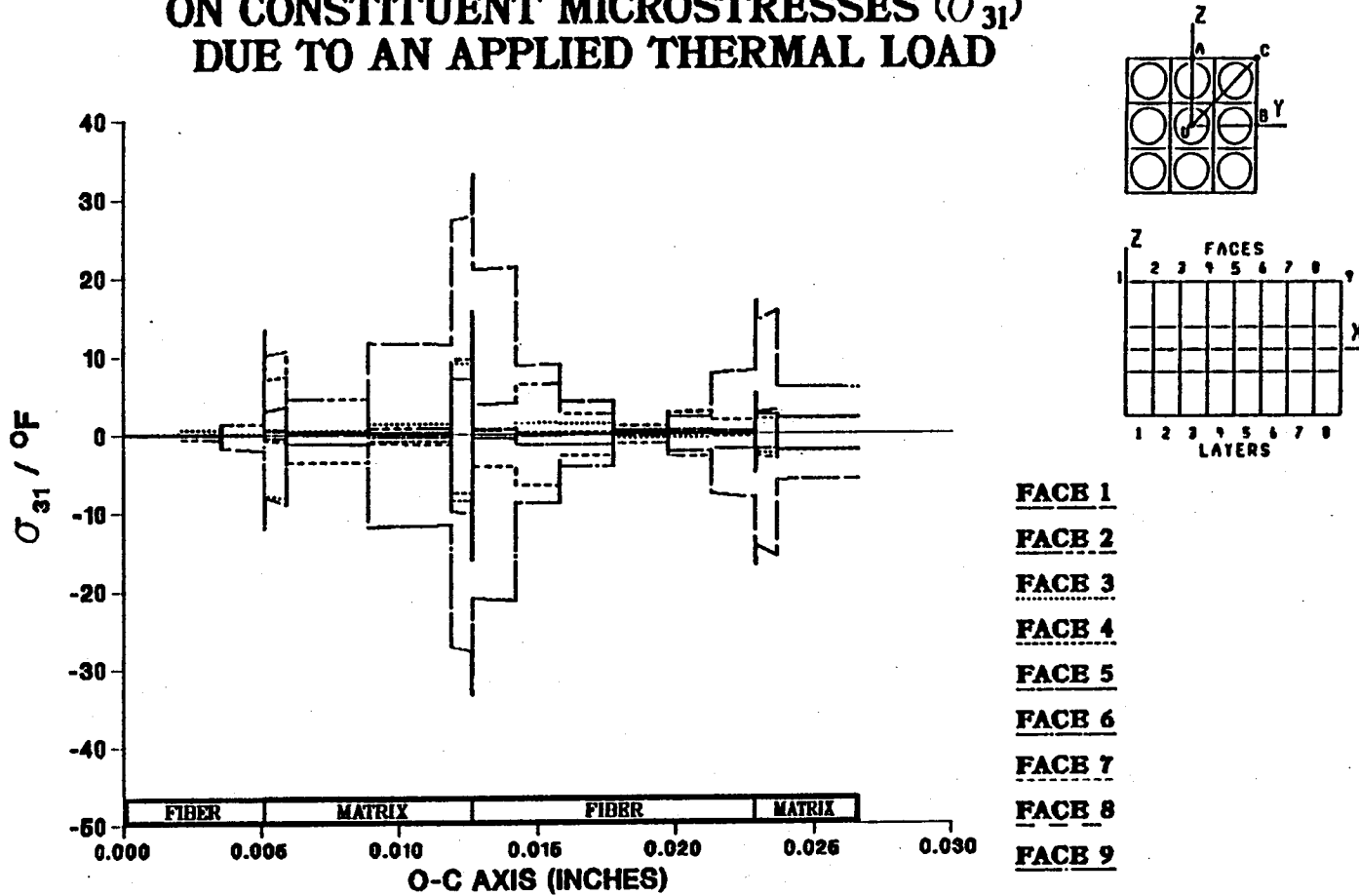


Figure A.161 - σ_{31} Normalized Microstresses, O-C Direction, 9.72% Debonding, Thermal Loading

EFFECT OF 11.1% FIBER LENGTH DEBONDING ON CONSTITUENT MICROSTRESSES (σ_{31}) DUE TO AN APPLIED THERMAL LOAD

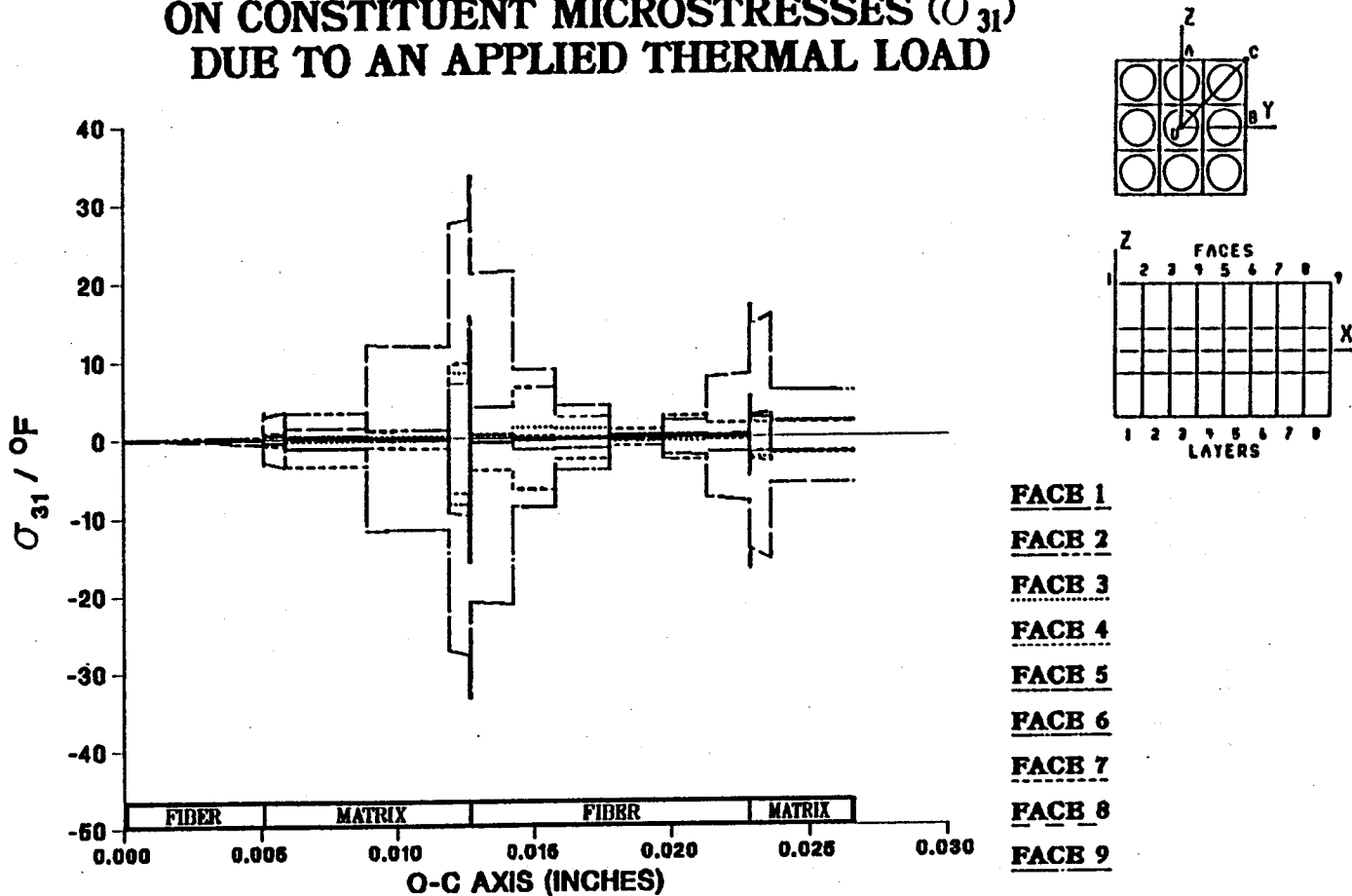


Figure A.162 - σ_{31} Normalized Microstresses, O-C Direction, 11.1% Debonding, Thermal Loading

EFFECT OF 0.0% FIBER LENGTH DEBONDING ON CONSTITUENT MICROSTRESSES (σ_{12}) DUE TO AN APPLIED THERMAL LOAD

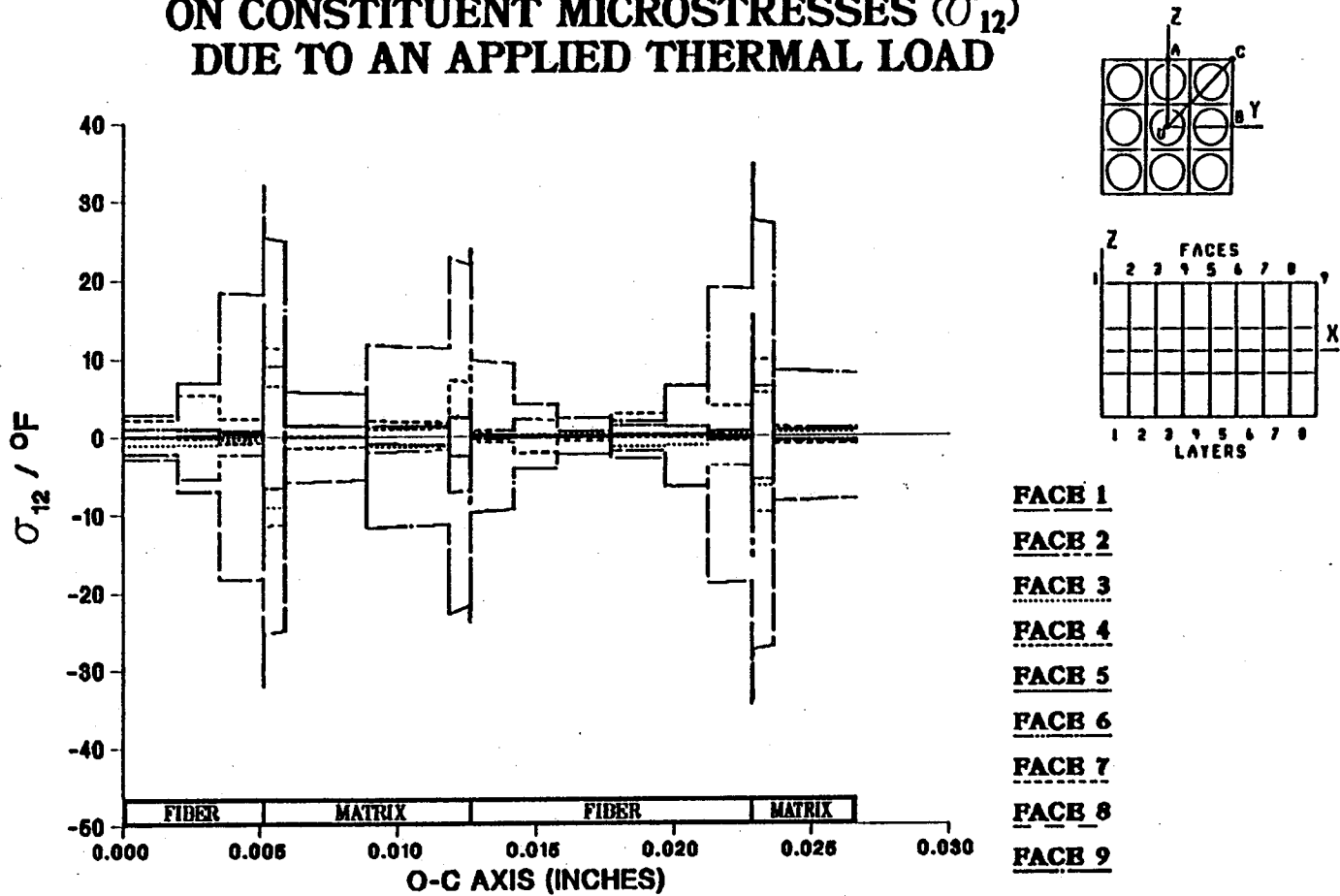


Figure A.163 - σ_{12} Normalized Microstresses, O-C Direction, 0.0% Debonding, Thermal Loading

EFFECT OF 1.39% FIBER LENGTH DEBONDING ON CONSTITUENT MICROSTRESSES (σ_{12}) DUE TO AN APPLIED THERMAL LOAD

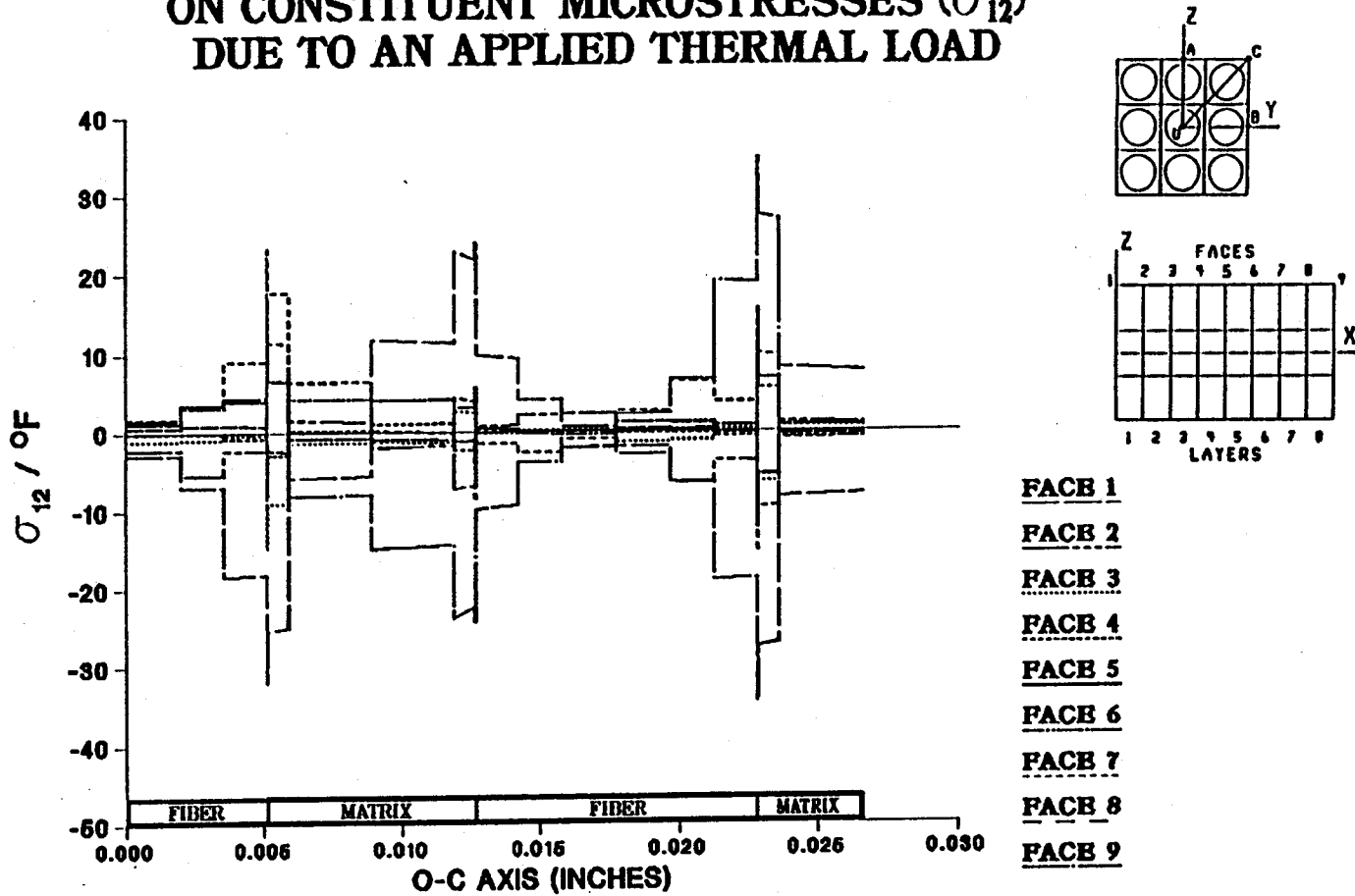


Figure A.164 – σ_{12} Normalized Microstresses, O–C Direction, 1.39% Debonding, Thermal Loading

EFFECT OF 2.78% FIBER LENGTH DEBONDING ON CONSTITUENT MICROSTRESSES (σ_{12}) DUE TO AN APPLIED THERMAL LOAD

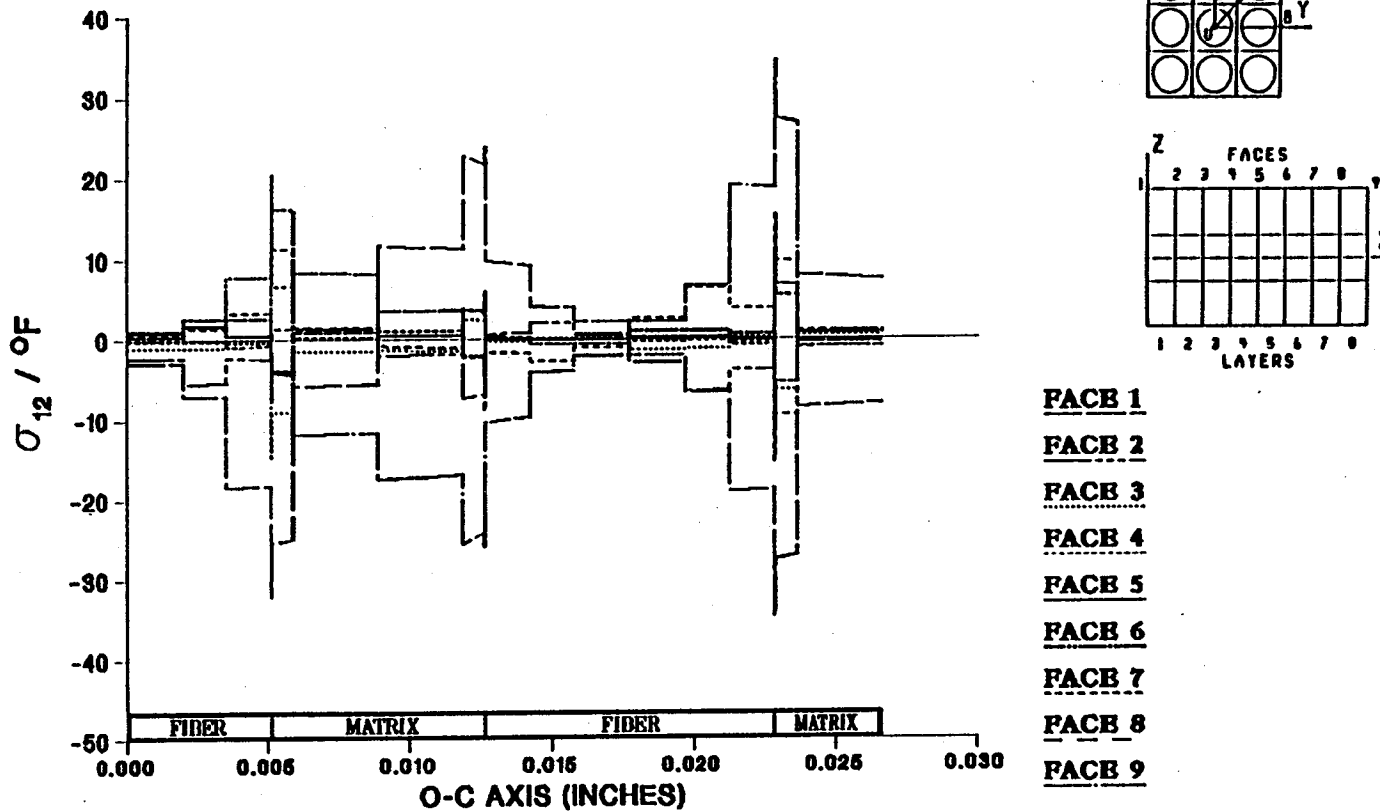


Figure A.165 - σ_{12} Normalized Microstresses, O-C Direction, 2.78% Debonding, Thermal Loading

EFFECT OF 4.17% FIBER LENGTH DEBONDING ON CONSTITUENT MICROSTRESSES (σ_{12}) DUE TO AN APPLIED THERMAL LOAD

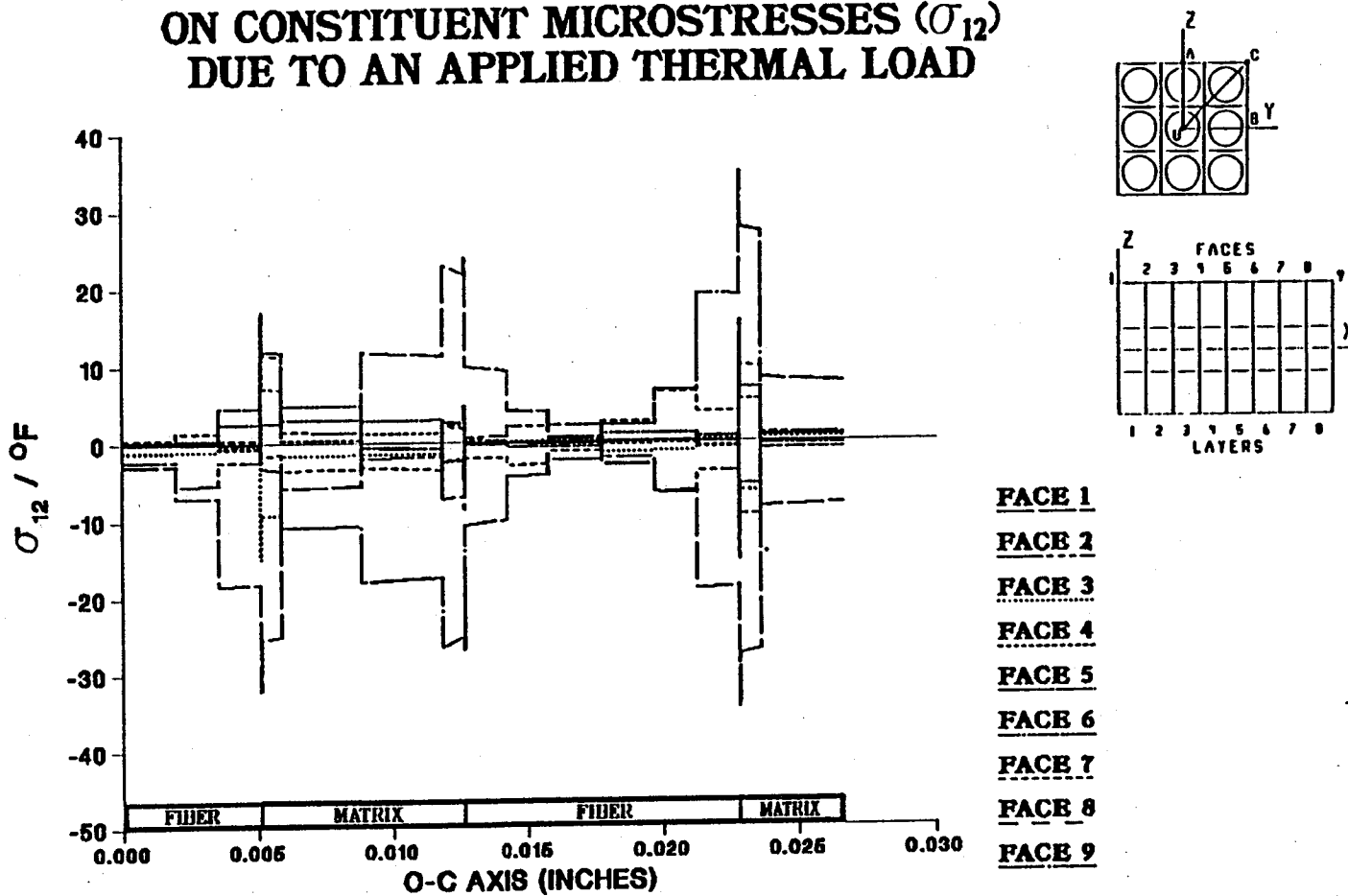


Figure A.166 - σ_{12} Normalized Microstresses, O-C Direction, 4.17% Debonding, Thermal Loading

EFFECT OF 5.56% FIBER LENGTH DEBONDING ON CONSTITUENT MICROSTRESSES (σ_{12}) DUE TO AN APPLIED THERMAL LOAD

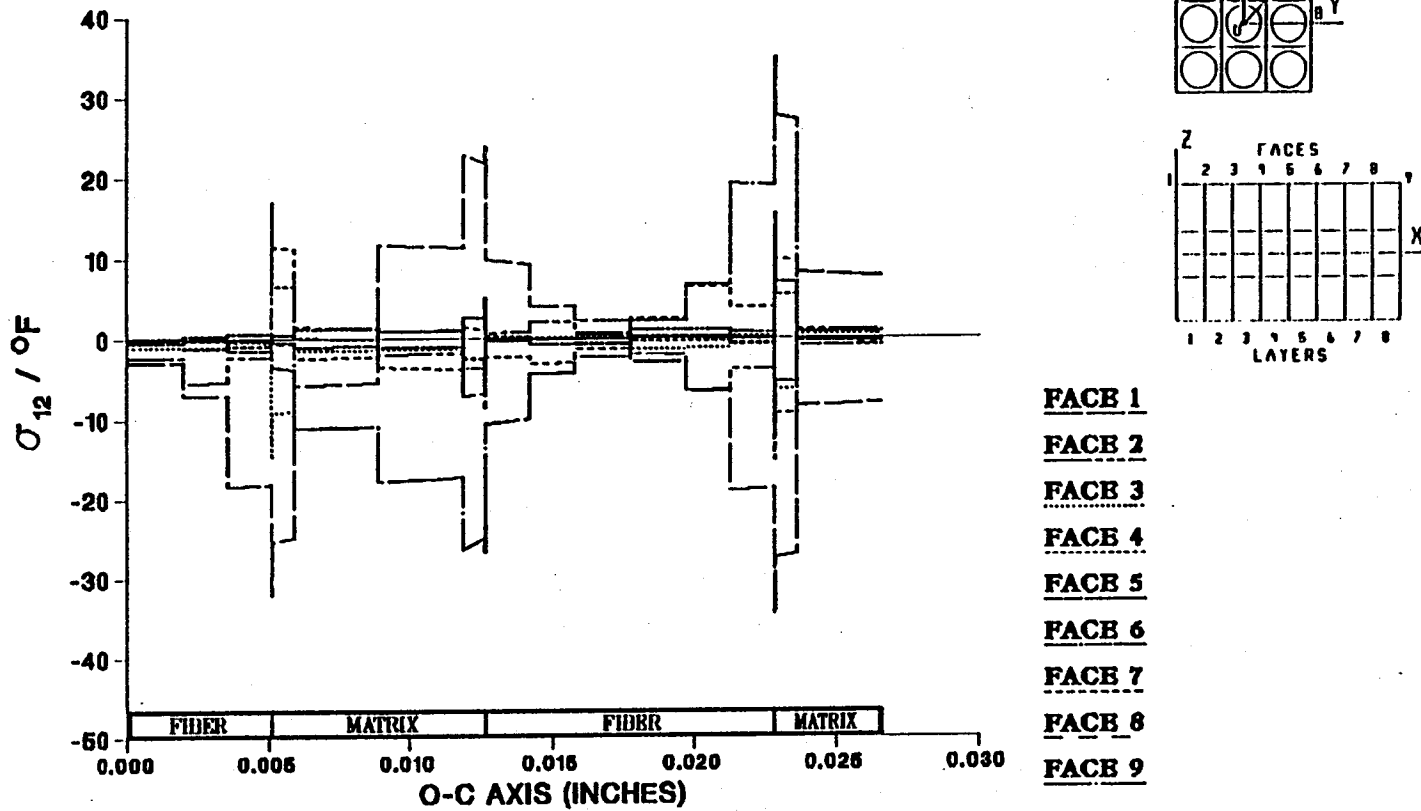


Figure A.167 - σ_{12} Normalized Microstresses, O-C Direction, 5.56% Debonding, Thermal Loading

EFFECT OF 6.94% FIBER LENGTH DEBONDING ON CONSTITUENT MICROSTRESSES (σ_{12}) DUE TO AN APPLIED THERMAL LOAD

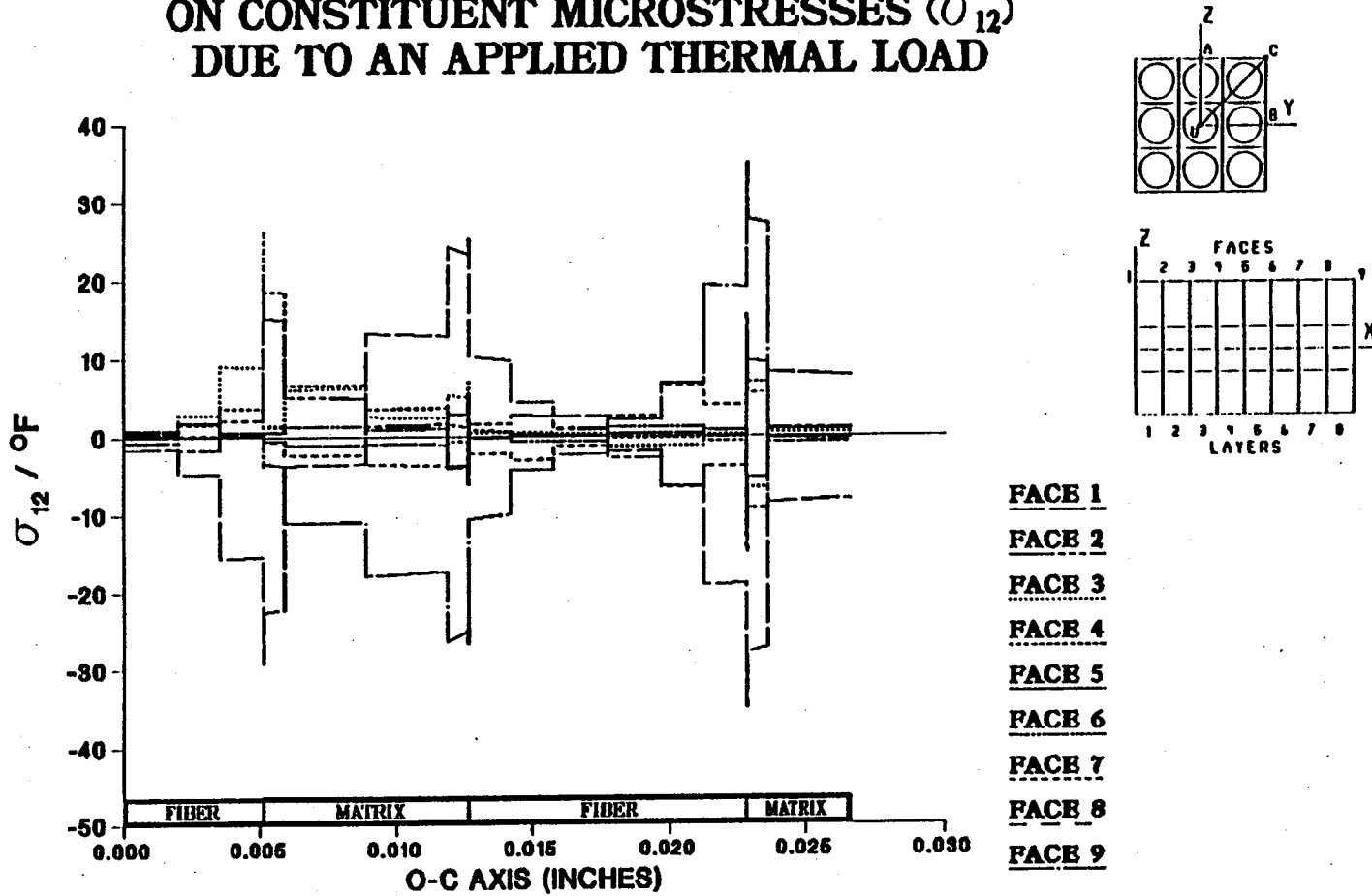


Figure A.168 - σ_{12} Normalized Microstresses, O-C Direction, 6.94% Debonding, Thermal Loading

EFFECT OF 8.33% FIBER LENGTH DEBONDING ON CONSTITUENT MICROSTRESSES (σ_{12}) DUE TO AN APPLIED THERMAL LOAD

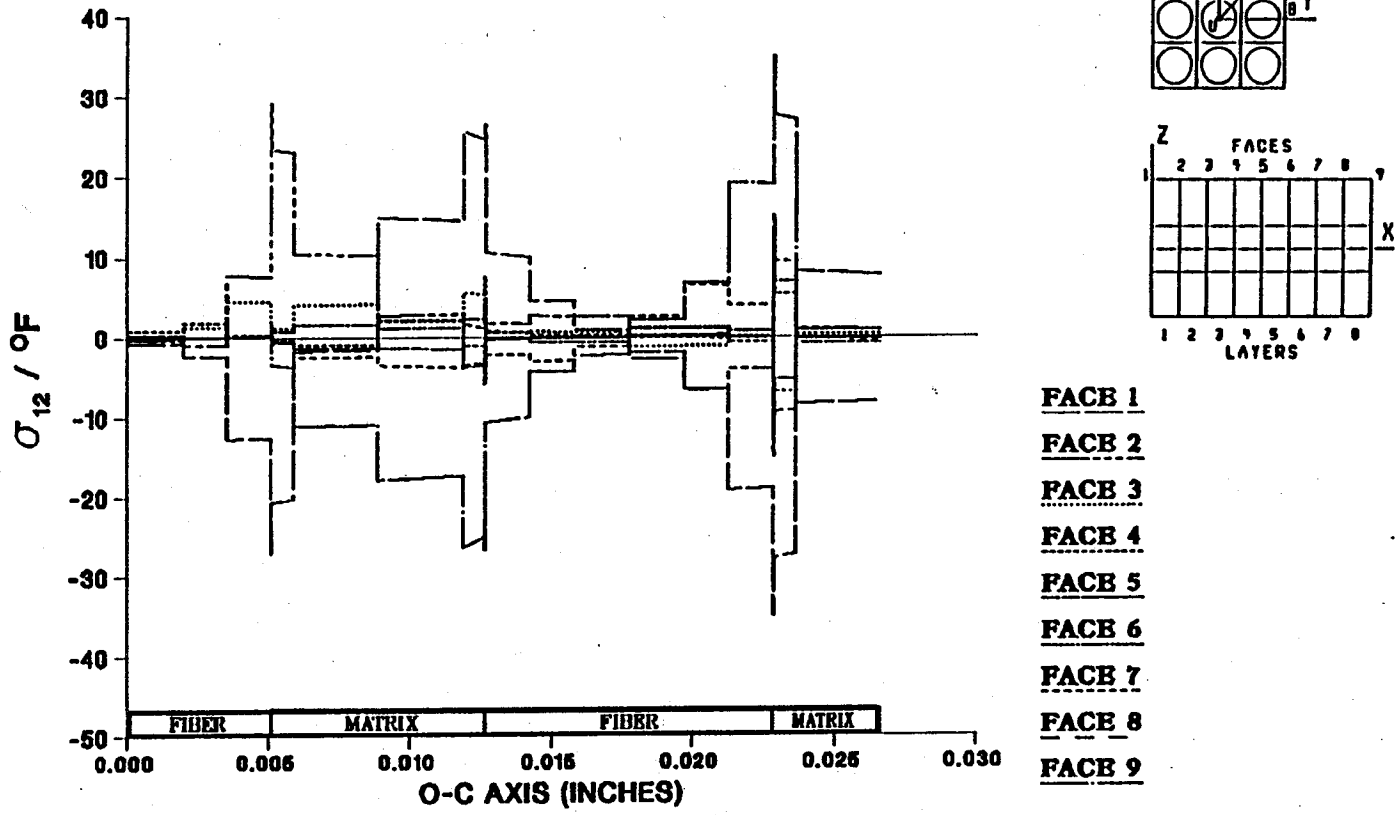


Figure A.169 - σ_{12} Normalized Microstresses, O-C Direction, 8.33% Debonding, Thermal Loading

**EFFECT OF 9.72% FIBER LENGTH DEBONDING
ON CONSTITUENT MICROSTRESSES (σ_{12})
DUE TO AN APPLIED THERMAL LOAD**

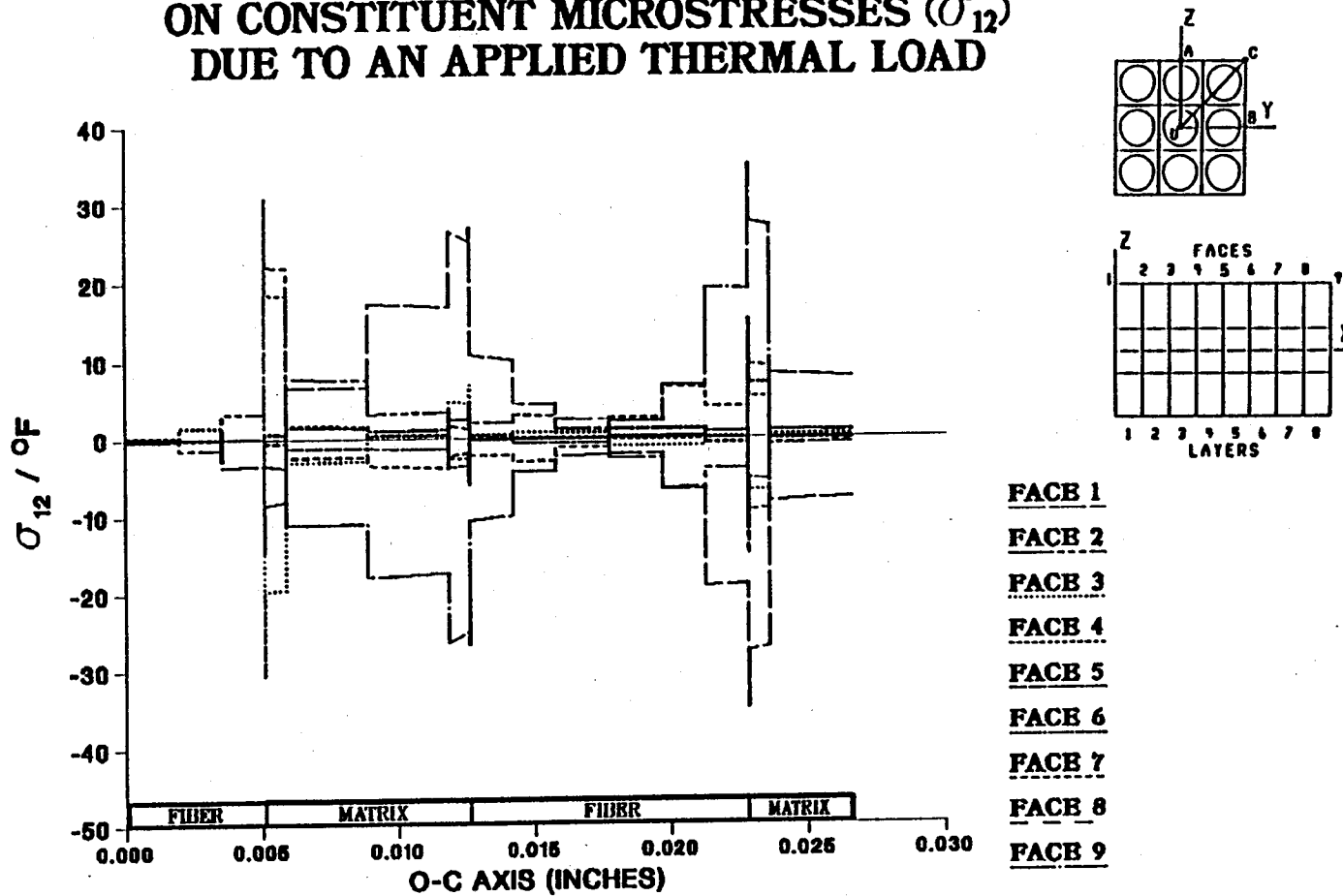


Figure A.170 — σ_{12} Normalized Microstresses, O-C Direction, 9.72% Debonding, Thermal Loading

EFFECT OF 11.11% FIBER LENGTH DEBONDING ON CONSTITUENT MICROSTRESSES (σ_{12}) DUE TO AN APPLIED THERMAL LOAD

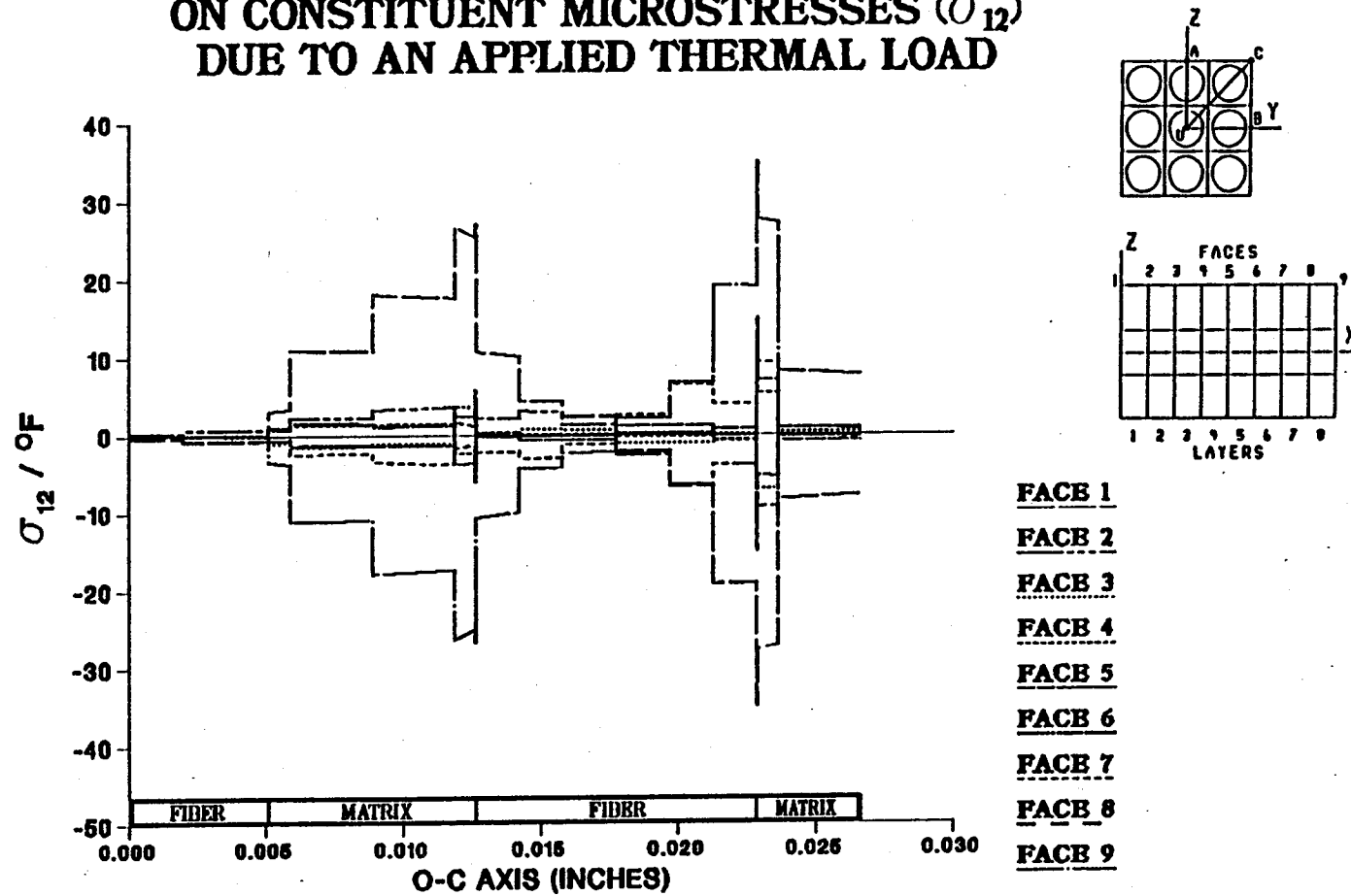
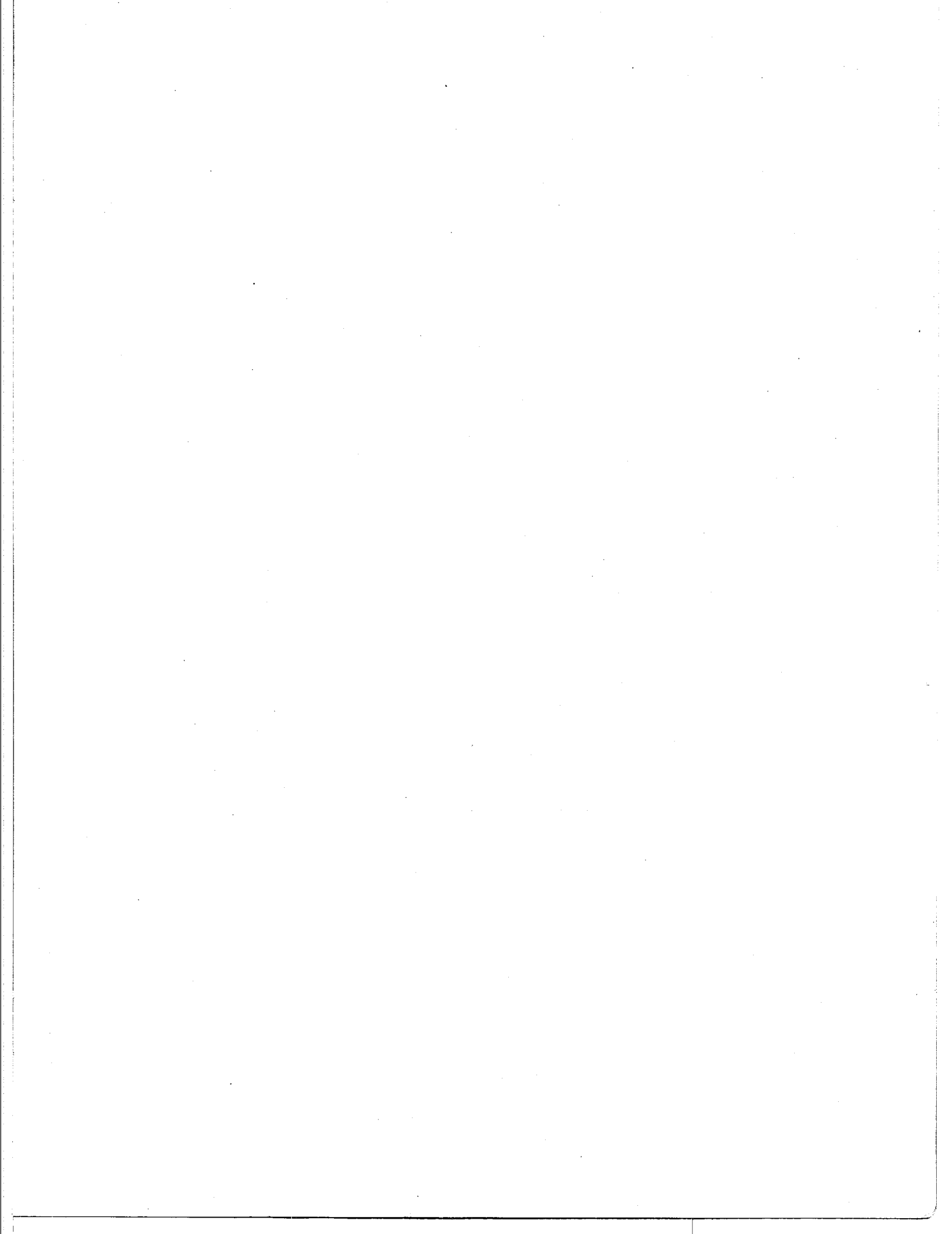


Figure A.171 - σ_{12} Normalized Microstresses, O-C Direction, 11.11% Debonding, Thermal Loading

REPORT DOCUMENTATION PAGEForm Approved
OMB No. 0704-0188

Public reporting burden for this collection of information is estimated to average 1 hour per response, including the time for reviewing instructions, searching existing data sources, gathering and maintaining the data needed, and completing and reviewing the collection of information. Send comments regarding this burden estimate or any other aspect of this collection of information, including suggestions for reducing this burden, to Washington Headquarters Services, Directorate for Information Operations and Reports, 1215 Jefferson Davis Highway, Suite 1204, Arlington, VA 22202-4302, and to the Office of Management and Budget, Paperwork Reduction Project (0704-0188), Washington, DC 20503.

1. AGENCY USE ONLY (Leave blank)		2. REPORT DATE November 1991	3. REPORT TYPE AND DATES COVERED Final Contractor Report - May 89	
4. TITLE AND SUBTITLE Superelement Methods in High Temperature Metal Matrix Composites			5. FUNDING NUMBERS WU-505-63-5B G-NAG3-50	
6. AUTHOR(S) Daniel Trowbridge				
7. PERFORMING ORGANIZATION NAME(S) AND ADDRESS(ES) University of Akron Department of Civil Engineering Akron, Ohio 44325			8. PERFORMING ORGANIZATION REPORT NUMBER None	
9. SPONSORING/MONITORING AGENCY NAMES(S) AND ADDRESS(ES) National Aeronautics and Space Administration Lewis Research Center Cleveland, Ohio 44135-3191			10. SPONSORING/MONITORING AGENCY REPORT NUMBER NASA CR-189070	
11. SUPPLEMENTARY NOTES Project Manager, J.C. Caruso and C.C. Chamis, Structures Division, NASA Lewis Research Center, (216) 433-3252. Report was submitted as a thesis in partial fulfillment of the requirements for the degree Master of Civil Engineering to the University of Akron, Akron, Ohio in May 1989.				
12a. DISTRIBUTION/AVAILABILITY STATEMENT Unclassified - Unlimited Subject Category 24			12b. DISTRIBUTION CODE	
13. ABSTRACT (Maximum 200 words) An investigation into fiber fracture and debonding in metal matrix composites is conducted using the finite element method. The superelement finite element technique was used to model a metal matrix composite under various loading condition and with varying degrees of fiber debonding. The use of superelements saved many man hours by allowing for alteration of only the primary superelement to manipulate partial bonding for the entire model. The composite's material properties were calculated and the effects of fiber debonding on these properties were noted. The internal stress state of the composite while under various loads was also investigated. Special interest was devoted to the change in stress state as a result of increasing fiber debonding.				
14. SUBJECT TERMS Composite properties; Microstresses; Debending; Interface; Modules; Expansion coefficients; Poissons ratios; Temperature effects; Application procedure; Nine-cell model; Results; Tabular; Graphical			15. NUMBER OF PAGES 394	
			16. PRICE CODE A17	
17. SECURITY CLASSIFICATION OF REPORT Unclassified	18. SECURITY CLASSIFICATION OF THIS PAGE Unclassified	19. SECURITY CLASSIFICATION OF ABSTRACT Unclassified	20. LIMITATION OF ABSTRACT	



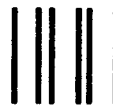
National Aeronautics and
Space Administration

Lewis Research Center
Cleveland, Ohio 44135

Official Business
Penalty for Private Use \$300

FOURTH CLASS MAIL

ADDRESS CORRECTION REQUESTED



Postage and Fees Paid
National Aeronautics and
Space Administration
NASA-451

J. Starness
NASA-Langley Research C.
Library - MS 185
Hampton, VA 23665

NASA
